The international journal of science / 9 February 2023

# nature



# HOW TO MAKE A MUMMY

Ancient Egyptian workshop reveals recipe for embalming the dead

**Mind your language**
Why the world needs to have a conversation about AI chatbots

**Drying out**
300 years of human activity cut global wetlands by one-fifth

**Dogged by reservoirs**
How HIV-infected cells evade drugs to persist in the body

VISIT…

LANZAROTE Caliente.com

# Nature.2023.02.11

[Sat, 11 Feb 2023]


- **This Week**
- **News in Focus**
- **Books & Arts**
- **Opinion**
- **Work**
- **Research**
- **Amendments & Corrections**

# This Week

- **Global pandemic treaty: what we must learn from climate-change errors** [07 Feb 2023]
  • The WHO's draft agreement proposes a COP-like process. That's unlikely to improve on the world's disastrous COVID response.
- **Indoor air pollution kills and science needs to step up** [08 Feb 2023]
  • Researchers and policymakers are only now waking up to the effects of dirty indoor air. As ever, low-income and marginalized communities are most exposed.

- EDITORIAL
- 07 February 2023

# Global pandemic treaty: what we must learn from climate-change errors

The WHO’s draft agreement proposes a COP-like process. That’s unlikely to improve on the world’s disastrous COVID response.




Researchers and policymakers need to investigate alternatives to a climate COP-like process for pandemic response and prevention.Credit: Mohammed Abed/AFP/Getty

The global response to COVID-19 represented a “catastrophic failure of the international community in showing solidarity and equity”. This frank assessment comes in the opening line of the first, or ‘zero’, draft of a new international pandemic agreement, published by the World Health Organization (WHO) last week. The agreement is intended to help the world to better prepare for future pandemics. Negotiations over the details are due to start later this month and are likely to last at least a year.

Although it doesn’t say so explicitly, the WHO’s statement can be read as a rebuke to the leaders of high-income nations, highlighting the fact that their response to the ongoing pandemic has not been a model of cooperation or compassion. A promise to properly support a vaccine-distribution scheme called COVAX went unfulfilled, undermining its potential. Rich countries over-ordered and hoarded vaccines, stopping them from reaching people in other countries who needed them. Some of the world’s best-known and well-respected pharmaceutical companies fought to stop intellectual property (IP) being shared. Had they not done so, more manufacturers could have produced vaccines and treatments, and more lives could have been saved. The treaty drafted by the WHO is intended to ensure that this behaviour is never repeated. But as *Nature* has argued before, a treaty on its own offers no guarantee that promises will be kept.

## Share and share alike

The draft text encourages the waiving of applicable IP rights for a defined period during a pandemic. In addition, at least one-fifth of relevant vaccines must be deposited with the WHO, to ensure that sufficient numbers reach the world’s poorest and most vulnerable people at the same time as they reach people in richer countries. Prices and contracts should be made public — something that didn’t happen during the COVID-19 pandemic, allowing countries to outbid each other for vaccines by offering higher prices that only pharmaceutical companies were a party to.




[What the WHO's new treaty could mean for the next pandemic]

The current wording also recognizes the importance of open science and the sharing of data such as viral genome sequences. Last month, the WHO urged China's authorities to share sequence data, as well as information on cases, hospitalizations and vaccination rates. Another point emphasized in the zero draft is that countries that share their scientific knowledge — as many low-income countries did during the pandemic — should also share in the benefits.

All of this is necessary and overdue, and has the backing of scientists and campaigning organizations. But researchers are rightly concerned about the lack of clarity on how the treaty will work in practice, and how signatories will be held to their promises. The WHO recommends that countries make decisions through a conference of the parties (COP), a democratic forum in which all countries have an equal voice in decision-making.

But COPs are expensive to run, and the creation of such a framework would mean that the WHO — which faces a constant struggle to get countries to fund it properly — would struggle even more. COPs also take their time to reach decisions, as we know all too well from those governing international action on concerns such as climate change and biodiversity loss.

Perhaps most important of all, a forum of 200-odd countries, plus tens of thousands of observers and lobbyists, is, arguably, not the best way to ensure that an agreement is adhered to, especially when the onus for action lies with a relatively small number of high-income nations. There's good evidence from the climate-change COP process that even legally binding agreements cannot compel nations to meet their commitments.



Even after COVID, the world's vaccine strategy is failing

Sensibly, the WHO wants countries to agree on some kind of monitoring system — a way to get them to report back on whether promises on funding, IP or vaccines are being kept. But negotiators and their teams would also be well advised to explore alternative ways of achieving the agreement's aims. Researchers who study the impact of international treaties could advise on other potential models.

It's clear from the WHO's zero draft text that the agency is determined to avoid a repeat of some of the worst of the behaviours seen during the pandemic. And it is reassuring to see, throughout the text, encouragement for governments and companies to be transparent and willing to share, particularly when it comes to know-how and products that are based on publicly funded research. Had this happened previously, the coronavirus pandemic might well have been behind us by now.

The world has little more than a year to convert the draft into finished text. The commitments in the current version will probably be watered down before an agreement is reached. But as researchers prepare to publish their studies, and campaigners rush to accelerate campaigning, it is easy to forget the need to determine the kinds of institution and structure that are essential to ensuring an agreement is delivered on. Institutional structures are as important as the content of treaties. The WHO and national negotiators need to ask themselves what value an agreement has if it includes everything in the WHO's zero draft, but proves unworkable in practice.

*Nature* **614**, 195-196 (2023)

*doi: https://doi.org/10.1038/d41586-023-00339-z*

---

This article was downloaded by **calibre** from https://www.nature.com/articles/d41586-023-00339-z

- EDITORIAL
- 08 February 2023

# Indoor air pollution kills and science needs to step up

Researchers and policymakers are only now waking up to the effects of dirty indoor air. As ever, low-income and marginalized communities are most exposed.



The World Health Organization’s most recent guidelines on damp and mould are from 2009.Credit: Michael A. McCoy/The Washington Post/Getty

The image of air pollution is often one of chimney stacks and smoggy cities. But this can be a misleading picture. Indoor air pollution killed more than 3

million people in 2020, almost as many as did its outdoor counterpart. And yet it has been mostly invisible to science, and to policy.

In a Comment article in *Nature* this week, three researchers describe how that needs to change. Christopher Whitty, the UK government's chief medical adviser, and colleagues Deborah Jenkins and Alastair Lewis, show what researchers and policymakers must do to improve our understanding of, and ultimately to reduce, indoor air pollution. Most people spend 80–90% of their time indoors, in homes, schools and places of work, the authors observe. But, in contrast to detailed and legally enforceable national standards for outdoor pollution that exist in many parts of the world, indoor spaces are mostly not subject to similar air-quality controls.



Hidden harms of indoor air pollution — five steps to expose them

The authors are right to draw attention to something that has been neglected for too long. Progress is hampered by our ignorance of basic facts, such as what indoor air pollution actually consists of. It includes familiar compounds such as carbon monoxide and carbon dioxide from coal burning, and nitrogen oxides from natural-gas boilers. But there is also a multiplicity of other sources, for example chemicals from synthetic compounds in paints and fabrics, mould from damp buildings and viruses and bacteria from human breath. Researchers need to be doing more to understand how all of

these circulate, how they interact with each other, their impact on human health and how they will be affected by climate change.

Although indoor air pollution is a global problem, the right strategies for combating it will vary between regions, countries and even localities. “Construction styles and materials, climate and energy sources, as well as behaviours and cultural practices, all affect indoor air”, the authors point out.

What’s clear, however, is that, just as poorer and marginalized people are disproportionately affected by bad outdoor air quality (A. Jbaily *et al*. *Nature* **601**, 228–233; 2022), indoor air pollution is a source of inequality, too. In sub-Saharan Africa, for example, 700,000 people are estimated to have died from indoor air pollution in 2019, many of them from the effects of particles from indoor biomass stoves (B. Khavari *et al*. *Nature Sustain.* https://doi.org/grqrbg; 2023). Cleaner alternatives do exist, but their large-scale use needs a panoply of research-based interventions — from engineering and design to behavioural sciences.

In richer or colder countries, people on lower incomes tend to rely on gas or solid fuels for heating, or live in homes affected by damp and mould. Targeted interventions to improve air quality by, for example, incentivizing the switch to cleaner fuels, can be a win–win situation, with the happy complementary effect of assisting decarbonization, too. (The reverse is, perhaps, less true: interventions to improve energy efficiency by better insulating indoor environments might have a negative effect on air quality, a relationship that must be carefully examined.) But, as the authors write, “it is essential that decarbonization, building improvement and gains in indoor air quality are, as much as possible, delivered equitably across society.”

Indoor air pollution clearly needs to attract urgent attention from policymakers — the most recent guidelines from the World Health Organization on damp and mould were published in 2009. That’s where Whitty and colleagues’ article, coming from researchers who advise governments, will undoubtedly help. Ultimately, science must be better prepared for when it is called on to advise about the various strategies. Indoor air pollution should become as mainstream a public-health concern as its outdoor sibling, with all the requisite funding that flows towards it. This is one good intention that shouldn’t go up in a puff of smoke.

*Nature* **614**, 196 (2023)

*doi: https://doi.org/10.1038/d41586-023-00338-0*

---

This article was downloaded by **calibre** from https://www.nature.com/articles/d41586-023-00338-0

| Section menu | Main menu |

# News in Focus

- **When will COVID stop being a global emergency?** [01 Feb 2023]
  • The World Health Organization has decided the crisis isn't over yet — but it's at a transition point.
- **The surprising chemicals used to embalm Egyptian mummies** [01 Feb 2023]
  • Resins used to prepare bodies for the afterlife are found in vessels in an ancient workshop.
- **The Milky Way in spellbinding detail and more — January's best science images** [01 Feb 2023]
  • The month's sharpest science shots, selected by Nature's photo team.
- **CRISPR voles can't detect 'love hormone' oxytocin — but still mate for life** [27 Jan 2023]
  • Prairie voles lacking oxytocin receptors bonded with mates and cared for pups.
- **Flu, MERS and Ebola — the disease outbreaks most frequently reported** [27 Jan 2023]
  • The World Health Organization's disease reports reflect public-health priorities and surveillance capabilities.
- **Weird supernova remnant blows scientists' minds** [26 Jan 2023]
  • Fireworks display from rare dying star is unlike anything astronomers have seen.
- **Stricter US guidelines for 'gain-of-function' research are on the way — maybe** [27 Jan 2023]
  • A biosecurity panel met, expecting to approve recommendations, but myriad concerns complicated the proceedings.
- **Will an AI be the first to discover alien life?** [30 Jan 2023]
  • SETI, the search for extraterrestrial intelligence, is deploying machine-learning algorithms that filter out Earthly interference and spot signals humans might miss.
- **How India is battling deadly rain storms as climate change bites** [08 Feb 2023]

• South Asian weather is becoming increasingly difficult to forecast as monsoons grow more erratic — and global warming is raising the risks posed by violent rain storms.

- **What ChatGPT and generative AI mean for science** [06 Feb 2023]
  • Researchers are excited but apprehensive about the latest advances in artificial intelligence.

---

| Next section | Main menu | Previous section |

- NEWS
- 01 February 2023

# When will COVID stop being a global emergency?

The World Health Organization has decided the crisis isn’t over yet — but it’s at a transition point.

- David Adam



COVID-19 testing sites have closed in some parts of the world.Credit: Cynthia Lee/Alamy

The World Health Organization (WHO) says that the COVID-19 outbreak will probably stop being a global emergency soon — but we're not there just yet.

After a meeting of its emergency committee on 27 January, the WHO said this week that it still considers the outbreak what it calls a public health emergency of international concern (PHEIC), but that the COVID-19 pandemic is at an inflection point — meaning that high levels of immunity to the virus SARS-CoV-2 are beginning to limit its impact and reach. The agency said that nations must remain vigilant, however, and laid the groundwork for administrative changes to keep pressure on the virus in a post-pandemic world.



How the world failed to curb COVID

Many researchers agree with the WHO's assessment. "The WHO can't say that the public-health emergency is over when you've got millions of cases and you've got thousands of deaths a day," says Salim Abdool Karim, an epidemiologist who advises the South African government on COVID-19 and directs the Durban-based Centre for the AIDS Programme of Research in South Africa. For instance, China has seen a surge in infections and deaths across the country since it lifted its zero-COVID policy at the end of last year.

But others think that the pandemic has already moved beyond the legal criteria used to define an infectious-disease outbreak as a PHEIC

(pronounced ‘fake’). The WHO’s decision came on the same day that President Joe Biden announced that the United States would end its own COVID-19 emergency declarations on 11 May.

## A weighty term

The granting and lifting of a PHEIC matters on a global and national scale because it triggers actions and redirects resources worldwide. The WHO emergency status compels the agency’s member nations to report cases of infection, for instance.

In particular, how the WHO labels the outbreak is important as a cue for the global community, Karim says. “What signal is it sending to the international air travel agency? What signal is it sending to researchers, to manufacturers and investigators developing new drugs and new vaccines?”

That’s why some researchers think it isn’t yet time to lift the PHEIC. “Declaring the public-health emergency over would give governments and some public-health agencies permission to look away and move on to other things,” says Mark Woolhouse, an epidemiologist at the University of Edinburgh, UK. “It remains a very significant public-health problem. About a quarter of the world is still unvaccinated, and that’s potentially a lot of vulnerable people.”

## An extraordinary event

The WHO first declared COVID-19 a PHEIC in January 2020. The emergency status is revisited every three months, when a committee of experts discusses the situation and then makes a recommendation.



[Why did the world’s pandemic warning system fail when COVID hit?]

The next opportunity for the WHO to lift the designation will come in April — and some say that should be the end of it. A PHEIC is defined by the WHO’s binding rules, the International Health Regulations (IHRs), as “an extraordinary event” that risks spreading an infectious disease internationally.

That definition doesn’t really apply to COVID-19 anymore, says Preben Aavitsland, director for surveillance at the Norwegian Institute of Public Health in Oslo. “The disease has already spread to every corner of the world. When the virus is already abundantly present in Nairobi, Napoli, Nashville, Nagoya, Nagpur and Nanjing, there is no extra risk introduced by travel and trade.”

“Given the strict definition of a Public Health Emergency (PHEIC), I’m not sure how the Committee concluded COVID still meets the criteria,” tweeted Devi Sridhar, a public-health researcher at the University of Edinburgh, on 30 January. “Of course it’s still a major global health problem alongside many other ones but PHEIC is a specific alarm bell.”

David Heymann, an epidemiologist at the London School of Hygiene & Tropical Medicine who chaired a WHO emergency committee on a Zika virus outbreak in 2016, says the decision on whether to remove the PHEIC status from COVID-19 will be driven by politics, as well as mortality rates and other data.

"This is a political tool, and governments pay attention," he says. "I expect that's one of the reasons why [the WHO has] continued the public-health emergency." Committee members did not respond to *Nature*'s requests for comment.

## An inflection point

The situation is made more complex by the term 'pandemic'. This is legally and operationally distinct from PHEIC, but is often used interchangeably with it to describe the state of the COVID-19 outbreak.

The WHO does not have the mandate or power to declare the start or end of a pandemic, because, unlike PHEIC, the term is not a category in the IHRs.




Monkeypox declared a global emergency: will it help contain the outbreaks?

The WHO first called the COVID-19 a pandemic in March 2020, but contrary to reports, says WHO spokesperson Tarik Jašarević, this did not mean that the agency had declared a pandemic. Instead, it merely "characterized the situation".

By saying this week that the COVID-19 crisis is at an inflection point, the WHO's emergency committee seems to be preparing to end the PHEIC in April, Aavitsland says. As part of that transition, the WHO is encouraging

countries to integrate COVID-19 surveillance and vaccination into routine programmes.

“I guess the WHO now will start making the plan for the transition and have this ready for the next meeting, in three months’ time,” he says.

*Nature* **614**, 201-202 (2023)

*doi: https://doi.org/10.1038/d41586-023-00294-9*

---

This article was downloaded by **calibre** from https://www.nature.com/articles/d41586-023-00294-9

- NEWS
- 01 February 2023
- Clarification 07 February 2023

# The surprising chemicals used to embalm Egyptian mummies

Resins used to prepare bodies for the afterlife are found in vessels in an ancient workshop.

- Ewen Callaway



A body is embalmed in an underground chamber (artist’s impression).Credit: Nikola Nevenov

Labelled pots found in a 2,500-year-old embalming workshop have revealed the plant and animal extracts used to prepare ancient Egyptian mummies —

including ingredients originating hundreds and even thousands of kilometres away.

Chemical analysis of the pots' contents has identified complex mixtures of botanical resins and other substances, some of them from plants that grow as far away as southeast Asia. The discovery was reported in a 1 February paper in *Nature*[1].

Previously, insights into the embalming process have come from two main sources: historical texts and chemical analyses of the mummies themselves. But linking these strands of information has proved difficult, says Salima Ikram, an archaeologist and mummy specialist at the American University in Cairo who was not involved in the research. "You might have the name of something, but you don't know what the hell it is, except the hieroglyphics suggesting it's an oil or a resin."

That has now changed thanks to an underground embalming workshop discovered in 2016 at Saqqara, an ancient Egyptian burial ground in use from 2900 bc or earlier. The site also includes burial chambers, and it is likely that elite members of society were interred there, the authors say. Inside the Saqqara workshop, which dates to 664–525 bc, archaeologists discovered dozens of ceramic vessels used in the embalming process, many labelled with the ingredients they contain and their use. "This is the first time you've got jars with labels of the contents," says Ikram.



Vessels from the embalming workshop display a variety of colours and shapes.Credit: Saqqara Saite Tombs Project, University of Tübingen, Tübingen, Germany; Photo: M. Abdelghaffar

To identify the specific contents of the vessels, an Egyptian–German team analysed the mixtures using a technique called gas chromatography–mass spectrometry, at a National Research Centre laboratory in Giza, Egypt. This showed that the pots contained substances previously linked to mummification, including extracts from juniper bushes, cypress trees and cedar trees, which grow in the eastern Mediterranean region. The team also found bitumen from the Dead Sea, along with animal fats and beeswax, probably of local origin.

But the researchers also identified two surprising ingredients: one resin called elemi, which comes from *Canarium* trees that grow in rainforests in Asia and Africa; and another called dammar that comes from *Shorea* trees found in tropical forests in southern India, Sri Lanka and southeast Asia.

“Egypt was resource poor in terms of many resinous substances, so many were procured or traded from distant lands,” says Carl Heron, an archaeological scientist at the British Museum in London who was not involved in the research.

## Imported ingredients

Ancient trade networks connected India and southeast Asia with the Mediterranean region. But it’s not clear whether Egyptian embalmers sought out these specific ingredients or came across them through trial and error, says Ikram. “Absolutely amazing”, she says. “Who would have thought that they were getting stuff that might be coming from India?”

Ancient Egyptian embalmers had a sophisticated understanding of the raw materials’ properties, the authors say. Pots contained complex mixtures of ingredients that, in some cases, had been carefully heated or distilled. Many of the resins had antimicrobial properties — one bowl containing elemi and animal fat was inscribed “to make his odour pleasant” — or characteristics that promoted preservation.

“Their knowledge of these substances was incredible,” says study co-author Maxime Rageot, a biomolecular archaeologist at the University of Tübingen in Germany.

Chemical studies of mummies suggest that embalming recipes became more complex over time, notes Rageot. But one open question is how ancient Egyptians developed specific embalming procedures and recipes — and why they selected certain ingredients over others, said study co-author Mahmoud Bahgat, a biochemist at Egypt’s National Research Centre in Cairo, at a press briefing. “We need to be as clever as them to discover the intentions.”

*Nature* **614**, 202-203 (2023)

*doi: https://doi.org/10.1038/d41586-022-04400-1*

Read the related News & Views: ‘Recipes and ingredients for ancient Egyptian mummification’.

### Updates & Corrections

- **Clarification 07 February 2023**: This article has been amended to note that two scientists who were quoted were not authors of the paper.

## References


1. Rageot, M. *et al. Nature* https://doi.org/10.1038/s41586-022-05663-4 (2023).

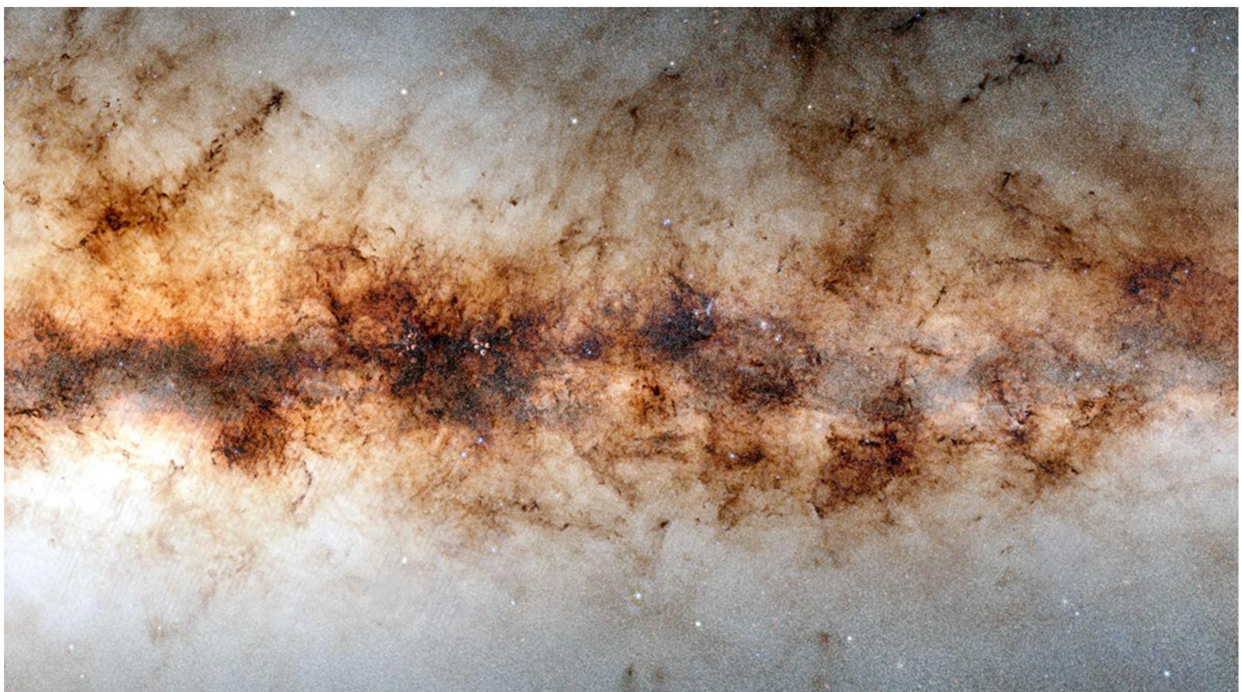

---


This article was downloaded by **calibre** from https://www.nature.com/articles/d41586-022-04400-1

# The Milky Way in spellbinding detail and more — January's best science images

The month's sharpest science shots, selected by *Nature's* photo team.

**Emma Stoye**
1 February 2023



of the northern United States and Canada over the holiday season, disrupting travel plans for millions of people and stranding many inside their homes. A blizzard left these houses in Fort Erie, Canada, coated in thick ice and knocked out power supplies for thousands of residents. The bomb cyclone, which was more than 3,000 kilometres wide, was caused by cold Arctic winds — the polar vortex — moving south.

Credit: DECaPS2/DOE/FNAL/DECam/CTIO/NOIRLab/NSF/AURA. Image processing: M. Zamani & D. de Martin (NSF's NOIRLab) (CC BY 4.0)

Credit: DECaPS2/DOE/FNAL/DECam/CTIO/NOIRLab/NSF/AURA. Image processing: M. Zamani & D. de Martin (NSF's NOIRLab) (CC BY 4.0)

Credit: U.S. Geological Survey/Handout via REUTERS

Credit: U.S. Geological Survey/Handout via REUTERS

**Lava lake.** Hawaii’s youngest and most active volcano, Kīlauea, began erupting on 5 January, creating a pool of lava in the Halemaʻumaʻu crater — seen in this shot taken by a US Geological Survey surveillance camera. The volcano has been erupting sporadically since 2018, when a months-long lava flow destroyed hundreds of homes.

Credit: Samantha Stephens/cupoty.com

Credit: Samantha Stephens/cupoty.com

**A taste for flesh.** Two unfortunate salamanders have fallen victim to a carnivorous northern pitcher plant (*Sarracenia purpurea*). The picture was the overall winner of the Close-up Photographer of the Year competition. Pitcher plants grow in nutrient-poor soils and usually feed on insects and other small invertebrates, trapping them in jug-shaped leaves. But this population of plants in Algonquin Provincial Park, Canada, regularly consumes vertebrate prey. “On the day I made this image, I was following researchers on their daily surveys of the plants,” says photographer Samantha Stephens. “When I saw a pitcher that had two salamanders, both at the same stage of decay floating at the surface of the pitcher’s fluid, I knew it was a special and fleeting moment.”

Credit: Will Palmer/SWpix.com/Shutterstock

Credit: Will Palmer/SWpix.com/Shutterstock

**Wandering walrus.** An Atlantic walrus (*Odobenus rosmarus*) nicknamed Thor drew crowds in Scarborough, UK, when it rested in the harbour on New Year’s Eve. A cordon was put in place and town authorities cancelled a fireworks display to allow the animal to sleep. It is thought to be the first sighting of a walrus in Yorkshire — the animals’ usual range is much further north, although they occasionally venture into warmer waters. Thor had been spotted even further south, in Hampshire, earlier in December, and another male called Wally hauled out on several British beaches in 2021.

Credit: Raytheon Technologies

Credit: Raytheon Technologies

**Moon crater.** This shot of the Tycho Crater is one the most detailed images of the lunar surface to be captured from Earth. It was taken by the Green Bank Telescope in West Virginia using the prototype of a next-generation planetary radar system that could be used to study and track objects in the Solar System, including near-Earth asteroids.

Credit: Patri Mora Riudavets, member of the Qubbat al-Hawā team (CC BY 4.0)

Credit: Patri Mora Riudavets, member of the Qubbat al-Hawā team (CC BY 4.0)

**Been a while, crocodile.** The remains of ten crocodile mummies that had lain undisturbed for centuries were found in an ancient Egyptian tomb underneath a Byzantine-era rubbish dump. The linen bandages that would have wrapped the bodies had been eaten away by insects, allowing the researchers to identify two species — *Crocodylus niloticus* and *Crocodylus suchus*. Egyptologists say that the mummies' presence offers insight into how ancient Egyptians might characterize the animals' role in the afterlife.

Credit: PT Hirschfield/Ocean Art 2022/Underwater Photography

Credit: PT Hirschfield/Ocean Art 2022/Underwater Photography

**Precious cargo.** A weedy seadragon (*Phyllopteryx taeniolatus*) carries bright pink eggs under its tail. These unusual-looking fish are related to seahorses, and it is the male that carries and cares for the eggs before they hatch, usually for about a month. This snap, taken off the southeast coast of Australia, won the Compact Behaviour category at the 2022 Ocean Art underwater-photography competition.

(This video has no sound and contains flashing images.) Credit: Quingyuan Wang *et al./Matter*

(This video has no sound and contains flashing images.) Credit: Quingyuan Wang *et al./Matter*

**He’ll be back.** This tiny shape-shifting metal ‘robot’ can escape from a cage by melting and re-forming on command. It is made from microscopic particles of a magnetic material mixed with gallium, a metal that is liquid at 35 °C. Applying magnetic fields at alternating currents increases the robot’s temperature enough for it to melt. Once transformed, it can be steered through the bars of its cage using more magnets, and cooled to room temperature to restore its solid form. Its creators say such materials could be used in flexible electronics, health care and robotics.

---

**SPRINGER NATURE**
Springer Nature

- Privacy Policy
- Use of cookies
- Legal notice
- Terms & Conditions
- Accessibility statement

© 2023 Springer Nature Limited. All rights reserved.
TopBuilt with **Shorthand**

---

This article was downloaded by **calibre** from https://www.nature.com/articles/d41586-023-00215-w

- NEWS
- 27 January 2023

# CRISPR voles can’t detect ‘love hormone’ oxytocin — but still mate for life

Prairie voles lacking oxytocin receptors bonded with mates and cared for pups.

- Heidi Ledford



Prairie voles (*Microtus ochrogaster*) are known for their strong commitment to family, which has been attributed to the oxytocin system.Credit: Yva Momatiuk & John Eastcott/ Minden Pictures/Alamy

The humble prairie vole (*Microtus ochrogaster*) has long been revered for its unusual commitment to family. Pair-bonded couples huddle together, raise pups together and mate exclusively together — at least most of the time. Drop another couple's pups into a cage with pair-bonded prairie voles and the adults will often foster those young as their own — highly unusual behaviour for a rodent.

But a study published on 27 January in *Neuron*[1] challenges decades of research that suggests a protein that detects the 'love hormone' oxytocin is responsible for the voles' domestic bliss. Using CRISPR gene-editing, researchers found that prairie voles lacking the protein were still responsible parents and still formed monogamous relationships.

These surprising results highlight the importance of revisiting accepted dogma when new scientific techniques emerge, says neuroscientist Bianca Jones Marlin at the Columbia University Zuckerman Institute in New York City. "Neuroscientists grew up in our field understanding that prairie voles pair bonded because of the distribution of oxytocin receptors and oxytocin," she says. "That was canon."

For decades, neuroscientists interested in understanding the biological underpinnings of human social behaviours have been fascinated by prairie voles. "There's a sort of eerie similarity between prairie vole social behaviours and human social behaviours," says Nirao Shah, a neuroscientist at Stanford University in California. "Prairie voles are one of the few mammalian species that exhibit social attachment."

## Social attachment

The hormone oxytocin has long been thought to have a pivotal role in social behaviours. A protein that binds to oxytocin, called oxytocin receptor, is expressed differently in prairie vole brains than in the brains of other voles that do not form monogamous relationships. In humans, oxytocin levels rise in response to social interactions, and the hormone is important in stimulating uterine contractions during childbirth and the production of milk afterwards.

Drugs that block oxytocin receptor abolish monogamy and other pair-bonding behaviours in prairie voles. And in mice, pups born to mothers that lack oxytocin die of starvation soon after birth because their mothers are unable to let down milk in response to the pups' suckling.

So, when Shah and his colleagues used CRISPR to mutate the gene that encodes oxytocin receptor in prairie voles, they expected the effects to be similarly devastating.

Instead, the voles still formed pair bonds and cared for their pups. Gene-edited mothers were still able to let down milk for their offspring, although their milk supply was reduced, and the pups did not grow to be as big as their counterparts whose mothers produced the receptor.

Working independently, social neuroscientist Larry Young at Emory University in Atlanta, Georgia and his colleagues have conducted the same experiment with similar but as-yet unpublished results. That came as a shock to Young, who has long studied the link between oxytocin and prairie vole behaviour. "I said, 'Oh no, what's wrong here?'" he says. "I didn't believe it."

# Crucial system

In retrospect, it makes sense that these behaviours might be resilient to the loss of just one protein, says Devanand Manoli, a behavioural neuroscientist at the University of California, San Francisco, and a co-author of the *Neuron* study. "The wiring for attachment is so important," he says. "It would be a little surprising if there were a single point of failure."

A hormone called vasopressin has also been associated with social attachment in prairie voles, but Manoli and his colleagues did not find any sign that vasopressin production kicks into overdrive when the oxytocin receptor is missing.

Even so, Manoli speculates that there could be other developmental mechanisms that partially compensate for the loss of oxytocin receptor. Such mechanisms might not be activated when a prairie vole with a working oxytocin-signalling system suddenly loses it, as in the animals treated with

drugs that block oxytocin receptor. By contrast, the gene-edited voles never had the oxytocin receptor.

It is also possible that those drugs affected more than just oxytocin receptor. Young says this is unlikely, given the drugs' specificity, but has not been ruled out. Alternatively, oxytocin could affect the brain using other receptors — something that has been proposed in some previous studies but not firmly proved, says Shah.

For years, researchers have been studying oxytocin's role in human social attachments — and whether it could contribute to a treatment for conditions in which those attachments can be affected, such as autism. Thus far, however, the results have not been conclusive. "It's fair to say that a lot more needs to be done before we can really say that this qualifies as a love hormone," says Shah. "And it seems fairly clear that oxytocin is not going to be a cure-all for conditions where social attachment has been disrupted."

Ultimately, it could be that oxytocin receptor is less an on–off switch and more of a way to fine-tune responses to social cues, says Young. But that doesn't mean it isn't important. "You don't find any species of mammal that doesn't have oxytocin receptors in the brain," he says. "They must be doing something absolutely critical."

*Nature* **614**, 204-205 (2023)

*doi: https://doi.org/10.1038/d41586-023-00197-9*

# References

1. Berendzen, K. M. *et al. Neuron* https://doi.org/10.1016/j.neuron.2022.12.011 (2023).

---

This article was downloaded by **calibre** from https://www.nature.com/articles/d41586-023-00197-9

- NEWS
- 27 January 2023

# Flu, MERS and Ebola — the disease outbreaks most frequently reported

The World Health Organization’s disease reports reflect public-health priorities and surveillance capabilities.

- Sara Reardon



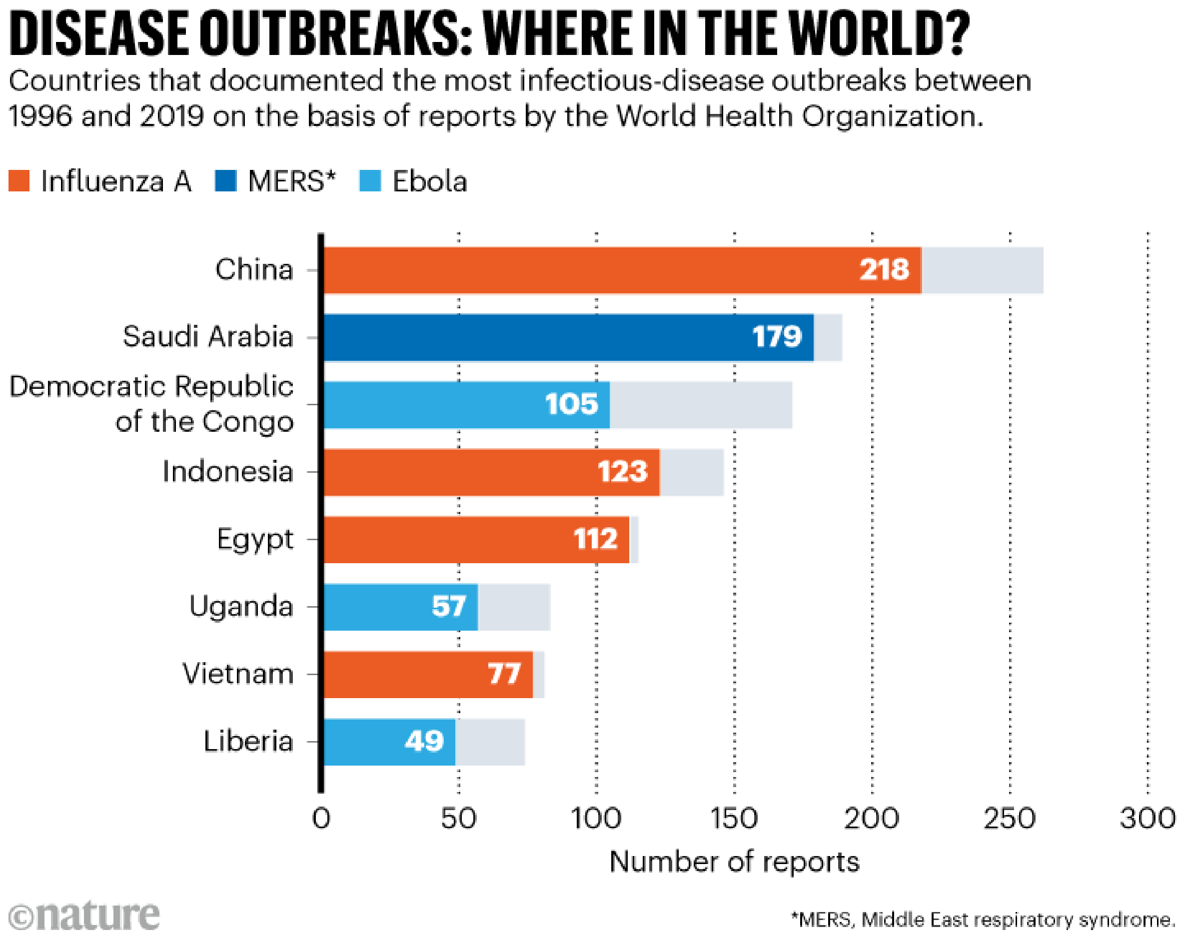
Middle East respiratory syndrome, thought to be transmitted by camels, was a commonly reported infectious disease between 1996 and 2019.Credit: Fayez Nureldine/AFP via Getty

Globally, influenza has been responsible for more outbreaks than any other infectious disease over the past 23 years, followed by Middle East respiratory syndrome (MERS) and Ebola, finds an analysis of disease reports by the World Health Organization (WHO)[1]. The study also reveals the subjective way in which disease outbreaks are often reported, suggesting that this can affect how resources are allocated.

Public-health authorities use several data sources to track infectious-disease outbreaks, but the WHO’s Disease Outbreak News (DON) is one of the most influential. Global-health researcher Rebecca Katz at Georgetown University in Washington DC and her colleagues collected all 2,789 DON reports issued between 1996 and 2019 in a searchable database. The database includes the metadata pulled from each report, such as the location of the outbreak, type of disease and timeframe over which it progressed.

The researchers found that in most years, influenza, especially the H5N1 variant, was reported at the highest frequency of any infectious disease — 776 outbreaks have been documented since 1996.

China reported the most outbreaks — 262 in total, of which 218 were of influenza — followed by Saudi Arabia, which documented MERS 179 times, and the Democratic Republic of the Congo, which reported 105 Ebola outbreaks (see ‘Disease outbreaks’). Few reports were associated with countries in Eastern Europe.




Source: Ref. 1.

Katz says that the diversity in reporting patterns results from the disparate surveillance capacities of various countries, along with the diseases that national health authorities prioritize and, ultimately, what the WHO decides to concern itself with. “There are a lot of humans involved here, and humans are making different calls,” she says. For instance, Ebola is reported much more often than other haemorrhagic fevers that periodically erupt in Africa.

Other variations can be explained by the quality of country’s health systems. For example, Egypt has reported 115 outbreaks — mostly of influenza — in the 23-year time span that Katz’s team analysed. But no outbreaks have ever been reported by nearby Libya, which has an underfunded and unstable health system as a result of two civil wars during that period. Timothy Brewer, an infectious-disease researcher at the University of California, Los

Angeles, says the analysis also shows that the WHO cannot track all outbreaks around the world, and so must pick and choose.

## Transparent reporting systems

The team's searchable database could be a useful tool in providing verified information about large outbreaks and documenting the history of infectious diseases, says Mark Smolinski, president of the non-profit organization Ending Pandemics in San Francisco, California. Having transparent, complementary outbreak-reporting systems is an important goal, he adds. "The faster we find out there's a real threat anywhere around the world and make that information available, the better off we all are."

The database will allow researchers to look at the factors that determine how much money is spent to suppress a specific outbreak, or how external circumstances such as conflicts or weather events affect them, says Katz. However, the study notes that DON reports do not mention all known outbreaks in every region.

Katz says the WHO could improve the DON reports by increasing transparency around how it prioritizes the thousands of notifications it receives, creating more-specific criteria for an outbreak's inclusion, and adding information about contextual factors such as climate hazards or outbreaks in animal populations.

A spokesperson for the WHO said it is drafting a publication detailing its decision-making process and criteria for DON reports, as well as restructuring its website to make the reports easier to search. The agency adds that it standardized the structure and format of the DON reports in 2021 — after the period that Katz's study analysed. "WHO is a learning organization, and this extends to the DON," the WHO wrote in a statement.

*Nature* **614**, 205 (2023)

*doi: https://doi.org/10.1038/d41586-023-00196-w*

## References

1. Carlson, C. J. *et al.* *PloS Glob. Public Health* **3**, e0001083 (2023).

---

This article was downloaded by **calibre** from https://www.nature.com/articles/d41586-023-00196-w

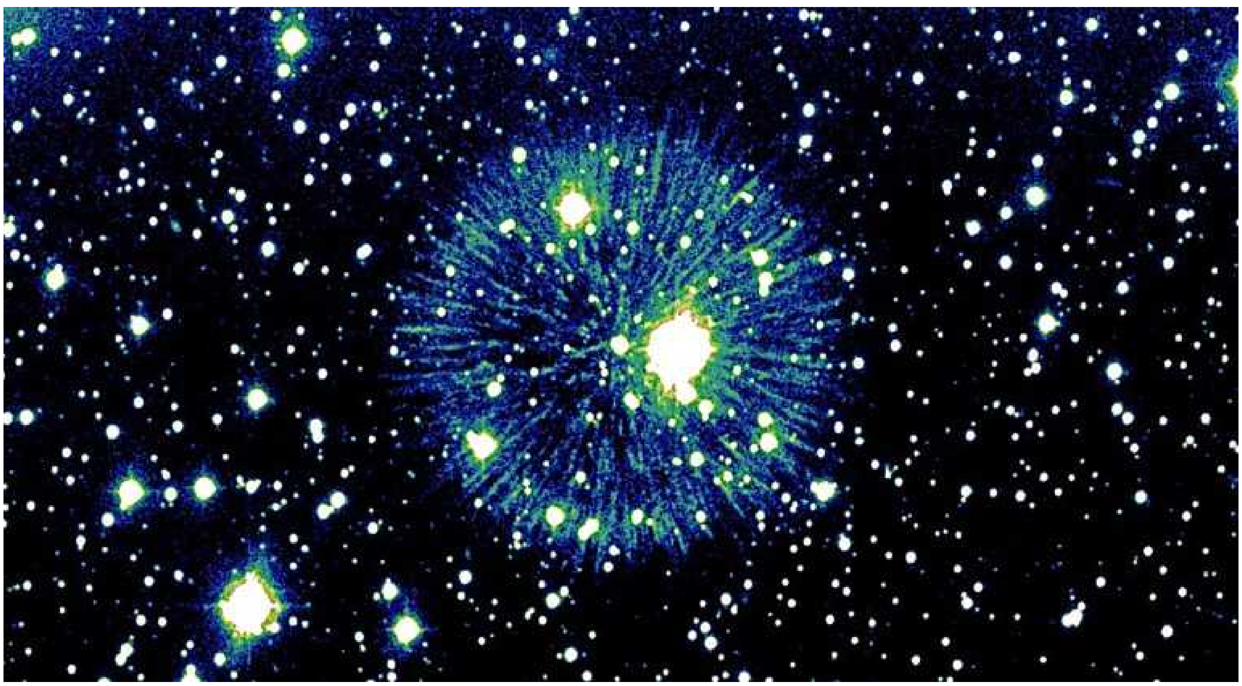
| Section menu | Main menu |

- NEWS
- 26 January 2023

# Weird supernova remnant blows scientists’ minds

Fireworks display from rare dying star is unlike anything astronomers have seen.

- Shannon Hall



Researchers imaged Pa 30’s fireworks display using an optical filter that is sensitive to sulfur. Credit: Robert Fesen (Dartmouth College)

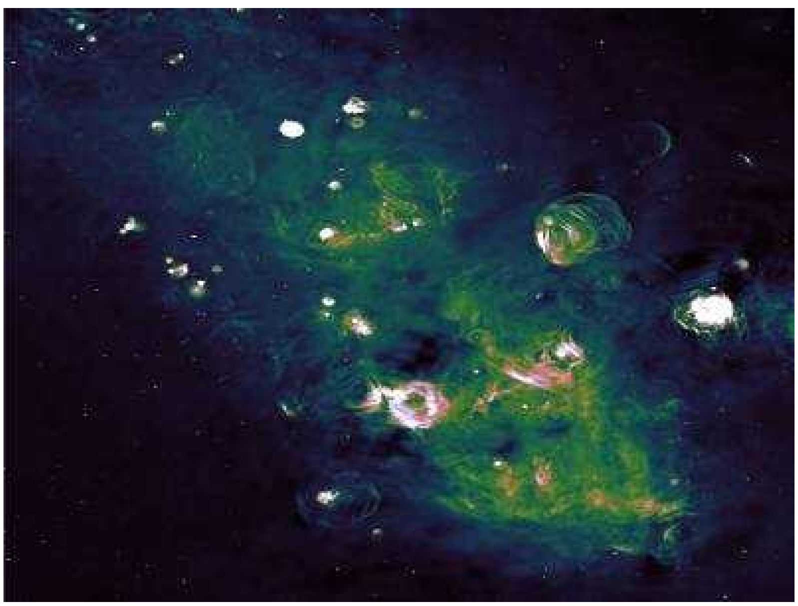
When dying stars explode as supernovae, they usually eject a chaotic web of dust and gas. But a new image of a supernova’s remains looks completely different — as though its central star sparked a cosmic fireworks display. It is the most unusual remnant that researchers have ever found, and could

point to a rare type of supernova that astronomers have long struggled to explain.

"I have worked on supernova remnants for 30 years, and I've never seen anything like this," says Robert Fesen, an astronomer at Dartmouth College in Hanover, New Hampshire, who imaged the remnant late last year. He reported his findings at a meeting of the American Astronomical Society on 12 January and posted them in a not-yet-peer-reviewed preprint on the same day[1].

## An 850-year-old firework

In 2013, amateur astronomer Dana Patchick discovered the object in archived images from NASA's Wide-field Infrared Survey Explorer. Over the next decade, several teams studied the remnant, known as Pa 30, but the results became only more and more baffling.



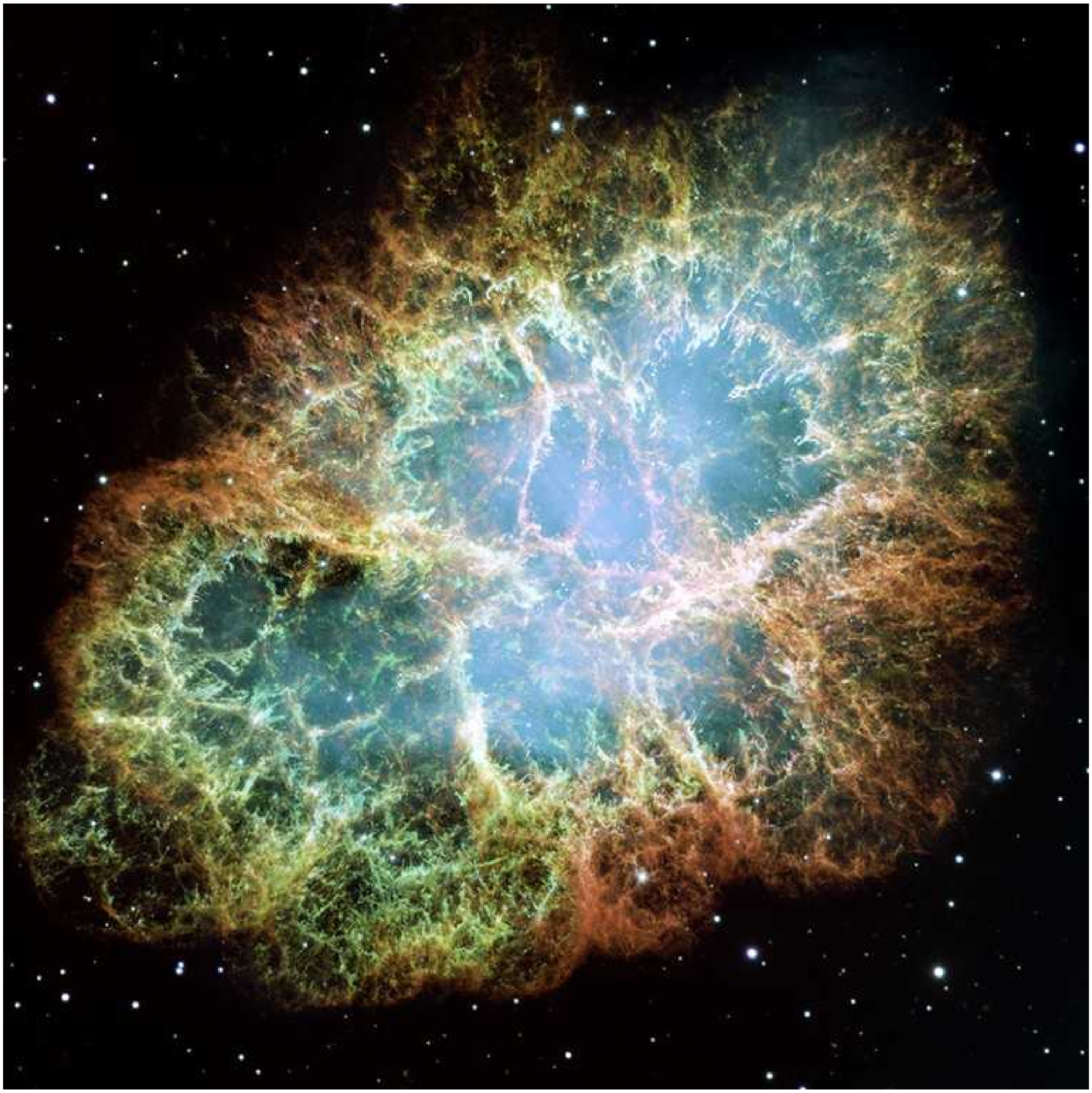
Star graveyard revealed in super-clear image of the Milky Way

Vasilii Gvaramadze, an astronomer at Lomonosov Moscow State University in Russia, and his colleagues found an extremely unusual star in 2019 at the dead centre of Pa 30[2]. That star had a surface temperature of roughly 200,000 kelvin, with a stellar wind travelling outwards at 16,000 kilometres

per second — roughly 5% of the speed of light. “Stars simply don’t have 16,000-kilometre-per-second winds,” Fesen says. Speeds of 4,000 kilometres per second aren’t unheard of, he says — but 16,000 is wild.

Pa 30 was again the subject of intrigue in 2021, when Andreas Ritter, an astronomer at the University of Hong Kong, and his colleagues proposed that the remnant is the aftermath of a supernova that lit up the sky nearly 850 years ago, in 1181[3]. Chinese and Japanese astronomers observed the object for roughly six months before it faded.

During their examination of Pa 30, Ritter and his colleagues noted that the remnant’s emission spectrum contained a particular line associated with the element sulfur. Intrigued, Fesen’s group later imaged the remnant with an optical filter that is sensitive to that line, using the 2.4-metre Hiltner Telescope at the Michigan–Dartmouth–MIT Observatory at Kitt Peak, Arizona.



The Crab Nebula is a more standard example of a supernova remnant, in which a dying star ejects a chaotic web of gas and dust.Credit: NASA, ESA, J. Hester and A. Loll (Arizona State University)

The data they collected not only helped to confirm that Pa 30 is indeed what's left of the supernova observed in 1181, but also yielded an image of the remnant unlike any other. It contains hundreds of fine filaments radiating outwards. Normally, researchers expect supernova remnants to look like the Crab Nebula — which looks less like a crab and more like a sea anemone, with a smooth region at the centre of an oval-shaped mass of tentacle-like

filaments. They also commonly look like the Tycho Supernova, which looks like a sphere of jumbled knots.

But Pa 30 comparatively makes for “just an amazing image”, says Saurabh Jha, an astronomer at Rutgers University in Piscataway, New Jersey. “I’ve never seen anything like it before. It’s really mind-blowing.”

## Cheating death

What could have caused such a remnant? In 2021, Ritter and his colleagues speculated that it was a rare supernova explosion classified as type Iax[3].

A normal type-Ia supernova occurs when a white dwarf siphons material from a companion star, eventually growing so massive that it can no longer support the extra weight and blows itself to smithereens — dispersing its innards across the galaxy. But in a type-Iax supernova, the star somehow survives. “We often call these zombie stars,” Jha says.



A supernova could light up the Milky Way at any time. Astronomers will be watching

Although theorists have developed many possible mechanisms to explain type-Iax supernovae, Ritter and his colleagues think that two white dwarfs

slammed together to produce Pa 30's fireworks. That's clear from the amount of sulfur in the remnant, which is a by-product of a white-dwarf explosion, and the lack of lighter elements that you would see from more massive stars.

Anthony Piro, an astronomer at Carnegie Observatories in Pasadena, California, thinks these findings crystallize at least one path through which a type Iax can form. But it is different from the previously favoured scenario, in which a white dwarf siphons material from a companion. That idea was developed in 2014, when astronomers successfully identified the stars involved in a Iax explosion by looking through archived images from before the event took place[4].

So, the Pa 30 finding "definitely broadens, in my mind, what could have led to a type-Iax supernova", Jha says.

These rare explosions tend to occur in distant galaxies, making them difficult to study. But Pa 30 (if it is truly type Iax) is only 2.3 kiloparsecs away — meaning that future observations will shed more light on this unusual type of supernova.

Already, Fesen has applied for observing time on both the Hubble Space Telescope and the newer James Webb Space Telescope (JWST). "The optical image that was taken, I think, gives only a hint of what it really looks like," Fesen says. "But the JWST image will be simply amazing."

*Nature* **614**, 206 (2023)

*doi: https://doi.org/10.1038/d41586-023-00202-1*

# References

1. Fesen, R. A., Schaefer, B. E. & Patchick, D. Preprint at https://arxiv.org/abs/2301.04809 (2023).

2. Gvaramadze, V. V. *et al. Nature* **569**, 684–687 (2019).

3. Ritter, A. *et al. Astrophys. J. Lett.* **918**, L33 (2021).

4. McCully, C. *et al.* *Nature* **512**, 54–56 (2014).

---

This article was downloaded by **calibre** from https://www.nature.com/articles/d41586-023-00202-1

| Section menu | Main menu |

- NEWS
- 27 January 2023
- Correction 30 January 2023
- Correction 31 January 2023

# Stricter US guidelines for ‘gain-of-function’ research are on the way — maybe

A biosecurity panel met, expecting to approve recommendations, but myriad concerns complicated the proceedings.

- Sara Reardon



Some scientists would like more rigorous oversight of risky pathogen research conducted at high-level biosecurity facilities.Credit: Patrick Semansky/AP/Shutterstock

A long-awaited report on how US health officials should regulate research involving dangerous pathogens has been approved — sort of. On 27 January, a panel of experts joined a virtual meeting of the US National Science Advisory Board for Biosecurity (NSABB) expecting to vote on a set of recommendations developed by a pair of working groups. So many concerns were lodged, however, that the meeting ended with an agreement to modify the report — although without a firm plan for how to do so.



Risky ‘gain-of-function’ studies need stricter guidance, say US researchers

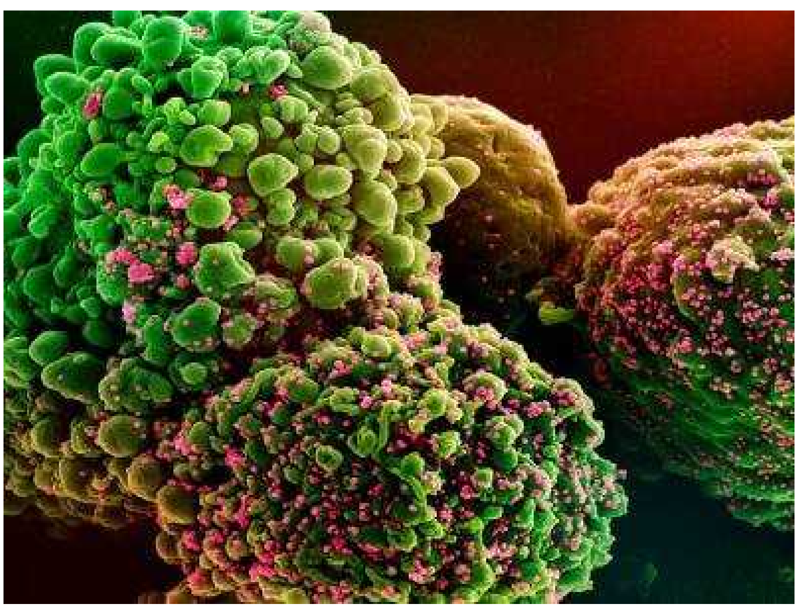
Board members — a mix of infectious-disease researchers, biosecurity experts and bioethicists — and other scientists at the meeting expressed discomfort with how the draft report’s vague language and recommendations for expanded oversight of such experiments could stifle crucial research, slowing scientists’ ability to respond to public-health emergencies. They also worried about issues such as how privately funded risky research would be regulated, the role of research institutions in identifying potentially dangerous research, and whether institutions in and outside the United States would have sufficient funding to meet US biosafety standards.

Once the report is finalized, the NSABB will send it to the US Department of Health and Human Services (HHS) for the department to consider when it crafts new policy guidelines. The HHS is "going to have to provide the 'how' level of details", said NSABB chair Gerry Parker. But when that will happen is unclear.

Given how the meeting ended, there could still be a long road ahead before the report is even finalized, a frustration for attendees. "The momentum is such that nobody wants to have another meeting to discuss it, even though some serious suggestions and criticisms were raised," says Gigi Kwik Gronvall, an immunologist at Johns Hopkins University in Baltimore, Maryland, who attended the meeting.

## Year of contention

The NSABB report is the culmination of a process that began more than a decade ago amid an uproar over a pair of publications[1,2] describing how researchers had engineered influenza viruses to become more transmissible in order to understand how they might evolve in the wild. In response, in 2014 the US National Institutes of Health (NIH) abruptly halted funding for around two dozen projects involving such 'gain-of-function' research that could enhance a pathogen's transmissibility or deadliness.



Which COVID studies pose a biohazard? Lack of clarity hampers research

The agency lifted the moratorium in December 2017, after the HHS proposed a new framework that included extended review of research involving certain pathogens that have the potential to start a pandemic. Since then, only three projects — all of which involved influenza-virus research — have undergone the official review process put in place by the HHS.

That low number concerns Marc Lipsitch, an epidemiologist at the Harvard T.H. Chan School of Public Health in Boston, Massachusetts. "The big loophole at this stage is that most things never get to the stage of being reviewed" because they aren't flagged as risky, he says. He points to proposed experiments at the NIH that would attempt to evolve a monkeypox virus to see whether certain mutations could make it more lethal to mice, and a study[3] in which researchers inserted a gene from the Omicron variant of SARS-CoV-2 into an earlier strain of the virus in an effort to understand how Omicron causes disease. Neither underwent the HHS's extended-review process.

The COVID-19 pandemic has highlighted the difficulty of designing guidelines that protect against research that is unreasonably risky without hampering crucial studies with regulatory red tape. It has also put a spotlight on risky pathogen research, with concerns raised over the safety and transparency of practices at laboratories in China that investigate bat coronaviruses.

"Before COVID, we were thinking of [pandemics as] something in the future that may happen," says Arturo Casadevall, a microbiologist at Johns Hopkins University. "The amount of damage to the world has been unbelievable."

## Myriad concerns

The new report's recommendations include increased transparency in the review process, a more defined role for research institutions in evaluating the risks and benefits of proposed experiments, and improved regulation of NIH-funded research performed in other countries.

The report also suggests that the HHS reevaluates its long-established list of 15 agents and toxins that could have ‘dual-use’ as biological weapons and therefore require special review before certain experiments can be performed. Instead, the report advises that the HHS evaluates all experiments that could be “reasonably anticipated” to make a pathogen more transmissible or dangerous.



The shifting sands of ‘gain-of-function’ research

Lipsitch says that this vague wording is useful — after all, scientists don’t always initially know where their research is going to lead. “We’re talking about low-probability, but high-consequence events,” he says. He remains concerned, however, that the wording could also allow high-risk research to proceed without extended review, depending on how the phrase is interpreted.

Conversely, Gronvall worries that “reasonably anticipated” could be interpreted so broadly that it could delay a wide swathe of experiments, such as those involved in vaccine development during an outbreak, or even those used in synthetic biology to engineer bacteria so that they produce biomaterials. “Almost all things are dual-use,” she says. “By not doing this research, we’re not making ourselves safer.”

At the NSABB meeting, board member Mark Denison, an infectious-disease researcher at Vanderbilt University Medical Center in Nashville, Tennessee, also mentioned the difficulty of determining which experiments could be risky. If identifying the function of a common protein might reveal that a mutation could make it more dangerous, for instance, would that identification constitute a risk? “We need a better definition of gain-of-function,” he said.

## Visible hesitancy

Gronvall’s concerns echo those of an 18 January report from the US Government Accountability Office (GAO), which recommended that the HHS develops a clear, public standard for what “reasonably anticipated” means. The GAO called for more transparency around the HHS’s evaluation process, and said that the US Centers for Disease Control and Prevention in Atlanta, Georgia, should evaluate whether exemptions for public-health emergencies constitute a risk.



US government lifts ban on risky pathogen research

Gronvall and others also question the NSABB report’s recommendation that the HHS evaluates the safety of research involving pathogen surveillance and vaccine development, which are currently exempt from these

regulations. “What got us out of the pandemic as quickly as it did was all the scientists who jumped in,” says Michael Imperiale, a microbiologist at the University of Michigan in Ann Arbor. “I don’t want to see any guidance ending up throwing sand in the gears of important experiments that need to be done because people don’t want to jump through hoops.”

At the meeting, after NIH acting science-policy director Lyric Jorgenson said that rejecting the report would require the group to reconvene, the panel members — some with visible hesitancy — voted to approve the report with modifications. But when or how those modifications would be made, or which of the panel’s many concerns they would address, was not clear.

In the meantime, scientists working with pathogens worry that the intent of the research is being lost in the debate. “The thing you have to remember is that if I’m not running a safe lab, the people most at risk are me and the people in my lab,” Imperiale says.

*Nature* **614**, 206-207 (2023)

*doi: https://doi.org/10.1038/d41586-023-00257-0*

### Updates & Corrections

- **Correction 30 January 2023**: An earlier version of this story stated that a study in which researchers inserted a gene from the Omicron variant of SARS-CoV-2 into an older strain of the virus was posted online without peer review. An early-access version of it has now been published in *Nature*.

- **Correction 31 January 2023**: An earlier version of this story located Gigi Kwik Gronvall in Washington DC. She is at Johns Hopkins University in Baltimore, Maryland.

# References

1. Imai, M. *et al. Nature* **486**, 420–428 (2012).

2. Herfst, S. *et al. Science* **336**, 1534–1541 (2012).

3. Chen, D.-Y. *et al.* *Nature* https://doi.org/10.1038/s41586-023-05697-2 (2023).

---

This article was downloaded by **calibre** from https://www.nature.com/articles/d41586-023-00257-0

- NEWS EXPLAINER
- 30 January 2023

# Will an AI be the first to discover alien life?

SETI, the search for extraterrestrial intelligence, is deploying machine-learning algorithms that filter out Earthly interference and spot signals humans might miss.

- Alexandra Witze



Machine learning is good at picking out unconventional signals that might have come from an E.T.Credit: Universal Pictures/Allstar/Alamy

From the hills of West Virginia to the flats of rural Australia, some of the world's largest telescopes are listening for signals from distant alien civilizations. The search for extraterrestrial intelligence, known as SETI, is an effort to find artificial-looking electromagnetic-radiation signals that might have come from a technologically advanced civilization in a far-away solar system. A study published today[1] describes one of several efforts to use machine learning, a subset of artificial intelligence (AI), to help astronomers sift quickly through the reams of data such surveys yield. As AI reshapes many scientific fields, what promise does it hold for the search for life beyond Earth?

"It is a new era for SETI research that is opening up thanks to machine-learning technology," says Franck Marchis, a planetary astronomer at the SETI Institute in Mountain View, California.

The problem of big data is relatively new for SETI. For decades, the field was constrained by having hardly any data at all. Astronomer Frank Drake pioneered SETI in 1960, when he pointed a telescope in Green Bank, West Virginia, towards two stars and listened for radio transmissions. Most of the SETI searches that followed were also limited to a small number of stars.

But in 2015, billionaire Yuri Milner funded the biggest SETI programme ever, in Berkeley, California: the Breakthrough Listen project to search one million stars for signs of intelligent life. Using telescopes in West Virginia, Australia and South Africa, the project looks for radio emissions that come from the direction of a star and that change steadily in frequency, as would happen if an alien transmitter were on a planet moving with respect to Earth.

# Data blizzard

The trouble is that these searches yield a blizzard of data — including false positives produced by Earthly interference from mobile phones, GPS and other aspects of modern life.

“The biggest challenge for us in looking for SETI signals is not at this point getting the data,” says Sofia Sheikh, an astronomer at the SETI Institute. “The difficult part is differentiating signals from human or Earth technology from the kind of signals we’d be looking for from technology somewhere else out in the Galaxy.”



The Robert C. Byrd Green Bank Telescope in West Virginia is one of several helping to look for alien civilizations.Credit: Jim West/Alamy

Going through millions of observations manually isn’t practical. A common alternative approach is to use algorithms that look for signals matching what astronomers think alien beacons could look like. But those algorithms can overlook potentially interesting signals that are slightly different from what astronomers are expecting.

Enter machine learning. Machine-learning algorithms are trained on large amounts of data and can learn to recognize features that are characteristic of Earthly interference, making them very good at filtering out the noise.

## Overlooked signals

Machine learning is also good at picking up candidate extraterrestrial signals that don't fall into conventional categories and so might have been missed by earlier methods, says Dan Werthimer, a SETI scientist at the University of California, Berkeley.

Peter Ma, a mathematician and physicist at the University of Toronto, Canada, and lead author of today's paper, agrees. "We can't always be anticipating what ET might send to us," he says.

Ma and his colleagues sifted through Breakthrough Listen observations of 820 stars, made using the 100-metre Robert C. Byrd Green Bank Telescope. They built machine-learning software to analyse the data; this netted nearly three million signals of interest but discarded most as Earth-based interference. Ma then manually reviewed more than 20,000 signals and narrowed them down to 8 intriguing candidates.

The search ultimately came up empty — all eight signals disappeared when the team listened again. But the methods could be used on other data, such as a flood of observations from the MeerKAT array of 64 radio telescopes in South Africa, which Breakthrough Listen began using in December. The machine-learning algorithms could also be used on archived SETI data, says Ma, to seek signals that might previously have been overlooked.

## Citizen SETI

Machine learning is also at the heart of a separate SETI effort that will launch next month. On 14 February, astronomers at the University of California, Los Angeles (UCLA), will launch a community-science project in which volunteers from the public will sort through images of radio signals and classify them as potential types of interference, to train a machine-learning algorithm to search SETI data from Green Bank.

And AI can help with other stages of the SETI process. Werthimer and his colleagues have used machine learning to come up with a ranking of stars to

be observed in an ongoing SETI project that uses the world’s largest single-dish telescope, the 500-metre FAST radio telescope in China.

Still, SETI will probably continue to use a mixture of classical and machine-learning approaches to sort through data, says Jean-Luc Margot, an astronomer at UCLA. Classical algorithms remain excellent at picking up candidate signals, and machine learning is “not a panacea”, he says.

“The machines can’t do it all, yet,” agrees Werthimer.

*Nature* **614**, 208 (2023)

*doi: https://doi.org/10.1038/d41586-023-00258-z*

## References

1. Ma, P. X. *et al. Nature Astron*. https://doi.org/10.1038/s41550-022-01872-z (2023).

---

This article was downloaded by **calibre** from https://www.nature.com/articles/d41586-023-00258-z

- NEWS FEATURE
- 08 February 2023

# How India is battling deadly rain storms as climate change bites

South Asian weather is becoming increasingly difficult to forecast as monsoons grow more erratic — and global warming is raising the risks posed by violent rain storms.

- Gayathri Vaidyanathan




Intense monsoonal rains caused catastrophic flooding in Kerala, India, during August 2018. Credit: Raj K Raj/Hindustan Times/Getty

## Western Ghats, Kerala

The rains did not let up all summer in 2018. By 14 August, most reservoirs had filled up and the people had grown weary of the monsoon. That day, Eby Emmanuel's phone started buzzing repeatedly with messages from neighbours warning that the Meenachil River was overflowing. He realized areas downhill could flood in hours, endangering a hamlet of 90 poor families living on the sandy riverbank.

Emmanuel, the secretary of the Meenachil River Protection Council in Kidangoor, a collective of local river conservationists, quickly organized with other community workers and the Kottayam fire department to evacuate the people. But one resident, T. Raju, refused to abandon his belongings. He lay down on his stringed bed frame, figuring he had seen plenty of bad rains. Then, his bed moved and his television floated by. This wasn't normal.

Raju jumped up, grabbed some clothes and 270 rupees (US$3.30) and fled to the evacuation site, he recalled in an interview with *Nature* last October. The water filled his home during the 2018 flood, Raju said, pointing to a water stain about 1.5 metres up his wall.

The state of Kerala, where the Meenachil River is located, received 164% more rainfall[1] than normal that August, triggering what residents call the *Pralayam* — a flood to end the Universe in the Hindu religion. It was the biggest in the state since 1924. More than 400 people died, more than one million were displaced and damages amounted to US$4.25 billion, according to an Indian government report[2].

Since 2018, "the sound of the rain beginning really disturbs my mood," says Emmanuel. "It is not like before — we were sleeping peacefully even when it's raining all season. But not any more."



Eby Emmanuel is secretary of the Meenachil River Protection Council in Kidangoor, and runs the flood early-warning system there.Credit: Gayathri Vaidyanathan

The extreme rains of 2018 spurred Emmanuel and a team of community members to create an early-warning system for floods — a project that is unusual in South Asia because it was developed and funded by local residents, say researchers who have advised on the effort. It consists of a network of improvised rain and river gauges along the 75-kilometre Meenachil River. Schoolchildren, teachers and other residents take

measurements daily, and even hourly during a storm. Using their knowledge of the local conditions and a growing data set, Emmanuel and his team issue flood alerts through community groups on the messaging service WhatsApp, and have earned widespread recognition for their efforts.

It's a system that the India Meteorological Department (IMD) simply cannot compete with — for now — because it is difficult to issue flood warnings at such local scales, say researchers. In terms of early warnings, "we will need to wait for that golden period somewhere in the far future", says Roxy Koll, a climate scientist at the Indian Institute of Tropical Meteorology in Pune, who is the scientific adviser for the community group.

There is a growing need for these kinds of warning system as the pace of climate change picks up. Throughout South Asia, natural weather disasters are occurring more frequently and with greater intensity — which some researchers link to alterations in the monsoon, changes to the natural landscape and global warming. This area is home to almost one-quarter of the global population, with 60% of people there relying on farming and living close to the land. That makes them especially vulnerable to climate change.

"South Asia is like a poster child for climate change," says Koll. "Even as a climate scientist, I cannot imagine the impacts that South Asia would see. We are not prepared for the events that we already have."

There has been a surge of bad news in the region over the past year. During March and April, a heatwave gripped India and Pakistan, killing at least 90 people and destroying wheat crops, which exacerbated a worldwide shortage of grain caused by the war in Ukraine. May saw landslides, floods and heavy downpours in northeast India. The monsoon arrived in June and there was widespread flooding, from Afghanistan to Sri Lanka. August spelled doom for Pakistan, when the nation was flooded after weeks of intense rainfall. More than 1,500 people died and damages exceeded $30 billion.



These girls were the first to create a rough river-height gauge on the Meenachil River after the 2018 floods.Credit: Gayathri Vaidyanathan

Scientists are racing to improve their forecasts and early-warning systems, especially for rainfall-related catastrophes, which cause the most loss of life in the region. It is a challenge because tropical weather is inherently more fickle than conditions in the mid-latitudes, where the wealthiest nations are located. And weather forecasting models were not originally designed for this part of the globe. What's more, heavy rainfall and storms are related to the South Asian summer monsoon, a notoriously complex weather phenomenon. The situation has become even more complicated because climate change and urban development have changed the risks and even altered the behaviour of weather.

"In the tropical region, this problem of predictability is there, everywhere," says K. S. Hosalikar, head of climate research and services at the IMD in

Pune. “And climate change is adding fury to it.”

## A changing monsoon

Every June, South Asia nervously awaits the summer monsoon, also called the southwest monsoon, which decides the fortunes of hundreds of millions of people. As the Northern Hemisphere tilts closer to the Sun during May, the land heats up and the warm air above it rises. The trade winds reverse course and flow in from the Arabian Sea, pushing moisture-laden rain clouds up the towering Western Ghats mountain range in Kerala and nearby parts of southwest India, triggering rain.

Within days, the winds find gaps in the topography of the Western Ghats and take rain across the subcontinent. By the time the monsoon ends in India, usually in September, it will have dumped an average of 850 millimetres of rain — more than three-quarters of the country’s annual total.

Scientists have noticed that the monsoon has become erratic over the past seven decades, with a propensity towards extreme rainfall and sudden droughts. Koll says this is caused, in part, by a supercharged Indian Ocean, which has warmed by 1.4 °C since 1870, more than other oceans[3]. There are frequent marine heatwaves that cause extreme rises in ocean temperatures, he says. And the trade winds seem to have weakened.

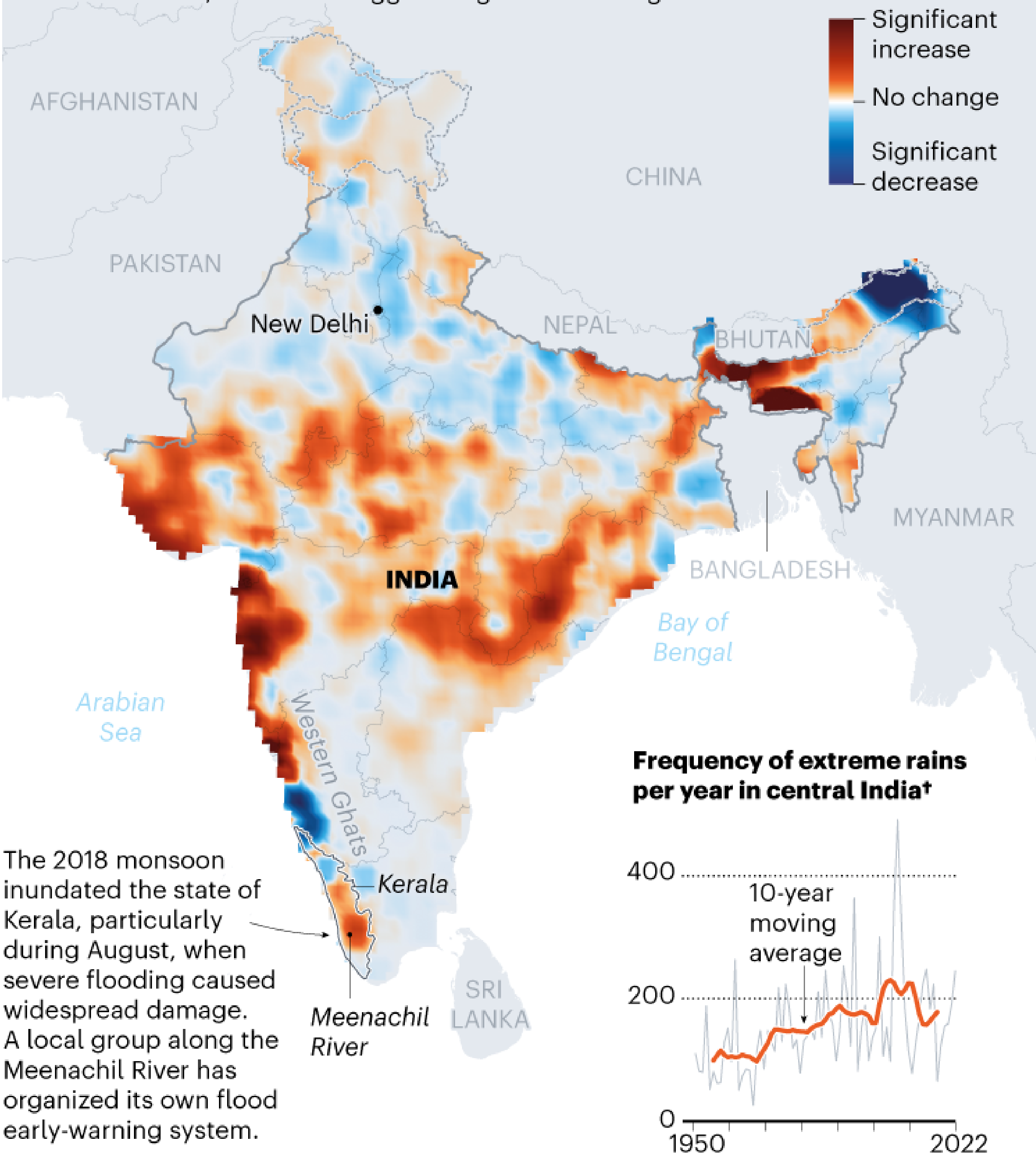
“Extreme weather events are responding to this huge change, because the oceans are a reservoir of continuous heat that supports all these weather systems,” Koll says. “To a large extent, most extreme weather events — particularly extreme rains, even droughts over land and cyclones — are tied to the Indian Ocean.”

Researchers don’t yet fully understand how changes in the ocean and the winds affect the monsoon and, by extension, local weather. But they have seen that the rains are not the same as they were 70 years ago. By 2015, the amount of rain falling over India had declined by about 6% from 1951 levels[3]. Droughts are now more frequent and widespread. There are prolonged dry spells and more intense wet spells[4]. And extreme rainfall events, which dump more than 150 millimetres in a single day, became

nearly twice as frequent between 1951 and 2022 (see ‘Severe storms’). Widespread extreme downpours have tripled in frequency since 1950 over central India, where about 500 million people live[5].

# SEVERE STORMS

The average rainfall from the monsoons over central India has decreased since 1950, but more rain is falling in extreme bursts, which can trigger dangerous flooding.




The 2018 monsoon inundated the state of Kerala, particularly during August, when severe flooding caused widespread damage. A local group along the Meenachil River has organized its own flood early-warning system.



*Extreme rain events are defined as 150 millimetres per day falling in an map grid cell measuring 0.25° latitude by 0.25° longitude.

†Number of grid cells exceeding 150 millimetres of rain in the region between 75°–85° E and 19°–26° N.

Nature publications remain neutral with regard to contested jurisdictional claims in published maps.

©nature

Source: Ref. 5; Additional data for 2015–22 from M. K. Roxy

Last year, 95% of India's extreme weather deaths resulted from thunderstorms, lightning and heavy rainfall, according to government data (see go.nature.com/3jmkrt3). The rains are no longer predictable. In the worst cases, clouds can grow rapidly and deposit more than 100 millimetres of rainfall in an hour over a single neighbourhood.

Tropical rain and thunderstorms, and their impacts, are difficult to forecast sufficiently in advance, particularly at the scale of neighbourhoods or towns. And communicating forecasts is challenging, because many of the two billion people in South Asia live in remote villages and do not receive news alerts.

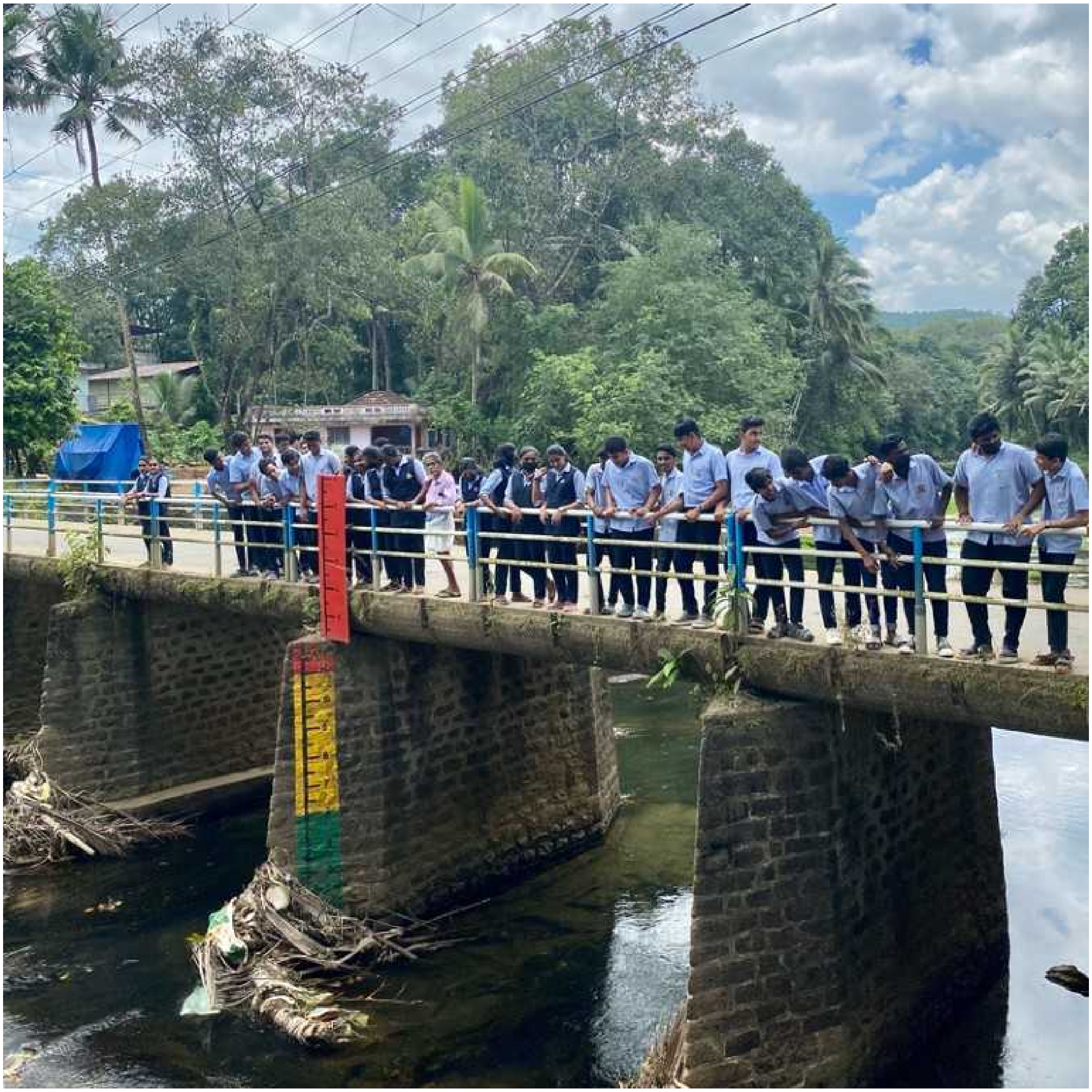
"We have a wide spectrum of users," says Soma Sen Roy, an atmospheric scientist at the IMD in New Delhi. "We have people who are advanced at handling mobiles or computers. And there are people who have never seen a computer or mobile in their life."

## Stormy weather

Kerala is a sliver of land between the Arabian Sea and the towering Western Ghats, where the monsoon first makes landfall. In August 2018, strong trade winds crashed against the Ghats and climbed over the mountains. Immense clouds, fuelled by bands of moisture from the sea, clustered and swirled against the range. Some grew as high as 15 kilometres. The weather system covered nearly the entire state and remained locked there by distant events, including a typhoon in the South China Sea.

Across the world, more than half of all annual tropical rainfall is caused by such widespread systems of clouds — spanning hundreds of square kilometres or more — that spring up when hot air carrying moisture rises and cools at high altitudes[6]. Such 'mesoscale' systems of thunderstorms can grow quickly in the tropics, and their development is difficult to spot on patchy meteorological networks. And because scientists are still learning how they grow, their behaviour and impacts are difficult to forecast in

advance. In 2019, similar mesoscale systems dropped 50 millimetres of rain within two hours in Kerala, leading to flash floods and landslides.



A flood gauge along the Meenachil River.Credit: Gayathri Vaidyanathan

Farther north, close to the Himalayas, individual thunderstorms called cloudbursts can drop more than 100 millimetres of rain in less than an hour, accompanied by strong winds and lightning, over areas of up to 30 square kilometres[7]. Very little is known about these cloudburst events. “Climate change is making [extreme rainfall] more erratic and the weather forecasting

models are unable to account for that increase in chaos," Koll says. "It is a challenge in the tropics."

The IMD can forecast some of these rainfall events with about 70% accuracy two days before they happen. But the accuracy drops to 60% for forecasts 5 days ahead, and its 10-day forecasts are even less accurate, it says.

"The monsoons are one of the hardest natural processes to be understood," says Arpita Mondal, a climate scientist at the Indian Institute of Technology Bombay. Add to that the unpredictability of mesoscale convective storms, and long-range forecasting in this region becomes even more challenging, says Vimal Mishra, a climate scientist at the Indian Institute of Technology Gandhinagar.

Forecasting storms before they develop requires a dense array of observation stations, which does not exist in the region. The IMD has the best set-up in South Asia, and it gets data from 33 doppler weather radars, 56 balloon-launching sites, 25 lightning-detection sensors and 725 automatic weather stations, as well as meteorological satellites, ships and other sources. The Indian government and agencies such as the US National Oceanic and Atmospheric Administration also operate observation buoys on the Indian Ocean.

But only some of these data are shared or used in monsoon forecasts, Koll says. "Data ideally should be available in the open domain so that we can use it for cutting-edge research." He adds that the IMD sometimes releases data when requested, but the process is slow and it doesn't provide all data. The IMD's Hosalikar responds that data are freely available for researchers, except for commercial purposes.



Climate scientist Roxy Koll studies extreme rains and advises the Meenachil River Protection Council.Credit: Gayathri Vaidyanathan

The observations feed into the Global Forecast System, developed by the US National Centers for Environmental Prediction, which the IMD has tailored to local conditions. But models created in the United States and Europe do not account for how much South Asia's unique farming practices and dense population can change the weather, says Mondal. Forecasting "becomes unimaginably complex because there is a blurred line between human and natural systems", she says.

Every year before the monsoon, millions of smallholder farmers on the Indo-Gangetic Plain turn on pump sets and flood their rice fields during the dry season. The weather forecasting models predict that evaporation of this irrigation water should cool the land surface and ease heatwaves. But Mondal and her colleagues found that existing forecast models overestimate the cooling by almost five times[8]. "There's so much happening at the local scale, which is also hard to measure and predict," she says. "That is creating

this gap of what is being predicted and what is actually happening on the ground."

Indian meteorologists run the models twice a day at a 12-kilometre resolution to generate weekly forecasts. That's too coarse to be able to forecast convective storms, which need a resolution finer than 4 kilometres, says Thara Prabhakaran, a cloud scientist at the Indian Institute of Tropical Meteorology. She studies the formation of such storms using data obtained by aircraft, fitted with lasers and other instruments, that fly through rain clouds to measure droplets and aerosols. The hope is that these data can improve forecasting models. "Nowadays, there are very heavy rains happening in a short period of time," she says. "How does it happen? What are the physics in the model that we are missing?"

Acknowledging the inherent difficulties of the problem, the IMD has focused since 2017 on issuing short-range warnings called nowcasts ahead of thunderstorms in major cities. These use cloud and wind data from radar, and a 3-kilometre-resolution model to issue forecasts that are accurate, on average, 80% of the time, according to the IMD. But Hosalikar acknowledges that even this isn't good enough. India's megacities are complex environments containing highways, crooked lanes, skyscrapers, slums and quick changes of elevation. The urban structures channel winds and create pockets of instability, meaning it can rain hard in one neighbourhood while the next one over remains dry. "We should use a 600-metre model," Hosalikar says. But that is impractical without more data and improved models.

False alarms for short-range forecasts, within 48 hours, can be as high as 40% in some regions, Mondal says. With that kind of uncertainty, a reservoir operator might decide not to open the sluice gates of a dam, leading to catastrophic flooding, according to some researchers. Deaths from extreme rainfall and storms have not declined in recent years, even with the IMD's nowcasts, says Sen Roy.

## Changing landscape

Before the 1990s, when people farmed the Meenachil River watershed, floods were welcome. During every monsoon, the river would flow predictably into paddy fields and fertilize them with silt. Children would fashion canoes out of banana-tree trunks and row them down streets. When 75-year-old retired teacher Elizabeth Koshy bought land in these rain-prone hills, she chose an elevated patch that wouldn't flood.

But people have changed how the water flows downhill. Villas have been built on paddy fields that once absorbed water, irrigation canals have become roads and the riverbed has been mined for sand. In 2018, for the first time, Koshy's home flooded.

"If rain is there for one day all over Kerala, the entire Kerala is flooded. Not because there is more water, but because the water has no way to flow easily," says S. Ramachandran, president of the Meenachil River Protection Council.

Flooding and droughts happen when the local water cycle is overwhelmed because of changes in how people use the land, and sometimes because reservoir managers make the wrong decisions as a result of imprecise forecasts, says Mondal.

The human element in extreme weather risk makes it challenging for meteorologists to issue granular 'impact-based forecasts' that warn people about events such as flooding, lightning strikes and landslides in their immediate vicinity. That's why Emmanuel and his community on the Meenachil River decided to take matters into their own hands. "We are not following the IMD," Emmanuel says, referring to government forecasts. "We are depending on our trusted volunteers' reporting."



Students use rain gauges to take daily measurements of precipitation along the Meenachil River.Credit: Gayathri Vaidyanathan

## Home-grown warning system

On a beautiful day a week after last summer's monsoon ended, Emmanuel walked into the courtyard at St Joseph's Upper Primary School in Malayinchippara, where he was greeted by the deafening sound of a marching band. This is one of 220 outposts where Emmanuel has set up rain- and river-monitoring gauges. He says the visit is meant to motivate his volunteers, but the students already take this effort seriously. Job Jose, aged 10, says a landslide demolished his neighbour's house and his family lost their well. Meera Binoy, who is 11, saw flood waters enter her house and damage some stored timber. Speaking in Malayalam, "A cloud burst open," she says, alluding to a convective storm.

The schoolchildren log daily rainfall and river-flow measurements in their rain book and send the data by WhatsApp to a group that oversees the operation. In a nearby village, 70-year-old retired bank manager P. C. Jose collates the data. He is part of a team that analyses the readings from 220 river gauges and 13 rain gauges spread across the 1,272-square-kilometre watershed. When there's no rain, measurements are taken once a day. During the rains, the team increases the frequency to once an hour or more.

Emmanuel and his team have deep knowledge of the surrounding topography and, aided by the data, are able to predict when areas downhill will flood. It's not yet entirely scientific, but it works, says Emmanuel. The group is collaborating with Koll, whose family hails from this area, to ensure scientifically rigorous data collection through an online portal so they can automate forecasts in the future.

This effort is "the best working example" of grassroots action, says Koll, which is something that the United Nations' Intergovernmental Panel on Climate Change has called on local communities to do to adapt to climate change. The early-warning system along the Meenachil River "can be tailored for climate action across similar environments across South Asia that face similar climate challenges and land–river use changes", adds Koll.

As well as producing finer-resolution flood forecasts than the IMD does, the local early-warning system reaches people through trusted networks. Koshy, the retired teacher, relies solely on the alerts from the group every monsoon, she says. "If I don't get correct information, I'll be in trouble because I cannot remain in this house if it gets flooded."

A few months after the 2018 floods, Koshy had a top floor built on her house, along with a ramp to accommodate her wheelchair. Others in her village have also built upwards in response to flooding, she says.

After visiting his volunteers all day, Emmanuel took a break in an office he shares with another community group. He pointed at a traditional lunar calendar hanging on a wall. Farmers use it to plan their planting and harvesting schedule, but these days, nature's rhythm is wonky: there is less constant rainfall, and more unpredictable fury. The early-warning system is sorely needed, he says. But keeping volunteers on track, recruiting new

members, ensuring data collection, getting buy-in from local officials and securing funding for gauges all take up a lot of his time. Emmanuel is committed to the community because his ancestors were elected leaders and social workers here; it's his family's legacy.

But he knows it might not outlast him unless he is able to build a strong team. "Something may stop when I stand still at any time. But I hope that is not going to happen."

*Nature* **614**, 210-213 (2023)

*doi: https://doi.org/10.1038/d41586-023-00341-5*

Additional reporting by Neelima Namboodiri.

## References

1. Hunt, K. M. R. & Menon, A. *Clim. Dyn.* **54**, 2433–2446 (2020).
2. United Nations Office for Disaster Risk Reduction. *Report of the Committee Constituted for Formulation of Strategy for Flood Management Works in Entire Country and River Management Activities and Works Related to Border Areas (2021–26)* (UNDRR, 2021).
3. Roxy, M. K. *et al.* In *Assessment of Climate Change Over the Indian Region* (eds Krishnan, R. *et al.*) 191–206 (Springer, 2020).
4. Roxy, M. *et al. Nature Commun.* **6**, 7423 (2015).
5. Roxy, M. K. *et al. Nature Commun.* **8**, 708 (2017).
6. Schumacher, R. S. & Rasmussen, K. L. *Nature Rev. Earth Environ.* **1**, 300–314 (2020).
7. Dimri, A. P. *et al. Earth Sci. Rev.* **168**, 1–23 (2017).
8. Jha, R., Mondal, A., Devanand, A., Roxy, M. K. & Ghosh, S. *Nature Commun.* **13**, 4275 (2022).

This article was downloaded by **calibre** from https://www.nature.com/articles/d41586-023-00341-5

- NEWS FEATURE
- 06 February 2023
- Correction 08 February 2023

# What ChatGPT and generative AI mean for science

Researchers are excited but apprehensive about the latest advances in artificial intelligence.

- Chris Stokel-Walker &
- Richard Van Noorden

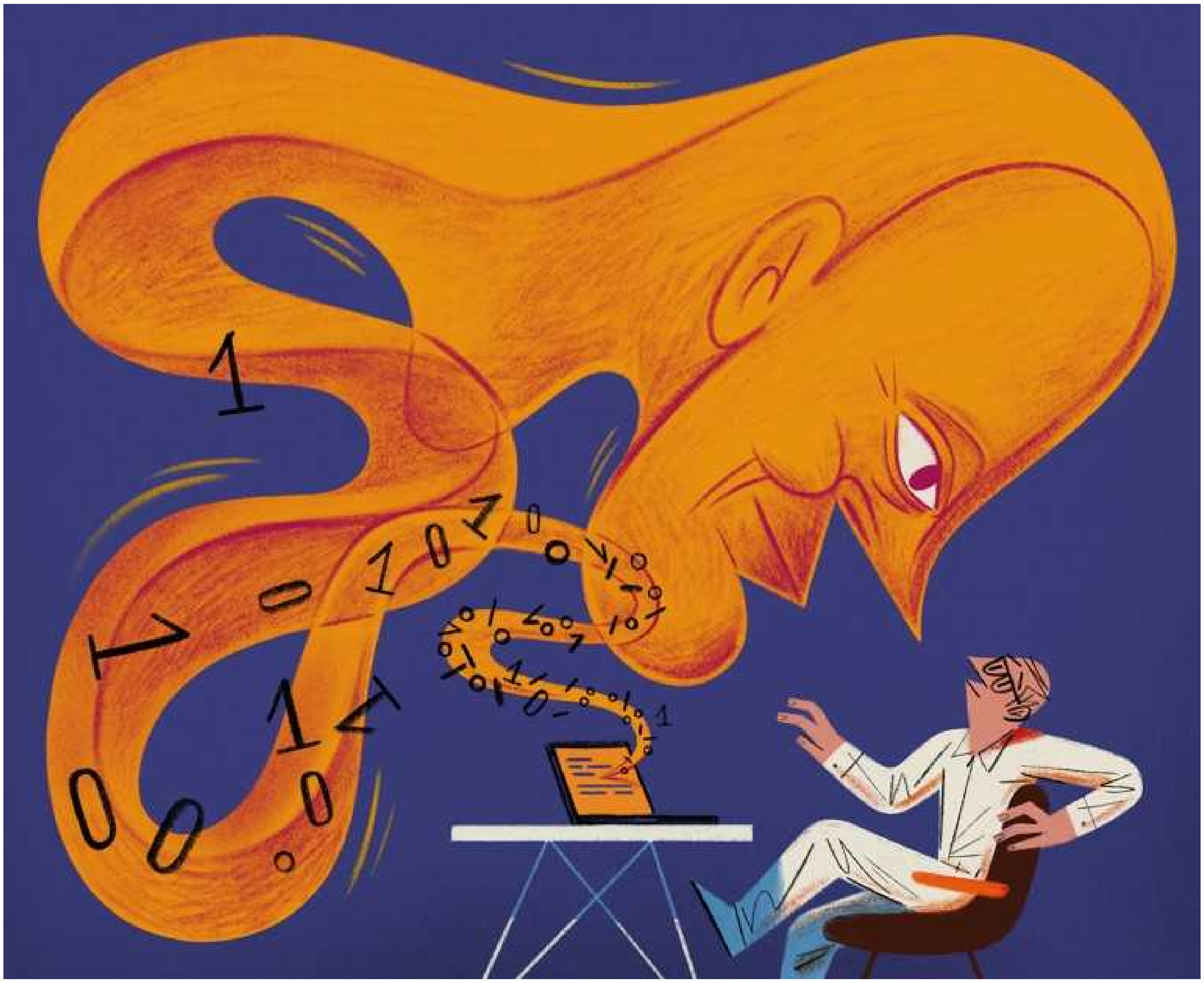


Illustration by Paweł Jońca

In December, computational biologists Casey Greene and Milton Pividori embarked on an unusual experiment: they asked an assistant who was not a scientist to help them improve three of their research papers. Their assiduous aide suggested revisions to sections of documents in seconds; each manuscript took about five minutes to review. In one biology manuscript, their helper even spotted a mistake in a reference to an equation. The trial didn't always run smoothly, but the final manuscripts were easier to read — and the fees were modest, at less than US$0.50 per document.

This assistant, as Greene and Pividori reported in a preprint[1] on 23 January, is not a person but an artificial-intelligence (AI) algorithm called GPT-3, first released in 2020. It is one of the much-hyped generative AI chatbot-style tools that can churn out convincingly fluent text, whether asked to

produce prose, poetry, computer code or — as in the scientists' case — to edit research papers (see 'How an AI chatbot edits a manuscript' at the end of this article).

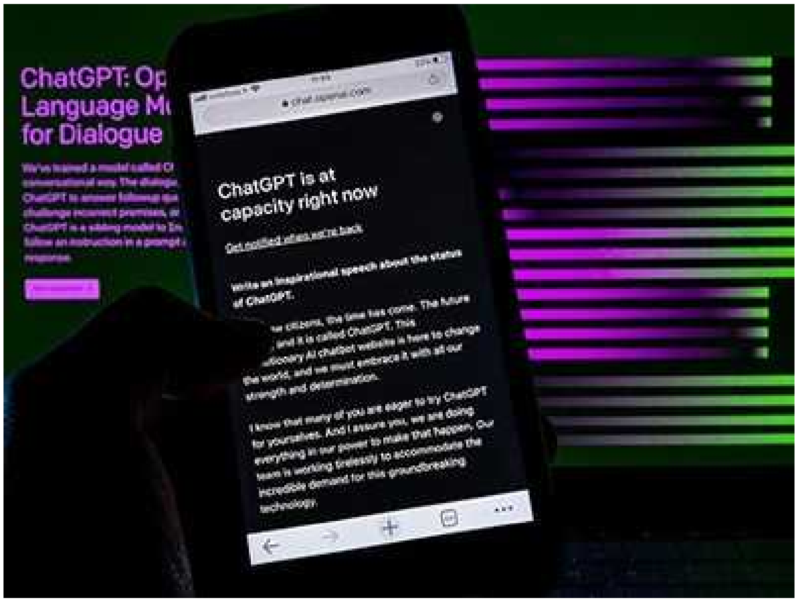
The most famous of these tools, also known as large language models, or LLMs, is ChatGPT, a version of GPT-3 that shot to fame after its release in November last year because it was made free and easily accessible. Other generative AIs can produce images, or sounds.

"I'm really impressed," says Pividori, who works at the University of Pennsylvania in Philadelphia. "This will help us be more productive as researchers." Other scientists say they now regularly use LLMs not only to edit manuscripts, but also to help them write or check code and to brainstorm ideas. "I use LLMs every day now," says Hafsteinn Einarsson, a computer scientist at the University of Iceland in Reykjavik. He started with GPT-3, but has since switched to ChatGPT, which helps him to write presentation slides, student exams and coursework problems, and to convert student theses into papers. "Many people are using it as a digital secretary or assistant," he says.

## What's your experience with ChatGPT? Take Nature's poll

*Nature* wants to hear your views on how ChatGPT and other generative artificial-intelligence tools could be used in research. Take our poll here.

LLMs form part of search engines, code-writing assistants and even a chatbot that negotiates with other companies' chatbots to get better prices on products. ChatGPT's creator, OpenAI in San Francisco, California, has announced a subscription service for $20 per month, promising faster response times and priority access to new features (although its trial version remains free). And tech giant Microsoft, which had already invested in OpenAI, announced a further investment in January, reported to be around $10 billion. LLMs are destined to be incorporated into general word- and data-processing software. Generative AI's future ubiquity in society seems assured, especially because today's tools represent the technology in its infancy.




ChatGPT: five priorities for research

But LLMs have also triggered widespread concern — from their propensity to return falsehoods, to worries about people passing off AI-generated text as their own. When *Nature* asked researchers about the potential uses of chatbots such as ChatGPT, particularly in science, their excitement was tempered with apprehension. “If you believe that this technology has the potential to be transformative, then I think you have to be nervous about it,” says Greene, at the University of Colorado School of Medicine in Aurora. Much will depend on how future regulations and guidelines might constrain AI chatbots’ use, researchers say.

## Fluent but not factual

Some researchers think LLMs are well-suited to speeding up tasks such as writing papers or grants, as long as there’s human oversight. “Scientists are not going to sit and write long introductions for grant applications any more,” says Almira Osmanovic Thunström, a neurobiologist at Sahlgrenska University Hospital in Gothenburg, Sweden, who has co-authored a manuscript[2] using GPT-3 as an experiment. “They’re just going to ask systems to do that.”

Tom Tumiel, a research engineer at InstaDeep, a London-based software consultancy firm, says he uses LLMs every day as assistants to help write code. “It’s almost like a better Stack Overflow,” he says, referring to the popular community website where coders answer each others’ queries.



ChatGPT listed as author on research papers: many scientists disapprove

But researchers emphasize that LLMs are fundamentally unreliable at answering questions, sometimes generating false responses. “We need to be wary when we use these systems to produce knowledge,” says Osmanovic Thunström.

This unreliability is baked into how LLMs are built. ChatGPT and its competitors work by learning the statistical patterns of language in enormous databases of online text — including any untruths, biases or outmoded knowledge. When LLMs are then given prompts (such as Greene and Pividori’s carefully structured requests to rewrite parts of manuscripts), they simply spit out, word by word, any way to continue the conversation that seems stylistically plausible.

The result is that LLMs easily produce errors and misleading information, particularly for technical topics that they might have had little data to train on. LLMs also can’t show the origins of their information; if asked to write an academic paper, they make up fictitious citations. “The tool cannot be

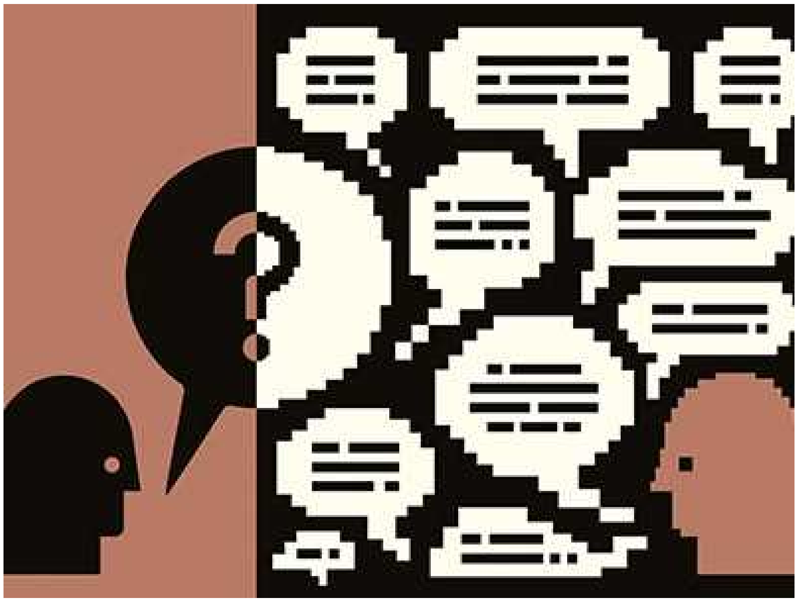
trusted to get facts right or produce reliable references," noted a January editorial on ChatGPT in the journal *Nature Machine Intelligence*[3].

With these caveats, ChatGPT and other LLMs can be effective assistants for researchers who have enough expertise to directly spot problems or to easily verify answers, such as whether an explanation or suggestion of computer code is correct.

But the tools might mislead naive users. In December, for instance, Stack Overflow temporarily banned the use of ChatGPT, because site moderators found themselves flooded with a high rate of incorrect but seemingly persuasive LLM-generated answers sent in by enthusiastic users. This could be a nightmare for search engines.

## Can shortcomings be solved?

Some search-engine tools, such as the researcher-focused Elicit, get around LLMs' attribution issues by using their capabilities first to guide queries for relevant literature, and then to briefly summarize each of the websites or documents that the engines find — so producing an output of apparently referenced content (although an LLM might still mis-summarize each individual document).



Could AI help you to write your next paper?

Companies building LLMs are also well aware of the problems. In September last year, Google subsidiary DeepMind published a paper[4] on a 'dialogue agent' called Sparrow, which the firm's chief executive and co-founder Demis Hassabis later told *TIME* magazine would be released in private beta this year; the magazine reported that Google aimed to work on features including the ability to cite sources. Other competitors, such as Anthropic, say that they have solved some of ChatGPT's issues (Anthropic, OpenAI and DeepMind declined interviews for this article).

For now, ChatGPT is not trained on sufficiently specialized content to be helpful in technical topics, some scientists say. Kareem Carr, a biostatistics PhD student at Harvard University in Cambridge, Massachusetts, was underwhelmed when he trialled it for work. "I think it would be hard for ChatGPT to attain the level of specificity I would need," he says. (Even so, Carr says that when he asked ChatGPT for 20 ways to solve a research query, it spat back gibberish and one useful idea — a statistical term he hadn't heard of that pointed him to a new area of academic literature.)

Some tech firms are training chatbots on specialized scientific literature — although they have run into their own issues. In November last year, Meta — the tech giant that owns Facebook — released an LLM called Galactica, which was trained on scientific abstracts, with the intention of making it particularly good at producing academic content and answering research questions. The demo was pulled from public access (although its code remains available) after users got it to produce inaccuracies and racism. "It's no longer possible to have some fun by casually misusing it. Happy?," Meta's chief AI scientist, Yann LeCun, tweeted in a response to critics. (Meta did not respond to a request, made through their press office, to speak to LeCun.)

## Safety and responsibility

Galactica had hit a familiar safety concern that ethicists have been pointing out for years: without output controls LLMs can easily be used to generate

hate speech and spam, as well as racist, sexist and other harmful associations that might be implicit in their training data.

Besides directly producing toxic content, there are concerns that AI chatbots will embed historical biases or ideas about the world from their training data, such as the superiority of particular cultures, says Shobita Parthasarathy, director of a science, technology and public-policy programme at the University of Michigan in Ann Arbor. Because the firms that are creating big LLMs are mostly in, and from, these cultures, they might make little attempt to overcome such biases, which are systemic and hard to rectify, she adds.

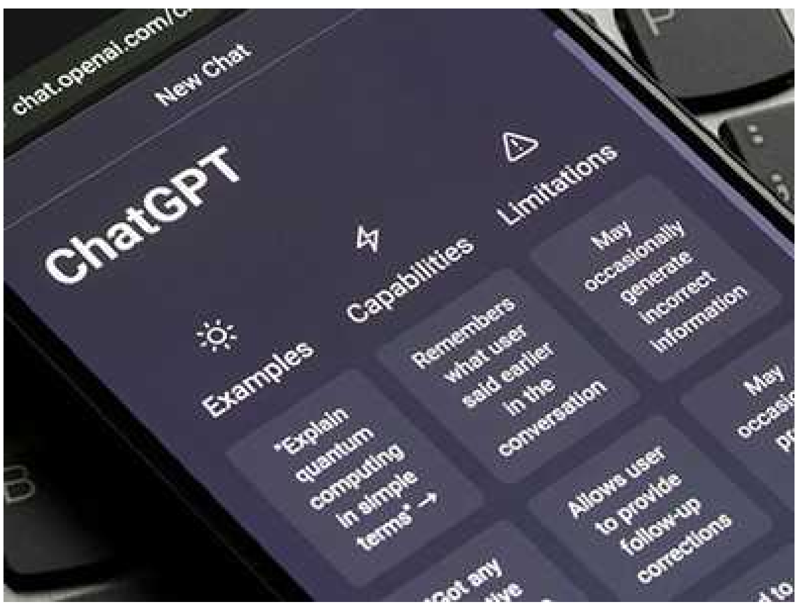


How language-generation AIs could transform science

OpenAI tried to skirt many of these issues when deciding to openly release ChatGPT. It restricted its knowledge base to 2021, prevented it from browsing the Internet and installed filters to try to get the tool to refuse to produce content for sensitive or toxic prompts. Achieving that, however, required human moderators to label screeds of toxic text. Journalists have reported that these workers are poorly paid and some have suffered trauma. Similar concerns over worker exploitation have also been raised about social-media firms that have employed people to train automated bots for flagging toxic content.

OpenAI’s guardrails have not been wholly successful. In December last year, computational neuroscientist Steven Piantadosi at the University of California, Berkeley, tweeted that he’d asked ChatGPT to develop a Python program for whether a person should be tortured on the basis of their country of origin. The chatbot replied with code inviting the user to enter a country; and to print “This person should be tortured” if that country was North Korea, Syria, Iran or Sudan. (OpenAI subsequently closed off that kind of question.)

Last year, a group of academics released an alternative LLM, called BLOOM. The researchers tried to reduce harmful outputs by training it on a smaller selection of higher-quality, multilingual text sources. The team involved also made its training data fully open (unlike OpenAI). Researchers have urged big tech firms to responsibly follow this example — but it’s unclear whether they’ll comply.




Tools such as ChatGPT threaten transparent science; here are our ground rules for their use

Some researchers say that academics should refuse to support large commercial LLMs altogether. Besides issues such as bias, safety concerns and exploited workers, these computationally intensive algorithms also require a huge amount of energy to train, raising concerns about their ecological footprint. A further worry is that by offloading thinking to

automated chatbots, researchers might lose the ability to articulate their own thoughts. "Why would we, as academics, be eager to use and advertise this kind of product?" wrote Iris van Rooij, a computational cognitive scientist at Radboud University in Nijmegen, the Netherlands, in a blogpost urging academics to resist their pull.

A further confusion is the legal status of some LLMs, which were trained on content scraped from the Internet with sometimes less-than-clear permissions. Copyright and licensing laws currently cover direct copies of pixels, text and software, but not imitations in their style. When those imitations — generated through AI — are trained by ingesting the originals, this introduces a wrinkle. The creators of some AI art programs, including Stable Diffusion and Midjourney, are currently being sued by artists and photography agencies; OpenAI and Microsoft (along with its subsidiary tech site GitHub) are also being sued for software piracy over the creation of their AI coding assistant Copilot. The outcry might force a change in laws, says Lilian Edwards, a specialist in Internet law at Newcastle University, UK.

# Enforcing honest use

Setting boundaries for these tools, then, could be crucial, some researchers say. Edwards suggests that existing laws on discrimination and bias (as well as planned regulation of dangerous uses of AI) will help to keep the use of LLMs honest, transparent and fair. "There's loads of law out there," she says, "and it's just a matter of applying it or tweaking it very slightly."

At the same time, there is a push for LLM use to be transparently disclosed. Scholarly publishers (including the publisher of *Nature*) have said that scientists should disclose the use of LLMs in research papers (see also *Nature* **613**, 612; 2023); and teachers have said they expect similar behaviour from their students. The journal *Science* has gone further, saying that no text generated by ChatGPT or any other AI tool can be used in a paper[5].

One key technical question is whether AI-generated content can be spotted easily. Many researchers are working on this, with the central idea to use LLMs themselves to spot the output of AI-created text.



‘Arms race with automation’: professors fret about AI-generated coursework

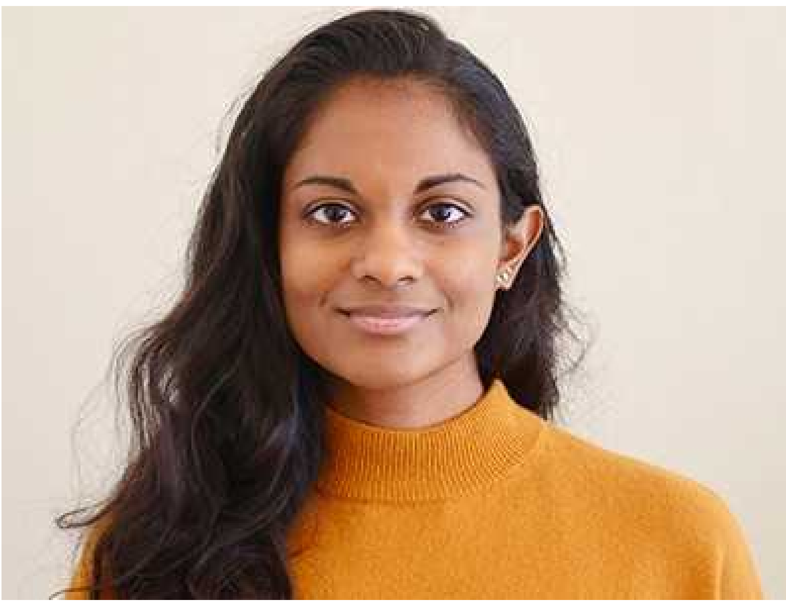
Last December, for instance, Edward Tian, a computer-science undergraduate at Princeton University in New Jersey, published GPTZero. This AI-detection tool analyses text in two ways. One is ‘perplexity’, a measure of how familiar the text seems to an LLM. Tian’s tool uses an earlier model, called GPT-2; if it finds most of the words and sentences predictable, then text is likely to have been AI-generated. The tool also examines variation in text, a measure known as ‘burstiness’: AI-generated text tends to be more consistent in tone, cadence and perplexity than does that written by humans.

Many other products similarly aim to detect AI-written content. OpenAI itself had already released a detector for GPT-2, and it released another detection tool in January. For scientists’ purposes, a tool that is being developed by the firm Turnitin, a developer of anti-plagiarism software, might be particularly important, because Turnitin’s products are already used by schools, universities and scholarly publishers worldwide. The company says it’s been working on AI-detection software since GPT-3 was released in 2020, and expects to launch it in the first half of this year.

However, none of these tools claims to be infallible, particularly if AI-generated text is subsequently edited. Also, the detectors could falsely suggest that some human-written text is AI-produced, says Scott Aaronson, a computer scientist at the University of Texas at Austin and guest researcher with OpenAI. The firm said that in tests, its latest tool incorrectly labelled human-written text as AI-written 9% of the time, and only correctly

identified 26% of AI-written texts. Further evidence might be needed before, for instance, accusing a student of hiding their use of an AI solely on the basis of a detector test, Aaronson says.

A separate idea is that AI content would come with its own watermark. Last November, Aaronson announced that he and OpenAI were working on a method of watermarking ChatGPT output. It has not yet been released, but a 24 January preprint[6] from a team led by computer scientist Tom Goldstein at the University of Maryland in College Park, suggested one way of making a watermark. The idea is to use random-number generators at particular moments when the LLM is generating its output, to create lists of plausible alternative words that the LLM is instructed to choose from. This leaves a trace of chosen words in the final text that can be identified statistically but are not obvious to a reader. Editing could defeat this trace, but Goldstein suggests that edits would have to change more than half the words.



Don’t ask if artificial intelligence is good or fair, ask how it shifts power

An advantage of watermarking is that it rarely produces false positives, Aaronson points out. If the watermark is there, the text was probably produced with AI. Still, it won’t be infallible, he says. “There are certainly ways to defeat just about any watermarking scheme if you are determined enough.” Detection tools and watermarking only make it harder to deceitfully use AI — not impossible.

Meanwhile, LLM creators are busy working on more sophisticated chatbots built on larger data sets (OpenAI is expected to release GPT-4 this year) — including tools aimed specifically at academic or medical work. In late December, Google and DeepMind published a preprint about a clinically-focused LLM it called Med-PaLM[7]. The tool could answer some open-ended medical queries almost as well as the average human physician could, although it still had shortcomings and unreliabilities.

Eric Topol, director of the Scripps Research Translational Institute in San Diego, California, says he hopes that, in the future, AIs that include LLMs might even aid diagnoses of cancer, and the understanding of the disease, by cross-checking text from academic literature against images of body scans. But this would all need judicious oversight from specialists, he emphasizes.

The computer science behind generative AI is moving so fast that innovations emerge every month. How researchers choose to use them will dictate their, and our, future. “To think that in early 2023, we’ve seen the end of this, is crazy,” says Topol. “It’s really just beginning.”

# HOW AN AI CHATBOT EDITS A MANUSCRIPT

Computational biologists Casey Greene and Milton Pividori constructed a program to get GPT-3 to edit research papers. The AI receives sections of a manuscript in turn, each with their own editing instructions (or 'prompts'). The prompts are adapted — in automated fashion — to suit the needs of each section, such as the methods or conclusion. In this example from their work, GPT-3 was fed an introduction section and the prompt below.

**Prompt:**

```
"Revise the following paragraph from the introduction of an
academic paper (with the title 'An efficient not-only-linear
correlation coefficient based on machine learning' and keywords
'correlation coefficient, nonlinear relationships, gene
expression') so most of the citations to other academic papers
are kept, the text minimizes the use of jargon, the text grammar
is correct, spelling errors are fixed, and the text is in active
voice and has a clear sentence structure."
```

**Paragraph:**

New technologies have vastly improved data collection, generating a deluge of information across different disciplines. This large amount of data provides new opportunities to address unanswered scientific questions, provided we have efficient tools capable of identifying multiple types of underlying patterns. Correlation analysis is an essential statistical technique for discovering relationships between variables [1]. Correlation coefficients are often used in exploratory data mining techniques, such as clustering or community detection algorithms, to compute a similarity value between a pair of objects of interest such as genes [2] or disease-relevant lifestyle factors [3]. Correlation methods are also used in supervised tasks, for example, for feature selection to improve prediction accuracy [4,5]. The Pearson correlation coefficient is ubiquitously deployed across application domains and diverse scientific areas. Thus, even minor and significant improvements in these techniques could have enormous consequences in industry and research.

**GPT-3 edits:**

~~New technologies have vastly improved data collection, generating a deluge of information across different disciplines.~~ The increasing availability of data has opened up new possibilities for scientific exploration. ~~This large amount of data provides new opportunities to address unanswered scientific questions, provided we have efficient tools capable of identifying multiple types of underlying patterns.~~ Correlation analysis is ~~an essential~~ a useful statistical technique ~~for discovering~~ to uncover such relationships ~~between variables~~ [1]. Correlation coefficients are often used in ~~exploratory~~ data mining techniques, such as clustering or community detection ~~algorithms~~, to ~~compute a~~ calculate the similarity ~~value~~ between ~~a pair of~~ two objects ~~of interest such as~~ , like genes [2] or ~~disease-relevant~~ lifestyle factors related to diseases [3]. ~~Correlation methods~~ They are also used in supervised tasks, ~~for example, for~~ like feature selection, to ~~improve~~ boost prediction accuracy [4,5]. The Pearson correlation coefficient is ~~ubiquitously deployed~~ widely used across many application domains and ~~diverse~~ scientific ~~areas~~ disciplines. ~~Thus~~ Therefore , even ~~minor and significant~~ small improvements in ~~these techniques could~~ this technique can have ~~enormous consequences in~~ a huge impact on industry and research.

**Final paragraph:**

The increasing availability of data has opened up new possibilities for scientific exploration. To take advantage of this, we need efficient tools to identify multiple types of relationships between variables. Correlation analysis is a useful statistical technique to uncover such relationships [1]. Correlation coefficients are often used in data mining techniques, such as clustering or community detection, to calculate the similarity between two objects, like genes [2] or lifestyle factors related to diseases [3]. They are also used in supervised tasks, like feature selection, to boost prediction accuracy [4,5]. The Pearson correlation coefficient is widely used across many application domains and scientific disciplines. Therefore, even small improvements in this technique can have a huge impact on industry and research.

©nature

Source: Adapted from ref 1.

*Nature* **614**, 214-216 (2023)

*doi: https://doi.org/10.1038/d41586-023-00340-6*

### Updates & Corrections

- **Correction 08 February 2023**: This News feature misrepresented Scott Aaronson's views on the accuracy of watermarking in identifying AI-produced text. Human-produced text might also be flagged as having a watermark, but the probability is extremely low.

## References

1. Pividori, M. & Greene, C. S. Preprint at bioRxiv https://doi.org/10.1101/2023.01.21.525030 (2023).

2. GPT, Osmanovic Thunström, A. & Steingrimsson, S. Preprint at HAL https://hal.science/hal-03701250 (2022).

3. *Nature Mach. Intell.* **5**, 1 (2023).

4. Glaese, A. *et al.* Preprint at https://arxiv.org/abs/2209.14375 (2022).

5. Thorp, H. H. *Science* **379**, 313 (2023).

6. Kirchenbauer, J. *et al.* Preprint at https://arxiv.org/abs/2301.10226 (2023).

7. Singhal, K. *et al.* Preprint at https://arxiv.org/abs/2212.13138 (2022).

---

This article was downloaded by **calibre** from https://www.nature.com/articles/d41586-023-00340-6

# Books & Arts

- **How genetics unmasked the Golden State Killer — and the uncomfortable ethical aftermath** [06 Feb 2023]
  • Barbara Rae-Venter’s account of her genetic sleuthing illustrates the power of technologies to bring criminals to justice. But should there be limits to their use?
- **The magic of physics, and why we have childhood: Books in brief** [06 Jan 2023]
  • Andrew Robinson reviews five of the best science picks.

- BOOK REVIEW
- 06 February 2023

# How genetics unmasked the Golden State Killer — and the uncomfortable ethical aftermath

Barbara Rae-Venter’s account of her genetic sleuthing illustrates the power of technologies to bring criminals to justice. But should there be limits to their use?

- Brendan Maher



Barbara Rae-Venter helped to identify the Golden State Killer and crack other unsolved cases.

**I Know Who You Are: How an Amateur DNA Sleuth Unmasked the Golden State Killer and Changed Crime Fighting Forever** *Barbara Rae-Venter* Ballantine (2023)

In April 2018, California authorities arrested one of the most vicious serial killers in US history. A man known variously as the East Area Rapist, the Original Night Stalker and, eventually, the Golden State Killer committed at least 13 murders, more than 50 rapes and 100 burglaries from the mid-1970s to about 1986. For around 40 years, local and federal investigators sought to identify him. Not once had the actual perpetrator, former police officer Joseph DeAngelo, come under suspicion. In the end, it took about four months of work by a retired patent attorney, Barbara Rae-Venter, to identify the culprit using investigative genetic genealogy (IGG).




[The ethics of catching criminals using their family's DNA]

IGG involves pinpointing individuals by constructing detailed family trees using public records and genetic information that people have uploaded to consumer DNA databases, usually to research their own ancestry and family history. The Golden State Killer wasn't the first cold case to be solved using the technique. It wasn't even Rae-Venter's first. Her start in criminal justice

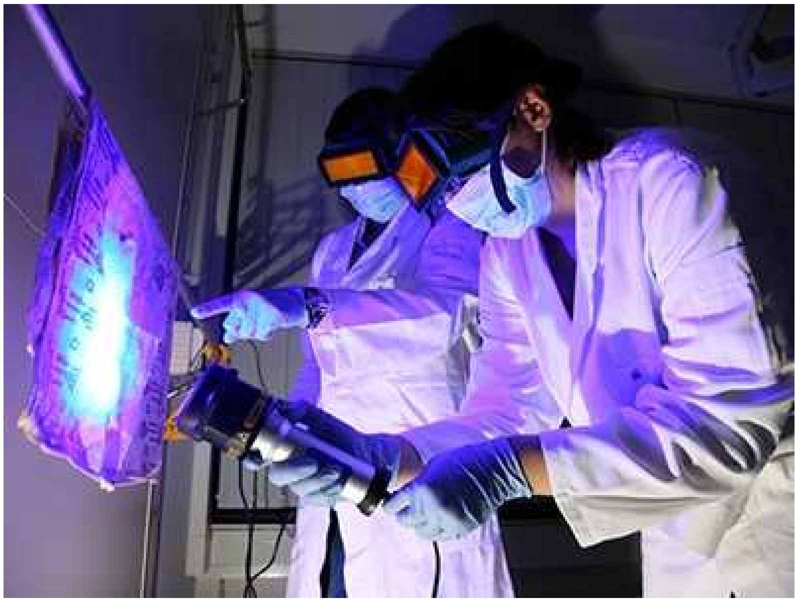
came in part through the case of Lisa Jensen, who had been abducted as a child and knew nothing about her past — not even her real name. Rae-Venter and other volunteers from a group that helps people who were adopted find their birth parents turned their skills to identifying Jensen. It took about a year to reveal her true identity, and that information set investigators on a path towards linking Jensen's abductor, Terry Rasmussen, to a grisly trail of murders.

Word of Rae-Venter's success spread and caught the attention of Paul Holes, a California detective with dreams of closing the Golden State Killer case before he retired. Unlike Jensen's, this investigation required sleuths to create a fake profile using crime-scene DNA from an unwitting database participant — the putative killer — without their consent. Most DNA-database companies, including 23andMe and Ancestry, prohibit that. But one, GEDmatch, did not expressly forbid law-enforcement searches in its terms of service. Another, FamilyTreeDNA, agreed to create and upload the Golden State Killer's profile in secret.

## Genealogy in the spotlight

In *I Know Who You Are*, Rae-Venter tells of her involvement in identifying Jensen, Rasmussen, DeAngelo and others. Written with bestselling author Alex Tresniowski, it is a gripping story tracing the hundreds of hours spent rifling through people's family ties to find killers and identify bodies. But the book disappoints when examining the ethical quandaries that Rae-Venter's actions have sparked.

DeAngelo's arrest put IGG under a white-hot spotlight. Although genealogists knew that this technique could be used to solve crimes, Rae-Venter was one of the first to break the glass and actually do it. IGG was hailed by some as the biggest scientific advance in crime-fighting since the introduction of DNA evidence. *Nature* named Rae-Venter one of ten people who mattered in science that year.



[The controversial company using DNA to sketch the faces of criminals]

But as law-enforcement officials started pushing the boundaries of the tool's use, there was a backlash. In May 2019, it was revealed that, for another case, investigators had uploaded a DNA sample from a non-sexual assault to GEDmatch. The move violated the site's updated terms of service, which allowed submissions by law-enforcement agencies only in cases of homicide and sexual assault. That signalled to critics that their fears of a slippery slope were well founded. Confronting user anger, GEDmatch made a U-turn, allowing law-enforcement officers to search the data only of people who had explicitly given their consent. Further consternation was caused in August that year when an investigation by *The Wall Street Journal* revealed FamilyTreeDNA's secret agreement with investigators.

Matters of privacy and transparency began to divide the genetic-genealogy field. Law-enforcement officials were scouring personal family details in ways that website users didn't expect and didn't necessarily sign up for. As one genealogist put it in a news article for *The Atlantic*, genetic genealogy "was built for reuniting families, and now it is being used essentially to get families to put their members in jail".

Rae-Venter scoffs at these concerns, arguing that the horrendous nature of the crimes under investigation is justification enough: "It simply did not strike me as a complicated ethical issue." She quotes critics of IGG, but she

doesn’t deeply explore their arguments about where the line should be drawn in applying the technique. She makes passing reference, for example, to the concerns about using IGG to identify the remains of abandoned infants, ostensibly to find and prosecute the mothers. But she doesn’t fully consider what such prosecutions mean for justice and public safety: research has shown that neonaticide is rarely the act of a violent criminal and more often involves factors such as social isolation and inadequate access to health care.




Supercharged crime-scene DNA analysis sparks privacy concerns

Rae-Venter observes that most cold cases to which IGG is applied involve white people who had been killed or raped, reflecting a preferential bias in law enforcement. But she also notes that the over-representation of white people in consumer DNA databases means that IGG will be most successful at identifying white suspects. She strangely refers to this as a reverse bias, presumably alluding to the systemic racism in US law enforcement that otherwise sees disproportionately high rates of incarceration among Black people. That she takes time to discuss how to address this limitation, but not others, in IGG is troubling.

Her nonchalance on such sensitive matters in dealing with the ethics of IGG mars an otherwise compelling book. IGG is a powerful tool. It has brought closure to more than 1,000 cold cases, by Rae-Venter’s estimates. And as the field grows and consolidates from the domain of hobbyists and volunteers to

that of a few well-funded companies, it’s worth not only recounting the details of its ascension — but also analysing more fully its shortcomings and potential for abuse.

*Nature* **614**, 217-218 (2023)

*doi: https://doi.org/10.1038/d41586-023-00342-4*

---

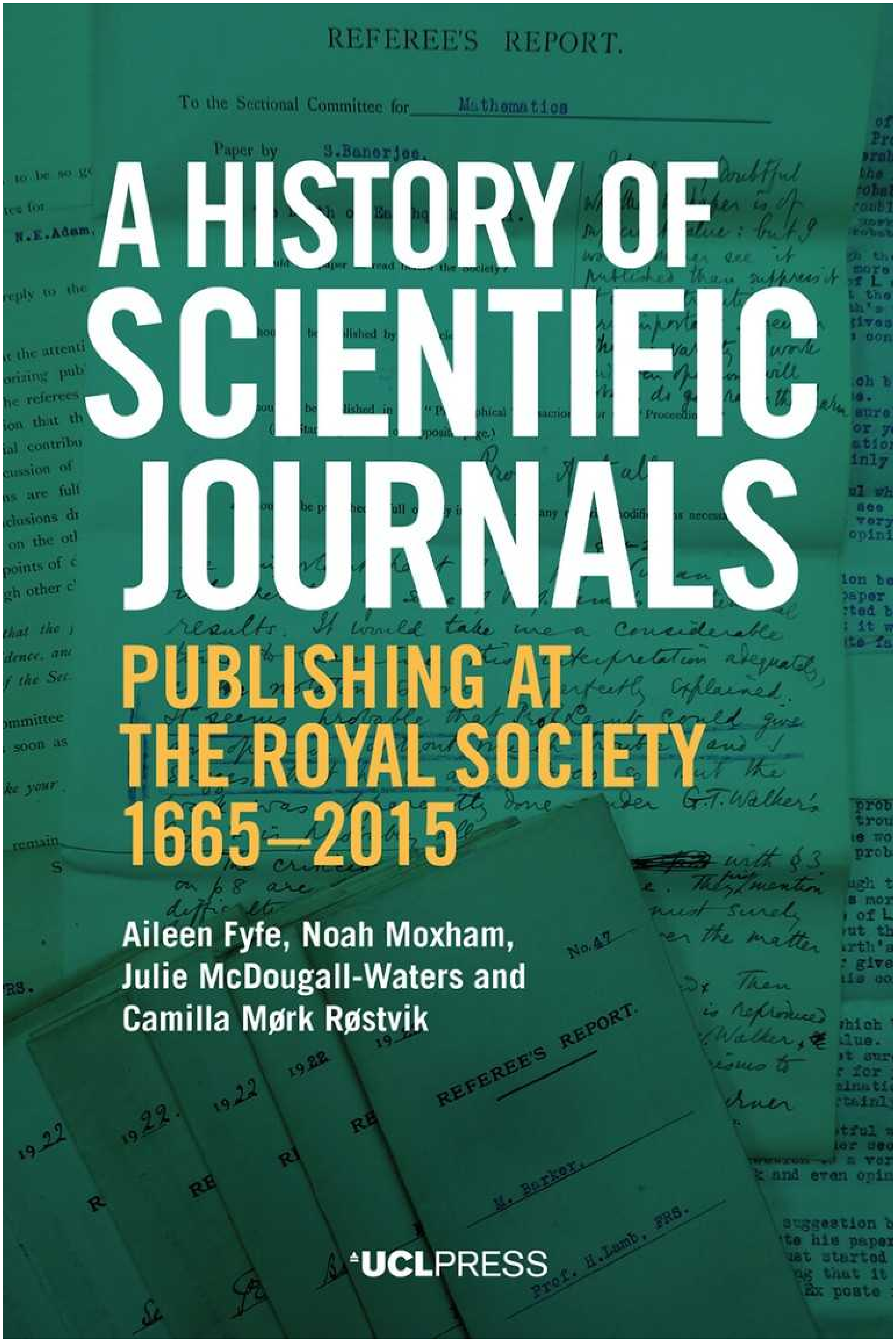
This article was downloaded by **calibre** from https://www.nature.com/articles/d41586-023-00342-4

- BOOK REVIEW
- 06 January 2023

# The magic of physics, and why we have childhood: Books in brief

Andrew Robinson reviews five of the best science picks.

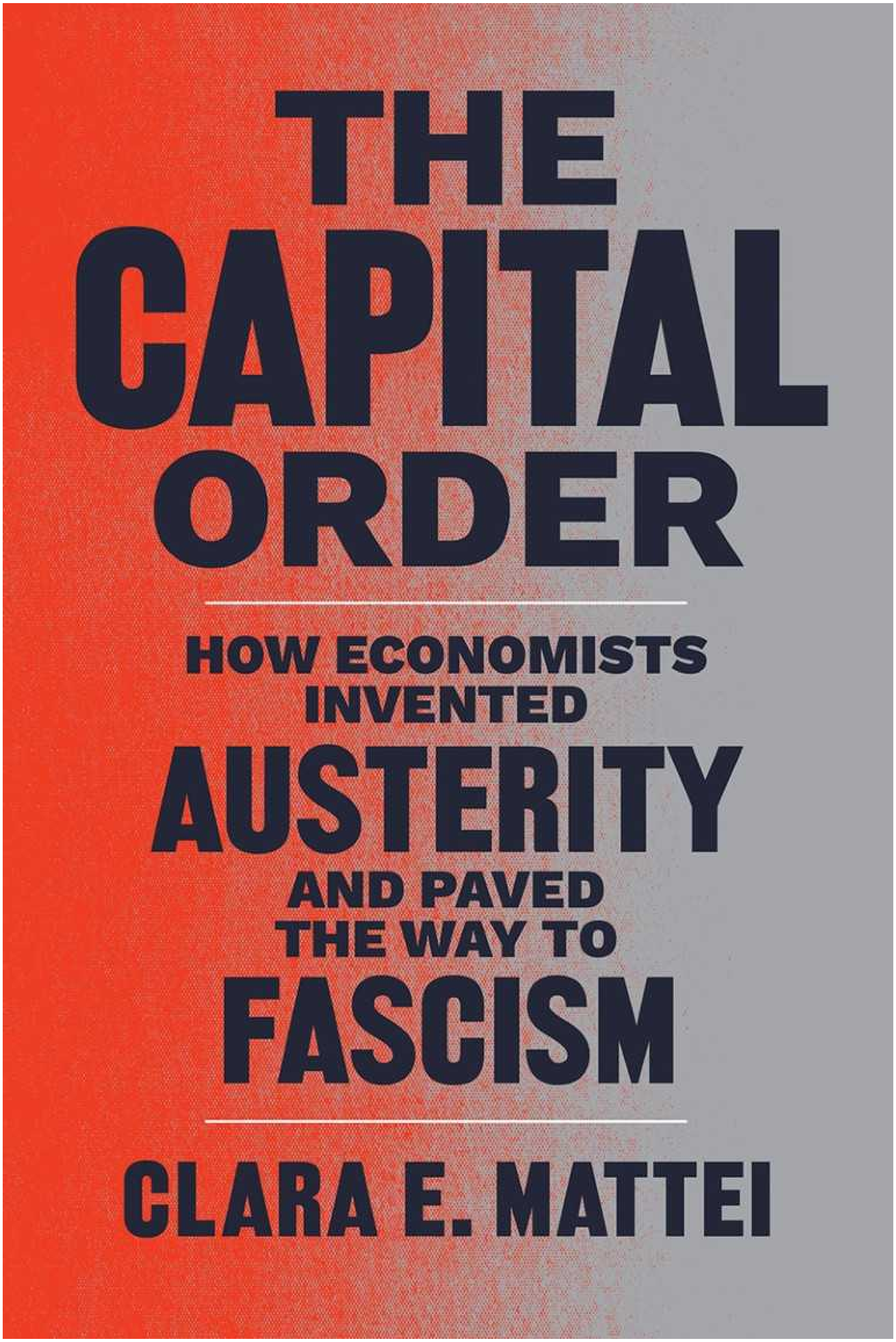
- Andrew Robinson


REFEREE'S REPORT.
To the Sectional Committee for Mathematics
A HISTORY OF
SCIENTIFIC
JOURNALS
PUBLISHING AT
THE ROYAL SOCIETY
1665–2015
Aileen Fyfe, Noah Moxham,
Julie McDougall-Waters and
Camilla Mørk Røstvik
REFEREE'S REPORT
UCLPRESS

**A History of Scientific Journals**

Aileen Fyfe *et al*. *UCL Press* (2022)

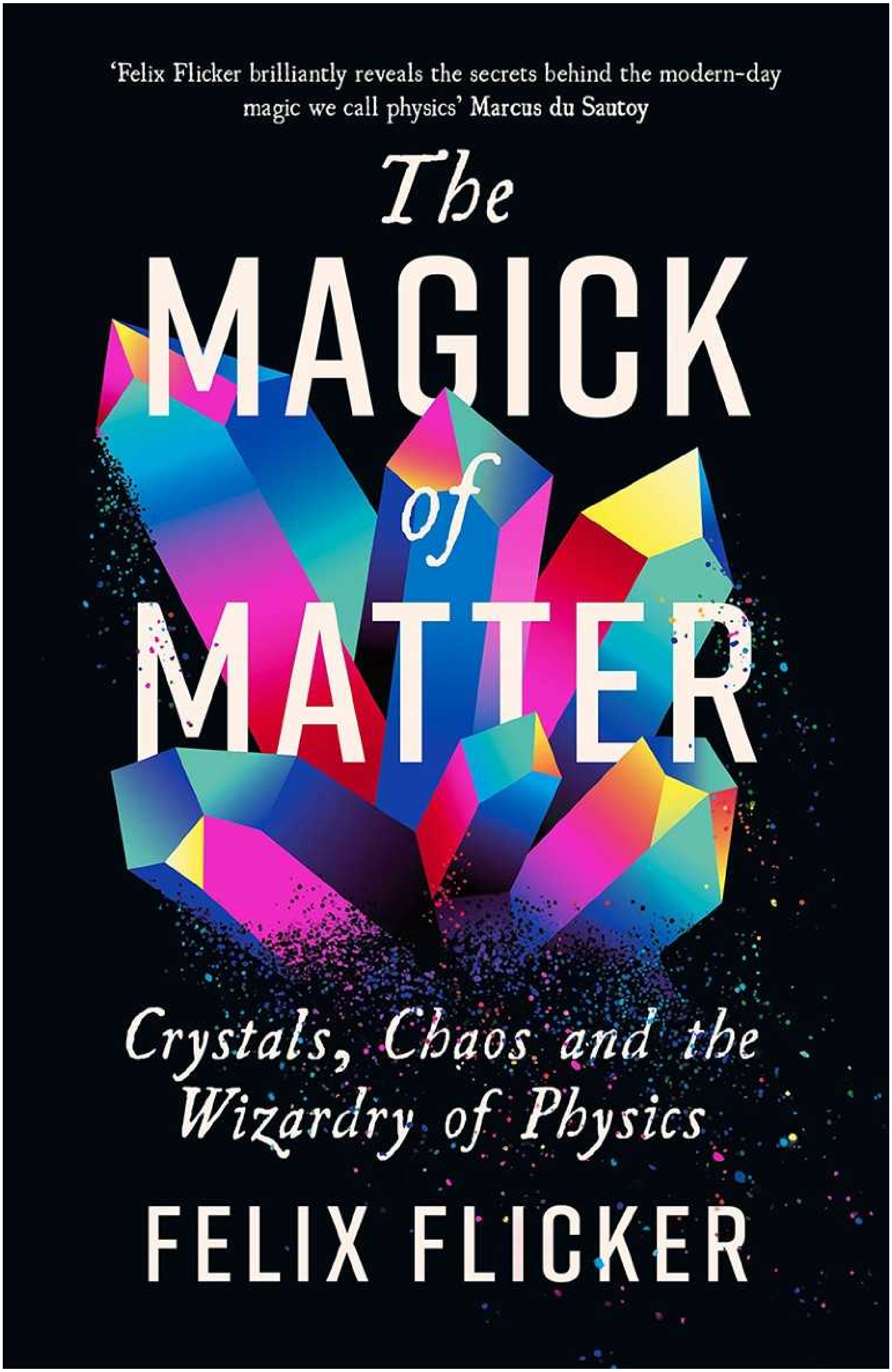
*Philosophical Transactions of the Royal Society*, published from 1665 in London, is regarded as the first scientific journal. In this study, four historians recount and analyse the society's publishing history up to 2015 — including the journal *Proceedings*, launched in 1831 — with erudition and acuteness. They reject the idea that the 1665 journal established four basic principles of current scientific publishing: registration, verification (peer review), dissemination and archiving. Instead, they show how these emerged gradually as science evolved.


THE CAPITAL ORDER
HOW ECONOMISTS INVENTED AUSTERITY AND PAVED THE WAY TO FASCISM
CLARA E. MATTEI

**The Capital Order**

Clara E. Mattei *Univ. Chicago Press* (2022)

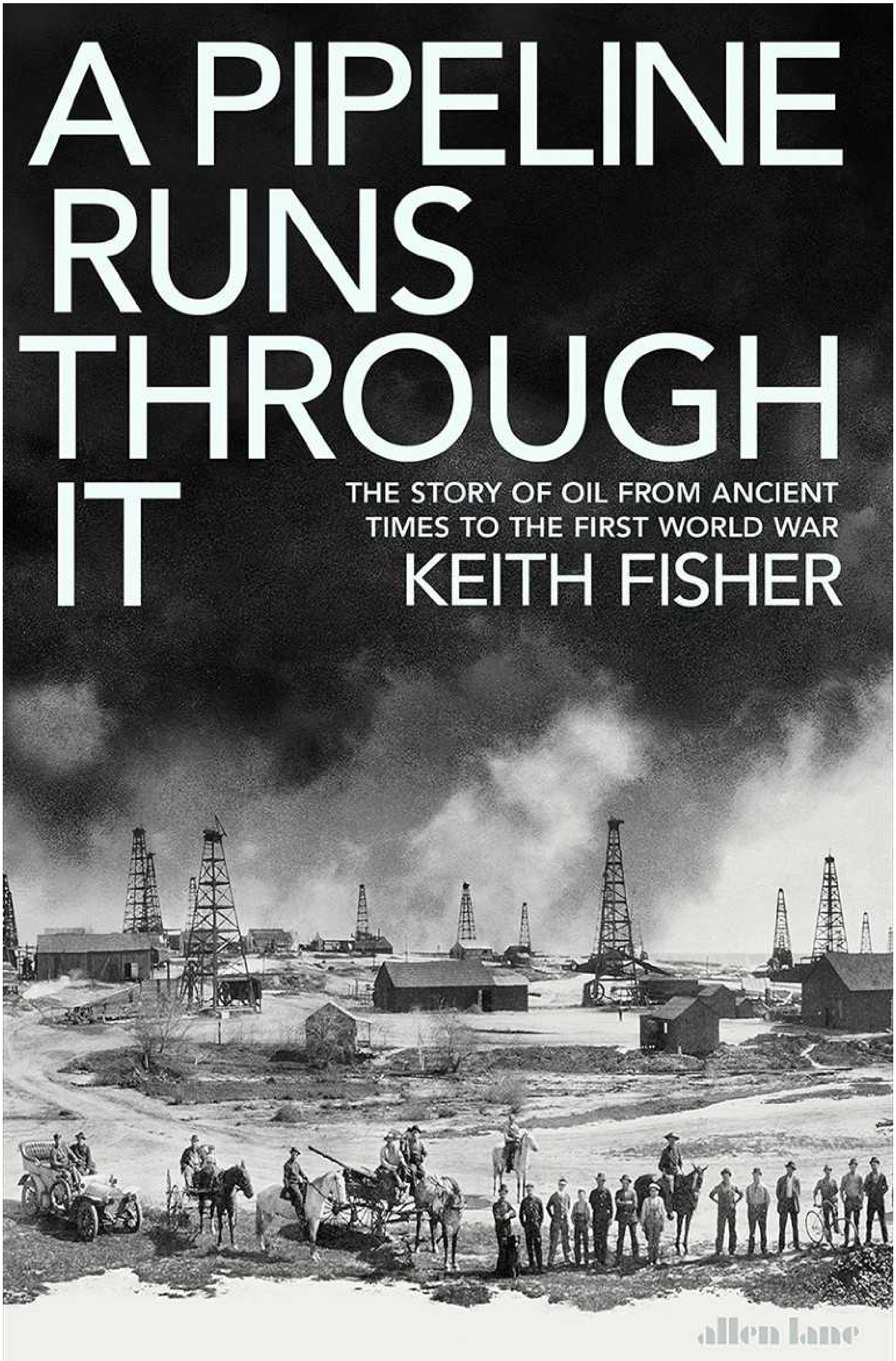
In the United States, the median male worker today earns less in real terms than in 1973, whereas the richest 400 families pay an overall tax rate lower than any other income group's. Such shocking disparities underlie economist Clara Mattei's topical study of austerity measures — fiscal tightening and cuts in wages and benefits — promoted over the past century. Focusing on 1920s liberal-democracy Britain and fascist Italy, she argues that the profitable application of austerity to these dissimilar nations licensed its use as a capitalist "tool of class control".


'Felix Flicker brilliantly reveals the secrets behind the modern-day magic we call physics' Marcus du Sautoy
The
MAGICK
of
MATTER
Crystals, Chaos and the Wizardry of Physics
FELIX FLICKER

**The Magick of Matter**

Felix Flicker *Profile* (2022)

Wolfgang Pauli, a founder of quantum mechanics, dismissed condensed-matter physics as *Schmutzphysik*, “the physics of dirt”. Physicist Felix Flicker makes this the opening chapter title in his imaginative introduction to the field, which employs one-third of today’s physicists. He stresses the ‘magical’ phenomenon of emergence: “The whole is more than the sum of the parts.” For example, sound travels through matter as emergent quasiparticles, phonons, which can be measured — yet, in a vacuum, they do not exist.


A PIPELINE RUNS THROUGH IT
THE STORY OF OIL FROM ANCIENT TIMES TO THE FIRST WORLD WAR
KEITH FISHER
allen lane

**A Pipeline Runs Through It**

Keith Fisher *Allen Lane* (2022)

During the First World War, monthly fuel-oil consumption by Britain’s warships surged: from 60,000 tonnes in 1914 to around 310,000 tonnes in 1918, most of it imported from the United States after Russian and Romanian supplies were cut off. Oil might even have been a catalyst for the war’s outbreak, proposes Keith Fisher, a journalist and researcher on corporate and environmental issues. His deeply researched, inevitably lengthy history of oil from Neanderthals to 1918 includes its purported use in waterproofing Noah’s Ark.

Brenna Hassett



'A gem of a book'
Alice Roberts

# growing up human

## the evolution of childhood



BLOOMSBURY

## Growing Up Human

Brenna Hassett *Bloomsbury Sigma* (2022)

Bioarchaeologist Brenna Hassett's PhD was in dental anthropology: looking for clues to human lives in ancient teeth. Her intriguing, entertaining book looks at a different facet of life: childhood. Why do humans take so long to grow up? When other apes are starting to reproduce, we are still playing. What, she asks, is the "weird, unique human childhood" for? She examines distinctive aspects from messy mating and dangerous pregnancies to the puzzling human fondness for formal education and love of the written word.

*Nature* **614**, 218 (2023)

*doi: https://doi.org/10.1038/d41586-022-04570-y*

---

This article was downloaded by **calibre** from https://www.nature.com/articles/d41586-022-04570-y

# Opinion

- **Hidden harms of indoor air pollution — five steps to expose them** [08 Feb 2023]
  • Dirty outdoor air might grab the headlines, but learning how pollutants inside buildings form, accumulate and affect our health is equally crucial.
- **ChatGPT: five priorities for research** [03 Feb 2023]
  • Conversational AI is a game-changer for science. Here’s how to respond.

- COMMENT
- 08 February 2023

# Hidden harms of indoor air pollution — five steps to expose them

Dirty outdoor air might grab the headlines, but learning how pollutants inside buildings form, accumulate and affect our health is equally crucial.


- Alastair C. Lewis,
- Deborah Jenkins &
- Christopher J. M. Whitty



Cooking stoves emit large amounts of particulate matter, which can have inflammatory and carcinogenic properties.Credit: Youngduk Ko/EyeEm

Air pollution is a leading cause of illness — from asthma[1] to heart disease, stroke, lung cancer[2] and, probably, dementia[3]. For outdoor air pollution, improved standards and regulations, guided by science, have over the past three decades markedly driven down emissions of particulates, nitrogen oxides and sulfur dioxide in many parts of the world[4]. Indoor air pollution hasn't received the same attention, even though it might cause almost as many deaths globally — 3.2 million in 2020, according to the World Health Organization (WHO), compared with around 3.5 million linked to polluted outdoor air (see go.nature.com/3jngf7x).

In industrialized nations, most people spend 80–90% of their time indoors — in private homes as well as in public spaces such as schools, workplaces, transport hubs, hospitals and supermarkets. Such spaces are typically not

subject to legally enforceable ambient air-quality standards. By contrast, global recommendations for how countries should assess and manage their outdoor air quality, made by the WHO, the United Nations Environment Programme and others, have been widely adopted. These are delivered through national regulations and laws that set minimum air-quality standards to protect the public[5].



Indoor air pollution kills and science needs to step up

The science of indoor air pollution is also less developed than that of outdoor air, making it hard for governments to target policies and controls. Building owners and operators might not consider air quality their responsibility, or might not know how to improve it or the risks of not doing so. Furthermore, the types and behaviours of pollutants differ inside from outside. Ventilation has a crucial role indoors. Pollutants such as carbon monoxide, which are diluted outdoors, can accumulate inside a room. In addition to pollution, respiratory pathogens, including coronaviruses and influenza viruses, can build up and spread between individuals more readily indoors — as the COVID-19 pandemic and the latest flu outbreaks have demonstrated.

Over years, the health harms of living with poor air quality can cascade. For example, persistent exposure to cancer-causing materials or particulates might increase the risk of heart disease and stroke.

Here we highlight five areas in which the science of indoor air pollution needs to be developed to inform standards and policies, identify engineering opportunities and provide advice for the public, especially those who are most vulnerable to the health risks.

## Understand what’s harmful

Indoor air contains a more diverse range of pollutants than does outdoor air. Some are common to both. For example, wood and coal fires and cooking stoves emit large amounts of particulate matter (those with grain sizes of 2.5 micrometres or less are known as $PM_{2.5}$). Natural-gas boilers give off nitrogen oxides ($NO_x$). Other pollutants are much more common indoors. Carbon monoxide is released from incomplete combustion, formaldehyde from building materials and glues, and radon from natural radioactivity in bedrock beneath buildings. All of these can accumulate and reach higher concentrations inside than outside[6].

Building materials, fabrics and furniture also give off chemicals that can irritate the lungs and eyes. Volatile organic compounds are released from paints, carpets and wood treatments and other household products. Persistent chemicals such as brominated fire retardants are embedded in modern furniture. These chemicals can react to produce secondary pollutants, such as formaldehyde and $PM_{2.5}$, that have inflammatory and carcinogenic properties.

Moulds thrive in damp, poorly ventilated buildings. Inhaling airborne fungal spores from mould can have adverse health impacts for some, such as increased severity of asthma[7]. For example, in November 2022, a UK coroner ruled that the death of a two-year-old boy had been caused by prolonged exposure to black mould in the rented flat he lived in.



Moulds thrive in damp, poorly ventilated buildings.Credit: Katherine Frey/The Washington Post via Getty

Occupants themselves affect indoor air quality. In closed rooms containing many people, such as offices and classrooms, levels of carbon dioxide can become high enough to cause cognitive impairment. Human breath can release droplets or smaller aerosols that carry viruses and bacteria, spreading infections[8]. Volatile organic compounds might also be exhaled, and be produced and absorbed by the skin, affecting how secondary pollutants form.

Such diversity makes it challenging to define what good indoor air quality looks like. Ventilation systems often use $CO_2$ as a proxy. This metric works well for assessing emissions linked to people and respiration, but says little about the prevalence of volatiles from solvents or spores from mould, for instance.

Researchers need to devise, and policymakers to use, a broad set of metrics for indoor air quality. Such metrics can then be applied to help inform research priorities, control emissions, predict effects, limit exposure and

measure outcomes — and to underpin the basic framework of air-quality science that has worked well for controlling outdoor pollution.

## Model how pollutants form and accumulate

A pollutant's concentration indoors depends on five factors[6]. First, the size of sources that release it and sinks that remove it (for example, through filtration, deposition or chemical reaction); second, the concentration of outdoor pollutants, which might enter through vents and windows; third, the amount of airflow and turbulence, which disperse the pollutant; fourth, the extent of exchange of air between outdoors and indoors; and fifth, the dimensions of the space.



[Aerosols must be included in climate risk assessment]

Some of these parameters can be easily measured, such as the size of a room, outdoor concentration and the rate at which air is exchanged. Others, for example the strengths of sources and sinks, are much harder to assess. Emissions of outdoor pollutants are often quantified relative to activity, such as grams of $NO_x$ emitted per vehicle kilometre driven. These are compiled into emissions inventories, some being used for regulatory purposes, others for research. However, few such estimates are available for indoor air.

Researchers need to build better inventories for interior emissions arising from home appliances, materials and human activities. This will be challenging: for example, when measuring emissions of volatile organic compounds from hundreds of household products, how can their compositions and people's daily exposure to them be captured? $PM_{2.5}$ released per kilogram of food cooked needs to be established, and exhaled aerosols from human respiration estimated for a range of body types and levels of physical exertion. Dependencies on individual behaviours should also be explored.



Air purifiers can lower levels of particulates indoors, but are an expensive option.Credit: Jean Chung/Getty

Models of indoor air chemistry are needed to evaluate the rates at which pollutants are removed or form. Some models have been adapted from outdoor atmospheric-chemistry mechanisms, to account for reduction in light and ultraviolet levels and to estimate loss of pollution from indoor surfaces such as furnishings[9]. But the processes by which chemicals degrade indoors differ from those for outdoors. Oxidation (the loss of one or more

electrons by a molecule) is important, and can transform relatively benign indoor chemicals such as methane into harmful compounds, including formaldehyde and secondary $PM_{2.5}$ (ref. [10]). At low indoor UV levels, gases such as nitrate ($NO_3$), ozone and chlorine have a greater role in oxidation than do hydroxyl (OH) radicals, the dominant outdoor oxidant.



Atmospheric chemistry: China's choking cocktail

Observations against which to benchmark models are also scant for indoor air. It is difficult to access private spaces to gather data in homes or workplaces, for example. Experiments studying indoor air have historically been low on funders' priority lists. But research has picked up in the past five years; some data sets have been collected that cover a wide range of chemicals indoors, although only for a handful of test homes, mostly in the United States. Such data sets are key for testing whether assumptions about what controls air indoors are correct and whether interventions are likely to be effective[11]. They should be extended to diverse types of building and construction.

The toxicity of airborne pollutants such as $PM_{2.5}$ indoors also needs to be better established. It might differ from that outdoors, because such particles originate from different processes, such as cooking stoves rather than car exhausts. Most epidemiological studies that link air pollution to health

impacts have been conducted on data sets based on outdoor air quality. The effects of long-term, low-level exposure to pollutants indoors needs to be better understood.

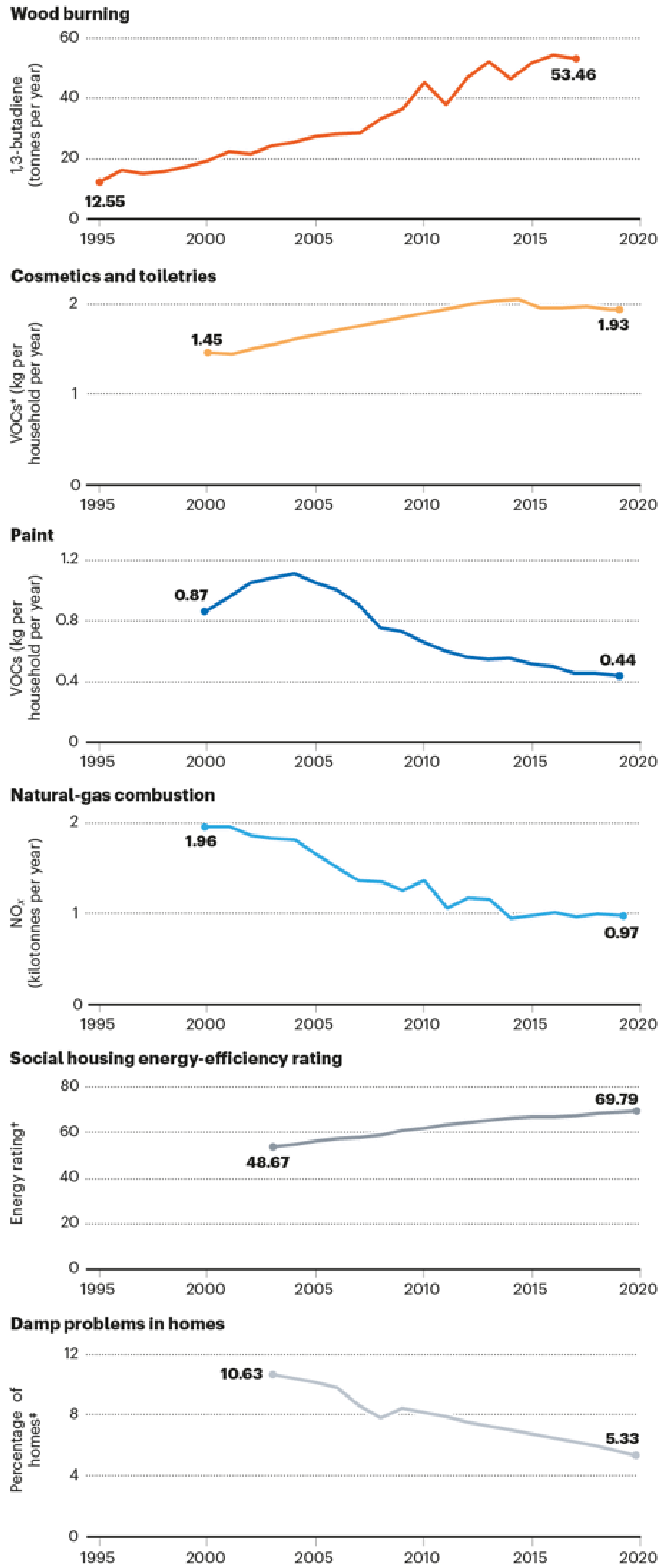
# Explore effects of local variations

The wide diversity in how buildings are constructed, ventilated, operated and occupied is the biggest challenge to the science of indoor air quality relevant to policy. Whereas outdoor-air measurements can be designed to be representative of a wide geographical area, indoor air quality might relate to only one room. It is often difficult to establish what a ‘typical’ indoor concentration of a pollutant might be. Construction styles and materials, climate and energy sources, as well as behaviours and cultural practices, all affect indoor air. In identical houses on the same street, concentrations of volatile organic compounds can differ by factors of around 1,000 owing to differences in occupant behaviour alone[12]. Homes in the United States, Japan or Nigeria, say, can contain different pollutants because of differences in the products used and living arrangements. Such variations could also point to solutions, however, by looking at practices in homes with little pollution.

Long-term data sets and representative surveys on concentrations of indoor-air pollution still need to be established, although some trends can be seen (see ‘Indicators of indoor air quality’). In England, for example, the proportion of homes with damp has more than halved in the past 25 years, in part owing to the wider use of central heating. Domestic coal use, cigarette smoking, chemicals from paints and emissions of $NO_x$ from gas combustion are all in decline. By contrast, emissions of volatile organic compounds from cosmetics and personal-care products have risen, as have pollutants associated with wood burning — which is now popular. Ventilation in homes has, on average, fallen as the energy efficiency of housing stock has improved. This is good for reducing $CO_2$ emissions but not necessarily for indoor air quality. How these trends have combined to affect air in homes and public spaces is unknown.

## INDICATORS OF INDOOR AIR QUALITY

In English homes, pollutants from wood fires and personal-care products are rising as those from paints, gas stoves and boilers decline. More energy-efficient homes have less damp and mould. The combined effects on health need to be better monitored.




*VOCs: volatile organic compounds; †Based on UK government 'Standard Assessment Procedure'; ‡England and Wales.

©nature

Sources: *English Housing Survey 2020–2021*. https://go.nature.com/4tljhzj; UK National Atmospheric Emissions Inventory. (Data and analysis courtesy Shona E. Wilde (Univ. York) & Tim Murrells (Ricardo Energy and Environment)

The impacts of climate change, adaptation and decarbonization on indoor air also need to be explored. A shift to wetter, windier conditions tends to reduce outdoor pollutants such as $PM_{2.5}$ but might increase damp and moulds inside. Hotter conditions can increase outdoor ozone, which can be drawn indoors. Residents might open windows and increase ventilation, or keep them closed and switch on air conditioning. Climate impacts on indoor air will depend on the age and construction of a building.

## Understand the best ways to improve indoor air quality

Decision makers need scientific evidence to help them prioritize groups of interventions and to develop strategies for improving indoor air quality. There are many options, but it is difficult to quantify the effect of each intervention (see go.nature.com/3wv28vt). Generally, as for outdoors, removing the largest sources of emission is most effective. That might mean replacing gas cookers with electric stoves, or reformulating products — for example, changing sprays such as deodorants and air fresheners that contain butane and propane to use nitrogen or air instead. Some indoor sources are surprisingly large — in the United Kingdom, compressed-aerosol cans now release more volatile organic compounds than do petrol cars[13].

For moulds, bioaerosols and $CO_2$, good building-management practices that ensure adequate heating, airflow and air exchange with outdoors are effective[14]. Increasing ventilation will create energy trade-offs, because heat is lost in colder weather, but engineered solutions are feasible.



Huge gaps in detection networks plague emissions monitoring

Air filters (sometimes called purifiers) are good at lowering levels of particulates indoors, including $PM_{2.5}$, bioaerosols and viruses, but are less effective for gaseous pollutants. Air filtration is expensive and energy-consuming; in some places, it might be more effective to open a window. Predictive models providing bespoke advice for building owners are needed.

Decarbonizing buildings affords an opportunity to rethink how indoor air quality can be managed and improved. Balancing the need to increase ventilation yet minimize energy loss through heating (in colder countries) or cooling (in hotter ones) is an important engineering challenge. Better insulation to reduce energy consumption needs to be set against adequate ventilation to avoid pollution collecting indoors.

Heat exchangers offer one solution, by recapturing energy in a fluid before air leaves the house. But these are expensive and hard to install in older buildings. The effects of various technologies designed mainly for decarbonization need to be quantified.

## Bolster science-based advice

A scientific road map to cleaner indoor air will need to work through many challenges. Who is most exposed and where? What are the key sources of pollution? What beneficial actions (technical, behavioural and regulatory) would have the greatest impacts? The scientific community must provide evidence to make these decisions and encourage action. Whereas scientific efforts must be global if they are to capture the ranges of buildings, behaviours and weather, science-based advice for cleaner indoor air will inevitably be country- and region-specific.

Monitoring the indoor environment for pollution should become standard practice in public spaces. Indoor emission inventories need urgent investment. Better advice on reducing indoor exposure without reducing energy efficiency will need to lean heavily on measurements. Long time series must be established in representative public buildings and homes to inform future building standards.

Interventions such as ventilation and innovations involving filtration and UV need to be fully characterized. Each solution will address only a subset of effects, and multiple actions will be needed. As with most public-health interventions, many incremental improvements leading to wholesale change are more likely to be effective than is waiting for a small number of transformational improvements.

It is essential that decarbonization, building improvement and gains in indoor air quality are, as much as possible, delivered equitably across society. Strategies that rely on householders investing in, for example, installing heat pumps, air filters and ventilation systems will skew benefits towards those who can afford to pay.

People most affected by poor indoor air quality, and who are in poor health to begin with, tend to be those on lower incomes, living in homes that rely on older gas or solid-fuel heating, homes with damp and those situated in areas of high outdoor pollution. Supporting these people is essential. Low- and middle-income countries face extra challenges, for example where solid fuel such as wood, charcoal or coal remains a major part of indoor cooking and heating.

Local and national governments must ensure that good indoor air quality is delivered for those in shared, social or rented accommodation, and for public indoor spaces. For example, in France, monitoring of a range of pollutants is mandatory in schools. Beyond state intervention, employers must ensure safe, healthy workplaces, including good-quality air.

Just as for outdoors, improving air quality indoors globally requires sustained investment in scientific and engineering research and international collaborations that share best practice in measurement, modelling and abatement. It is time for researchers to develop the evidence that will allow governments, businesses and individuals to take up the baton and devise science-based global standards for indoor air quality, to reduce emissions, exposure and harms.

*Nature* **614**, 220-223 (2023)

*doi: https://doi.org/10.1038/d41586-023-00287-8*

# References

1. Sacks, J. *et al. Integrated Science Assessment for Particulate Matter* (EPA, 2019).

2. WHO. *Noncommunicable Diseases and Air Pollution* (WHO, 2019).

3. Peters, R., Mudway, I., Booth, A., Peters, J. & Anstey, K. J. *Neuroepidemiology* **55**, 253–265 (2021).

4. Department of Health and Social Care. *Chief Medical Officer's Report 2022: Air Pollution* (DHSC, 2022).

5. WHO. *WHO Global Air Quality Guidelines: Particulate Matter (PM2.5 and PM10), Ozone, Nitrogen Dioxide, Sulfur Dioxide and Carbon Monoxide* (WHO, 2021).

6. Air Quality Expert Group. *Indoor Air Quality* (DEFRA, 2022).

7. Rick, E. M., Woolnough, K., Pashley, C. H. & Wardlaw, A. J. *J. Invest. Allergol. Clin. Immunol.* **26**, 344–354 (2016).

8. Wang, C. C. *et al. Science* **373**, eabd9149 (2021).

9. Shaw, D. & Carslaw, N. *J. Open Source Softw.* **6**, 3224 (2021).

10. Abbatt, J. P. D. & Wang, C. *Environ. Sci. Process. Impacts* **22**, 25–48 (2020).

11. Farmer, D. K. *et al. Environ. Sci. Process. Impacts* **21**, 1280–1300 (2019).

12. Wang, C. M. *et al. Environ. Sci. Process. Impacts* **19**, 528–537 (2017).

13. Yeoman, A. M. & Lewis, A. C. *Elementa* **9**, 00177 (2021).

14. Cheek, E., Guercio, V., Shrubsole, C. & Dimitroulopoulou, S. *Sci. Total Environ.* **766**, 142585 (2021).

---

This article was downloaded by **calibre** from https://www.nature.com/articles/d41586-023-00287-8

| Section menu | Main menu |

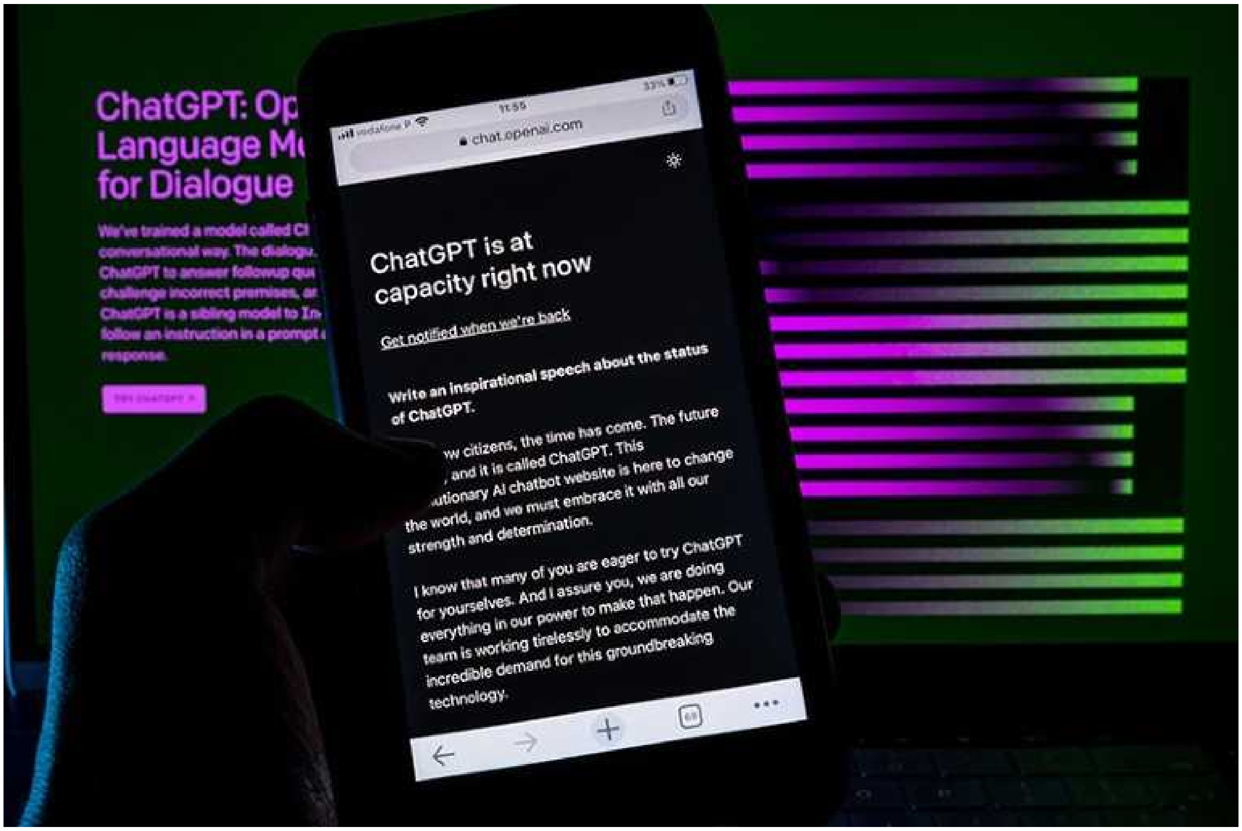
- COMMENT
- 03 February 2023

# ChatGPT: five priorities for research

Conversational AI is a game-changer for science. Here’s how to respond.


- Eva A. M. van Dis,
- Johan Bollen,
- Willem Zuidema,
- Robert van Rooij &
- …
- Claudi L. Bockting

Show authors




Credit: Vitor Miranda/Alamy

Since a chatbot called ChatGPT was released late last year, it has become apparent that this type of artificial intelligence (AI) technology will have huge implications on the way in which researchers work.

ChatGPT is a large language model (LLM), a machine-learning system that autonomously learns from data and can produce sophisticated and seemingly intelligent writing after training on a massive data set of text. It is the latest in a series of such models released by OpenAI, an AI company in San Francisco, California, and by other firms. ChatGPT has caused excitement and controversy because it is one of the first models that can convincingly converse with its users in English and other languages on a wide range of topics. It is free, easy to use and continues to learn.

This technology has far-reaching consequences for science and society. Researchers and others have already used ChatGPT and other large language models to write essays and talks, summarize literature, draft and improve papers, as well as identify research gaps and write computer code, including

statistical analyses. Soon this technology will evolve to the point that it can design experiments, write and complete manuscripts, conduct peer review and support editorial decisions to accept or reject manuscripts.

Conversational AI is likely to revolutionize research practices and publishing, creating both opportunities and concerns. It might accelerate the innovation process, shorten time-to-publication and, by helping people to write fluently, make science more equitable and increase the diversity of scientific perspectives. However, it could also degrade the quality and transparency of research and fundamentally alter our autonomy as human researchers. ChatGPT and other LLMs produce text that is convincing, but often wrong, so their use can distort scientific facts and spread misinformation.

We think that the use of this technology is inevitable, therefore, banning it will not work. It is imperative that the research community engage in a debate about the implications of this potentially disruptive technology. Here, we outline five key issues and suggest where to start.

# Hold on to human verification

LLMs have been in development for years, but continuous increases in the quality and size of data sets, and sophisticated methods to calibrate these models with human feedback, have suddenly made them much more powerful than before. LLMs will lead to a new generation of search engines[1] that are able to produce detailed and informative answers to complex user questions.

But using conversational AI for specialized research is likely to introduce inaccuracies, bias and plagiarism. We presented ChatGPT with a series of questions and assignments that required an in-depth understanding of the literature and found that it often generated false and misleading text. For example, when we asked ‘how many patients with depression experience relapse after treatment?’, it generated an overly general text arguing that treatment effects are typically long-lasting. However, numerous high-quality studies show that treatment effects wane and that the risk of relapse ranges from 29% to 51% in the first year after treatment completion[2–4]. Repeating

the same query generated a more detailed and accurate answer (see Supplementary information, Figs S1 and S2).

Next, we asked ChatGPT to summarize a systematic review that two of us authored in *JAMA Psychiatry*[5] on the effectiveness of cognitive behavioural therapy (CBT) for anxiety-related disorders. ChatGPT fabricated a convincing response that contained several factual errors, misrepresentations and wrong data (see Supplementary information, Fig. S3). For example, it said the review was based on 46 studies (it was actually based on 69) and, more worryingly, it exaggerated the effectiveness of CBT.

Such errors could be due to an absence of the relevant articles in ChatGPT's training set, a failure to distil the relevant information or being unable to distinguish between credible and less-credible sources. It seems that the same biases that often lead humans astray, such as availability, selection and confirmation biases, are reproduced and often even amplified in conversational AI[6].




[Abstracts written by ChatGPT fool scientists]

Researchers who use ChatGPT risk being misled by false or biased information, and incorporating it into their thinking and papers. Inattentive reviewers might be hoodwinked into accepting an AI-written paper by its beautiful, authoritative prose owing to the halo effect, a tendency to over-

generalize from a few salient positive impressions[7]. And, because this technology typically reproduces text without reliably citing the original sources or authors, researchers using it are at risk of not giving credit to earlier work, unwittingly plagiarizing a multitude of unknown texts and perhaps even giving away their own ideas. Information that researchers reveal to ChatGPT and other LLMs might be incorporated into the model, which the chatbot could serve up to others with no acknowledgement of the original source.

Assuming that researchers use LLMs in their work, scholars need to remain vigilant. Expert-driven fact-checking and verification processes will be indispensable. Even when LLMs are able to accurately expedite summaries, evaluations and reviews, high-quality journals might decide to include a human verification step or even ban certain applications that use this technology. To prevent human automation bias — an over-reliance on automated systems — it will become even more crucial to emphasize the importance of accountability[8]. We think that humans should always remain accountable for scientific practice.

# Develop rules for accountability

Tools are already available to predict the likelihood that a text originates from machines or humans. Such tools could be useful for detecting the inevitable use of LLMs to manufacture content by paper mills and predatory journals, but such detection methods are likely to be circumvented by evolved AI technologies and clever prompts. Rather than engage in a futile arms race between AI chatbots and AI-chatbot-detectors, we think the research community and publishers should work out how to use LLMs with integrity, transparency and honesty.

Author-contribution statements and acknowledgements in research papers should state clearly and specifically whether, and to what extent, the authors used AI technologies such as ChatGPT in the preparation of their manuscript and analysis. They should also indicate which LLMs were used. This will alert editors and reviewers to scrutinize manuscripts more carefully for potential biases, inaccuracies and improper source crediting. Likewise,

scientific journals should be transparent about their use of LLMs, for example when selecting submitted manuscripts.

Research institutions, publishers and funders should adopt explicit policies that raise awareness of, and demand transparency about, the use of conversational AI in the preparation of all materials that might become part of the published record. Publishers could request author certification that such policies were followed.

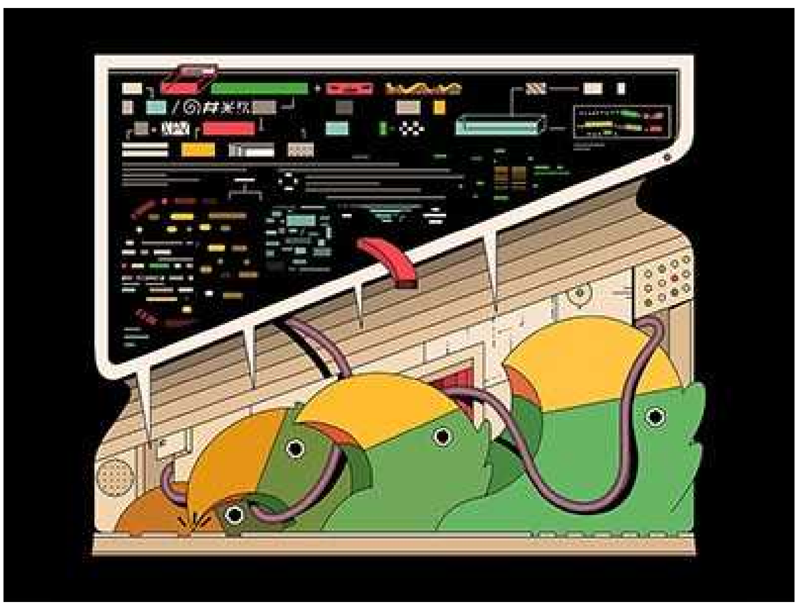
For now, LLMs should not be authors of manuscripts because they cannot be held accountable for their work. But, it might be increasingly difficult for researchers to pinpoint the exact role of LLMs in their studies. In some cases, technologies such as ChatGPT might generate significant portions of a manuscript in response to an author's prompts. In others, the authors might have gone through many cycles of revisions and improvements using the AI as a grammar- or spellchecker, but not have used it to author the text. In the future, LLMs are likely to be incorporated into text processing and editing tools, search engines and programming tools. Therefore they might contribute to scientific work without authors necessarily being aware of the nature or magnitude of the contributions. This defies today's binary definitions of authorship, plagiarism and sources, in which someone is either an author, or not, and a source has either been used, or not. Policies will have to adapt, but full transparency will always be key.

Inventions devised by AI are already causing a fundamental rethink of patent law[9], and lawsuits have been filed over the copyright of code and images that are used to train AI, as well as those generated by AI (see go.nature.com/3y4aery). In the case of AI-written or -assisted manuscripts, the research and legal community will also need to work out who holds the rights to the texts. Is it the individual who wrote the text that the AI system was trained with, the corporations who produced the AI or the scientists who used the system to guide their writing? Again, definitions of authorship must be considered and defined.

## Invest in truly open LLMs

Currently, nearly all state-of-the-art conversational AI technologies are proprietary products of a small number of big technology companies that have the resources for AI development. OpenAI is funded largely by Microsoft, and other major tech firms are racing to release similar tools. Given the near-monopolies in search, word processing and information access of a few tech companies, this raises considerable ethical concerns.

One of the most immediate issues for the research community is the lack of transparency. The underlying training sets and LLMs for ChatGPT and its predecessors are not publicly available, and tech companies might conceal the inner workings of their conversational AIs. This goes against the move towards transparency and open science, and makes it hard to uncover the origin of, or gaps in, chatbots' knowledge[10]. For example, we prompted ChatGPT to explain the work of several researchers. In some instances, it produced detailed accounts of scientists who could be considered less influential on the basis of their h-index (a way of measuring the impact of their work). Although it succeeded for a group of researchers with an h-index of around 20, it failed to generate any information at all on the work of several highly cited and renowned scientists — even those with an h-index of more than 80.



Robo-writers: the rise and risks of language-generating AI

To counter this opacity, the development and implementation of open-source AI technology should be prioritized. Non-commercial organizations such as universities typically lack the computational and financial resources needed to keep up with the rapid pace of LLM development. We therefore advocate that scientific-funding organizations, universities, non-governmental organizations (NGOs), government research facilities and organizations such as the United Nations — as well tech giants — make considerable investments in independent non-profit projects. This will help to develop advanced open-source, transparent and democratically controlled AI technologies.

Critics might say that such collaborations will be unable to rival big tech, but at least one mainly academic collaboration, BigScience, has already built an open-source language model, called BLOOM. Tech companies might benefit from such a program by open sourcing relevant parts of their models and corpora in the hope of creating greater community involvement, facilitating innovation and reliability. Academic publishers should ensure LLMs have access to their full archives so that the models produce results that are accurate and comprehensive.

## Embrace the benefits of AI

As the workload and competition in academia increases, so does the pressure to use conversational AI. Chatbots provide opportunities to complete tasks quickly, from PhD students striving to finalize their dissertation to researchers needing a quick literature review for their grant proposal, or peer-reviewers under time pressure to submit their analysis.

If AI chatbots can help with these tasks, results can be published faster, freeing academics up to focus on new experimental designs. This could significantly accelerate innovation and potentially lead to breakthroughs across many disciplines. We think this technology has enormous potential, provided that the current teething problems related to bias, provenance and inaccuracies are ironed out. It is important to examine and advance the validity and reliability of LLMs so that researchers know how to use the technology judiciously for specific research practices.



ChatGPT listed as author on research papers: many scientists disapprove

Some argue that because chatbots merely learn statistical associations between words in their training set, rather than understand their meanings, LLMs will only ever be able to recall and synthesize what people have already done and not exhibit human aspects of the scientific process, such as creative and conceptual thought. We argue that this is a premature assumption, and that future AI-tools might be able to master aspects of the scientific process that seem out of reach today. In a 1991 seminal paper, researchers wrote that "intelligent partnerships" between people and intelligent technology can outperform the intellectual ability of people alone[11]. These intelligent partnerships could exceed human abilities and accelerate innovation to previously unthinkable levels. The question is how far can and should automation go?

AI technology might rebalance the academic skill set. On the one hand, AI could optimize academic training — for example, by providing feedback to improve student writing and reasoning skills. On the other hand, it might reduce the need for certain skills, such as the ability to perform a literature search. It might also introduce new skills, such as prompt engineering (the process of designing and crafting the text that is used to prompt conversational AI models). The loss of certain skills might not necessarily be problematic (for example, most researchers do not perform statistical analyses by hand any more), but as a community we need to carefully

consider which academic skills and characteristics remain essential to researchers.

If we care only about performance, people's contributions might become more limited and obscure as AI technology advances. In the future, AI chatbots might generate hypotheses, develop methodology, create experiments[12], analyse and interpret data and write manuscripts. In place of human editors and reviewers, AI chatbots could evaluate and review the articles, too. Although we are still some way from this scenario, there is no doubt that conversational AI technology will increasingly affect all stages of the scientific publishing process.

Therefore, it is imperative that scholars, including ethicists, debate the trade-off between the use of AI creating a potential acceleration in knowledge generation and the loss of human potential and autonomy in the research process. People's creativity and originality, education, training and productive interactions with other people will probably remain essential for conducting relevant and innovative research.

## Widen the debate

Given the disruptive potential of LLMs, the research community needs to organize an urgent and wide-ranging debate. First, we recommend that every research group immediately has a meeting to discuss and try ChatGPT for themselves (if they haven't already). And educators should talk about its use and ethics with undergraduate students. During this early phase, in the absence of any external rules, it is important for responsible group leaders and teachers to determine how to use it with honesty, integrity and transparency, and agree on some rules of engagement. All contributors to research should be reminded that they will be held accountable for their work, whether it was generated with ChatGPT or not. Every author should be responsible for carefully fact-checking their text, results, data, code and references.

Second, we call for an immediate, continuing international forum on development and responsible use of LLMs for research. As an initial step, we suggest a summit for relevant stakeholders, including scientists of

different disciplines, technology companies, big research funders, science academies, publishers, NGOs and privacy and legal specialists. Similar summits have been organized to discuss and develop guidelines in response to other disruptive technologies, such as human gene editing. Ideally, this discussion should result in quick, concrete recommendations and policies for all relevant parties. We present a non-exhaustive list of questions that could be discussed at this forum (see ‘Questions for debate’).

One key issue to address is the implications for diversity and inequalities in research. LLMs could be a double-edged sword. They could help to level the playing field, for example by removing language barriers and enabling more people to write high-quality text. But the likelihood is that, as with most innovations, high-income countries and privileged researchers will quickly find ways to exploit LLMs in ways that accelerate their own research and widen inequalities. Therefore, it is important that debates include people from under-represented groups in research and from communities affected by the research, to use people’s lived experiences as an important resource.

Science, similar to many other domains of society, now faces a reckoning induced by AI technology infringing on its most dearly held values, practices and standards. The focus should be on embracing the opportunity and managing the risks. We are confident that science will find a way to benefit from conversational AI without losing the many important aspects that render scientific work one of the most profound and gratifying enterprises: curiosity, imagination and discovery.

## Questions for debate

Issues for discussion at a forum about conversational AIs.

• Which research tasks should or should not be outsourced to large language models (LLMs)?

• Which academic skills and characteristics remain essential to researchers?

• What steps in an AI-assisted research process require human verification?

• How should research integrity and other policies be changed to address LLMs?

• How should LLMs be incorporated into the education and training of researchers?

• How can researchers and funders aid the development of independent open-source LLMs and ensure the models represent scientific knowledge accurately?

• What quality standards should be expected of LLMs (for example, transparency, accuracy, bias and source crediting) and which stakeholders are responsible for the standards as well as the LLMs?

• How can researchers ensure that LLMs promote equity in research, and avoid risks of widening inequities?

• How should LLMs be used to enhance principles of open science?

• What legal implications do LLMs have for scientific practice (for example, laws and regulations related to patents, copyright and ownership)?

*Nature* **614**, 224-226 (2023)

*doi: https://doi.org/10.1038/d41586-023-00288-7*

## References

1. Grant, N. & Metz, C. *The New York Times* (21 December 2022).
2. Jelovac, A., Kolshus, E. & McLoughlin, D. M. *Neuropsychopharmacol.* **38**, 2467–2474 (2013).
3. Kato, M. *et al. Mol. Psychiatry* **26**, 118–133 (2021).
4. Vittengl, J. R., Clark, L. A., Dunn, T. W. & Jarrett, R. B. *J. Consult. Clin. Psychol.* **75**, 475–488 (2007).
5. van Dis, E. A. M. *et al. JAMA Psychiatry* **77**, 265–273 (2020).

6. Rich, A. S. & Gureckis, T. M. *Nature Mach. Intell*. **1**, 174–180 (2019).

7. Thorndike, E. L. *J. Appl. Psychol.* **4**, 25–29 (1920).

8. Skitka, L. J., Mosier, K. & Burdick, M. D. *Int. J. Human-Comp. Stud.* **52**, 701–717 (2000).

9. George, A. & Walsh, T. *Nature* **605**, 616–618 (2022).

10. Rudin, C. *Nature Mach. Intell.* **1**, 206–215 (2019).

11. Salomon, G., Perkins, D. N. & Globerson, T. *Edu. Res.* **20**, 2–9 (1991).

12. Melnikov, A. A. *et al. Proc. Natl Acad. Sci. USA* **115**, 1221–1226 (2018).

---

This article was downloaded by **calibre** from https://www.nature.com/articles/d41586-023-00288-7

| Section menu | Main menu |

# Work

- **Measuring societal impact: how to go beyond standard publication metrics** [06 Feb 2023]
  • Approaches to capturing the benefits of research on society are improving — but huge challenges remain.
- **Smart microscopes spot fleeting biology** [07 Feb 2023]
  • Automated microscopes that adapt to each sample’s quirks can capture elusive biological phenomena at high resolution.
- **This baby turtle surprised scientists by swimming against the current** [06 Feb 2023]
  • Satellite transmitters help Cristina Miranda to understand the movements and habitats of endangered hawksbill sea turtles in the eastern Pacific Ocean.

- CAREER FEATURE
- 06 February 2023

# Measuring societal impact: how to go beyond standard publication metrics

Approaches to capturing the benefits of research on society are improving — but huge challenges remain.

- Chris Woolston

Find a new job



Research can lead to major societal impact on the ground, especially in lower-income countries.

Every researcher wants their work to matter — and increasing competition for funding is compelling scientists to show their worth. But what is the real value of an experiment, a finding or a public lecture?

Science and scientists affect so many aspects of society that capturing the full breadth of their impacts is a complicated task, says Ingeborg Meijer, a policy researcher at Leiden University in the Netherlands. Still, she says, it's crucial to fully recognize and reward scientists for their contributions. In her view, embracing a broad view of research impact is the only way to ensure that scientists fulfil their part of the social contract. "Society expects a lot from universities to help solve big problems," she says. "If you want to do that, you have to make sure science is connected to society at the very early stages."

The impacts that are potentially the most meaningful, however, are those that are the most challenging to measure, says Lutz Bornmann, a science-policy researcher at the Max Planck Society, who is based in Munich, Germany. "It's very difficult to find or produce good metrics of societal impact," he says. But this has not prevented numerous attempts over the past few years to measure impacts, such as cancer drugs extending people's lives; child-development theories informing school policies; or artificial-intelligence bots, including ChatGPT, redefining how society views creative writing. At a time when impact factors and citation counts are under more scrutiny than ever, the search is on for more approaches that can measure societal impact and help to strengthen the case for public investment in science.

## Quality assessment

Efforts by governments and funding bodies over the past decade to better understand their return on investment in research have helped to lay the groundwork for a fuller appreciation of impact. For example, the UK Research Excellence Framework (REF) — which was launched in 2014, and repeated in 2021 — measures the quality of research contributions by UK universities by assigning a score for impact, which it defines as any effect on

or benefit to "economy, society, culture, public policy or services, health, the environment or quality of life beyond academia". It's a step beyond its predecessor, the Research Assessment Exercise, which periodically assessed UK research from 1986 to 2008 but did not look separately at societal impact. For the 2021 REF, expert panels considered nearly 6,800 impact case studies (most are available in a searchable database; see go.nature.com/3y6rs), documents put together by university departments that attempt to explain the reach of their research beyond academia. Take, for example, the Crisis Resolution Team Optimisation and Relapse Prevention programme at University College London, designed to provide evidence-based guidance to mental-health professionals responding to people in acute crisis. The programme was deemed by its case study to have changed "national and international policy and practice in mental health crisis care, with resulting benefits for patients (in particular reduced use of hospital detention) and significant cost savings" to the UK National Health Service.



Why the party is over for Britain's Research Excellence Framework

In 2016, the Netherlands Association of Universities of Applied Sciences (NAUAS) took a broad view of scientific contributions in a document called *Onderzoek met Impact* (Research with Impact) (see go.nature.com/3wtq3). The report outlined ten areas of society that university research should affect, including health and vitality, education and talent development, societal resilience, sustainable transportation, sustainable agriculture and

responsible business. The document underscored the NAUAS's interest in proving the worth of research, but, as Meijer explains, it didn't include any methodology for actually tracking impact.

However, there's often a big gap between expressing an intention to measure broad impacts and actually creating a system to do so. "The evaluation culture hasn't hit science to the extent that it might," says Paul Nightingale, a science-policy researcher at the University of Sussex in Brighton, UK. When the government spends money on roads, education or welfare schemes, it has a decent idea of what its return on investment might be in terms of social and economic value. "In the UK, science is the only area of significant public funding where there isn't proper impact evaluation."

Assessing impact is challenging, but there's still a good reason to try, Nightingale says: "If you could do proper evaluations, the return on investment [into science] would be very high." Efforts over the past few years by Bornmann, Meijer and others are laying the groundwork for a fuller evaluation of science and the effects it has on policy, the economy and other areas.

## Policy impact

In theory, it should be possible to systematically track connections between research and policy, including government policies and clinical guidelines, says Martin Szomszor, a freelance data scientist based in London. Szomszor co-wrote a November 2022 paper[1] investigating a database of policy documents that had been collected from governments, think tanks, intergovernmental organizations and charities. As Szomszor explains, a citation in a policy document can be more meaningful than a citation in a highly read journal. "It's an important way to show that research actually changed behaviour," he says.

Szomszor and co-author Euan Adie, the founder and director of Overton, the London-based firm that created the database, found that articles published in social-science and humanities journals were especially likely to be cited in policy documents. According to the database, the almost 37,000 articles in these fields that were published in 2010 generated nearly 260,000 policy

citations in the following decade, a rate of almost seven policy citations per article. By contrast, close to 18,000 articles were published in physical-science and engineering journals in 2010 — but these generated roughly 63,000 policy citations in the same timeframe, a rate of about 3.5 policy citations per article. The sheer amount of available data raises the real possibility of creating a policy impact metric similar to the *h*-index, one number that measures research quality and productivity, Szomszor says. "Decision makers love to have a single number. It's cheap, and it enables a more straightforward process."



[Why I'm a garbage collector for the world's oceans]

But such a score would probably over-simplify the impact of research and fail to recognize the scientists who have truly changed the actions of governments, medical societies or other institutions. Szomszor and Adie compared the policy-citation scores of particular universities with their scores in the 2014 REF impact database. Their analysis suggested that institutions with the most policy citations tended to have been given higher scores by peer reviewers in the REF, but the correlation wasn't especially strong. One take-home lesson: a simple score derived from a policy database is likely to fall short, Szomszor says. Including some form of peer review "that would allow you to judge the worth of policy influence" would be preferable.

Still, he says, collecting and categorizing policy citations will help to broaden the picture of research impact. “The evidence of policy impact that these kinds of databases can give for research is going to become really important,” he says. “It provides a more holistic view of research contributions. It will be interesting to see how this develops.”

## Innovation and economic impact

Research often drives the development of new technologies and products, but tracking the innovation impact of a particular researcher can be a tricky process, says Sacha Wunsch-Vincent, an economist at the World Intellectual Property Organization, a United Nations agency based in Geneva, Switzerland. The organization produces the annual Global Innovation Index (GII), a publication that considers some 80 metrics across a range of areas — including the political environment, scientific and educational resources and patent creation — to rank the innovation impact of 132 economies. Switzerland scored highest in the latest edition[2], just above the United States — but less-developed nations with good innovation performance, such as Vietnam and Rwanda, are also highlighted.



A marine ecologist works on a station for monitoring the effects of climate change on coral in the Red Sea.Credit: Lukasz Larsson Warzecha/Getty

Innovations are essential for science and society — and it's becoming increasingly important to identify the most consequential projects and researchers, Wunsch-Vincent says. But the simplest metrics for measuring innovation might not be the most illuminating. "We're doing particularly well at measuring intermediate innovation outputs, such as patents or citations," he says. "But there are serious downsides." Just as researchers often cite themselves in their publications to boost their own impact factor, inventors often cite their own work in patent applications. In certain countries, he says, it's common for innovators to cite patents from only that country, partly to avoid possible international copyright disputes.

University research can have broad economic impacts that go far beyond patents or spin-off companies, Nightingale says, starting with the creation of a skilled workforce. "The most important thing that we generate from research and teaching is students. If you look at things like future income,

it's a huge amount of value." He points to the far-reaching consequences of economic research: work in the 1970s and 1980s helped the UK government to adopt new strategies to target inflation, which substantially strengthened the economy.

AUTM, a non-profit organization based in Washington DC, conducted a survey[3] to measure the innovation outputs of 197 research institutions for the fiscal year 2020. Those institutions generated more than 27,000 'invention disclosures', preliminary steps towards patents that are a signal of innovation. Discoveries made at academic research centres led directly to the creation of more than 1,000 start-up businesses. Tracking such results at the level of individual researchers would help to identify the major innovators in science, Wunsch-Vincent says. He adds that, in his experience, professors in Switzerland — the number-one economy in the GII — would generally score highly by any measure. He says that it would be very common for a robotics or biotechnology professor in Zurich to have a spin-off company that is attracting buy-out offers from influential companies, such as Google or Novartis.

# Social and environmental impact

The immense societal impacts of research are harder to measure than economic impacts, but that doesn't diminish their significance, Nightingale says. "There are amazing impacts from research that aren't economic," he says. "Researchers do critical work in humanities and social sciences that causes us to rethink the things that we value and call out inequalities." Scholarship in feminism, for example, has arguably helped lead to greater equity in society and the workplace, he says.

At an even wider level, science has the potential to transform the planet by tackling global environmental crises, such as climate change, and to improve the well-being of poorer communities. The UN Sustainable Development Goals (SDGs), a set of 17 targets that address the biggest global challenges, including poverty, hunger and clean energy, are increasingly being used to measure such impact.



How the pandemic inspired a new generation of creators

Universities and researchers commonly tout their commitment to the SDGs — but a 2022 report[4] by Steering Research and Innovation for Global Goals (STRINGS), a consortium of researchers at the University of Sussex, University College London and the United Nations Development Programme, based in New York City, suggests that research is largely failing to meet the goals. The report found that 95–98% of patents and inventions and 60–80% of academic publications are "poorly aligned with SDGs". The report found that only about 30–40% of research conducted in high- or middle-income countries has any connection to the SDGs — much less than the 60–80% in low-income countries — and describes the dearth of data and understanding about how funding for sustainability-related research is actually used, and how the impact of that research spreads beyond academia. It concludes that "major investment is also needed to gather data about knowledge and innovation investment and production across all contexts and sectors".

## Cultural impact

Alternative metrics, or 'altmetrics', attempt to track the reach of research through social media, news sites and other outlets, rather than academic citations. They were created to tell more fully the story of research impact,

but Bornmann says they have so far fallen short of that goal. For example, he says, counting mentions of a paper on social media doesn't reveal much about its true significance: anyone can share a paper on social media, including those that don't put stock in the results, are doing it to criticize the research or are spreading false information about its findings. "If you take a look at tweets on papers, it's clear that in most cases there is no deep understanding or deep reading of the paper," he says. "One can really question how such data could be used for researcher evaluation."



[Nature Index: Innovation](#)

Bornmann co-authored a 2020 study[5] that examined altmetric scores — figures based on social-media posts, news mentions and Wikipedia entries, as gathered by the data company Altmetric — of about 200 researchers who applied for funding at the Competence Center Environment and Sustainability, an environmental research centre based at the Swiss Federal Institute of Technology in Zurich. The study found only a weak correlation between altmetric scores and the likelihood of securing funding, a sign that the scores were a poor proxy of research quality.

Alternative metrics need to be refined and validated if they are ever going to be a reliable basis for funding decisions, says Bornmann, who adds that it is "a bad situation" if such metrics are being used even if "it's not clear

whether they are valid". "There needs to be a longer period of research on these metrics, and then they can be used in evaluation," he says.

## All hands on deck

Despite the many challenges, capturing the full breadth of research impact is far from a lost cause. Inspired by the ambitious goals of the Research with Impact initiative, Meijer has been exploring frameworks that could measure the diverse impacts of researchers at Dutch universities. In a paper[6] that she co-authored in 2021, she noted that any successful approach must include input from the researchers, as well as from industry, government and the funders that support the work.

In the paper, Meijer points to the promising approach of 'contribution mapping', a method that uses structured interviews to track the connections between individual scientists and non-scientists. The mapping happens in real time, starting at the beginning of a project and following it through project management, a time- and labour-intensive process that by definition spans both academia and industry. But she says that such an approach will work only if all of the actors are willing to participate in the evaluation, which has proven difficult for sectors that extend beyond the university. "External users are more difficult to find and more difficult to engage," she says. "They either want to be paid or they are not interested." And this, perhaps, illustrates a major barrier to measuring societal impact. Until there are agreed international methods for tracking influence — like those that are used to quantify academic impact — the promising but time-consuming and complex solutions that already exist need honing.

*Nature* **614**, 375-377 (2023)

*doi: https://doi.org/10.1038/d41586-023-00345-1*

## References

1. Szomszor, M. & Adie, E. *Quant. Sci. Stud.* **3**, 624–650 (2022).

2. Dutta, S., Lanvin, B., León, L. R. & Wunsch-Vincent, S. (eds) *Global Innovation Index 2022* 15th edn (WIPO, 2022).

3. AUTM *2020 Licensing Activity Survey* (AUTM, 2020).

4. Ciarli, T. (ed.) *Changing Directions: Steering Science, Technology and Innovation Towards the Sustainable Development Goals* (STRINGS, 2022).

5. Kassab, O., Bornmann, L. & Haunschild, R. *Quant. Sci. Stud.* **1**, 792–809 (2020).

6. Coombs, S. & Meijer, I. *Sci. Public Policy* **48**, 226–234 (2021).

---

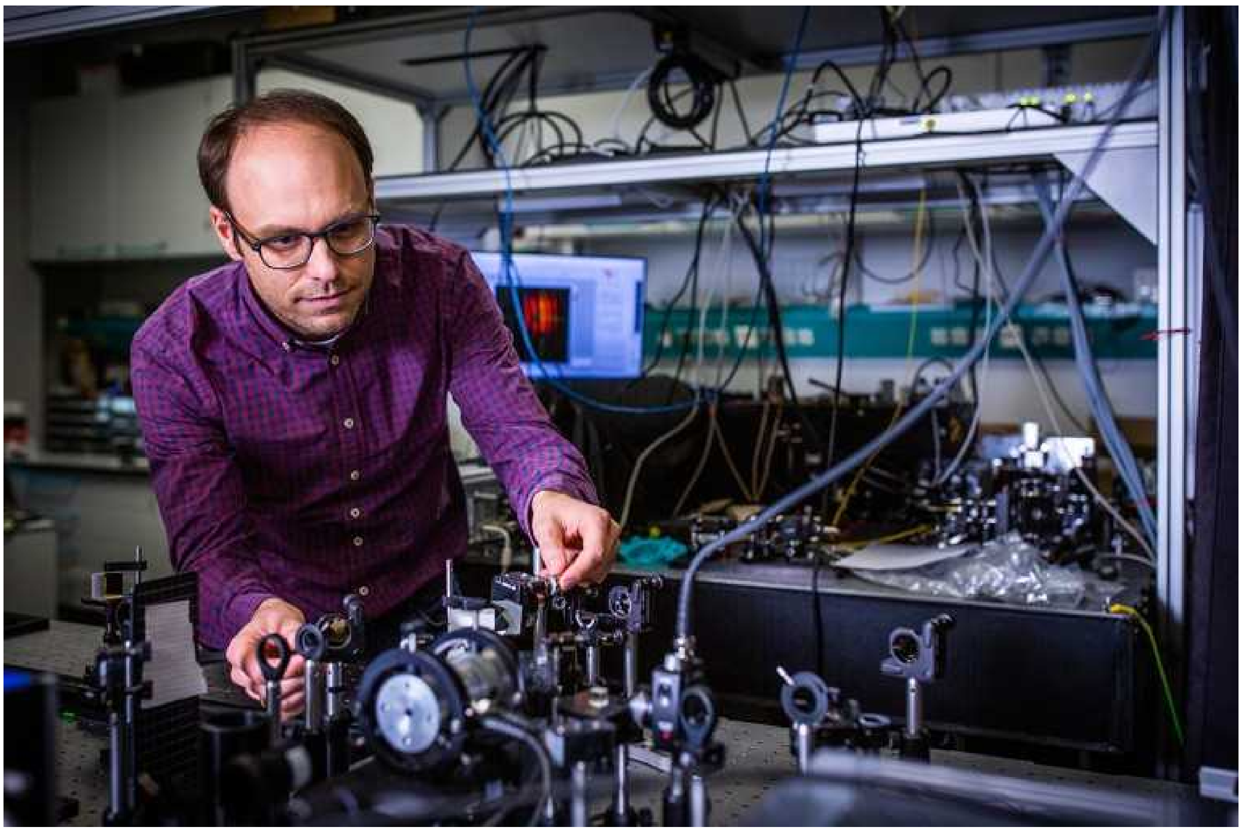
This article was downloaded by **calibre** from https://www.nature.com/articles/d41586-023-00345-1

- TECHNOLOGY FEATURE
- 07 February 2023
- Correction 07 February 2023

# Smart microscopes spot fleeting biology

Automated microscopes that adapt to each sample's quirks can capture elusive biological phenomena at high resolution.

- Jyoti Madhusoodanan



Physicist Robert Prevedel builds microscopes that can quickly measure neuron activity while adapting to movements in the live mouse brain. Credit:

EMBL

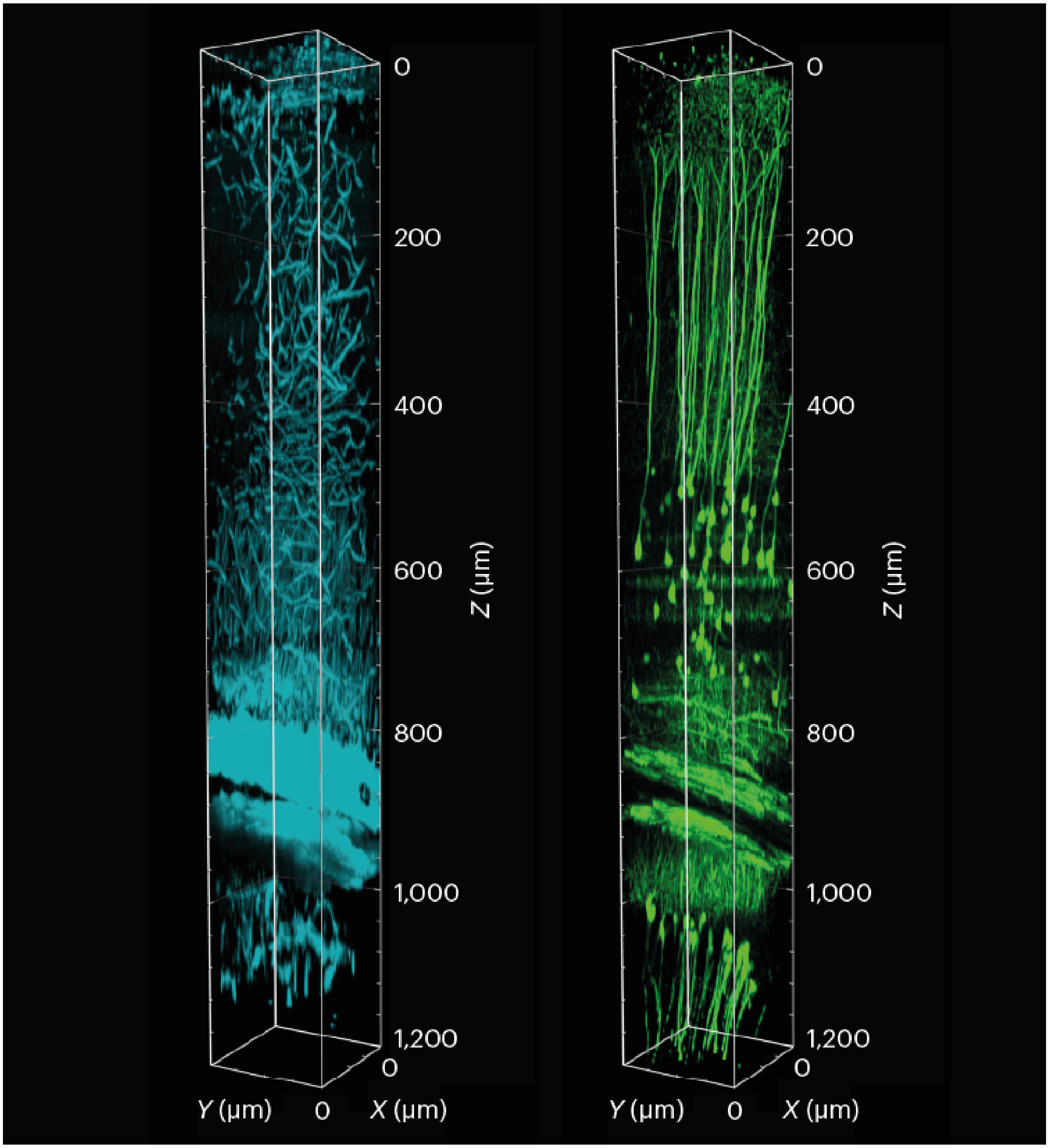
A mouse's heart beats roughly 600 times each minute. With every beat, blood pumping through vessels jiggles the brain and other organs. That motion doesn't trouble the mouse, but it does pose a challenge for physicist Robert Prevedel.

Prevedel designs and builds microscopes to solve research problems at the European Molecular Biology Laboratory in Heidelberg, Germany. In his case, the issue is how to capture neural activity deep inside the brain when the organ itself is moving. "The deeper we image, the more aberrations we accumulate," he says. "So, we have to build our microscope to quickly measure and adapt."

Typically, microscopes struggle to peer deeper than about one millimetre into tissues. Beyond that, light bouncing off intracellular structures creates distortions, blurring the images — even when the sample is not moving to a heartbeat.

In 2021, Prevedel and his colleagues engineered a microscope that combines an approach called three-photon fluorescence imaging, which is used to probe inside tissues, with an adaptive optical system. The latter strategy was first developed in astronomy, and directs light using mirrors and lenses made of deformable membranes instead of rigid optical materials. Software tools quickly alter the membranes' shapes in response to variations in the sample, bending light in specific ways to peek through surface structures. Rather than needing a human operator, this 'sample-adaptive' approach relies on the microscope itself adjusting the optics in real time to continually produce high-quality images.

Prevedel's microscope had to go one step further to compensate for the vibrations of the animal's pumping heart. By timing photos to the heartbeat, the team was able to image cells nearly 1.5 millimetres beneath the brain's surface in a region called the hippocampus, and 0.5 mm deeper than previous efforts[1]. "It was really exciting to see that it worked much farther down than we were expecting," Prevedel says.




A 3D reconstruction of a section of the mouse visual cortex and hippocampus, showing tissue structure (cyan) and neurons (green). The sample was imaged to a depth of 1.2 mm using three-photon fluorescence microscopy with an adaptive optical system.L. Streich *et al.*/*Nature Methods* (CC BY 4.0)

Prevedel’s microscope is just one of a suite of smart microscopes that rely on adaptive optical systems such as deformable membranes, coupled with machine-learning approaches, to peer deeper into tissues than ever before, and to zoom in at crucial moments to capture fleeting moments in the life of a cell.

Often involving custom-built hardware and software components that can make them inaccessible to the broader biological community, these efforts are producing tools that do more than just produce clear images. They’re also gentler on living systems, allowing researchers to observe prolonged processes without damaging their samples, thus expanding the reach of microscopy.

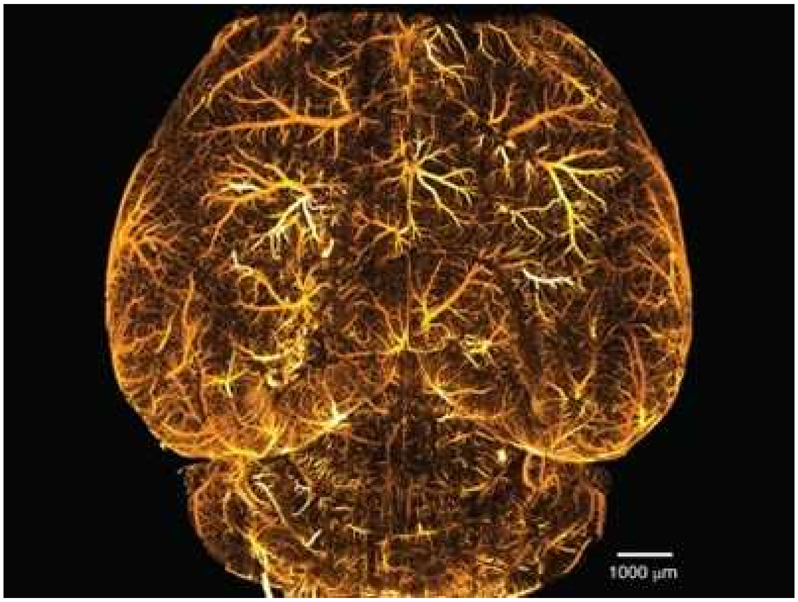
“If all your research involves looking at cells on slides, you don’t need adaptive microscopy,” says Martin Booth, an optical-systems engineer at the University of Oxford, UK. “But if you’re going tens or hundreds of micrometres deep into living specimens, that’s when this becomes really useful.”

## Sampling in space and time

For Kate McDole, now a developmental biologist at the MRC Laboratory of Molecular Biology in Cambridge, UK, the key consideration in designing her adaptive microscope was sample size.

As a postdoctoral fellow at the Howard Hughes Medical Institute’s Janelia Research Campus in Ashburn, Virginia, McDole and her colleagues developed a microscope to study how clumps of cells form complex tissues as the mouse embryo develops[2]. Led by developmental biologist Philipp Keller, the team wanted to image the developing embryo over three days, during which its diameter grows from about 200 micrometres to nearly 3 millimetres. Anchored on one end, the embryo, McDole says, is “free to sway in the breeze — it moves”, and its density and other optical properties change over time. “The microscope needed to keep up with all of that,” McDole says.

She and her colleagues started with a technique known as simultaneous multiview light-sheet microscopy, which Keller's team had developed to track cell movement in developing fruit-fly embryos. To adapt it for the mouse, they altered the optical design and built software to control such factors as the angle of the light source and the positions of optical elements. The software was able to gauge the data quality of the images as they were collected, and could tweak these factors to optimize images throughout the experiment.




[Microscopy made to order]

The microscope was also automated to detect the growing embryo's position in the sample chamber and keep it centred in the field of view, adjusting the distances to ensure consistent image quality. "A lot of biological specimens like to roam around, so you need to keep them centred," McDole says.

McDole and her team used this system to observe mouse embryo development over a 48-hour period, imaging the embryonic heart and other developing organs at single-cell resolution. They have subsequently imaged brain organoids for up to two weeks. "That's kind of the future of autonomous microscopy — letting the microscope decide when and where and how to act on specific events," McDole says. "You can teach the microscope: 'It's going to be 3:00 a.m. when this cell division happens, and I

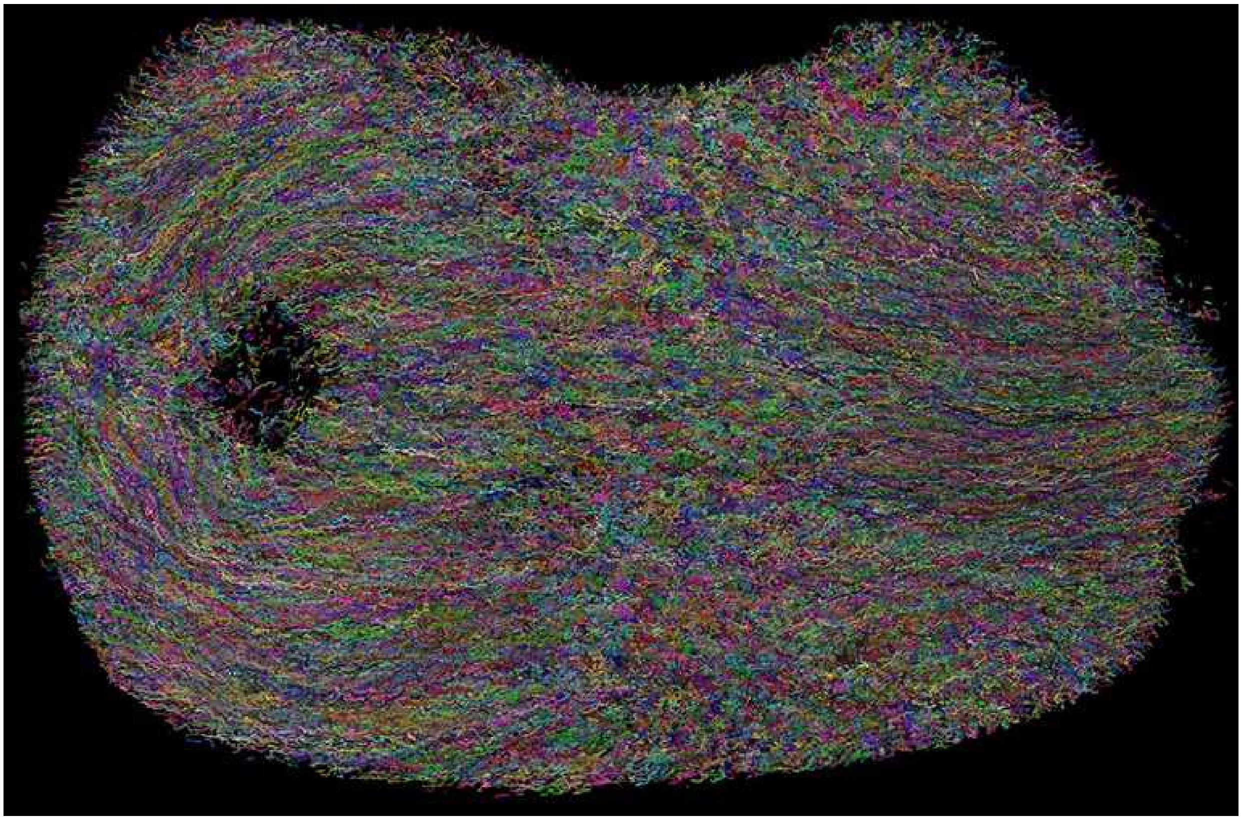
want you to zoom in and do something and then go back to normal imaging.'"

The Keller group has released schematics for building such an instrument, and the software is freely available online (see go.nature.com/3huukh9). Researchers who already use a light-sheet microscope can expect to spend about US$30,000 to add these capabilities to their system, Keller says. "It's a pretty small extra investment" to achieve deep-tissue, single-cell resolution, he notes.

## Subcellular scales

Smart microscopes are also being developed to image smaller structures. Physicist Ilaria Testa at the KTH Royal Institute of Technology in Stockholm, for instance, built one to observe subcellular vesicles as they release calcium at neural synapses when nerve cells fire — a key step in signal transmission. "These are rare events and it's not always easy to capture them," she says.

One option was to image a specimen continually in the hope of capturing the moment. But vesicle-release events are transient and the structures too small for standard microscopy. Super-resolution imaging can reveal more detail, but it requires high-intensity light sources that can be used only briefly before the sample is damaged. The team tried various time-lapse approaches, in which images are captured at regular intervals. But that, Testa says, was like watching a soccer match and missing a goal because you are looking elsewhere at the crucial moment. "It was a bit frustrating," she says. "The resolution would have been fine if we only knew where to look."



Individual cell tracks in a developing mouse embryo, imaged over 48 hours using adaptive light-sheet microscopy and a deep-learning algorithm for automated tracking.Credit: Kate McDole

To help them keep their eyes on the ball, Testa and her team combined two microscopy approaches: a fluorescent wide-field microscope and a form of super-resolution microscopy known as stimulated emission depletion (STED). They developed a software system to control these microscopy modes: when the software detected a change in fluorescence, the system would switch automatically to the higher-resolution STED mode. This allowed the team to capture — with nanometre precision — how cells reorganize their synaptic vesicles after releasing calcium[3]. “We’re basically guiding the acquisition of the image in a smarter way,” Testa says.

Testa and her team took about two years to build the microscope, she says, using mostly custom 3D-printed hardware. The only commercial component was the upper part that includes the eyepiece, known as the microscope head. The set-up cost about $200,000: most expensive were the lasers, which cost some $60,000. But the result is an automated system that works more

efficiently than a researcher trying to switch between microscopes, Testa says. “We’re actually delegating something that the computer can do much better than a human.” The set-up also reduces the effort required to home in on the fleeting moments of biology that really matter, Prevedel adds. “The microscope just acquires the few seconds that you really care about.”

## Expanded access

Testa’s software is available on GitHub and her team has published the hardware schematics[3], so the microscope could — in principle — be used by anyone. But it requires a super-resolution microscope, which not all labs are able to access, particularly in resource-poor regions of the world, she points out.

For now, researchers using sample-adaptive approaches tend to collaborate with colleagues who can build or modify custom microscopes. But when it comes to DIY projects, software and instrument tweaks are often required, notes Booth. The Keller team spent months identifying the best metrics and computational strategies to use in their adaptive microscope, McDole says. Even so, the equipment is often constantly changing, and “users require significantly more training than on your standard commercial microscope”, she says.



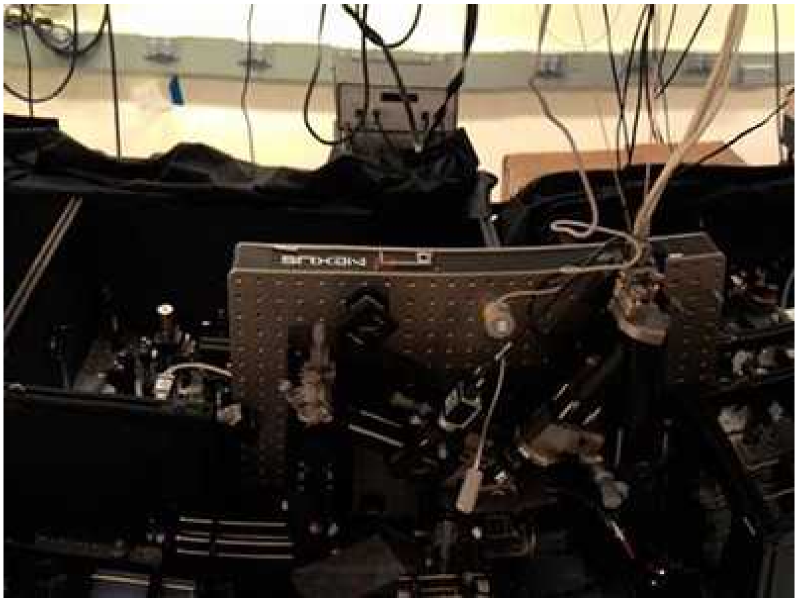
## Microscopy: hello, adaptive optics

Biologists wanting to team up with engineers to access custom microscopes might only be able to do so at large, well-funded universities and research centres. Cell biologist Ricardo Henriques was keenly aware of this issue because of his experiences working in the United Kingdom and South Africa during his graduate studies.

“Almost everything that we’ve done in terms of creating technology has been designed to be accessible to everyone,” says Henriques, who now leads a research group at the Gulbenkian Institute of Science in Lisbon in his native Portugal. “We are particularly sensitive to the fact that there’s a big difference between the global south and the global north when it comes to accessing these resources.”

In 2016, Henriques and his team devised a computational method called super-resolution radial fluctuations (SRRF) to extend super-resolution microscopy to conventional fluorescence microscopes, which are generally widely accessible[4]. The method now relies on a machine-learning approach that adapts the microscope to acquire images at high speeds and then parse the data to identify sample-specific blips in fluorescence. Users capture 100 images of their sample at high speeds to minimize chemical damage to fluorescent labels, known as bleaching, as well as to reduce blurring from movements. The data are then fed into an algorithm that looks for variations in fluorescence.

The fluorescent molecules, or fluorophores, that are used to label cellular structures fluctuate in brightness depending on their location and other sample properties. “Every time [the algorithm] picks up a fluctuation, it’s able to pinpoint the exact centre of the fluctuation and if it’s coming from a fluorophore or not,” Henriques explains. “So, it generates something that’s crisper than the original.”



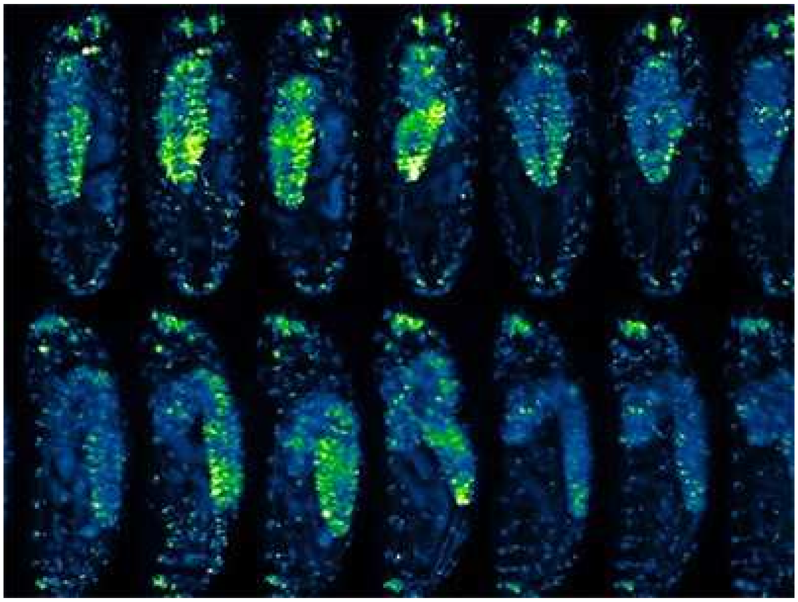
Lattice light-sheet microscopy gets an AO upgrade

Microscopist Adán Guerrero at the National Autonomous University of Mexico's National Advanced Microscopy Laboratory in Cuernavaca was one of the first researchers to adopt the SRRF method, choosing it to explore the subcellular location of a bacterial protein[5]. Guerrero's institute had super-resolution microscopes at the time, but users often had to wait weeks to use them. Because Henriques and his team had released their SRRF tool as a plug-in for the image-processing program ImageJ, it could be used with the institute's readily available microscopes, making the tool especially practical, Guerrero says. The plug-in element was also valuable, he adds, because his users were uncomfortable doing their own coding. "There were other, similar technologies published earlier or around the same time, but the speed of getting data and the plug-in made SRRF more accessible."

The possibility of obtaining higher-quality images without the need for expensive instrumentation has made a huge difference to his research community, Guerrero adds. But users must still cross-validate their images with other techniques, such as biochemical studies or electron microscopy, to avoid mistakes, warns Caron Jacobs, an imaging scientist at the University of Cape Town in South Africa.

For instance, when Jacobs was a graduate student in Henriques' lab, she tried to image how HIV engages with protein receptors on the surfaces of the

immune cells that the virus infects, called T cells. After using SRRF, Jacobs and her colleagues saw a distinct "honeycomb-like lattice" — but the protein receptors, the team knew, were actually evenly distributed. "As we saw the honeycomb pattern, we knew it was an artefact," Jacobs says. "But if you don't know the underlying biology, there's a danger of thinking it's real."



The microscope makers putting ever-larger biological samples under the spotlight

Henriques' team has developed another computational tool called SQUIRREL (super-resolution quantitative image rating and reporting of error locations) that allows users to check their images for such artefacts[6]. But similar problems can occur with any computationally intense microscopy technique, says Jacobs, who now helps biologists to image a wide range of samples. When students approach her for advice on super-resolution or other microscopy techniques, Jacobs encourages them to think about the data they want. "If you drill down to the scientific question, nine times out of ten they don't need either [approach] — just good wide-field microscopy and sample-preparation strategies."

But if a sample proves to be especially sensitive, or the biology seems difficult to pin down or you're sifting through reams of data to find one interesting moment, it might be worth considering an adaptive approach, Prevedel says.

# A toolkit for all

In principle, sample-adaptive systems would be neatly bolted on to existing microscopes, but the adaptive optical element is currently too large to fit on to commercial microscopes, Booth says. “It’s been a challenge because of the physical constraints,” he says. “You already have a designed microscope and you’ve got to somehow add these optics in the middle of it.”

Costs for the devices can range from $20,000 to $50,000, so will have to get cheaper to make such tools widely accessible, he adds. The software required to control adaptive optics needs to improve, too. “There are several things that limit the wider use of these techniques,” says optical engineer Fabrice Harms, who works at Imagine Optic in Paris, one of a handful of companies that produces various sample-adaptive systems. But most cannot switch between modalities, as Testa’s microscope does, for instance. “A robust system that is able to deliver a better image under any imaging conditions is not something that’s currently been industrialized,” Harms says.

If those barriers can be overcome, says Booth, the technology’s reach can grow. Not everyone will need it, but for those who do, smart microscopes that can adjust to the samples under their lenses can make the difference between experimental success and failure. “If people are happy with their data, there’s no need to change anything,” Prevedel says. “But if you’re getting very frustrated with your data, then you should consider a sample-adaptive approach.”

*Nature* **614**, 378-380 (2023)

*doi: https://doi.org/10.1038/d41586-023-00336-2*

## Updates & Corrections

- **Correction 07 February 2023**: An earlier version of this article gave the wrong caption for the image of individual cell tracks in a developing mouse embryo.

# References

1. Streich, L. *et al. Nature Methods* **18**, 1253–1258 (2021).
2. McDole, K. *et al. Cell* **175**, 859–876 (2018).
3. Alvelid, J., Damenti, M., Sgattoni, C. & Testa, I. *Nature Methods* **19**, 1268–1275 (2022).
4. Gustafsson, N. *et al. Nature Commun.* **7**, 12471 (2016).
5. Vega-Cabrera, L. A. *et al. PLoS ONE* **12**, e0172737 (2017).
6. Culley, S. *et al. Nature Methods* **15**, 263–266 (2018).

---

This article was downloaded by **calibre** from https://www.nature.com/articles/d41586-023-00336-2

| Section menu | Main menu |

- WHERE I WORK
- 06 February 2023

# This baby turtle surprised scientists by swimming against the current

Satellite transmitters help Cristina Miranda to understand the movements and habitats of endangered hawksbill sea turtles in the eastern Pacific Ocean.

- Virginia Gewin



Credit: Felipe Vallejo/Equilibrio Azul

In 2008, I had just begun volunteering at Equilibrio Azul — a non-profit marine-research and -conservation organization based in Quito — when

colleagues discovered a hawksbill sea turtle (*Eretmochelys imbricata*) nesting at La Playita beach in Ecuador. The eastern Pacific population of hawksbill sea turtles is one of the most endangered in the world and was considered functionally extinct in the region before this turtle and others were observed.

That discovery was a tipping point for hawksbill research in Ecuador and throughout the Pacific Ocean. Since 2008, we've found about 20 nests each year at La Playita, and one season, we documented 50.

We have tagged 11 adult females with satellite transmitters. Previously, most of our understanding of these turtles had been based on observations in the Caribbean, where the reptiles are strictly coral-reef dwellers. But Ecuador's reefs are mostly rocky, with patches of coral, and we were surprised to see females migrate south to mangroves, mainly for food.



Women in science

In this image, we have just attached a transmitter to a baby turtle — a first for hawksbill turtles this young and in the eastern Pacific region. We did not know much about hawksbills at this young age. It is tricky working with baby turtles, because they grow very fast, and the transmitters, which give us location data, can easily fall off. We've used cement to glue the devices to the shells of six newborns so far. The longest the transmitters have lasted is

three months and the shortest period was only six weeks — but the devices provided our first insights into the ‘lost years’ of sea-turtle biology.

Our findings have overturned assumptions that neonates were just carried along by currents. Instead, we found that one-day-old turtles can swim against the current. They aim for a specific direction — north by northwest — as they learn to dive and swim. We tracked one-year-old hawksbills to Costa Rican waters, a journey of roughly 2,000 kilometres, before we lost their signal.

Cristina Miranda is a scientific coordinator at Equilibrio Azul in Quito, Ecuador. Interview by Virginia Gewin.

*Nature* **614**, 382 (2023)

*doi: https://doi.org/10.1038/d41586-023-00335-3*

---

This article was downloaded by **calibre** from https://www.nature.com/articles/d41586-023-00335-3

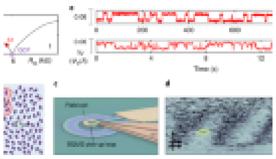
# Research

- **Coherent correlation imaging for resolving fluctuating states of matter** [18 Jan 2023]
  • Nanoscale magnetic fluctuations are spatiotemporally resolved beyond conventional resolution limits using coherent correlation imaging, in which frames in Fourier space are recorded and analysed using an iterative hierarchical clustering algorithm.
- **Biomolecular analyses enable new insights into ancient Egyptian embalming** [01 Feb 2023]
  • Philological analysis of labels and instructions, together with gas chromatography–mass spectrometry analysis of residues on vessels recovered from a 26th Dynasty embalming workshop at Saqqara, Egypt provide insights into ancient Egyptian embalming practices.
- **Mesolimbic dopamine adapts the rate of learning from action** [18 Jan 2023]
  • Analysis of data collected from mice learning a trace conditioning paradigm shows that phasic dopamine activity in the brain can regulate direct learning of behavioural policies, and dopamine sets an adaptive learning rate rather than an error-like teaching signal.
- **Stigma receptors control intraspecies and interspecies barriers in Brassicaceae** [25 Jan 2023]
  • A signalling mechanism ensuring intraspecies and interspecies reproductive barriers in flowering plants is uncovered.
- **Phenotypic signatures of immune selection in HIV-1 reservoir cells** [04 Jan 2023]
  • A proteogenomic profiling analysis of single cells from the blood and lymph nodes of individuals living with HIV-1 reveals that CD4+ memory T cells harbouring intact provirus show signatures associated with resistance to immune-mediated killing and cell survival.
- **HIV silencing and cell survival signatures in infected T cell reservoirs** [04 Jan 2023]
  • HIV-infected memory CD4 T cells under antiretroviral therapy are a distinctive population of cells with transcriptomic patterns that favour HIV silencing, cell survival and cell proliferation.
- **mRNA ageing shapes the Cap2 methylome in mammalian mRNA** [01 Feb 2023]

• Cap2 methylation increases on transcripts as they age, reducing activation of innate immunity.

---

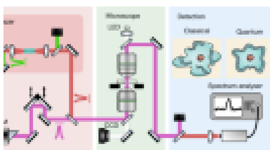
| Next section | Main menu | Previous section |



## Imaging quantum fluctuations near criticality

20 August 2018

A. Kremen, H. Khan, … B. Kalisky



## Quantum-enhanced nonlinear microscopy

09 June 2021

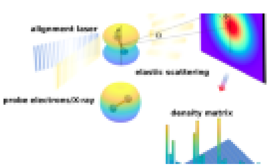
Catxere A. Casacio, Lars S. Madsen, … Warwick P. Bowen



## Ultrafast current imaging by Bayesian inversion

06 February 2018

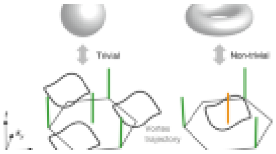
S. Somnath, K. J. H. Law, … R. K. Vasudevan



## Quantum state tomography of molecules by ultrafast diffraction

14 September 2021

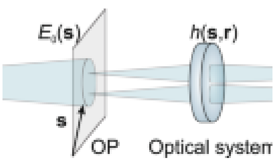
Ming Zhang, Shuqiao Zhang, … Zheng Li



## [Measuring topology from dynamics by obtaining the Chern number from a linking number]

15 April 2019

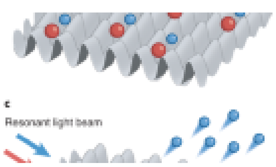
Matthias Tarnowski, F. Nur Ünal, … Christof Weitenberg




## [Lost photon enhances superresolution]

09 August 2021

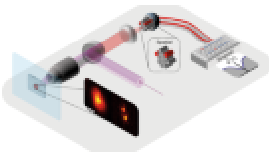
A. B. Mikhalychev, P. I. Novik, … D. S. Mogilevtsev



## [Microscopes go molecular]

11 August 2022

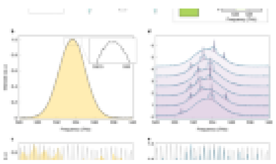
Christof Weitenberg



[Super-resolution with quantum light](#)

24 January 2019

Andrew Forbes & Valeria Rodriguez-Fajardo



[Spectral super-resolution spectroscopy using a random laser](#)

02 December 2019

Alice Boschetti, Andrea Taschin, … Diederik S. Wiersma

- Article
- Open Access
- Published: 18 January 2023

# Coherent correlation imaging for resolving fluctuating states of matter


- Christopher Klose,
- Felix Büttner ,
- Wen Hu ,
- Claudio Mazzoli,
- Kai Litzius,
- Riccardo Battistelli,

- Ivan Lemesh,
- Jason M. Bartell,
- Mantao Huang,
- Christian M. Günther,
- Michael Schneider,
- Andi Barbour,
- Stuart B. Wilkins,
- Geoffrey S. D. Beach,
- Stefan Eisebitt &
- …
- Bastian Pfau

Show authors


*Nature* **volume 614**, pages 256–261 (2023)


- 3833 Accesses

- 146 Altmetric

- Metrics details


## Abstract

Fluctuations and stochastic transitions are ubiquitous in nanometre-scale systems, especially in the presence of disorder. However, their direct observation has so far been impeded by a seemingly fundamental, signal-limited compromise between spatial and temporal resolution. Here we develop coherent correlation imaging (CCI) to overcome this dilemma. Our method begins by classifying recorded camera frames in Fourier space. Contrast and spatial resolution emerge by averaging selectively over same-state frames. Temporal resolution down to the acquisition time of a single frame arises independently from an exceptionally low misclassification rate, which we achieve by combining a correlation-based similarity metric[1,2] with a modified, iterative hierarchical clustering algorithm[3,4]. We apply CCI to study previously inaccessible magnetic fluctuations in a highly degenerate magnetic stripe domain state with nanometre-scale resolution. We uncover

an intricate network of transitions between more than 30 discrete states. Our spatiotemporal data enable us to reconstruct the pinning energy landscape and to thereby explain the dynamics observed on a microscopic level. CCI massively expands the potential of emerging high-coherence X-ray sources and paves the way for addressing large fundamental questions such as the contribution of pinning[5,6,7,8] and topology[9,10,11,12] in phase transitions and the role of spin and charge order fluctuations in high-temperature superconductivity[13,14].

# Main

The difficulty of imaging stochastic processes traces back to a conceptual dilemma: to gain spatiotemporal resolution, both full-field and scanning imaging approaches must distribute the detected signal over thousands of pixels. Thus, the better the spatial resolution targeted the larger the signal needed. But the number of sample–probe interactions per volume and time is limited—not only owing to source, optics and detector constraints, but ultimately owing to sample perturbations such as heating, strain, electronic excitations, contrast bleaching, and even sample destruction[15,16]. High spatial resolution therefore requires extensive temporal signal averaging. If, by lack of better knowledge, this averaging is indiscriminate, it leads to a loss of temporal resolution and to motion-blurred images. Under certain conditions, one may recover characteristic spatiotemporal 'modes' of a dynamic system beyond this conventional temporal resolution limit. However, mode decomposition only enhances the signal-to-noise ratio of modes that repeat in time[17,18]; denoising of irregular temporal signals is beyond its scope[18]. Alternatively, mixed-state ptychography may be used to reconstruct static images of the most visited states within the averaging time period[19]. In any case, if the actual sequence of events is of interest, the trade-off between spatial and temporal resolution appears to be fundamental.

CCI overcomes this limit. The key idea is to record snapshots of Fourier-space coherent scattering patterns as raw data, and to exploit that even at low photon count—where imaging is not possible—each scattering pattern contains speckle fingerprints of the real-space state of the system. By combining developments in photon-correlation spectroscopy, nanoparticle

tomography[1,2] and genome research[3], we use this sensitivity to accurately classify the state of each snapshot, and hence the timestamps of each state, in a sequence of thousands of frames. Spatial resolution arises independently from the informed average of same-state scattering patterns, which we here convert to real-space images by holographically aided phase retrieval (see Methods). CCI allows us to discover rich fluctuation dynamics in an otherwise well-explored magnetic material, which illustrates the breadth of unexpected physics hidden in fluctuating states of matter and highlights the power of CCI in exploring this territory.

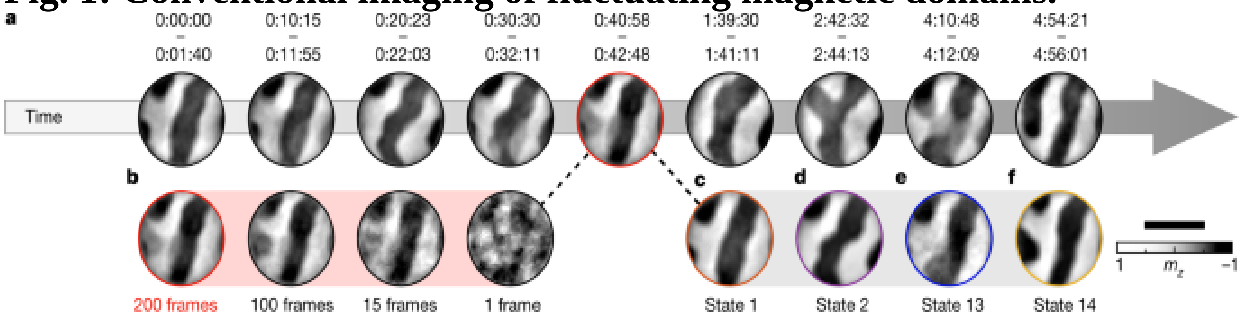
To develop and demonstrate CCI, we study a textbook example of a fluctuating state of matter[20,21]: the finite temperature dynamics of a highly degenerate magnetic ground state. We focus on meandering domains[22] in a [Pt (2.7 nm)/$Co_{60}Fe_{20}B_{20}$ (0.8 nm)/MgO (1.5 nm)]$_{\times 15}$ multilayer[23]—a low-pinning, thin-film perpendicular-magnetic ferromagnet, which represents a class of materials widely consideredas a platform for future information technologies[24]. Because of the low pining in the material, thermal activation is expected to drive magnetic configuration transitions in this system, which is not only critical for any information encoded but also fundamentally a largely unexplored field.

Here, we investigate the nature of such magnetic configuration fluctuations by recording a nearly continuous sequence of snapshots of the out-of-plane magnetization component $m_z(\mathbf{x}, t)$ in a fixed field of view and at a constant cryostat temperature of 310 K ($\mathbf{x}$ is the spatial coordinate and $t$ is the time interval of the snapshot). Snapshots $I(\mathbf{q}, t)$ were recorded in momentum space ($\mathbf{q}$ is the photon momentum transfer) by resonant X-ray scattering in forward geometry combined with a holographic mask to robustly reconstruct real-space images of $m_z(\mathbf{x}, t)$ by phase retrieval. For technical details, see Methods.

Figure 1a shows images of the natural evolution of $m_z(\mathbf{x}, t)$ reconstructed from successive averages of 200 snapshots (camera frames). Most images show almost binary black-and-white contrast, and the resulting patterns can be interpreted as static maze-like domains of $m_z$, interrupted only by the expected domain wall regions of vanishing contrast. However, as time progresses, these domain states change. Their thermal dynamics is mostly

characterized by a gradual evolution of the domain wall network. Surprisingly, the dynamics is discrete (the magnetic states $\{{m}_{z}^{i}({\bf{x}}),i=1,2,3,\ldots \}$ are countable) and recurring (the same states are revisited after a random set of intermediate states).

**Fig. 1: Conventional imaging of fluctuating magnetic domains.**



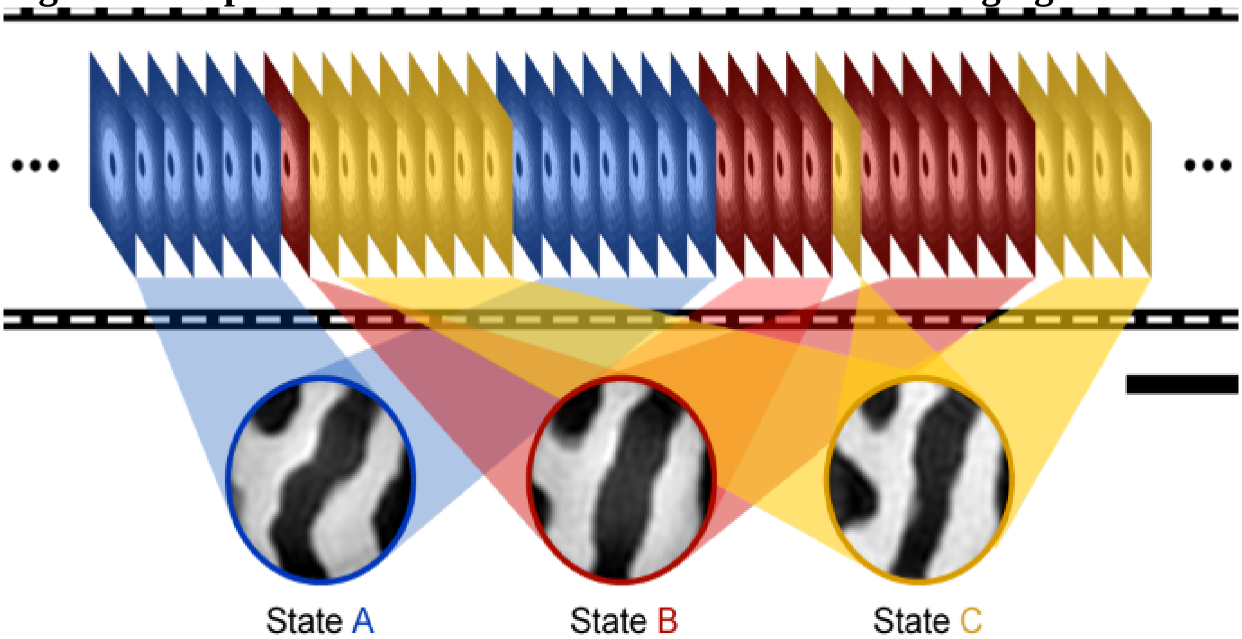

**a**, Example images of the thermally evolving magnetic maze domain states at 310 K. Each image has been reconstructed by Fourier-transform holography from scattering data sequentially averaged over the indicated time intervals. High-contrast regions indicate stationary behaviour of the local out-of-plane magnetization $m_z$, and grey features correspond to unresolved dynamics during the averaging period. **b**, Example images reconstructed from averages of fewer frames. **c**–**f**, Disentangled magnetic domain states corresponding to the time interval of **b**. The domain states were identified and reconstructed using CCI. Scale bar, 500 nm.

Some images contain regions of grey contrast, which suggests that the image is a superposition of dynamically evolving domain states. One can attempt to resolve the intermediate dynamics by averaging fewer exposures (Fig. 1b). However, this comes at a loss of image resolution and contrast. Indeed, we find that without increasing the incident intensity to a perturbative regime, it is impossible to temporally resolve the superimposed magnetic states (Fig. 1c–f) forming Fig. 1b in the traditional way of blindly averaging successive frames.

CCI can solve this dilemma, as sketched in Fig. 2, by classifying all scattering patterns prior to any spatial or temporal averaging by their underlying domain states. High-resolution real-space images of the pure domain states ${m}_{z}^{i}({\bf{x}})$ can then be reconstructed from an informed signal average ${\langle I({\bf{q}},t)\rangle }_{t| {m}_{z}}$

({\bf{x}},t)={m}_{z}^{i}({\bf{x}})}\). By contrast, temporal resolution emerges from the precision by which each snapshot, and hence timestamp, is assigned to the correct state. The temporal resolution of CCI is hence independent of the spatial resolution, that is, the captured *q* range, but instead depends on the similarity between states, the speckle contrast, the exposure time, and on the precision (jitter) of the recorded timestamps.

**Fig. 2: Principle of time-resolved coherent correlation imaging.**

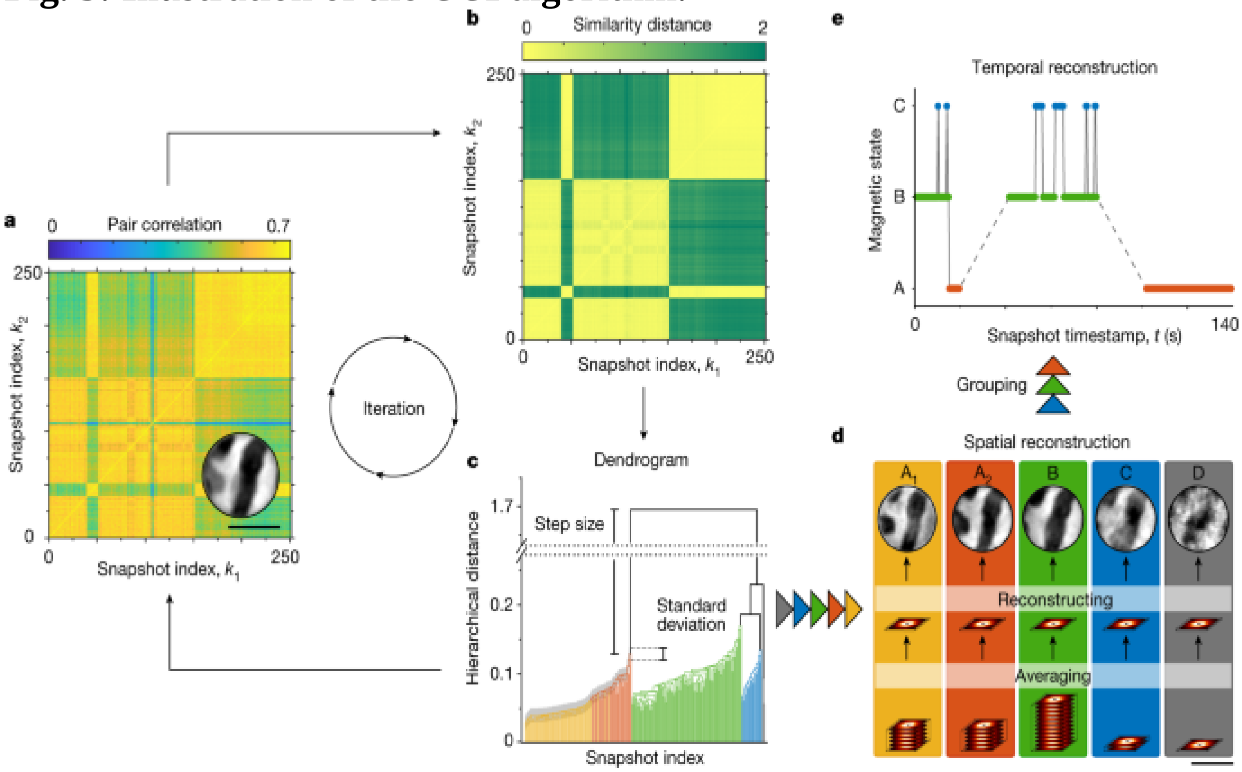



Top, sequence of camera frames showing Fourier-space coherent scattering patterns. Coherent correlation imaging classifies scattering frames by their underlying domain state, as indicated by the colours. Bottom, real-space images reconstructed from an informed average of same-state frames. Scale bar, 500 nm.

The classification of snapshots is based on a low-noise measure of similarity, or ‘distance’, between snapshots and is performed in three phases, as shown in Fig. 3. First, based on clustering[4] known from gene identification[3], we obtain an as-complete-as-possible set of magnetic domain configurations encoded in the ensemble of all snapshots. Second, we evaluate the misclassification error of assigning single frames to these domain configurations as a function of the similarity between the configurations. And third, based on an acceptable misclassification error threshold defined by the physics of interest (here we use an error of less than 1%), we group

similar domain configurations until the assignment error between frames and groups is below this acceptable threshold. We call the groups ‘states’ because we can resolve them in space and time, and the configurations within the groups ‘internal modes’ to emphasize that they are resolved in space but not in time. For details, see Methods and Extended Data Figs. 2–6.

**Fig. 3: Illustration of the CCI algorithm.**

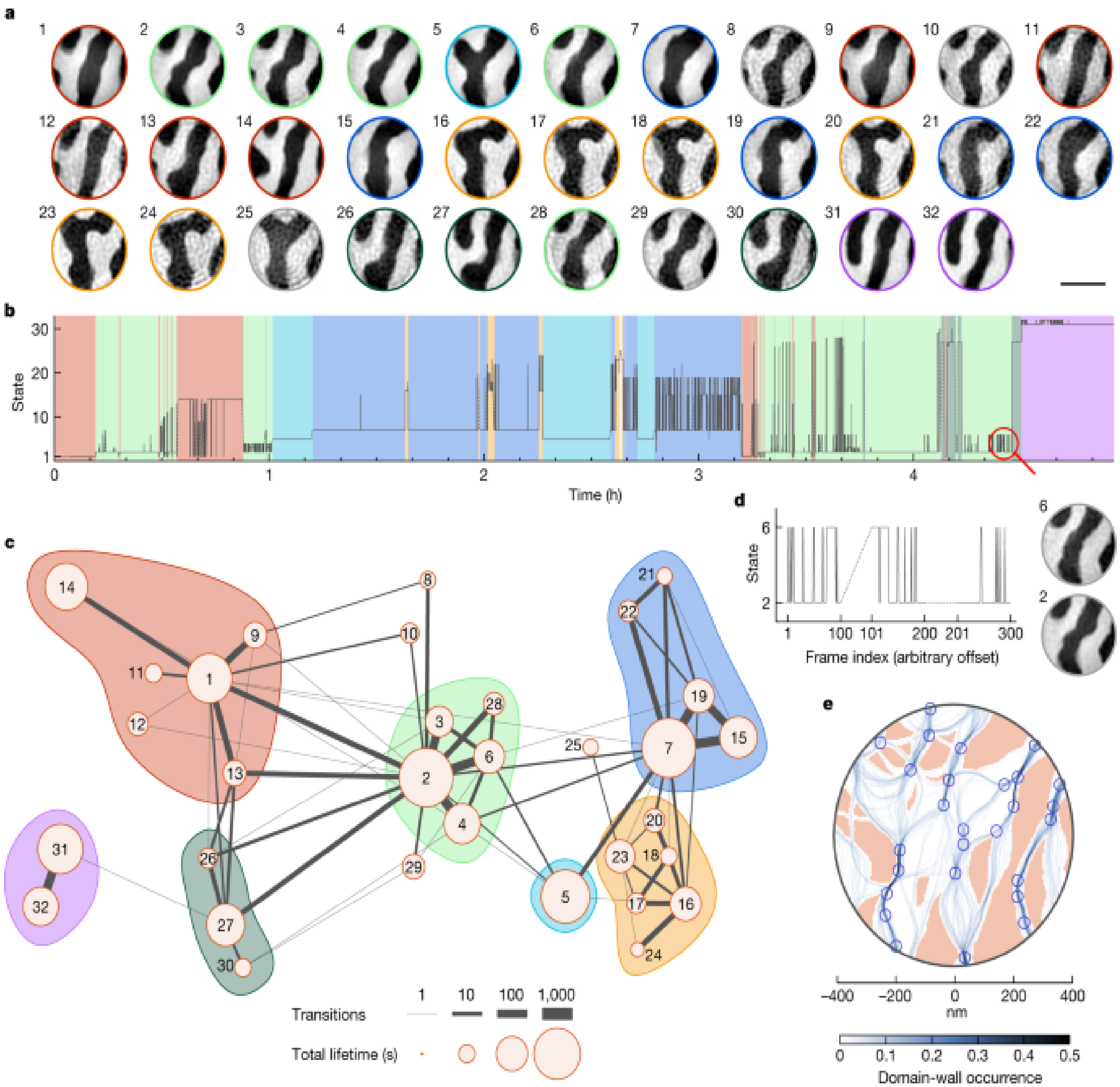



**a**, Pair correlation map of an exemplary set of 250 camera snapshots. The inset shows the magnetic image reconstructed from the sequential average of all 250 snapshots. **b**, Similarity distance derived from the normalized pair correlation of the pattern in **a**. **c**, Dendrogram calculated from **b** by an agglomerative, hierarchical clustering algorithm. Natural divisions are identified by exceptionally large inconsistencies between the vertical step size and the standard deviation of lower-level links, as indicated by the colour. The complete separation into the clusters in **d** is performed iteratively as indicated. See Methods for details. **d**, Spatially resolved set of domain configurations reconstructed from an informed average of all snapshots of each cluster. **e**, Reconstructed temporal evolution of states, as obtained by grouping domain configurations from **d**, that is, by grouping the internal

modes $A_1$ and $A_2$. Dashed lines indicate times without data points. Scale bars, 500 nm.

Overall, CCI assigns 99.5% of our 28,800 frames to one of 32 temporally resolved states (Fig. 4a and supplementary video 1), which are composed of 72 internal modes (Extended Data Figs. 4, 6, and supplementary video 2). The dynamics of these states is surprising in several aspects, as summarized in Fig. 4. Already their temporal sequence, depicted in Fig. 4b, reveals unexpected behaviour. First, unlike previously reported thermally activated processes in magnetic materials (such as two-state hopping[20,21,25,26], domain wall creep motion[27], Barkhausen reversal[20,28], and Brownian motion of skyrmions[29]), the dynamics observed is neither cyclic nor evolving, at least not at the timescales resolved here. Second, the number of states is slowly growing, but the dynamics is largely confined to the already explored set of states. And third, we find no obvious temporal order, such as repeating sequences or a preferred switching frequency. Instead, rapid oscillations often randomly follow extended calm periods, and a given state (for example, state 2) can sometimes be stable for tens of minutes and at other times perform excessive hopping on subsecond timescales, see Fig. 4b,d. Assuming that the existence of internal modes does not interfere with the concept of ‘lifetime’ of a state as a whole, this behaviour is incompatible with the established picture of Arrhenius activation over a fixed energy barrier, where longer lifetimes are expected to be exponentially suppressed. Instead, this observation suggests a dynamic energy landscape due to correlation effects of the multi-domain state.

**Fig. 4: CCI resolved dynamics of the fluctuating domain network.**




**a**, Real-space images of all domain states. The circular coloured borders refer to the agglomerates indicated in **c**. **b**, Temporal evolution of the states. The background shades refer to the agglomerates. Dashed lines indicate times without data points. **c**, Transition network of the domain configurations. The distance between nodes approximately represents the Pearson distance of the corresponding states. The width of the connecting lines indicates the number of observed pair transitions. The diameter of the circular orange contours illustrates the total observed lifetime of each state. Background colours highlight state agglomerates. **d**, Magnification of the region marked with a magnifying glass in **b**. The displayed real-space

images were reconstructed exclusively from the corresponding set of frames. **e**, Map of attractive (blue dots) and repulsive (red areas) pinning sites. The background shows the position of the domain walls and their relative occurrence in the internal modes. Scale bar, 500 nm.

A more detailed picture of the dynamics emerges when considering the similarity distance of transitions, as shown in the transition network in Fig. 4c. The extent of the network in this similarity space remains almost constant after state 7 (states are numbered by occurrence), which underlines the non-evolving character of the dynamics. More importantly, however, the hopping frequency is not obviously linked to the hopping distance (compare, for example, states 2, 3, 4, 27). Instead, an underlying order arises if we combine the distance and the frequency of transitions observed (see Methods). With this metric, the network separates into agglomerates, see Fig. 4b,c. Transitions within these agglomerates are much more common than between them. Interestingly, many agglomerates are centred around one or a few ‘linker states’ that mediate most of the intra- and inter-agglomerate transitions, for example, states 1, 2 and 7.

Although the time and spatial frequency domain data are sufficient to extract many relevant features of the dynamics (Fig. 4b,c), spatial and spatiotemporal imaging is key to understanding the microscopic mechanism underlying these observations. Figure 4e illustrates the level of detail that is accessible from real-space data. First, from the spatially resolved internal modes, we can reconstruct a map of possible domain-wall pathways in the field of view (Fig. 4e and Extended Data Fig. 7c). These paths fan out in some parts of the sample whereas in others their distribution collapses to a single point—a behaviour reminiscent of a snaring guitar string. Following this analogy, we identify the points where many domain-wall paths merge as attractive pinning sites (see Methods and Extended Data Fig. 7d for the exact criteria). The distribution of attractive pinning sites is shown in Fig. 4e.

In addition to attractive pinning sites, our data also point to the presence of repulsive interactions that restrict the positions of domain walls. Specifically, we find extended areas where no quasistatic domain wall configurations were observed during the acquisition. Often, even straight-line connections between attractive pinning sites are missing. From the spatiotemporal data we can extract how often $m_z$ has switched in these areas (see Extended Data

Fig. 7e) and hence estimate how easily they can be traversed by a domain wall. Combining this information, we have identified the strongest repulsive pinning sites, as shown in Fig. 4e.

We are now in a position to explain the physics behind the dynamics observed. At the core of it is the conceptual difference between attractive and repulsive pinning sites that derives from a strong topological constraint: domain walls cannot end in the interior of a material. As illustrated in Extended Data Fig. 8, this constraint implies that for domain walls, attractive pinning sites have a point-like action (domain walls are pinned most strongly to the bottom of a depression in the energy landscape), whereas repulsive pinning sites have a two-dimensional character (energetically elevated areas are avoided entirely). This difference explains the separation of the dynamics into agglomerates. Specifically, inter-agglomerate transitions are predominately associated with hopping over one or more repulsive pinning sites, whereas most intra-agglomerate transitions involve only attractive pinning sites (see Extended Data Fig. 9, where we also show exceptions from this rule). Owing to their area-shaped action, repulsive pinning sites add an energetic cost to an entire domain wall section during a transition. Likewise, they inhibit ‘zipper-type transitions’, that is, one-by-one reordering of a domain wall between multiple attractive pinning sites. These conceptual differences lead to lower activation energies of intra-agglomerate transitions and therefore explain why they occur more frequently than inter-agglomerate ones. Moreover, the fragmentation of the material by extended prohibited areas explains why we observe such a small number of states out of all the possibilities to connect the attractive pinning sites. Finally, the seemingly chaotic time trace can be attributed to the intrinsic long-range stray-field interactions, which add a nonlocal, configuration-dependent contribution from areas outside the field of view to the energy landscape.

Stochastic dynamics are very common in systems with spatially varying order parameters. Examples include domain fluctuations in antiferromagnets[30,31], fluctuations of spin and charge density waves in high-transition-temperature ($T_c$) superconductor materials[13,14], the dynamics of frustrated systems such as artificial spin-ice materials[32,33], thermally activated motion of crystallographic domain boundaries[34], as well as virtually any dynamics during or close to a phase transition. These collective

dynamics at the nanometre scale provide, on one hand, an exciting playground in which to explore the underlying—often competing—fundamental interactions, and, on the other hand, to exploit the richness of the emerging physics for advanced devices. Many of such phenomena were previously studied by coherent X-ray or electron scattering experiments, but, with a few exceptions, not via high-resolution real-space imaging owing to insufficient signal on a timescale faster than the relevant dynamics or the state lifetimes. Hence, many details uniquely accessible by time-resolved imaging—such as the shape, morphology, connectivity and topology of locally ordered regions, the dynamics of these properties, and their relation to material inhomogeneities—have remained unexplored, preventing a fundamental understanding of the underlying materials physics. CCI now enables such direct imaging research, at least for all those systems which are currently investigated in reciprocal space and which return, within the duration of the experiment and within a limited field of view, to the same configuration or a close approximation thereof (such that 'binning' into a discrete set of 'states' is possible).

CCI is a natural extension of any reciprocal-space coherent imaging technique and may be combined with mode decomposition techniques to analyse the resulting real-space dynamics[18] or to eliminate timing uncertainties of the nominal time stamps of the reconstructed images[17]. CCI is applicable to fully or partially coherent sources from visible light to soft or hard X-rays or even electrons, both in transmission and reflection geometries[35], and requires no modification of existing coherent imaging set-ups. Moreover, CCI promises a change of paradigm in time-resolved imaging at sources such as free-electron X-ray lasers and high-harmonic generation sources, where a single probe pulse may carry enough information to identify a state, in particular when combined with few-photon correlation techniques[2] and machine-learning classification[36]. Under such conditions, CCI overcomes the triggerability and repeatability limitations of pump–probe schemes and enables nonperturbative imaging of both equilibrium and nonequilibrium dynamics. In conjunction with the next generation of free-electron X-ray lasers running at MHz repetition rates, real-time imaging with submicrosecond temporal resolution as well as nondestructive pump–probe imaging with femtosecond resolution and wavelength-limited spatial resolution will be feasible. This advancement is

illustrated in Extended Data Table 1, where CCI is compared to existing coherent imaging techniques.

Our results demonstrate that coherent scattering signals encode enough information to overcome the long-standing dilemma between spatial and temporal resolution. By means of CCI, the spatiotemporal evolution of a system is now accessible from such coherent scattering data down to the single-frame acquisition limit, even in the absence of repeating characteristic sequences. We have demonstrated that this approach performs well even in weak-contrast systems where differential imaging is required. CCI revealed otherwise inaccessible insights into the domain-wall dynamics of degenerate maze domain states, where it uncovered an intricate transition network with unexpected agglomeration in similarity distance space and a seemingly chaotic temporal behaviour. Most importantly, CCI provided spatiotemporal data based on which we developed a general mechanistic understanding of how these complex dynamics arise from a combination of attractive and repulsive pinning and intrinsic configurational energies, with direct consequences for any potential devices using domain walls. With these capabilities, CCI promises to become a powerful tool to answer some of the large open questions in condensed-matter physics and materials science, such as the role of thermal fluctuations and material defects in microelectronics[37] or batteries[38], the role of fluctuations and nanometre-scale material inhomogeneities in high-$T_c$ superconductivity[6,7,13,14], the dynamics of magnetic monopole excitations in frustrated spin-ice systems[32,33], and the role of fluctuations and topological states in ultrafast phase transitions[5,10,11,12,39,40].

# Methods

## Sample fabrication

The thin-film magnetic multilayer [Pt (2.7 nm)/$Co_{60}Fe_{20}B_{20}$ (0.8 nm)/MgO (1.5 nm)]$_{x15}$ with Pt (2.7 nm) capping layer on a Ta (2.3 nm)/Pt (3.7 nm) seed layer was sputter-deposited onto a silicon nitride membrane. Ta, Pt and $Co_{60}Fe_{20}B_{20}$ were grown by d.c. magnetron sputtering and MgO was grown by radio frequency sputtering at Ar pressures of 3.5 mtorr (for Pt) and 3

mtorr for all other materials. The material has a Curie temperature of 650 K, as reported previously[23]. The zero-temperature, zero-field magnetic ground state of this material is a state of parallel stripe-shaped domains of the out-of-plane magnetic order parameter $m_z$, but any meandering configuration of these stripe domains is almost equal in energy and in practice all these configurations are energetically degenerate[23].

The back side of the silicon nitride membrane was coated with [Cr (5 nm)/Au(55 nm)]$_{x20}$ to block the incident soft X-rays[41]. Three circular apertures were milled by focused-ion-beam lithography into this opaque layer, one with 720 nm in diameter defining the field of view and two reference holes 60 nm and 40 nm in diameter providing reference beams for holography. These hole diameters represent a geometry that was developed for time-resolved X-ray holography of out-of-plane magnetic domains[41,42,43]. They represent a good compromise between sensitivity for small changes (which is easier revealed with smaller object holes) and contextual information (for which larger field of views are preferred).

## Data acquisition and sample environment

The experiment was performed at the coherent soft X-ray scattering beamline (CSX) of the National Synchrotron Light Source II, Brookhaven National Laboratory. Partially coherent, circularly polarized X-rays were focused onto the sample in transmission geometry. A 50-µm upstream pinhole was used to increase the coherence and to reduce the overall flux to limit beam-induced heating. Magnetic contrast was achieved by tuning the X-ray energy to the Co $L_3$ absorption edge (778 eV), where the X-ray magnetic circular dichroism (XMCD) contrast is maximum[44]. A Sydor Fast CCD camera, mounted in-vacuum 33 cm downstream of the sample, recorded the coherently scattered and phase-encoded X-rays as a hologram. The direct beam was blocked by a beamstop. To image the dynamics in a time series, holograms (frames) were recorded continuously and stored individually with their respective timestamps. To separate magnetic from topographic contrast (see below), the helicity was reversed every 100 frames. The exposure time of each single frame was set to 0.3 s, slightly below the saturation limit of individual detector pixels. The effective readout time was

0.087 s. A full set of stacks at both helicities was recorded in $\sim$120 s. This includes the time to change the undulator. Timestamps of the frames were recorded by the beamline controls and acquisition system, with computer precision and hence negligible temporal error compared to the exposure and readout time. That is, the temporal resolution of our experiment was 0.387 s. A liquid helium flow cryostat was used to control of the sample temperature with $\Delta T < 0.01$ K precision.

## Algorithm to subtract static topography holograms

Topography holograms $I_{\mathrm{sum}}$ were recorded as a sum of positive and negative helicity holograms. Only holograms without dynamics during the acquisition were used for topography data. That is, we only considered sets where the magnetic reconstruction from the difference of positive and negative helicity holograms showed full contrast across the entire field of view. The topography holograms were manually updated along the temporal frame sequence as needed. In total we used 26 topography holograms, each averaged over at least 100 frames per helicity. To determine if the topography image still represented the current state of the sample, we determined if the topographically induced airy pattern from the circular aperture was successfully suppressed in the difference holograms. Moreover, we checked that our topography holograms were free of any magnetic contrast via the pair correlation maps. To this end, we note that spurious magnetic contribution would produce an offset in the magnetic pair correlation map. The sign of this offset would be inverted at every helicity change, leading to a characteristic checkerboard pattern in the correlation maps. We confirmed that such patterns are absent in our data.

Subsequently, we subtracted $I_{\mathrm{sum}}$ from all magnetic holograms $I_{\pm}$ recorded with either positive or negative helicity X-rays to obtain the difference hologram $I_{\mathrm{diff}}$ without mask scattering. To compensate for intensity drift, we used a dynamic factor $\alpha$, that is, $I_{\mathrm{diff}} = \pm(I_{\pm} - \alpha I_{\mathrm{sum}})$. The dynamic factor was automatically determined for each image from the scalar product of the full topographic and the magnetic holograms as $\alpha = \langle I_{\pm}, I_{\mathrm{sum}}\rangle / \langle I_{\mathrm{sum}}, I_{\mathrm{sum}}\rangle$. This equation is based on the approximation that topography and magnetic signal are uncorrelated and hence orthogonal. Importantly, this approach leaves

only one time-dependent signal in the reconstruction process ($I_{\pm}$) and, moreover, produces the same output $I_{\rm diff}$ for the same state regardless of whether it was recorded with positive or negative helicity light. Thus, after this step, the temporal resolution of CCI equals the temporal resolution (here the acquisition time) of the original single frame $I_{\pm}$.

## Real-space image reconstruction

Images in Figs. 1, 3 were reconstructed by Fourier-transform holography (FTH)[42,45,46], which is a linear operation and therefore best suited to illustrate the effect of limited signal-to-noise ratio (SNR) and blind averaging. The final, high-SNR images of the magnetic states and modes (Figs. 2, 4, Extended Data Figs. 4, 6, 7, 9 and supplementary videos) were reconstructed by holographically aided iterative phase retrieval[47,48], which offers increased resolution and contrast of the resulting images as long as the underlying scattering data are of low noise.

Whereas FTH images were processed based on difference holograms, our phase retrieval algorithm relies on the positive values in the scattering plane. Therefore, we started by calculating the single helicity holograms for every mode discerned by our CCI algorithm using the following equation:

$${I}_{\pm ,i}=\sum _{k\in {\varphi }^{i}}{I}_{\pm ,k}=\sum _{k\in {\varphi }^{i}}\frac{2{\alpha }_{k}{I}_{{\rm{sum}},k}\pm {I}_{{\rm{diff}},k}}{2}$$
(1)

where $I_{\pm,k}$ is a frame belonging to the set of frames $\phi^{i}$ assigned to a particular mode $i$, $I_{{\rm sum},k}$ is the topography image associated with that specific frame and $\alpha_k$, $I_{{\rm diff},k}$ are its associated dynamic factor and difference image, respectively (see Methods section ‘Algorithm to subtract static topography holograms’ for the definition of the dynamic factor, $\alpha$). Such a procedure allowed us to obtain single helicity images for each frame with the photon statistics of both helicities.

The resulting holograms were then centred, and any present (readout) offset was subtracted. A support mask for the phase retrieval algorithm was

manually generated by selectively thresholding the absolute value of the FTH reconstruction of the average hologram. The same mask was used to reconstruct all images. The holograms were then fed to an iterative phase retrieval algorithm designed for dichroic imaging[48]. First, the positive helicity exit wave of the sample was reconstructed using a combination of two different phase retrieval algorithms. The starting guess used was derived from the support mask multiplied by a constant, adjusted according to the intensity of the input hologram. We first applied a modified version of the iterative relaxed averaged alternating reflections (RAAR) algorithm[49] (700 iteration steps with a relaxation parameter $\beta$ smoothly going from 1 to 0.5), where the nonnegativity reflector constraint was removed, owing to its inadequacy to deal with complex holograms. The positive helicity reconstruction was completed by the error reduction algorithm[50] (50 iteration steps).

Then, the negative helicity exit wave was reconstructed using the error reduction algorithm (50 iteration steps) using the phase of the reconstructed positive helicity complex hologram as a starting guess. This approach enables us to avoid any shift between the two different helicity images. Finally, the magnetic reconstruction was obtained by computing the ratio between the difference and the sum of the two reconstructed images to extract the pure XMCD contrast.

The phase retrieval algorithm yields reconstructions with higher contrast and better resolution compared to the FTH reconstruction. We achieve diffraction-limited resolution of 18 nm for internal modes with 250 frames or more contributing to the reconstruction. The resolution was determined via Fourier ring correlation[51] using the half-bit threshold criterion[52]. Displaying the ratio between the difference and sum, instead of the bare difference, allows to neglect topographic features and widens the field of view of the technique to 810 nm, as the borders of the object hole partially covered in gold present the same contrast as the centre, despite less light being transmitted.

## Algorithm to calculate magnetic pair correlations in Fourier space

In our X-ray holography geometry, we can determine the magnetic pair correlation directly in Fourier space, as illustrated in Extended Data Fig. 1. We start by subtracting the topography hologram from the recorded single-helicity hologram to obtain the difference hologram $h_{\rm diff}$ (Extended Data Fig. 1a). Fourier-transforming the difference hologram yields the so-called Patterson map (Extended Data Fig. 1b). The Patterson map includes four reference-reconstructed real-space images of the out-of-plane magnetization $m_z(\mathbf{x}, t)$ in the off-centre region, and the interference between object hole charge scattering and magnetic scattering in the centre.

We next eliminate the reference-induced modulations as these are mostly adding noise, owing to their sensitivity to fluctuations of the incident beam. We therefore first crop the central part of the Patterson map excluding the reconstructions and, second, transform back to Fourier space. The resulting filtered difference hologram ${\widetilde{I}}_{{\rm{diff}}}$, depicted in Extended Data Fig. 1c, exhibits high intensity at small reciprocal vectors **q** and needs to be flattened before performing the correlation analysis. Mathematically, ${\widetilde{I}}_{{\rm{diff}}}\propto {\rm{Re}}({\mathcal{F}}\,[m]){\mathcal{F}}\,[{T}_{{\rm{mask}}}]$, where ${\mathcal{F}}\,[{T}_{{\rm{mask}}}]$ is the Airy-disk scattering of the approximately binary transmission $T_{\rm mask}$ of the circular mask defining the field of view. This identity is derived in ref. [53]. We therefore extract the pure magnetic scattering ${S}_{i}={\widetilde{I}}_{{\rm{diff}}}({t}_{i})/\sqrt{{\widetilde{I}}_{\text{sum}}}\propto {\rm{Re}}({\mathcal{F}}\,[m])$ by dividing the filtered difference hologram by the square root of the topographic sum hologram ${\widetilde{I}}_{{\rm{sum}}}\propto {\mathcal{F}}\,{[{T}_{{\rm{mask}}}]}^{2}$. Then, the Fourier-space pair correlation matrix (Extended Data Fig. 1d), calculated using

$${c}_{ij}=\frac{\langle {S}_{i},{S}_{j}\rangle }{\parallel {S}_{i}\parallel \,\parallel {S}_{j}\parallel },$$
(2)

is essentially equivalent to the pair correlation matrix of the underlying real-space textures $m_z(\mathbf{x}, t)$, see ref. [53]. Note that $\langle ., .\rangle$ is the scalar product of the unravelled pixel arrays and $\|.\|$ is the norm according to this scalar product.

## Robust classification of frames

Our method to classify frames corresponding to the same physical state is illustrated in Fig. 3. It is based on two ingredients: (i) a low-noise metric $d_{ij}$ that quantifies the pair-wise similarity ('distance') of two camera frames $\phi_i$ and $\phi_j$ recorded at times $t_i$ and $t_j$ and (ii) an iterative, hierarchical clustering algorithm[3,4] that groups frames into same-state sets.

We start with the frame-wise pair correlation map of magnetic textures, $c_{ij}$, see previous section. As shown in Fig. 3a and Extended Data Fig. 2, already $c_{ij}$ resolves clear grid-shaped fingerprints of state changes at a single-frame level, with approximately ten times better signal-to-noise ratio than a similar analysis based on holographic real-space reconstructions (see Extended Data Fig. 3). We further reduce the noise of the metric by the following consideration: If $S_\alpha$ and $S_\beta$ represent the same state (A) then the correlation of $S_\alpha$ with any arbitrary frame should be the same as the correlation of $S_\beta$ with that frame. This follows from the transitivity of the equivalence relation. Hence, each pair correlation $c_{\alpha\gamma}$ for any $\gamma$ is a fingerprint of state A and the entire vector $c(S_\alpha) \equiv (c_{\alpha 1}, c_{\alpha 2}, \ldots, c_{\alpha n})$ has considerably better photon statistics than the single scattering pattern $S_\alpha$ alone. We therefore define our low-noise fourth-order Pearson distance metric $d_{ij}$ as

$${d}_{ij}=1-{c}_{ij}^{(4)}=1-\frac{\langle c({S}_{i})-\bar{c}({S}_{i}),c({S}_{j})-\bar{c}({S}_{j})\rangle }{\parallel c({S}_{i})-\bar{c}({S}_{i})\parallel \,\parallel c({S}_{j})-\bar{c}({S}_{j})\parallel },$$

(3)

where $\bar{c}({S}_{i})=\frac{1}{n}{\sum }_{j=1}^{n}{c}_{ij}$ is the mean of the vector $c(S_i)$. That is, the matrix ${c}_{ij}^{(4)}$ is the normalized Pearson correlation matrix of $c_{ij}$. The resulting distance matrix is shown in Fig. 3b.

On the basis of the measure of distance, we identify distinctive clusters of highly similar frames through an iterative variant (Fig. 3a–c) of a concept

know from gene identification[3] as UPGMA (unweighted pair group method with arithmetic mean) to construct a hierarchical cluster tree from $d_{ij}$. In this bottom-up process, the nearest two clusters are combined into a higher-level cluster, starting with single frames on the lowest level[3,4] and ending with a single final cluster. The UPGMA clustering was performed using the MATLAB function ‘linkage’ specified with the ‘correlation’ metric to compute the proximity of two scattering patterns $S_i$ and $S_j$ by autocorrelation of the input matrix $d_{ij}$. This additional application of the correlation function results in a nonlinear similarity metric enhancing the numerical separation of high correlation values (similar states) and low correlation values (dissimilar states). The resulting so-called dendrogram is presented in Fig. 3c. The vertical level, or height, of each link in the dendrogram corresponds to the distance (abstract, nonlinear in our case) between the linked clusters. If two linked clusters represent the same physical state of the sample, the step size, or height difference, between the old and the new hierarchy level is small. Conversely, a large step, also known as an inconsistency, indicates a natural division in the data set, that is, the merging of different physical states. The largest step size is naturally observed at the topmost node in the tree. We aim to make the most robust classification and therefore split the tree only at the top node into two subclusters. Instead of dividing the dendrogram into a complete set of clusters in a single step, we iterate through the whole clustering procedure, separating the dendrogram in each iteration at most into two subgroups (at the topmost link). The iterations enable us to extract domain configurations beyond the conventional UPGMA, for example, to separate configurations $A_1$ and $A_2$ in Fig. 3c.

The next iteration step is to decide if our two identified subclusters represent pure or mixed states, that is, if they comprise frames from a single state or multiple states. To this end, we quantify the distinctness of the topmost link in the dendrogram by the inconsistency coefficient $\xi$, where $\xi$ is given as the ratio of the average absolute deviation of the step height to the standard deviation of all lower-level links included in the calculation. Both the step height and the standard deviation are indicated in Fig. 3c. On this basis, we identify all clusters that undercut an inconsistency threshold as pure-state clusters whereas, complementarily, mixed states are present in clusters exceeding this threshold.

The iteration steps are repeated for mixed-state clusters until—within our temporal resolution and available signal-to-noise ratio—complete separation into clusters containing only pure states is achieved. The frames of each pure-state cluster are then averaged, and a real-space image of the corresponding domain configuration is reconstructed (Fig. 3d). The knowledge of which frames entered each cluster, and the time stamps of when these frames were recorded, yields the temporal reconstruction, as shown in Fig. 3e (see Methods section 'Estimation of the temporal discrimination threshold and reconstruction of the 32 states' for more details about the temporal reconstruction).

Applied to our data, we find that the modified clustering algorithm performs well for thresholds of the inconsistency coefficient $\xi$ in the range 1.7 to 2.2. The upper limit is determined by the minimal sensitivity needed to separate the most evident mixed-states (for example, identified by motion-blurred contrast, as in Fig. 1b). The lower limit is set by the total number of frames (here 99%) that can be assigned to clusters that yield acceptable real-space reconstructions, which we assume as 15 frames per cluster. Specifically, we chose $\xi = 1.85$ because it produces the lowest frame misclassification probability while assigning 99.5% of our 28,800 frames to clusters with >15 frames (see Methods section 'Estimation of the temporal discrimination threshold and reconstruction of the 32 states' for more details about the evaluation of the frame misclassification).

We note that major drawbacks of hierarchical clustering are the so-called chaining phenomenon and the sensitivity towards outliers, merging inconsistent clusters or creating minor cluster with few elements. Whereas the former is effectively minimized in the iteration process by choosing a sufficiently low inconsistency threshold, the latter leads to the fragmentation of a pure state into several inseparable clusters. In our case, the algorithm finds 119 magnetic configurations, of which many are visibly indistinguishable. To eliminate duplicates in this set, we calculated the similarity between all identified clusters $A$ and $B$ by averaging the pair correlation values $c_{AB}$ for all combinations of frames $\phi_A$ and $\phi_B$ belonging to these clusters. Using a conventional (noniterative) agglomerative UPGMA algorithm we then processed the resulting reduced 119 × 119 cell cluster-correlation matrix to group clusters that actually represented the same

domain configurations. We verified that our final clusters are pure states by applying the same iterative scheme as mentioned above.

The result is a set of 72 domain configurations forming the basis for further separation into discretized internal modes (discretized versions of the just spatially resolved domain configurations) and states (spatiotemporally resolved configurations).

## Discretizing of the internal modes

To extract the positions of domain walls from sometimes noisy or inhomogeneously illuminated real-space images reconstructed by the phase retrieval algorithm, we discretized the 72 domain configurations identified in the cluster analysis (see Extended Data Fig. 4). To this end, we started with a low-pass filter: the cluster-averaged difference holograms were first cropped with a circular binary mask before reconstructing real-space images to reduce high-frequency noise in the images. The radius of the filter in Fourier space was determined individually for each internal mode as the maximum $q$ beyond which the noise dominates over the total magnetic scattering signal of all frames of that mode. Although this filter reduces the spatial resolution, the location of the domain wall remains unaffected. The domain segmentation was based on the sign of the reconstructed phase $\varphi(r)$ of the complex-valued images instead of its real part because the phase shows the most distinct separation of the up and down magnetization. The reconstructed phase was centred around zero to achieve maximum contrast observed by a phase transition of $\pm\pi$ at the domain wall locations. We considered domains smaller than 50 pixels as artefacts caused by noise and merged them therefore with their surrounding domains. Images that were strongly affected by the artefacts were adjusted manually.

Some of the original real-space reconstructions of the 72 internal modes show evidence of mixed-state superposition, see Extended Data Fig. 4b. Such mixed states inevitably emerge if the domain state changes during the acquisition of a single frame (that is, if the dynamics is faster than our minimum temporal resolution). Hence, simply binarizing a domain image as the one shown in Extended Data Fig. 4b would constitute a loss of information. However, we find that the whole set of binarized internal modes forms a representative basis, based on which the original greyscale images

can be decomposed, as illustrated in Extended Data Fig. 4b. In practice, we evaluated the similarity between the domain images and all binary internal modes by the real-space correlation[53]. In a next step, we applied a multilinear regression to decompose each individual greyscale image into those binary internal modes which have >88% similarity to the grayscale image. We find that the weighted superposition of internal modes accurately represents all domain configurations, with the exception of state 32, where an additional binary domain configuration 73 was manually created (we attribute this to the fact that state 32 is the last state in our time series and insufficient data were available to automatically decompose it). The discrete representation of all 72 internal domain modes is shown in Extended Data Fig. 6. The set of original domain images along with their low-pass filtered phase images, their adjusted binarized versions, and their decomposition into binary internal modes is compiled in supplementary video 2.

## Estimation of the temporal discrimination threshold and reconstruction of the 32 states

Cluster analysis is a method to classify data into natural divisions with similar features, for example, coincident magnetic domain states in this work. Any such algorithm applied to noisy data will eventually produce assignment errors. These errors have a crucial role in the temporal reconstruction, where every misclassified frame is a falsely detected or neglected transition. However, finding the genuine assignment becomes increasingly difficult for states that are very similar (see domain configurations $A_1$ and $A_2$ in Fig. 3d). Of the 72 internal modes identified by the clustering algorithm, some exhibit real-space similarities of up to 99%. Given this extremely close similarity, the question arises how accurate the assignment of a single frame to a particular magnetic state is. We address this question by estimating the frame misclassification probability, which we derive from the robustness of assigning a frame between two clusters.

In the bottom-up clustering approach used in our analysis, links between clusters created on lower levels strongly influence higher-level clustering. The whole linkage tree, that is, the dendrogram, is particularly sensitive to the links created at lowest levels for low-distance high-noise data, where small changes of the initial distance may lead to deviating final assignments.

Conversely, the robustness against variations of the initial set of frames is a measure of the quality of a clustering assignment. Based on this rationale, we developed the following analysis to verify the accuracy and sensitivity of our cluster analysis.

In our analysis, we validate the clustering assignment of frames between every pair of clusters $A$ and $B$. We assume that our full cluster analysis already outputs a representative estimate of the members $\phi^A$ and $\phi^B$ belonging to $A$ and $B$, respectively. For error analysis, we now compare clustering runs starting with different initial frame sets—on the one hand, the original frame set $\phi^A + \phi^B$ and, on the other hand, ten newly assembled subsets ${\widetilde{\varphi }}^{A}+{\widetilde{\varphi }}^{B}$. Each subset ${\widetilde{\varphi }}^{A}$ and ${\widetilde{\varphi }}^{B}$ contains a randomly selected half of the parent frame set $\phi^A$ and $\phi^B$, respectively. We separate the assembled frame sets into exactly two clusters using the same iterative agglomerative UPGMA algorithm as described previously. The robustness of the clustering is evaluated by comparing the original frame-to-cluster assignment with the new assignment, that is, if frames that are grouped in $A$ or $B$ are still grouped in $\widetilde{A}$ or $\widetilde{B}$, respectively. Otherwise, frames are considered as misclassified and we define the misclassification probability as the average fraction of misclassified frames in ${\widetilde{\varphi }}^{A}+{\widetilde{\varphi }}^{B}$.

For the majority of mode pairs (87%) we find perfect coincidence in the clustering with random subsets. We find that the robustness of the frame classification substantially drops if at least one of the clusters contains a very low number of frames. We exclude clusters with less than 100 frames—the number of frames for a standard FTH image of a single hologram stack—from further analysis because recording more frames is not a fundamental challenge.

In Extended Data Fig. 5, we show the frame misclassification probability of all remaining mode pairs as a function of their similarity, represented by their pair correlation. Notable misclassification rates occur for very similar domain configurations only. Specifically, we find that the frame misclassification probability is below 1% for similarities of the underlying magnetic textures of up to 93.8%. We define this as the sensitivity threshold

in our analysis. Internal domain modes with higher similarity were grouped allowing their temporal discrimination with an acceptable misclassification rate, as shown in Fig. 3e. These groups of modes are referred to as spatially and temporally resolved magnetic ‘states’. In practice, we successively combined the nearest modes until the distance between any pair of modes of two dissimilar states exceeded the 100% − 93.8 % = 6.2% similarity distance defined by the sensitivity threshold. An overview of the identified states and their associated internal domain modes is shown in Extended Data Fig. 6. We note in this context that the correlation between domain wall hopping in different parts of the field of view is not an artefact of the clustering algorithm but instead emerges from the intrinsic physics of the material, namely from the desire of the material to retain a constant domain width as set by the competition of domain wall energies and long-range stray field energies.

The number of states and internal modes may vary with particular choices of model parameters, but the conclusions drawn in the text remain robust in a broad range of parameters discussed above. We note further that this approach of ‘binning’ of similar configurations into ‘states’ makes CCI broadly applicable even to systems exhibiting nonrecurring dynamics, especially when combined with a fixed and finite field of view.

## Determination of agglomerates in the transition network

Already in its raw representation, the transition network (Fig. 4c) visually segregates into agglomerates of states. To quantify this observation, we defined a new distance metric that takes into account the similarity distance as well as the frequency of transitions between states. To this end, we use the simplest approach, where we just add the two distance measures as

$${d}_{AB}=2-\left({c}_{{\rm{state}}}(A,B)+\frac{\widetilde{\theta }(A,B)}{{\widetilde{\theta }}_{\max }}\right).$$

where $d_{AB}$ is the distance between states $A$ and $B$ according to this new metric, $c_{\rm{state}}$ is the state similarity distance and $\mathop{\theta }\limits^{\sim }(A,B)=\log (1+\theta T)$ is the logarithm of the transition frequency $\theta$ between $A$ and $B$, $T$ is the duration of the experiment, and \

${\widetilde{\theta }}_{\max }$ denotes the highest observed $\widetilde{\theta }$ across all states. We then applied a UPGMA hierarchical clustering algorithm to create a dendrogram from the states according to this distance metric (Extended Data Fig. 10). The separation threshold that defines the agglomerates was manually set at the large step around 0.38 in this dendrogram.

## Determination of attractive pinning sites

Our approach to determine the position of attractive pinning sites is based on the domain-wall occupation probability and the averaged domain-wall curvature. First, we extracted domain-wall locations that were observed in at least 20% of all internal modes shown in Extended Data Fig. 7c. Among these hotspots, there are point-like and line-shaped areas with an increased occupation probability indicating pinning sites. We used the points of maximum occupation probability to determine the pinning sites of point-like hotspots directly.

Second, we used the averaged domain wall curvature illustrated in Extended Data Fig. 7d to localize the pinning sites of line-shaped hotspots. Namely, we extract extended areas with an averaged curvature larger than 1.5 $\mu m^{-1}$. Among those areas, we defined the point of the highest curvature as the location of the pinning sites in the line-shaped hotspots. To ensure a sufficient spatial separation, only pinning sites that are at least 8 pixels apart were considered.

## Comparison of CCI to existing time-resolved coherent imaging methods

In Extended Data Table 1 we compare CCI with existing time-resolved coherent imaging methods with magnetic contrast. The figures are based on the following considerations: Line 1: Results for conventional coherent imaging in this work. The diffraction-limited resolution of 18 nm is achieved when averaging over ~250 frames (see Methods section ‘Real-space image reconstruction’), which corresponds to ~100 s. Of course, to achieve the best resolution, the system has to be static over the integration time. Line 2: Spatial and temporal resolution achieved in this work by employing CCI. To

achieve the reported diffraction-limited spatial resolution, the same number of frames as in conventional imaging had to be averaged, but due to CCI without loss of temporal resolution. Statistical errors in the assignment of a state to a frame as well as uncertainties from grouping several internal modes into a state are not included in the resolutions specified and have to be considered additionally. Line 3: Anticipated potential of conventional coherent X-ray imaging with sub-10 nm resolution (a regime that is difficult to reach with noncoherent X-ray imaging techniques). The integration time drastically increases as the target spatial resolution increases because scattering signals typically decay strongly at high *q*. Line 4: CCI at synchrotron radiation sources. The frame rate reported here corresponds to the detector frame rate of the MOENCH detector[54], a particularly fast detector in the soft X-ray regime. Line 5: CCI at high-repetition-rate X-ray free-electron lasers. The perspective given here is based on the specifications of the European XFEL (EuXFEL)[55]. Time resolution is limited by the maximum bunch frequency (currently 1/(220 ns) at EuXFEL) and maximum duration is limited by the length of a bunch train (currently 600 µs at EuXFEL). Line 6: CCI in a pump–probe scheme at an XFEL, where the time resolution is limited by the pulse duration and the duration by the maximum pump–probe delay available. Line 7: Based on ref. [43]. Line 8: Based on refs. [56,57]. Line 9: Based on a combination of ref. [58], where nondestructive single-shot holographic magnetic imaging was demonstrated, and ref. [59], where it was shown that an image of the same specimen at two different times can be encoded in such a single-shot hologram.

# Data availability

The data reported in this study are available with identifiers at https://doi.org/10.5281/zenodo.7180988.

# Code availability

The code reported in this study is available with identifiers at https://doi.org/10.5281/zenodo.7180988.

# References

1. Gaffney, K. J. & Chapman, H. N. Imaging atomic structure and dynamics with ultrafast X-ray scattering. *Science* **316**, 1444–1448 (2007).

2. von Ardenne, B., Mechelke, M. & Grubmüller, H. Structure determination from single molecule X-ray scattering with three photons per image. *Nat. Commun.* **9**, 2375 (2018).

3. Sherlock, G. Analysis of large-scale gene expression data. *Curr. Opin. Immunol.* **12**, 201–205 (2000).

4. Murtagh, F. & Contreras, P. Algorithms for hierarchical clustering: an overview, II. *WIREs Data Min. Knowl. Discov.* **7**, e1219 (2017).

5. Vidas, L. et al. Imaging nanometer phase coexistence at defects during the insulator–metal phase transformation in $VO_2$ thin films by resonant soft X-ray holography. *Nano Lett.* **18**, 3449–3453 (2018); correction **21**, 7426 (2021).

6. Chen, X. M. et al. Charge density wave memory in a cuprate superconductor. *Nat. Commun.* **10**, 1435 (2019).

7. Vojta, M. Lattice symmetry breaking in cuprate superconductors: stripes, nematics, and superconductivity. *Adv. Phys.* **58**, 699–820 (2009).

8. Reichhardt, C., Reichhardt, C. J. O. & Milosevic, M. V. Statics and dynamics of skyrmions interacting with disorder and nanostructures. *Rev. Mod. Phys.* **94**, 035005 (2022).

9. Chmiel, F. P. et al. Observation of magnetic vortex pairs at room temperature in a planar $\alpha$-$Fe_2O_3$/Co heterostructure. *Nat. Mater.* **17**, 581–585 (2018).

10. Vogelgesang, S. et al. Phase ordering of charge density waves traced by ultrafast low-energy electron diffraction. *Nat. Phys.* **14**, 184–190 (2018).

11. Zong, A. et al. Evidence for topological defects in a photoinduced phase transition. *Nat. Phys.* **15**, 27–31 (2019).

12. Büttner, F. et al. Observation of fluctuation-mediated picosecond nucleation of a topological phase. *Nat. Mater.* **20**, 30–37 (2021).

13. Ghiringhelli, G. et al. Long-range incommensurate charge fluctuations in (Y,Nd)$Ba_2Cu_3O_{6+x}$. *Science* **337**, 821–825 (2012).

14. Arpaia, R. et al. Dynamical charge density fluctuations pervading the phase diagram of a Cu-based high-$T_c$ superconductor. *Science* **365**, 906–910 (2019).

15. Nagler, B. et al. Turning solid aluminium transparent by intense soft X-ray photoionization. *Nat. Phys.* **5**, 693–696 (2009).

16. Schneider, M. et al. Ultrafast demagnetization dominates fluence dependence of magnetic scattering at Co M edges. *Phys. Rev. Lett.* **125**, 127201 (2020).

17. Fung, R. et al. Dynamics from noisy data with extreme timing uncertainty. *Nature* **532**, 471–475 (2016).

18. Giannakis, D. Data-driven spectral decomposition and forecasting of ergodic dynamical systems. *Appl. Comput. Harmon. Anal.* **47**, 338–396 (2019).

19. Thibault, P. & Menzel, A. Reconstructing state mixtures from diffraction measurements. *Nature* **494**, 68–71 (2013).

20. Burgess, Ja. J. et al. Quantitative magneto-mechanical detection and control of the Barkhausen effect. *Science* **339**, 1051–1054 (2013).

21. Tetienne, J.-P. et al. Nanoscale imaging and control of domain-wall hopping with a nitrogen-vacancy center microscope. *Science* **344**, 1366–1369 (2014).

22. Seul, M. & Andelman, D. Domain shapes and patterns: the phenomenology of modulated phases. *Science* **267**, 476–483 (1995).

23. Lemesh, I. et al. Current-induced skyrmion generation through morphological thermal transitions in chiral ferromagnetic heterostructures. *Adv. Mater.* **30**, 1805461 (2018).

24. Barla, P., Joshi, V. K. & Bhat, S. Spintronic devices: a promising alternative to CMOS devices. *J. Comput. Electron.* **20**, 805–837 (2021).

25. Romming, N. et al. Writing and deleting single magnetic skyrmions. *Science* **341**, 636–639 (2013).

26. Eltschka, M. et al. Nonadiabatic spin torque investigated using thermally activated magnetic domain wall dynamics. *Phys. Rev. Lett.* **105**, 056601 (2010).

27. Metaxas, P. J. et al. Creep and flow regimes of magnetic domain-wall motion in ultrathin Pt/Co/Pt films with perpendicular anisotropy. *Phys. Rev. Lett.* **99**, 217208 (2007).

28. Schwarz, A. et al. Visualization of the Barkhausen effect by magnetic force microscopy. *Phys. Rev. Lett.* **92**, 077206 (2004).

29. Zázvorka, J., Jakobs, F., Heinze, D., Keil, N. & Kromin, S. Thermal skyrmion diffusion used in a reshuffler device. *Nat. Nano.* **14**, 658–661 (2019).

30. Shpyrko, O. G. et al. Direct measurement of antiferromagnetic domain fluctuations. *Nature* **447**, 68–71 (2007).

31. Chen, X. M. et al. Spontaneous magnetic superdomain wall fluctuations in an artificial antiferromagnet. *Phys. Rev. Lett.* **123**, 197202 (2019).

32. Kapaklis, V. et al. Thermal fluctuations in artificial spin ice. *Nat. Nano.* **9**, 514–519 (2014).

33. Farhan, A. et al. Emergent magnetic monopole dynamics in macroscopically degenerate artificial spin ice. *Sci. Adv.* **5**, eaav6380 (2019).

34. Winning, M., Gottstein, G. & Shvindlerman, L. S. Stress-induced grain boundary motion. *Acta Mater.* **49**, 211–219 (2001).

35. Levitan, A. L. et al. Single-frame far-field diffractive imaging with randomized illumination. *Opt. Express* **28**, 37103–37117 (2020).

36. Zimmermann, J. et al. Deep neural networks for classifying complex features in diffraction images. *Phys. Rev. E* **99**, 063309 (2019).

37. Holler, M. et al. High-resolution non-destructive three-dimensional imaging of integrated circuits. *Nature* **543**, 402–406 (2017).

38. Merryweather, A. J., Schnedermann, C., Jacquet, Q., Grey, C. P. & Rao, A. Operando optical tracking of single-particle ion dynamics in batteries. *Nature* **594**, 522–528 (2021).

39. Seaberg, M. H. et al. Spontaneous fluctuations in a magnetic Fe/Gd skyrmion lattice. *Phys. Rev. Res.* **3**, 033249 (2021).

40. Danz, T., Domröse, T. & Ropers, C. Ultrafast nanoimaging of the order parameter in a structural phase transition. *Science* **371**, 371–374 (2021).

41. Büttner, F. et al. Automatable sample fabrication process for pump–probe X-ray holographic imaging. *Opt. Express* **21**, 30563–30572 (2013).

42. Büttner, F. Dynamic imaging with X-ray holography. In *Holographic Materials and Optical Systems* (eds. Naydenova, I. et al.) https://doi.org/10.5772/66689 (InTech, 2017).

43. Büttner, F. et al. Dynamics and inertia of skyrmionic spin structures. *Nat. Phys.* **11**, 225–228 (2015).

44. Scherz, A. et al. Phase imaging of magnetic nanostructures using resonant soft X-ray holography. *Phys. Rev. B* **76**, 214410 (2007).

45. Eisebitt, S. et al. Lensless imaging of magnetic nanostructures by X-ray spectro-holography. *Nature* **432**, 885–888 (2004).

46. Pfau, B. & Eisebitt, S. X-Ray holography. In *Synchrotron Light Sources and Free-Electron Lasers: Accelerator Physics, Instrumentation and Science Applications* (eds. Jaeschke, E. J. et al.) 1093–1133 (Springer, 2016); https://doi.org/10.1007/978-3-319-14394-1_28.

47. Flewett, S. et al. Holographically aided iterative phase retrieval. *Opt. Express* **20**, 29210–29216 (2012).

48. Kfir, O. et al. Nanoscale magnetic imaging using circularly polarized high-harmonic radiation. *Sci. Adv.* **3**, eaao4641 (2017).

49. Luke, D. R. Relaxed averaged alternating reflections for diffraction imaging. *Inverse Prob.* **21**, 37–50 (2005).

50. Gerchberg, R. W. & Saxton, W. O. A practical algorithm for the determination of phase from image and diffraction plane pictures. *Optik* **35**, 237–246 (1972).

51. Banterle, N., Bui, K. H., Lemke, E. A. & Beck, M. Fourier ring correlation as a resolution criterion for super-resolution microscopy. *J. Struct. Biol.* **183**, 363–367 (2013).

52. van Heel, M. & Schatz, M. Fourier shell correlation threshold criteria. *J. Struct. Biol.* **151**, 250–262 (2005).

53. Klose, C. et al. Photon correlation spectroscopy with heterodyne mixing based on soft X-ray magnetic circular dichroism. *Phys. Rev. B* **105**, 214425 (2022).

54. Cartier, S. et al. Micron resolution of MÖNCH and GOTTHARD, small pitch charge integrating detectors with single photon sensitivity. *J. Instrum.* **9**, C05027–C05027 (2014).

55. Tschentscher, T. et al. Photon beam transport and scientific instruments at the European XFEL. *Applied Sciences* **7**, 592 (2017).

56. von Korff Schmising, C. et al. Imaging ultrafast demagnetization dynamics after a spatially localized optical excitation. *Phys. Rev. Lett.* **112**, 217203 (2014).

57. Zayko, S. et al. Ultrafast high-harmonic nanoscopy of magnetization dynamics. *Nat. Commun.* **12**, 6337 (2021).

58. Wang, T. et al. Femtosecond single-shot imaging of nanoscale ferromagnetic order in Co/Pd multilayers using resonant X-ray holography. *Phys. Rev. Lett.* **108**, 267403 (2012).

59. Günther, C. M. et al. Sequential femtosecond X-ray imaging. *Nat. Photon* **5**, 99–102 (2011).

# Acknowledgements

We thank C. Ropers, R. Comin, A. Menzel and D. Giannakis for discussions and advice. Work at MIT was supported by the DARPA TEE programme. Work at MBI was supported by the Leibniz Collaborative Excellence programme. Work at HZB was supported by the Helmholtz Young Investigator Group Program. This research used resources (beamline 23-ID-1, CSX) of the National Synchrotron Light Source II, a US Department of Energy (DOE) Office of Science User Facility operated for the DOE Office of Science by Brookhaven National Laboratory under contract no. DE-SC0012704.

# Funding

Open access funding provided by Helmholtz-Zentrum Berlin für Materialien und Energie GmbH.

# Author information

Author notes

1. These authors contributed equally: Claudio Mazzoli, Bastian Pfau

## Authors and Affiliations

1. Max Born Institute, Berlin, Germany

Christopher Klose, Michael Schneider, Stefan Eisebitt & Bastian Pfau

2. Department of Materials Science and Engineering, Massachusetts Institute of Technology, Cambridge, MA, USA

   Felix Büttner, Kai Litzius, Ivan Lemesh, Jason M. Bartell, Mantao Huang & Geoffrey S. D. Beach

3. National Synchrotron Light Source II, Brookhaven National Laboratory, Upton, NY, USA

   Felix Büttner, Wen Hu, Claudio Mazzoli, Andi Barbour & Stuart B. Wilkins

4. Helmholtz-Zentrum für Materialien und Energie, Berlin, Germany

   Felix Büttner & Riccardo Battistelli

5. Zentraleinrichtung Elektronenmikroskopie (ZELMI), Technische Universität Berlin, Berlin, Germany

   Christian M. Günther

6. Institut für Optik und Atomare Physik, Technische Universität Berlin, Berlin, Germany

   Stefan Eisebitt

## Contributions

F.B., W.H., C.M., S.B.W., G.S.D.B. and B.P. conceived the project. F.B., I.L., M.S. and C.M.G. prepared the samples. C.K., F.B., W.H., I.L., J.M.B. and M.H. performed the experiments with support from C.M. and S.B.W.; C.K. analysed the data with supervision from B.P. and S.E.; R.B. performed the CDI reconstructions. C.K., F.B., W.H., C.M. and B.P. interpreted the data with input from K.L., A.B. and S.B.W.; W.H., C.M., C.K., F.B. and B.P. developed the CCI technique. C.K., F.B., W.H., C.M. and B.P. wrote the paper with comments from all authors.

### Corresponding authors

Correspondence to Felix Büttner or Wen Hu.

## Ethics declarations

### Competing interests

The authors declare no competing interests.

## Peer review

### Peer review information

*Nature* thanks Serguei Molodtsov and the other, anonymous, reviewer(s) for their contribution to the peer review of this work. Peer reviewer reports are available.

## Additional information

**Publisher's note** Springer Nature remains neutral with regard to jurisdictional claims in published maps and institutional affiliations.

## Extended data figures and tables

### Extended Data Fig. 1 Algorithm to calculate the magnetic pair correlations map.

**a**, The calculation starts with the experimental data, that is, the magnetic difference hologram $h_{diff}(t)$ obtained at time $t$ from the difference of a circular polarization hologram and a topography hologram. Inset, scanning electron micrograph of the sample, superimposed by an image of the magnetic domain state. Scale bar, 500 nm. **b**, Patterson map obtained from an inverse Fourier transformation of $h_{diff}(t)$. The cross-correlation appears in

the centre while the real-space magnetic-contrast image (‘reconstruction’) is offset from the centre by the object–reference distance. **c**, A low-pass filtered difference hologram is calculated from the Fourier transformation of the cross-correlation cropped from the Patterson map. Further normalization (flattening) is performed using the amplitudes of the topography scattering, i.e., the square-root of the reference-filtered topography hologram. **d**, Normalized pair correlation map calculated by the scalar product ⟨., .⟩ of the flattened difference holograms (equation (1). For illustration purposes, all panels are based on sequential averages of 100 hologram frames.
See Methods for the mathematical steps.

## Extended Data Fig. 2 Complete pair correlation map.

**a**, Pair correlation map of all recorded frames (indexed sequentially). **b**, Magnified section of the correlation map, marked with a red square in **a**, now plotted as a function of the wall time (time stamp) when the respective frames were recorded. Each block represents a stack of 100 acquired frames. White areas indicate time intervals where no images were recorded, mostly due to helicity change events.

## Extended Data Fig. 3 Signal-to-noise ratio of the real- and Fourier-space method of calculating correlation maps.

**a**, Fourier-space correlation map calculated with the algorithm presented in Extended Data Fig. 1, showing a transition between two states. **b**, The same correlation map calculated using single-frame real-space reconstructions (see Extended Data Fig. 1b). **c**, Histograms showing the distribution of observed pair correlation values. The distributions were obtained from the same-state regions in each of the correlation maps (visible as yellow regions in **a**). To estimate the signal-to-noise ratio (SNR), both distributions were fitted with a Gaussian function. We define the SNR by the expectation value divided by the standard deviation of the fit. We find that the Fourier-space SNR is more than 10 times higher (29.3 ± 1.0) than the real space SNR (SNR 2.5 ± 0.2).

## Extended Data Fig. 4 Discretization of the internal domain modes.

**a**, Creation of binary internal domain modes. The up and down magnetization of all domain images is binarized using image segmentation based on threshold filtering of the CDI reconstructions. The representations of images with a low signal-to-noise ratio were adjusted manually. **b**, Illustration of the multi-level discretization of internal domain modes. The CDI reconstruction of a domain image is decomposed into a set of binarized internal modes. The binary images of the internal modes are superimposed to create a discretized representation of the domain image with multiple contrast level. A fitting process determines the weighting coefficients from the image of the domain mode. For further details about the procedure, see Methods. Scale bar, 500 nm.

## Extended Data Fig. 5 Sensitivity limit of the temporal reconstruction.

Frame misclassification probability of a two-state system as a function of the similarity of the underlying two domain states. A similarity value of one corresponds to indistinguishable states. Data points below 87% similarity show a misclassification probability of zero and were therefore excluded from the log-log plot. The light-blue band is a guide to the eye. Our sensitivity threshold is marked by the dashed blue lines. The horizontal line indicates the largest acceptable misclassification rate for temporal assignment (1%). The vertical line depicts the maximum similarity of two states before and after a temporally resolved transition (93.8%), which was chosen such that all data points left of this line are below the misclassification threshold. For further details, see Methods.

## Extended Data Fig. 6 Overview of the reconstructed discretized internal modes.

We identified a total of 72 internal modes, ranging up to 99% in similarity (see Methods). The modes are subsets of the 32 domain states (see Fig. 4), as indicated by the grey background shading. Modes are defined by a high pair correlation of >93.8%, which means that their exact temporal sequence is inaccessible but statistical information, such as the real-space images and the number of contributing frames, can still be reconstructed reliably. Scale bar, 500 nm.

## Extended Data Fig. 7 Statistical analysis of the real-space reconstructions.

**a**, Average of all domain configurations observed during the experiment weighted according to the number of frames for each configuration. **b**, Similar average of the discretized domain configurations. **c**, Superposition (sum) of the domain wall positions of all internal modes, normalized by the total number of modes. **d**, Average curvature of the domain walls. Only walls showing a considerable curvature are visualized in colour. Grey lines mark remaining domain walls. **e**, Number of magnetization switching events observed locally in the temporal evolution of the domain configuration. Scale bar, 500 nm.

## Extended Data Fig. 8 Illustration of the conceptual difference between attractive and repulsive pinning.

String-shaped magnetic domain walls (grey lines) located in an energy landscape with attractive and repulsive Gaussian-shaped pinning potentials. The attractive pinning sites (blue) induce depressions in the energy landscape trapping the domain walls at their minimum, whereas the repulsive pinning site (red) forms an area-like potential barrier repelling the domain walls.

## Extended Data Fig. 9 Domain-wall rearrangement during transition between two states.

**a**,**b**, Selected examples for inter-agglomerate (**a**) and intra-agglomerate (**b**) transitions. The colour code is explained below both panels. The summed contrast shows areas without magnetization changes as purple or white and areas with switched magnetization as blue or red. Areas containing repelling pinning sites are marked with semi-transparent grey shadows, whereas attractive pinning sites are marked with black dots. Scale bar, 500 nm.

## Extended Data Fig. 10 Dendrogram of state agglomeration.

An UPGMA hierarchical clustering algorithm groups the 32 domain states shown in Fig. 4 into 11 agglomerates based on the state's similarity distances and the frequency of transitions between the states. The separation threshold was manually set at a generally large step in the hierarchical distance (0.38) as indicated by the dashed red line. The colour coding separates the different agglomerates and corresponds to Fig. 4. Single, short-lived states which are not colour-coded in Fig. 4 are shown in grey here.

**Extended Data Table 1 Comparison of CCI to existing time-resolved coherent X-ray imaging methods**

## Supplementary information

### Peer review file

### Supplementary Video 1

### Supplementary Video 2

## Rights and permissions

**Open Access** This article is licensed under a Creative Commons Attribution 4.0 International License, which permits use, sharing, adaptation, distribution and reproduction in any medium or format, as long as you give appropriate credit to the original author(s) and the source, provide a link to the Creative Commons licence, and indicate if changes were made. The images or other third party material in this article are included in the article's Creative Commons licence, unless indicated otherwise in a credit line to the material. If material is not included in the article's Creative Commons licence and your intended use is not permitted by statutory regulation or exceeds the permitted use, you will need to obtain permission directly from the copyright holder. To view a copy of this licence, visit http://creativecommons.org/licenses/by/4.0/.

Reprints and Permissions

# About this article

## Cite this article

Klose, C., Büttner, F., Hu, W. *et al.* Coherent correlation imaging for resolving fluctuating states of matter. *Nature* **614**, 256–261 (2023). https://doi.org/10.1038/s41586-022-05537-9

- Received: 21 October 2021
- Accepted: 08 November 2022
- Published: 18 January 2023
- Issue Date: 09 February 2023
- DOI: https://doi.org/10.1038/s41586-022-05537-9

## Share this article

Anyone you share the following link with will be able to read this content:

Get shareable link

Sorry, a shareable link is not currently available for this article.

Copy to clipboard

Provided by the Springer Nature SharedIt content-sharing initiative

---

This article was downloaded by **calibre** from https://www.nature.com/articles/s41586-022-05537-9

## A combined physical–chemical and microbiological approach to unveil the fabrication, provenance, and state of conservation of the Kinkarakawa-gami art

02 October 2020

Elena Piacenza, Alessandro Presentato, … Delia Francesca Chillura Martino

## Archaeometric evidence for the earliest exploitation of lignite from the bronze age Eastern Mediterranean

17 December 2021

Stephen Buckley, Robert C. Power, … Philipp W. Stockhammer

## Multiproxy study of 7500-year-old wooden sickles from the Lakeshore Village of La Marmotta, Italy

02 September 2022

Niccolò Mazzucco, Mario Mineo, … Juan F. Gibaja

## 2000 Year-old Bogong moth (Agrotis infusa) Aboriginal food remains, Australia

17 December 2020

Birgitta Stephenson, Bruno David, … John Hellstrom

## New results with regard to the Flora bust controversy: radiocarbon dating suggests nineteenth century origin

15 April 2021

Ina Reiche, Lucile Beck & Ingrid Caffy

### Using microartifacts to infer Middle Pleistocene lifeways at Schöningen, Germany

15 December 2022

Flavia Venditti, Bárbara Rodríguez-Álvarez, … Nicholas J. Conard

### Interpreting ancient food practices: stable isotope and molecular analyses of visible and absorbed residues from a year-long cooking experiment

27 August 2020

Melanie J. Miller, Helen L. Whelton, … Christine A. Hastorf

### The arrival of millets to the Atlantic coast of northern Iberia

03 November 2022

Borja González-Rabanal, Ana B. Marín-Arroyo, … Manuel R. González-Morales

### Ancient proteins from ceramic vessels at Çatalhöyük West reveal the hidden cuisine of early farmers

03 October 2018

Jessica Hendy, Andre C. Colonese, … Eva Rosenstock

- Article
- Open Access
- Published: 01 February 2023

# Biomolecular analyses enable new insights into ancient Egyptian embalming


- Maxime Rageot ,
- Ramadan B. Hussein,
- Susanne Beck,
- Victoria Altmann-Wendling,
- Mohammed I. M. Ibrahim,
- Mahmoud M. Bahgat,
- Ahmed M. Yousef,
- Katja Mittelstaedt,
- Jean-Jacques Filippi,
- Stephen Buckley,
- Cynthianne Spiteri &
- …
- Philipp W. Stockhammer

Show authors


*Nature* **volume 614**, pages 287–293 (2023)


- 33k Accesses

- 1 Citations

- 2764 Altmetric

- Metrics details


## Abstract

The ability of the ancient Egyptians to preserve the human body through embalming has not only fascinated people since antiquity, but also has always raised the question of how this outstanding chemical and ritual process was practically achieved. Here we integrate archaeological, philological and organic residue analyses, shedding new light on the practice and economy of embalming in ancient Egypt. We analysed the organic contents of 31 ceramic vessels recovered from a

26th Dynasty embalming workshop at Saqqara[1,2]. These vessels were labelled according to their content and/or use, enabling us to correlate organic substances with their Egyptian names and specific embalming practices. We identified specific mixtures of fragrant or antiseptic oils, tars and resins that were used to embalm the head and treat the wrappings using gas chromatography–mass spectrometry analyses. Our study of the Saqqara workshop extends interpretations from a micro-level analysis highlighting the socio-economic status of a tomb owner[3,4,5,6,7] to macro-level interpretations of the society. The identification of non-local organic substances enables the reconstruction of trade networks that provided ancient Egyptian embalmers with the substances required for mummification. This extensive demand for foreign products promoted trade both within the Mediterranean[8,9,10] (for example, *Pistacia* and conifer by-products) and with tropical forest regions (for example, dammar and elemi). Additionally, we show that at Saqqara, *antiu* and *sefet*—well known from ancient texts and usually translated as ‘myrrh’ or ‘incense’[11,12,13] and ‘a sacred oil’[13,14]—refer to a coniferous oils-or-tars-based mixture and an unguent with plant additives, respectively.

## Main

Ancient Egyptians developed an outstanding ability to protect the human body from decomposition or destruction after death—instigated by the belief that the decomposition of the corpse presented a physical obstacle toward attaining the afterlife[15]. Performed by specialized and learned individuals (ritualist embalmers), embalming was both a chemical and a ritual process[14]. From a chemical perspective, the practice evolved from simple natural preservation (through desiccation), via a proto-embalming treatment during prehistoric times[16] (around 4,300–3,100 bc), to the sophisticated pharaonic procedures of anthropogenic desiccation (using natron), excerebration, evisceration and the use of antibacterials, antifungals, barrier materials and fixatives[3,15]. This preservation procedure, which could take up to 70 days to complete, ensured the transformation of a vulnerable body into a durable mummy. Embalming also entailed sets of ritualized acts and the recitation of liturgical texts, through which the chemically treated body would be revived and acquired a new identity as a justified or glorified deceased, worthy of living on in the netherworld[17].

Our present-day knowledge of embalming substances is derived from two main sources: ancient written sources such as embalming papyri[14,18], and organic residue analyses (ORA) of Egyptian mummies. Substances used in embalming have been named in ancient Egyptian texts and by Greek authors such as Herodotus and Diodorus. However, debates have arisen concerning the specific substances to which

these terms correspond[11,15,19,20]. In recent years, ORA has been applied to study residues recovered from mummies and embalming vessels in individual tombs (for example, in ref. [3]). Although these analyses have successfully identified various substances used in embalming, the roles of these balms in this process as well as the overall procedure have so far remained unclear.

The discovery of embalming facilities at Saqqara presented here reshapes our knowledge and understanding of ancient Egyptian mummification. Dated to around 664–525 bc (26th Dynasty), the embalming workshop is located a few metres to the south of the pyramid of King Unas. It includes a subterranean evisceration facility (the *wabet*), a multifunctional aboveground structure (probably corresponding to the *ibu*) and communal burial spaces[1,2] (Fig. 1; for a detailed description of the archaeological evidence, see Supplementary Information, section 1). In addition to these structures, a cache of embalming pottery vessels was uncovered in the *wabet* facility. This cache includes a large corpus of potsherds and both broken and complete vessels, with some showing traces of burning as well as drippings of boiled substances on their outer surfaces. Among the finds are 121 beakers and bowls (a total of 59 ‘marl clay beakers’ and 62 ‘red goldfish bowls’; for shapes, refer to Fig. 1) inscribed with Hieratic and Demotic texts providing embalming instructions (for example, ‘to put on his head’ or ‘bandage or embalm with it’) and/or names of embalming substances (for example, ‘*sefet*’ or ‘dry *antiu*’) and sometimes with the title of an administrator of the embalming workshop or the necropolis (Extended Data Table 1). Out of this corpus, we selected 9 beakers and 22 red bowls with the most clearly readable labels for ORA. To establish a possible link with the vessels from the *wabet* facility, we included in our analyses four samples from two burial chambers (locations 3 and 4) at the bottom of the communal burial shaft: two red bowls, one faience cup and one red cylindrical vessel.

**Fig. 1: The embalming facilities and burial chambers of the Saqqara complex.**

figure 1

Orange arrows show the locations of the investigated vessels. The background image is a digital documentation of the Saqqara complex (copyright M. Lang, Universität Bonn). The two labelled vessels were uncovered in the embalming room and correspond to a ‘red goldfish bowl’ (inscription: ‘*sefet* + dry *antiu*’) and a ‘white clay beaker’ (inscription: ‘to be put on his head’). The unlabelled red bowl with black surface residue was uncovered in the burial chamber loc. 4.

## Organic residue analyses

A wide range of products was identified, including plant oils and tars, resins, and animal fats (details in Extended Data Table 1, Extended Data Fig. 1 and Supplementary Information, section 2).

Among the group of conifer by-products, juniper or cypress (hereafter juniper/cypress) by-products in the form of essential or fragrant oil or tar were identified in 21 vessels (60%). Their identification is supported by the association of totarol derivatives and cuparene-related sesquiterpenes[21,22] (Fig. 2). The cedar oil or tar is the second most commonly detected product in the Saqqara vessels (19 vessels (54%)). Its presence is indicated by the predominance or the equivalence of low

molecular weight sesquiterpenoids of the himachalene series over the characteristic diterpenes of the abietane family[22,23,24] (Fig. 2).

**Fig. 2: Partial gas chromatograms of organic residue extracts from bowls labelled 'dry *antiu*' and '*sefet*'.**

figure 2

Total ion chromatograms showing the molecular constituents of the essential oil or tar of cedar (brown) and juniper/cypress (purple), and animal fat (blue). Sesquiterpenes and diterpenes are labelled a–z. The prefix SSTP is an identifier for samples from the Saqqara Saite Tombs Project. Right, electron ionization mass spectra (70 eV) of characteristic corresponding sesquiterpenes from coniferous oils or tars. MAG, monoacylglycerol. *A*, abundance; $AI_{DB\text{-}5}$, arithmetic retention index; tent., tentative assignment; TMS, trimethylsilyl derivative; $t_r$, retention time.

With regard to angiosperm resins, we identified elemi in at least 15 vessels (43%) (Extended Data Fig. 1) on the basis of the combination of lupeol and α- and β-amyrin derivatives (Fig. 3). This assemblage is commonly associated with resin of Burseraceae, particularly that of *Canarium*[25,26,27,28,29] (also known as elemi) (Extended Data Table 2). *Bursera* and *Protium* resins could be excluded as they occur mainly in Central and South America[21,30]. α- and β-11-keto amyrins were identified in the 15 vessels (sometimes together with their acetate derivatives), in two cases together with traces of brein (urs-12-ene-3,16-diol). These biomarkers are documented in elemis from the Asian rainforest[25,26,29] but elemis from the African rainforest should not be excluded (Extended Data Table 2). Finally, the compounds, olean-9(11),12-dien-3-ol and urs-9(11),12-dien-3-ol were detected in 14 samples (Fig. 3 and Extended Data Table 2). These were previously identified in artificially aged elemis from Manila and Mexican copal[28]. In addition, *Pistacia* resin was detected in five vessels (14%). The identification was on the basis of the presence of characteristic biomarkers[5,8,31] (for example, moronic, oleanonic, isomasticadienonic and masticadienonic acids) (Fig. 3). Triterpenic markers of heat treatment[8] were also

identified in four vessels (Extended Data Fig. 1). A Dipterocarpaceae resin, commonly known as dammar, was detected in one red bowl from burial chamber, location 4. This resin is characterized by a broad assemblage of triterpenic markers from dammarane, nor-ursane and oleanane families. Although some of these biomarkers are ubiquitous, the co-occurrence of dammaradien-3-ol, nor-α-amyrone, δ-amyrone and oxidation products such as 20,24-epoxy-25-hydroxydammaren-3-ol is a convincing argument for the identification of dammar. To our knowledge, these compounds have not been found together in any other resin[31,32,33,34] (Fig. 3).

**Fig. 3: Partial gas chromatograms showing the molecular constituents of *Pistacia* resin, dammar and beeswax.**

figure 3

**a**,**b**, Total ion chromatograms showing the molecular constituents of *Pistacia* resin (visible surface residue), dammar and beeswax (absorbed residue) (**a**) and elemi (**b**). **c**, Electron ionization mass spectra (70 eV) of triterpenic palmitates. Green circles indicate markers of *Pistacia* resin, pink circles indicate markers of dammar resin and yellow circles indicate markers of elemi. Filled circles are biomarkers present in fresh resin, empty circles are degradation markers linked to natural oxidation and/or heat treatment and half-filled circles are biomarkers and/or degradation markers. Numbers prefixed with W are the number of carbon atoms in the long-chain esters associated with the corresponding peak. Triterpenes are labelled numerically as follows: 1, 28-norolean-12, 17-dien-3-one; 2, olean-9(11),12-dien-3-one; 3, 3-epi-β-amyrin; 4, 3-epi-α-amyrin; 5, 3-epi-lupeol; 6, olean-9(11)-en-3-one; 7, urs-9(11),12-dien-3-one; 8, olean-9(11),12-dien-3-ol; 9, nor-β-amyrone (28-norolean-12-en-3-one); 10, α-amyrenone isomer (urs-9(11)-en-3-one); 11, β-amyrenone; 12, dammaradien-3-one; 13, olean-18-en-3-one; 14, 28-noroleandien-3-one or 28-norursdien-3-one (tent.); 15, nor-α-amyrenone (28-norurs-12-en-3-one); 16, urs-9(11),12-dien-3-ol; 17, 28-norolean-17-en-3-one; 18, olean-3,12-dien-16-ol (dehydroxymaniladiol); 19, oleandienol; 20, nor-β-amyrin (28-norolean-12-ene-3-ol); 21, α-amyrenone; 22, dammaradien-3-ol (3β-hydroxy-20,24-dammarediene); 23, β-amyrin; 24, lupenone; 25, olean-9(11),12-dien-3-yl acetate; 26, nor-α-amyrin (28-norurs-12-ene-3-ol); 27, α-amyrin; 28, lupeol; 29, ursa-9(11),12-dien-3-yl acetate; 30, δ-amyrenone (olean-13(18)-en-3-one); 31, noroleanenol or norursenol (tent.); 32, maniladiol (olean-12-ene-3,16-diol); 33, 11-oxo-β-amyrin epi-isomer (tent.); 34, 11-oxo-α-amyrin epi-isomer (tent.); 35, dammarenolic acid; 36, shoreic acid; 37, lupeol isomer; 38, brein (urs-12-ene-3,16-diol); 39, β-amyrin acetate; 40, α-amyrin acetate; 40′, 20,24-epoxy-25-hydroxydammaren-3-one; 41, hydroxydammaradienone (tent.); 42, oleandien-28-ol (tent. erythro-3-en-28-ol); 43, hydroxydammarenone; 44, oleanonic aldehyde; 45, moronic acid; 46, oleanonic acid; 46′, 20,24-epoxy-25-hydroxydammaren-3-ol; 47, 11-oxo-β-amyrenone; 48, hydroxydammarenol; 49, oleanol derivative or ursol derivative; 50, 11-oxo-α-amyrenone; 51, oleanolic acid; 51′, ursonic acid (3-oxours-12-en-28-oic acid); 52, 11-oxo-β-amyrin; 53, ursolic aldehyde; 54, oleanolic aldehyde; 55, 11-oxo-α-amyrin; 56, ursolic acid; 57, lupane derivative (tent. canaric acid); 58, isomasticadienonic acid; 59, 11-oxo-β-amyrin acetate; 60, 11-oxo-α-amyrin acetate; 61, 11-oxo-oleanonic acid; 62, hydroxy oleanolic acid; 63, masticadienonic acid; 64, α-amyrin palmitate (urs-12-en-3-yl palmitate); 65, oxo-oleanene palmitate; 66, 11-oxo-β-amyrin palmitate; 67, 11-oxo-α-amyrin palmitate.

Animal fat was detected in 18 vessels (51% of vessels). Its presence was indicated by a narrow distribution of saturated triacylglycerols (TAGs) (46:0 to 54:0 (carbon atoms:unsaturated carbon–carbon bonds)) and diacylglycerols[35] (32:0 to 36:0). Furthermore, traces of saturated TAGs with an odd number of carbon atoms (53:0,

51:0 and 49:0), which are characteristic of ruminant animal fats[36], were identified in 7 vessels (Extended Data Figs. 1 and 2). Plant oils were detected in 5 vessels (14%). In 4 of them, a plant oil, type olive (although degraded argan or hazelnut oils cannot be excluded) was indicated by the specific distribution of unsaturated TAGs (54:3, 52:2, 50:1) and diacylglycerols[37] (34:1, 36:2 and 32:0) (Extended Data Fig. 3). The detection of ricinoleic acid together with a substantial amount of oleic acid and its mono- and dihydroxylated degraded markers in one beaker suggests that it may have contained castor oil, possibly mixed with other oils[38,39,40] (Extended Data Fig. 4). Although ricinoleic acid has also been associated with the activity of ergot fungi on Gramineae[41], the castor oil hypothesis remains the most plausible in the Saqqara context, where embalming vessels were dedicated to the preparation of antiseptic and antifungal substances for mummification. Beeswax was identified in 5 vessels (14%) by the presence of its characteristic even-numbered fatty acids (22:0 to 28:0, with 24:0 being the most important) and long-chain ($C_{40}$ to $C_{48}$) palmitic esters[5,42] (Fig. 3).

Bitumen was found in two vessels recovered from the burial chambers at locations 3 and 4, based on the characteristic hopanes and steranes[3,23,43,44] (Extended Data Fig. 5). Its chemical composition suggests that it originated from the Dead Sea[23] (Supplementary Information, section 2).

Finally, we identified molecular markers of recipes that involve the mixing and heating of resinous substances with fat or oil in three vessels (triterpenic palmitates; Supplementary information 2 and ref. [45]). Elemi was prepared together with animal fat and/or plant oil in two beakers and dammar was prepared with beeswax and/or animal fat in a bowl (Fig. 3 and Extended Data Fig. 1).

## Treatment of the body in the workshop

The inscriptions on the vessels of the Saqqara workshop contain instructions for the treatment of specific body parts, especially the head, and for the preparation of linen bandages. Some of these treatments involved the preparation and application of several mixtures.

Eight vessels are inscribed with instructions for the treatment of the head. Our samples show that the embalmers used three different mixtures (mixtures A, B and C in Fig. 4 and Extended Data Fig. 1), which can include elemi, *Pistacia* resin an oil or tar of juniper/cypress and cedar, animal fat, beeswax, probably castor oil, and a plant oil (type olive). To our knowledge, the use of elemi and oil or tar of juniper/cypress for embalming the head has not previously been reported. However,

previous ORA studies of early mummies from the first millennium bc suggest, in accordance with our results, that castor oil and *Pistacia* resin were used specifically for the treatment of the head[6,40,46]. Beeswax, Pinaceae by-product, and fat or oil were additionally used for different parts of the body[3,4,5,6].

**Fig. 4: Organic contents of vessels providing embalming instructions.**

figure 4

Organic substances and/or mixtures identified in the pottery and the inscriptions associated with these vessels. Mummy drawing copyright S. Lucas.

We extracted samples from eight vessels (four beakers and four red bowls) with labels indicating for 'wrapping or embalming with it', which were probably used for preparing mummy linen bandages. The organic contents of seven vessels were mixtures (mixtures D and E; Fig. 4 and Extended Data Fig. 1), and one bowl contained only animal fat. Mixture E was the most frequently detected (five vessels) and consisted of oil or tar of juniper/cypress and cedar, animal fat and/or plant oil and elemi. In two of these vessels, we additionally identified heating markers of elemi resin together with fat or oil. Previous studies of mummy bandages from the 4th millennium bc and later provide evidence for the use of fat or oil and conifer by-product in most of the balms, but none for the use of elemi[3,4,5,6,16]. However, one

sample from the 1st millennium bc was treated with a mixture including fat or oil, a conifer by-product and a triterpenic resin resembling mixture E[5]. Previous studies have provided evidence that bitumen and beeswax were regularly incorporated into balms for bandages during this period[3,4,5,7]. However, neither of these substances were detected in vessels used for the mummy bandages at Saqqara (although the limited amount of residue absorbed prevented the application of targeted methods[6,47]). Instead, we found two new substances—elemi and juniper/cypress.

Six other sherds provided information on substances used for washing the body, reducing bodily odour and softening the skin, as well as a recipe for the treatment of the liver and another for the stomach. The bowl labelled with 'to wash', contained markers of oil or tar of conifer, and the bowl inscribed with 'to make his odour pleasant' showed evidence of ruminant animal fat (adipose or dairy) and degraded Burseraceae resin (Extended Data Table 2). In the vessel with inscriptions related to the treatment of the skin, which may have occurred on the third day of embalming (Extended Data Table 1), we identified a mixture of animal ruminant fat (adipose or dairy) combined with heated beeswax.

Two of the sampled vessels were inscribed: one with the name of the god Imseti, who protects the liver, and the other with the god Duamutef, who protects the stomach. One of these vessels (Imseti/liver) contained a mixture of oil or tar of juniper/cypress and elemi, whereas the other (Duamutef/stomach) contained only heated beeswax (potentially similar content of two 26th Dynasty canopic jars is described in ref. [7]).

Another bowl was inscribed with the title of an administrator of the embalming workshop and the necropolis—the seal bearer—who carried out specific embalming procedures, related mainly to the treatment of the head[14]. This vessel yielded fat or oil and oil or tar of juniper/cypress, which is identical to mixture D, for treating linen bandages and which could have been used to wrap the head.

## Embalming vessels in the burial chambers

The embalmers of the workshop also provided additional services, including the burial of the deceased in communal burial spaces[1]. We analysed four vessels from two communal burial chambers (locations 3 and 4) to evaluate similarities and differences among the substances used during burial.

One bowl from location 4 was used multiple times and for different substances. A visible black residue lining its surface was identified as a pure heated *Pistacia* resin. However, the ceramic sample taken from its inner wall showed markers of oils or

tars of cedar and juniper/cypress, bitumen and dammar mixed with beeswax and/or animal fat. This points to the complex and extended usage of the vessel, used first to prepare the different substances (ceramic impregnation) and subsequently to contain a heated *Pistacia* resin (last deposit).

From burial chamber location 3, we analysed a small faience cup and a red cylindrical pottery vessel. The cup still contained a cake-like substance, consisting of oil or tar of cedar, animal fat, heated *Pistacia* resin and heated beeswax. The cylindrical vessel contained oil or tar of cedar and possibly of juniper/cypress as well as bitumen and a fat or oil.

With the exception of the dammar and bitumen, all the substances detected in the vessels recovered from the burial chambers matched those identified in the embalming workshop.

## Properties and management of substances

These results suggest that the embalmers used the substances for their specific biochemical properties, as *Pistacia* resin, elemi, dammar, oils, bitumen and beeswax have antibacterial or antifungal and odoriferous properties, and thus help to preserve human tissue and reduce unpleasant smells[4,33,42,44]. Animal fat, plant oil and beeswax were also essential ingredients in recipes for the treatment of different body parts, as well as in ointments used to moisturize the skin[48]. Finally, the hydrophobic and adhesive properties of tars, resins, bitumen and beeswax were useful to seal skin pores, exclude moisture and to treat linen wrappings. The colour or appearance of these products may also have been desirable[4].

The embalming substances identified point to the existence of a management system of bio-products, from harvest, transportation, transformation and application. For example, obtaining plant oil and animal fat necessitate an extraction system, and the production of wood tar (pyrolysis) or oil (steam distillation) involves thermal processing and the specific controlled management of the raw material[49]. In addition, the thermal treatment of substances (such as *Pistacia* resin and beeswax) and the subsequent production of recipes (for example, those based on elemi and dammar resins) required specialized knowledge, technical skills and tools to obtain balms with the desired properties. Our results demonstrate that the embalmers indeed carried out activities that require specific know-how and benefited from institutional organization.

## *Antiu* and *sefet*

An important challenge for understanding Egyptian embalming practices on the basis of textual sources has always been the translation of substance-related terms[20]. Lexicographically, *antiu* has tentatively been associated with myrrh on the basis of philological conjectures[11,12,13]. However, five vessels from the embalmers' workshop that carry the label *antiu* yield a mixture of oil or tar of cedar and juniper/cypress together with animal fat (Extended Data Fig. 1; the use of cedar and/or juniper/cypress oil in ancient Egypt is described in refs. [22,23,46,50,51]). The labels indicate that *antiu* could have been used alone in dry form or mixed with *sefet*. However, in all cases we find markers of a mixture of coniferous volatile products with animal fat. This strongly suggests that *antiu* is a product that was purposefully manufactured by the embalmers and whose preparation entails the transformation of at least two different coniferous oils or tars and then mixing them with animal fat. In the Saqqara context, translations of *antiu* as a raw material such as myrrh can be excluded.

In Egyptology, *sefet* is usually described as an unidentified oil[12,13,48]. It was one of the '7 sacred oils' that were used in embalming and the 'opening of the mouth' ritual[13,14]. In three vessels from the embalmers' workshop with the label '*sefet*', we identified markers of animal fats, which were mixed in two of these vessels with oil or tar of juniper/cypress. The third vessel contained the markers of ruminant fat (adipose or dairy) with elemi. This indicates that, at least at Saqqara, *sefet* was a scented unguent (fat-based formula) with plant additives, particularly Cupressaceae or Burseraceae by-products. It is possible that the scented *sefet* unguent was also prepared with other plant oils. Moreover, its composition may have evolved over time[14,46,51].

## Egyptian mummification and the world economy

The majority of the substances used at the Saqqara workshop were imported—many of them from a considerable distance. The Saqqara context (Extended Data Figs. 6, 7 and 8) provides only a glimpse into the trade and exchange systems required to run a comprehensive embalming industry[3,15,52]. These findings confirm the known pattern of the diversification and complexification of embalming practices after around 1000 bc[3,5]. The origin of the different substances provides evidence for an almost global network (Fig. 5). The bitumen identified in Saqqara most probably originated from the Dead Sea, confirming previous findings that the asphalt from this region was exported to Egypt in the first millennium bc specifically for mummification[4,53]. *Pistacia* trees producing high yields of resin (*Pistacia lentiscus* or *Pistacia terebinthus*), olive trees, cedar, juniper and cypress are absent in Egypt[8,11,21,30], but grow in different locations in the Mediterranean basin (Fig. 5).

The related by-products were also imported, most probably from the Levant (for example, *Cedrus libani*), which had important trade networks with Egypt[8,9,10].

**Fig. 5: Potential origins of imported bioresources at Saqqara complex.**

figure 5

Coloured areas indicates the potential origins of the raw materials that were used for the preparation of balms and the mummification processes at Saqqara. Map copyright S. Lucas.

Although intensified trade networks and cross-cultural exchanges are well-documented for the regions of the Mediterranean basin, the Saqqara workshop provides additional evidence for long-distance trade networks via the vivid Indo-Mediterranean trade routes, which seem to have existed since the 2nd millennium bc[54]. This is particularly true for resins, which are endemic to rainforests. *Canarium* species, which produce elemi, are distributed in both Asian and African rainforests[21,30], whereas dammars are harvested from Dipterocarpaceae trees that grow exclusively in Asian tropical forests[21,30]. Thus, it is possible that elemi reached Egypt by the same route as dammar[55]. Consequently, the embalming and funerary services of the 7th century bc Saqqara workshop kept the demand for such biomaterials from distant lands active and supported the flourishing of international trade networks connecting Egypt with the eastern Mediterranean in addition to Asian and possibly African rainforests.

## Conclusion

We have identified several specific mixtures used for embalming the head or wrapping the body. The mummification specialists seem to have been aware of both the chemical properties and the bioactivity of the substances used and to have obtained complex knowledge about the preparation of different balms of particular ingredients. We identified *antiu* and *sefet* as mixtures of different fragrant oils or tars and fats. *Antiu* should be less restrictively designated—that is, not exclusively as myrrh or incense. Egyptian mummification was built upon and fostered long-distance exchange and routes, including imports from the Mediterranean basin as well as Asian and possibly African rainforest regions.

# Methods

Upon the discovery of the embalming vessels of the Saqqara workshop, a multinational team of researchers from the Universities of Tübingen and the Ludwig Maximilian University of Munich (Germany), and the National Research Centre (NRC) of Cairo (Egypt) was formed. Vessels were sampled on site at Saqqara and samples were delivered to the NRC laboratories for extraction and analyses.

## Sample treatment before GC–MS analyses

ORA was carried out at the NRC, Chromatographic Laboratories Network, Giza, Egypt. One gram of pottery powder was drilled out from the inner walls of the vessel (layer 2), following cleaning of its surfaces in order to remove any exogenous lipids. The characterization of the lipid constituents present was based on the analytical results obtained from layer 2. The ceramic powder collected during surface cleaning (layer 1) was retained for potential additional analysis. Powdered sherds were solvent-extracted (dichloromethane:methanol, 2:1 by volume) by ultrasonication to target lipid and resin compounds following established protocols[56]. 50% of the total lipid extract were trimethylsilylated (40 °C for 20 min) using *N*,*O*-bis(trimethylsilyl)trifluoroacetamide (BSTFA) (50 μl) and a catalytic reagent (pyridine) (4 μl) before analysis by gas chromatography–mass spectrometry (GC–MS).

Modern and aged (30-year-old) angiosperm resins, which included *Pistacia*, dammars, frankincense, elemi and myrrh (Extended Data Table 3) were ground, then extracted by ultrasonication in dichloromethane (1 mg $ml^{-1}$) and trimethylsilylated following established protocols[49].

## Gas chromatography and GC–MS analyses

The analysis of trimethylsilylated samples was performed by GC–MS using an Agilent 7890B GC system and Agilent 5977 MSD.

The analyses were carried out using helium as a carrier gas, with a split/splitless injection system (SSL), operating in the splitless mode with a flow rate of 3.0 ml min$^{-1}$ of helium and a constant pressure at the head of the column of 8.6667 psi. Samples were analysed using an Agilent J&W DB-5HT-column (15 m × 0.32 mm internal diameter; 0.1 μm film thickness). The temperature of the oven was set at 50 °C for 1 min then ramped to 100 °C at 15 °C min$^{-1}$, then to 240 °C at 4 °C min$^{-1}$ and to 380 °C at 20 °C min$^{-1}$ (held isothermally for 7 min). The inlet temperature was set at 300 °C. Mass spectra were acquired using electron ionization at 70 eV and obtained by scanning between *m*/*z* values 50 and 950. The interface and the ion source temperatures were 300 °C and 230 °C, respectively.

Some samples composed of triterpenoid markers and determined to be free of high molecular weight components (absence of wax esters, TAGs, triterpene palmitate) by the conditions described above, were analysed using an Agilent J&W DB-5MS column (30 m × 0.25 mm internal diameter; 0.25 μm film thickness). The inlet temperature was fixed at 300 °C. The oven temperature was ramped from 50 °C (held isothermally for 1 min) to 150 °C at 10 °C min$^{-1}$, and then increased to 320 °C at 4 °C min$^{-1}$ (held isothermally for 15 min). The analyses were carried out using helium as a carrier gas, with a flow rate at 2.0 ml min$^{-1}$ and the operating in the splitless mode with a purge flow of 3.0 ml min$^{-1}$ and a split ratio of 3:1. Mass spectra were acquired using electron ionization at 70 eV. The mass range was scanned for *m*/*z* 50–950. The ion source temperature was set at 230 °C and the transfer line at 250 °C.

Chromatograms and mass spectra were matched against authentic standards (lupeol, lupenone, α- and β-amyrin, saturated and unsaturated triglycerides, fatty acids, *n*-alkanes)[8,22,28,31,57,58,59] and the National Institute of Standards and Technology (NIST) library[60].

Retention indices were calculated based on a series of straight chain hydrocarbons from 7 to 40 carbons and were also used to confirm the identification of sesquiterpenes and diterpenes. The arithmetic retention indexes (AI) used in ref. [59] were computed as: $AI(x) = 100z + 100[(RT(x) - RT(P_z))/(RT(P_z + 1) - RT(P_z))]$, according to Van den Dool and Kratz[61]; *x*, analyte; RT, retention time; $P_z$ are paraffins (*n*-alkanes) with *z* carbon atoms.

## Reporting summary

Further information on research design is available in the Nature Portfolio Reporting Summary linked to this article.

## Data availability

All information on the samples and the data generated and analysed in this study is included in the manuscript, supplementary information files and Extended Data files.

## References


1. Hussein, R. B. in *Guardian of Ancient Egypt. Studies in Honor of Zahi Hawass, II* (ed Kamrin, J. et al.) 627–682 (Czech Institute of Egyptology, 2020).

2. Hussein, R. B. & Marchand, S. A mummification workshop in Saqqara: the pottery from the main shaft K24. Saqqara Saite Tombs Project (SSTP). *Bulletin de Liaison de la Céramique Égyptienne* **29**, 101–132 (2019).

3. Evershed, R. P. & Clark, K. A. in *The Handbook of Mummy Studies: New Frontiers in Scientific and Cultural Perspectives* (eds Shin, D. H. & Bianucci, R.) 653–715 (Springer, 2021).

4. Clark, K. A., Ikram, S. & Evershed, R. P. The significance of petroleum bitumen in ancient Egyptian mummies. *Philos. Trans. A* **374**, 20160229 (2016).

5. Buckley, S. & Evershed, R. P. Organic chemistry of embalming agents in Pharaonic and Graeco-Roman mummies. *Nature* **413**, 837–841 (2001).

6. Łucejko, J., Connan, J., Orsini, S., Ribechini, E. & Modugno, F. Chemical analyses of Egyptian mummification balms and organic residues from storage jars dated from the Old Kingdom to the Copto-Byzantine period. *J. Archaeolog. Sci.* **85**, 1–12 (2017).

7. Connan, J. in *Encyclopédie Religieuse de L'Univers Végétal Croynces Phytoreligieuses de L'Egypte Ancienne (ERUV) III* (ed. Aufrère, S. H.) (OrMondp XVI, 2005).

8. Stern, B., Heron, C., Corr, L., Serpico, M. & Bourriau, J. Compositional variations in aged and heated *Pistacia* resin found un Late Bronze age Canaanite amphorae and bowls from Arman, Egypt. *Archaeometry* **45**, 457–469 (2003).

9. Serpico, M. in *Metron. Measuring the Aegean Bronze Age. Proc. 9th International Aegean Conference, Yale University 18-21 April, 2002. Annales d'Archéologie Égéenne de l'Université de Liège* (ed. Laffineur, R.) 224–230 (2003).

10. Moreno García, J. C. in *Markets and Exchanges in Pre-Modern and Traditional Societies* (ed. García, J. C. M.) 198–229 (Oxbow Books, 2021).

11. Germer, R. *Handbuch der Altägyptischen Heilpflanzen* 4349 (Harrasowitz, 2008).

12. Kemna, C. M. in *Im Schatten der Zeder. Eine Kulturübergreifende Spurensuche zu der Identität und Kultischen Verwendung des ꜥš-Baumes* 149–155 (Göttiner Miszellen, 2018).

13. Koura, B. in *Die '7-Heiligen Öle' und andere Öl- und Fettnamen. Eine Lexikographische Untersuchung zu den Bezeichnungen von Ölen, Fetten und Salben bei den alten Ägyptern von der Frühzeit bis zum Anfang der Ptolemäerzeit (von 3000 v.Chr.–ca. 305 v.Chr.)* (Shaker, 1999).

14. Töpfer, S. *Das Balsamierungsritual. Eine (Neu-)Edition der Textkomposition Balsamierungsritual* (Harrassowitz, 2015).

15. Ikram, S. & Dodson, A. *The Mummy in Ancient Egypt: Equipping the Dead for Eternity* (Thames and Hudson, 1998).

16. Jones, J., Higham, T. F., Oldfield, R., O'Connor, T. P. & Buckley, S. A. Evidence for prehistoric origins of Egyptian mummification in late Neolithic burials. *PLoS ONE* **9**, e103608 (2014).

17. Assmann, J. *Death and Salvation in Ancient Egypt* (trans: Lorton, D.) (Cornell Univ. Press, 2005).

18. Quack, J. F. in *Texte zur Wissenskultur* (eds Janowski, B. & Schwemer, D.) 418–438 (Gütersloh, 2020).

19. García-Jiménez, L. in *Pharmacy and Medicine in Ancient Egypt: Proceedings of the Conference held in Barcelona* (2018) (ed. Solà, R. D.) 15–29 (Archaeopress, 2021).

20. Pommerening, T. in *Zwischen Philologie und Lexikographie des Ägyptisch-Koptischen. Akten der Leipziger Abschlusstagung des Akademienprojekts*

‘*Altägyptisches Wörterbuch*’ (eds Dils, P. & Popko, L.) 82–111 (S. Hirzel, 2016).

21. Mills, J. S. & white, R. Natural resins of art and archaeology their sources, chemistry, and identification. *Stud. Conserv.* **22**, 12–31 (1977).

22. Sarret, M. et al. Organic substances from Egyptian jars of the Early Dynastic period (3100–2700 bce): Mode of preparation, alteration processes and botanical (re)assessment of ‘cedrium’. *J. Archaeol. Sci. Rep.* **14**, 420–431 (2017).

23. Buckley, S., clark, K. A. & Evershed, R. P. Complex organic chemical balms of Pharaonic animal mummies. *Nature* **431**, 294–299 (2004).

24. Huber, B., Vassão, D. G., Roberts, P., Wang, Y. V. & Larsen, T. Chemical modification of biomarkers through accelerated degradation: implications for ancient plant identification in archaeo-organic residues. *Molecules* **27**, 3331 (2022).

25. Bandaranayake, W. M. Terpenoids of *Canarium zeylanicum*. *Phytochemistry* **19**, 255–257 (1980).

26. Hinge, V. K., Wagh, A. D., Paknikar, S. K. & Bhattacharyya, S. C. Terpenoids—LXXI: constituents of Indian black dammar resin. *Tetrahedron* **21**, 3197–3203 (1965).

27. Cartoni, G., Russo, M. V., Spinelli, F. & Talarico, F. GC–MS characterisation and identification of natural terpenic resins employed in works of art. *Ann. Chim.* **94**, 767–782 (2004).

28. De la Cruz-Cañizares, J., Doménech-Carbó, M.-T., Gimeno-Adelantado, J.-V., Mateo-Castro, R. & Bosch-Reig, F. Study of Burseraceae resins used in binding media and varnishes from artworks by gas chromatography–mass spectrometry and pyrolysis–gas chromatography–mass spectrometry. *J. Chromatogr. A* **1093**, 177–194 (2005).

29. Kikuchi, T. et al. Melanogenesis inhibitory activity of sesquiterpenes from *Canarium ovatum* resin in mouse B16 melanoma cells. *Chem. Biodivers.* **9**, 1500–1507 (2012).

30. Langenheim, J. H. *Plant Resins: Chemistry, Evolution, Ecology, and Ethnobotany* (Timber Press, 2003).

31. van der Doelen, G. A. et al. Analysis of fresh triterpenoid resins and aged triterpenoid varnishes by high-performance liquid chromatography–atmospheric pressure chemical ionisation (tandem) mass spectrometry. *J. Chromatogr. A* **809**, 21–37 (1998).

32. Burger, P., Charrié-Duhaut, A., Connan, J., Flecker, M. & Albrecht, P. Archaeological resinous samples from Asian wrecks: taxonomic characterization by GC–MS. *Anal. Chim. Acta* **648**, 85–97 (2009).

33. Charrié-Duhaut, A., Burger, P., Maurer, J., Connan, J. & Albrecht, P. Molecular and isotopic archaeology: top grade tools to investigate organic archaeological materials. *Comptes Rendus Chim.* **12**, 1140–1153 (2009).

34. Colombini, M. P. & Modugno, F. *Organic Mass Spectrometry in Art and Archaeology* (Willey, 2009).

35. Regert, M. Analytical strategies for discriminating archeological fatty substances from animal origin. *Mass Spectrom. Rev.* **30**, 177–220 (2011).

36. Charrié-Duhaut, A. et al. The canopic jars of Rameses II: real use revealed by molecular study of organic residues. *J. Archaeolog. Sci.* **34**, 957–967 (2007).

37. Rageot, M. et al. New insights into Early Celtic consumption practices: organic residue analyses of local and imported pottery from Vix-Mont Lassois. *PLoS ONE* **14**, e0218001 (2019).

38. Regert, M., Bland, H. A., Dudd, S. N., Bergen, P. F. V. & Evershed, R. P. Free and bound fatty acid oxidation products in archaeological ceramic vessels. *Proc. R. Soc. Lond. B* **265**, 2027–2032 (1998).

39. Copley, M. S., Bland, H. A., Rose, P., Horton, M. & Evershed, R. P. Gas chromatographic, mass spectrometric and stable carbon isotopic investigations of organic residues of plant oils and animal fats employed as illuminants in archaeological lamps from Egypt. *Analyst* **130**, 860–871 (2005).

40. Yatsishina, E. B., Pozhidaev, V. M., Sergeeva, Y. E., Malakhov, S. N. & Slushnaya, I. S. An integrated study of the hair coating of ancient Egyptian mummies. *J. Anal. Chem.* **75**, 262–274 (2020).

41. Lucejko, J. J. et al. Long-lasting ergot lipids as new biomarkers for assessing the presence of cereals and cereal products in archaeological vessels. *Sci. Rep.* **8**, 3935 (2018).

42. Regert, M., Colinart, S., Degrand, L. & Decavallas, O. Chemical alteration and use of beeswax through time :accelerated ageing test and analysis of archaeological samples from various environmental contexts. *Archaeometry* **43**, 549–569 (2001).

43. Connan, J. Use and trade of bitumen in antiquity and prehistory: molecular archaeology reveals secrets of past civilizations. *Philos. Trans. R Soc. Lond. B Biol. Sci.* **354**, 33–50 (1999).

44. Fulcher, K. & Budka, J. Pigments, incense, and bitumen from the New Kingdom town and cemetery on Sai Island in Nubia. *J. Archaeol. Sci. Rep.* **33**, 102550 (2020).

45. Dudd, S. N. & Evershed, R. P. Unsual triterpenoid fatty acyl ester component of archaeological birch bark tars. *Tetrahedron Lett.* **40**, 359–362 (1999).

46. Serpico, M. & White, R. Chemical analysis of coniferous resins from ancient Egypt using gas chromatography/mass spectrometry (GC/MS). In *Proc. 7th International Congress of Egyptologists, Leuven* (1998).

47. Fulcher, K., Serpico, M., Taylor, J. H. & Stacey, R. Molecular analysis of black coatings and anointing fluids from ancient Egyptian coffins, mummy cases, and funerary objects. *Proc. Natl Acad. Sci. USA* **118**, e2100885118 (2021).

48. Deines, H. V. & Westendorf, W. *Wörterbuch der Medizinischen Texte. Grundriss der Medizin der Alten Ägypter 7* (Akademie, 1961).

49. Rageot, M. et al. Birch bark tar production: experimental and biomolecular approaches to the study of a common and widely used prehistoric adhesive. *J. Archaeol. Method Theor.* **26**, 276–312 (2019).

50. Koller, J., Baumer, U., Kaup, Y., Schmid, M. & Weser, U. Ancient materials: analysis of a pharaonic embalming tar. *Nature* **425**, 784 (2003).

51. Serpico, M. in *Ancient Egyptian Materials and Technology* (eds Nicholson, P. T. & Shaw, I.) 430–474 (Cambridge Univ. Press, 2000).

52. Quack, J. F. in *Ägyptische Mumien. Unsterblichkeit im Land der Pharaonen* 19–27 (Landesmuseum Württemberg, 2007).

53. Nissenbaum, A. & Buckley, S. Dead Sea asphalt in Ancient Egyptian mummies —why? *Archaeometry* **55**, 563–568 (2013).

54. Scott, A. et al. Exotic foods reveal contact between South Asia and the Near East during the second millennium bce. *Proc. Natl Acad. Sci. USA* **118**, e2014956117 (2021).

55. Kockelmann, H. & Rickert, A. *Von Meroe bis Indien. Fremdvölkerlisten und Nubische Gabenträger in den Griechisch-Römischen Tempeln, Soubassementstudien V, Studien zur Spätägyptischen Religion 12*. 53–54 (Harrassowitz, 2015).

56. Mottram, H. R., Dudd, S. N., Lawrence, G. J., Stott, A. W. & Evershed, R. P. New chromatographic, mass spectrometric and stable isotope approaches to the classification of degraded animal fats preserved in archaeological pottery. *J. Chromatogr. A* **833**, 209–221 (1999).

57. van den Berg, K. J., Boon, J. J., Pastorova, I. & Spetter, L. F. M. Mass spectrometric methodology for the analysis of highly oxidized diterpenoid acids in old master paintings. *J. Mass Spectrom.* **35**, 512–533 (2000).

58. Mathe, C., Culioli, G., Archier, P. & Vieillescazes, C. Characterization of archaeological frankincense by gas chromatography–mass spectrometry. *J. Chromatogr. A* **1023**, 277–285 (2004).

59. Adams, R. P. *Identification of Essential Oil Components by Gas Chromatography/Mass Spectrometry* edn 4.1 (Allured Business Media, 2017).

60. National Institute of Standards and Technology (NIST). *NIST Library*, 2014 edn (2014).

61. Van den Dool, H. & Kratz, P. D. A generalization of the retention index system including linear temperature programmed gas-liquid partition chromatography. *J. Chromatography* **11**, 463–471 (1963).

## Acknowledgements

This study was funded by the European Research Council (ERC) under the European Union’s Horizon 2020 research innovation programme (ERC-2015-StG 678901-Food-Transforms) as part of ERC Starting Grant project ‘FoodTransforms: Transformations of Food in the Eastern Mediterranean Late Bronze Age’ (P.W.S.) and the DFG Project Saqqara Saite Tombs Project (directed by R.B.H.; project number 288139336). The authors thank M. Regert for providing some reference resins and K. Ryholt for helping with the Demotic inscriptions.

# Author information

Author notes

1. Deceased: Ramadan B. Hussein

## Authors and Affiliations


1. Institute for Pre- and Protohistoric Archaeology and Archaeology of the Roman Provinces, Ludwig Maximilian University of Munich, Munich, Germany

   Maxime Rageot, Victoria Altmann-Wendling, Katja Mittelstaedt & Philipp W. Stockhammer

2. Department of Pre- and Protohistory, Eberhard Karls University of Tübingen, Tübingen, Germany

   Maxime Rageot, Stephen Buckley & Cynthianne Spiteri

3. Department of Egyptology, Eberhard Karls University of Tübingen, Tübingen, Germany

   Ramadan B. Hussein & Susanne Beck

4. Department of Egyptology, Julius-Maximilians University, Würzburg, Würzburg, Germany

   Victoria Altmann-Wendling

5. The Central Laboratories Network, the National Research Centre, Cairo, Egypt

   Mohammed I. M. Ibrahim & Mahmoud M. Bahgat

6. Packaging Materials Department, the National Research Centre, Cairo, Egypt

   Ahmed M. Yousef

7. Analytical Research Department, Robertet S.A., Grasse, France

   Jean-Jacques Filippi

8. BioArCh, University of York, York, UK

Stephen Buckley

9. Department of Life Sciences, University of Turin, Turin, Italy

Cynthianne Spiteri

10. Max Planck Institute for Evolutionary Anthropology, Leipzig, Germany

Philipp W. Stockhammer

### Contributions

M.R. and R.B.H. designed and performed the research. M.R. and A.M.Y. sampled the pottery at Saqqara. M.R., K.M. and M.I.M.I. processed the ORA of ceramic sherds. M.R. interpreted the organic residue data with the help of J.-J.F. and S. Buckley. R.B.H. directed the excavation of the site of Saqqara. R.B.H., S. Beck and V.A.-W. performed the study of Hieratic and Demotic texts and provided historical background. M.R., R.B.H. and P.W.S. wrote the paper. M.M.B. and C.S. proofread the manuscript.

### Corresponding authors

Correspondence to Maxime Rageot or Philipp W. Stockhammer.

## Ethics declarations

### Competing interests

The authors declare no competing interests.

## Peer review

### Peer review information

*Nature* thanks Carl Heron and the other, anonymous, reviewer(s) for their contribution to the peer review of this work.

## Additional information

**Publisher's note** Springer Nature remains neutral with regard to jurisdictional claims in published maps and institutional affiliations.

## Extended data figures and tables

### Extended Data Fig. 1 Organic substances identified in the pottery from the Saqqara embalming workshop and communal burial spaces.

Flame = molecular markers associated with heat treatment of the substance. Dotted squares = markers present in the substances, but the assemblage is not specific enough.

### Extended Data Fig. 2 Characteristic biomarkers of ruminant fat.

Partial Total Ion Chromatograms and mass spectra (EI, 70 eV) showing even and odd saturated triacylglycerols (TAGs).

### Extended Data Fig. 3 Characteristic biomarkers of plant oil.

Partial Total Ion Chromatograms and mass spectra (EI, 70 eV) showing unsaturated di- and triacylglycerols (DAGs and TAGs).

### Extended Data Fig. 4 TIC showing the molecular constituents of castor oil and possibly other plant oils (blue), oil/tar of cedar oil/tar (brown) and juniper/cypress (purple) in a white beaker labelled "head".

Cx:y = fatty acid with x carbon atoms and y representing the number of unsaturation; OH-C = hydroxy fatty acid; diOH-C = dihydroxy fatty acid; Ric-OH = ricinoleic acid. $AI_{DB\text{-}5}$ = arithmetic retention index.

### Extended Data Fig. 5 Bitumen biomarkers.

Ion extract chromatogram (m/z 191 and 217) showing **a** the hopanes and **b** the steranes. Hopanes = TM: 17α(H), 22,29,30-trisnorhopane; H29: 17α(H),21β(H)-norhopane (C29); H30: 17 α (H),21β(H)-hopane (C30); H31S: 22S-30-homohopane (C31); H31R: 22R-30-homohopane (C31); GCR: gammacerane; H32S: 22S-30,31-bishomohopane (C32); H32R: 22R-30,31-bishomohopane (C32); H33S: 22S-30,31,32-trishomohopane (C33); H33R: 22R-30,31,32-trishomohopane (C33);

H34S: 22S-30,31,32,33-tetrakishomohopane (C34); H34R: 22R-30,31,32,33-tetrakishomohopane (C34); H35S: 22S-30,31,32,33,34-pentakishomohopane (C35); H35R: 22R-30,31,32,33,34-pentakishomohopane (C35). Steranes = C27Sααα: 20S-5α(H),14α(H),17α(H)-cholestane (C27); C27Rαββ: 20R-5α(H),14β(H),17β(H)-cholestane (C27); C27Sαββ: 20S-5α(H),14β(H),17β(H)-cholestane (C27); C27Rααα: 20R-5α(H),14α(H),17α(H)-cholestane (C27); C28Sααα: 20S-5α(H),14α(H),17α(H)-ergostane (C28); C28Rαββ: 20R-5α(H),14β(H),17β(H)-ergostane (C28); C28Sαββ: 20S-5α(H),14β(H),17β(H)-ergostane (C28); C28Rααα: 20R-5α(H),14α(H),17α(H)-ergostane (C28); C29Sααα: 20S-5α(H),14α(H),17α(H)-stigmastane (C29); C29Rαββ: 20R-5α(H),14β(H),17β(H)-stigmastane (C29); C29Sαββ: 20S-5α(H),14β(H),17β(H)-stigmastane (C29); C29Rααα: 20R-5α(H),14α(H),17α(H)-stigmastane (C29).

### Extended Data Fig. 6 Saqqara complex and location of the investigated vessels in the embalming facilities and burial chambers.

Background = digital documentation of Saqqara complex. Copyright M. Lang, Universität Bonn.

### Extended Data Fig. 7 Photograph of Shaft M23-II (left side).

Embalming workshop/cachette room with ledge-like bed and drainage channel, looking east. Copyright SSTP.

### Extended Data Fig. 8 Photograph of Shaft M23-II (right side).

Embalming workshop/cachette room with the ledge-line bed and the large fumigation vessel on the right side, looking east. Copyright SSTP.

**Extended Data Table 1 List of samples including the vessels' inscription, ORA results and quantification**
**Extended Data Table 2 Synthesis of the triterpenoid components of Burseraceae resins and comparison with the products identified in Saqqara**
**Extended Data Table 3 Modern and aged angiosperm resins used as references**

## Supplementary information

### Supplementary Information

The Supplementary Information contains Supplementary Sections 1 and 2 which present a detailed description of the archaeological context of the Saqqara complex (embalming workshop and ancient Egyptian embalming facilities) and of the results of the organic residue analyses (molecular assemblages associated with the identified substances).

**Reporting Summary**

## Rights and permissions

**Open Access** This article is licensed under a Creative Commons Attribution 4.0 International License, which permits use, sharing, adaptation, distribution and reproduction in any medium or format, as long as you give appropriate credit to the original author(s) and the source, provide a link to the Creative Commons licence, and indicate if changes were made. The images or other third party material in this article are included in the article's Creative Commons licence, unless indicated otherwise in a credit line to the material. If material is not included in the article's Creative Commons licence and your intended use is not permitted by statutory regulation or exceeds the permitted use, you will need to obtain permission directly from the copyright holder. To view a copy of this licence, visit http://creativecommons.org/licenses/by/4.0/.

Reprints and Permissions

## About this article

### Cite this article

Rageot, M., Hussein, R.B., Beck, S. *et al.* Biomolecular analyses enable new insights into ancient Egyptian embalming. *Nature* **614**, 287–293 (2023). https://doi.org/10.1038/s41586-022-05663-4

- Received: 10 August 2022
- Accepted: 15 December 2022
- Published: 01 February 2023
- Issue Date: 09 February 2023
- DOI: https://doi.org/10.1038/s41586-022-05663-4

### Share this article

Anyone you share the following link with will be able to read this content:

Get shareable link

Sorry, a shareable link is not currently available for this article.

Copy to clipboard

Provided by the Springer Nature SharedIt content-sharing initiative

## This article is cited by

- **The surprising chemicals used to embalm Egyptian mummies**
    - Ewen Callaway

  *Nature* (2023)

### How mummies were prepared: Ancient Egyptian pots spill secrets

- Nick Petrić Howe
- Benjamin Thompson

Nature Nature Podcast 01 Feb 2023

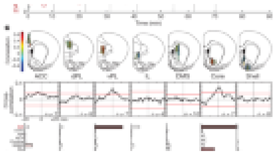
### Recipes and ingredients for ancient Egyptian mummification

- Salima Ikram

Nature News & Views 01 Feb 2023

---

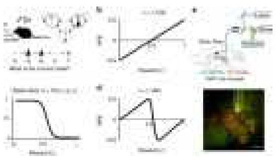
This article was downloaded by **calibre** from https://www.nature.com/articles/s41586-022-05663-4



## Dissociable dopamine dynamics for learning and motivation

22 May 2019

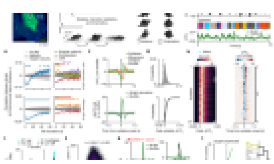
Ali Mohebi, Jeffrey R. Pettibone, … Joshua D. Berke



## Belief state representation in the dopamine system

14 May 2018

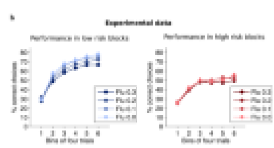
Benedicte M. Babayan, Naoshige Uchida & Samuel. J. Gershman



## Spontaneous behaviour is structured by reinforcement without explicit reward

18 January 2023

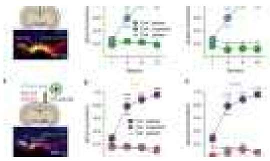
Jeffrey E. Markowitz, Winthrop F. Gillis, … Sandeep Robert Datta



## Dopamine blockade impairs the exploration-exploitation trade-off in rats

01 May 2019

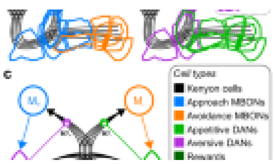
François Cinotti, Virginie Fresno, … Mehdi Khamassi



## Dopamine neurons create Pavlovian conditioned stimuli with circuit-defined motivational properties

23 July 2018

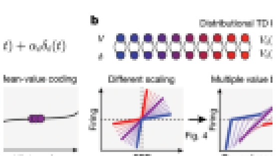
Benjamin T. Saunders, Jocelyn M. Richard, … Patricia H. Janak



## Learning with reinforcement prediction errors in a model of the Drosophila mushroom body

07 May 2021

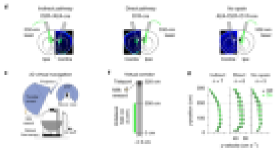
James E. M. Bennett, Andrew Philippides & Thomas Nowotny



## A distributional code for value in dopamine-based reinforcement learning

15 January 2020

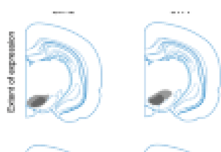
Will Dabney, Zeb Kurth-Nelson, … Matthew Botvinick



[Opponent control of behavior by dorsomedial striatal pathways depends on task demands and internal state]

07 March 2022

Scott S. Bolkan, Iris R. Stone, … Ilana B. Witten



[Dopamine transients do not act as model-free prediction errors during associative learning]

08 January 2020

Melissa J. Sharpe, Hannah M. Batchelor, … Geoffrey Schoenbaum

- Article
- Open Access
- Published: 18 January 2023

# Mesolimbic dopamine adapts the rate of learning from action


- Luke T. Coddington ,
- Sarah E. Lindo &

- Joshua T. Dudman


*Nature* **volume 614**, pages 294–302 (2023)


- 9350 Accesses
- 49 Altmetric
- Metrics details


# Abstract

Recent success in training artificial agents and robots derives from a combination of direct learning of behavioural policies and indirect learning through value functions[1,2,3]. Policy learning and value learning use distinct algorithms that optimize behavioural performance and reward prediction, respectively. In animals, behavioural learning and the role of mesolimbic dopamine signalling have been extensively evaluated with respect to reward prediction[4]; however, so far there has been little consideration of how direct policy learning might inform our understanding[5]. Here we used a comprehensive dataset of orofacial and body movements to understand how behavioural policies evolved as naive, head-restrained mice learned a trace conditioning paradigm. Individual differences in initial dopaminergic reward responses correlated with the emergence of learned behavioural policy, but not the emergence of putative value encoding for a predictive cue. Likewise, physiologically calibrated manipulations of mesolimbic dopamine produced several effects inconsistent with value learning but predicted by a neural-network-based model that used dopamine signals to set an adaptive rate, not an error signal, for behavioural policy learning. This work provides strong evidence that phasic dopamine activity can regulate direct learning of behavioural policies, expanding the explanatory power of reinforcement learning models for animal learning[6].

# Main

Biological and artificial agents learn how to optimize behaviour through experience with an environment. Reinforcement learning theory describes

the algorithms that allow an agent to iteratively improve its success through training[3]. Experience with the environment can be evaluated either by the success of an agent's behavioural 'policy' that directly determines the actions performed ('policy learning') or by an agent's subjective expectations of reward that indirectly guide action ('value learning'). Over the past several decades much work has explored how midbrain dopamine neuron (mDA) activity matches the predicted update signals (reward prediction errors (RPEs)[7]) for value learning[4]. However, mDA activity also reflects a heterogeneous mix of signals and functions that may not be completely addressed by the predictions of value learning models[8,9,10,11,12]. Phasic mDA activity can be intertwined with the production and monitoring of action[10,13,14,15,16,17,18] and is determined at least in part by inputs from areas involved in determining behavioural policy[19]. This calls for an exploration of how broadening the scope of considered reinforcement learning algorithms might inform our understanding of phasic mDA signals in biological agents.

Direct policy learning specifically offers untapped potential[5,20] to provide 'computational and mechanistic primitives'[6] that explain the functions of dopamine, especially in the context of novel task acquisition by animals. First, direct policy learning methods have achieved substantial success in embodied learning problems in robotics that resemble problems faced by a behaving animal[1]. Second, under a wide set of conditions policy learning is the most parsimonious reinforcement learning model that explains learned behaviour[5]. Third, policy learning can be directly driven by behavioural performance error (PE) signals, in lieu of, or in addition to, RPEs[21,22], connecting them to diverse observations of learning in dopamine-recipient brain areas[23,24]. Finally, policy learning methods facilitate explicit modelling of meaningful variability[25] in individual behavioural learning trajectories as a search through the space of policy parameterizations[1].

It can in fact be a criticism of policy search that learning trajectories can be too variable; although conducive to modelling individual differences, this feature can produce suboptimal learning[26,27]. A powerful solution is to set an optimal update size for each trial according to some heuristic for how useful each trial could be for learning[2]. Doing so independently of the performance

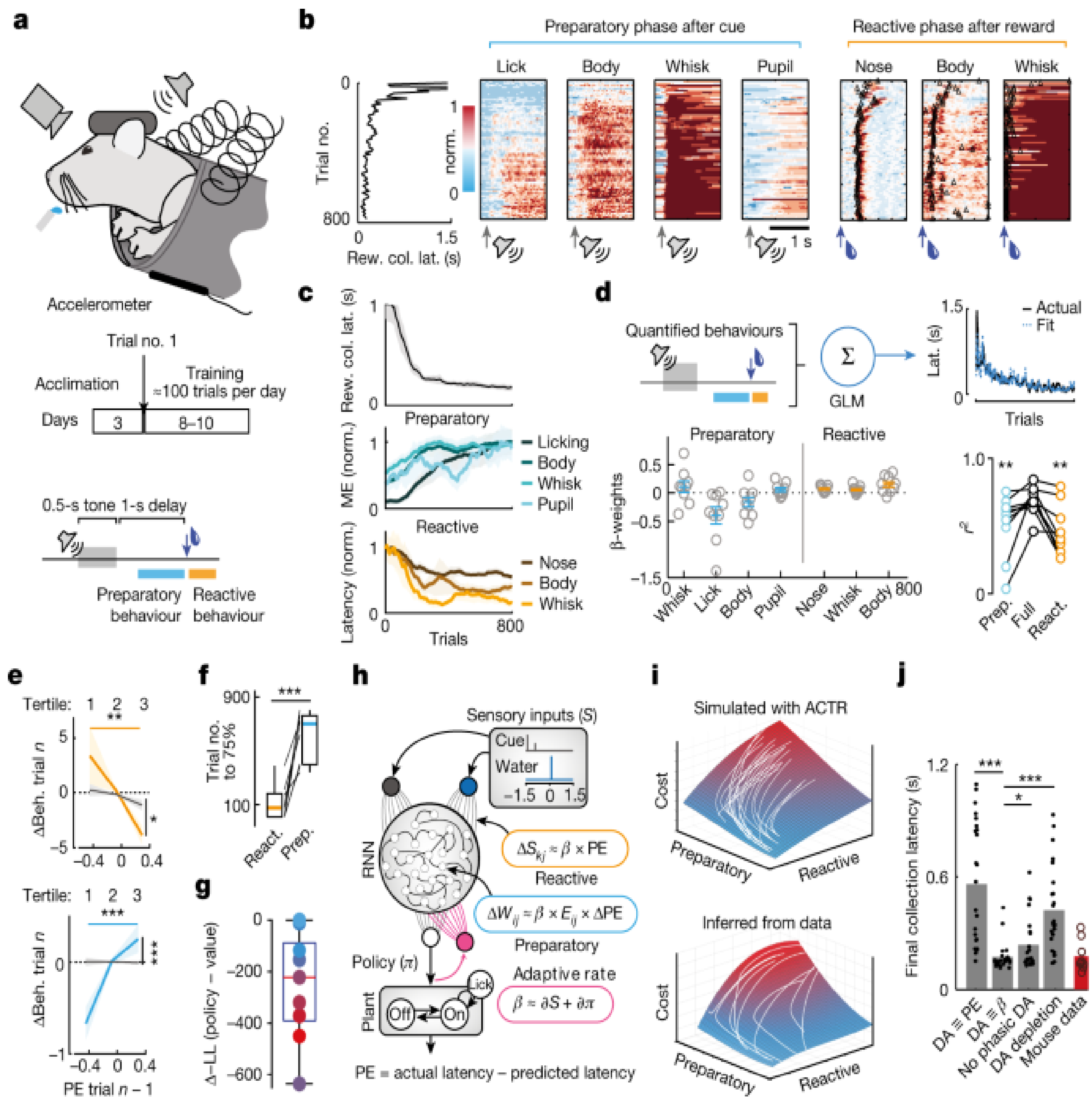
feedback that directs learning can enhance useful variability while suppressing noise[1,26,28]. Such 'adaptive learning rates' have led to fundamental advances in machine learning[28], and can also make models of animal learning more accurate[29]. Thus, insights from policy learning lead to an intriguing hypothesis for phasic mDA activity that has not, so far, been explored. Phasic mDA activity could be a useful adaptive learning rate signal, given its correlations to novel and salient stimuli[12], upcoming actions[13] and prediction errors[7], all of which are useful heuristics for identifying key moments during which learning rates should be elevated. Alternatively, mDA activity correlates with PEs during avian song learning[30], suggesting that in mammals it could also dictate error-based updates to behavioural policies—a role more analogous to conveying RPEs for value learning. The establishment of policy learning models of canonical animal behavioural tasks is required to distinguish among these possibilities.

Here we develop a policy learning account of the acquisition of classical trace conditioning in which behaviour is optimized to minimize the latency to collect reward once it is available, inspired by observations of this process in naive mice. A multidimensional dataset of behavioural changes during acquisition could be seen to drive improvements in reward collection performance, and a novel policy learning model quantitatively accounted for the diverse learned behaviour of individual animals. mDA activity predicted by the component of this model that sets an adaptive learning rate closely matched fibre photometry recordings of mDA activity made continuously throughout learning. Individual differences in initial phasic mDA responses predicted learning outcome hundreds of trials later in a manner consistent with dopamine modulating learning rate. Optogenetic manipulation of ventral tegmental area (VTA) dopamine neurons was calibrated to physiological signals and triggered in closed-loop with behaviour to provide a key test of the hypothesis that phasic mDA activity modulates learning rate as a distinct alternative to signalling signed errors. Together, these results define a novel function for mesolimbic dopamine in adapting the learning rate of direct policy learning (summarized in Extended Data Fig. 10).

## Task design and learning trajectories

We tracked multiple features of behavioural responses to classical trace conditioning in thirsty mice that had been acclimated to head fixation but had received no other ‘shaping’ or pre-training. Sweetened water reward was ‘cued’ by a 0.5-s auditory cue (10-kHz tone) followed by a 1-s delay, except on a small number of randomly interleaved ‘uncued’ probe trials (about 10% of total trials). Although reward was delivered irrespective of behaviour, mice still learned to optimize reward collection, as assayed by monotonic decreases in latency to collect reward across training (Fig. 1a–c). We measured multiple features of behaviour to understand how idiosyncratic learning across individual mice subserved performance improvements: an accelerometer attached to the movable basket under the mice summarized body movements[9], while high-resolution video was used to infer lick rate, whisking state, pupil diameter and nose motion. We reasoned that reward collection performance could be improved along two dimensions: preparation for reward delivery and reaction to its sensory components (Fig. 1d–f). ‘Preparatory’ behaviour was assayed across lick, body, whisker and pupil measurements as the total amount of activity during the delay period between cue and reward. ‘Reactive’ behaviour was assayed across nose, body and whisker measurements as the latency to initiate following reward delivery.

**Fig. 1: Changes to behavioural policy correlate with improved reward collection performance.**



**a**, Experimental design. **b**, Ten-trial binned behavioural quantification across the first 800 training trials. Reward collection latency (Rew. col. lat.; leftmost column) compared to normalized (Norm.) heat maps of preparatory (middle four columns; grey arrows: cue start) and reactive behaviour (right three columns; blue arrows: reward delivery; black triangles: mean first response). **c**, One-hundred-trial moving means of reward collection latency (top), and normalized preparatory (middle, motion energy (ME)) and reactive (bottom, latency) measures ($n = 9$ mice). **d**, Top: behavioural measures predicted reward collection latency in a GLM for each mouse.

Bottom left: GLM predictor weights for each of nine mice. Bottom right: preparatory (Prep.; blue) or reactive (React.; orange) predictors alone performed worse than the full model. Significance testing: Friedman's. **e**, Trialwise reactive (top, orange) and preparatory (bottom, blue) behaviour (Beh.; binned into tertiles of PE magnitudes) correlated with inferred PE on the previous trial (black lines: shuffled control of trialwise PE for all other mice). *n*, trial number. Significance testing: two-way ANOVA; Tukey–Cramer post hoc. **f**, Trials to reach 75% maximum learned performance for reactive (orange) and preparatory (blue) behaviours ($n = 9$ mice). $P < 0.001$; two-tailed rank sum test. **g**, Difference between fits (in negative log likelihood (−LL)) for versions of ACTR model (grey bars (smaller number equals better fit) for each mouse (coloured circles). **h**, The ACTR model learned a lick plant control policy ($\pi$) as the output from an RNN receiving sensory inputs following cue onset/offset (purple) and reward delivery (red). $e_{ij}$, eligibility trace for node perturbation at the synapse between the *i*th neuron and the *j*th neuron. Learning rules (blue and orange boxes) updated the weights of sensory inputs ($S_{kj}$) and internal connections ($W_{ij}$) using a mDA-like adaptive learning rate ($\beta$, pink). **i**, Top: cost surface calculated from ACTR model, overlaid with trajectories from individual initializations (white). Bottom: cost surface fitted from mouse data, overlaid with individual trajectories (white). **j**, Final performance for versions of ACTR model (grey bars; individuals as dots; $n = 24$) with the indicated differences in dopamine function (see main text) compared to observed performance in mice (red bar; individuals as circles; $n = 9$). Significance testing: rank sum. All error bars denote ±s.e.m. Box plots represent the median at their centre bounded by the 25th and 75th percentile of the data, with whiskers to each extreme. *$P < 0.05$; **$P < 0.01$; ***$P < 0.001$.

Although preparatory and reactive components of learned behaviour exhibited roughly monotonic trajectories on average (Fig. 1c), this belied heterogeneity in the dynamics of learning across individuals (Extended Data Fig. 1a–c). To assess the relationship between learned behaviours and reward collection performance on an individual basis, we built generalized linear models (GLMs) to predict reward collection latency across training in each mouse (Fig. 1d). GLMs using preparatory and reactive behavioural measures as predictors captured much of the variance in reward collection efficiency over training ($r^2 = 0.69 \pm 0.11$; $r^2$ with shuffled responses $= 0.01 \pm 3 \times 10^{-4}$).

Each predictor's weighting could vary widely from mouse to mouse, with preparatory licking having the most consistent relation to reward collection latency (Fig. 1d). However, both preparatory and reactive variables were necessary to most accurately predict reward collection latency (Fig. 1d; Friedman's: $P = 0.0003$; preparatory alone $r^2 = 0.51 \pm 0.24$, versus full model $P = 0.004$; reactive alone $r^2 = 0.46 \pm 0.20$, versus full model $P = 0.002$). Consistent with direct policy updates by a PE related to reward collection latency, our observations showed that updates to both the reactive and preparatory behaviour on each current trial were significantly related to reward collection latency on the previous trial (Fig. 1e). The significantly different time courses of preparatory and reactive learning (Fig. 1f) further confirm that these two learning components are dissociable processes.

We thus describe updates to the behavioural policy for each mouse as a trajectory through an abstract 'learning space' spanned by two components (preparation and reaction) that together explain improvements in reward collection performance optimized by minimizing reaction times and maximizing preparation (Fig. 1i and Extended Data Fig. 1b,c).

# ACTR policy learning model

The above data suggest that naive acquisition of trace conditioning could be considered as a problem of optimizing an effective control policy for reward collection through direct policy learning rather than indirectly through value learning. To formalize this comparison, we took an exemplar of a low-parameter value learning model that accounts for variable learning rates across individuals[31] and implemented a matched direct policy learning algorithm of the REINFORCE class[21] with equal free parameters (Methods). We next compared the negative log likelihood (−LL) and Akaike information criterion for the data given the optimal parameterization of each model class as carried out previously[32]. We found that the policy learning variant achieved significantly better fits (lower −LL and Akaike information criterion) when comparing optimally parameterized versions across nine mice ($\Delta$LL = −252.6 ± 70.8; $P < 0.01$, signrank; Extended Data Fig. 1d,e). We also found that the policy learning formulation was markedly less brittle

($\Delta LL_{median} = -3.8 \times 10^3 \pm 0.8 \times 10^3$; $P < 0.01$, signrank; Extended Data Fig. 1f).

This model comparison indicates that for these broad algorithmic classes, a policy learning instantiation is a better descriptor of learning behaviour, as observed previously in human dynamic foraging[32] and sensorimotor adaptation tasks[33]. However, these low-parameter models enable only limited comparisons to behavioural and neurophysiological measurements. First, our experimental data clearly indicated two dissociable components of learning (reactive and preparatory) that have no clear analogy to abstract policy or value learning models in large part because there is no explicit modelling of the control of behaviour. Second, although model comparison reveals that policy learning algorithms in general may be superior, this is a broad class of algorithm that prescribes properties of the learning rule, but depending on model structure can be computed in many different ways[21]. Thus, we next sought to implement a circuit-inspired policy learning model that might facilitate direct comparisons to neurophysiological measurements.

To address these issues, we first specified a behavioural 'plant' (Extended Data Fig. 2d and Fig. 1h) that captured the statistics of rodent licking behaviour as a state model that transitions between quiescence and a licking state that emits a physiological lick frequency. A continuous control policy ($\pi(t)$) determined the forward transition rate to active licking. The reverse transition rate reflects a bias towards quiescence that decreases in the presence of water such that licking is sustained until collection is complete (Methods). The control policy was learned as the additive combination of output from a recurrent neural network (RNN) modelling preparatory learning and a feedforward sensorimotor pathway modelling reactive learning (Fig. 1h; see Methods for model details and code). Notably, optimal policies for speeding reward collection (identified by a search through the space of potential RNNs; Extended Data Fig. 2a,b) required preparatory cued licking that depends on sustained dynamics in the RNN output.

The PE used to train the model was proportional to the difference between performance, as measured by the latency to collect the water reward, and a correlate of expected performance, the activity of the output unit at the time of reward delivery (Methods). Both reactive and preparatory learning

occurred in proportion to this PE, but they were implemented at different positions within the network. Reactive learning was modelled as changes to feedforward weights from sensory inputs to behavioural policy output ($S_{kj}$; Fig. 1h), to replicate the optimization of behavioural responses to reward delivery in both cued and uncued trials (Extended Data Fig. 2e). Preparatory learning was modelled as changes to internal weights in the RNN ($W_{ij}$; Fig. 1h), and was proportional to the relative change in PE (customary in many policy learning algorithms[21]). The combination of reactive and preparatory learning robustly converged on stable, near-optimal policies that led to marked reductions in the latency to collect reward over several hundreds of training trials (Fig. 1i,j). To stabilize policy across a range of model initializations, an adaptive learning rate for each trial was controlled by a feedback unit (pink output unit in Fig. 1h); activity of the feedback unit was the sum of the state change in the behavioural plant (akin to an efference copy of reward-related action initiation commands) and the change in behavioural policy at the time of reward delivery (akin to reward-related sensory evidence informing behaviour[9]). This feedback scheme has a direct and intentional parallel to the phasic activity of mDA neurons in this task, which is well described as the sum of action- and sensory-related components of reward prediction[9,13] and occurs in parallel to direct sensorimotor outputs[34]. Notably, this scheme closely reproduces mDA activity across naive learning as measured by both somatic spiking[9] and $Ca^{2+}$-sensor dynamics (Fig. 4). Overall, our approach adds an adaptive rate component inspired by supervised learning optimization methods[26,28,35] to an unsupervised, biologically plausible rule for training RNNs[36] that itself drew inspiration from node perturbation methods and the classic direct policy optimization method whose acronym is REINFORCE[3,21]. Hence, we refer to the complete model as ACTR (for adaptive rate, cost of performance to REINFORCE).

ACTR successfully reproduced many meaningful aspects of mouse behavioural learning data. For repeated ACTR simulations ($n = 24$) with a range of initializations, latency to collect rewards declined comparably to observed mouse behaviour over training (Fig. 1i–j, including an equivalent cued performance gain (Extended Data Fig. 2e)). Learning trajectories and cost surfaces calculated from a range of model initializations compared well

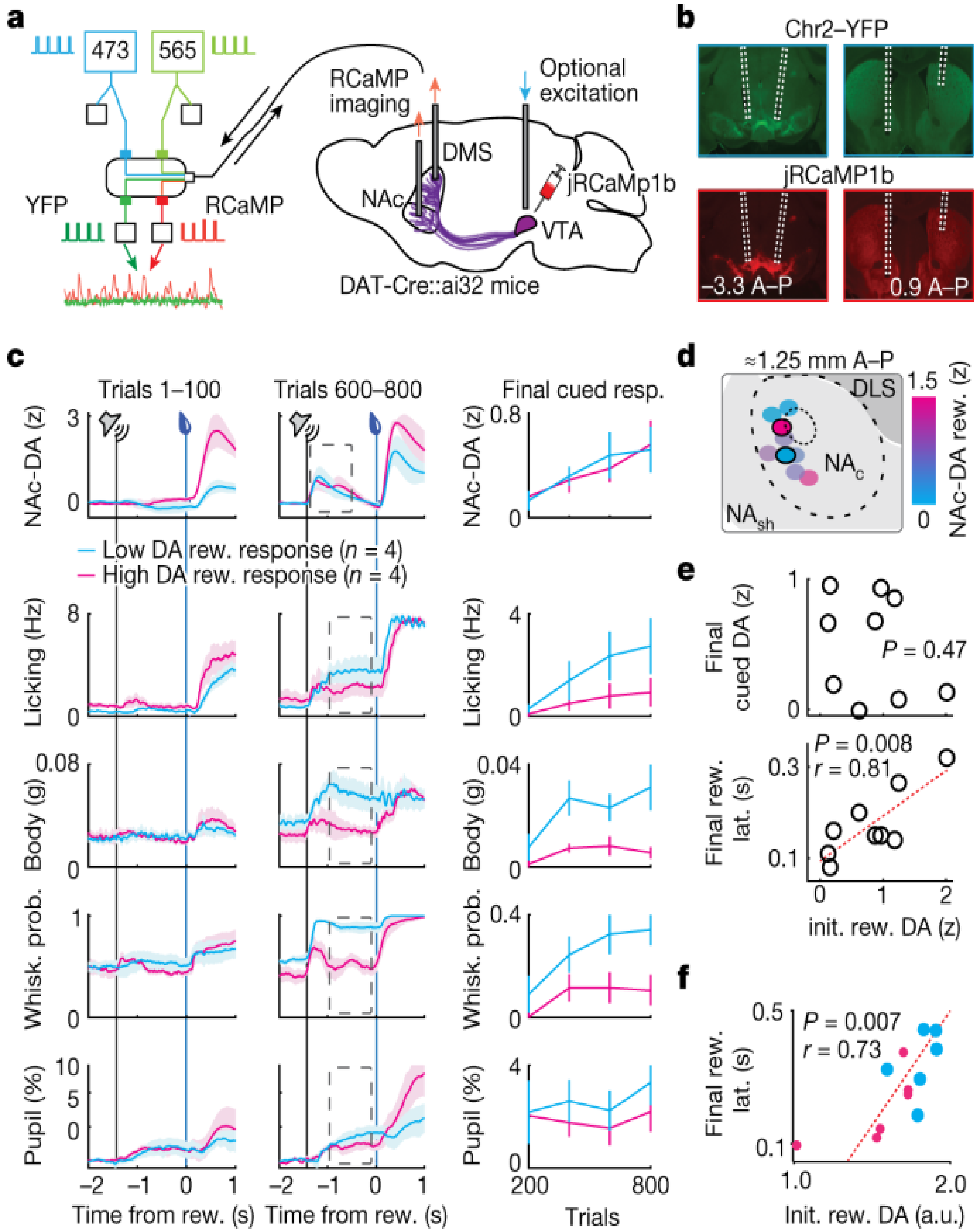
qualitatively and quantitatively to those inferred from mouse data (Fig. 1i, Extended Data Fig. 2c and Methods). Finally, modelling the adaptive rate term ($\beta$) after phasic mDA activity (see Fig. 4 for comparison of modelled to actual) was well supported by comparing end performance of the full model to modified versions (Fig. 1j) in which: the mDA-like feedback unit signalled PE instead of rate (Extended Data Fig. 2f; significantly worse performance, rank sum $P < 2 \times 10^{-7}$); learning rate was globally reduced (akin to dopamine depletion[37]; significantly worse performance, rank sum $P < 2 \times 10^{-6}$); a basal learning rate was intact but there was no adaptive component (akin to disruption of phasic mDA reward signalling[38]; significantly worse performance, rank sum $P = 0.02$). Thus, naive trace conditioning is well described as the optimization of reward collection behaviour, and best approximated when mDA-like signals act not as signed errors directing changes to the policy, but instead adapting the size of the learned update on each trial.

## Change in dopamine activity over learning

We measured mDA activity in the above mice, which were DAT-Cre::ai32 mice that transgenically expressed Chr2 under control of the dopamine transporter promoter, by injecting a Cre-dependent jRCaMP1b virus across the ventral midbrain[9] (Fig. 2a,b). This combined optogenetic–fibre photometry strategy also allowed for calibrated dopamine manipulations in later experiments. Optical fibres were implanted bilaterally over the VTA, and unilaterally in the nucleus accumbens core (NAc), and in the dorsomedial striatum (DS; Fig. 2a). We recorded jRCaMP1b signals from the NAc (‘NAc–DA’) in all mice, with some additional simultaneous recordings from ipsilateral VTA ($n = 3$, ‘VTA–DA’) or contralateral DS ($n = 6$, ‘DS–DA’). NAc–DA reward responses became better aligned to reward delivery across training but did not decrease significantly (trials 1–100: 0.82 ± 0.21 z, trials 700–800: 1.16 ± 0.23 z, signed rank $P = 0.13$), even as cue responses steadily increased (Extended Data Fig. 3a,b). These dynamics recapitulated our previous observations from somatic activity[9] and indeed closely resembled simultaneously recorded VTA–DA signals (Extended Data Fig. 3a–e). By contrast, DS–DA developed cue and reward responses only on further training, matching previous reports[39,40] (Extended Data Fig.

3a–e), and indicating that mesolimbic (for example, VTA-to-NAc) reward signals are of specific interest during the initial learning period studied here.

**Fig. 2: Individual differences in mesolimbic dopamine signals correlate with learned behavioural policy.**




**a**, Schematic for fibre photometry with optional simultaneous optogenetic stimulation of midbrain dopamine neurons. **b**, Fibre paths and virus

expression from an example experiment. A–P, anterior–posterior. **c**, Left and middle: NAc–DA, licking, body movements, whisking probability and pupil diameter measurements for the mean of animals with lowest (blue, $n = 4$) and highest (pink, $n = 4$) NAc–DA reward signals over the initial 100 trials, shown for trials 1–100 (left) compared to trials 600–800 (middle). Right: means of responses (resp.) in the analysis windows indicated at left (dashed grey boxes) across training. **d**, Illustration of fibre locations for each mouse ($n = 9$), colour-coded according to the size of their initial NAc–DA reward signals. DLS, dorsolateral striatum; $NA_{sh}$, nucleus accumbens shell. **e**, Initial (Init.) NAc–DA reward responses (trials 1–100) were correlated with final latency to collect reward (bottom, Pearson's $r = 0.81$, $P = 0.008$), but not with final cued NAc–DA response (top, Pearson's $P = 0.47$) ($n = 9$ mice). **f**, ACTR simulations with low (small pink dots, $n = 6$) or high (large blue dots, $n = 6$) initial reward-related sensory input exhibited a significant correlation between initial (trials 1–100) predicted mDA reward response and final reward collection latency. a.u., arbitrary units. All error bars denote ±s.e.m.

We thus proceeded to examine how individual differences in mesolimbic reward signals were related to the individual differences in behavioural learning. We found substantial inter-animal variance in initial NAc–DA responses in the first 100 trials that was not related to anatomical location of fibres (Fig. 2c,d; initial NAc–DA reward: anterior–posterior: $P = 0.5$, medial–lateral: $P = 0.4$, dorsal–ventral: $P = 0.5$; multiple linear regression all axes, $P = 0.7$). Unexpectedly, initial NAc–DA reward signals were negatively correlated with the amount of preparatory behaviour at the end of training (Fig. 2c and Extended Data Fig. 3f; NAc–DA $\text{reward}_{\text{trials 1–100}}$ versus preparatory $\text{index}_{\text{trials 700–800}}$, $r = -0.85$, $P = 0.004$), as well as the speed of reward collection (Fig. 2e; NAc–DA $\text{reward}_{\text{trials 1–100}}$ versus reward collection $\text{latency}_{\text{trials 700–800}}$, $r = 0.81$, $P = 0.008$). This relationship was specific for preparatory behaviours (Extended Data Fig. 3g; NAc–DA $\text{reward}_{\text{trials 1–100}}$ versus reactive $\text{index}_{\text{trials 700–800}}$, $P = 0.24$), and was robust as each mouse's initial dopamine reward signals could be accurately predicted from quantifications of final preparatory behaviour (Extended Data Fig. 3h; actual versus predicted $r = 0.99$, $P < 0.0001$).

The negative correlation between dopaminergic reward signaling and behavioural learning is not consistent with the magnitude of phasic mDA

activity determining or correlating with the error used for a learning update. However, it is potentially consistent with phasic mDA activity reflecting action-related and sensory-related components of the control policy. At initialization of the ACTR model, no preparatory actions have been learned, so the dopamine signal is dominated by the initial reactive response to sensory input at reward delivery. Adjusting the strength of this sensory input at model initialization scales the initial dopamine reward response magnitudes similarly to the range observed in mice (Fig. 2f). These initialization differences in ACTR simulations predicted a delayed collection latency at the end of training (Extended Data Fig. 3i; $r = 0.73$, $P = 0.007$) due to a reduced development of a preparatory licking policy (Extended Data Fig. 3j), mirroring our results in mice and demonstrating that stronger reactive responses to sensory information can impair the learned development of preparatory responses (and thus ultimately impair performance). These insights from the ACTR model suggest that, in real mice, initial sensitivity to reward-related sensory stimuli is reported by increased mDA reward signalling, and this initial condition can explain meaningful individual differences in the courses of future learning.

# Calibrated dopamine stimulation

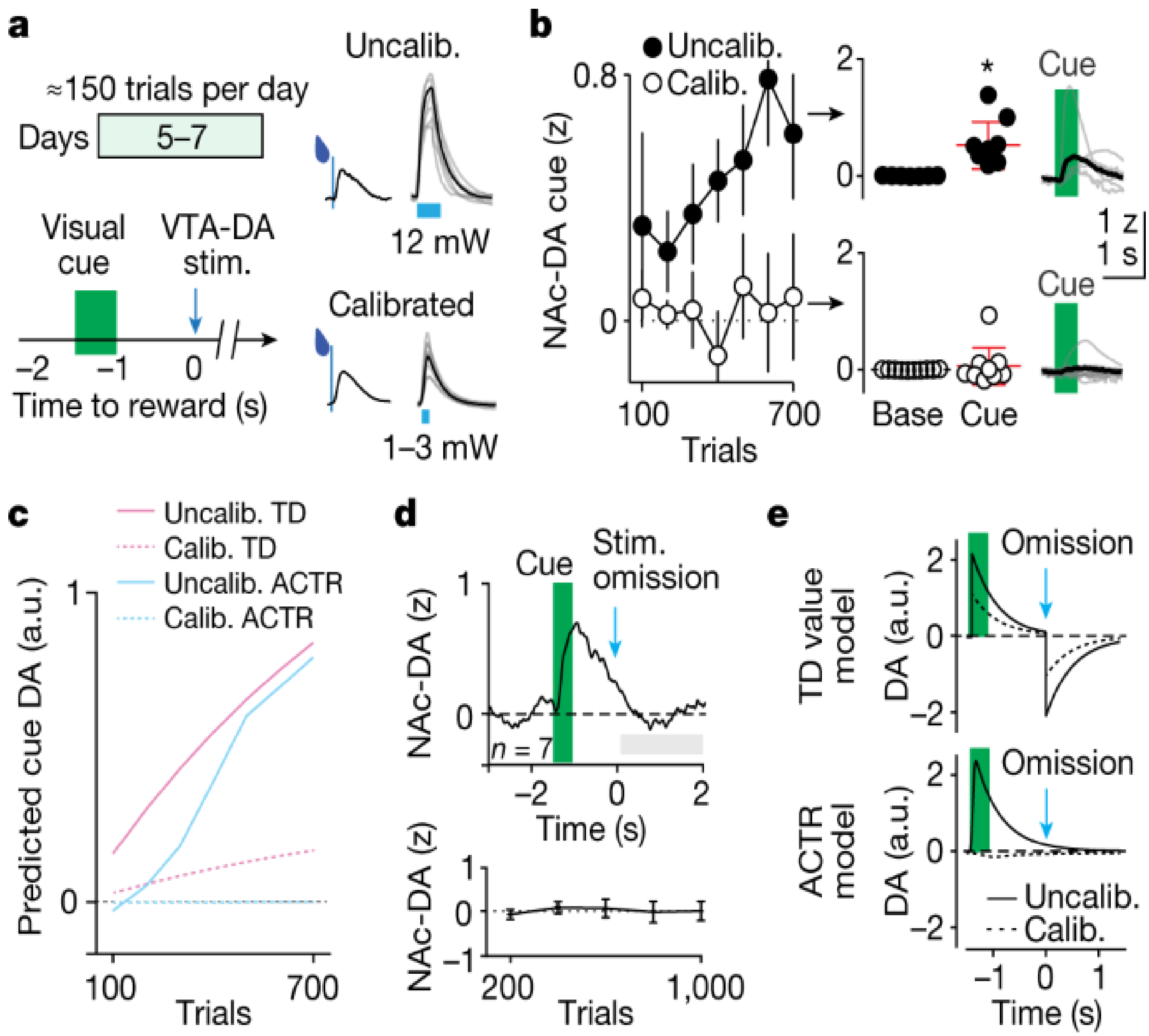
Work exploring direct roles of dopamine in movement[10] or motivation[41] suggests that phasic cue responses provoke or invigorate preparatory behaviour. Indeed, learned NAc–DA cue responses were correlated with cued licking across mice (Extended Data Fig. 4c). However, at the end of regular training some mice experienced an extra session in which VTA–DA stimulation was triggered on cue presentation on a random subset of trials (Extended Data Fig. 4). Increasing mesolimbic cue responses in this way had no effect on cued licking in the concurrent trial (control 2.3 ± 1.1 Hz, stimulation 2.3 ± 1.0 Hz, $P > 0.99$). Thus, within this context (although not necessarily others[42]), the magnitude of NAc–DA cue signals correlates only with learned changes in behavioural policy but does not seem to directly regulate preparatory behaviour in anticipation of reward delivery[9,43].

Notably, individual differences in initial NAc–DA reward signals were not correlated with the learning of NAc–DA cue signals ($\text{reward}_{\text{trials 1–100}}$ versus

$cue_{trials\ 700–800}$, $P = 0.5$; Fig. 2e). This could argue that dopamine reward signals are not a driving force in the learning of cue signals. This is surprising given that results in rodents[43,44] and monkeys[45] provide specific evidence for value learning effects following exogenous VTA–DA stimulation. However, reward-related mDA bursting is brief (≤0.2 s) in our task[9] as well as in canonical results across species[4], raising the question of whether high-power, longer-duration stimulation recruits the same learning mechanisms as briefer, smaller reward-sized responses. We next used our ability to simultaneously manipulate and measure mesolimbic dopamine[9] to examine the function of brief dopamine transients calibrated to match reward responses from our task.

Following initial training on the trace conditioning paradigm (Supplementary Table 1), we introduced mice to a novel predictive cue—a 500-ms flash of light directed at the chamber wall in front of the mouse. After ten introductory trials, this visible cue stimulus was paired with exogenous VTA–DA stimulation after 1 s delay for five daily sessions (about 150 trials per session; Fig. 3a). One group of randomly selected mice received VTA–DA stimulation calibrated to uncued reward responses (150 ms at 30 Hz and 1–3 mW steady-state power, stimulation response = 1.4 ± 0.3 uncued reward response, $n = 10$), whereas the complement received larger, uncalibrated stimulations (500 ms at 30 Hz and 10 mW steady-state power, stimulation response = 5.5 ± 0.8 uncued reward response, $n = 7$; Fig. 3a,b). After five sessions, the group receiving calibrated, reward-sized stimulation did not exhibit NAc–DA cue responses above baseline (0.0 ± 0.2 z, $P = 0.8$), whereas the large, uncalibrated stimulation group exhibited substantial NAc–DA cue responses (0.5 ± 0.2 z, $P = 0.02$; Fig. 3b).

**Fig. 3: Large mesolimbic dopamine manipulations drive value-like learning.**




**a**, Left: experimental design for VTA–DA stimulation (stim.) predicted by a 0.5-s light flash at the front of the behavioural chamber. Right: mean uncued NAc–DA reward responses versus VTA–DA stimulation responses (right, individuals in grey, mean in black) for mice that received either large, uncalibrated (Uncalib.) stimulation (top; 30 Hz, 12 mW for 500 ms) or stimulation calibrated to reward responses (bottom; 30 Hz, 1–3 mW for 150 ms). **b**, Left: jRCaMP1b NAc–DA cue responses across training for mice that received large stimulations (5× the size of reward responses; filled circles, *n* = 7) or calibrated (Calib.) stimulations (1× the size of reward responses; open circles, *n* = 10). Right: quantified and raw data for mean NAc–DA traces after 750 training trials (5 sessions) with uncalibrated (top, two-tailed signed rank versus baseline, **P* = 0.02, *n* = 7) and calibrated

(bottom, two-tailed signed rank versus baseline $P = 0.8$, $n = 10$) stimulation. **c**, Predicted dopamine cue responses for the experiment in **a** simulated with a TD value learning model (light pink) versus ACTR (light blue). **d**, Top: mean NAc–DA signal after seven sessions of uncalibrated stimulation training, on probe trials with omitted stimulation that were delivered 10% of the time, with quantification over training (bottom). **e**, Predicted dopamine responses by TD (top) and ACTR (bottom) models, for uncalibrated (bold line) and calibrated (dotted line) dopamine stimulation. All error bars denote ±s.e.m.

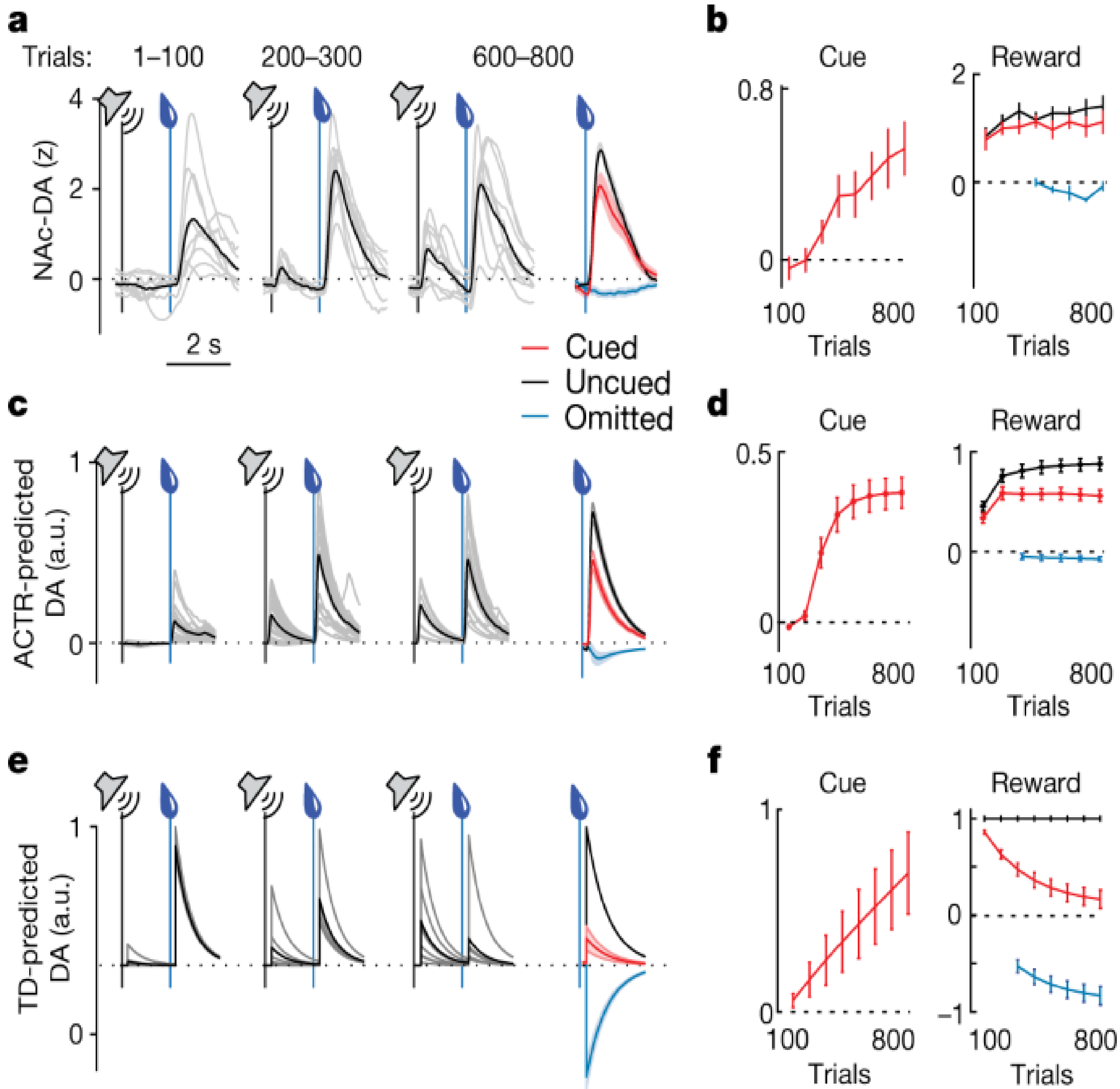
The emergence of cue signals following uncalibrated dopamine stimulation was captured in ACTR by introducing a nonlinearity in which larger, more sustained dopamine activation was modelled as a large modulation of learning rate coupled with a change in PE encoding (Fig. 3c–e and Methods). This coupled effect in the model enhanced cue encoding in a manner similar to the predictions of value learning; however, it was also distinct in that this change in the encoding of cues was not accompanied by the suppression of dopamine activity on omission of the laser stimulus expected from value learning models (Fig. 3d,e). In contrast to previous observations of inhibition following omission of expected stimulation in the context of consistent, overt behavioural responses to cues[17,46], only a brief bout of body movement accompanied cue learning in the current paradigm (Extended Data Fig. 5). This suggests that dopamine inhibition observed following omission of expected rewards may depend on concurrent control[9,13] or evaluation[17] of action.

In separate experiments, calibrated and uncalibrated VTA–DA stimulations had a similar spatial profile of response magnitude across the medial prefrontal cortex and the dorsal-to-ventral axis of the striatum, suggesting that the recruitment of value-like cue learning by uncalibrated stimulation was related to the magnitude or duration of the uncalibrated signal rather than an increased spatial spread (Extended Data Fig. 6). Together, these data provide further evidence that phasic mDA reward responses of the magnitude measured in our task are not sufficient to drive value-like learning of predictive cue responses, but larger stimulation flooding the same downstream regions with higher dopamine concentrations are sufficient to teach phasic responses to a cue that predicts dopamine stimulation.

## Dopamine sets an adaptive learning rate

We next elaborate on the role of dopamine reward signals in performance-driven direct policy learning. NAc–DA signals predicted by ACTR and temporal difference (TD) value learning can be visualized by convolving their dopamine signals (the adaptive rate signal in ACTR and the RPE signal from the optimized TD model parameters; Extended Data Fig. 1) with a temporal kernel matched to the kinetics of jRCaMP1b (Fig. 4 and Methods). ACTR's predicted phasic mDA photometry signal corresponds closely to experimentally measured NAc– and VTA–DA activity across training (Fig. 4a–d and Extended Data Fig. 3a). Notably, ACTR's modelling of mDA activity as the sum of action and sensory components in a control policy reproduces the emergence of differences between expected and unexpected rewards, despite the lack of an explicit RPE computation (Fig. 4b and Extended Data Fig. 7). This scheme also predicts that mDA reward signals should reflect the evolution of reward collection policy across learning. Although animals' policies are not directly observable, the presence or absence of preparatory licking on a given trial of behaviour is a noisy correlate of differences in underlying behavioural policy. Indeed, both ACTR and mouse data exhibited differential reward responses on trials with ('lick+') or without ('lick−') preparatory licking as learning progressed (Extended Data Fig. 8a–d).

**Fig. 4: Dopaminergic adaptive rate signals correlate with RPEs.**

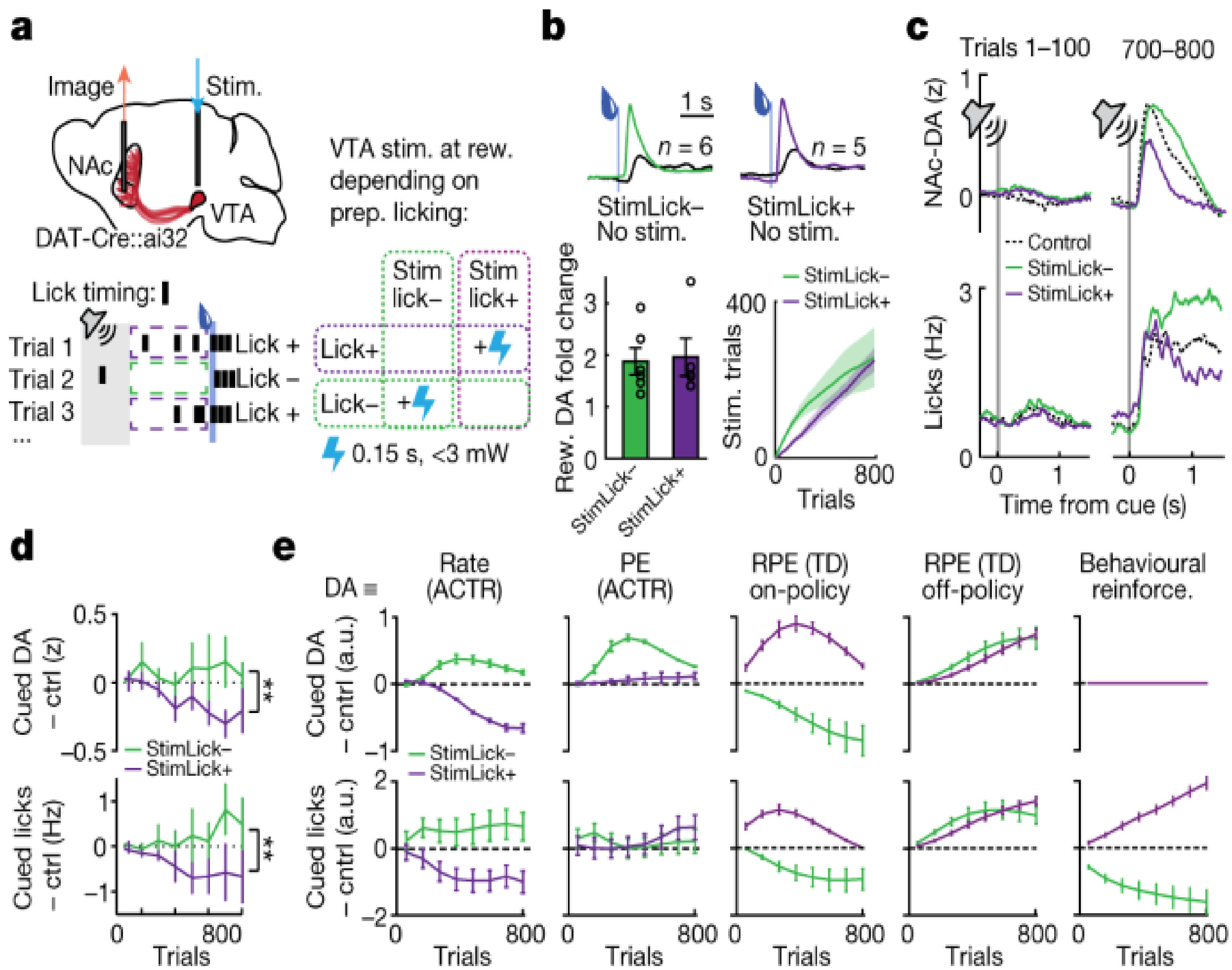



**a**, Measured NAc–DA responses for mice across training, including mean responses to reward on cued (red), uncued (black) and omission (blue, aligned to point at which reward should have been delivered) trials. **b**, Mean cue and reward responses binned in 100-trial blocks across training ($n = 9$). **c**,**d**, Same as **a**,**b** except for predicted dopamine responses in the ACTR model ($n = 9$ model initializations). **e**,**f**, As in **a**,**b** except for predicted dopamine responses in the TD learning model ($n = 9$ model initializations) using parameters that gave the best fit to behavioural learning (from Extended Data Fig. 1). All error bars denote ±s.e.m.

A close examination of the learning signals on lick− versus lick+ trials indicates that those trial types are capturing different distributions of PEs, as estimated from reward collection latency and anticipatory licking (Methods). Although lick+ trials are critical for optimal performance, generally lick+ trials are associated with negative PEs and lick− trials are associated with positive PEs (Extended Data Fig. 8f). Our modelling provides some insight into why this effect is expected and can be most easily illustrated by considering the limiting cases. If the policy is optimal then trials are lick+ and stochasticity in the licking plant or fluctuations in the policy can result only in deviations towards worse than expected reward collection latencies (that is, resulting in a bias towards negative PEs). By contrast, if the policy is as bad as possible, trials are lick− and stochastic initiation of the lick plant right after reward delivery or stochastic fluctuations in the underlying policy (even without inducing a pre-reward lick) can only improve reward collection relative to expected latency of a poor policy (that is, resulting in a bias towards positive PEs).

It then follows that disrupting the balance of dopamine signalling between lick+ and lick− trials should systematically affect learning given the biases in PEs between the two trial types. Owing to their average negative PE, increasing the learning rate exogenously (by increasing the dopamine signal) only on lick+ trials should bias away from robust preparatory policies and decrease final learned preparatory licking. The converse is true for lick− trials, for which selective amplification of positive PEs should bias to more preparatory licking. These paradoxical effects of enhanced rates impairing learning of the contingent behaviour can be demonstrated in ACTR simulations, as trial-type-dependent enhancement of the dopaminergic learning rate signal indeed produced opposite signed effects on preparatory licking behaviour (Extended Data Fig. 8e). Furthermore, this closed-loop stimulation paradigm offers the unique ability to distinguish between many competing models of dopamine function: when dopamine reward signals are modelled as signed errors (PEs in ACTR or RPEs in value learning models) or as a simple behavioural reinforcement signal, the same closed-loop stimulation paradigm biases dopamine cue signals and preparatory licking in opposite directions for at least one of the two trial types (Fig. 5e).

**Fig. 5: Closed-loop manipulation of mesolimbic dopamine distinguishes learning rate signalling from error signalling.**




**a**, Top: simultaneous measurement and manipulation of mesolimbic dopamine. Bottom: closed-loop experiment design, in which different groups of mice received bilateral VTA stimulation (0.15 s, 30 Hz, power calibrated to roughly double control reward response) concurrent with reward delivery on either lick− trials ('stimLick–') or lick+ trials ('stimLick+'). **b**, Top: mean NAc–DA reward responses across training (trials 1–800) for each mouse, with (coloured traces) and without (black traces) exogenous stimulation, for stimLick− (left and green, *n* = 6) and stimLick+ (right and purple, *n* = 5) cohorts of mice. Bottom: fold increase in NAc–DA reward signals on stimulated trials and cumulative sum of stimulated trials across training for stimLick− (green) and stimLick+ (purple). **c**, NAc–DA (top) and licking (bottom) during early (trials 1–100, left) and late (trials 700–800, right) training for control (black), stimLick− (green) and stimLick+ (purple) animals. **d**, NAc–DA cue responses (top) and cued licking (bottom) for stimLick− (green, *n* = 6) and stimLick+ (purple, *n* = 5) mice across training,

shown as the difference from control mice. Two-way ANOVA, **$P$ = 0.002. **e**, Modelling results for the difference of dopamine cue responses (top) and cued licking (bottom) from control in stimLick− and stimLick+ contingencies, compared for five possible functions of phasic dopamine signals. Left to right: the adaptive rate term ($\beta$) in the ACTR policy learning model, biasing the PE term in the ACTR, the RPE signal in on-policy and off-policy TD value learning models, or reinforcing contingent behaviour without affecting learning of dopamine signals ($n$ = 9 simulations for each condition (control, stimLick− and stimLick+) for each model version (Methods)). All error bars denote ±s.e.m.

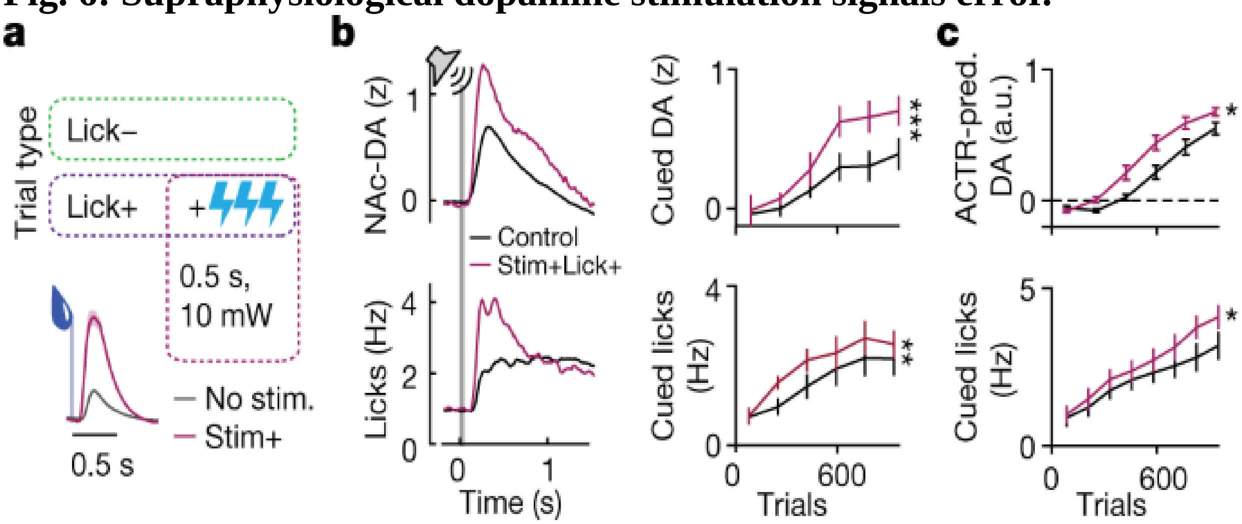
We thus performed this experiment in mice, selectively increasing dopamine reward signals through optogenetic stimulation in the VTA contingent on preparatory cued behaviour. Separate groups of animals experienced each of the following stimulation contingencies: ‘stimLick+’ animals received VTA–DA stimulation at the moment of reward delivery on trials in which we detected licking in the 750 ms preceding reward delivery, whereas ‘stimLick−’ animals received the same stimulation on trials in which no licking was detected during the delay interval (Fig. 5a). Crucially, stimulation was brief (150 ms) and low power (3 mW), approximately doubling the endogenous NAc–DA reward response (Fig. 5b). To account for the large discrepancy in stimulated trials that would arise between the two stimulation groups due to eventual predominance of lick+ trials, stimLick+ animals were limited to having a maximum of 50% of total trials stimulated in a given session. This resulted in a comparable number of stimulated trials between the two groups by the end of the training period (Fig. 5b). We also confirmed post hoc that stimulation captured systematically different ($P$ = 0.004, rank sum test) positive and negative PEs for each condition as expected (Extended Data Fig. 8g).

Calibrated enhancement of reward-related activity in mesolimbic projections in this way had opposite effects on emerging delay-period behaviour across the two stimLick contingencies (Fig. 5b–d and Extended Data Fig. 8h). As in the ACTR model, behaviour was biased in opposite directions for each contingency, with stimLick+ animals exhibiting lower and stimLick− animals exhibiting higher preparatory licking (trials 600–800, stimLick+ 1.0 ± 0.7, stimLick− 0.6 ± 0.1, analysis of variance (ANOVA) $F_{1,72}$ = 10.5, $P$ = 0.002; Fig. 5d). Furthermore, NAc–DA cue signals were biased in matching

directions, with the stimLick− group also exhibiting higher NAc-DA cue responses versus stimLick+ (trials 600–800, stimLick+ 0.3 ± 0.1 z, stimLick− 2.6 ± 0.7 z, ANOVA $F_{1,72}$ = 10.1, $P$ = 0.002; Fig. 5d). Baseline licking examined just before trials began across training showed no correlation with the extent of learning ($P$ = 0.9) or initial NAc–DA magnitude ($P$ = 0.8), confirming that preparatory licking learning was indeed driven by the predictive cue (Extended Data Fig. 9).

The differences in effects of calibrated and uncalibrated stimulations (Fig. 3) suggest that uncalibrated stimulation could paradoxically reverse the effect on suppression of cued licking seen in the stimLick+ condition above. To test this possibility, we repeated the stimLick+ experiment with a new set of mice, but this time augmented rewards on lick+ trials with large, uncalibrated VTA–DA stimulation (500 ms, at 30 Hz and about 10 mW power; Fig. 6a). Indeed, this new larger exogenous stimulation contingency ('stim+Lick+') now resulted in increased NAc–DA cue responses (Fig. 5b, two-way ANOVA, stimulation group $F_{1,66}$ = 11.7, $P$ = 0.001) and increased cued licking (Fig. 5b, two-way ANOVA, stimulation group $F_{1,60}$ = 7.1, $P$ = 0.01), reversing the sign of the effects of calibrated stimLick+ stimulation (Fig. 5d). These effects were well predicted by a modified version of the ACTR model in which large dopamine stimulations biased towards positive errors in addition to modulating learning rate (Fig. 6c), exactly as in the previous experiment in which large uncalibrated stimulation caused the emergence of NAc–DA responses to a predictive cue (Fig. 3a–c).

**Fig. 6: Supraphysiological dopamine stimulation signals error.**



**a**, Top: experimental design for new group of mice that experienced a 'stim+Lick+' contingency: they received large, uncalibrated VTA–DA stimulation on lick+ trials. Bottom: NAc–DA reward responses on stimulated (magenta) and unstimulated (grey) trials. **b**, NAc–DA cue responses (top) and cued licking (bottom) for control (black, $n = 9$) and stim+Lick+ (light purple, $n = 4$) mice. Two-way ANOVA, $^{**}P = 0.01$, $^{***}P = 0.001$. **c**, Predicted cue responses (top) and cued licking (bottom) in a version of the ACTR model altered for the large-amplitude stimulations to bias PE in addition to setting the adaptive learning rate ($n = 9$ simulations). Two-way ANOVA, $^{*}P < 0.05$. All error bars denote ±s.e.m.

# Discussion

The discovery that the phasic activity of mDA neurons in several species correlated with a key quantity (RPE) in value learning algorithms has been a marked and important advance suggesting that the brain may implement analogous processes[4,7]. At the same time, reinforcement learning constitutes a large family of algorithms[1,3] that include not only learning about expected values of environmental states, but also directly learning parameterized policies for behavioural control. Close analysis of our trace conditioning paradigm indeed revealed that behavioural learning was better explained by direct policy learning as compared to value learning. The fact that signed RPEs are not required for policy learning opened up the possibility that mDA activity could map onto a different quantity. This led us to develop a biologically plausible network-based formulation of policy learning that is consistent with many aspects of individual behavioural trajectories, but also closely matches observed mDA neuron activity during naive learning. This is distinct from standard 'actor–critic' models of dopamine function in the basal ganglia[47] in multiple ways, including in the function of dopamine in the model and the proposition that the ventral striatum is part of the 'actor' that determines policy, rather than the 'critic'. However, both emphasize the need to understand how policy is implemented in dopamine-recipient circuits as an abstracted action-control signal.

Regardless of the specific reinforcement learning algorithm favoured, our analyses and experiments discriminate between two potential biological functions of dopamine: a signed error signal that governs the direction of

learned changes and an unsigned adaptive rate signal that governs how much of the error is captured on a given trial. A role in modulating learning rate as opposed to signalling an error predicts that stimulation of mDA neurons will often enhance learning as previously observed, but could paradoxically slow learning in some contingencies. Slowed learning would be paradoxical if dopamine activity functioned as an error or as a reinforcer of past action. Stimulation of mDA neurons without respect to ongoing behaviour, as routinely carried out, fails to distinguish between these possibilities and thus a new experiment was required—calibrated manipulation of mDA activity in closed-loop operation with behaviour (inferred policy state). We found a remarkable agreement between policy learning model-based predictions and experimental observations. Intriguingly, we also discovered that uncalibrated mDA stimulation 3–5 times stronger than endogenous mDA activity (but with parameters common in the field at present) was well explained by our model as a bias in a signed error in addition to modulating learning rate. This suggests that dopamine-dependent attribution of motivational value to cues[46,48,49] is at least partially dissociable from the regulation of policy learning rate within the same mesolimbic circuits. Such parallel functions could be complementary, intriguingly mirroring the system of parallel policy and value learning networks implemented in AlphaGo[50], a landmark achievement in modern artificial intelligence.

Value-like error signalling following higher-power, longer stimulation may depend on specific receptor recruitment within a circuit[51] (as suggested by similar input–output relationships across tested regions (Extended Data Fig. 6)), and/or differential recruitment of diverse[8,52,53,54] dopaminergic circuits. This predicts that recipient areas should exhibit distinct electrophysiological responses to supraphysiological stimulation, which can be tested in future experiments. Our data indicate that both strongly enhanced dopmaine signalling and oversensitivity to sensory input can bias towards value-like learning that leads an animal to exhibit excessively strong reactive responses to cues at the expense of optimal behaviour. This may be akin to the excessive acquired and innate sensitivity to drug-predictive cues thought to underlie the development of addiction[55], and connects our results to previous observations of correlations between the magnitude of phasic dopamine signalling and individual differences in reward-related behaviours[49]. This suggests that policy learning, and specifically the reactive component in our

ACTR model, may be a useful way to model the acquisition of incentive salience[41] (although not its expression, as phasic dopamine signals could be shown to modulate only learning, and not apparent incentive salience on the current trial (Extended Data Fig. 4)). Our results promote the practice of matching exogenous manipulations of neuromodulators to physiological signals[9,56], and support the modelling of addictive maladaptive learning[57] with extended, high-magnitude mDA stimulation.

There are many opportunities to extend the current ACTR model formulation to capture more biological reality and evaluate the biologically plausible, but so far incompletely tested, cellular and circuit mechanisms of posited ACTR learning rules. There is prior evidence for the capacity of mDA activity to capture eligibility traces and modulate synaptic plasticity[58,59]; however, our behavioural data and modelling call for further examination of multiple coordinated learning rules governing reactive-like and preparatory-like learning. Given that adaptive control over the magnitude of learning rate can be a key determinant of machine learning performance in deep neural networks[2,28] and RNNs[35], studying how adaptive control of learning rates is implemented in animal brains, and especially across diverse tasks, may provide additional algorithmic insights to those developed here. Recent evidence also suggests that other neuromodulators in the brain may play distinct, putatively complementary roles in controlling the rate of learning[60]. Here we effectively identify a key heuristic apparent in phasic mDA activity that adapts learning rates to produce more stable and performant learning; however, we focused on a single behavioural learning paradigm and dopamine is known to be critical for a broad range of putative behavioural policies. Our work provides a perspective for future work to expand on and identify other aspects of mDA activity that may be critical for the adaptive control of learning from action.

# Methods

## Animals

All protocols and animal handling procedures were carried out in strict accordance with a protocol (no. 19–190) approved by the Janelia Institutional Animal Care and Use Committee and in compliance with the

standards set forth by the Association for Assessment and Accreditation of Laboratory Animal Care.

For behaviour and juxtacellular recordings, we used 24 adult male DAT-Cre::ai32 mice (3–9 months old) resulting from the cross of DAT$^{IRES\textit{cre}}$ (The Jackson Laboratory stock 006660) and Ai32 (The Jackson Laboratory stock 012569) lines of mice, such that a Chr2–EYFP fusion protein was expressed under control of the endogenous dopamine transporter *Slc6a3* locus to specifically label dopaminergic neurons. Mice were maintained under specific-pathogen-free conditions. Mice were housed on a free-standing, individually ventilated (about 60 air changes hourly) rack (Allentown Inc.). The holding room was ventilated with 100% outside filtered air with >15 air changes hourly. Each ventilated cage (Allentown) was provided with corncob bedding (Shepard Specialty Papers), at least 8 g of nesting material (Bed-r'Nest, The Andersons) and a red mouse tunnel (Bio-Serv). Mice were maintained on a 12:12-h (8 am–8 pm) light/dark cycle and recordings were made between 9 am and 3 pm. The holding room temperature was maintained at 21 ± 1 °C with a relative humidity of 30% to 70%. Irradiated rodent laboratory chow (LabDiet 5053) was provided ad libitum. Following at least 4 days recovery from headcap implantation surgery, animals' water consumption was restricted to 1.2 ml per day for at least 3 days before training. Mice underwent daily health checks, and water restriction was eased if mice fell below 75% of their original body weight.

## Behavioural training

Mice were habituated to head fixation in a separate area from the recording rig in multiple sessions of increasing length over ≥3 days. During this time they received some manual water administration through a syringe. Mice were then habituated to head fixation while resting in a spring-suspended basket in the recording rig for at least two sessions of 30+ min each before training commenced. No liquid rewards were administered during this recording rig acclimation; thus, trial 1 in the data represents the first time naive mice received the liquid water reward in the training environment. The reward consisted of 3 μl of water sweetened with the non-caloric sweetener saccharin delivered through a lick port under control of a solenoid. A 0.5-s, 10-kHz tone preceded reward delivery by 1.5 s on 'cued' trials, and 10% of

randomly selected rewards were ‘uncued’. Matching our previous training schedule[9], after three sessions, mice also experienced ‘omission’ probe trials, in which the cue was delivered but not followed by reward, on 10% of randomly selected trials. Intertrial intervals were chosen from a randomly permuted exponential distribution with a mean of about 25 s. Ambient room noise was 50–55 dB, and an audible click of about 53 dB accompanied solenoid opening on water delivery and the predictive tone was about 65 dB loud. Mice experienced 100 trials per session and one session per day for 8–10 days. In previous pilot experiments, it was observed that at similar intertrial intervals, behavioural responses to cues and rewards began to decrease in some mice at 150–200 trials. Thus, the 100 trials per session limit was chosen to ensure homogeneity in motivated engagement across the dataset.

Some animals received optogenetic stimulation of VTA–DA neurons concurrent with reward delivery, contingent on their behaviour during the delay period (see technical details below). Mice were randomly assigned to stimulation group (control, stimLick−, stimLick+) before training. Experimenter was not blinded to group identity during data collection. Following trace conditioning with or without exogenous dopamine stimulation, five mice experienced an extra session during which VTA–DA neurons were optogenetically stimulated concurrently with cue presentation (Extended Data Fig. 4). Mice were then randomly assigned to groups for a new experiment in which a light cue predicted VTA–DA stimulation with no concurrent liquid water reward (5–7 days, 150–200 trials per day). The light cue consisted of a 500-ms flash of a blue light-emitting diode (LED) directed at the wall in front of head fixation. Intertrial intervals were chosen from randomly permuted exponential distributions with a mean of about 13 s. Supplementary Table 1 lists the experimental groups each mouse was assigned to in the order in which experiments were experienced.

## Video and behavioural measurement

Face video was captured at 100 Hz continuously across each session with a single camera (Flea 3, FLIR) positioned level with the point of head fixation, at an approximately 30º angle from horizontal, and compressed and streamed to disk with custom code written by J. Keller (available at

https://github.com/neurojak/pySpinCapture). Dim visible light was maintained in the rig so that pupils were not overly dilated, and an infrared LED (model#) trained at the face provided illumination for video capture. Video was post-processed with custom MATLAB code available on request.

Briefly, for each session, a rectangular region of interest (ROI) for each measurement was defined from the mean of 500 randomly drawn frames. Pupil diameter was estimated as the mean of the major and minor axis of the object detected with the MATLAB regionprops function, following noise removal by thresholding the image to separate light and dark pixels, then applying a circular averaging filter and then dilating and eroding the image. This noise removal process accounted for frames distorted by passage of whiskers in front of the eye, and slight differences in face illumination between mice. For each session, appropriateness of fit was verified by overlaying the estimated pupil on the actual image for about 20–50 randomly drawn frames. A single variable, the dark/light pixel thresholding value, could be changed to ensure optimal fitting for each session. Nose motion was extracted as the mean of pixel displacement in the ROI *y* axis estimated using an image registration algorithm (MATLAB imregdemons). Whisker pad motion was estimated as the absolute difference in the whisker pad ROI between frames (MATLAB imabsdiff; this was sufficiently accurate to define whisking periods, and required much less computing time than imregdemons). Whisking was determined as the crossing of pad motion above a threshold, and whisking bouts were made continuous by convolving pad motion with a smoothing kernel. Licks were timestamped as the moment pixel intensity in the ROI in between the face and the lick port crossed a threshold.

Body movement was summarized as basket movements recorded by a triple-axis accelerometer (Adafruit, ADXL335) attached to the underside of a custom-designed three-dimensionally printed basket suspended from springs (Century Spring Corp, ZZ3-36). Relative basket position was tracked by low-pass filtering accelerometer data at 2.5 Hz. Stimulations and cue deliveries were coordinated with custom-written software using Arduino Mega hardware (https://www.arduino.cc). All measurement and control signals were synchronously recorded and digitized (at 1 kHz for behavioural data, 10 kHz for fibre photometry data) with a Cerebus Signal Processor

(Blackrock Microsystems). Data were analysed using MATLAB software (Mathworks).

## Preparatory and reactive measures and abstract learning trajectories

To describe the relationship between behavioural adaptations and reward collection performance, for each mouse in the control group a GLM was created to predict reward collection latency from preparatory and reactive predictor variables on each trial. Preparatory changes in licking, whisking, body movement and pupil diameter were quantified by measuring the average of each of those signals during the 1-s delay period preceding cued rewards. The nose motion signal was not included as it did not display consistent preparatory changes. Reactive responses in the whisking, nose motion and body movement were measured as the latency to the first response following reward delivery. For whisking, this was simply the first moment of whisking following reward delivery. For nose motion, the raw signal was convolved with a smoothing kernel and then the first response was detected as a threshold crossing of the cumulative sum of the signal. For body movement, the response was detected as the first peak in the data following reward delivery. On occasional trials no event was detected within the analysis window. Additionally, discrete blocks of trials were lost owing to data collection error for mouse 3, session 7; mouse 4, session 5; and mouse 9, session 4. To fit learning curves through these absent data points, missing trials were filled in using nearest-neighbour interpolation.

Trial-by-trial reward collection latencies and predictor variables (preparatory licking, whisking, body movement and pupil diameter; and reactive nose motions, whisking and body movement) were median filtered (MATLAB medfilt1(signal,10)) to minimize trial-to-trial variance in favour of variance due to learning across training. Collection latency was predicted from $z$-scored predictor variables using MATLAB glmfit to fit $\beta$-values for each predictor. The unique explained variance of each predictor was calculated as the difference in explained variance between the full model and a partial model in which $\beta$-values were fitted without using that predictor.

Preparatory and reactive predictor variables were used to define abstract learning trajectories that were plots of collection latency against the inferred reactive and preparatory variables for each of the first 800 cue–reward trials of training. Reactive and preparatory variables were calculated as the first principal component of the individual reactive and preparatory variables used in the GLM fits. For visualization, we fitted a parametric model to all three variables (single exponential for preparatory, double exponentials for reactive and latency using the MATLAB fit function). Quality of fits and choice of model were verified by visual inspection of all data for all mice. An individual mouse's trajectory was then visualized by plotting downsampled versions of the fit functions for latency, reactive and preparatory. Arrowheads were placed at logarithmically spaced trials.

To quantify the total amount of preparatory behaviour in each mouse at a given point in training (final prep. behav., Extended Data Fig. 3f), each preparatory measure (pupil, licking, whisking and body movement) was *z*-scored and combined across mice into a single data matrix. The first principal component of this matrix was calculated and loading onto PC1 was defined as a measure of an inferred underlying 'preparatory' component of the behavioural policy. This created an equally weighted, variance-normalized combination of all preparatory measures to allow comparisons between individual mice. An analogous method was used to reduce the dimensionality of reactive variables down to a single 'reactive' dimension that captures most variance in reactive behavioural variables across animals (final reactive behav., Extended Data Fig. 3g). Initial NAc–DA signals were predicted from trained behaviour at trials 700–800 by multiple regression (specifically, pseudoinverse of the data matrix of reactive and preparatory variables at the end of training multiplied by data matrix of physiological signals for all animals).

## Combined fibre photometry and optogenetic stimulation

In the course of a single surgery session, DAT-Cre::ai32 mice received: bilateral injections of AAV2/1-CAG-FLEX-jRCaMP1b in the VTA (150 nl at the coordinates −3.1 mm anterior–posterior (A–P), 1.3 mm medial–lateral (M–L) from bregma, at depths of 4.6 and 4.3 mm) and in the substantia nigra pars compacta (100 nl at the coordinates −3.2 mm A–P, 0.5 mm M–L, depth

of 4.1, mm); custom 0.39-NA, 200-μm fibre cannulas implanted bilaterally above the VTA (−3.2 mm A–P, 0.5 mm M–L, depth of −4.1 mm); and fibre cannula implanted unilaterally in the DS (0.9 mm A–P, 1.5 mm M–L, depth of 2.5 mm) and NAc (1.2 mm A–P, 0.85 mm M–L, depth of 4.3 mm). Hemisphere choice was counterbalanced across individuals. A detailed description of the methods has been published previously[56].

Imaging began >20 days post-injections using custom-built fibre photometry systems (Fig. 2a)[56]. Two parallel excitation–emission channels through a five-port filter cube (FMC5, Doric Lenses) allowed for simultaneous measurement of RCaMP1b and eYFP fluorescence, the latter channel having the purpose of controlling for the presence of movement artefacts. Fibre-coupled LEDs of 470 nm and 565 nm (M470F3, M565F3, Thorlabs) were connected to excitation ports with acceptance bandwidths of 465–490 nm and 555–570 nm, respectively, with 200-μm, 0.22-NA fibres (Doric Lenses). Light was conveyed between the sample port of the cube and the animal by a 200-μm-core, 0.39-NA fibre (Doric Lenses) terminating in a ceramic ferrule that was connected to the implanted fibre cannula by a ceramic mating sleeve (ADAL1, Thorlabs) using index matching gel to improve coupling efficiency (G608N3, Thorlabs). Light collected from the sample fibre was measured at separate output ports (emission bandwidths 500–540 nm and 600–680 nm) by 600-μm-core, 0.48-NA fibres (Doric Lenses) connected to silicon photoreceivers (2151, Newport).

A time-division multiplexing strategy was used in which LEDs were controlled at a frequency of 100 Hz (1 ms on, 10 ms off), offset from each other to avoid crosstalk between channels. A Y-cable split each LED output between the filter cube and a photodetector to measure output power. LED output power was 50–80 μW. This low power combined with the 10% duty cycle used for multiplexing prevented local ChR2 excitation[56] by 473 nm eYFP excitation. Excitation-specific signals were recovered in post-processing by only keeping data from each channel when its LED output power was high. Data were downsampled to 100 Hz, and then band-pass filtered between 0.01 and 40 Hz with a second-order Butterworth filter. Although movement artefacts were negligible when mice were head-fixed in the rig (the movable basket was designed to minimize brain movement with respect to the skull[9]), according to standard procedure the least-squares fit of

the eYFP movement artefact signal was subtracted from the jRCaMP1b signal. d*F*/*F* was calculated by dividing the raw signal by a baseline defined as the polynomial trend (MATLAB detrend) across the entire session. This preserved local slow signal changes while correcting for photobleaching. Comparisons between mice were carried out using the z-scored d*F*/*F*.

Experimenters were blind to group identity during the initial stages of analysis when analysis windows were determined and custom code was established to quantify fibre photometry signals and behavioural measurements. Analysis windows were chosen to capture the extent of mean phasic activations following each kind of stimulus. For NAc–DA and VTA–DA, reward responses were quantified from 0 to 2 s after reward delivery and cue responses were quantified from 0 to 1 s after cue delivery. DS–DA exhibited much faster kinetics, and thus reward and cue responses were quantified from 0 to 0.75 s after delivery.

Somatic Chr2 excitation was carried out with a 473-nm laser (50 mW, OEM Laser Systems) coupled by a branching fibre patch cord (200 μm, Doric Lenses) to the VTA-implanted fibres using ceramic mating sleeves. Burst activations of 30 Hz (10 ms on, 23 ms off) were delivered with durations of either 150 ms for calibrated stimulation or 500 ms for large stimulations. For calibrated stimulation, laser power was set between 1 and 3 mW (steady-state output) to produce a NAc–DA reactive of similar amplitude to the largest transients observed during the first several trials of the session. This was confirmed post hoc to have roughly doubled the size of reward-related NAc–DA transients (Figs. 3a and 5b). For large stimulations, steady-state laser output was set to 10 mW.

## ACTR computational learning model

### Behavioural plant

An important aspect of this modelling work was to create a generative agent model that would produce core aspects of reward-seeking behaviour in mice. To this end, we focused on licking, which in the context of this task is the unique aspect of behaviour critical for reward collection. A reader may look at the function dlRNN_Pcheck_transfer.m within the software repository to

appreciate the structure of the plant model. We describe the function of the plant briefly here. It is well known that during consumptive, repetitive licking mice exhibit preparatory periods of about 7 Hz licking. We modelled a simple fixed rate plant with an active, ‘lick’ state that emitted observed licks at a fixed time interval of 150 ms. The onset of this lick pattern relative to entry into the lick state was started at a variable phase of the interval (average latency to lick initialization from transition into lick state about 100 ms). Stochastic transitions between ‘rest’ and ‘lick’ states were governed by forward and backward transition rates. The reverse transition rate was a constant that depended on the presence of reward ($5 \times 10^{-3}$ ms without reward, $5 \times 10^{-1}$ ms with reward). This change in the backwards rate captured the average duration of consumptive licking bouts. The forward rate was governed by the scaled policy network output and a background tendency to transition to licking as a function of trial time (analogous to an exponential rising hazard function; □ = 100 ms). The output unit of the policy network was the sum of the RNN output unit (constrained {−1,1} by the tanh activation function) and a large reactive transient proportional to the sensory weight ({0,max_scale}), in which max_scale was a free parameter generally bounded from 5 to 10 during initialization. This net output was scaled by $S = 0.02\ \mathrm{ms}^{-1}$ to convert to a scaled transition rate in the policy output. Behaviour of the plant for a range of policies is illustrated in Extended Data Fig. 2. A large range of parameterizations were explored with qualitatively similar results. Chosen parameters were arrived at by scanning many different simulations and matching average initial and final latencies for cue–reward pairings across the population of animals. More complicated versions (high-pass filtered, nonlinear scaling) of the transition from RNN output to transition rate can be explored in the provided code. However, all transformations were found to produce qualitatively similar results, and thus the simplest (scalar) transformation was chosen for reported simulations for clarity of presentation.

## RNN

As noted in the main text, the RNN component of the model and the learning rules used for training drew on inspiration from ref. [36], which itself drew on inspiration variants of node perturbation methods[61] and the classic policy optimization methods known as REINFORCE rules[3,21]. Briefly, ref. [36]

demonstrated that a relatively simple learning rule that computed a nonlinear function of the correlation between a change in input and change in output multiplied by the change in performance on the objective was sufficiently correlated with the analytic gradient to allow efficient training of the RNN. We implemented a few changes relative to this prior work. Below we delve into the learning rule as implemented here or a reader may examine the commented open source code to get further clarification as well. First, we describe the structure of the RNN and some core aspects of its function in the context of the model. The RNN was constructed largely as described in ref. [36], and was very comparable to the structure of a re-implementation of that model in ref. [62].

Although we explored a range of parameters governing RNN construction, many examples of which are shown in Extended Data Fig. 2, the simulations shown in the main results come from a network with 50 units ($N_{\rm u}$ = 50; chosen for simulation efficiency; larger networks were explored extensively as well), densely connected ($P_{\rm c}$ = 0.9), spectral scaling to produce preparatory dynamics ($\boldsymbol{g}$ = 1.3), a characteristic time constant ($\tau$ = 25 ms) and a standard tanh activation function for individual units. Initial internal weights of the network ($W_{ij}$) were assigned according to the equation (in RNN-dudlab-master-LearnDA.m)

$${W}_{ij}={\boldsymbol{g}}\times {\mathscr{N}}(0,1)\times {({P}_{{\rm{c}}}\times {N}_{{\rm{u}}})}^{-1/2}$$
(1)

The RNN had a single primary output unit with activity that constituted the continuous time policy (that is, $\pi(t)$) input to the behaviour plant (see above), and a ‘feedback’ unit that did not project back into the network as would be standard, but rather was used to produce adaptive changes in the learning rate (described in more detail in the section below entitled Learning rules).

## Objective function

Evaluation of model performance was calculated according to an objective function that defines the cost as the performance cost (equation (2), $\text{cost}_{\rm P}$)

and an optional network stability cost (equation (3), $\mathrm{cost}_{\mathrm{N}}$) (for example, lines 269 and 387 in dlRNN-train_learnDA.m, for equations (4) and (5), respectively)

$${{\rm{cost}}}_{{\rm{P}}}={1-{\rm{e}}}^{-\Delta {\rm{t}}/500}$$
(2)

$${{\rm{cost}}}_{{\rm{N}}}={\rm{sum}}({\rm{| }}\,{\boldsymbol{\delta }}{\boldsymbol{\pi }}(t)/{\boldsymbol{\delta }}t| )$$
(3)

$${R}_{{\rm{obj}}}=(1-{{\rm{cost}}}_{{\rm{P}}})-{\boldsymbol{\pi }}({t}_{{\rm{reward}}})$$
(4)

$$\langle R(T)\rangle ={{\boldsymbol{\alpha }}}_{{\rm{R}}}\times {R}_{{\rm{obj}}}(T)+\left(1-{{\boldsymbol{\alpha }}}_{{\rm{R}}}\right)\times {R}_{{\rm{obj}}}(T-1)$$
(5)

in which $T$ is the trial index. In all presented simulations, $W_{\mathrm{N}} = 0.25$. A filtered average cost, **R**, was computed as before[36] with $\boldsymbol{\alpha}_{\mathrm{R}} = 0.75$ and used in the update equation for changing network weights through the learning rule described below. For all constants a range of values were tried with qualitatively similar results. The performance objective was defined by $\mathrm{cost}_{\mathrm{P}}$, for which $\Delta t$ is the latency to collected reward after it is available. The network stability cost ($\mathrm{cost}_{\mathrm{N}}$) penalizes high-frequency oscillatory dynamics that can emerge in some (but not all) simulations. Such oscillations are inconsistent with observed dynamics of neural activity so far.

### Identifying properties of RNN required for optimal performance

To examine what properties of the RNN were required for optimal performance, we scanned through thousands of simulated network configurations (random initializations of $W_{ij}$) and ranked those networks according to their mean cost ($R_{\mathrm{obj}}$) when run through the behaviour plant for 50 trials (an illustrative group of such simulations is shown in Extended Data Fig. 2). This analysis revealed a few key aspects of the RNN required for optimality. First, a preparatory policy that spans time from the detection of

the cue through the delivery of water reward minimizes latency cost. Second, although optimal RNNs are relatively indifferent to some parameters (for example, $P_c$), they tend to require a coupling coefficient ($g$) ≧ 1.2. This range of values for the coupling coefficient is known to determine the capacity of an RNN to develop preparatory dynamics[63]. Consistent with this interpretation, our findings showed that optimal policies were observed uniquely in RNNs with large leading eigenvalues (Extended Data Fig. 2; that is, long-time-constant dynamics[64]). These analyses define the optimal policy as one that requires preparatory dynamics of output unit activity that span the interval between the cue offset and reward delivery and further reveal that an RNN with long-timescale dynamics is required to realize such a policy. Intuitively: preparatory anticipatory behaviour, or ‘conditioned responding’, optimizes reward collection latency. If an agent is already licking when reward is delivered the latency to collect that reward is minimized.

## RNN initialization for simulations

All mice tested in our experiments began training with no preparatory licking to cues and a long latency (about 1 s or more) to collect water rewards. This indicates that animal behaviour is consistent with an RNN initialization that has a policy $\pi(t) \approx 0$ for the entire trial. As noted above, there are many random initializations of the RNN that can produce clear preparatory behaviour and even optimal performance. Thus, we carried out large searches of RNN initializations (random matrices $W_{ij}$) and used only those that had approximately 0 average activity in the output unit. We used a variety of different initializations across the simulations reported (Fig. 1 and Extended Data Fig. 2) and indeed there can be substantial differences in the observed rate of convergence depending on initial conditions (as there are across mice as well). For simulations of individual differences (Fig. 1j and Extended Data Fig. 2), distinct network initializations were chosen (as described above), and paired comparisons were made for the control initialization and an initialization in which the weights of the inputs from the reward to the internal RNN units were tripled.

## Learning rules

Below we articulate how each aspect of the model acronym, ACTR (adaptive rate cost of performance to REINFORCE), is reflected in the learning rule that governs updates to the RNN. The connections between the variant of node perturbation used here and REINFORCE[21] has been discussed in detail previously[36]. There are two key classes of weight changes governed by distinct learning rules within the ACTR model. First, we will discuss the learning that governs changes in the 'internal' weights of the RNN ($W_{ij}$). The idea of the rule is to use perturbations (1–10 Hz rate of perturbations in each unit; simulations reported used 3 Hz) to drive fluctuations in activity and corresponding changes in the output unit that could improve or degrade performance. To solve the temporal credit assignment problem, we used eligibility traces similar to those described previously[36]. One difference here was that the eligibility trace decayed exponentially with a time constant of 500 ms and it was unclear whether decay was a feature of prior work. The eligibility trace ($\mathcal{e}$) for a given connection *i*,*j* could be changed at any time point by computing a nonlinear function ($\mathcal{S}$) of the product of the derivative in the input from the *i*th unit ($x_i$) and the output rate of the *j*th unit ($r_j$) in the RNN according to the equation (in dlRNN_engine.m)

$${\mathcal{e}}_{i,j}(t)={\mathcal{e}}_{i,j}(t-1)+{\boldsymbol{\varphi}}[{r}_{j}(t-1)\times ({x}_{i}(t)-\langle {x}_{i}\rangle )]$$
(6)

As noted in ref. [36], the function $\mathcal{S}$ need only be a signed, nonlinear function. Similarly, in our simulations we also found that a range of functions could all be used. Typically, we used either $\boldsymbol{\phi}(y) = y^3$ or $\boldsymbol{\phi}(y) = |y| \times y$, and simulations presented were generally the latter, which runs more rapidly.

The change in a connection weight ($W_{ij}$) in the RNN in the original formulation[36] is then computed as the product of the eligibility trace and the change in PE scaled by a learning rate parameter. Our implementation kept this core aspect of the computation, but several critical updates were made and will be described. First, as the eligibility trace is believed to be 'read out' into a plastic change in the synapse by a phasic burst of dopamine

firing[58], we chose to evaluate the eligibility at the time of the computed burst of dopamine activity estimated from the activity of the parallel feedback unit (see below for further details). Again, models that do not use this convention can also converge, but in general converge worse than and less similarly to observed mice. The update equation is thus (for example, line 330 in dlRNN-train_learnDA.m)

$${{\rm{W}}}_{i,j}(T)={{\rm{W}}}_{i,j}(T-1)+{{\boldsymbol{\beta }}}_{{\rm{DA}}}\times {\eta }_{{\mathscr{S}}}\times {e}_{i,j}({t}_{{\rm{DA}}})\times ({R}_{{\rm{obj}}}(T)-\langle R(T)\rangle )$$
(7)

in which ${\eta }_{{\mathcal{S}}}$ is the baseline learning rate parameter and is generally used in the range $5 \times 10^{-4} \pm 1 \times 10^{-3}$ and $\beta_{\mathrm{DA}}$ is the ‘adaptive rate’ parameter that is a nonlinear function (sigmoid) of the sum of the derivative of the policy at the time of reward plus the magnitude of the reactive response component plus a tonic activity component, $T$ ($T = 1$ except in Extended Data Fig. 2 where noted and $\boldsymbol{\phi}$ is a sigmoid function mapping inputs from {0,10} to {0,3} with parameters: $\boldsymbol{\sigma} = 1.25$, $\boldsymbol{\mu} = 7$) (for example, line 259 in dlRNN-train_learnDA.m):

$${{\boldsymbol{\beta }}}_{{\rm{DA}}}=T+{\boldsymbol{\varphi }}(\Delta {\boldsymbol{\pi }}({t}_{{\rm{reward}}})+{{\mathscr{S}}}_{i,{\rm{reward}}})$$
(8)

As noted in the description of the behavioural data described in Fig. 1, it is clear that animal behaviour exhibits learning of both preparatory behavioural responses to the cue as well as reactive learning that reduces reaction times between sensory input (either cues or rewards) and motor outputs. This is particularly prominent in early training during which a marked decrease in reward collection latency occurs even in the absence of particularly large changes in the preparatory component of behaviour. We interpreted this reactive component as a ‘direct’ sensorimotor transformation consistent with the treatment of reaction times in the literature[65], and thus reactive learning updates weights between sensory inputs and the output unit (one specific element of the RNN indexed as ‘o’ below). This reactive learning was also

updated according to PEs. In particular, the difference between $R_{obj}(T)$ and the activity of the output unit at the time of reward delivery. For the cue, updates were proportional to the difference between the derivative in the output unit activity at the cue and the PE at the reward delivery. These rates were also scaled by the same $\beta_{DA}$ adaptive learning rate parameter (for example, line 346 in dlRNN-train_learnDA.m):

$${W}_{{\rm{trans}},{\rm{o}}}(T)={W}_{{\rm{trans}},{\rm{o}}}(T-1)+{{\boldsymbol{\beta }}}_{{\rm{DA}}}\times {\eta }_{{\mathscr{S}}}\times ({R}_{{\rm{obj}}}(T)-{\boldsymbol{\pi }}({t}_{{\rm{reward}}}))$$

(9)

in which $\eta_I$ is the baseline reactive learning rate and typical values were about 0.02 in presented simulations (again a range of different initializations were tested).

We compared acquisition learning in the complete ACTR model to observed mouse behaviour using a variety of approaches. We scanned about two orders of magnitude for two critical parameters $\eta_I$ and $\eta_W$. We also aimed to sample the model across a range of initializations that approximately covered the range of learning curves exhibited by control mice. To scan this space, we followed the following procedure. We initialized 500–1,000 networks with random internal weights and initial sensory input weights (as described above). As no mice that we observed initially exhibited sustained licking, we selected six network initializations with preparatory policies approximately constant and 0. For these 6 net initializations, we ran 24 simulations with 4 conditions for each initialization. Specifically, we simulated input vectors with initial weights ${\mathcal{S}}$ = [0.1, 0.125, 0.15, 0.175] and baseline learning rates $\eta_I = [2, 2.25, 2.5, 2.75] \times 8 \times 10^{-3}$. Representative curves of these simulations are shown in Fig. 1j.

## Visualizing the objective surface

To visualize the objective surface that governs learning, we scanned a range of policies (combinations of reactive and preparatory components) passed through the behaviour plant. The range of reactive components covered was

[0:1.1] and preparatory was [−0.25:1]. This range corresponded to the space of all possible policy outputs realizable by the ACTR network. For each pair of values, a policy was computed and passed through the behaviour plant 50 times to get an estimate of the mean performance cost. These simulations were then fitted using a third-order, two-dimensional polynomial (analogous to the procedure used for experimental data) and visualized as a three-dimensional surface.

In the case of experimental data, the full distribution of individual trial data points across all mice ($N = 7,200$ observations) was used to fit a third-order, two-dimensional polynomial (MATLAB; fit). Observed trajectories of preparatory versus reactive were superimposed on this surface by finding the nearest corresponding point on the fitted two-dimensional surface for the parametric preparatory and reactive trajectories. These data are presented in Fig. 1j.

### Simulating closed-loop stimulation of mDA experiments

We sought to develop an experimental test of the model that was tractable (as opposed to inferring the unobserved policy for example). The experimenter in principle has access to real-time detection of licking during the cue–reward interval. In simulations, this also can easily be observed by monitoring the output of the behavioural plant. Thus, in the model we kept track of individual trials and the number of licks produced in the cue–reward interval. For analysis experiments (Fig. 5e), we tracked these trials and separately calculated the predicted dopamine responses depending on trial type classification (lick– vs lick+). For simulations in Fig. 5e, we ran simulations from the same initialization in nine replicates (matched to the number of control mice) and error bars reflect the standard error.

To simulate calibrated stimulation of mDA neurons, we multiplied the adaptive rate parameter, $\boldsymbol{\beta}_{\mathrm{DA}}$, by 2 on the appropriate trials For simulations reported in Fig. 5e, we used three conditions: control, stimLick– and stimLick+. For each of these three conditions, we ran 9 simulations (3 different initializations, 3 replicates) for 27 total learning simulations (800 trials). This choice was an attempt to estimate the expected experimental

variance as trial classification scheme is an imperfect estimate of underlying policy.

**Pseudocode summary of model**

Here we provide a description of how the model functions in pseudocode to complement the graphical diagrams in the main figures and the discursive descriptions of individual elements that are used below.

Initialize trial to $T = 0$

Initialize ACTR with $W(0)$, ${\mathcal{S}}_{\text{rew}}(T)$, ${\mathcal{S}}_{\text{cue}}(T)$

repeat

Run RNN simulation engine for trial $T$

Compute plant input $\boldsymbol{\pi}(T) = O(T) + {\mathcal{S}}(T)$

Compute lick output $L(t) = \text{Plant}(\boldsymbol{\pi}(T))$

Compute latency to collect reward $t_{\text{collect}} \leftarrow$ find $L(t) > t_{\text{reward}}$

Compute $\text{cost}(T) = 1 - \exp(-\Delta t/500)$

Evaluate eligibility trace at collection ${\mathcal{e}} \leftarrow {\mathcal{e}}_{i,j}(t_{\text{collect}})$

Compute $\boldsymbol{\beta}_{\text{DA}} = 1 + \boldsymbol{\phi}(\Delta\boldsymbol{\pi}(t_{\text{reward}}) + {\mathcal{S}}_{\text{rew}})$

Compute $R_{\text{obj}}(T) = 1 - (1 - \exp(-\Delta t/500)) - O(T, t_{\text{reward}} - 1)$

Estimate objective gradient $\text{PE} = R_{\text{obj}}(T) - \langle R(T) \rangle$

Compute update $\Delta W = -\eta_{\text{J}} \times {\mathcal{e}} \times \text{PE} \times \boldsymbol{\beta}_{\text{DA}}$

Update $W(T + 1) \leftarrow W(T) + \Delta W$

Update $\mathcal{S}_{reward}(T+1) \leftarrow \mathcal{S}_{rew}(T) + \eta_{\mathcal{S}} \times R_{obj}(T) \times \boldsymbol{\beta}_{DA}$

Update $\mathcal{S}_{cue}(T+1) \leftarrow \mathcal{S}_{cue}(T) + \eta_{\mathcal{S}} \times R_{obj}(T) \times \boldsymbol{\beta}_{DA}$

Until $T == 800$

in which $T$ is the current trial and $t$ is time within a trial, $W$ is the RNN connection weight matrix, $\mathcal{S}$ is the sensory input strength, $O$ is the RNN output, $\pi$ is the behavioural policy, $\Delta t = t_{collect} - t_{reward}$, $\boldsymbol{\phi}$ is the nonlinear (sigmoid) transform, $\langle R(T) \rangle$ is the running mean PE, $\eta_J$ is the baseline learning rate for $W$ and $\eta_{\mathcal{S}}$ is the baseline learning rate for input $\mathcal{S}$.

## ACTR model variants

In Fig. 1k, we consider three model variants equivalent to dopamine signalling PEs, dopamine depletion and loss of phasic dopamine activity—all manipulations that have been published in the literature. To accomplish these simulations, we: changed $\boldsymbol{\beta}_{DA}$ to equal PE; changed $\boldsymbol{\beta}_{DA}$ offset to 0.1 from 1; and changed $\boldsymbol{\beta}_{DA}$ to equal 1 and removed the adaptive term.

In Figs. 3 and 5, calibrated stimulation was modelled as setting $\boldsymbol{\beta}_{DA}$ to double the maximal possible magnitude of $\boldsymbol{\beta}_{DA}$ under normal learning. In Figs. 3c–e and 5i, we modelled uncalibrated dopamine stimulation as setting PE = +1 in addition to the calibrated stimulation effect.

## TD learning model

To model a standard TD value learning model we reimplemented a previously published model that spanned a range of model parameterizations from ref. [66].

### Policy learning model equivalent to the low-parameter TD learning model

The ACTR model that we articulate seeks to provide a plausible mechanistic account of naive trace conditioning learning using: RNNs; a biologically plausible synaptic plasticity rule; conceptually accurate circuit organization of mDA neurons; a ‘plant’ to control realistic behaviour; and multiple components of processing of sensory cues and rewards. However, to facilitate formal comparison between value learning and direct policy learning models, we sought to develop a simplified model that captures a key aspect of ACTR (the specific gradient it uses) and allows for explicit comparison against existing value learning models with the same number of free parameters. To model a low-parameter (as compared to ACTR) policy learning equivalent of the TD value learning model from ref. [67], we used the same core structure, basis function representation and free parameters. However, rather than using an RPE (value gradient) for updating, we follow previous work[32] and consider a direct policy learning version in which a policy gradient is used for updates as originally described in ref. [21] and equivalent in terms of the effective gradient to the ACTR implementation. First, we consider the latency to collect reward rather than the reward value per se as used in TD models. The latency to collect reward is a monotonic function of the underlying policy such that increased policy leads to increased anticipatory licking as a reduction in the collection latency (Fig. 1). Typically one uses a nonlinearity that saturates towards the limits 0,1. For simplicity, we choose a soft nonlinearity (half-Gaussian) for convenience of the simple policy gradient that results. Regardless of the scaling parameter of the Gaussian (sigma), the derivative of the log of the policy is then proportional to $1 - p_t$, in which $p_t$ is the policy on trial $t$ (subject to scaling by a constant proportional to sigma that is subsumed into a learning rate term in the update equation). According to the REINFORCE algorithm family[21], we have an update function proportional to $(r_{\text{curr}} - b) \times (1 - p_t)$, in which $r_{\text{curr}}$ is the current trial reward collection latency and $b$ is a local average of the latency calculated by $b = \boldsymbol{\upsilon} \times r_{\text{curr}} + (1 - \boldsymbol{\upsilon}) \times b$. Typical values for $\boldsymbol{\upsilon}$ were 0.25 (although a range of different calculations for $b$, including $b = 0$, yield consistent results as noted previously[21]).

## Formal model comparison

As in previous work[32], we sought to compare the relative likelihood of the observed data under the optimal parameterization of either the value learning (TD) model or the direct policy learning model. The data we aimed to evaluate were the frequency of anticipatory licking during the delay period over the first approximately 1,000 trials of naive learning for each mouse. We used a recent model formalization proposed to describe naive learning[67] and used grid search to find optimal values of the parameters $\boldsymbol{\lambda}$, $\boldsymbol{\alpha}$ and $\boldsymbol{\gamma}$. To compute the probability of observing a given amount of anticipatory licking as a function of the value function or policy, respectively, we used a normal probability density (sigma = 1) centred on the predicted lick frequency (7 Hz × value or policy). Initial examination revealed that sigma = 1 minimized the LL for all models, but the trends were the same across a range of sigma. The −LL of a given parameterization of the model was computed as the negative sum of log probabilities over trials for all combinations of free parameters. We also computed the Akaike information criterion[68]—sum of ln(sum(residuals$^2$))—as preferred in some previous work[69]. The results were consistent and the number of free parameters was equivalent; thus, we primarily report −LL in the manuscript. For direct comparison, we took the minimum of the −LL for each model (that is, its optimal parameterization) and compared these minima across all animals. To examine the 'brittleness' of the model fit, we compare the median −LL across the entire grid search parameter space for each model.

## Estimating PEs from behavioural data

First, we assume that on average the number of anticipatory licks is an unbiased estimate of the underlying policy (the core assumption of the low-parameter models described above). The latency to collect reward can be converted into a performance cost using the same equation (2) described for ACTR. The PE was then computed as in equation (4). A smoothed baseline estimate was calculated by smoothing PE with a 3-order, 41-trial-wide

Savitzky–Golay filter and the baseline subtracted PE calculated analogous to equations (4) and (5).

### Histology

Mice were killed by anaesthetic overdose (isoflurane, >3%) and perfused with ice-cold phosphate-buffered saline, followed by paraformaldehyde (4% wt/vol in phosphate-buffered saline). Brains were post-fixed for 2 h at 4 °C and then rinsed in saline. Whole brains were then sectioned (100 μm thickness) using a vibrating microtome (VT-1200, Leica Microsystems). Fibre tip positions were estimated by referencing standard mouse brain coordinates[70].

### Statistical analysis

Two-sample, unpaired comparisons were made using Wilcoxon's rank sum test (MATLAB rank sum); paired comparisons using Wilcoxon signed rank test (MATLAB signrank). Multiple comparisons with repeated measures were made using Friedman's test (MATLAB friedman). Comparisons between groups across training were made using two-way ANOVA (MATLAB anova2). Correlations were quantified using Pearson's correlation coefficient (MATLAB corr). Linear regression to estimate contribution of fibre position to variance in mDA reward signals was fitted using MATLAB fitlm. Polynomial regression used to fit objective surfaces were third order and (MATLAB fit). Errors are reported as s.e.m. Sample sizes (*n*) refer to biological, not technical, replicates. No statistical methods were used to predetermine sample size. Data visualizations were created in MATLAB or GraphPad Prism.

### Reporting summary

Further information on research design is available in the Nature Portfolio Reporting Summary linked to this article.

## Data availability

The dataused to generate results supporting the findings of this study are available at https://janelia.figshare.com/account/collections/6369111 or https://doi.org/10.25378/janelia.c.6369111; the primary dataset is 10.25378/janelia.21816054.

# Code availability

All code relating to simulating the ACTR model and for a reader to explore both described parameterizations and explore a number of implemented, but unused in this manuscript, features is available at https://github.com/dudmanj/RNN_learnDA. Specific line numbers are provided within the code for a subset of critical computations in the model.

# References


1. Kober, J., Bagnell, J. A. & Peters, J. Reinforcement learning in robotics: a survey. *Int J. Rob. Res.* **32**, 238–1274 (2013).

2. Bottou, L., Curtis, F. E. & Nocedal, J. Optimization methods for large-scale machine learning. *SIAM Rev.* **60**, 223–311 (2018).

3. Sutton, R. S. & Barto, A. G. *Reinforcement Learning: an Introduction* (MIT Press, 1998).

4. Schultz, W. Neuronal reward and decision signals: from theories to data. *Physiol. Rev.* **95**, 853–951 (2015).

5. Bennett, D., Niv, Y. & Langdon, A. Value-free reinforcement learning: policy optimization as a minimal model of operant behavior. *Curr. Opin. Behav. Sci.* **41**, 114–121 (2021).

6. Collins, A. G. E. & Cockburn, J. Beyond dichotomies in reinforcement learning. *Nat. Rev. Neurosci.* **21**, 576–586 (2020).

7. Schultz, W., Dayan, P. & Montague, P. R. A neural substrate of prediction and reward. *Science* **275**, 1593–1599 (1997).

8. Engelhard, B. et al. Specialized coding of sensory, motor and cognitive variables in VTA dopamine neurons. *Nature* **570**, 509–513 (2019).

9. Coddington, L. T. & Dudman, J. T. The timing of action determines reward prediction signals in identified midbrain dopamine neurons. *Nat. Neurosci.* **21**, 1563–1573 (2018).

10. Howe, M. W. & Dombeck, D. A. Rapid signalling in distinct dopaminergic axons during locomotion and reward. *Nature* **535**, 505–510 (2016).

11. Kremer, Y., Flakowski, J., Rohner, C. & Lüscher, C. Context-dependent multiplexing by individual VTA dopamine neurons. *J. Neurosci.* **40**, 7489–7509 (2020).

12. Redgrave, P. & Gurney, K. The short-latency dopamine signal: a role in discovering novel actions? *Nat. Rev. Neurosci.* **7**, 967–975 (2006).

13. Coddington, L. T. & Dudman, J. T. Learning from action: reconsidering movement signaling in midbrain dopamine neuron activity. *Neuron* **104**, 63–77 (2019).

14. Syed, E. C. J. et al. Action initiation shapes mesolimbic dopamine encoding of future rewards. *Nat. Neurosci.* **19**, 34–36 (2016).

15. Jin, X. & Costa, R. M. Start/stop signals emerge in nigrostriatal circuits during sequence learning. *Nature* **466**, 457–462 (2010).

16. Dodson, P. D. et al. Representation of spontaneous movement by dopaminergic neurons is cell-type selective and disrupted in parkinsonism. *Proc. Natl Acad. Sci. USA* **113**, E2180–E2188 (2016).

17. Hollon, N. G. et al. Nigrostriatal dopamine signals sequence-specific action-outcome prediction errors. *Curr. Biol.* **31**, 5350–5363 (2021).

18. Bova, A. et al. Precisely timed dopamine signals establish distinct kinematic representations of skilled movements. *Elife* **9**, e61591 (2020).

19. Dudman, J. T. & Gerfen, C. R. in *The Rat Nervous System* (ed. Paxinos, G.) 4th edn, 391–440 (Academic Press, 2015).

20. Mongillo, G., Shteingart, H. & Loewenstein, Y. The misbehavior of reinforcement learning. *Proc. IEEE* **102**, 528–541 (2014).

21. Williams, R. J. Simple statistical gradient-following algorithms for connectionist reinforcement learning. *Mach. Learn.* **8**, 229–256 (1992).

22. Silver, D. A. RL course - lecture 7: policy gradient methods. *YouTube* https://www.youtube.com/watch?v=KHZVXao4qXs (2015).

23. Park, J., Coddington, L. T. & Dudman, J. T. Basal ganglia circuits for action specification. *Annu. Rev. Neurosci.* **43**, 485–507 (2020).

24. Turner, R. S. & Desmurget, M. Basal ganglia contributions to motor control: a vigorous tutor. *Curr. Opin. Neurobiol.* **20**, 704–716 (2010).

25. Werkhoven, Z. et al. The structure of behavioral variation within a genotype. *Elife* **10**, e64988 (2021).

26. Schulman, J., Wolski, F., Dhariwal, P., Radford, A. & Klimov, O. Proximal policy optimization algorithms. Preprint at https://arxiv.org/abs/1707.06347 (2017).

27. Konda, V. R. & Tsitsiklis, J. N. Actor-critic algorithms. *Advances in Neural Information Processing Systems* **12**, 1008–1014 (1999).

28. Kingma, D. P. & Ba, J. Adam: a method for stochastic optimization. Preprint at https://arxiv.org/abs/1412.6980 (2014).

29. Pearce, J. M. & Hall, G. A model for Pavlovian learning: variations in the effectiveness of conditioned but not of unconditioned stimuli. *Psychol. Rev.* **87**, 532–552 (1980).

30. Gadagkar, V. et al. Dopamine neurons encode performance error in singing birds. *Science* **354**, 1278–1282 (2016).

31. Amo, R. et al. A gradual temporal shift of dopamine responses mirrors the progression of temporal difference error in machine learning. *Nat. Neurosci.* **25**, 1082–1092 (2022).

32. Li, J. & Daw, N. D. Signals in human striatum are appropriate for policy update rather than value prediction. *J. Neurosci.* **31**, 5504–5511 (2011).

33. Hadjiosif, A. M., Krakauer, J. W. & Haith, A. M. Did we get sensorimotor adaptation wrong? Implicit adaptation as direct policy updating rather than forward-model-based learning. *J. Neurosci.* **41**, 2747–2761 (2021).

34. Pan, W.-X., Coddington, L. T. & Dudman, J. T. Dissociable contributions of phasic dopamine activity to reward and prediction. *Cell Rep.* **36**, 109684 (2021).

35. Sussillo, D. & Abbott, L. F. Generating coherent patterns of activity from chaotic neural networks. *Neuron* **63**, 544–557 (2009).

36. Miconi, T. Biologically plausible learning in recurrent neural networks reproduces neural dynamics observed during cognitive tasks. *Elife* **6**, e20899 (2017).

37. Palmiter, R. D. Dopamine signaling in the dorsal striatum is essential for motivated behaviors: lessons from dopamine-deficient mice. *Ann. N. Y. Acad. Sci.* **1129**, 35–46 (2008).

38. Parker, J. G. et al. Absence of NMDA receptors in dopamine neurons attenuates dopamine release but not conditioned approach during Pavlovian conditioning. *Proc. Natl Acad. Sci. USA* **107**, 13491–13496 (2010).

39. Brown, H. D., McCutcheon, J. E., Cone, J. J., Ragozzino, M. E. & Roitman, M. F. Primary food reward and reward-predictive stimuli evoke different patterns of phasic dopamine signaling throughout the striatum. *Eur. J. Neurosci.* **34**, 1997–2006 (2011).

40. Willuhn, I., Burgeno, L. M., Everitt, B. J. & Phillips, P. E. M. Hierarchical recruitment of phasic dopamine signaling in the striatum during the progression of cocaine use. *Proc. Natl Acad. Sci. USA* **109**, 20703–20708 (2012).

41. Berridge, K. C., Robinson, T. E. & Aldridge, J. W. Dissecting components of reward: ‘liking’, ‘wanting’, and learning. *Curr. Opin. Pharmacol.* **9**, 65–73 (2009).

42. Hamilos, A. E. et al. Slowly evolving dopaminergic activity modulates the moment-to-moment probability of reward-related self-timed movements. *Elife* **10**, e62583 (2021).

43. Lee, K. et al. Temporally restricted dopaminergic control of reward-conditioned movements. *Nat. Neurosci.* **23**, 209–216 (2020).

44. Steinberg, E. E. et al. A causal link between prediction errors, dopamine neurons and learning. *Nat. Neurosci.* **16**, 966–973 (2013).

45. Stauffer, W. R. et al. Dopamine neuron-specific optogenetic stimulation in rhesus cacaques. *Cell* **166**, 1564–1571 (2016).

46. Saunders, B. T., Richard, J. M., Margolis, E. B. & Janak, P. H. Dopamine neurons create Pavlovian conditioned stimuli with circuit-defined motivational properties. *Nat. Neurosci.* **21**, 1072-1083 (2018).

47. Joel, D., Niv, Y. & Ruppin, E. Actor–critic models of the basal ganglia: new anatomical and computational perspectives. *Neural Netw.* **15**, 535–547 (2002).

48. Mohebi, A. et al. Dissociable dopamine dynamics for learning and motivation. *Nature* **570**, 65–70 (2019).

49. Flagel, S. B. et al. A selective role for dopamine in stimulus-reward learning. *Nature* **469**, 53–57 (2011).

50. Silver, D. et al. Mastering the game of Go with deep neural networks and tree search. *Nature* **529**, 484–489 (2016).

51. Arbuthnott, G. W. & Wickens, J. Space, time and dopamine. *Trends Neurosci.* **30**, 62–69 (2007).

52. de Jong, J. W. et al. A neural circuit mechanism for encoding aversive stimuli in the mesolimbic dopamine system. *Neuron* **101**, 133–151 (2019).

53. Stelly, C. E., Girven, K. S., Lefner, M. J., Fonzi, K. M. & Wanat, M. J. Dopamine release and its control over early Pavlovian learning differs between the NAc core and medial NAc shell. *Neuropsychopharmacology* **46**, 1780–1787 (2021).

54. Hamid, A. A., Frank, M. J. & Moore, C. I. Wave-like dopamine dynamics as a mechanism for spatiotemporal credit assignment. *Cell* **184**, 2733–2749 (2021).

55. Lüscher, C., Robbins, T. W. & Everitt, B. J. The transition to compulsion in addiction. *Nat. Rev. Neurosci.* **21**, 247–263 (2020).

56. Coddington, L. T. & Dudman, J. T. In vivo optogenetics with stimulus calibration. *Methods Mol. Biol.* **2188**, 273–283 (2021).

57. Pascoli, V. et al. Stochastic synaptic plasticity underlying compulsion in a model of addiction. *Nature* **564**, 366–371 (2018).

58. Shindou, T., Shindou, M., Watanabe, S. & Wickens, J. A silent eligibility trace enables dopamine-dependent synaptic plasticity for reinforcement learning in the mouse striatum. *Eur. J. Neurosci.* **49**, 726–736 (2019).

59. Yagishita, S. et al. A critical time window for dopamine actions on the structural plasticity of dendritic spines. *Science* **345**, 1616–1620 (2014).

60. Grossman, C. D., Bari, B. A. & Cohen, J. Y. Serotonin neurons modulate learning rate through uncertainty. *Curr. Biol.* **32**, 586–599 (2022).

61. Fiete, I. R., Fee, M. S. & Seung, H. S. Model of birdsong learning based on gradient estimation by dynamic perturbation of neural conductances. *J. Neurophysiol.* **98**, 2038–2057 (2007).

62. Michaels, A. J. & Scherberger, H. HebbRNN: a reward-modulated Hebbian learning rule for recurrent neural networks. *J. Open Source Softw.* **1**, 60 (2016).

63. Driscoll, L. N., Golub, M. D. & Sussillo, D. Computation through cortical dynamics. *Neuron* **98**, 873–875 (2018).

64. Vogels, T. P., Rajan, K. & Abbott, L. F. Neural network dynamics. *Annu. Rev. Neurosci.* **28**, 357–376 (2005).

65. Noorani, I. & Carpenter, R. H. S. The LATER model of reaction time and decision. *Neurosci. Biobehav. Rev.* **64**, 229–251 (2016).

66. Amo, R., Matias S, Yamanaka, A., Tanaka, K. F., Uchida, N & Watabe-Uchida, M. A gradual backward shift of dopamine responses mirrors the progression of temporal difference error in machine learning. *Nat. Neurosci.* **25**, 1082-1092 (2022).

67. Mikhael, J. G., Kim, H. R., Uchida, N. & Gershman, S. J. The role of state uncertainty in the dynamics of dopamine. *Curr. Biol.* **32**, 1077–1087 (2022).

68. Akaike, H. in *Selected Papers of Hirotugu Akaike* (eds Parzen, E. et al.) 199–213 (Springer, 1998).

69. Kim, H. R. et al. A unified framework for dopamine signals across timescales. *Cell* **183**, 1600–1616 (2020).

70. Paxinos, G. & Franklin, K. B. J. *Paxinos and Franklin's the Mouse Brain in Stereotaxic Coordinates* (Academic, 2019).

# Acknowledgements

We thank L. Grima and J. Keller and all the members of the Dudman laboratory, B. Mensh, A. Hermundstad, S. Romani and J. Day for project feedback; J. Arnold, Janelia Experimental Technologies and J. Keller for technical assistance; the Janelia GENIE team for designing and supplying viral vectors; and M. Copeland and B. Foster for histology. This work was supported by the Howard Hughes Medical Institute, where J.T.D. is a Senior Group Leader at the Janelia Research Campus.

# Author information

## Authors and Affiliations

1. Howard Hughes Medical Institute, Janelia Research Campus, Ashburn, VA, USA

   Luke T. Coddington, Sarah E. Lindo & Joshua T. Dudman

## Contributions

L.T.C. and J.T.D. conceived of the project and experiments, analysed data, and wrote the manuscript with input from S.E.L. J.T.D. built models with input from L.T.C. and ran simulations. S.E.L. carried out animal surgeries. L.T.C. collected all experimental data.

## Corresponding authors

Correspondence to Luke T. Coddington or Joshua T. Dudman.

# Ethics declarations

## Competing interests

The authors declare no competing interests.

# Peer review

### Peer review information

*Nature* thanks the anonymous reviewers for their contribution to the peer review of this work. Peer reviewer reports are available.

## Additional information

**Publisher's note** Springer Nature remains neutral with regard to jurisdictional claims in published maps and institutional affiliations.

## Extended data figures and tables

### Extended Data Fig. 1 Comparison of low dimensional policy learning and value learning model fits to behavioral learning.

**a**) Reward collection latency (leftmost column) compared to normalized heat maps of preparatory measures of licking, body movement, whisking probability and pupil diameter (middle 4 columns), and reactive measures of nose motion, body movements, and whisking probability (right 3 columns, with mean first response following reward delivery indicated by black triangles) for standard trials in which a 0.5 s auditory cue (grey arrows at cue start) predicted 3 µL sweetened water reward (blue arrows), averaged in 10-trial bins across training. Each color-coded row corresponds to a separate example mouse, with the background color identifying the same mice in the low dimensional learning trajectories in Extended Data Fig. 1b, c. **b**) Abstract learning trajectories were described as exponential fits to the first principal. component of "preparatory" (left) and "reactive" (right) behavioral measurements. (example mice from panel A: red, yellow, grey; all other mice: thin black, total n = 9 mice). **c**) The relationship of inferred policy updates to reward collection performance visualized for each mouse as exponential fits to the first principal component of reactive and preparatory measurement variables (as shown in panel B), then plotted against the latency to collect reward (example mice from panel a: red, yellow, grey; all other mice: thin black, total n = 9 mice). **d**) Fits of value (blue) and policy (orange) learning models for each mouse across the space of possible parameterizations, measured as -log likelihood (smaller number

is better fit) (n = 9 mice). **e**) Comparison of optimally parameterized policy and value models for each mouse, quantified by -log likelihood (left) or Aikake information criterion per trial (right). **f**) Comparison of median parameterized policy and value models for each mouse, quantified by -log likelihood (left) or Aikake information criterion per trial (right).

## Extended Data Fig. 2 ACTR model details.

**a**) top) Schematic of ACTR policy recurrent neural network (RNN) and licking output from example different network initialization (right). **b**) Thousands of randomized initial network configurations ranked according to their performance cost (Fig. 1h; cost is a combination of latency and a network variance cost, see methods for details). Displayed are the latency to collect reward (black), network sparsity (blue), coupling coefficient (red), leading eigenvalue (purple). This analysis reveals a few key aspects. First, a sustained policy that spans time from the detection of the cue through the delivery of water reward is necessary to minimize latency cost. Second, while optimal RNNs are relatively indifferent to some parameters (sparsity of connectivity) they tend to require a strong coupling coefficient which is known to determine the capacity of a RNN to develop sustained dynamics[86], and thus optimal policies were observed uniquely in RNNs with large leading eigenvalues (i.e. long time constant dynamics[87]). These analyses indicate that there are realizable RNN configurations sufficient to produce an optimal policy, given an effective learning rule. **c**) Different ratios of sustained vs transient learning rates (inset color code) produced a range of trajectories similar to observed trajectories in individual mice (Fig. 1e). **d**) (top row) Licking behavior was modeled as a two state ({off,on}) plant that emitted 7 Hz lick bouts from the 'on' state. Forward transition rate (off→on) was determined by a policy *π(t)*. Reverse transition rate (on→off) was a constant modulated by the presence of water. Bottom three rows illustrate example licking behavior produced by the plant for three different constant policies (red, purple, blue) before and after water reward delivery (vertical black line) for 100 repetitions of each policy. **e**) Learning quantified by a decrease in reward collection latency over training. As training progressed, a predictive cue led to faster reward collection (red) as compared to uncued probe trials (black) in both the ACTR model (top, trials 600–800, cued: 146 ± 21 ms, uncued: 205 ± 7 ms, two-tailed signed rank p

= 0.01) and mouse data (bottom, cued: 176 ± 26 ms, uncued: 231 ± 23 ms, two-tailed signed rank p = 0.03). **f**, Cost surface (red = high, blue = low) overlaid with trajectories of individual initializations (white) as in Fig 1g, except having a constant learning rate and using the dopamine-like feedback unit to set the performance error (PE) instead of an adaptive learning rate (β), showing that the dopamine-like signal does not perform well as the PE in the ACTR learning rule. All error bars and bands represent +/− SEM around the mean.

## Extended Data Fig. 3 Dopamine signals across learning.

**a**) (left 3 columns) jRCaMP1b dopamine signals in the nucleus accumbens core (NAc, black, n = 9) and simultaneous recordings in the ventral tegmental area (VTA, purple, n = 3) and dorsal striatum (DS, green, n = 6), for cued reward trials in the trial bins indicated across training. (right) Reward or omission signals in NAc (top), VTA (middle), and DS (bottom) in trials 600–800, for cued (red), uncued (black), and cued but omitted (blue) trials. **b**) Mean signals from the data in panel (a) during the 1 s following cue delivery (left) and 2 s following reward delivery (right) across training for NAc (black, n = 9), VTA (purple, n = 3), and DS (green, n = 6). **c**) Example simultaneous recordings from NAc + VTA (top) and NAc + DS (bottom). **d**) Mean cross correlations for simultaneously measured NAc + VTA signals (top row, n = 3) and NAc + DS signals (bottom row, n = 6) in trials 1–100 (left) and trials 700–800 (right) within trial periods (1 s before cue to 3 s after reward). **e**) Peak cross correlation coefficients between NAc + VTA (purple, n = 3) and NAc + DS (green, n = 6) signal pairs across training, within "trial periods" defined as the time between cue start and 3 s after reward delivery. **f**) Correlation of initial NAc–DA reward signals with final combined preparatory behaviors (see Methods) (Pearson's r = −0.85, p = 0.004). **g**) No correlation of initial NAc–DA reward signals with final combined reactive behaviors (Pearson's p = 0.25). **h**) Correlation of initial NAc–DA reward signals predicted from behavior measures in trials 700–800 (see Methods) to observed initial NAc–DA reward signals (Pearson's r = 0.99, p < 0.0001). **i**) Reward collection latency for simulations with low (cyan) and high (magenta) initial reward-related sensory input. **j**) Preparatory cued licking for simulations with low (cyan) and high (magenta) initial reward-related

sensory input. All error bars and bands represent +/− SEM around the mean.

## Extended Data Fig. 4 Augmenting mesolimbic cue signals does not affect cued behavior.

**a**) To test for a causal connection between the size of mesolimbic dopamine cue responses and cued behavior, in a new session after regular training was complete, we delivered large, uncalibrated VTA–DA stimulation on a random subset of cued reward trials (light green). Shown are NAc–DA responses (top) and licking (bottom) for this session. **b**) Quantification of cued preparatory licking during the delay period for unstimulated (black) vs stimulated (green) trials. **c**) Cued licking was correlated with the size of NAc–DA cue responses across animals (Pearson's $r = 0.78$, $p = 0.01$), even though manipulations did not support a causal relationship. All error bands represent +/− SEM around the mean.

## Extended Data Fig. 5 Movement correlates after learning induced by exogenous VTA-DA stimulation.

**a**) NAc–DA responses (top) and body movement measured as acceleration of the basket holding the mice (bottom) at the end of training in the paradigm in Fig 3a–e in which a visual cue predicted VTA–DA stimulation calibrated to measured uncued reward responses. **b**) Same as (a) except for larger, uncalibrated stimulation. All error bands represent +/− SEM around the mean.

## Extended Data Fig. 6 Exogenous stimulation produces similar input-output ratios across sampled mDA projection targets.

**a**) Dopamine responses measured through the same fiber for the low (black), medium (dark red), and high (bright red) stim parameters indicated at right, inserted either in the mPFC or at the indicated depth in the striatum. **b**) Schematic of experiment. **c**) Input-output ratio (response to high stim parameters divided by response to low stim parameters at each recording site in two separate mice (blue and orange).

## Extended Data Fig. 7 ACTR-modeled dopamine dynamics are robust to initialization conditions.

**a**) Predicted dopamine responses to cues for 5 random initializations of the ACTR model. **b**) Predicted dopamine responses to rewards over the same initializations as (a), comparing cued (red), uncued (black) and omitted (blue) reward trials ($n = 5$ simulations per initialization). RPE correlates emerged robustly across initializations. All error bars represent +/− SEM around the mean.

## Extended Data Fig. 8 Relationship of NAc–DA signals and performance errors to the presence of preparatory licking.

**a**) Trial types defined as "lick+" trials (purple) with at least one lick during the delay between cue and reward and "lick-" trials (green) with no delay period licking. **b**) Percent of total trials that are "lick+" (top) and reward collection latency (bottom), for best 4 (green) and worst 4 (purple) performing mice, as determined by their reward collection latency in trials 700–800. **c**) NAc–DA signals in the second half of training (trials 400–800) lick- (green) and lick+ (purple) trials, for ACTR simulations (top) and worst (left) and best (right) top 4 performing mice in terms of reward collection latency in trials 700–800. **d**) The ratio of NAc–DA reward signals on lick- vs lick+ trials was correlated with the final reward collection latency (Pearson's $r = -0.71$, $p = 0.03$). **e**) Enhancing the mDA-like adaptive learning rate signal at reward on either lick- (green) or lick+ (purple) trials (schematic at left) in the ACTR model biases future licking behavior in opposite directions from the stimulation contingency across training (right) for $n = 9$ initializations. In other words, enhancing mDA-like reward signals on trials with cued licking decreases cued licking in the future. **f**) The average change in performance error (ΔPE, the learning signal for preparatory learning in the ACTR model (Fig. 1i)) for each control mouse ($n = 9$) switched sign on lick+ or lick- trial types (two-tailed signed rank test $p < 0.001$). **g**) Average ΔPE on all stimulated trials in each mouse that received VTA–DA stimulation depending on whether they licked during the delay period preceding reward ("StimLick+", $n = 5$), or whether they did not lick during the delay period ("StimLick-", $n = 6$) (two-tailed signed rank

p < 0.004 StimLick+ vs StimLick-). **h**) 3d learning trajectories as in Fig. 1e, comparing preparatory and reactive components of behavior to the latency to collect reward across training. All error bands represent +/− SEM around the mean. Box plots represent the median at their center bounded by the 25th and 75th percentile of the data, with whiskers to each extreme.

## Extended Data Fig. 9 Baseline licking across training in all animals.

**a**) Licking behavior showed in extended time before and after reward delivery to illustrate baseline intertrial licking behavior across the indicated training trials, for control (black), stimLick- (green), and stimLick+ (purple) mice. Grey numbered blocks indicate analysis epochs for panel (b). **b**) (top) Quantification of baseline licking at analysis epoch 1 (indicated at right of panel (a)) across training. (bottom) Quantification of baseline licking at analysis epoch 2. **c**) Mean baseline licking rate (final 300 trials of training) for all the experimental groups shown in Fig 1–6. No stimulation controls (white, n = 9), stimLick- (green, n = 6), stimLick+ (dark purple, n = 5), stim+Lick+ (light purple, n = 4). **d**) Licking behavior over the 3 s preceding uncued trials at the end of training (trials 600–800) for the best 4 and worst 4 performing mice displayed an insignificant trend towards more baseline licking in bad learners. **e**) (left) No correlation between baseline licking and final latency to collect reward (a measure of learned performance) for all mice (Pearson's p = 0.46, n = 20). (right) No correlation between baseline licking and final latency to collect reward (a measure of learned performance) for only control mice that received no exogenous dopamine manipulations during training (corresponding to data from Fig 1–2, Pearson's p = 0.9, n = 9). **f**) No correlation between baseline licking and initial NAc–DA reward responses for control mice (Pearson's p = 0.75). All error bands represent +/− SEM around the mean.

## Extended Data Fig. 10 Logic Outline.

**A**) Key points of the paper grouped by theme (left), with location in figures for primary supporting data (blue). **B**) In Reinforcement Learning, an agent learns iteratively from environmental feedback to improve a policy, which

is a set of parameters (Θ) describing an action (a) that is performed given a state (s). In policy learning, the agent applies a learning rule.

## Supplementary information

### Supplementary Table 1

### Reporting Summary

### Peer Review File

## Rights and permissions

**Open Access** This article is licensed under a Creative Commons Attribution 4.0 International License, which permits use, sharing, adaptation, distribution and reproduction in any medium or format, as long as you give appropriate credit to the original author(s) and the source, provide a link to the Creative Commons licence, and indicate if changes were made. The images or other third party material in this article are included in the article's Creative Commons licence, unless indicated otherwise in a credit line to the material. If material is not included in the article's Creative Commons licence and your intended use is not permitted by statutory regulation or exceeds the permitted use, you will need to obtain permission directly from the copyright holder. To view a copy of this licence, visit http://creativecommons.org/licenses/by/4.0/.

Reprints and Permissions

## About this article

### Cite this article

Coddington, L.T., Lindo, S.E. & Dudman, J.T. Mesolimbic dopamine adapts the rate of learning from action. *Nature* **614**, 294–302 (2023). https://doi.org/10.1038/s41586-022-05614-z

- Received: 05 May 2021
- Accepted: 30 November 2022
- Published: 18 January 2023
- Issue Date: 09 February 2023
- DOI: https://doi.org/10.1038/s41586-022-05614-z

## Share this article

Anyone you share the following link with will be able to read this content:

Get shareable link

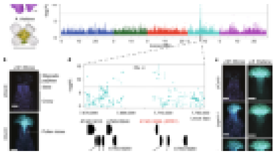
Sorry, a shareable link is not currently available for this article.

Copy to clipboard

Provided by the Springer Nature SharedIt content-sharing initiative

---

This article was downloaded by **calibre** from https://www.nature.com/articles/s41586-022-05614-z



## A stigmatic gene confers interspecies incompatibility in the Brassicaceae

01 July 2019

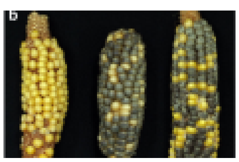
Sota Fujii, Takashi Tsuchimatsu, … Seiji Takayama



## Incompatible pollen abortion and late-acting self-incompatibility in Schima superba

16 September 2022

Rui Zhang, Hanbo Yang & Zhichun Zhou



## A pistil-expressed pectin methylesterase confers cross-incompatibility between strains of Zea mays

24 May 2019

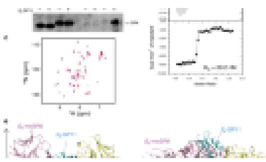
Yongxian Lu, Samuel A. Hokin, … Mathew M. S. Evans



## [Widespread coexistence of self-compatible and self-incompatible phenotypes in a diallelic self-incompatibility system in Ligustrum vulgare (Oleaceae)]

04 September 2021

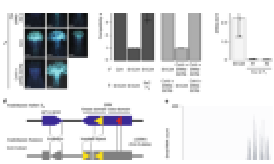
Isabelle De Cauwer, Philippe Vernet, … Pierre Saumitou-Laprade



## [Mechanism of self/nonself-discrimination in Brassica self-incompatibility]

01 October 2020

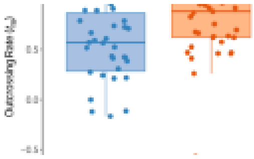
Kohji Murase, Yoshitaka Moriwaki, … Seiji Takayama



## [Parallel evolution of dominant pistil-side self-incompatibility suppressors in Arabidopsis]

16 March 2020

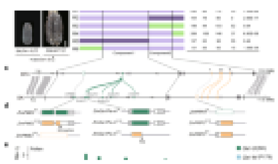
Sota Fujii, Hiroko Shimosato-Asano, … Seiji Takayama



[Outcrossing rates in an experimentally admixed population of self-compatible and self-incompatible Arabidopsis lyrata]

16 December 2021

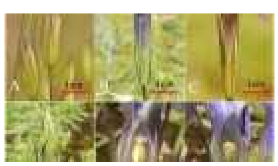
Christina Steinecke, Courtney E. Gorman, … Marcel E. Dorken



[Three types of genes underlying the Gametophyte factor1 locus cause unilateral cross incompatibility in maize]

03 August 2022

Yuebin Wang, Wenqiang Li, … Jianbing Yan



[Correlation between the timing of autonomous selfing and floral traits: a comparative study from three selfing Gentianopsis species (Gentianaceae)]

26 February 2018

Ji-Qin Yang, Yong-Li Fan, … Xing-Fu Zhu

- Article
- Open Access

- Published: 25 January 2023


# Stigma receptors control intraspecies and interspecies barriers in Brassicaceae


- Jiabao Huang,
- Lin Yang,
- Liu Yang,
- Xiaoyu Wu,
- Xiaoshuang Cui,
- Lili Zhang,
- Jiyun Hui,
- Yumei Zhao,
- Hongmin Yang,
- Shangjia Liu,
- Quanling Xu,
- Maoxuan Pang,
- Xinping Guo,
- Yunyun Cao,
- Yu Chen,
- Xinru Ren,
- Jinzhi Lv,
- Jianqiang Yu,
- Junyi Ding,
- Gang Xu,
- Nian Wang,
- Xiaochun Wei,
- Qinghui Lin,
- Yuxiang Yuan,
- Xiaowei Zhang,
- Chaozhi Ma,
- Cheng Dai,
- Pengwei Wang,

- Yongchao Wang,
- Fei Cheng,
- Weiqing Zeng,
- Ravishankar Palanivelu,
- Hen-Ming Wu,
- Xiansheng Zhang,
- Alice Y. Cheung &
- …
- Qiaohong Duan

Show authors

*Nature* **volume 614**, pages 303–308 (2023)

- 10k Accesses
- 1 Citations
- 68 Altmetric
- Metrics details

## Abstract

Flowering plants have evolved numerous intraspecific and interspecific prezygotic reproductive barriers to prevent production of unfavourable offspring[1]. Within a species, self-incompatibility (SI) is a widely utilized mechanism that rejects self-pollen[2,3] to avoid inbreeding depression. Interspecific barriers restrain breeding between species and often follow the SI × self-compatible (SC) rule, that is, interspecific pollen is unilaterally incompatible (UI) on SI pistils but unilaterally compatible (UC) on SC pistils[1,4,5,6]. The molecular mechanisms underlying SI, UI, SC and UC and their interconnections in the Brassicaceae remain unclear. Here we demonstrate that the SI pollen determinant *S*-locus cysteine-rich protein/*S*-locus protein 11 (SCR/SP11)[2,3] or a signal from UI pollen binds to the SI female determinant *S*-locus receptor kinase (SRK)[2,3], recruits FERONIA (FER)[7,8,9] and activates FER-mediated reactive oxygen species production in

SI stigmas[10,11] to reject incompatible pollen. For compatible responses, diverged pollen coat protein B-class[12,13,14] from SC and UC pollen differentially trigger nitric oxide, nitrosate FER to suppress reactive oxygen species in SC stigmas to facilitate pollen growth in an intraspecies-preferential manner, maintaining species integrity. Our results show that SRK and FER integrate mechanisms underlying intraspecific and interspecific barriers and offer paths to achieve distant breeding in Brassicaceae crops.

# Main

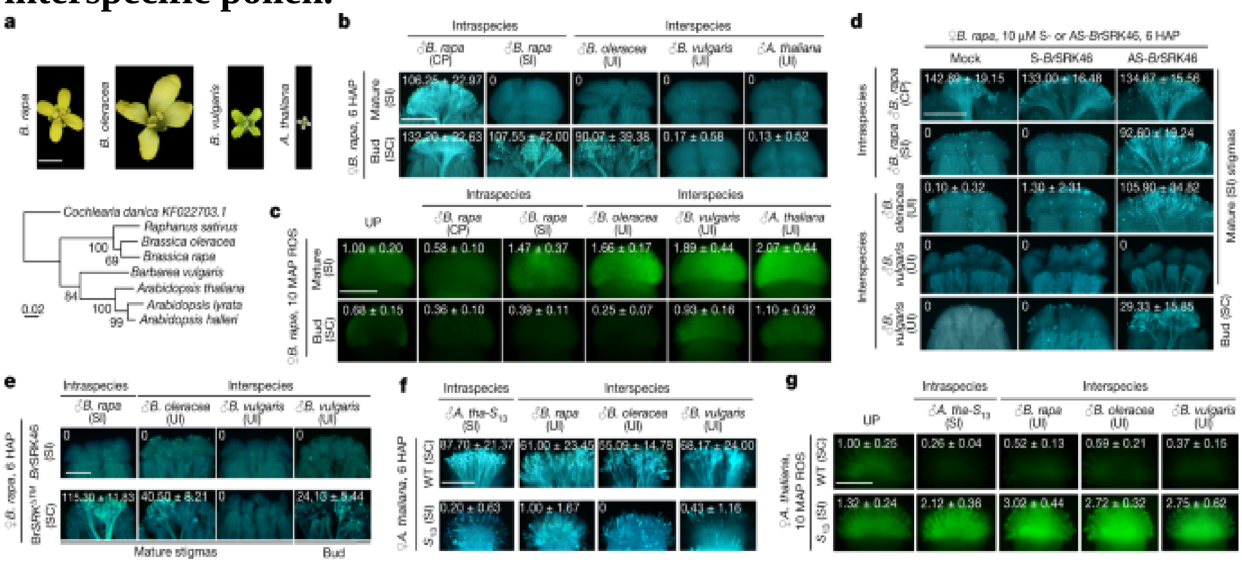
In flowering plants, prezygotic reproductive barriers may occur at one or more check points before fertilization to prevent production of unfavourable offspring[1]. In nature, the stigma of an open flower is exposed to pollen from its own species, closely and distantly related interspecies, therefore must respond accordingly. Within a species, SI is widely utilized as a mechanism to avoid inbreeding depression and promote hybrid vigour by rejecting self-pollen and accepting intraspecific cross-compatible (CP) pollen[2,3]. Between species, interspecific incompatibility maintains species integrity and often follows the SI × SC rule, that is, interspecific pollen is UI on SI pistils but UC on SC pistils[1,4,5,6]. So far, little is known about the molecular mechanisms regulating these compatibility systems and their interconnections in the Brassicaceae.

In Brassicaceae SI, self-pollen is recognized by the ligand–receptor interaction between the pollen-expressed SCR/SP11 and its receptor, the stigma-expressed, plasma membrane-localized SRK[2,3]. This activates two downstream positive regulators of SI, the *M*-locus protein kinase (MLPK)[15] and ARM-repeat containing 1 (ARC1) E3 ubiquitin ligase[16]. How MLPK functions remains unclear[2,15,17]. ARC1 targets compatible factors such as the exocyst component EXO70A1 for degradation, blocking pollen hydration[2,16,18]. We discovered that the female fertility regulator FER receptor kinase[7,8,9] maintains a stigmatic gate in *Arabidopsis thaliana*[14] and has a dual role in rejecting SI pollen and facilitating SC pollen germination in *Brassica rapa*[10,11] by signalling a rapid elevation of stigmatic reactive oxygen species (ROS) or its decline, respectively.

# SRK controls rejection of UI pollen

We first characterized pollen-induced responses during SI, SC, UI or UC pollination in *B. rapa* and *A. thaliana* stigmas by depositing pollen from *B. rapa*, closely related interspecific *Brassica oleracea*, more distant intergeneric *Barbarea vulgaris* and *A. thaliana*[19,20] (Fig. 1a). Of particular interest is crosses involving *B. vulgaris* owing to its high resistance to fungal and insect pathogens[21,22], but intergeneric barriers prevent introgression of its desirable traits into *Brassica* crops.

### Fig. 1: SRK controls stigmatic ROS in SI to reject intraspecific and interspecific pollen.




**a**, Open flowers and phylogenetic tree for Brassicaceae species from maximum likelihood analysis using internal transcribed spacer sequences. Distantly related *Cochlearia danica* served as an outgroup. Scale bar, mean number of nucleotide substitutions per site. **b**, Aniline blue staining showing intraspecific and interspecific pollen growth in mature and bud-stage *B. rapa* stigmas. **c**, $H_2$DCFDA staining of ROS in unpollinated (UP) or pollinated *B. rapa* stigmas. **d**,**e**, Relaxed SI and UI in AS-*Br*SRK46-treated *B. rapa* $S_{46}$ stigmas (**d**) and stigmas from SRK-defective *B. rapa*, Br*SRK*$^{\Delta TM}$ (**e**). **f**,**g**, Intraspecific and interspecific pollen (**f**) and ROS responses (**g**) in stigmas from SC *A. thaliana*, that is, wild type (WT), and stigmas from SI *A. thaliana* expressing *A. halleri* $S_{13}$ genes (*A. tha*-$S_{13}$). The values in the **b**–**g**

images, shown as average ± s.d., indicate average number of pollen tubes in the stigma (**b**,**d**,**e**,**f**) and average ROS intensity (**c**,**g**). The same data are also presented in box plots with all data points (Extended Data Figs. 1, 2). Scale bars, 0.5 cm (**a**), 500 μm (**b**–**e**) and 200 μm (**f**,**g**). Each experiment was repeated at least three times with consistent results.

We used *B. rapa* var. *pekinensis*, an economically important vegetable crop also called heading Chinese cabbage, as a representative SI species for pollen-induced responses on the stigma. A hallmark of SI in Brassicaceae is that its strength is developmentally regulated, due to the progressive increase in the amount of SRK accumulation from bud stage to maturity[23] (Extended Data Fig. 1a). Compared with extensive CP pollen tube penetration into mature *B. rapa* stigmas, SI and interspecific pollen were severely inhibited (Fig. 1b and Extended Data Fig. 1b). Bud-stage *B. rapa* stigmas were comparably well penetrated by both SI and *B. oleracea* pollen, reflecting the involvement of an SRK-mediated mechanism in UI, mimicking SI. However, they remained impenetrable by *B. vulgaris* and *A. thaliana* pollen (Fig. 1b and Extended Data Fig. 1b), and it is likely that even the low level of SRK in bud-stage *B. rapa* stigmas is enough to reject intergeneric pollen.

Given that the profile of SRK expression aligns with that of ROS accumulation[10], we examined whether stigmatic redox status has a crucial role in the UI response. Like the SI-induced stigmatic ROS increase[10,11] but contrary to CP-induced ROS decline, UI pollen stimulated notable ROS increase in mature *B. rapa* stigmas. Bud-stage stigma ROS was reduced by *B. oleracea* pollen but was increased by *B. vulgaris* and *A. thaliana* pollen by 10 min after pollination (Fig. 1c and Extended Data Fig. 1c,d). Furthermore, sequestrating ROS by sodium salicylate (Na-SA)[8,24,25] not only broke the barrier for *B. oleracea* pollen on mature *B. rapa* stigmas but also the barrier for *B. vulgaris* pollen on bud-stage stigmas (Extended Data Fig. 1e–g). Together, these results support UI pollen-induced ROS being essential for their rejection on SI stigmas.

Next, we tested whether SRK, in addition to rejecting SI pollen, also underlies the UI response. Treating $S_{46}$ *B. rapa* with AS-*Br*SRK46 (antisense oligodeoxyribonucleotide (AS-ODN) that specifically suppresses *Br*SRK46)[10], allowed the penetration of *B. oleracea* pollen tubes into mature

stigmas and *B. vulgaris* pollen tubes into bud-stage stigmas, consistent with ROS reduction (Fig. 1d and Extended Data Fig. 2a–d). Moreover, '*B. rapa* fast plant self-compatible (FPsc)' expresses a transmembrane domain-deleted SRK, hereafter named Br$SRK^{\Delta TM}$, failed to respond with SI and UI pollen-triggered ROS increase and showed compromised rejection of SI and UI pollen (Fig. 1e and Extended Data Fig. 2e–j). Together, these results clearly demonstrate that SRK not only controls SI but also the rejection of interspecific and intergeneric pollen.

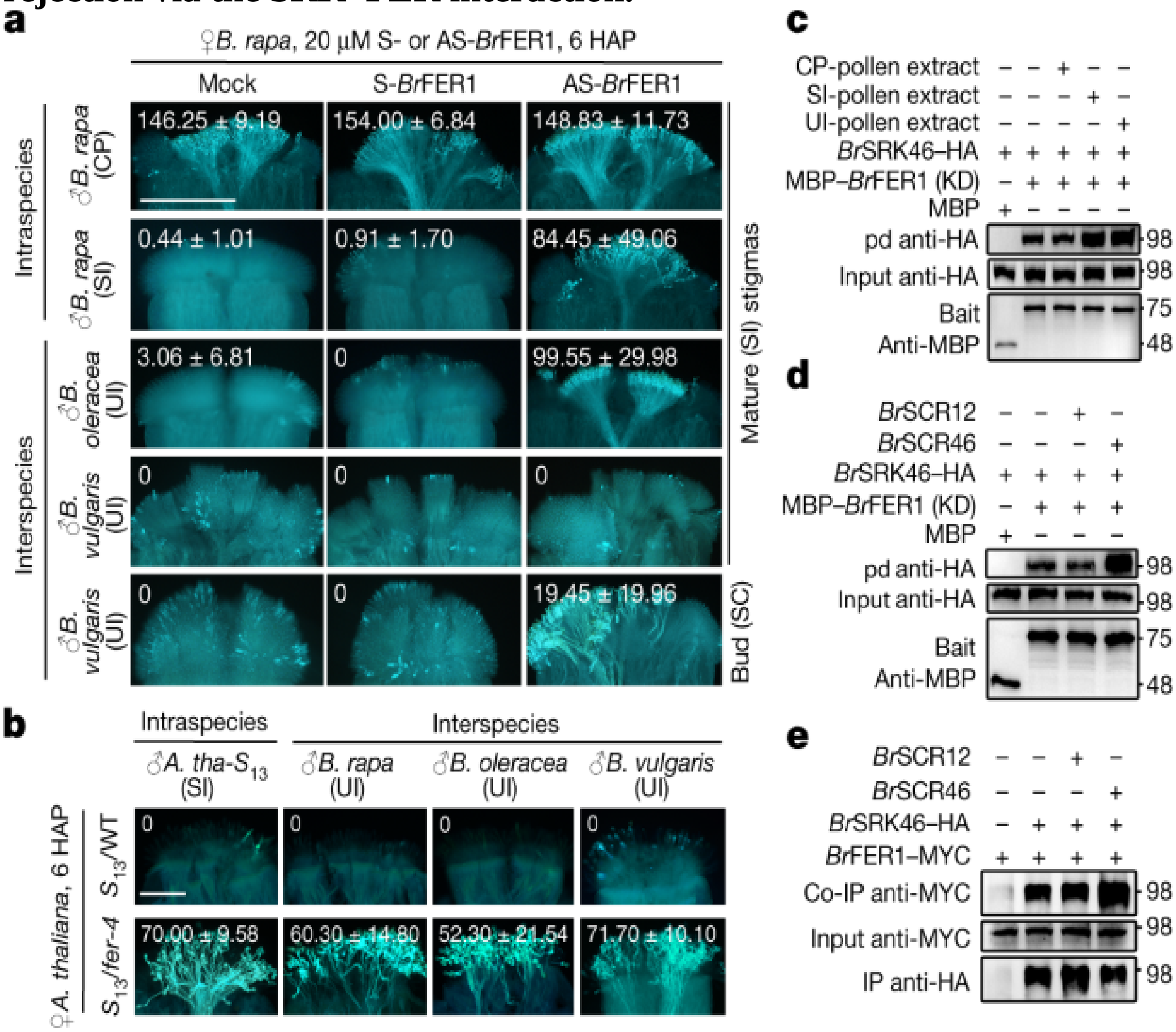
Furthermore, *A. thaliana*, a typical SC Brassicaceae with loss-of-function mutations or complete deletions of the *SRK* and/or *SCR* genes[23,26,27], allowed pollen penetration from *A. thaliana*, *B. rapa*, *B. oleracea* and *B. vulgaris*, and showed stigmatic ROS reduction after pollination. However, transgenic *A. thaliana* expressing SP11/SCR, SRK and ARC1 from the *A. halleri* of $S_{13}$ (referred to as *A. tha*-$S_{13}$ hereafter), which recapitulates SI[28], strongly inhibited interspecific pollen and rapidly increased stigmatic ROS (Fig. 1f,g and Extended Data Fig. 2k–m). In addition, *B. oleracea* $S_{36}$ pollen was similarly rejected by *B. rapa* stigmas of several different *S*-haplotypes (Extended Data Fig. 2n), suggesting that SRK variations do not differ in their function in UI. Together, these results demonstrated unambiguously that SRK and SRK-dependent high stigmatic ROS levels positively correlate with the rejection of UI pollen, similar to the SI response.

# UI and SI activate SRK–FER-regulated ROS

Given the role of FER in regulating ROS[8,29], we suppressed Br*FER1* in *B. rapa* stigmas by AS-ODN or crossed *fer-4* mutant into SI *Arabidopsis*, and observed effective inhibition of SI and UI pollen-triggered stigmatic ROS increase, and marked SI and UI breakdown (Fig. 2a,b and Extended Data Fig. 3a–g). Suppressing *Br*ANJEA1 (*Br*ANJ1), which complexes with FER[14], or *Br*RBOHF, which produces ROS[10], also severely inhibited ROS increase and compromised SI and UI pollen rejection (Extended Data Figs. 3h–l and 4). Furthermore, yeast two-hybrid, bimolecular fluorescent complementation (Extended Data Fig. 5a,b) and protein pull-down assays demonstrated that *Br*SRK46 interacted with *Br*FER1 (Fig. 2c,d). Furthermore, protein extracts from SI and UI pollen, and SI determinant

*Br*SCR46, markedly augmented *Br*SRK46–HA pulled down by MBP–*Br*FER1 (kinase domain (KD)), whereas CP pollen extracts and *Br*SCR12 had no effect (Fig. 2c,d and Extended Data Fig. 5c–f). Moreover, when co-expressed in tobacco leaves, *Br*SCR46 enhanced *Br*FER1–MYC co-immunoprecipitation with *Br*SRK46–HA and ROS production in tobacco leaves (Fig. 2e and Extended Data Fig. 5g–i). Together, these results suggest that SCR from SI pollen[2,3] and an unknown signal from UI pollen trigger SRK-dependent activation of FER-regulated ROS production by boosting SRK–FER interaction to reject the incompatible pollen.

**Fig. 2: UI and SI converge on stigmatic ROS activation for pollen rejection via the SRK–FER interaction.**



**a**,**b**, Treating *B. rapa* stigmas with AS-*Br*FER1 or crossing *fer-4* into SI *A. thaliana* stigmas, $S_{13}$/*fer-4*, relaxed SI and UI. The values in the **a**,**b** images, shown as average ± s.d., indicate average number of pollen tubes in the stigma. The same data are also presented in box plots with all data points (Extended Data Fig. 3). **c**–**e**, Pull-down (pd) (**c**,**d**) and co-immunoprecipitation (co-IP) (**e**) assays showing protein extracts from SI and UI pollen. *Br*SCR46 augmented the *Br*SRK46–*Br*FER1 interaction. The protein samples were derived from the same experiment and the blots were processed in parallel (**c**–**e**). For gel source data, see Supplementary Fig. 1. Scale bars, 500 μm (**a**) and 200 μm (**b**). Each experiment was repeated at least three times with consistent results.

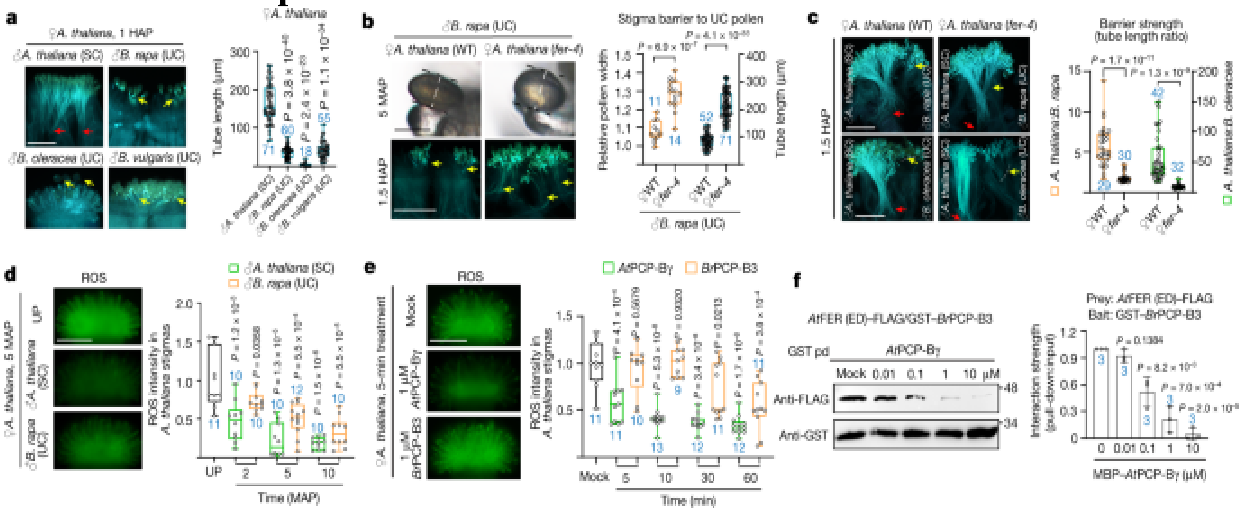
We then explored how the FER–ROS signalling pathway might connect with known SRK signalling[15,16,17,18]. Suppressing *Br*MLPK and *Br*ARC1 by AS-ODN allowed the penetration of SI as well as *B. oleracea* pollen tubes in mature *B. rapa* stigmas (Extended Data Fig. 6a–d). However, although AS-*Br*MLPK inhibited SI and UI-triggered ROS increase, AS-*Br*ARC1 did not (Extended Data Fig. 6e,f). Together, these results suggest that after SRK senses SI and UI pollen, it activates two parallel intracellular signalling pathways: the FER to ROS pathway that mediates pollen rejection, possibly involving MLPK, and the ARC1-mediated pathway for the degradation of compatible factors required for pollen growth.

## FER and PCP-Bs favour SC over UC pollen

We used *A. thaliana* for pollen-induced responses on SC stigmas. Although pollen tubes from *B. rapa*, *B. oleracea* or *B. vulgaris* all penetrated *A. thaliana* stigmas by 6 h after pollination (HAP) (Fig. 1f), UC pollen tubes were much shorter than SC pollen tubes when examined earlier (1 HAP) (Fig. 3a), suggesting a more stringent barrier for UC pollen. We determined that FER has an important role in suppressing UC pollen in *A. thaliana* stigma as *B. rapa* pollen hydrated considerably faster and their tubes were much longer in *fer-4* stigmas than those in wild type by 1.5 HAP (Fig. 3b). Moreover, simultaneous deposition of *A. thaliana* with *B. rapa* pollen, or *A. thaliana* with *B. oleracea* pollen on the same *A. thaliana* stigma showed a notable reduction in stigmatic barrier strength in *fer* and *rbohd* stigmas (Fig. 3c and Extended Data Fig. 7a–c). UC pollen was also slower than SC pollen

in inducing ROS decline (Fig. 3d), consistent with FER-mediated ROS functioning as a barrier in SC stigmas to discriminate against interspecific pollen for species integrity.

**Fig. 3: Species-preferential interaction between PCP-Bs and FER maintains interspecies barrier.**



**a**, In *A. thaliana* stigmas, *A. thaliana* pollen tubes were longer than those of *B. rapa*, *B. oleracea* and *B. vulgaris* at 1 HAP. **b**, Faster hydration and growth of *B. rapa* pollen on *A. thaliana fer-4* stigmas. The orange plots indicate relative pollen width and the blue plots indicate pollen tube length. The equatorial diameter of a pollen grain, indicated by white dashed lines, was measured in ImageJ for pollen width. **c**, Relaxed interspecies barrier in *fer-4* stigmas. Ratios of pollen tube length in intraspecies and interspecific crosses are used as a measure for barrier strength. In **a**–**c**, the arrows indicate pollen tube front. **d**,**e**, Species-preferential ROS reduction in *A. thaliana* stigmas by pollen (**d**) and PCP-Bs (**e**) from intraspecies and interspecies. **f**, Pull-down assay showing *At*PCP-Bγ competed dose-dependently with GST–*Br*PCP-B3 for interaction with *At*FER (ED)–FLAG. The protein samples were derived from the same experiment and the blots were processed in parallel (**f**). For gel source data, see Supplementary Fig. 1. Scale bars, 200 μm (**a**–**e**) and 20 μm (pollen in **b**). For box plots (**a**–**e**), the centre line indicates the median, the box limits denote the lower and upper quartiles, the dots indicate individual data points, and the whiskers denote the highest and lowest data points. *P* values were determined by two-tailed Student *t*-tests. *n* (in blue) indicates the number of stigmas or pollen grains. In **f**, for the data bar, average ± s.d. is shown; average intensities from three

biological replicates of the blot are represented on the left (two-tailed *t*-test, $n = 3$). Each experiment was repeated at least three times with consistent results.

Source data

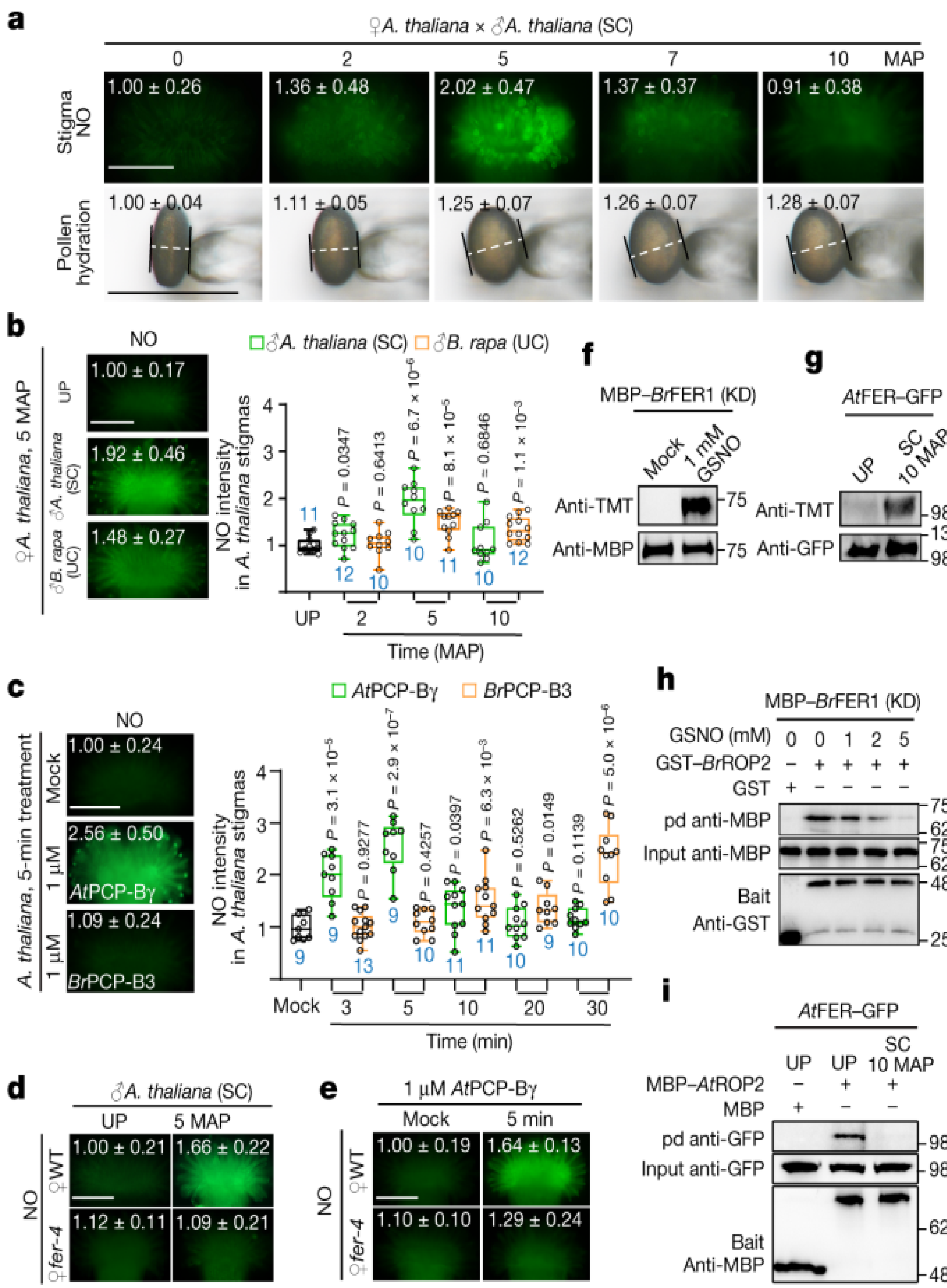
Pollen coat proteins B-class (PCP-Bs) are highly polymorphic cysteine-rich peptides that are widespread in the Brassicaceae (Extended Data Fig. 7d,e) and are important for pollen hydration[12,13,14]. In *A. thaliana*, PCP-Bγ binds to FER and reduces stigmatic ROS to allow pollen growth[14]. We therefore examined the efficacy of PCP-Bs from different species in suppressing ROS. On *A. thaliana* stigmas, *At*PCP-Bγ induced a marked reduction of ROS as early as 5 min after treatment, but *Br*PCP-B3 (ref. [12]) reduced ROS to comparable levels only by 60 min after treatment. Reciprocally, *B. rapa* stigma ROS responded to *Br*PCP-B3 earlier than *A. thaliana* stigmas (Fig. 3e and Extended Data Fig. 7f,g). Moreover, species-specific PCP-B-induced ROS suppression was recapitulated in *Arabidopsis* roots, which also express FER[29] (Extended Data Fig. 7h,i), thus providing further support. Pull-down assays showed that *At*PCP-Bγ competed dose-dependently with *Br*PCP-B3, but not vice versa, for interaction with the *At*FER extracellular domain (ED) (Fig. 3f and Extended Data Fig. 7j). Together, these results suggest that the species-specific match between PCP-Bs and FER is important for a rapid compatibility response and serves as an interspecific barrier to favour intraspecific pollen for fertilization.

# Compatible pollen induced-NO reduces ROS

As signalling of ROS and nitric oxide (NO) is intimately engaged[30,31], we investigated whether NO regulates stigmatic ROS during SC and UC responses. In *A. thaliana* stigmas, NO levels increased rapidly, as early as 2 min after pollination with SC pollen, reaching a maximum by 5 min after pollination, and declined sharply to pre-pollination level, paralleling that of pollen hydration (Fig. 4a, upper panel, and Extended Data Fig. 8a,b). However, *B. rapa* pollen and *Br*PCP-B3 were notably slower than *A. thaliana* pollen and *At*PCP-Bγ, respectively, in stimulating NO in *A. thaliana* stigmas (Fig. 4b,c). Furthermore, unlike wild type, *fer-4* stigma NO was non-responsive to SC pollination and *At*PCP-Bγ treatment (Fig. 4d,e and

Extended Data Fig. 8c,d). Species-preferential PCP-B-induced NO increase was also recapitulated in roots (Extended Data Fig. 8e–g). The intraspecific and interspecific pollen and respective PCP-B-induced differential NO increases (Fig. 4b,c) were opposite to their induced changes in ROS (Fig. 3d,e), revealing an inverse functional relationship between NO and ROS in discriminating against interspecific compatible pollen.

**Fig. 4: Compatible pollination induces NO to suppress FER-mediated ROS production.**



a
♀A. thaliana × ♂A. thaliana (SC)
0
2
5
7
10
MAP
Stigma NO
1.00 ± 0.26
1.36 ± 0.48
2.02 ± 0.47
1.37 ± 0.37
0.91 ± 0.38
Pollen hydration
1.00 ± 0.04
1.11 ± 0.05
1.25 ± 0.07
1.26 ± 0.07
1.28 ± 0.07
b
NO
♀A. thaliana, 5 MAP
UP
1.00 ± 0.17
♂A. thaliana (SC)
1.92 ± 0.46
♂B. rapa (UC)
1.48 ± 0.27
♂A. thaliana (SC)
♂B. rapa (UC)
NO intensity in A. thaliana stigmas
P = 0.0347
P = 0.6413
P = 6.7 × 10⁻⁶
P = 8.1 × 10⁻⁵
P = 0.6846
P = 1.1 × 10⁻³
UP
2
5
10
Time (MAP)
c
NO
A. thaliana, 5-min treatment
Mock
1.00 ± 0.24
1 μM AtPCP-Bγ
2.56 ± 0.50
1 μM BrPCP-B3
1.09 ± 0.24
AtPCP-Bγ
BrPCP-B3
NO intensity in A. thaliana stigmas
P = 3.1 × 10⁻⁵
P = 0.9277
P = 2.9 × 10⁻⁷
P = 0.4257
P = 0.0397
P = 6.3 × 10⁻³
P = 0.5262
P = 0.0149
P = 0.1139
P = 5.0 × 10⁻⁶
Mock
3
5
10
20
30
Time (min)
d
♂A. thaliana (SC)
UP
5 MAP
NO
♀WT
1.00 ± 0.21
1.66 ± 0.22
♀fer-4
1.12 ± 0.11
1.09 ± 0.21
e
1 μM AtPCP-Bγ
Mock
5 min
NO
♀WT
1.00 ± 0.19
1.64 ± 0.13
♀fer-4
1.10 ± 0.10
1.29 ± 0.24
f
MBP–BrFER1 (KD)
Mock
1 mM GSNO
Anti-TMT
Anti-MBP
g
AtFER–GFP
UP
SC 10 MAP
Anti-TMT
Anti-GFP
h
MBP–BrFER1 (KD)
GSNO (mM)
GST–BrROP2
GST
pd anti-MBP
Input anti-MBP
Bait Anti-GST
i
AtFER–GFP
UP
UP
SC 10 MAP
MBP–AtROP2
MBP
pd anti-GFP
Input anti-GFP
Bait Anti-MBP

**a**, DAF-FM DA staining of pollination-induced NO responses and pollen hydration in *A. thaliana* stigmas. The equatorial diameter of a pollen grain, indicated by white dashed lines, was measured in ImageJ for pollen width. **b**,**c**, Species-preferential elevation of NO in *A. thaliana* stigmas. **d**,**e**, FER-dependent NO elevation in *A. thaliana* stigmas induced by pollen (**d**) and *At*PCP-Bγ (**e**). The values in the **a**–**e** images, shown as average ± s.d., indicate average NO intensity (**a**–**e**) and equatorial diameter of pollen grains (**a**). The same data are also presented in box plots with all data points (Extended Data Fig. 8). **f**,**g**, Nitrosation of FER. *Br*FER1 was nitrosated in vitro by the NO donor GSNO (**f**), and *At*FER–GFP from transformed *A. thaliana* stigmas was nitrosated in vivo by SC pollination (**g**). **h**,**i**, Pull-down assays showing that nitrosation of FER in vitro (**h**) and by pollination (**i**) reduced its interaction with the downstream ROP2 signalling module. The protein samples were derived from the same experiment and the blots were processed in parallel (**f**–**i**). For gel source data, see Supplementary Fig. 1. Scale bars, 200 μm (**a**–**e**) and 50 μm (pollen in **a**). For box plots (**b**,**c**), the centre line indicates the median, the box limits denote the lower and upper quartiles, the dots indicate individual data points, and the whiskers denote the highest and lowest data points. *n* (in blue) indicates the number of stigmas or pollen grains. *P* values were determined by two-tailed Student *t*-tests. Each experiment was repeated at least three times with consistent results.

Source data

Additional observations further supported the role of NO in regulating stigmatic ROS and pollen growth. Scavenging *A. thaliana* stigma NO by cPTIO[31] suppressed SC-induced NO increase and ROS reduction and prevented SC pollen growth (Extended Data Fig. 8h,i). Pollination experiments carried out in NO-deficient[32,33,34] and NO-overaccumulating[35] mutants similarly supported the importance of NO involvement (Extended Data Fig. 8j–p). Furthermore, in *B. rapa*, stigmatic NO responded similarly, stimulated by SC but not by SI or UI pollen (Extended Data Fig. 9a,b). Scavenging or increasing NO by cPTIO or *S*-nitrosoglutathione (GSNO), respectively, also induced opposite changes in ROS and pollen growth in *B. rapa* stigmas (Extended Data Fig. 9c–h). These results established firmly that NO is specifically induced in stigmas by compatible pollen for ROS reduction and pollen growth.

## NO nitrosates FER in compatible response

A major bioactivity of NO is *S*-nitrosation of specific cysteines in many proteins[9,36,37]. Given the role of FER and RBOHs examined here (Extended Data Figs. 3 and 4), they could be targets for nitrosation. A tandem mass tag-switch analysis[9,38] of GSNO-treated MBP–*Br*FER1 showed nitrosation of Cys730, and Cys752 in the KD, which are conserved among FERs from many Brassicaceae species (Fig. 4f and Extended Data Fig. 9i–l). *At*FER–GFP in transformed *A. thaliana* stigmas[8,29] was also nitrosated after SC pollination (Fig. 4g), suggesting that nitrosation of FER has important roles during the compatible response.

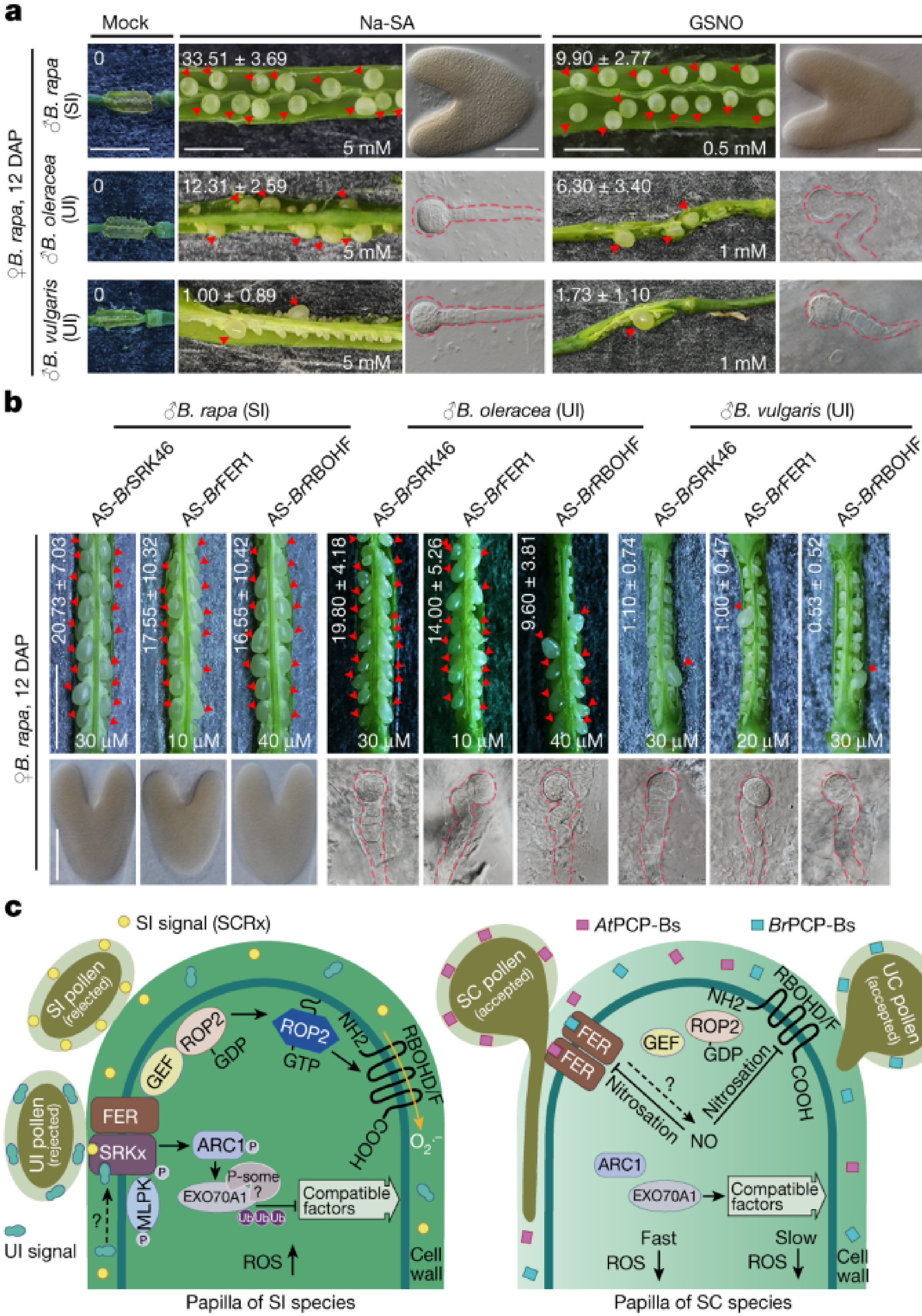
Nitrosation of proteins may affect their stability, biochemical properties and interaction with other proteins[9,39]. GSNO-treated *Br*FER1 (KD) and a Cys730Trp (*Br*FERC730W) conversion, which mimics nitrosation[40], both showed compromised interaction with its downstream *Br*ROP2 signalling complex (Fig. 4h and Extended Data Fig. 9m,n). We also observed substantial reduction in *At*FER–GFP pulled down by *At*ROP2 in *A. thaliana* stigmas with SC pollen (Fig. 4i). Moreover, stigma-expressed RBOHs were also nitrosated in vitro and by pollination (Extended Data Fig. 9o–t), similar to immunity signalling-induced nitrosation[36]. Together, these results indicate that stigmatic ROS decline is a consequence of compatible pollination-stimulated NO, nitrosating FER to inactivate downstream RAC/ROP-regulated RBOH-dependent ROS production, and the already produced RBOHs to rapidly quell ROS-producing activity in stigmas.

## Breaking the barrier for distant breeding

Having established the mechanisms underlying the interspecific barrier at the stigma, we next explored to what extent breaking the barrier might promote distant breeding. We treated *B. rapa* pistils with Na-SA to reduce the levels of ROS and GSNO to increase NO levels, or AS-ODNs to disrupt the *Br*SRK–*Br*FER interaction and *Br*FER-to-*Br*RBOH signalling, then pollinated them with SI and UI pollen. By 12 days after pollination, SI *B. rapa* pollen, *B. oleracea* pollen and *B. vulgaris* pollen all resulted in enlarged ovules with developing embryos in these treated pistils (Fig. 5a,b

and Extended Data Fig. 10). Additional barriers beyond the stigma must have precluded robust cross-fertilization and hampered hybrid embryo development (Fig. 5a,b and Extended Data Fig. 10). Combining the strategies used here with embryo rescue, an in vitro culture technique widely utilized in distant breeding[41], should allow successful development of interspecific hybrid embryos into viable plants.

**Fig. 5: Breaking the stigmatic barrier for distant breeding of Brassicaceae crops.**



a
Mock
Na-SA
GSNO
♀B. rapa, 12 DAP
♂B. rapa (SI)
♂B. oleracea (UI)
♂B. vulgaris (UI)
0
33.51 ± 3.69
5 mM
9.90 ± 2.77
0.5 mM
12.31 ± 2.59
6.30 ± 3.40
1 mM
1.00 ± 0.89
1.73 ± 1.10
b
♂B. rapa (SI)
♂B. oleracea (UI)
♂B. vulgaris (UI)
AS-BrSRK46
AS-BrFER1
AS-BrRBOHF
20.73 ± 7.03
17.55 ± 10.32
16.55 ± 10.42
19.80 ± 4.18
14.00 ± 5.26
9.60 ± 3.81
1.10 ± 0.74
1.00 ± 0.47
0.53 ± 0.52
30 μM
10 μM
40 μM
20 μM
c
SI signal (SCRx)
SI pollen (rejected)
UI pollen (rejected)
UI signal
GEF
ROP2
GDP
GTP
NH2
RBOHD/F
COOH
FER
SRKx
MLPK
ARC1
P-some
EXO70A1
Compatible factors
ROS
Cell wall
Papilla of SI species
AtPCP-Bs
BrPCP-Bs
SC pollen (accepted)
UC pollen (accepted)
Nitrosation
NO
Fast ROS
Slow ROS
Papilla of SC species

**a**,**b**, Reducing stigmatic ROS by a ROS scavenger, increasing NO by a NO generator (**a**), and disrupting the *Br*SRK–*Br*FER interaction and *Br*FER1-to-*Br*RBOH signalling by AS-ODNs (**b**) alleviated the interspecific and intergeneric reproductive barrier. The arrowheads indicate enlarged ovules. The dashed lines denote the outline of hybrid embryos. The values in the **a**,**b** images, shown as average ± s.d., indicate average number of enlarged ovules in the pod. The same data are also presented in box plots with all data points (Extended Data Fig. 10). Scale bars, 0.5 cm (siliques) and 100 µm (emb ryos). Each experiment was repeated at least three times with consistent results. **c**, Model of FER-regulated ROS as a shared signalling node in SI, UI, SC and UC responses. In stigmas from SI species, SI pollen and UI pollen activate ROS via the SRK–FER–ROP2–RBOHs pathway, functioning along with the ARC1-mediated processes. Stigmas from SC species are compatible to interspecific pollen, but species-preferential interaction between PCP-Bs and FER initiates a faster compatible response via NO-mediated nitrosation of FER and RBOHs to suppress ROS production, promoting intraspecies precedence and protecting species integrity. The dashed lines and '?' indicate 'to be determined'. P, phosphate; P-some, proteosome; Ub, ubiquitin.

# Discussion

Upon pollination, pollen and stigma engage in a series of communications to facilitate growth of desirable pollen and discourage invaders and less desirable pollen[1]. Exploring SI, UI, SC and UC together in one study, we demonstrate how the interplay between two receptor kinases, SRK and FER, provides the capacity to perceive different pollen signals to fine tune the stigmatic redox conditions and determine acceptance or rejection of pollen from intraspecies or sympatric interspecies with similar flowering time. As summarized in our working model (Fig. 5c), we demonstrate how incompatible signals from SI and UI pollen activate FER-mediated ROS production for pollen rejection in SI stigmas, functioning in parallel with ARC1-mediated processes[2]. We also demonstrate how the species-preferential interaction of PCP-Bs and FER leads to interspecific barriers in SC stigmas.

The Brassicaceae includes many important vegetable and oil crops. Breeding within a species is far from maximizing hybrid vigour owing to the relatively narrow genetic diversity. Breeding between species enriches germplasm resources but is restricted by interspecific barriers, rendering distant breeding with slim chances of success. Achieving interspecific and intergeneric fertilization here by breaking the stigmatic barrier in *B. rapa*, in particular the production of hybrid embryos with the fungal-resistant and insect-resistant *B. vulgaris*[21,22] (Fig. 5a,b), represents a remarkable feat and major breakthrough, enabling introgression of desirable traits into crops from distant species.

# Methods

## Plant materials and growth conditions

Stigmas from *B. rapa* var. *pekinensis*, also known as heading Chinese cabbage, and *A. thaliana* were mostly used for pollination responses. For interactions on SI stigmas, *B. rapa* stigmas from a double haploid line of $S_{46}$ were pollinated with pollen from *B. rapa* $S_{46}$ or $S_{12}$ as SI or CP pollinations, or pollen from *B. oleracea* ($S_{36}$), *B. vulgaris* (SC) and *A. thaliana* (SC) as UI pollinations. For interactions on SC stigmas, a variety FPsc with a defective allele of SRK that lacks the coding sequence for the transmembrane domain and SC *A. thaliana* were used. *B. rapa* stigmas from $S_{46,}$ $S_{12,}$ $S_{9,}$ $S_{40}$ and $S_{38}$ were pollinated with *B. oleracea* ($S_{36}$) for haplotype-dependent analysis. Transgenic SI *A. thaliana*[28], *p*At*FER::*At*FER–GFP*[29] plants, homozygous *fer-4* (GK-106A06, GABI-Kat)[29], *srn* (the γ-ray mutant)[42], *hot5-4* (FLAG_298F11, Versailles Genomic Resource Centre)[35], *noa1* (CS6511)[9], *rbohd-3* (Salk_070610C)[10] and *rbohd-4* (CS9555)[10] mutants and their corresponding wild-type plants Col-0, C24 or WS have been previously described. Transgenic plants *p*At*FER::GFP*–At*RBOHD* were generated by the *Agrobacterium tumefaciens*-mediated floral dip method[43]. $S_{13}$/*fer-4* was generated by crossing *fer-4* mutant into SI Arabidopsis ($S_{13}$ of *A. halleri*); / indicates that these two genetic modifications are in the same *Arabidopsis* plant.

Seeds of *B. rapa*, *B. oleracea* and *B. vulgaris* were germinated in potted soil (Pindstrup substrate, Denmark). Vernalization was performed in a growth chamber with 10 °C–5 °C, 14 h–10 h light–dark cycles, and light intensity of 100 mmol $m^{-2}$ $s^{-1}$. After 1 month of cold treatment for 1-week-old *B. rapa*, and 3 months for 7–8 leaf stage *B. oleracea* and *B. vulgaris* plants, these plants were planted in soil under greenhouse conditions with 25 °C–15 °C, 16 h–8 h light–dark cycles, and light intensity of 300 mmol $m^{-2}$ $s^{-1}$. Seeds of *A. thaliana* and *Nicotiana benthamiana* were germinated and grew in potted soil in a greenhouse at 22 °C, 16–8 h light–dark cycle with a relative humidity of 60%.

## Statistical analysis

Data involving ROS, NO, pollen hydration and pollen tube length were presented as box plots generated in GraphPad Prism v8.0.1. Unless otherwise indicated, the centre line of box plots denotes the median, the box limits denote the lower and upper quartiles, and the whiskers denote the lowest and highest data points. Protein plots and quantitative PCR with reverse transcription (qRT–PCR) related data were presented as data bars (average ± s.d., $n = 3$). Data involving changes of stigma NO over time after pollination were presented as a line chart (average ± s.d.; $n$ indicates the number of stigmas). All statistics data were labelled with the exact $P$ value, and dots in data bars and box plots denote individual data points. Each experiment was repeated at least three times with consistent results.

## Stigma treatment and pollen growth observation

Compatibility was demonstrated by the number of pollen tubes that had penetrated the stigma papilla cells. Stigma feeding assays followed that of refs. [10,44]. *B. rapa* flowers that have just opened but before anther dehiscence, or bud-stage flowers were emasculated and cut at 3 mm away from the stigmatic surface. Excised stigmas were inserted into basic PGM (5 mM $CaCl_2$, 5 mM KCl, 0.01% $H_3BO_3$, 1 mM $MgSO_4 \cdot 7H_2O$, 10% sucrose and 0.8% agarose, pH 7.5) or the treatment medium and kept in a chamber with constant temperature (22.5 °C) and humidity (45%) for the indicated period of time (S-ODNs or AS-ODNs for 1 h; Na-SA, GSNO and cPTIO for 6 h). Treated stigmas were transferred to basic PGM medium and manually

pollinated with similar amount of SI, CP or various UI pollen and maintained in the same condition for 6 h or as indicated. Stigmas were then fixed in Canoy's fixative (ethanol to acetic acid 3:1), softened in 10 M NaOH, and stained in 0.1% aniline blue. Pollen tubes were visualized by epifluorescence (Ex375-328, DM415 and BA351p) on a Nikon Eclipse Ni. Images were captured by a DS-Ri2 digital camera.

For in planta treatment, just open flowers, or bud-stage flowers, on inflorescences of *B. rapa* plants were treated twice at a 30-min interval, with S-ODN and AS-ODN, Na-SA, GSNO or the corresponding mock solution, supplemented with 0.0125% Tween, then pollinated with a similar amount of SI, CP, *B. oleracea* or *B. vulgaris* pollen. The number of enlarged ovules was counted at 12 days after pollination. Embryo clearing and observation followed that of ref. [45] with modifications. Enlarged ovules were cleared in Hoyer's medium (7.5 g gum arabic, 100 g chloral hydrate, 5 ml glycerol and 60 ml $H_2O$) for 5 days, then observed under differential interference contrast on a Nikon Eclipse Ni microscope equipped with a DS-Ri2 digital camera.

The effect of chemicals or the mutation of stigma-expressed genes on the growth of intraspecific or interspecific pollen on SC *A. thaliana* stigmas was demonstrated by the rate of pollen hydration or pollen tube length. SC *A. thaliana* flowers were emasculated at stage 12 (ref. [46]), cultured in PGM for 14 h, then pollinated with *A. thaliana* pollen or *B. rapa* pollen. For pollen hydration, images were taken at each time point after pollination under differential interference contrast on a Nikon Eclipse Ni microscope equipped with a DS-Ri2 digital camera. The equatorial diameters of pollen grains at various time points were measured in ImageJ v1.53c. For pollen tube length, *A. thaliana* stigmas with *A. thaliana* pollen, *B. rapa* pollen or *B. oleracea* pollen were processed for aniline blue staining at 1 or 1.5 HAP. In dual-pollination assays, *A. thaliana* WT and *fer*-mutant pistils (or other mutant pistils) were simultaneously pollinated with *A. thaliana* pollen on half and either *B. rapa* or *B. oleracea* pollen on the other half of the same stigma, with a clear boundary in between. Pollen growth from each half of the stigma was clearly confined to the corresponding half of the pistils and readily distinguishable.

## ODN design and treatment

ODN design and treatment of stigmas followed that of ref. [10]. S-ODNs and AS-ODNs were used to target the following genes (accession numbers shown in Supplementary Table 1): *Br*SRK46, *Br*FER1 and *Br*RBOHF. S-ODNs or AS-ODNs were designed based on Sfold (https://sfold.wadsworth.org/cgi-bin/soligo.pl). The BLAST program (https://blast.ncbi.nlm.nih.gov/Blast.cgi) was used to assess potential off-target effect. The ODNs were synthesized in the Beijing Genomics Institution (BGI). Three bases at both 5′ and 3′ end of S-ODN and AS-ODN were phosphorothioate-modified to maintain stability. The sequences of S-ODNs and AS-ODNs were listed in Supplementary Table 2. Stigmas were excised at the style 1 mm away from the top, inserted in PGM containing the S-ODN or AS-ODN and treated for 1 h. Stigmas were subjected to aniline blue assay at 6 HAP to observe pollen growth.

## Staining of ROS and NO

For stigmatic ROS staining, *B. rapa* stigmas or *A. thaliana* stigmas, unpollinated or at 10 min after pollination with SI, CP or UI pollen, were pretreated in MES buffer (10 mM MES, 5 μM KCl and 50 μM $CaCl_2$, pH 6.15) for 30 min, stained with 50 μM $H_2$DCF-DA (2′,7′-dichlorofluorescein diacetate; Sigma-Aldrich) for 30 min, respectively, then washed at least three times in buffer before observation. For stigmatic NO staining, *B. rapa* stigmas or *A. thaliana* stigmas before or after pollination were soaked in Tris buffer (10 mM Tris-HCl and 10 mM KCl, pH 7.5) for 30 min, stained with 20 μM DAF-FM DA (3-amino,4-aminomethyl-2′,7′-difluorescein diacetate; Thermo Scientific) for 1 h, then washed at least three times in buffer before observation.

For treatments, stigmas were first soaked in MES buffer for 30 min, then treated with S-ODNs or AS-ODNs, chemicals, peptides or pollen extracts at indicated concentration and duration in MES buffer supplemented with 0.0125% Tween 20. After washing three times in MES buffer, treated stigmas were stained for ROS or NO as above described.

For root ROS or NO staining, 3-day-old *A. thaliana* seedlings or 2-day-old *B. rapa* seedlings were soaked in the corresponding buffer for 30 min,

treated with 0.1 μM of *At*PCP-Bγ or *Br*PCP-B3 for the indicated period of time, then stained with 50 μM $H_2$DCF-DA or 20 μM DAF-FM DA for 1 h.

Imaging was carried out under eGFP epifluorescence (Ex470-440, DM4951p and BA525/550), using a Nikon Eclipse Ni and equipped with a DS-Ri2 digital camera. The exposure time for all comparative samples were exactly the same within one experiment. Average ROS or NO signals outlined in the dotted area were measured in Image J v1.53c; ROS or NO in control stigmas were set at 1 for comparative analyses.

For comparison, stigmas were directly stained with the same concentrations of $H_2$DCF-DA or DAF-FM DA for 10 min without buffer pretreatment, and imaged under a confocal microscope (Zeiss LSM880). Changes of ROS and NO were consistent with those imaged under wide-field fluorescence microscope. Wide-field observation, due to its considerably high expedition to sample entire stigma specimens, was used for the massive amount of data gathering required for this study.

For ROS staining of infiltrated tobacco leaves, agrobacterium cells containing *Br*FER1–MYC, GFP–*Br*RBOHD2 and *Br*SRK46–HA were mixed and infiltrated into tobacco leaves. Two days after infiltration, 10 μM GST–*Br*SCR12 or GST–*Br*SCR46 were injected into the same leaf and treated for 10 min. Nitro blue tetrazolium (NBT) staining[47] was used to detect ROS of the infiltrated leaves. The leaves were vacuum infiltrated with 5 mg $ml^{-1}$ NBT (in 10 mM sodium citrate, pH 7.0) for 40 min at room temperature. Leaves were then decolourized three times by boiling in decolourized solution (95% ethanol to glycerine 3:1) for 10 min. The images were captured by a digital camera and measured for ROS intensity in Image J v1.53c. For ROS staining of protoplasts, protoplasts were isolated from the above infiltrated tobacco leaves co-expressing *Br*FER1–MYC, GFP–*Br*RBOHD2 and *Br*SRK46–HA, following that of ref. [48]. Protoplasts were then treated with buffer, *Br*SCR12 and *Br*SCR46, respectively, for 15 min, before staining with 10 μM $H_2$DCF-DA for 10 min. Protoplasts from tobacco leaves infiltrated with buffer were stained for ROS as a control.

## Enzymatic activity of RBOHs

Stigmas before or after pollination or treatment were washed three times with the MES buffer and then freezed in liquid $N_2$. Enzymatic activity of RBOHs was measured following the manufacturer's instructions (Nanjing JC bio). In brief, approximately 0.05 g stigma tissue (approximately 100 stigmas) was ground in liquid $N_2$, extracted in buffer (0.2 M $NaH_2PO_4$ and 0.2 M $Na_2HPO_4$, pH 7.2) and centrifuged at 4,000*g* for 20 min at 4 °C. The resulting supernatant was used to measure RBOH activity spectrophotometrically at 340 nm using FAD and NADPH as substrates. The result was shown as the average of three technical replicates of one sample.

## RNA isolation and qRT–PCR

Total RNA was extracted via the SteadyPure Universal RNA Extraction Kit (AG21017, Accurate Biotechnology) and reverse transcribed with HiScript III 1st Strand cDNA Synthesis Kit (Vazyme). qRT–PCR was performed on a QuantStudio 3 system (Applied Biosystems) with ChamQ SYBR qPCR Master Mix (Vazyme), using Br*ACTIN2* as internal controls. A list of gene-specific primers used for qRT–PCR is included in Supplementary Table 3.

## Molecular cloning

For the *Br*SRK46–HA or *Br*RBOHD2–GFP construct, sequences encoding the full length of *Br*SRK46 or *Br*RBOHD2 were amplified from *B. rapa* stigma cDNA using 2× Phanta Max Master Mix (Vazyme). The fragment was cloned into the modified pCAMBIA1300 vector with a HA or GFP tag using pEASY-Basic Seamless Cloning and Assembly Kit (TransGen Biotech). For the GST fusion protein constructs, sequences encoding *Br*PCP-B3 (residues 1–76), *Br*SCR46 (residues 1–78), *Br*SCR12 (residues 1–76), full length of *Br*ROP2, C-terminal cytoplasmic region of *Br*RBOHD1 (CT; residues 758–923), *Br*RBOHD2 (CT; residues 614–904) and *Br*RBOHF (CT; residues 767–949) were amplified and cloned into a pGEX-4T-1 vector. For the MBP fusion protein constructs, sequences encoding ED of *Br*FER1 (residues 14–420), KD of *Br*FER1 (residues 486–783), mature *At*PCP-Bγ (residues 23–76) and *At*ROP2 were amplified and cloned into a pMAL-p2X vector. For the FLAG fusion protein construct, the ED of *At*FER (residues 29–446) and the KD of *Br*SRK46 (residues 448–860) were amplified and cloned into the pFLAG-CTS vector. For the MYC fusion

protein construct, *Br*FER1 (residues 1–788) was amplified and cloned into pCXSNF. For the bimolecular fluorescent complementation constructs, the KD of *Br*SRK46 (residues 448–860) and *Br*FER1 (residues 486–783) were amplified and cloned into pDONR207 by the Gateway BP reaction via Gateway BP Clonase Enzyme Mix (Invitrogen Life Technologies) and cloned into the pEARLY GATE 201 vector or pEARLY GATE 202 by the LR reaction via Gateway LR Clonase Enzyme Mix (Invitrogen Life Technologies). For the yeast two-hybrid constructs, the KD of *Br*SRK46 (residues 448–860) and the KD of *Br*FER1 (residues 486–783) were amplified and cloned into the pGADT7 or pGBKT7 vectors. For MBP–*Br*FER1$^{C730W}$ (KD), the mutant fragment was amplified from the MBP–*Br*FER1 (KD) vector with appropriate PCR primers using the Fast Mutagenesis System (TransGen Biotech) according to the manufacturer's instructions. A list of gene-specific primers used for the above constructs is included in Supplementary Table 4.

## Protein expression and purification

The constructs of GST, MBP and FLAG fusion protein were transformed into *Escherichia coli* BL21 (DE3) for protein expression. After induction by 0.5 mM IPTG at 37 °C for 4–6 h, the cells were spun down and resuspended in 5 ml PBS (140 mM NaCl, 2 mM KCl, 2 mM $KH_2PO_4$ and 10 mM $Na_2HPO_4.7H_2O$). Sonicated (SCIENTZ) protein was purified by magnetic GSH beads (BEAVER), amylose magnetic beads (PuriMag Pro) or anti-FLAG magnetic beads (BeyoMag), respectively. The eluted protein was separated by SDS–PAGE and detected by the corresponding antibody after western blot.

For peptide preparation, MBP–*At*PCP-Bγ and GST–*Br*PCP-B3 were expressed in *E. coli* BL21 cells and purified by corresponding magnetic beads. The *At*PCP-Bγ (residues 23–76) peptides were also synthesized by Scilight Biotechnology with more than 95% of purity. The peptides were diluted to 1 mM in sterile $ddH_2O$ as stock solution.

For proteins expressed in tobacco leaves, *Agrobacterium tumefaciens* GV3101 (Weidi) cells containing corresponding constructs were infiltrated into *N. benthamiana* leaves following standard procedure[48]. In brief,

*Agrobacterium* cells were spun down at 5,000*g* for 10 min at 4 °C and resuspended to an optical density at 600 nm of 0.6 in the infiltration buffer (10 mM MES, 10 mM $MgCl_2$ and 0.5% glucose, pH 6.5), with 100 μM acetosyringone added before infiltration. Leaves from 5–6-week-old tobacco plants were infiltrated using a 1-ml syringe. Two days after infiltration, leaves were homogenized in liquid $N_2$, mixed in 1 ml plant protein extraction buffer (75 mM KAc, 300 mM NaCl, 100 mM arginine, 10 mM EDTA, 0.25% Triton X-100, pH 7.4, 1 mM PMSF and 1 mM cocktail protease inhibitor) in a 1.5-ml centrifuge tube and stayed on ice for 20 min. After centrifuge at 13,800*g* for 10 min at 4 °C, the supernatant was transferred into a new tube for pull-down or co-IP assays.

## Protein interaction assays

For the yeast two-hybrid assay of *Br*FER1 (KD) and *Br*SRK46 (KD), vector construction, yeast transformation, growth on drop out medium and X-Gal staining followed standard procedure[29].

For the bimolecular fluorescent complimentary assay, the pEARLY GATE 201 containing *Br*FER1 (KD)–nYFP and the pEARLY GATE 202 containing *Br*SRK46 (KD)–cYFP were transformed into *Agrobacterium tumefaciens* strain GV3101. Equal volumes of two cultures were mixed and infiltrated into *N. benthamiana* leaves as described above. Two days after infiltration, imaging was carried out under eGFP epifluorescence (Ex470-440, DM4951p and BA525/550), using a Nikon Eclipse Ni and equipped with a DS-Ri2 digital camera.

For the pull-down assay of *Br*SRK46–HA by MBP–*Br*FER1 (KD), *Br*SRK46–HA protein was extracted from infiltrated tobacco leaves, mixed with amylose magnetic beads (PuriMag Pro)-bound MBP–*Br*FER1 (KD) bait protein for 6 h at 4 °C. The beads were washed three times in pull-down buffer (50 mM Tris-HCl, pH 7.0, 100 mM NaCl and 0.1% Triton X-100 (v/v)) and boiled in SDS–PAGE loading buffer for 5 min. The proteins were then processed for SDS–PAGE, western blot and immunodetection by anti-MBP antibody (1:15,000; Abmart) or anti-HA antibody (1:5,000; Abmart), and with anti-mouse horseradish peroxidase (HRP)-conjugated secondary antibody (1:15,000; Abmart) followed by the HRP detection kit (Vazyme)

analysis with a chemiluminescence imaging system (TIAN NENG). For the effect of peptides, GST–*Br*SCR46 or GST–*Br*SCR12, or protein extracts from SI ($S_{46}$), CP ($S_{12}$) pollen or interspecific (*B. oleracea*) pollen on the interaction of *Br*SRK46–*Br*FER1 (KD), 0.5 μM peptides or 0.65 mg $ml^{-1}$ protein extracts were incubated with *Br*SRK46–HA protein for 1 h before the pull-down assay.

For the co-IP assay of *Br*FER1–MYC by *Br*SRK46–HA, GV3101 *Agrobacterium* cells containing *35S::*Br*SRK46–HA* or *35S::*Br*FER1–MYC* were mixed and infiltrated together into *N. benthamiana* leaves. Two days after infiltration, 10 μM GST–*Br*SCR12 or GST–*Br*SCR46 were infiltrated into the same leaf and treated for 10 min. The leaves were then used for protein extraction. Aliquots of 1 ml supernatant were incubated with 100 μl anti-HA magnetic beads (PuriMag Pro) at 4 °C overnight with rotation. After washing three times, the beads were boiled and the proteins were processed for SDS–PAGE, western bolt and immunodetection by anti-MYC antibody (1:5,000; Abmart) and anti-HA antibody (1:5,000; Abmart) and anti-mouse HRP-conjugated secondary antibody (1:10,000; Abmart).

For the pull-down assay of MBP–*Br*FER1 (KD) by GST–*Br*ROP2, MBP–*Br*FER1 (KD) protein was treated with 1, 2 and 5 mM GSNO for 3 h at room temperature, then mixed with GSH bead (BEAVER)-bound, GST–*Br*ROP2 bait protein for 6 h at 4 °C. The beads were boiled and processed for SDS–PAGE, western bolt and immunodetection by anti-MBP antibody (1:15,000; Abmart) or anti-GST antibody (1:5,000; Abmart), and with anti-mouse HRP-conjugated secondary antibody (1:15,000; Abmart). MBP–*Br*FER1$^{C730W}$ (KD), without GSNO treatment, was processed similarly for the pull-down assay with GST–*Br*ROP2.

For the pull-down of *At*FER–GFP by MBP–*At*ROP2, MBP or MBP–*At*ROP2 bait proteins were bound with amylose magnetic beads (PuriMag Pro) for 6 h and washed three times with pull-down buffer. *A. thaliana* stigmas from *p*At*FER::*At*FER–GFP* transgenic plants, unpollinated or 10 min after pollination, were used for total protein extraction. *At*FER–GFP protein was incubated with corresponding bait protein for 8 h at 4 °C. After washing three times, the beads were boiled and processed for SDS–PAGE, western bolt and immunodetection by anti-GFP antibody (1:10,000; Abmart)

or anti-MBP antibody (1:15,000; Abmart), and with anti-mouse HRP-conjugated secondary antibody (1:10,000; Abmart).

For the pull-down assay to examine peptide competition, anti-FLAG magnetic bead (BeyoMag)-bound *At*FER (ED)–FLAG bait protein was incubated with GST–*Br*PCP-B3 with rotation at 4 °C for 2 h, then increasing concentrations of *At*PCP-Bγ peptides were added for competition at 4 °C for 3 h. The competition by GST–*Br*PCP-B3 peptides with MBP–*At*PCP-Bγ in interaction with *At*FER (ED)–FLAG bait protein was performed similarly. The beads were boiled and processed for SDS–PAGE, western bolt and immunodetection by anti-FLAG antibody (1:5,000; Abmart), anti-GST antibody (1:5,000; Abmart) or anti-MBP antibody (1:15,000; Abmart), and anti-mouse HRP-conjugated secondary antibody (1:5,000; Abmart).

## Protein nitrosation assay

In vitro *S*-nitrosation assay followed that of ref. [35] with modifications, using Pierce *S*-Nitrosylation Western Blot Kit (90105, Thermo Scientific). Purified proteins of GST–*Br*RBOHD1 (CT), GST–*Br*RBOHD2 (CT), GST–*Br*RBOHF (CT) and MBP–*Br*FER1 (KD) were desalted by acetone precipitation and resuspended in HENS buffer (100 mM HEPES, pH 7.0, 1 mM EDTA, 0.1 mM neocuproine and 2.5% SDS). Approximately 150 µg proteins per sample were incubated with 1 mM GSNO in a reaction volume of 100 µl HENS buffer for 2 h at room temperature in the dark. The sample was precipitated with cold acetone and resuspended in 100 µl HENS buffer. After incubation at 50 °C for 1 h with 200 mM *N*-ethylmaleimide (Solarbio) and at room temperature for 30 min, the sample was precipitated with cold acetone and resuspended in HENS buffer. The sample was treated with 60 mM sodium ascorbate and 0.4 mM iodoTMTzero label reagent for 2 h. All the above steps were carried out in the dark. The proteins were finally precipitated by cold acetone and resuspended in 2 M urea buffer. Aliquots of each protein were separated by SDS–PAGE and then analysed by immunoblotting with anti-TMT antibody (1:5,000; Thermo Scientific) and goat anti-mouse IgG (H+L)–HRP (1:10,000; Thermo Scientific) were used for detection of nitrosated protein. In parallel, the proteins were detected for loading with anti-GST antibody (1:5,000; Abmart) or anti-MBP antibody (1:15,000; Abmart), and goat anti-mouse IgG–HRP (1:10,000; Abmart).

For the analysis of *S*-nitrosation in stigmas before and after pollination, 200 stigmas (approximately 0.1 g) from *A. thaliana* plants expressing *p*At*FER::*At*FER–GFP* or *p*At*FER::GFP*–At*RBOHD*, unpollinated or at 10 min after pollination with intraspecific compatible pollen (WT *Arabidopsis* pollen), were homogenized in liquid $N_2$ and resuspended in 0.7 ml of the plant protein extraction buffer. Protein extracts, 1.5 mg in 150 µl, were precipitated with cold acetone and resuspended in HENS buffer for the detection of nitrosated proteins similar to in vitro nitrosation detection.

## Mass spectrometry analysis of nitrosated residue

Mass spectrometric identification of *S*-nitrosated cysteine residues was carried out by Shanghai Bioprofile Biotechnology (China). The protein pellets were resolved with HENS buffer and *N*-ethylmaleimide (Sigma) was used to block the free cysteine. The *S*-nitrosation sites of protein were reduced by the sodium ascorbate (Sigma) specifically and then labelled with iodoTMT zero reagent (Thermo Scientific). The processed proteins were digested with trypsin in 50 mM $NH_4HCO_3$ overnight at 37 °C. The peptides were then desalted with C18 cartridge (Thermo Scientific). The iodoTMT-labelled peptides were enriched by anti-TMT resin as instructed by the manufacturer (Thermo Scientific). Then, the enriched peptides were loaded into liquid chromatography–mass spectrometry for analysis. The Q Exactive HF-X mass spectrometer coupled to Easy nLC1200 (Thermo Scientific) were performed on a 2-h time gradient for peptide mass spectrometry detection. The mass spectrometry raw data were imported into MaxQuant software v1.6.0.16 for data interpretation and protein identification against the *B. rapa* genome database[49] (http://brassicadb.cn). The search results were filtered and exported with a less than 1% false discovery rate at the site level, peptide-spectrum-matched level and protein level. MaxQuant analysis was filtered only for those nitrosated sites (iodoTMT labelled) that were confidently localized (class I, localization probability of more than 0.75) and the score of the modified peptide was more than 40.

## Bioinformatic analysis

All sequences analysed were retrieved from the *B. rapa* genome database[49] (http://brassicadb.cn), NCBI GenBank[50]

(https://www.ncbi.nlm.nih.gov/genbank) or EnsemblPlants[51] (http://plants.ensembl.org/index.html) or Phytozome[52] (https://phytozome-next.jgi.doe.gov). *C. danica* was selected as the outgroup to infer the species relationships among *B. rapa*, *B. oleracea*, *B. vulgaris*, *A. thaliana*, *Raphanus sativus*, *Arabidopsis lyrata* and *A. halleri*. The maximum likelihood tree based on the alignment of nuclear ribosomal internal transcribed spacers from the above-mentioned species was inferred under a Tamura–Nei nucleotide substitution model with 1,000 bootstraps. For the phylogenetic tree of RBOHs, PCPs and SRKs, corresponding sequences were aligned using the MUSCLE algorithm implemented in MEGA X[53], and constructed using the neighbour-joining method in MEGA X with 1,000 bootstraps. The amino acid sequence of PCP-Bs and FER alignment was performed by the online software Clustal Omega[54] (https://www.ebi.ac.uk/Tools/msa/clustalo) with default parameters then import into ESPript 3.0 (ref. [55]) (https://espript.ibcp.fr/ESPript/cgi-bin/ESPript.cgi) to generate pictures.

### Figure preparation

Average ROS and NO signals, pollen grain width and pollen tube length were measured by Image J v1.53c (https://imagej.net). Histograms were prepared by GraphPad Prism v8.0.1 (https://www.graphpad-prism.cn). The main figures were assembled in Adobe Illustrator; all other figures were assembled in Adobe Photoshop. Some cartoon components were from www.figdraw.com for model drawing.

### Reporting summary

Further information on research design is available in the Nature Portfolio Reporting Summary linked to this article.

## Data availability

The source data for Figs. 1–5 and Extended Data Figs. 1–10 are provided with the paper. Raw, uncropped gels and gene accession numbers used in this paper are shown in the Supplementary Information. Source data are provided with this paper.

# References


1. Broz, A. K. & Bedinger, P. A. Pollen–pistil interactions as reproductive barriers. *Annu. Rev. Plant Biol.* **72**, 615–639 (2021).

2. Jany, E., Nelles, H. & Goring, D. R. The molecular and cellular regulation of Brassicaceae self-incompatibility and self-pollen rejection. *Int. Rev. Cell Mol. Biol.* **343**, 1–35 (2019).

3. Nasrallah, J. B. Self-incompatibility in the Brassicaceae: regulation and mechanism of self-recognition. *Curr. Top. Dev. Biol.* **131**, 435–452 (2019).

4. Lewis, D. & Crowe, L. K. Unilateral incompatibility in flowering plants. *Heredity* **12**, 233–256 (1958).

5. Kitashiba, H. & Nasrallah, J. B. Self-incompatibility in Brassicaceae crops: lessons for interspecific incompatibility. *Breed Sci.* **64**, 23–37 (2014).

6. Bedinger, P. A., Broz, A. K., Tovar-Mendez, A. & McClure, B. Pollen–pistil interactions and their role in mate selection. *Plant Physiol.* **173**, 79–90 (2017).

7. Escobar-Restrepo, J. M. et al. The FERONIA receptor-like kinase mediates male–female interactions during pollen tube reception. *Science* **317**, 656–660 (2007).

8. Duan, Q. et al. Reactive oxygen species mediate pollen tube rupture to release sperm for fertilization in *Arabidopsis*. *Nat. Commun.* **5**, 3129 (2014).

9. Duan, Q. et al. FERONIA controls pectin- and nitric oxide-mediated male–female interaction. *Nature* **579**, 561–566 (2020).

10. Zhang, L. et al. FERONIA receptor kinase-regulated reactive oxygen species mediate self-incompatibility in *Brassica rapa*. *Curr. Biol.* **31**, 3004–3016 (2021).

11. Franklin-Tong, N. & Bosch, M. Plant biology: stigmatic ROS decide whether pollen is accepted or rejected. *Curr. Biol.* **31**, R904–R906 (2021).

12. Wang, L. et al. PCP-B class pollen coat proteins are key regulators of the hydration checkpoint in *Arabidopsis thaliana* pollen–stigma interactions. *New Phytol.* **213**, 764–777 (2017).

13. Doughty, J., Wong, H. Y. & Dickinson, H. G. Cysteine-rich pollen coat proteins (PCPs) and their interactions with stigmatic S (incompatibility) and S-related proteins in *Brassica*: putative roles in SI and pollination. *Ann. Bot.* **85**, 161–169 (2000).

14. Liu, C. et al. Pollen PCP-B peptides unlock a stigma peptide-receptor kinase gating mechanism for pollination. *Science* **372**, 171–175 (2021).

15. Murase, K. et al. A membrane-anchored protein kinase involved in *Brassica* self-incompatibility signaling. *Science* **303**, 1516–1519 (2004).

16. Gu, T., Mazzurco, M., Sulaman, W., Matias, D. D. & Goring, D. R. Binding of an arm repeat protein to the kinase domain of the *S*-locus receptor kinase. *Proc. Natl Acad. Sci. USA* **95**, 382–387 (1998).

17. Kitashiba, H., Liu, P., Nishio, T., Nasrallah, J. B. & Nasrallah, M. E. Functional test of *Brassica* self-incompatibility modifiers in *Arabidopsis thaliana*. *Proc. Natl Acad. Sci. USA* **108**, 18173–18178 (2011).

18. Stone, S. L., Anderson, E. M., Mullen, R. T. & Goring, D. R. ARC1 is an E3 ubiquitin ligase and promotes the ubiquitination of proteins during the rejection of self-incompatible *Brassica* pollen. *Plant Cell* **15**, 885–898 (2003).

19. Bailey, C. D. et al. Toward a global phylogeny of the Brassicaceae. *Mol. Biol. Evol.* **23**, 2142–2160 (2006).

20. Cai, X. et al. Impacts of allopolyploidization and structural variation on intraspecific diversification in *Brassica rapa*. *Genome Biol.* **22**, 166

(2021).

21. Nielsen, J. K., Nagao, T., Okabe, H. & Shinoda, T. Resistance in the plant, *Barbarea vulgaris*, and counter-adaptations in flea beetles mediated by saponins. *J. Chem. Ecol.* **36**, 277–285 (2010).

22. Badenes-Perez, F. R., Reichelt, M., Gershenzon, J. & Heckel, D. G. Using plant chemistry and insect preference to study the potential of Barbarea (Brassicaceae) as a dead-end trap crop for diamondback moth (Lepidoptera: Plutellidae). *Phytochemistry* **98**, 137–144 (2014).

23. Nasrallah, M. E., Liu, P. & Nasrallah, J. B. Generation of self-incompatible *Arabidopsis thaliana* by transfer of two *S* locus genes from *A. lyrata*. *Science* **297**, 247–249 (2002).

24. Luo, X. & Lehotay, D. C. Determination of hydroxyl radicals using salicylate as a trapping agent by gas chromatography–mass spectrometry. *Clin. Biochem.* **30**, 41–46 (1997).

25. Liszkay, A., van der Zalm, E. & Schopfer, P. Production of reactive oxygen intermediates (superoxide, H2O2, and hydroxyl radical) by maize roots and their role in wall loosening and elongation growth. *Plant Physiol.* **136**, 3114–3123 (2004).

26. Bechsgaard, J. S., Castric, V., Charlesworth, D., Vekemans, X. & Schierup, M. H. The transition to self-compatibility in *Arabidopsis thaliana* and evolution within S-haplotypes over 10 Myr. *Mol. Biol. Evol.* **23**, 1741–1750 (2006).

27. Tsuchimatsu, T. et al. Evolution of self-compatibility in *Arabidopsis* by a mutation in the male specificity gene. *Nature* **464**, 1342–1346 (2010).

28. Zhang, T. et al. Generation of transgenic self-incompatible *Arabidopsis thaliana* shows a genus-specific preference for self-incompatibility genes. *Plants (Basel)* **8**, 570 (2019).

29. Duan, Q., Kita, D., Li, C., Cheung, A. Y. & Wu, H. M. FERONIA receptor-like kinase regulates RHO GTPase signaling of root hair development. *Proc. Natl Acad. Sci. USA* **107**, 17821–17826 (2010).

30. Besson-Bard, A., Pugin, A. & Wendehenne, D. New insights into nitric oxide signaling in plants. *Annu. Rev. Plant Biol.* **59**, 21–39 (2008).

31. Domingos, P., Prado, A. M., Wong, A., Gehring, C. & Feijo, J. A. Nitric oxide: a multitasked signaling gas in plants. *Mol. Plant* **8**, 506–520 (2015).

32. Guo, F., Okamoto, M. & Crawford, N. M. Identification of a plant nitric oxide synthase gene involved in hormonal signaling. *Science* **302**, 100–103 (2003).

33. Moreau, M., Lee, G. I., Wang, Y., Crane, B. R. & Klessig, D. F. AtNOS/AtNOA1 is a functional *Arabidopsis thaliana* cGTPase and not a nitric-oxide synthase. *J. Biol. Chem.* **283**, 32957–32967 (2008).

34. Tewari, R. K., Prommer, J. & Watanabe, M. Endogenous nitric oxide generation in protoplast chloroplasts. *Plant Cell Rep.* **32**, 31–44 (2013).

35. Lee, U., Wie, C., Fernandez, B. O., Feelisch, M. & Vierling, E. Modulation of nitrosative stress by *S*-nitrosoglutathione reductase is critical for thermotolerance and plant growth in *Arabidopsis*. *Plant Cell* **20**, 786–802 (2008).

36. Yun, B. W. et al. *S*-nitrosylation of NADPH oxidase regulates cell death in plant immunity. *Nature* **13**, 264–268 (2011).

37. Hess, D. T. & Stamler, J. S. Regulation by *S*-nitrosylation of protein post-translational modification. *J. Biol. Chem.* **10**, 4411–4418 (2012).

38. Qu, Z. et al. Proteomic quantification and site-mapping of *S*-nitrosylated proteins using isobaric iodoTMT reagents. *J. Proteome Res.* **13**, 3200–3211 (2014).

39. Feng, J., Chen, L. & Zuo, J. Protein *S*-nitrosylation in plants: current progresses and challenges. *J. Integr. Plant Biol.* **61**, 1206–1223 (2019).

40. Zhan, N. et al. *S*-nitrosylation targets GSNO reductase for selective autophagy during hypoxia responses in plants. *Mol. Cell* **71**, 142–154 (2018).

41. Nishi, S., Toda, M. & Toyoda, T. Studies on the embryos culture in vegetable crops. III. On the conditions affecting to embryo culture of interspecific hybrids between cabbage and Chinese cabbage. *Bull. Hort. Res. Sta.* **9**, 75–100 (1970).

42. Rotman, N. et al. Female control of male gamete delivery during fertilization in *Arabidopsis thaliana*. *Curr. Biol.* **4**, 432–436 (2003).

43. Clough, S. J. & Bent, A. F. Floral dip: a simplified method for *Agrobacterium*-mediated transformation of *Arabidopsis thaliana*. *Plant J.* **16**, 735–743 (1998).

44. Huang, J. et al. Programmed cell death in stigmatic papilla cells is associated with senescence-induced self-incompatibility breakdown in Chinese cabbage and radish. *Front. Plant Sci.* **11**, 586901 (2020).

45. Liu, C. & Meinke, D. W. The titan mutants of *Arabidopsis* are disrupted in mitosis and cell cycle control during seed development. *Plant J.* **16**, 21–31 (1998).

46. Smyth, D. R., Bowman, J. L. & Meyerowitz, E. M. Early flower development in *Arabidopsis*. *Plant Cell* **2**, 755–767 (1990).

47. Jambunathan, N. Determination and detection of reactive oxygen species (ROS), lipid peroxidation, and electrolyte leakage in plants. *Methods Mol. Biol.* **639**, 292–298 (2010).

48. Li, C. et al. Glycosylphosphatidylinositol-anchored proteins as chaperones and co-receptors for FERONIA receptor kinase signaling in *Arabidopsis*. *eLife* **4**, e06587 (2015).

49. Chen, H. X. et al. BRAD V3.0: an upgraded Brassicaceae database. *Nucleic Acids Res.* **50**, 1432–1441 (2022).

50. Benson, D. A. et al. GenBank. *Nucleic Acids Res.* **41**, 36–42 (2013).

51. Howe, K. L. et al. Ensembl Genomes 2020-enabling non-vertebrate genomic research. *Nucleic Acids Res.* **48**, 689–695 (2020).

52. Goodstein, D. M. et al. Phytozome: a comparative platform for green plant genomics. *Nucleic Acids Res.* **40**, 1178–1186 (2012).

53. Kumar, S., Stecher, G., Li, M., Knyaz, C. & Tamura, K. MEGA X: molecular evolutionary genetics analysis across computing platforms. *Mol. Biol. Evol.* **35**, 1547–1549 (2018).

54. Madeira, F. et al. The EMBL-EBI search and sequence analysis tools APIs in 2019. *Nucleic Acids Res.* **47**, 636–641 (2019).

55. Robert, X. & Gouet, P. Deciphering key features in protein structures with the new ENDscript server. *Nucleic Acids Res.* **42**, W320–W324 (2014).

# Acknowledgements

We thank many people from Shandong Agricultural University for their help in all directions: Y. Hao, Z. Bao and X. Zhang for sharing of equipment, and Z. Ren and C. Zhou for manuscript discussion; and L. Guo from Peking University Institute of Advanced Agricultural Sciences for help in retrieving the genomic sequence of SRK from FPsc. This work was supported by grants from the National Natural Science Foundation of China (32170365 to Q.D.), Shandong Natural Science Foundation (ZR2021ZD07 and ZR2020KC017 to Q.D.), Shandong Yiyi Agricultural Science and Technology Co., Ltd (Q.D.), National Major Scientific Research Program of China (2013CB945100 to Xiansheng Zhang), US National Science Foundation (MCB-1715764 and IOS-2101467 to A.Y.C. and H.-M.W.), and UMass NIFA/USDA (MAS00525 to A.Y.C.).

# Author information

Author notes

1. These authors contributed equally: Jiabao Huang, Lin Yang

## Authors and Affiliations

1. State Key Laboratory of Crop Biology, Shandong Agricultural University, Tai’an, China

Jiabao Huang, Lin Yang, Liu Yang, Xiaoyu Wu, Xiaoshuang Cui, Lili Zhang, Jiyun Hui, Yumei Zhao, Hongmin Yang, Shangjia Liu, Quanling Xu, Maoxuan Pang, Xinping Guo, Yunyun Cao, Yu Chen, Xinru Ren, Jinzhi Lv, Jianqiang Yu, Junyi Ding, Gang Xu, Nian Wang, Xiansheng Zhang & Qiaohong Duan

2. College of Horticulture Science and Engineering, Shandong Agricultural University, Tai’an, China

Jiabao Huang, Lin Yang, Liu Yang, Xiaoyu Wu, Xiaoshuang Cui, Lili Zhang, Jiyun Hui, Yumei Zhao, Hongmin Yang, Shangjia Liu, Quanling Xu, Maoxuan Pang, Xinping Guo, Yunyun Cao, Yu Chen, Xinru Ren, Jinzhi Lv, Jianqiang Yu & Qiaohong Duan

3. Institute of Horticulture, Henan Academy of Agricultural Sciences, Zhengzhou, China

Xiaochun Wei, Yuxiang Yuan & Xiaowei Zhang

4. Computer Network Information Centre, Chinese Academy of Sciences, Beijing, China

Qinghui Lin

5. National Key Laboratory of Crop Genetic Improvement, Huazhong Agricultural University, Wuhan, China

Chaozhi Ma, Cheng Dai & Pengwei Wang

6. Shandong Yiyi Agricultural Science and Technology Co., Ltd, Tai’an, China

Yongchao Wang

7. College of Horticulture, Qingdao Agricultural University, Qingdao, China

Fei Cheng

8. Trait Discovery, Corteva Agriscience, Johnston, IA, USA

Weiqing Zeng

9. School of Plant Sciences, University of Arizona, Tucson, AZ, USA

Ravishankar Palanivelu

10. Department of Biochemistry and Molecular Biology, Molecular Cell Biology and Plant Biology Programs, University of Massachusetts, Amherst, MA, USA

Hen-Ming Wu & Alice Y. Cheung

## Contributions

Q.D. conceptualized the study, designed the research plan and the experiments, and interpretated the results, with contributions from J. Huang, Lin Yang, A.Y.C., H.-M.W. and Xiansheng Zhang. Q.D. and A.Y.C. led the writing process with contribution from J.H., L.Y., Xiansheng Zhang, H.-M.W., R.P. and W.Z. in discussion and manuscript revision. J. Huang and Lin Yang performed major experiments and data analysis, with help from L.Z., Y.Z., Liu Yang, X.W., J. Hui, X.C., H.Y., S.L., Q.X., M.P., Y. Cao, Y. Chen, J.L. and J.Y. L.Z. performed stigma feeding experiments, with help from S.L., J.Y. and M.P. Y.Z. performed vector construction work, with help from Y. Cao, Y. Chen, X.R. and J.L. J. Hui performed the pollen hydration assay, with help from Q.X. X.W., Y.Y. and Xiaowei Zhang. generated Chinese cabbage germplasm resources and performed *S*-haplotype-related UI experiments. X.W. performed bioinformatic analysis, with help from J.D., N.W. and Q.L. C.M., C.D. and P.W. performed SI *A. thaliana*-related experiments. X.C. and H.Y. performed in planta breakdown of SI and UI, with help from F.C. and Y.W. G.X. participated in biochemical experiments and data analysis, with help from Liu Yang X.G. drew the working model. All authors participated in data collection, presentation and finalizing the manuscript.

### Corresponding authors

Correspondence to Alice Y. Cheung or Qiaohong Duan.

## Ethics declarations

### Competing interests

The authors declare no competing interests.

## Peer review

### Peer review information

*Nature* thanks Marcus Samuel and the other, anonymous, reviewer(s) for their contribution to the peer review of this work.

## Additional information

**Publisher's note** Springer Nature remains neutral with regard to jurisdictional claims in published maps and institutional affiliations.

## Extended data figures and tables

### Extended Data Fig. 1 ROS underlies the rejection of interspecific pollen during UI.

**a**, The developmentally regulated SI and the progressive increase in the amount of SRK from bud stage to maturity. **b**, The number of intra– and various interspecific pollen tubes in mature or bud-stage *B. rapa* stigmas. Mature *B. rapa* stigmas rejected SI and all the interspecific pollen examined, but bud-stage *B. rapa* stigmas allowed the growth of SI pollen and interspecific *B. oleracea* pollen, and still rejected intergeneric *B. vulgaris* and *A. thaliana* pollen. See Fig. 1b. **c**, Imaging of $H_2$DCFDA-stained ROS under confocal microscope and under wide-field fluorescence microscope

showed comparable changes of ROS in *B. rapa* stigmas Dotted line outlined the area for ROS quantification. Wide-field observation, with its considerably high expedition to sample entire stigma specimens, was used for the massive amount of data gathering required for this study. **d**, ROS intensity in unpollinated (UP) or pollinated *B. rapa* stigma. See Fig. 1c. **e**–**g**, Scavenging ROS by Na-SA suppressed stigmatic ROS induction, and promoted the growth of SI pollen and *B. oleracea* pollen in mature and *B. vulgaris* pollen in bud-stage *B. rapa* stigmas. Scale bars, 500 μm. Data bar (**a**): average ± SD. Average relative expression levels from three biological replicates of stigmas (two tailed *t*-test, n = 3). Box plots (**b**–**g**): centre line, median; box limits, lower and upper quartiles; dots, individual data points; whiskers, highest and lowest data points. n (in blue), number of stigmas. *P* values, two-tailed *t*-tests. Each experiment was repeated at least thrice with consistent results.

Source data

## Extended Data Fig. 2 SRK underlies the rejection of interspecific pollen during UI.

**a**, Quantitative RT-PCR showing AS-BrSRK46 treatment reduced *BrSRK46* expression in mature *B. rapa* stigmas ($S_{46}$) and further reduced its already low level in bud-stage stigmas ($S_{46}$). **b**, AS-BrSRK46 treatment of mature *B. rapa* stigmas ($S_{46}$) broke the inhibition to *B. oleracea* pollen not *B. vulgaris* pollen. AS-BrSRK46 treatment of bud-stage stigmas ($S_{46}$) broke inhibition to *B. vulgaris* pollen. See Fig. 1d. **c**, **d**, AS-BrSRK46 treatment reduced ROS in mature *B. rapa* stigmas ($S_{46}$) and further reduced its already low ROS in bud-stage stigmas ($S_{46}$). **e**–**g**, Sequence alignment (**e**), phylogenetic analysis (**f**) and expression of SRK in FPsc (Brara.G02663) (**g**). SRK from FPsc lacks the coding sequence for the transmembrane domain and we name it $BrSRK^{\Delta TM}$ hereafter. **h**–**j**, Mature and bud-stage stigmas of FPsc were defective in SI and UI pollen-triggered ROS increase **(h**, **i**) and the rejection of SI and UI pollen (**j**). See Fig. 1e. **k**, *SRK13* expression from SI *A. thaliana* stigmas transformed with *Arabidopsis halleri* AhSP11/SCR13-AhSRK13-AhARC1. These three transgenes were in a single construct. **l**, **m**, The number of intra– or interspecific pollen tubes (**l**) and ROS changes (**m**) in

SC *A. thaliana* stigmas and in SI *A. thaliana* stigmas. See Fig. 1f, g. **n**, *B. oleracea* pollen of $S_{36}$-haplotype was rejected in *B. rapa* stigmas of $S_{46}$, $S_{12}$, $S_{9}$, $S_{40}$, or $S_{38}$, showing the dependence on *S*RK but the independence of SCR-SRK interaction in the rejection of interspecific pollen. Scale bars, 500 µm (**c**, **d**, **h**, **i**, **n**). Data bars (**a**, **g**, **k**): average ± SD. Average relative expression levels from three biological replicates of stigmas (two tailed *t*-test, n = 3). Box plots (**b**–**d**, **h**–**j**, **l**–**n**): centre line, median; box limits, lower and upper quartiles; dots, individual data points; whiskers, highest and lowest data points. n (in blue), number of stigmas. *P* values, two-tailed *t*-tests. Each experiment was repeated at least thrice with consistent results.

Source data

## Extended Data Fig. 3 FER/ANJ signalling regulates stigmatic ROS during UI.

**a**, **b**, Quantitative RT-PCR showing AS-BrFER1 treatment suppressed the expression of *BrFER1*(**a**) and promoted the growth of SI pollen and *B. oleracea* pollen in mature *B. rapa* stigmas and *B. vulgaris* pollen in bud stage (**b**) *B. rapa* stigmas. See Fig. 2a. **c**, **d**, AS-BrFER1 treatment suppressed SI and UI-induced ROS increase in mature and bud stage *B. rapa* stigmas at 10 MAP. **e**, **f**, The expression of *FER* and *SRK* in stigmas of *A. tha* (SI)*/fer-4* (**e**) and loss of FER in SI *A. thaliana* promoted the growth of SI pollen, *B. oleracea* pollen and *B. vulgaris* pollen in SI *A. thaliana* stigmas (**f**). See Fig. 2b. **g**, Loss of FER in SI *A. thaliana* suppressed SI and UI-induced ROS increase in *A. tha* (SI)*/fer-4* stigmas at 10 MAP. **h**, Domain structures of BrANJs proteins showing only BrANJ1 have intact extracellular and intracellular domain. **i**, **j**, AS-BrANJ1 treatment suppressed the expression of *BrANJ1*(**i**) and promoted the growth of SI pollen and *B. oleracea* pollen in mature *B. rapa* stigmas and *B. vulgaris* pollen in bud stage *B. rapa* stigmas (**j**). **k**, **l**, AS-BrANJ1 treatment suppressed SI and UI-induced ROS increase in mature (**k**) and bud stage (**l**) *B. rapa* stigmas at 10 MAP. Scale bars, Scale bars, 500 µm (**c**, **d**, **j**, **k**, **l**), 200 µm (**g**). Data bars (**a**, **e**, **i**): average ± SD. Average relative expression levels from three biological replicates of stigmas (two tailed *t*-test, n = 3). Box plots (**b**–**d**, **f**, **g**, **j**–**l**): centre line, median; box limits, lower and upper quartiles; dots, individual data points; whiskers, highest and lowest data points. n (in blue), number of

stigmas. *P* values, two-tailed *t*-tests. Each experiment was repeated at least thrice with consistent results.

Source data

## Extended Data Fig. 4 ROS are produced by RBOHs during UI.

**a**, Quantitative RT-PCR showing AS-BrRBOHF treatment suppressed the expression of *BrRBOHF*. **b**, **c**, AS-BrRBOHF treatment suppressed SI and UI-induced ROS increase in mature (**b**) and bud-stage (**c**) *B. rapa* stigmas at 10 MAP. **d**, The RBOH enzymatic activity in mature *B. rapa* stigmas were increased after pollination with SI and UI pollen but decreased after pollination with CP pollen. **e**, AS-BrRBOHF treatment promoted the growth of SI pollen and *B. oleracea* pollen in mature and *B. vulgaris* pollen in bud-stage *B. rapa* stigmas. Scale bars, 500 μm. Data bar (**a**): average ± SD. Average relative expression levels from three biological replicates of stigmas (two tailed *t*-test, n = 3). Data bars (**d**): Average activity of ROS producing enzymes from three technical replicates of one stigma sample containing 100 stigmas (two tailed *t*-test, n = 3). Box plots (**b**, **c**, **e**): centre line, median; box limits, lower and upper quartiles; dots, individual data points; whiskers, highest and lowest data points. n (in blue), number of stigmas. *P* values, two-tailed *t*-tests. Each experiment was repeated at least thrice with consistent results unless otherwise specified.

Source data

## Extended Data Fig. 5 SRK is correlated with stigmatic ROS during UI.

**a**, **b**, BrSRK46 kinase domain (KD) interacts with BrFER1 (KD) in yeast two-hybrid assay (**a**) and BiFC (**b**). **c**, **d**, Protein extract from SI pollen and *B. oleracea* pollen ($S_{36}$), but not that from CP pollen ($S_{12}$), increased ROS in *B. rapa* stigmas ($S_{46}$) (**c**), and enhanced interaction between BrSRK46 and BrFER1 (**d**) in the pull-down assay. See Fig. 2c. **e**–**g**. ROS in *B. rapa* stigmas ($S_{46}$) were increased (**e**), and the BrSRK46-BrFER1 interaction enhanced in the pull-down (**f**) and Co-IP assays (**g**), by GST-BrSCR46, not GST-BrSCR12, which is active for $S_{12}$ stigma. The protein samples were

derived from the same experiment and the blots were processed in parallel (**d**, **f**, **g**). For gel source data, see Supplementary Fig. 1. See Fig. 2d, e. **h**, **i**, Nitro blue tetrazolium staining or tobacco leaves and $H_2$DCFDA staining of protoplasts from tobacco leaves co-expressing BrFER1, BrRBOHD2, and BrSRK46 showing the enhancement of ROS by BrSCR46, not by BrSCR12. Scale bars, 500 µm (**c**, **e**); 50 µm (**i**). Data bars (**d**, **f**, **g**): average ± SD. Average relative intensities from three biological replicates of the blots shown in Fig. 2c–e (two tailed *t*-test, n = 3). Box plots (**c**, **e**, **h**, **i**): centre line, median; box limits, lower and upper quartiles; dots, individual data points; whiskers, highest and lowest data points. n (in blue), number of stigmas, tobacco leaves, protoplast samples. *P* values, two-tailed *t*-tests. Each experiment was repeated at least thrice with consistent results.

Source data

## Extended Data Fig. 6 The relationship of FER-ROS signaling with MLPK and ARC1 during SI and UI.

**a**, **b**, Quantitative RT-PCR showing AS-BrMLPK and AS-BrARC1 treatment suppressed the expression of *BrMLPK* and *BrARC1*, respectively, in mature *B. rapa* stigmas. **c**, **d**, AS-BrMLPK (**c**) and AS-BrARC1 (**d**) treatment promoted the growth of SI and UI pollen tubes in mature *B. rapa* stigmas ($S_{46}$). **e**, AS-BrMLPK treatment of mature *B. rapa* stigmas ($S_{46}$) inhibited SI and UI pollen-induced ROS increase. **f**, AS-BrARC1 treatment of mature *B. rapa* stigmas ($S_{46}$) did not affect SI and UI pollen-induced ROS increase. Scale bars, 500 µm. Data bars (**a**, **b**): average ± SD. Average relative expression levels from three biological replicates of stigmas (two tailed *t*-test, n = 3). Data bar: average ± s.d. Box plots (**c**–**f**): centre line, median; box limits, lower and upper quartiles; dots, individual data points; whiskers, highest and lowest data points. n (in blue), number of stigmas. *P* values, two-tailed *t*-tests. Each experiment was repeated at least thrice with consistent results.

Source data

## Extended Data Fig. 7 Species-specific match of PCP-Bs and FER.

**a**–**c**, When observed at 1.5 HAP, the reduced reproductive barrier to *B. rapa* and *B. oleracea* pollen in *A. thaliana fer* mutant (**a**, *srn*) and *rbohd* mutant (**b**, **c**) stigmas was obvious. See also Fig. 3c. **d**, Phylogenetic analysis of PCP-B genes from *A. thaliana*, *B. oleracea*, and *B. rapa*. We name BrapaB3[12], an ortholog of AtPCP-Bγ, BrPCP-B3 hereafter. **e**, Amino acid sequence alignment of PCP-Bs from *A. thaliana*, *B. oleracea*, and *B. rapa* shows the comparison of PCP-B sequences. They all shared a common pattern of seven or eight cysteines in the mature polypeptide. Red rectangle shows the conserved cysteines (C30, C32, C33 of AtPCP-B), mutation of which render a loss in the ability for stigmatic ROS reduction and pollen hydration[14]. **f**, Synthetic AtPCP-Bγ and recombinant MBP-AtPCP-Bγ show similar function in reducing ROS of UP *A. thaliana* stigmas, but GST-BrPCP-B3 shows no effect in reducing ROS at 5 or 10 MAT. **g**, *B. rapa* stigmas and *A. thaliana* stigmas, which express divergent FER, responded species-preferentially to BrPCP-B3 in reducing ROS. **h**, AtPCP-Bγ was much faster than GST-BrPCP-B3 in reducing ROS of *A. thaliana* roots, which also express FER[28]. **i**, GST-BrPCP-B3 was more effective in reducing ROS of *B. rapa* roots than that of *A. thaliana* roots. **j**, Quantified data of pull-down assay showing the inefficiency of GST-BrPCP-B3 to compete with AtPCP-Bγ in interaction with AtFER (ED)-FLAG. The protein samples were derived from the same experiment and the blots were processed in parallel. For gel source data, see Supplementary Fig.1. See also Fig. 3f. Scale bars, 200 μm (**a**–**c**, **f**, **g**) and roots (**h**, **i**). Data bar (**j**): average ± SD. Average relative intensities from three biological replicates of the blot represented on the left (two tailed *t*-test, n = 3). Box plots (**a**–**c**, **f**, **g**–**i**): centre line, median; box limits, lower and upper quartiles; dots, individual data points; whiskers, highest and lowest data points. n (in blue), number of stigmas or roots. *P* values, two-tailed *t*-tests. Each experiment was repeated at least thrice with consistent results.

Source data

## Extended Data Fig. 8 Stigmatic NO is required for ROS reduction in *A. thaliana* stigmas during SC and UC.

**a**, **b**, Confocal and wide-field imaging showing the increase of stigmatic NO at 5 MAP with SC pollen (**a**) and quantified data of SC-induced NO and

pollen hydration in *A. thaliana* stigmas, both showed NO peaking at ~5 MAP (**b**). See Fig. 4a. **c**, **d**, FER-dependent elevation of NO in *A. thaliana* stigmas induced by pollen and At-PCP-Bγ .See Fig. 4d, e. **e**, AtPCP-Bγ was much faster than GST-BrPCP-B3 in increasing NO of *A. thaliana* roots. **f**, GST-BrPCP-B3 was more effective in increasing NO of *B. rapa* roots than that of *A. thaliana* roots. **g**, Roots of *fer-4* was not responsive to AtPCP-Bγ in inducing NO. **h**, **i**, (Left to right) cPTIO scavenged SC-induced NO, suppressed SC-induced ROS reduction, and inhibited SC pollen hydration and tube growth in *A. thaliana* stigmas. **j**–**n**, Relative to WT, *noa1* stigmas showed lower NO and higher ROS levels, and slower hydration of SC (WT *A. thaliana*) pollen and pollen tube growth (**j**, **k**, **l**). Relative to WT, *hot5-4* stigmas showed faster NO and lower ROS levels, and faster hydration of SC (WT *A. thaliana*) pollen and pollen tube growth (**j**, **m**, **n**). **o**, **p**, Mutations in NOA1, *noa1* (**o**) and GSNOR, *hot5-4* (**p**), enhanced and reduced, respectively, the reproductive barrier to *B. rapa* or *B. oleracea* pollen in *A. thaliana* stigmas at 1.5 HAP. Scale bars, 200 µm (**a**, **h**, **j**, **o**, **p**) and roots (**e**–**g**); 50 µm for pollen (**h**, **j**). Box plots (**a**–**p**): centre line, median; box limits, lower and upper quartiles; dots, individual data points; whiskers, highest and lowest data points. n (in blue), number of stigmas, pollen grains or roots. *P* values, two-tailed *t*-tests. Each experiment was repeated at least thrice with consistent results.

Source data

## Extended Data Fig. 9 The inverse relationship of NO and ROS and nitrosation of BrFER1 and RBOHs in *B. rapa* stigmas.

**a**, **b**, Intraspecific CP pollen (2$^{nd}$ row), but not SI and *B. oleracea* (UI) pollen, induced NO in *B. rapa* stigmas. **c**–**e**, Scavenging NO increased ROS (**c**) and RBOH enzymatic activity of UP *B.rapa* stigmas (**d**), and inhibited the growth of CP pollen tubes in *B. rapa* stigmas (**e**). **f**–**h**, GSNO treatment increased NO (**f**), reduced ROS (**f**) and RBOH enzymatic activity of UP *B. rapa* stigmas (**g**), and promoted the growth of SI or *B. oleracea* pollen in mature or *B. vulgaris* polen in bud-stage *B. rapa* stigmas (**h**). **i**, BrFER1(KD), not BrFER1 (ED), was nitrosated by GSNO. See also Fig. 4f. **j**, **k**, LC-MS spectrum showing the nitrosated cysteine residues in BrFER1 protein. **l**, FER amino acid sequence alignment showing the nitrosated

cysteines, Cys730 and Cys752 (*) are evolutionarily conserved. **m**, Pull-down assay shows GSNO treatment induced quantitative inhibition of MBP-BrFER1(KD) with GST-BrROP2 complex. See also Fig. 4h. **n**, The nitrosomimetic mutation, Cys730W, reduced the amount of BrFER1 that was pulled down by GFP-BrROP2. **o**, Phylogenetic analysis of BrRBOHs and AtRBOHD. BrRBOHD1 and BrRBOHD2 are closer to AtRBOHD than other BrRBOHs. **p**–**r**, RBOHD was nitrosated by NO. *In vitro* nitrosation of BrRBOHD1 by GSNO (**p**); CP-induced nitrosation of GFP-AtRBOHD protein from *A. thaliana* stigmas (**q**), and LC–MS spectra showing nitrosation of Cys891 of GST-BrRBOHD1 (CT, C-terminal) (**r**). Nitrosated amino acid residues were labelled with TMT. Proteins were representative of more than three independent preparations. **s**, **t**, GST-BrRBOHD2 (CT) (**s**) and GST-BrRBOHF (CT) (**t**) proteins were nitrosated *in vitro*. The protein samples were derived from the same experiment and the blots were processed in parallel (**i**, **m**, **n**, **p**, **q**, **s**, **t**). For gel source data, see Supplementary Fig. 1. Scale bars, 500 µm. Line chart (**b**): average ± SD. Average relative NO intensities from three biological replicates of stigmas shown in a (two tailed *t*-test, n = 3). Data bars (**d**, **g**): Average activity of ROS producing enzymes from three technical replicates of one stigma sample containing 100 stigmas (two tailed *t*-test, n = 3). Data bar (**m**, **n**): average ± SD. Average relative intensities from three biological replicates of stigmas in (**a**) and blots in Fig 4h and in (**n**) (two tailed *t*-test, n = 3). Box plots (**c**, **e**, **f**, **h**): centre line, median; box limits, lower and upper quartiles; dots, individual data points; whiskers, highest and lowest data points. n (in blue), number of stigmas. *P* values, two-tailed *t*-tests. Each experiment was repeated at least thrice with consistent results unless otherwise specified.

Source data

## Extended Data Fig. 10 Breaking interspecific barriers in *Brassica* crops.

**a**, **b**, Reducing ROS by Na-SA or increasing NO by GSNO increased the number of enlarged ovules in the pod of ♀*B. rapa* × ♂*B. oleracea* or ♀*B. rapa* × ♂*B. vulgaris*. See Fig. 5a. **c**, Suppressing the expression of *BrSRK46*, *BrBrFER1*, or *BrRBOHF* by AS-ODNs increased the number of enlarged ovules in the pod of ♀*B. rapa* × ♂*B. oleracea* or ♀*B. rapa* × ♂*B. vulgaris*.

See also Fig. 5b. **d**, *B. oleracea* pollen tubes or *B. vulgaris* pollen tubes in *B. rapa* pistils. The reduced number of enlarged ♀*B. rapa* × ♂*B. vulgaris* ovules is possibly due to fewer *B. vulgaris* pollen tubes had exited the transmitting tissue and targeted the *B. rapa* ovules due to additional barriers based on their evolutionary distance (Fig. 1a). Arrowheads point to bundles of pollen tubes in the transmitting tissue, stars point to ovules penetrated by a pollen tube. Scale bars, 100 µm (**d**). Box plots (**a**–**c**): centre line, median; box limits, lower and upper quartiles; dots, individual data points; whiskers, highest and lowest data points. n (in blue), number of pistils. *P* values, two-tailed *t*-tests. Each experiment was repeated at least thrice with consistent results.

Source data

# Supplementary information

## **Supplementary Information**

This file contains Supplementary Fig. 1 and Supplementary Tables 1–4.

## **Reporting Summary**

# Source data

## **Source Data Fig. 3**

## **Source Data Fig. 4**

## **Source Data Extended Data Fig. 1**

## **Source Data Extended Data Fig. 2**

## **Source Data Extended Data Fig. 3**

## **Source Data Extended Data Fig. 4**

**Source Data Extended Data Fig. 5**

**Source Data Extended Data Fig. 6**

**Source Data Extended Data Fig. 7**

**Source Data Extended Data Fig. 8**

**Source Data Extended Data Fig. 9**

**Source Data Extended Data Fig. 10**

## Rights and permissions

**Open Access** This article is licensed under a Creative Commons Attribution 4.0 International License, which permits use, sharing, adaptation, distribution and reproduction in any medium or format, as long as you give appropriate credit to the original author(s) and the source, provide a link to the Creative Commons licence, and indicate if changes were made. The images or other third party material in this article are included in the article's Creative Commons licence, unless indicated otherwise in a credit line to the material. If material is not included in the article's Creative Commons licence and your intended use is not permitted by statutory regulation or exceeds the permitted use, you will need to obtain permission directly from the copyright holder. To view a copy of this licence, visit http://creativecommons.org/licenses/by/4.0/.

Reprints and Permissions

## About this article

### Cite this article

Huang, J., Yang, L., Yang, L. *et al.* Stigma receptors control intraspecies and interspecies barriers in Brassicaceae. *Nature* **614**, 303–308 (2023). https://doi.org/10.1038/s41586-022-05640-x

- Received: 28 April 2022
- Accepted: 09 December 2022
- Published: 25 January 2023
- Issue Date: 09 February 2023
- DOI: https://doi.org/10.1038/s41586-022-05640-x

## Share this article

Anyone you share the following link with will be able to read this content:

Get shareable link

Sorry, a shareable link is not currently available for this article.

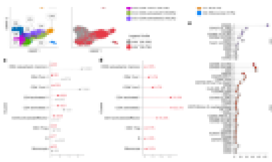
Copy to clipboard

Provided by the Springer Nature SharedIt content-sharing initiative

---

This article was downloaded by **calibre** from https://www.nature.com/articles/s41586-022-05640-x

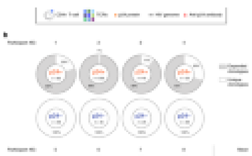
---



## Profound phenotypic and epigenetic heterogeneity of the HIV-1-infected CD4+ T cell reservoir

19 December 2022

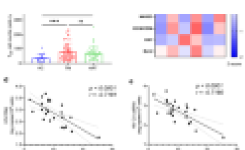
Vincent H. Wu, Jayme M. L. Nordin, … Michael R. Betts



## Single-cell TCR sequencing reveals phenotypically diverse clonally expanded cells harboring inducible HIV proviruses during ART

14 August 2020

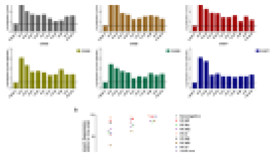
Pierre Gantner, Amélie Pagliuzza, … Nicolas Chomont



## Virtual memory CD8+ T cells restrain the viral reservoir in HIV-1-infected patients with antiretroviral therapy through derepressing KIR-mediated inhibition

24 March 2020

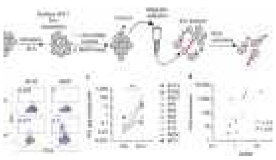
Jie-Hua Jin, Hui-Huang Huang, … Fu-Sheng Wang



## [HLA class II-Restricted CD8+ T cells in HIV-1 Virus Controllers]

15 July 2019

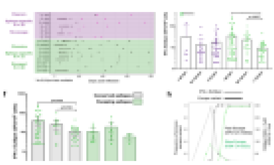
Tinashe E. Nyanhete, Alyse L. Frisbee, … Georgia D. Tomaras



## [Clonal CD4+ T cells in the HIV-1 latent reservoir display a distinct gene profile upon reactivation]

23 April 2018

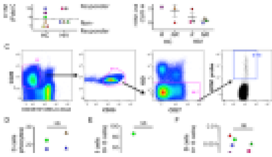
Lillian B. Cohn, Israel T. da Silva, … Michel C. Nussenzweig



## [Identification of human progenitors of exhausted CD8+ T cells associated with elevated IFN-γ response in early phase of viral infection]

07 December 2022

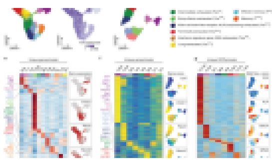
Curtis Cai, Jerome Samir, … Fabio Luciani



[Single Cell Profiling Reveals PTEN Overexpression in Influenza-Specific B cells in Aging HIV-infected individuals on Anti-retroviral Therapy]

21 February 2019

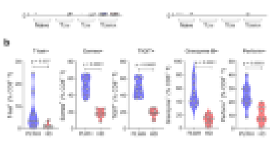
Lesley R. de Armas, Suresh Pallikkuth, … Savita Pahwa



[Divergent clonal differentiation trajectories of T cell exhaustion]

26 October 2022

Bence Daniel, Kathryn E. Yost, … Ansuman T. Satpathy



[Immune mobilising T cell receptors redirect polyclonal CD8+ T cells in chronic HIV infection to form immunological synapses]

01 November 2022

Zoë Wallace, Jakub Kopycinski, … Lucy Dorrell

- Article
- Open Access
- Published: 04 January 2023

# Phenotypic signatures of immune selection in HIV-1 reservoir cells


- Weiwei Sun,
- Ce Gao,
- Ciputra Adijaya Hartana,
- Matthew R. Osborn,
- Kevin B. Einkauf,
- Xiaodong Lian,
- Benjamin Bone,
- Nathalie Bonheur,
- Tae-Wook Chun,
- Eric S. Rosenberg,
- Bruce D. Walker,
- Xu G. Yu &
- …
- Mathias Lichterfeld

Show authors



*Nature* **volume 614**, pages 309–317 (2023)



- 8569 Accesses
- 2 Citations
- 455 Altmetric
- Metrics details


## Abstract


Human immunodeficiency virus 1 (HIV-1) reservoir cells persist lifelong despite antiretroviral treatment[1,2] but may be vulnerable to host immune responses that could be exploited in strategies to cure HIV-1. Here we used a

single-cell, next-generation sequencing approach for the direct ex vivo phenotypic profiling of individual HIV-1-infected memory $CD4^+$ T cells from peripheral blood and lymph nodes of people living with HIV-1 and receiving antiretroviral treatment for approximately 10 years. We demonstrate that in peripheral blood, cells harbouring genome-intact proviruses and large clones of virally infected cells frequently express ensemble signatures of surface markers conferring increased resistance to immune-mediated killing by cytotoxic T and natural killer cells, paired with elevated levels of expression of immune checkpoint markers likely to limit proviral gene transcription; this phenotypic profile might reduce HIV-1 reservoir cell exposure to and killing by cellular host immune responses. Viral reservoir cells harbouring intact HIV-1 from lymph nodes exhibited a phenotypic signature primarily characterized by upregulation of surface markers promoting cell survival, including CD44, CD28, CD127 and the IL-21 receptor. Together, these results suggest compartmentalized phenotypic signatures of immune selection in HIV-1 reservoir cells, implying that only small subsets of infected cells with optimal adaptation to their anatomical immune microenvironment are able to survive during long-term antiretroviral treatment. The identification of phenotypic markers distinguishing viral reservoir cells may inform future approaches for strategies to cure and eradicate HIV-1.

# Main

At present, a cure for HIV-1 infection is considered elusive owing to infected cells that harbour genome-intact, chromosomally integrated viral DNA and persist long-term despite suppressive antiretroviral treatment (ART)[1,2]. After initiation of ART, the frequency of these cells, here termed HIV-1 reservoir cells, declines over time[3]; however, this process is slow, and the mechanisms underlying this decline are not well understood. ART itself is unlikely to directly contribute to the longitudinal decrease of viral reservoir cells because antiviral drugs have no cytotoxic activity against virally infected cells; they merely protect HIV-uninfected cells against viral infection and prevent the seeding of new viral reservoir cells. Instead, it is likely that immune mechanisms have an important role in the longitudinal reduction of HIV-1 reservoir cells during ART, specifically for the decline of the small subset of cells encoding for functional, genome-intact proviral sequences,

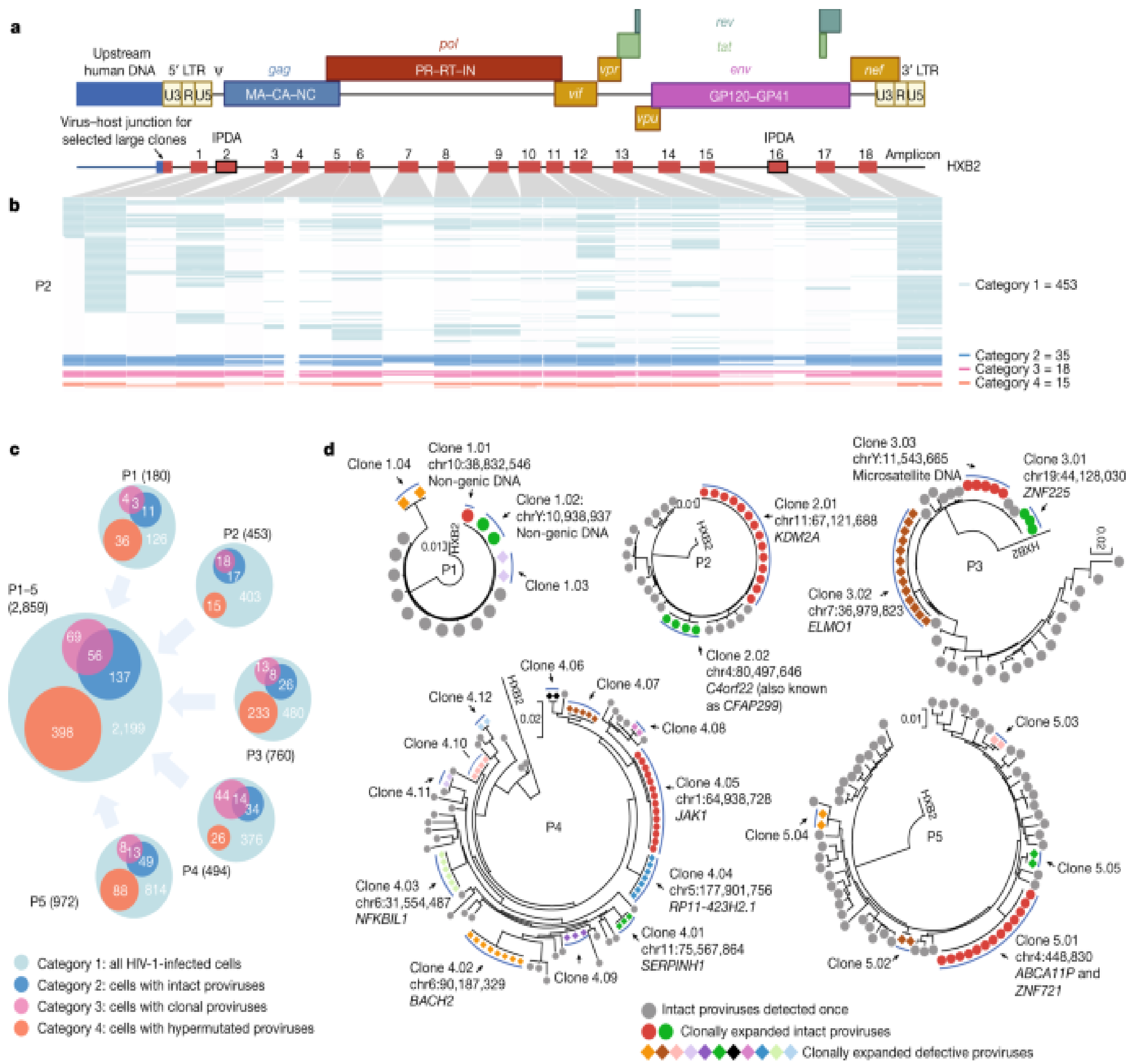
which seem to decrease faster compared to defective proviruses[4,5,6,7]. Footprints of antiviral immune effects against the HIV-1 reservoir cells may be more visible when qualitative features of HIV-1-infected cells, including proviral chromosomal integration sites and transcriptional activities, are analysed[8,9,10,11,12], and when viral reservoir profiles are evaluated over extended periods of suppressive ART. However, previous studies suggest that viral reservoir cells can frequently resist host selection forces, and long-term persistence of highly transcriptionally active proviruses that seem to effectively avoid host immune activity has been reported in multiple studies[10,13,14]. Mechanisms that allow HIV-1-infected cells to withstand host immune effects and to survive lifelong are not well defined at present.

# Single-cell proteogenomic profiling

Interrogation of the surface phenotype of HIV-1 reservoir cells may be highly informative for understanding the susceptibility or resistance of HIV-1 reservoir cells to host immune responses; however, such investigations have been precluded in the past by technical limitations that did not allow profiling the surface phenotype of these cells directly ex vivo, and instead relied on a phenotypic analysis of a small subset of reservoir cells that produce viral antigen in response to in vitro stimulation[15,16] or on a biocomputational inference of the reservoir cell profile[17]. As an alternative approach, we developed an experimental strategy, here termed ‘phenotypic and proviral sequencing’ (PheP-seq), which was designed to evaluate the phenotype of patient-derived HIV-1-infected cells, using a single-cell next-generation sequencing assay[18] (Extended Data Fig. 1a) that permits one to jointly profile phenotypic markers and selected parts of chromosomal DNA from single cells[19]. This approach complements recent studies using cellular indexing of transcriptomes and epitopes by sequencing (CITE-seq) that focus on a combined analysis of phenotypic markers and the cellular transcriptome in HIV-1 reservoir cells[20,21]. For our experiments, memory $CD4^+$ ($mCD4^+$) T cells isolated from the peripheral blood (PB) of study participants infected with HIV-1 ($n = 5$) were labelled with a cocktail of oligonucleotide-tagged antibodies directed to T cell surface markers ($n = 53$), without any type of prior in vitro activation or manipulation. Afterwards, cells were subjected to a single-cell analytic platform technique designed to

conduct a multiplex polymerase chain reaction (PCR) for amplifying small fragments of genomic HIV-1 DNA, coupled with amplification of corresponding antibody-bound oligonucleotide tags. Amplification products were then pooled, sequenced and biocomputationally deconvoluted to isolate sequencing reads originating from individual cells. For a deep interrogation of the proviral sequence in each infected cell, a total of 18 non-overlapping custom-designed primer pairs were synthesized that spanned strategically important and phylogenetically conserved regions in the HIV-1 proviral genome and allowed for simultaneous amplifications of small HIV-1 DNA fragments approximately 200–300 base pairs (bp) in length from single virally infected cells (Fig. 1a,b, Extended Data Fig. 1b and Supplementary Table 1); specifically, we included primers from the intact proviral DNA assay (IPDA)[22] that permit identifying proviruses with high probability to be genome-intact. For enhanced analytic depth, we also included primers spanning the virus–host chromosomal integration site junctions of large, sequence-identical proviral clones previously characterized in our study participants; amplification of such previously defined chromosomal regions allows one to unequivocally identify clonal HIV-1-infected cells with known proviral sequences and to relate phenotypic information of infected cells to proviral chromosomal locations.

**Fig. 1: Combined assessment of cellular phenotype and proviral sequence in HIV-1-infected cells (PheP-seq) from PB.**




**a**, The genomic location of 18 different HIV-1 amplification products incorporated in the PheP-seq assay; these 18 amplicons cover approximately 4,000 bp of the HIV-1 genome; gaps between amplification products are indicated. Note that additional amplicons corresponding to predefined virus–host junctions of large proviral clones were also included. Amplicons 2 and 16 were previously described for the IPDA assay. LTR, long terminal repeat. Ψ, retroviral psi packaging element. **b**, A virogram summarizing individual HIV-1 DNA amplification products in single HIV-1-infected cells from study participant 2 (P2). Each row represents data from one infected cell; the numbers of sequences meeting criteria for categories 1, 2, 3 and 4 are shown. For longer amplification products (amplicons 5, 10 and 12), centrally located

nucleotides could not be efficiently amplified using the Illumina NextSeq 2 × 150-bp sequencing read length used in this study. **c**, Venn diagrams summarizing the numbers of category 1–4 HIV-1-infected cells, shown separately for each study participant (P1–P5) and for all study participants combined. The numbers of sequences meeting criteria for different proviral categories are shown individually in each category. **d**, Circular maximum-likelihood phylogenetic trees of selected proviral sequences from each study participant, determined by PheP-seq. Clonal sequences are indicated; chromosomal integration sites are listed when available. Graphics in **a** were created using BioRender.com.

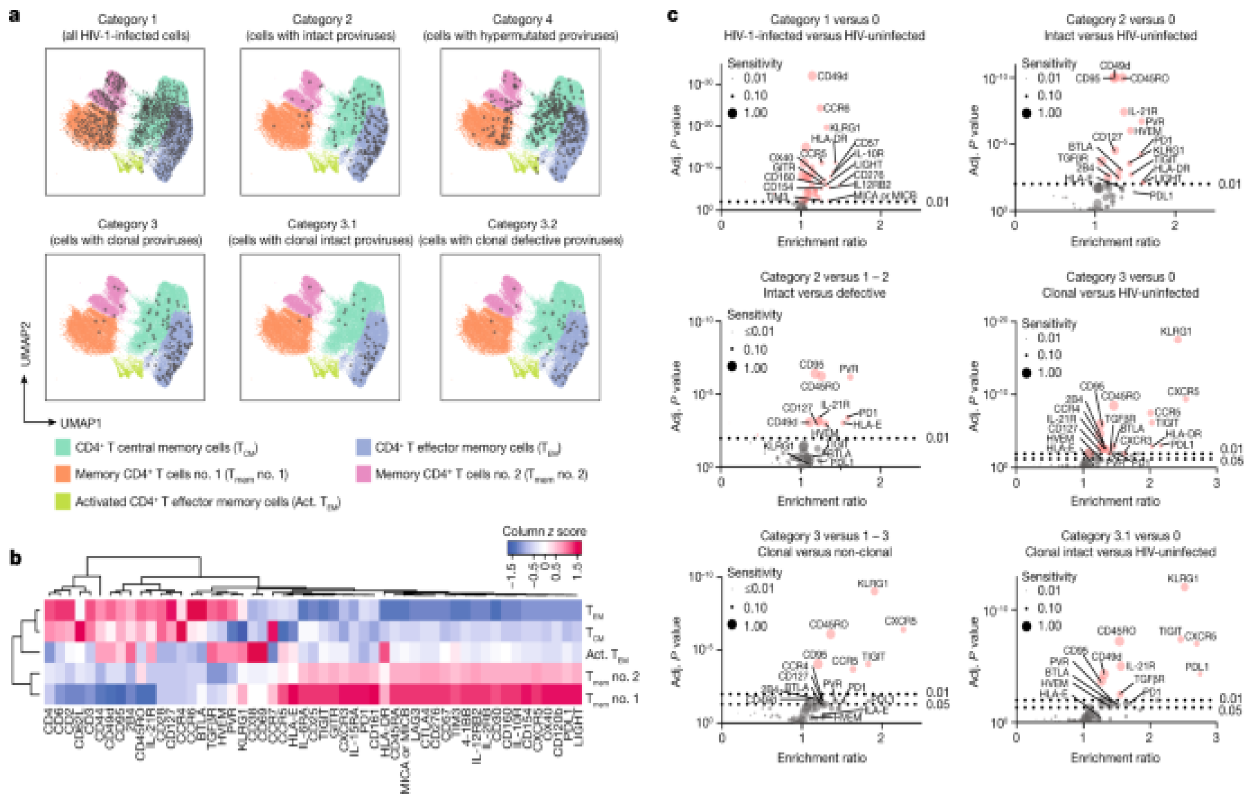
# Global analysis of HIV-1 reservoir cells

Using this assay, we analysed 530,143 individual mCD4$^+$ T cells in PB from five study participants (four who had remained on suppressive ART for approximately 10 years, and one maintaining undetectable levels of HIV-1 plasma viraemia in the absence of ART (Extended Data Fig. 2a,b). To analyse the proviral landscapes in infected cells, we introduced the following classification system (Fig. 1b,c, Extended Data Figs. 1b and 2c and Supplementary Table 2). Category 1 included cells (*n* = 2,859) considered HIV-1-infected and harbouring any type of HIV-1 proviruses; for added rigour, we required these cells to have a total of at least 20 proviral reads from at least two HIV-1 amplicons. Category 2 contained cells (*n* = 193) harbouring proviruses enriched for genome-intact HIV-1 sequences[23,24] and were defined by having a total of at least 20 sequencing reads from the two IPDA amplicons. In case an IPDA amplicon was missing (owing to, for example, suboptimal PCR performance), a total of at least 15 proviral amplicons had to be present to qualify for inclusion in category 2. Sequences showing statistically significant signs of hypermutation mediated by APOBEC3G or APOBEC3F were excluded from category 2. Category 3 included cells (*n* = 125) belonging to large clones of virally infected cells that were defined by amplicons spanning proviral integration sites (Extended Data Fig. 1c) or, in a limited number (*n* = 32) of cells, by completely identical proviral sequences from all available amplicons (Fig. 1d). This category was further subdivided into cells containing genome-intact clonal proviruses (category 3.1, *n* = 56 cells) and defective clonal proviruses (category 3.2, *n* = 69 cells), and exhibited expected clonal phylogenetic

clusters (Fig. 1d and Extended Data Fig. 2c). Category 4 (total of $n = 398$) cells harboured proviral genomes with statistically significant sequence hypermutations. For comparative purposes, cells without detectable proviral sequencing reads (category 0) were considered as HIV-uninfected cells.

For an initial global analysis of the phenotype of HIV-1-infected cells from PB, we visualized in silico-gated $CD3^{+}CD4^{+}$ cells (after exclusion of contaminating $CD45RA^{+}CCR7^{+}$ naive T cells) from the different categories on uniform manifold approximation and projection (UMAP)[25] plots, classifying the $mCD4^{+}$ T cell pool in five distinct, computationally defined phenotypic clusters (Fig. 2a,b). This analysis demonstrated a diverse distribution of category 1 HIV-1-infected cells across the entire spectrum of $mCD4^{+}$ T cells, with only minor under- or over-representation in specific cell clusters relative to HIV-uninfected cells; specifically, there was no evidence of enhanced clustering of virally infected category 1 cells in activated, HLA-$DR^{+}$ or $CD38^{+}mCD4^{+}$ T cells (Extended Data Fig. 3a–c). A similar observation was made for category 4 cells (harbouring hypermutated proviruses), which closely imitated the phenotypic distribution pattern of category 0 and 1 cells (Fig. 2a,b). The phenotypic profiles of category 2 and 3 cells were markedly biased in comparison to those of category 0, 1 and 4 cells; cells from both categories 2 and 3 were disproportionally enriched within clusters exhibiting features of a more mature, effector memory phenotype, characterized by high levels of expression of CD45RO and low levels of expression of CCR7 and CD62L (Fig. 2a,b and Extended Data Fig. 3a–c). Together, these results indicate that cells encoding intact proviruses and/or being part of large proviral clones exhibit distinct phenotypic properties; by contrast, virally infected cells in categories 1 and 4, mostly consisting of lymphocytes harbouring defective proviruses, remained phenotypically largely indistinguishable from HIV-uninfected cells in this global phenotypic analysis.

**Fig. 2: Phenotypic profile of patient-derived HIV-1-infected cells circulating in PB.**

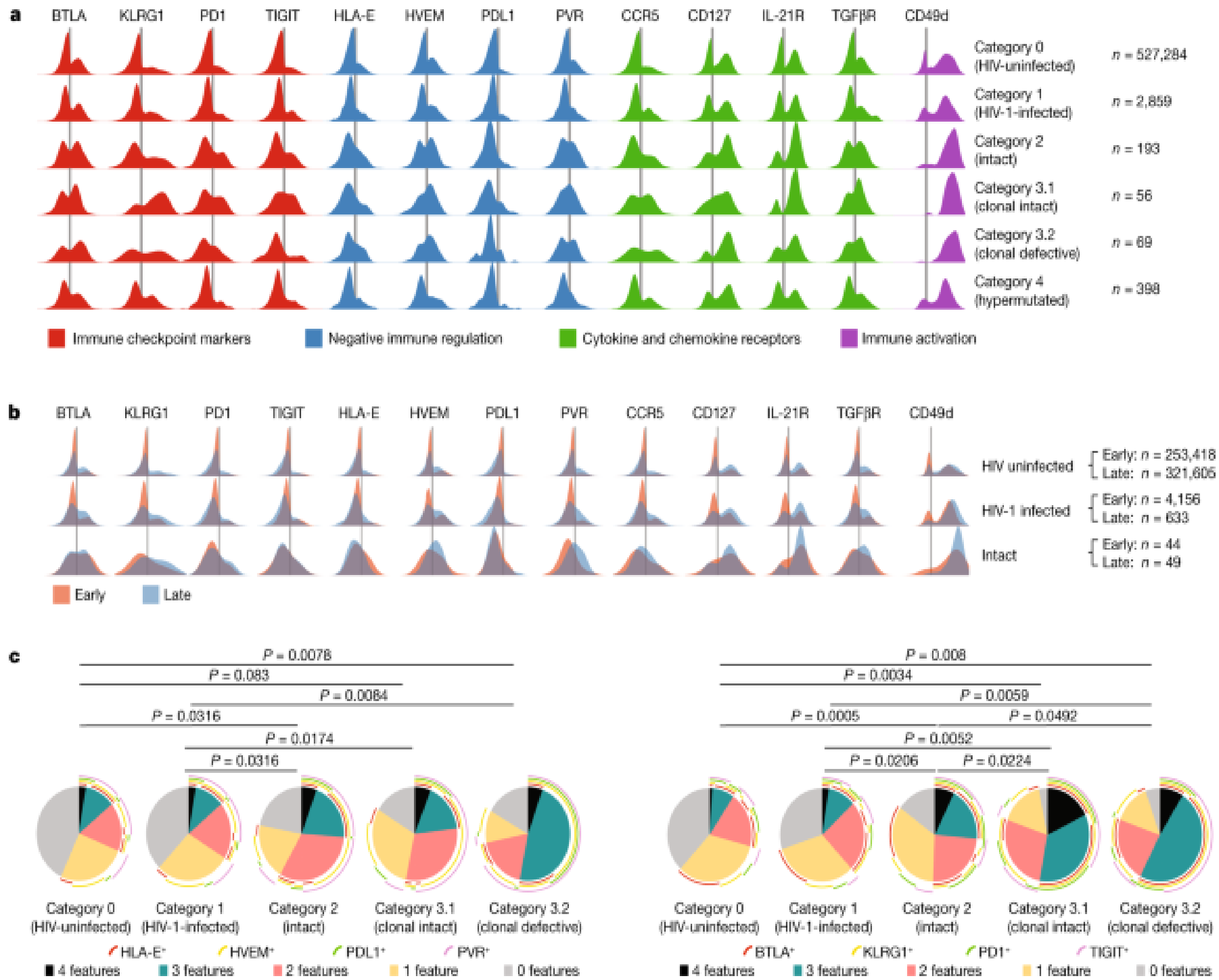



**a**, Global visualization of phenotypic properties of HIV-1-infected CD4$^+$ T cells from five study participants using two-dimensional UMAP plots; five computationally defined spherical clusters reflecting phenotypically distinct mCD4$^+$ T cell subsets are shown. One plot is shown for each cell category. **b**, A heatmap summarizing the normalized phenotypic profile of cells in each spherical cluster, based on 53 surface markers included in this study. **c**, Volcano plots showing enrichment ratios of marker-positive cells and corresponding FDR-adjusted (adj.) *P* values for all 53 surface markers included in this study; selected markers are labelled individually. Marker sensitivities, calculated as the proportions of marker-positive cells in the indicated categories of cells, are indicated by dot sizes. Comparisons between indicated categories of cells are depicted; bootstrapped data from all five participants are shown. Significance was tested using a two-sided chi-squared test; FDR-adjusted *P* values are shown.

For a formal statistical evaluation of the phenotypic profile of HIV-1-infected cells from PB, we first established an average read count for unspecific isotype control antibody binding, normalized to the total read count in each cell; this background was then used as a cutoff to calculate the

proportion of cells expressing a given surface marker in each category of virally infected cells, relative to the HIV-uninfected cells (Supplementary Table 3). To account for differences in the total number of virally infected cells available from each participant, which could disproportionately bias results by participants with higher numbers of HIV-1-positive cells, we used a bootstrapping analysis approach so that data from each participant had an equal impact on final statistical outcomes. Several surface markers with significant enrichment in category 1 HIV-1-infected cells were noted, relative to HIV-uninfected cells (Fig. 2c). Although differences for many of these markers reached very definitive levels of statistical significance owing to relatively high numbers of cells in category 1, their biological significance was questionable, given that only very small proportions of category 1 cells were positive for such markers, and/or there were rather limited fold enrichments relative to uninfected cells. This was true for expression of, for example, CD276, GITR, CD57, interleukin-10 receptor (IL-10R), HLA-DR, LIGHT and OX40. Overall, inter-individually consistent surface marker expression differences between category 1 cells and HIV-uninfected cells were modest, suggesting that category 1 cells frequently show only slight phenotypic variations relative to their uninfected counterparts (Figs. 2c and 3a and Extended Data Fig. 4). Notably, weaker phenotypic differences were also observed for category 4 cells relative to HIV-uninfected cells (Fig. 3a and Extended Data Figs. 4 and 5a).

**Fig. 3: Differentially expressed surface markers on patient-derived HIV-1-infected $CD4^+$ T cells circulating in PB.**




**a**, Density plots indicating the surface expression of selected phenotypic markers on indicated categories of cells in a cross-sectional analysis from all five participants after approximately 10 years of ART. **b**, Density plots reflecting surface expression of selected phenotypic markers in longitudinal samples collected at approximately year 1 (‘early’) and year 10 (‘late’) of ART in study participants P1 and P2. **c**, ‘Simplified Presentation of Incredibly Complex Evaluations’ (SPICE) diagrams reflecting the proportions of HIV-1-infected cells expressing ensemble phenotypic markers in a cross-sectional analysis of samples collected from five study participants after 10 years of ART. The pie charts indicate the relative proportions of cells expressing 0, 1, 2, 3 or 4 of the indicated markers; individual markers are shown as overlaying arches. One separate diagram is shown for each category of cells; the data in the left panel reflect phenotypic markers associated with resistance to immune-mediated killing, and the data in the

right panel show immune checkpoint markers. Significance was tested using an FDR-adjusted permutation test.

## Reservoir cells harbouring intact HIV-1

For PB cells harbouring proviruses with a high probability to be genome-intact (category 2 cells), we noted more pronounced statistical enrichments for a list of markers that are associated with functional inhibition of T cells (Figs. 2c and 3a and Extended Data Fig. 4). Such markers included the immune checkpoint receptors PD1, TIGIT, BTLA, 2B4 and KLRG1; only minor, nonsignificant changes were observed for CTLA4, TIM3 and LAG3. By increasing the threshold for cellular activation, these markers may limit proviral gene expression and reduce subsequent visibility and vulnerability of reservoir cells to host immune recognition mechanisms; pharmacological blockade of one checkpoint marker (PD1) was indeed shown to increase proviral gene expression in recent animal[26] and human clinical studies[27,28]. Notably, category 2 cells also showed elevated expression of several markers that act as ligands for inhibitory receptors expressed on immune effector cells and increase resistance of target cells to $CD8^+$ T or natural killer (NK) cell-mediated immune activity by conferring negative immunoregulatory impulses (Figs. 2c and 3a); overexpression of such markers might defend HIV-1-infected cells against cellular immune responses and may translate into a longitudinal selection advantage. In particular, we observed upregulation of the herpes virus entry mediator (HVEM), which negatively regulates T and NK cells through binding to BLAT[29] and CD160 (refs. [30,31]) and has a known role for protecting virally infected cells against host immune effects, supported by the discovery of the HVEM paralogue UL144 encoded by human CMV[32] (Fig. 3a). In addition, we noted upregulation of the poliovirus receptor (PVR), which can inhibit cytotoxic effects of T and NK cells by interactions with its high-affinity ligands TIGIT[33] and KIR2DL5 (ref. [34]), respectively. Enrichment within category 2 cells was also observed for PDL1 (the physiological ligand for PD1) and for HLA-E, a non-classical MHC class I molecule that acts as the high-affinity ligand for the inhibitory receptor NKG2A expressed on NK and T cells[35]; however, these markers were expressed on more limited numbers of cells and statistical scores were weaker (false discovery rate (FDR)-adjusted $P = 0.02$

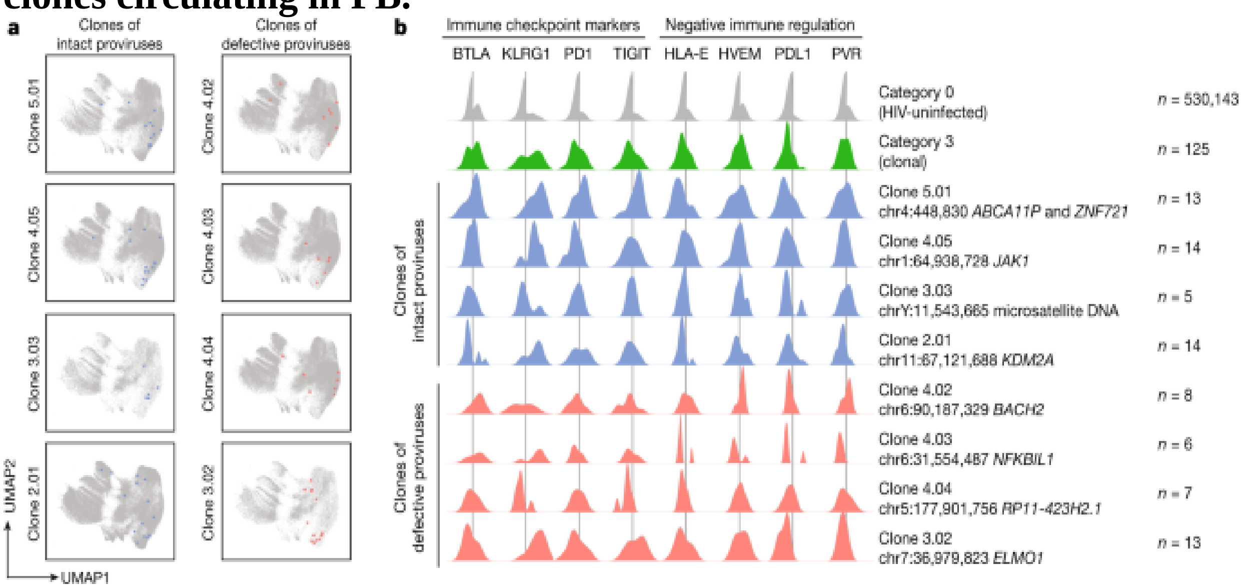
for HLA-E and $P = 0.04$ for PDL1). Category 2 cells harbouring intact HIV-1 DNA were further enriched for a higher level of surface expression of CD49d, CD45RO and CD95, all of which can be associated with T cell activation and differentiation towards an effector memory profile. Moreover, they exhibited elevated expression of the receptor for transforming growth factor β (TGFβ), which can promote proviral latency[36], of the receptor for IL-21, and of CD127, the receptor for the homeostatic cytokine IL-7. In a subsequent analysis, we noted little phenotypic variation between cells harbouring clonal genome-intact proviruses and intact proviruses detected only once, with the notable exception of KLRG1, which was more strongly expressed on the former (Extended Data Fig. 4a). Moreover, we compared the phenotypic profiles of category 2 cells with those of cells encoding for defective proviruses (category 1 cells after excluding category 2 cells; Figs. 2c and 3a); these analyses involved lower numbers of cells and reached lower levels of statistical significance, but also identified elevated surface expression of markers associated with resistance to immune-mediated killing (PVR, HLA-E and HVEM) as key distinguishing features for cells enriched for harbouring genome-intact HIV-1 DNA. Markers associated with functional inhibition of T cells, in particular PD1, were also upregulated in category 2 cells relative to cells harbouring defective proviruses (Figs. 2c and 3a).

# Phenotype of clonal reservoir cells

In a dedicated analysis of cells harbouring clonally expanded proviruses (category 3), we noted strong enrichment for expression of KLRG1, which, in addition to its role as an inhibitory checkpoint marker binding to E-cadherin[37], has been associated with terminal differentiation and cellular senescence[38]; enrichment of KLRG1 in category 3 cells probably reflects a history of strong clonal proliferative turnover in this specific cell population (Figs. 2c and 3). PDL1 emerged as a negative immunoregulatory marker with a more notable enrichment on category 3 cells, suggesting a role of this marker for protecting clonal HIV-1-infected target cells against T cell immune attacks. Among markers associated with functional inhibition of T cells, TIGIT exhibited the most notable upregulation in category 3 cells; expression of PD1 and BTLA was also increased on category 3 cells. For a more detailed analysis of individual clones of HIV-1 reservoir cells, we

investigated the phenotype of clonal HIV-1-infected cells sharing a common chromosomal integration site. In a global analysis, cells belonging to the same clone tended to cluster near one another on a UMAP plot, suggesting a rather homogenous phenotypic behaviour of HIV-1-infected cells derived from the same clone (Fig. 4a); however, some clones showed a higher level of phenotypic variability. Moreover, we noted that the upregulation of specific immunoregulatory markers on category 3 cells, including PDL1, HVEM and PVR, was not selectively driven by specific cell clones but occurred relatively consistently across most analysed clonal reservoir cell populations (Fig. 4b); nevertheless, some inter-clonal phenotypic diversity was noted and deserves additional investigation in future studies. Together, these findings suggest that clonal HIV-1-infected cells, which may be under more profound immune selection pressure due to a higher propensity for viral reactivation during cellular proliferation, may exhibit a specific surface phenotype that is likely to increase a cell's ability to resist host immune selection forces.

**Fig. 4: Phenotypic profile of individual HIV-1-infected CD4$^+$ T cell clones circulating in PB.**




**a**, Two-dimensional UMAP diagrams indicating the global phenotypic profile of selected HIV-1-infected CD4$^+$ T cell clones relative to HIV-uninfected mCD4 T cells. **b**, Density plots showing the surface expression of selected phenotypic markers on individual HIV-1-infected CD4$^+$ T cell clones, identified by proviral chromosomal integration sites. The data were

collected in a cross-sectional analysis from study participants after approximately 10 years of ART. Results from all clonal HIV-1-infected cells (category 3) and HIV-uninfected cells (category 0) are shown as references.

## Combinatorial and longitudinal analysis

We subsequently considered a combinatorial analysis of surface markers that may be jointly upregulated on HIV-1-infected cells from the PB, applying an algorithm previously developed for analysing multivariate flow cytometry datasets[39]. These additional studies demonstrated that after prolonged periods of viral suppression, proportions of cells expressing none of the markers associated with protection from killing by T or NK cells (HVEM, PVR, HLA-E and PDL1) were significantly higher in category 0 and category 1 cells, whereas the fractions of cells simultaneously expressing two or more of these markers were significantly increased among category 2 and 3 cells (Fig. 3c). A similar observation was made for immune checkpoint molecules (PD1, KLRG1, BTLA and TIGIT); by contrast, a combinatorial analysis failed to demonstrate a pronounced enrichment of category 2 or 3 cells with combinations of markers associated with immune activation (CD38, CD49d, CD95, CD69 and HLA-DR; Extended Data Fig. 5b). These findings were corroborated by experiments evaluating the frequencies of intact proviruses in sorted $mCD4^+$ T cells expressing the described marker combinations, although some variations in phenotypic patterns were noted among different study participants (Extended Data Figs. 6 and 7). Collectively, our results indicate that category 2 and 3 reservoir cells are characterized by ensemble phenotypic signatures of immune checkpoint molecules that probably reduce a cell's propensity to reactivate proviral gene transcription, and of marker combinations that can protect infected target cells against killing by T and NK cells. Such a phenotypic profile seems evolutionarily advantageous by minimizing exposure to and killing by host immune effector cells and is consistent with functional studies suggesting increased resistance of HIV-1 reservoir cells to T cell-mediated killing[40,41]. Functional experiments conducted with cells from our study participants also suggested enhanced resistance of reservoir cells encoding for intact HIV-1 DNA to HIV-1-specific $CD8^+$ T cell-mediated killing (Extended Data Fig. 8).

To longitudinally evaluate the stability of the reported phenotypic profile of HIV-1 reservoir cells, we carried out PheP-seq assays on PB samples collected early (1–2 years) after ART initiation in study participants 1 and 2, from whom such samples were available for analysis (Extended Data Fig. 2). In total, $n = 257{,}574$ individual $mCD4^+$ T cells were analysed from these early time points, of which $n = 4{,}156$ and $n = 44$ were classified as category 1 and 2 cells, respectively. Notably, category 2 reservoir cells already exhibited an increased level of expression of immune checkpoint markers and ligands for inhibitory receptors of T or NK cells at early time points after ART initiation, although such changes tended to be less pronounced relative to later time points of ART for some markers, specifically for PVR and HVEM (Fig. 3b and Extended Data Fig. 5c). Moreover, there was a trend for elevated expression for the receptors of IL-21 and TGFβ after more extended durations of ART. Together, these observations suggest that selection of reservoir cells starts early after ART initiation, possibly implying that only a small subset of category 2 cells with specific phenotypic properties are predestined to enter the long-lasting reservoir cell pool. As after longer durations of ART, category 1 reservoir cells from the early time point exhibited only limited phenotypic variations relative to uninfected cells from the same time point. Few cells analysed at early stages of ART meet our criteria for category 3 reservoir cells, precluding a specific comparison of such cells between early and late ART.

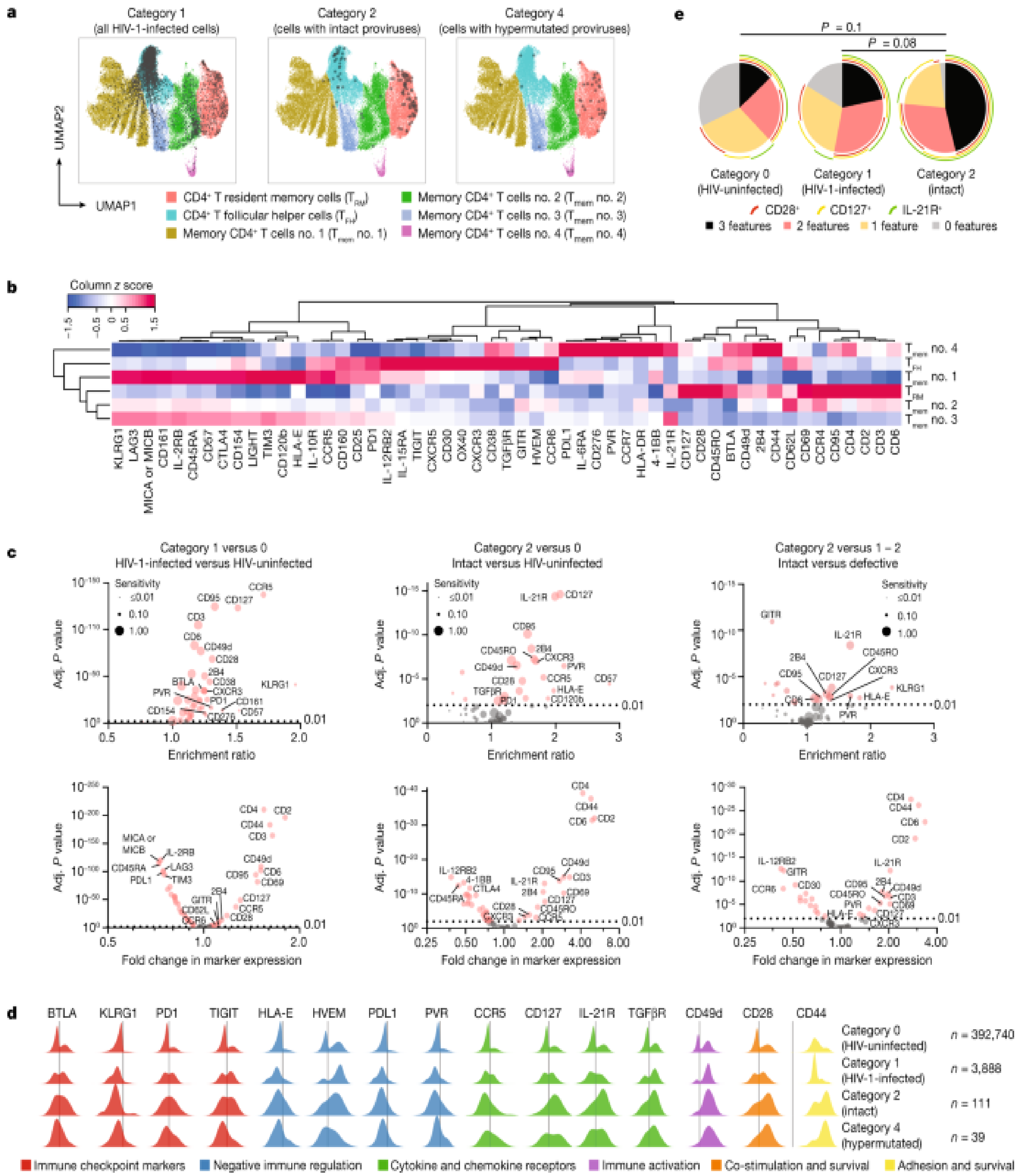
## HIV-1 reservoir cells in lymph nodes

As most HIV-1 reservoir cells are located in lymphoid tissues[42], we subsequently conducted a phenotypic analysis of virally infected cells from inguinal lymph nodes (LNs) collected by surgical excision from three people living with HIV-1 who remained on continuous suppressive ART for approximately 10–15 years (Extended Data Fig. 9a,b). In total, we analysed the phenotype of $n = 396{,}628$ single $mCD4^+$ T cells from these samples, of which $n = 3{,}888$, $n = 111$ and $n = 39$ met criteria for category 1, 2 and 4 cells, respectively; the small number of category 4 cells may be related to primer mismatches to hypermutated proviral sequences. Category 3 cells were not individually analysed in LN samples owing to the limited number of cells meeting our category 3 criteria (Extended Data Fig. 9c). A global analysis of the phenotypic landscape of HIV-1 reservoir cells from LNs (Fig. 5a,b)

indicated that viral reservoir cells exhibited focal enrichments in two different cell clusters, one characterized by high-level surface expression of CXCR5, indicative of T follicular helper ($T_{FH}$) cell polarization[43], and a second one characterized by elevated expression of CD127 and CD69, suggestive of a $CD4^+$ tissue resident memory T ($T_{RM}$) cell profile in LNs[44,45]. Whereas $T_{FH}$ cells accounted for most cells in category 1, consistent with prior results[46], category 2 cells were more equally balanced between the $T_{FH}$ cells and $T_{RM}$ cells. Subsequently, we conducted a detailed evaluation of differentially expressed surface markers between the different categories of HIV-1-infected cells, again using a bootstrapping analysis approach ensuring equal contribution of each study participant to statistical outcomes (Fig. 5c, Extended Data Fig. 10a,b and Supplementary Table 3). These evaluations demonstrated upregulation of some immune checkpoint markers on category 2 cells in LNs; however, statistical scores and enrichment ratios were weaker relative to category 2 reservoir cells from PB. Similarly, fewer markers conferring resistance to killing by T or NK cells were upregulated on category 2 cells in LNs relative to category 2 cells from PB, although both PVR and HLA-E met statistical criteria for upregulation on category 2 cells in LNs. These differential phenotypic profiles between category 2 cells from LNs versus blood may possibly be related to the predominant presence of non-cytolytic $CD8^+$ T cells in LNs[47,48], probably resulting in a more limited selection advantage for viral reservoir cells with phenotypic signs of increased resistance to immune-mediated killing in this tissue compartment. Markers that strongly distinguished category 2 reservoir cells from uninfected cells in LNs included CD44, the IL-21 receptor (CD360), the IL-7 receptor (CD127) and, to a lesser extent, CD28 (Fig. 5c,d); these markers were also upregulated on category 2 reservoir cells in LNs relative to LN cells harbouring defective proviruses (Fig. 5c) and to category 1 and 2 reservoir cells from PB (Extended Data Fig. 10B). All of these markers are functionally involved in mediating cell survival signals; in particular, CD44 can increase survival and apoptosis resistance of $CD4^+$ T cells through engagement of the phosphoinositide 3-kinase–AKT signalling pathway[49]. Moreover, T cell survival signals related to activation of the AKT signalling pathway also occur downstream of the IL-21 receptor[50,51]. Likewise, CD28 has a prominent role for supporting $CD4^+$ T cell survival; this is probably related to a CD28-mediated upregulation of cell-intrinsic

anti-apoptosis markers from the BCL-2 family[52]. Phenotypic signatures of increased cell survival were also detected on category 2 cells in LNs when a combinatorial analysis was applied (Fig. 5e). Notably, we also observed a trend for elevated expression of several members of the TNF receptor superfamily on category 2 cells in LNs, specifically of CD30, GITR and OX40, which have also been implicated in mediating cell survival signals[53] (Extended Data Fig. 10a). Phenotypic differences between category 2 and category 1 or 4 reservoir cells were not as definitive in LNs compared to PB cells, a finding that requires more attention in future studies. Together, our data demonstrate that category 2 reservoir cells from LNs predominantly show phenotypic features associated with apoptosis resistance and survival; upregulation of these markers on category 2 cells in LNs may promote their long-term persistence and can be viewed as a sign of immune adaptation of reservoir cells to the LN immune microenvironment.

**Fig. 5: Phenotypic analysis of HIV-1 reservoir cells from inguinal LNs.**



**a**, Global phenotypic analysis of HIV-1 reservoir cells from LNs by two-dimensional UMAP plots. Six computationally defined spherical clusters are indicated; one plot is shown each for category 1, category 2 and category 4 cells. **b**, A heatmap summarizing the phenotypic profile of cells in each spherical cluster, based on 53 surface markers included in this study. **c**,

Volcano plots showing enrichment ratios of marker-positive cells (upper panel) or fold changes in marker expression intensity (lower panel) and corresponding FDR-adjusted *P* values for all 53 surface markers included in this study; selected markers are labelled individually. Marker sensitivities, calculated as the proportions of marker-positive cells in the indicated categories of cells, are indicated by dot sizes. Comparisons between indicated categories of cells are depicted; bootstrapped data from all three donors of LN biopsies are shown. Significance was tested using a chi-squared test or two-sided *t*-test, FDR-adjusted *P* values are shown. **d**, Density plots indicating the expression of selected phenotypic markers on indicated categories of cells from all three LN donors. **e**, SPICE diagrams reflecting the proportions of HIV-1-infected LN cells expressing the ensemble phenotypic cell survival markers CD127, CD28 and IL-21R. The pie charts indicate the relative proportions of cells expressing none, one, two or three of the indicated markers; individual markers are shown as overlaying arches. One separate diagram is shown for each indicated population of cells. Significance was tested using an FDR-adjusted permutation test.

# Discussion

Our experiments, involving single-cell proteogenomic profiling data from a total of 1,184,345 individual patient-derived mCD4$^{+}$ T cells, indicate that following years of continuous ART, HIV-1-infected cells show several distinct phenotypic features, specifically when harbouring intact proviruses; however, they do not support the presence of a single unifying phenotypic marker that can effectively distinguish virally infected cells from uninfected cells. Given that a higher expression level of certain markers was more definitively observed on category 2 (in LNs and PB) and on category 3 cells (in PB), we propose that these phenotypic changes are not due to an intrinsic association with HIV-1 infection, or a higher susceptibility of cells expressing these markers to HIV-1 infection. Instead, they probably represent a consequence of immune selection mechanisms that promote preferential persistence of reservoir cells with a phenotypic profile offering optimal adaptation to their specific immunological microenvironment. We emphasize that the enrichment for the described phenotypic markers, specifically when analysed as isolated parameters, must be considered as

moderate, although there were stronger enrichments for specific marker combinations, suggesting that phenotypic marker ensembles allow for a more effective and, possibly, a more customized adaptation to host immune activity. Together, our findings strongly support the hypothesis that viral reservoir cells are subject to active host immune selection pressure, and that footprints of such immune selection are particularly visible in cells harbouring intact HIV-1 proviruses. Given their likely dependence on host immune selection activity, we suggest that phenotypic alterations of viral reservoir cells described here are unlikely to act as universal biomarkers of viral reservoir cells in all ART-treated people living with HIV-1; instead, the presence or absence of such phenotypic selection footprints may vary among different people and might be critically influenced by the intensity of host immune activities; evaluations of the longitudinal coevolution of host immune responses and phenotypic profiles of viral reservoir cells may represent an attractive future research perspective for understanding viral reservoir dynamics. Although we do not claim that the phenotypic markers identified here may represent direct targets for immunotherapeutic interventions in HIV-1 cure research, we suggest that clinical strategies designed to intensify and accelerate immune selection of HIV-1 reservoir cells may be of benefit for reducing HIV-1 long-term persistence and inducing a drug-free remission of HIV-1 infection.

# Methods

## Study participants

Individuals infected with HIV-1 were recruited as study participants at the Massachusetts General Hospital in Boston, MA, and at the NIH Clinical Center in Bethesda, MD. PB mononuclear cell (PBMC) samples were obtained according to protocols approved by the respective Institutional Review Boards. All study participants gave written informed consent for blood collection or for LN biopsies. Clinical characteristics of study participants are summarized in Extended Data Figs. 2 and 9. Study participants were preselected on the basis of high frequencies of HIV-1-infected CD4$^+$ T cells analysed in previous studies.

## LN biopsies

Inguinal LNs were excised surgically with informed consent of study participants, according to protocols approved by the Massachusetts General Hospital Institutional Review Board. LN tissue was dissected and mechanically disaggregated through a 70-µm nylon cell strainer in RPMI medium supplemented with 10% fetal bovine serum.

## Isolation of memory $CD4^+$ T cells

PBMCs and LN mononuclear cells (LNMCs) were isolated using Ficoll–Paque density centrifugation. PBMCs and LNMCs were viably frozen in 90–95% fetal bovine serum and 5–10% dimethylsulfoxide. For analysis, cells were thawed and subjected to negative immunomagnetic isolation of memory $CD4^+$ T cells, using a commercial product (Stemcell EasySep Human Memory $CD4^+$ T cell Enrichment Kit, no. 18000) per the manufacturer’s protocol.

## Surface labelling with monoclonal antibodies

Monoclonal antibodies tagged with distinct oligonucleotides were custom manufactured and supplied as lyophilized single-reaction vials by a commercial vendor (BioLegend). Antibodies to the following surface markers were used: PDL1 (clone 29E.2A3), CD276 (clone DCN.70), HVEM (clone 122), CD155 (clone SKII.4), CD154 (also known as CD40L) (clone 24-31), CCR4 (clone L291H4), PD1 (A17188B), TIGIT (clone A15153G), CD44 (clone BJ18), CXCR3 (clone G025H7), CCR5 (clone HEK/1/85a), CCR6 (clone G034E3), CXCR5 (clone J252D4), CCR7 (clone G043H7), KLRB1 (also known as CD161) (clone HP-3G10), CTLA4 (clone BNI3), LAG3 (clone 11C3C65), KLRG1 (clone 14C2A07), CD95 (clone, DX2), OX40 (also known as CD134) (clone Ber-ACT35), CD57 (clone HNK-1), TIM3 (clone F38-2E2), BTLA (also known as CD272); (clone MIH26), CD244 (also known as 2B4) (clone 2-69), IL-2R (clone TU27), CD137 (also known as 4-1BB) (clone 4B4-1), GITR (also known as CD357) (clone 108-17), CD28 (clone CD28.2), CD127 (clone A019D5), IL-6R (clone UV4), HLA-E (clone 3D12), MICA or MICB (clone 6D4), IL-15R (also known as CD215) (clone JM7A4), IL-21R (clone 2G1-K12), TNFR2 (clone 3G7A02), CD160 (clone BY55), LIGHT (also known as CD258) (clone T5-39), IL-10R (also known as CD210) (clone 3F9), TGFβR (clone W17055E),

IL-12R (clone S16020B), CD6 (clone BL-CD6), CD49d (clone 9F10), CD25 (clone BC96), CD30 (clone BY88), CD69 (clone FN50), CD45RA (clone HI100), CD38 (clone HIT2), HLA-DR (clone L243), CD4 (clone RPA-T4), CD2 (clone TS1/8), CD3 (clone UCHT1), CD62L (clone DREG-56), CD45RO (clone UCHL1). Two mouse IgG control antibodies (BioLegend, no. 400299, no. 400383), conjugated with distinct TotalSeq-D oligonucleotides were included as the isotype controls. The lyophilized antibody cocktails containing the above-mentioned antibodies were reconstituted with 60-µl of cell staining buffer (BioLegend, no. 420201). Cells were blocked with Human TruStain FcX (BioLegend, no. 422301) for 15 min on ice and then incubated with 50 µl of reconstituted antibody cocktail for 30 min on ice. After three washes with pre-chilled cell staining buffer, cells were filtered with a 40-µm cell Flowmi strainer (Fisher Scientific, no. 14-100-150), counted with an automated cell counter, and then loaded into a microfluidic cartridge for single-cell multiplex PCR assays.

## Single-cell multiplex PCR

Single-cell amplification of defined genomic DNA segments was carried out using the Tapestri platform (MissionBio) according to the manufacturer's protocol[18]. Viable single cells were encapsulated into droplets with a lysis buffer (containing protease and a mild detergent) and incubated for 1 h at 50 °C, followed by 10 min at 80 °C for heat inactivation of enzymes. Droplets containing single-cell barcoding beads (tagged with oligonucleotides carrying the cellular barcodes and custom-designed primers) were fused with encapsulated cell lysates. A panel of primers designed to amplify $n = 18$ different genomic regions in HIV-1 and $n = 27$ specific HIV–host DNA junctions of previously defined large clonal HIV-1-infected T cell populations in our study participants were used (Fig. 1b and Supplementary Table 1) in addition to two primer sets amplifying control genomic regions in the *RPP30* gene on chromosome 10. The droplets were placed under ultraviolet light to cleave PCR primers containing unique cell barcodes from beads. To amplify the selected genomic DNA segments and the antibody oligonucleotide tags, droplets were subjected to PCR for 24 cycles with temperature gradients recommended by the manufacturer.

## Sequencing library construction

Amplification products were pooled, mixed with AMPure XP beads (Beckman Coulter, no. A63882) at a ratio of 0.7 and placed in a magnetic field for separating the DNA and the protein tag libraries. The DNA library bound to AMPure beads was washed with 80% ethanol, and the supernatant containing the protein tag library was aspirated and incubated with a biotinylated oligonucleotide complementary to the 5′ end of the antibody tags, followed by magnetic isolation using streptavidin beads. For library amplification, PCRs were carried out with Illumina index primers P5 and P7 on purified DNA and protein libraries, respectively, according to the manufacturer’s protocol; 12 cycles were carried out for the DNA library, and 18 cycles were run for the protein tag library.

## Next-generation sequencing

The DNA and protein tag libraries were run on a High Sensitivity D1000 ScreenTape instrument (Agilent Technologies, 5067-5584) with the Agilent 4200 TapeStation System to evaluate DNA quality. Libraries were quantified by a fluorometer (Qubit 4.0, Invitrogen) and sequenced on Illumina next-generation sequencing platforms with a 20% spike-in of PhiX control DNA (Illumina, no. FC-110-3002). DNA and protein tag libraries were sequenced separately on a NextSeq 500 instrument (Illumina), using the NextSeq 500/550 High Output flow cell v2.5 (Illumina, no. 20022408) and the NextSeq 500/550 High Output Kit v2.5 (300 cycles; Illumina, no. 20024908) in 2 × 150-bp paired-end runs.

## Bioinformatic analysis

The Tapestri pipeline (MissionBio, v2.0.1) with minor modifications was used to process the sequencing data. Briefly, for DNA library data, cutadapt (v2.5)[54] was used to trim 5′ and 3′ adaptor sequences, and extract 18-bp cell barcode sequences from read 1. Cell barcodes that aligned to a unique barcode on a whitelist within a Hamming distance of 2 were used for downstream analysis. Using bwa (v0.7.12)[55], sequences were aligned to custom reference genomes built from the human genome (GRCh38) and patient-specific autologous HIV-1 sequences identified in prior studies.

Single-cell alignments were filtered according to criteria implemented in the Tapestri pipeline, and indexed using samtools (v1.9)[56]. Candidate HIV-1-infected cells were determined by the CellFinder algorithm built in the Tapestri pipeline. Bcftools (v1.9)[57] was used to call variants and generate consensus sequences. To reduce spurious alignments, viral sequencing reads were considered valid only if they covered at least 80% of the length of the reference sequence for each given amplicon; host sequencing reads had to cover at least 50% of the length of respective amplicon. For antibody library data, cell barcodes were similarly extracted using cutadapt. For reads with valid cell barcodes, 15-bp antibody barcodes were extracted from read 2. Antibody barcode sequences within a Hamming distance of 1 from known antibody barcodes were accepted. Candidate cells appearing in both libraries were processed for downstream analysis. Read counts for each antibody were normalized to the total read count in each cell using centred log-ratio transformation[58]. Cutoffs for a given phenotypic marker to be considered positive were defined by marker-specific read counts higher than 1 mean absolute deviation of the normalized median read count corresponding to unspecific IgG control antibodies. To generate a more homogenous cell population for analysis, centred log-ratio values of all candidate cells that were $CD3^{-}CD4^{-}$ (non-$CD4^{+}$ T cells) and $CCR7^{+}CD45RA^{+}$ (contaminating naive $CD4^{+}$ T cells) were excluded.

## Dimension reduction and clustering

UMAP embeddings in two dimensions of the centred log-ratio values was carried out through the Monocle 3 (ref. [59]) and uwot[60] packages with the number of principal components set to 15 for all cells, and to 10 for HIV-1-infected cells alone; numbers of neighbours to use during *k*-nearest neighbours graph construction were set to 9 and 5, respectively. All other settings were kept to the default values. The cells were clustered using the Leiden community detection algorithm through Monocle 3, with the *k*-near neighbours set to 500.

## Phylogenetic analysis of HIV-1

HIV-1 sequencing reads corresponding to each of the 18 HIV-1 amplification products and of additional amplification products corresponding to

predefined virus–host junctions were aligned to the reference HIV-1 genome HXB2, to autologous intact HIV-1 sequences and to the human reference genome GRCh38. The presence or absence of hypermutations associated with APOBEC3G or APOBEC3F was determined using the Los Alamos National Laboratory HIV Sequence Database Hypermut 2.0 program[61]. Sequence alignments were carried out using MUSCLE[62]. Phylogenetic distances between sequences were examined using maximum-likelihood trees in MEGA (https://www.megasoftware.net) and MAFFT (https://mafft.cbrc.jp/alignment/software), and visualized using highlighter plots (https://www.lanl.gov). Proviruses were classified in 4 different categories according to the following criteria—category 1 (any provirus): at least 20 total valid viral sequencing reads with at least 4 reads in at least 2 different HIV-1 amplicons each; category 2 (enriched for intact proviruses): a total of at least 20 viral sequencing reads with at least 4 sequencing reads from amplicons 2 and 16 (corresponding to IPDA amplicons) each or at least 4 reads from at least 15 amplification products each or at least 4 reads from amplification products spanning known virus–host junctions of intact proviruses (all viral sequencing reads in category 2 had to be without evidence of statistically significant hypermutation and could not correspond to virus–host junctions from known defective proviruses); category 3 (clonal proviruses): proviruses with identical proviral integration sites (based on at least 4 viral sequencing reads from amplification products of known virus–host junctions) or completely identical proviral sequences; category 4 (hypermutated proviruses): proviral sequences from category 1 that exhibited statistically significant sequence hypermutations (FDR-adjusted $P < 0.05$). Cells with HIV-1 sequencing reads that did not meet any of the above-mentioned criteria were excluded from the analysis. Category 0 cells were defined by complete absence of sequencing reads corresponding to HIV-1.

## Cell sorting and flow cytometry

Memory $CD4^+$ T cells isolated from PBMCs by negative immunomagnetic enrichment were incubated with defined fluorophore-labelled surface antibodies: CD3–PerCP–Cy5.5 (BioLegend, clone UCHT1, catalogue no. 300430), CD4–BUV395 (BD, clone RPA-T4, catalogue no. 564724), PD1–FITC (BioLegend, clone A17188B, catalogue no. 621612), TIGIT–BV421

(BioLegend, clone A15153G, catalogue no. 372710), PVR–PE (eBioscience, clone 2H7CD155, catalogue no. 12-1550-41), HVEM–APC (BioLegend, clone 122, catalogue no. 318808), BTLA–FITC (BioLegend, clone MIH26, catalogue no. 344524), KLRG1–APC (BioLegend, clone 14C2A07, catalogue no. 368606), HLA-E–BV421 (BioLegend, clone 3D12, catalogue no. 342612), PDL1–PE (BioLegend, clone MIH2, catalogue no. 393608). After 25 min of incubation, cells were washed, and indicated cell populations were sorted in a specifically designated biosafety cabinet (Baker Hood), using a FACSAria cell sorter (BD Biosciences) at 70 pounds per square inch. Cell sorting was carried out by the Ragon Institute Imaging Core Facility at Massachusetts General Hospital. Data were analysed using FlowJo software (Tree Star). Sorted cells were subjected to proviral sequencing analysis using the full-length individual proviral sequencing assay (FLIP-seq).

## Full-length HIV-1 sequencing assay

A previously described protocol was used[11,23]. In brief, genomic DNA was extracted from sorted cell populations using a QIAGEN DNeasy Blood & Tissue kit. DNA diluted to single-genome levels based on Poisson distribution statistics was subjected to single-genome amplification using Invitrogen Platinum Taq and nested primers spanning near-full-length HIV-1. PCR products were visualized by agarose gel electrophoresis; amplification products were subjected to single-genome sequencing on the Illumina platform. Resulting short reads were de novo assembled and aligned to HXB2 to identify large deleterious deletions, out-of-frame indels, premature/lethal stop codons, internal inversions or packaging signal deletions, using an automated in-house pipeline (https://github.com/BWH-Lichterfeld-Lab/Intactness-Pipeline). The presence or absence of hypermutations associated with APOBEC3G or APOBEC3F was determined using the Los Alamos HIV Sequence Database Hypermut 2.0 program. Viral sequences that lacked all lethal defects listed above were classified as genome-intact. Sequence alignments were carried out using MUSCLE. Phylogenetic distances between sequences were examined using Clustal X-generated neighbour-joining algorithms. Proviral species that were completely sequence-identical were considered as clonal.

## Ex-vivo HIV-1 reservoir cell killing assay

Memory $CD4^+$ T cells isolated from PBMCs by negative immunomagnetic enrichment were incubated in R10 medium with or without epitopic peptides for 1 h and washed thoroughly. Afterwards, cells were co-incubated with previously isolated HIV-1-specific $CD8^+$ T cell clones at selected effector-to-target (E/T) ratios for 16 h. After washing, cells were stained with blue viability dye (Invitrogen, catalogue no. L34962), CD3–FITC (BioLegend, clone UCHT1, catalogue no. 300406) and CD4–BV711 (BioLegend, clone RPA-T4, catalogue no. 300558) antibodies, followed by sorting of viable $CD3^+CD4^+$ events. Sorted cells were subjected to assessments of intact and total HIV-1 proviruses using the IPDA assay.

## IPDA

The IPDA uses digital droplet PCR to quantify proviruses lacking overt fatal defects, especially large deletions and hypermutations, and was carried out as previously described[22].

## Statistical analysis

The data are presented as pie charts, Venn diagrams, volcano plots, UMAP plots and heatmaps. Enrichment ratios between two cell populations for each marker were calculated as the ratio of the proportion of marker-positive cells in the first population divided by the proportion of marker-positive cells in the second population. Sensitivity values were calculated by dividing the number of marker-positive cells in each category of cells by the total number of cells in the respective category. A bootstrapped dataset was constructed by resampling equal numbers of cells from each cell category from each participant, while keeping the total number of cells from each cell category equal between the bootstrapped and raw datasets. Differences were tested for statistical significance using Fisher's exact test, chi-squared test, *t*-test or Mann–Whitney *U*-test, as appropriate. *P* values of $<0.05$ were considered significant; FDR correction was carried out using the Benjamini–Hochberg method[63] or the Bonferroni method. Analyses were carried out using Prism (GraphPad Software, Inc.), SPICE[39], R (R Foundation for Statistical

Computing[64]) and Python (Python Software Foundation). Figures were generated using Adobe Illustrator.

### Reporting summary

Further information on research design is available in the Nature Portfolio Reporting Summary linked to this article.

## Data availability

Data supporting conclusions in this Article are provided in Supplementary Tables 1–3. Owing to study participant confidentiality concerns, viral sequencing data cannot be publicly released, but will be made available to investigators upon reasonable request and after signing a data-sharing agreement.

## Code availability

No new computational codes are reported in this Article.

## References


1. Finzi, D. et al. Identification of a reservoir for HIV-1 in patients on highly active antiretroviral therapy. *Science* **278**, 1295–1300 (1997).

2. Wong, J. K. et al. Recovery of replication-competent HIV despite prolonged suppression of plasma viremia. *Science* **278**, 1291–1295 (1997).

3. Siliciano, J. D. et al. Long-term follow-up studies confirm the stability of the latent reservoir for HIV-1 in resting CD4$^+$ T cells. *Nat. Med.* **9**, 727–728 (2003).

4. Falcinelli, S. D. et al. Longitudinal dynamics of intact HIV proviral DNA and outgrowth virus frequencies in a cohort of ART-treated individuals. *J. Infect. Dis.* **224**, 92–100 (2020).

5. Peluso, M. J. et al. Differential decay of intact and defective proviral DNA in HIV-1-infected individuals on suppressive antiretroviral therapy. *JCI Insight* **5**, e132997 (2020).

6. Gandhi, R. T. et al. Selective decay of intact HIV-1 proviral DNA on antiretroviral therapy. *J. Infect. Dis.* **223**, 225–233 (2020).

7. Cho, A. et al. Longitudinal clonal dynamics of HIV-1 latent reservoirs measured by combination quadruplex polymerase chain reaction and sequencing. *Proc. Natl Acad. Sci. USA* **119**, e2117630119 (2022).

8. Einkauf, K. B. et al. Intact HIV-1 proviruses accumulate at distinct chromosomal positions during prolonged antiretroviral therapy. *J. Clin. Invest.* **129**, 988–998 (2019).

9. Cole, B. et al. In-depth single-cell analysis of translation-competent HIV-1 reservoirs identifies cellular sources of plasma viremia. *Nat. Commun.* **12**, 3727 (2021).

10. Einkauf, K. B. et al. Parallel analysis of transcription, integration, and sequence of single HIV-1 proviruses. *Cell* **185**, 266–282 (2022).

11. Jiang, C. et al. Distinct viral reservoirs in individuals with spontaneous control of HIV-1. *Nature* **585**, 261–267 (2020).

12. Lian, X. et al. Signatures of immune selection in intact and defective proviruses distinguish HIV-1 elite controllers. *Sci. Transl. Med.* **13**, eabl4097

13. Liu, R. et al. Single-cell transcriptional landscapes reveal HIV-1-driven aberrant host gene transcription as a potential therapeutic target. *Sci. Transl. Med.* **12**, eaaz0802 (2020).

14. Halvas, E. K. et al. HIV-1 viremia not suppressible by antiretroviral therapy can originate from large T cell clones producing infectious virus. *J. Clin. Invest.* **130**, 5847–5857 (2020).

15. Fromentin, R. et al. $CD4^+$ T cells expressing PD-1, TIGIT and LAG-3 contribute to HIV persistence during ART. *PLoS Pathog.* **12**, e1005761

(2016).

16. Baxter, A. E. et al. Single-cell characterization of viral translation-competent reservoirs in HIV-infected individuals. *Cell Host Microbe* **20**, 368–380 (2016).

17. Neidleman, J. et al. Phenotypic analysis of the unstimulated in vivo HIV CD4 T cell reservoir. *eLife* **9**, e60933 (2020).

18. Ruff, D. W., Dhingra, D. M., Thompson, K., Marin, J. A. & Ooi, A. T. High-throughput multimodal single-cell targeted DNA and surface protein analysis using the Mission Bio Tapestri platform. *Methods Mol. Biol.* **2386**, 171–188 (2022).

19. Demaree, B. et al. Joint profiling of DNA and proteins in single cells to dissect genotype-phenotype associations in leukemia. *Nat. Commun.* **12**, 1583 (2021).

20. Collora, J. A. et al. Single-cell multiomics reveals persistence of HIV-1 in expanded cytotoxic T cell clones. *Immunity* **55**, 1013–1031 e1017 (2022).

21. Weymar, G. H. J. et al. Distinct gene expression by expanded clones of quiescent memory $CD4^+$ T cells harboring intact latent HIV-1 proviruses. *Cell Rep.* **40**, 111311 (2022).

22. Bruner, K. M. et al. A quantitative approach for measuring the reservoir of latent HIV-1 proviruses. *Nature* **566**, 120–125 (2019).

23. Lee, G. Q. et al. Clonal expansion of genome-intact HIV-1 in functionally polarized Th1 $CD4^+$ T cells. *J. Clin. Invest.* **127**, 2689–2696 (2017).

24. Ho, Y. C. et al. Replication-competent noninduced proviruses in the latent reservoir increase barrier to HIV-1 cure. *Cell* **155**, 540–551 (2013).

25. Becht, E. et al. Dimensionality reduction for visualizing single-cell data using UMAP. *Nat. Biotechnol.* **37**, 38–44 (2019).

26. Harper, J. et al. CTLA-4 and PD-1 dual blockade induces SIV reactivation without control of rebound after antiretroviral therapy interruption. *Nat. Med.* **26**, 519–528 (2020).

27. Uldrick, T. S. et al. Pembrolizumab induces HIV latency reversal in people living with HIV and cancer on antiretroviral therapy. *Sci. Transl. Med.* **14**, eabl3836 (2022).

28. Lau, J. S. Y. et al. The impact of immune checkpoint therapy on the latent reservoir in HIV-infected individuals with cancer on antiretroviral therapy. *AIDS* **35**, 1631–1636 (2021).

29. Sedy, J. R. et al. B and T lymphocyte attenuator regulates T cell activation through interaction with herpesvirus entry mediator. *Nat. Immunol.* **6**, 90–98 (2005).

30. Cai, G. et al. CD160 inhibits activation of human $CD4^+$ T cells through interaction with herpesvirus entry mediator. *Nat. Immunol.* **9**, 176–185 (2008).

31. Peretz, Y. et al. CD160 and PD-1 co-expression on HIV-specific CD8 T cells defines a subset with advanced dysfunction. *PLoS Pathog.* **8**, e1002840 (2012).

32. Bitra, A. et al. Structure of human cytomegalovirus UL144, an HVEM orthologue, bound to the B and T cell lymphocyte attenuator. *J. Biol. Chem.* **294**, 10519–10529 (2019).

33. Yu, X. et al. The surface protein TIGIT suppresses T cell activation by promoting the generation of mature immunoregulatory dendritic cells. *Nat. Immunol.* **10**, 48–57 (2009).

34. Wojtowicz, W. M. et al. A human IgSF cell-surface interactome reveals a complex network of protein-protein interactions. *Cell* **182**, 1027–1043 (2020).

35. Lee, N. et al. HLA-E is a major ligand for the natural killer inhibitory receptor CD94/NKG2A. *Proc. Natl Acad. Sci. USA* **95**, 5199–5204 (1998).

36. Samer, S. et al. Blockade of TGF-beta signaling reactivates HIV-1/SIV reservoirs and immune responses in vivo. *JCI Insight* **7**, e162290 (2022).

37. Rosshart, S. et al. Interaction of KLRG1 with E-cadherin: new functional and structural insights. *Eur. J. Immunol.* **38**, 3354–3364 (2008).

38. Henson, S. M. & Akbar, A. N. KLRG1–more than a marker for T cell senescence. *Age* **31**, 285–291 (2009).

39. Roederer, M., Nozzi, J. L. & Nason, M. C. SPICE: exploration and analysis of post-cytometric complex multivariate datasets. *Cytometry A* **79**, 167–174 (2011).

40. Ren, Y. et al. BCL-2 antagonism sensitizes cytotoxic T cell-resistant HIV reservoirs to elimination ex vivo. *J. Clin. Invest.* **130**, 2542–2559 (2020).

41. Huang, S. H. et al. Latent HIV reservoirs exhibit inherent resistance to elimination by $CD8^+$ T cells. *J. Clin. Invest.* **128**, 876–889 (2018).

42. Estes, J. D. et al. Defining total-body AIDS-virus burden with implications for curative strategies. *Nat. Med.* **23**, 1271–1276 (2017).

43. Crotty, S. T follicular helper cell biology: a decade of discovery and diseases. *Immunity* **50**, 1132–1148 (2019).

44. Schenkel, J. M. & Masopust, D. Tissue-resident memory T cells. *Immunity* **41**, 886–897 (2014).

45. Sathaliyawala, T. et al. Distribution and compartmentalization of human circulating and tissue-resident memory T cell subsets. *Immunity* **38**, 187–197 (2013).

46. Banga, R. et al. $PD\text{-}1^+$ and follicular helper T cells are responsible for persistent HIV-1 transcription in treated aviremic individuals. *Nat. Med.* **22**, 754–761 (2016).

47. Buggert, M. et al. The identity of human tissue-emigrant $CD8^+$ T cells. *Cell* **183**, 1946–1961 (2020).

48. Reuter, M. A. et al. HIV-specific $CD8^+$ T cells exhibit reduced and differentially regulated cytolytic activity in lymphoid tissue. *Cell Rep.* **21**, 3458–3470 (2017).

49. Baaten, B. J. et al. CD44 regulates survival and memory development in Th1 cells. *Immunity* **32**, 104–115 (2010).

50. Yuan, Y., Yang, Y. & Huang, X. IL-21 is required for CD4 memory formation in response to viral infection. *JCI Insight* **2**, e90652 (2017).

51. Ostiguy, V., Allard, E. L., Marquis, M., Leignadier, J. & Labrecque, N. IL-21 promotes T lymphocyte survival by activating the phosphatidylinositol-3 kinase signaling cascade. *J. Leukoc. Biol.* **82**, 645–656 (2007).

52. Pagan, A. J., Pepper, M., Chu, H. H., Green, J. M. & Jenkins, M. K. CD28 promotes $CD4^+$ T cell clonal expansion during infection independently of its YMNM and PYAP motifs. *J. Immunol.* **189**, 2909–2917 (2012).

53. Ward-Kavanagh, L. K., Lin, W. W., Sedy, J. R. & Ware, C. F. The TNF receptor superfamily in co-stimulating and co-inhibitory responses. *Immunity* **44**, 1005–1019 (2016).

54. Martin, M. Cutadapt removes adapter sequences from high-throughput sequencing reads. *EMBnet J.* **17**, 10–12 (2011).

55. Li, H. & Durbin, R. Fast and accurate short read alignment with Burrows-Wheeler transform. *Bioinformatics* **25**, 1754–1760 (2009).

56. Li, H. et al. The Sequence Alignment/Map format and SAMtools. *Bioinformatics* **25**, 2078–2079 (2009).

57. Li, H. A statistical framework for SNP calling, mutation discovery, association mapping and population genetical parameter estimation from sequencing data. *Bioinformatics* **27**, 2987–2993 (2011).

58. Aitchison, J. Measures of location of compositional data sets. *Math. Geol.* **21**, 787–790 (1989).

59. Cao, J. et al. The single-cell transcriptional landscape of mammalian organogenesis. *Nature* **566**, 496–502 (2019).

60. Melville, J. uwot: the uniform manifold approximation and projection (UMAP) method for dimensionality reduction. R package version 0.1.9. https://CRAN.R-project.org/package=uwot (2020).

61. Rose, P. P. & Korber, B. T. Detecting hypermutations in viral sequences with an emphasis on G–> A hypermutation. *Bioinformatics* **16**, 400–401 (2000).

62. Edgar, R. C. MUSCLE: multiple sequence alignment with high accuracy and high throughput. *Nucleic Acids Res.* **32**, 1792–1797 (2004).

63. Benjamini, Y. & Hochberg, Y. Controlling the false discovery rate: A practical and powerful approach to multiple testing. *J. R. Stat. Soc. B* **57**, 289–300 (1995).

64. R Core Team *R: A Language and Environment for Statistical Computing*, http://www.R-project.org (R Foundation for Statistical Computing, 2019).

# Acknowledgements

M.L. is supported by NIH grants AI117841, AI120008, AI130005, DK120387, AI152979, AI155233, AI135940 and AI169768, by the American Foundation for AIDS Research (amfAR, no. 110181-69-RGCV) and by the Campbell Foundation. X.G.Y. is supported by NIH grants AI155171, AI116228, AI078799, HL134539 and DA047034, amfAR ARCHE grant no. 110393-72-RPRL and the Bill and Melinda Gates Foundation (INV-002703). M.L. and X.G.Y. are members of the DARE, ERASE, PAVE and BEAT-HIV Martin Delaney Collaboratories (UM1 AI164560, AI164562, AI164566 and AI164570). Collection of LN samples was supported by a donation from M. and L. Schwartz.

# Author information

Author notes

1. These authors contributed equally: Weiwei Sun, Ce Gao

2. These authors jointly supervised this work: Xu G. Yu, Mathias Lichterfeld

## Authors and Affiliations

1. Ragon Institute of MGH, MIT and Harvard, Cambridge, MA, USA

   Weiwei Sun, Ce Gao, Ciputra Adijaya Hartana, Matthew R. Osborn, Kevin B. Einkauf, Xiaodong Lian, Benjamin Bone, Nathalie Bonheur, Bruce D. Walker, Xu G. Yu & Mathias Lichterfeld

2. Infectious Disease Division, Brigham and Women's Hospital, Boston, MA, USA

   Weiwei Sun, Ce Gao, Kevin B. Einkauf, Xiaodong Lian, Benjamin Bone, Xu G. Yu & Mathias Lichterfeld

3. National Institute of Allergies and Infectious Diseases, Bethesda, MD, USA

   Tae-Wook Chun

4. Infectious Disease Division, Massachusetts General Hospital, Boston, MA, USA

   Eric S. Rosenberg & Bruce D. Walker

5. Howard Hughes Medical Institute, Chevy Chase, MD, USA

   Bruce D. Walker

6. Institute for Medical Engineering and Sciences and Department of Biology, Massachusetts Institute of Technology, Cambridge, MA, USA

Bruce D. Walker

### Contributions

Design and performance of PheP-seq assay: W.S., M.R.O., K.B.E., C.G., X.G.Y., M.L. Cell sorting: W.S., C.A.H., N.B. HIV-1 reservoir cell killing assay: W.S., C.A.H. HIV-1 sequencing assays: W.S., X.L., B.B. Biological specimen contribution: E.S.R., T.-W.C., B.D.W. Bioinformatics analysis: C.G. Data analysis, interpretation, presentation: C.G., W.S., M.R.O., C.A.H., X.G.Y., M.L. Study concept and supervision: X.G.Y., M.L. W.S. and C.G. contributed equally to this work and shared the first authorship; C.A.H. and M.R.O. contributed equally to this work and shared the second authorship.

### Corresponding author

Correspondence to Mathias Lichterfeld.

## Ethics declarations

### Competing interests

The authors declare no competing interests.

## Peer review

### Peer review information

*Nature* thanks the anonymous reviewers for their contribution to the peer review of this work. Peer reviewer reports are available.

## Additional information

**Publisher’s note** Springer Nature remains neutral with regard to jurisdictional claims in published maps and institutional affiliations.

# Extended data figures and tables

## Extended Data Fig. 1 Single-cell proteogenomic profiling of HIV-1 reservoir cells from peripheral blood.

(A): Schematic representation of the experimental workflow for the PheP-seq assay. (B): Virograms summarizing individual HIV-1 DNA amplification products in single HIV-1-infected cells from study participants 1, 3, 4 and 5. Each row represents data from one infected cell; numbers of sequences meeting criteria for categories 1, 2, 3 and 4 are shown. For longer amplification products (amplicons 5, 10, 12), centrally located nucleotides could not be efficiently amplified using the Illumina NextSeq 2 x 150-bp sequencing read length used in this study. (C): Highlighter plots reflecting representative clonal proviral sequences identified by PheP-seq. Sequencing data from all 18 amplification products from each single cell were fused. Sequencing reads corresponding to defined virus-host junctions and corresponding chromosomal IS are indicated. Gray areas reflect gaps in sequencing reads related to incomplete sequence coverage. Graphics in **a** and **b** were created using BioRender.com.

## Extended Data Fig. 2 Clinical and demographical data of study participants donating peripheral blood samples.

(A) summarizes longitudinal CD4 T cell counts and viral loads; red arrows indicate the timepoints of PBMC sample collection. Note that study participant 3 is an elite controller or post-treatment controller. In study participant 4, continuous suppressive antiretroviral therapy since 1995 was documented, but individual viral load test results were not available for review by study team. (B) demonstrates sex and age at the time of study participation. (C): Cell numbers analyzed at each timepoint from each study participant in each cell category.

## Extended Data Fig. 3 Global phenotypic analysis of HIV-1 reservoir cells from peripheral blood.

(A): Pie charts indicating proportional contributions of cells in each of the phenotypic clusters (defined in Fig. 2a) to the total number of cells in indicated cell categories. Heatmap reflects FDR-adjusted p-values from comparisons between individual pie charts, based on two-sided chi-squared tests. (B): UMAP plots displaying the expression of selected surface markers across all five UMAP spherical clusters. (C): UMAP plots generated from all category 1 cells; positioning of category 2-4 cells is indicated individually.

## Extended Data Fig. 4 Comprehensive phenotypic profile of HIV-1 reservoir cells from peripheral blood.

(A): Density plots reflecting surface expression of selected phenotypic markers in cells harboring intact proviruses detected only once (non-clonal intact, category 2.1) and in cells harboring clonal intact proviruses (clonal intact, category 3.1). (B): Density plots reflecting surface expression of indicated phenotypic markers on HIV-1-infected peripheral blood mCD4$^{+}$ T cells from categories 1-4. Category 0 cells are shown as reference.

## Extended Data Fig. 5 Additional phenotypic characteristics of HIV-1 reservoir cells from peripheral blood.

(A): Volcano plots displaying enrichment ratios and corresponding FDR-adjusted p-values for all 53 surface markers included in this study for comparisons between indicated HIV-1 reservoir cell populations. Selected markers are labeled individually. Marker sensitivities are indicated by the sizes of their corresponding dots. Bootstrapped data from comparisons between indicated categories of cells are shown. Significance was tested using a two-sided chi-squared test. (B): Ensemble expression of immune activation markers on HIV-1 reservoir cells. SPICE diagrams reflect proportions of cells in each category expressing 0, 1, 2, 3, 4 or 5 of the indicated T cell activation markers. Overlaying arches reflect proportions of cells expressing individual markers. (C): Ensemble expression of indicated phenotypic markers on category 0, 1, 2 HIV-1 reservoir cells at early and late

timepoints after ART initiation in study participants P1 and P2. (B-C): One diagram is shown for each indicated category of cells. Significance was tested using an FDR-adjusted permutation test.

## Extended Data Fig. 6 Orthogonal validation of phenotypic signatures of HIV-1 reservoir cells using fluorescence-activated cell sorting of patient-derived memory $CD4^+$ T lymphocytes.

(A): Representative flow cytometry dot plots demonstrating the gating strategy for $mCD4^+$ T cell populations isolated from peripheral blood; gates used for sorting (G1-G4) are indicated. (B): Flow cytometry plots for displaying expression of indicated markers on non-$CD4^+$ T cells are shown for comparative purposes. (C): Frequencies of intact proviruses, sequence-identical clonal proviruses (including both intact and defective proviruses) and non-clonal defective proviruses in indicated, sorted $mCD4^+$ T cell subpopulations, determined by near full-length proviral sequencing (FLIP-seq). (D): Phylogenetic tree of all intact proviruses retrieved from sorted $mCD4^+$ T cell subpopulations. Note that in study participant D, the majority of intact proviruses were detected within $mCD4^+$ T cells that were negative for PD-1, TIGIT, HVEM and PVR but positive for BTLA/KLRG-1 and/or HLA-E/PD-L1.

## Extended Data Fig. 7 Orthogonal validation of phenotypic signatures of HIV-1 reservoir cells using fluorescence-activated cell sorting of patient-derived memory $CD4^+$ T lymphocytes.

(A): Representative flow cytometry dot plots demonstrating the gating strategy for memory $CD4^+$ T cell populations isolated from peripheral blood; gates used for sorting (G1-G4) are indicated. (B): Flow cytometry plots for displaying expression of indicated markers on non-$CD4^+$ T cells are shown for comparative purposes. (C): Frequencies of intact proviruses, sequence-identical clonal proviruses (including both intact and defective proviruses) and non-clonal defective proviruses in indicated, sorted memory $CD4^+$ T cell subpopulations, determined by near full-length proviral sequencing (FLIP-seq). (D): Phylogenetic tree of all intact proviruses retrieved from

sorted mCD4$^+$ T cell subpopulations. Note that in study participant D, the majority of intact proviruses were detected within memory CD4$^+$ T cells that were negative for PD-1, TIGIT, HVEM and PVR but positive for BTLA/KLRG-1 and/or HLA-E/PD-L1.

## Extended Data Fig. 8 Evaluation of the susceptibility of HIV-1 reservoir cells to cytotoxic effects of HIV-1-specific CD8$^+$ T cell clones.

(A): Patient-derived memory CD4$^+$ T cells were pulsed with indicated epitopic peptides, followed by exposure to HIV-1-specific CD8$^+$ T cell clones matched to the indicated autologous HLA class I alleles and recognizing the epitopic peptides used for target cell pulsing. Following incubation for 16 h, viable CD3$^+$ CD4$^+$ T cells were sorted and subjected to assessments of intact proviruses using the IPDA. Data indicate frequencies of intact proviruses in patient-derived cells, relative to autologous control cells incubated with the same antigen-specific CD8$^+$ T cell clones in the absence of prior peptide pulsing. Frequencies of total HIV-1 DNA in sorted cells, evaluated by the IPDA, are shown for comparison. Experiments were conducted at indicated effector-to-target cell ratios, taking into consideration the CTL clone and target cell availability and the killing potency of the CTL clones. L. O. D. Limit of detection, reflecting the number of cells analyzed without target identification. (B): Summary of data shown in A. Geometric symbols reflect individual CTL and target cell pairs. p-value adjusted for multiple comparison was determined by two-sided Wilcoxon matched-pairs signed rank test.

## Extended Data Fig. 9 Clinical and demographical data of study participants donating lymph node samples.

(A) summarizes longitudinal CD4$^+$ T cell counts and viral loads; red arrows indicate the timepoints of LN sample collection. In study participants P6 and P8, continuous suppressive antiretroviral therapy since 2001/2002 was documented, but individual viral load test results were not available for review by study team. In study participant P7, undetectable plasma viremia was documented since 2004, but clinical records summarizing antiretroviral

treatment history prior to 2012 were not available to study team. (B) demonstrates sex and age at the time of study participation. (C): Cell numbers analyzed from each study participant in each cell category.

### Extended Data Fig. 10 Additional phenotypic properties of HIV-1 reservoir cells from lymph nodes.

(A): Density plots reflecting the surface expression of indicated phenotypic markers on HIV-1-infected $mCD4^{+}$ T cells in lymph nodes from categories 1, 2 and 4. Category 0 cells are shown for comparison. (B): Exploratory comparison of selected phenotypic markers between reservoir cells from peripheral blood and lymph nodes. Data reflect fold-changes in expression intensities of indicated surface markers in category 1 cells (all HIV-1-infected cells) and category 2 cells (enriched for cells harboring intact HIV-1 proviruses), normalized to category 0 cells (uninfected cells), from peripheral blood and lymph nodes. Significance was tested using two-sided Mann Whitney U tests, FDR-adjusted p-values are shown.

## Supplementary information

### Reporting Summary

### Peer Review File

### Supplementary Table 1

Primers used for amplification of 18 different HIV-1 segments and of indicated virus–host junctions.

### Supplementary Table 2

PheP-seq sequencing quality control metrics.

### Supplementary Table 3

Relative enrichment ratios for all phenotypic markers in indicated HIV-1 reservoir cell categories from PB and LNs.

## Rights and permissions

**Open Access** This article is licensed under a Creative Commons Attribution 4.0 International License, which permits use, sharing, adaptation, distribution and reproduction in any medium or format, as long as you give appropriate credit to the original author(s) and the source, provide a link to the Creative Commons licence, and indicate if changes were made. The images or other third party material in this article are included in the article's Creative Commons licence, unless indicated otherwise in a credit line to the material. If material is not included in the article's Creative Commons licence and your intended use is not permitted by statutory regulation or exceeds the permitted use, you will need to obtain permission directly from the copyright holder. To view a copy of this licence, visit http://creativecommons.org/licenses/by/4.0/.

Reprints and Permissions

## About this article

### Cite this article

Sun, W., Gao, C., Hartana, C.A. *et al.* Phenotypic signatures of immune selection in HIV-1 reservoir cells. *Nature* **614**, 309–317 (2023). https://doi.org/10.1038/s41586-022-05538-8

- Received: 02 March 2022
- Accepted: 08 November 2022
- Published: 04 January 2023
- Issue Date: 09 February 2023
- DOI: https://doi.org/10.1038/s41586-022-05538-8

### Share this article

Anyone you share the following link with will be able to read this content:

Get shareable link

Sorry, a shareable link is not currently available for this article.

Copy to clipboard

Provided by the Springer Nature SharedIt content-sharing initiative

## This article is cited by

- **[Silence, escape and survival drive the persistence of HIV]**
  - Nicolas Chomont

  *Nature* (2023)

### Silence, escape and survival drive the persistence of HIV

- Nicolas Chomont

Nature News & Views 04 Jan 2023

---

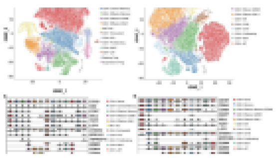
This article was downloaded by **calibre** from https://www.nature.com/articles/s41586-022-05538-8



## Profound phenotypic and epigenetic heterogeneity of the HIV-1-infected CD4+ T cell reservoir

19 December 2022

Vincent H. Wu, Jayme M. L. Nordin, … Michael R. Betts



## Global transcriptomic characterization of T cells in individuals with chronic HIV-1 infection

28 March 2022

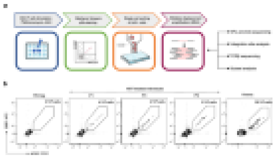
Xiang-Ming Wang, Ji-Yuan Zhang, … Fu-Sheng Wang



## Phenotypic signatures of immune selection in HIV-1 reservoir cells

04 January 2023

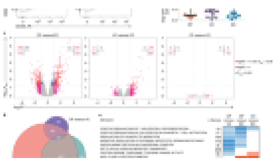
Weiwei Sun, Ce Gao, … Mathias Lichterfeld



## In-depth single-cell analysis of translation-competent HIV-1 reservoirs identifies cellular sources of plasma viremia

17 June 2021

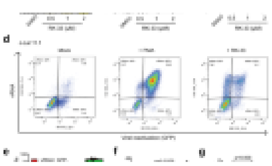
Basiel Cole, Laurens Lambrechts, … Linos Vandekerckhove



## Altered differentiation is central to HIV-specific CD4+ T cell dysfunction in progressive disease

15 July 2019

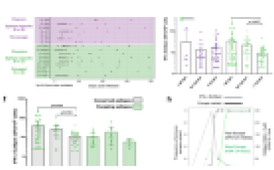
Antigoni Morou, Elsa Brunet-Ratnasingham, … Daniel E. Kaufmann



## Selective cell death in HIV-1-infected cells by DDX3 inhibitors leads to depletion of the inducible reservoir

30 April 2021

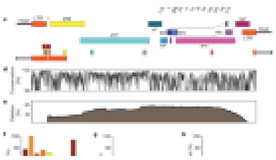
Shringar Rao, Cynthia Lungu, … Tokameh Mahmoudi



## Identification of human progenitors of exhausted CD8+ T cells associated with elevated IFN-γ response in early phase of viral infection

07 December 2022

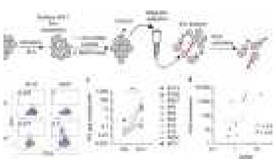
Curtis Cai, Jerome Samir, … Fabio Luciani



## A quantitative approach for measuring the reservoir of latent HIV-1 proviruses

30 January 2019

Katherine M. Bruner, Zheng Wang, … Robert F. Siliciano



## Clonal CD4+ T cells in the HIV-1 latent reservoir display a distinct gene profile upon reactivation

23 April 2018

Lillian B. Cohn, Israel T. da Silva, … Michel C. Nussenzweig

- Article
- Open Access
- Published: 04 January 2023

# HIV silencing and cell survival signatures in infected T cell reservoirs


- Iain C. Clark,
- Prakriti Mudvari,
- Shravan Thaploo,
- Samuel Smith,
- Mohammad Abu-Laban,
- Mehdi Hamouda,
- Marc Theberge,
- Sakshi Shah,
- Sung Hee Ko,
- Liliana Pérez,
- Daniel G. Bunis,
- James S. Lee,
- Divya Kilam,
- Saami Zakaria,
- Sally Choi,
- Samuel Darko,
- Amy R. Henry,
- Michael A. Wheeler,
- Rebecca Hoh,
- Salwan Butrus,
- Steven G. Deeks,
- Francisco J. Quintana,
- Daniel C. Douek,
- Adam R. Abate &
- …
- Eli A. Boritz


Show authors

*Nature* **volume 614**, pages 318–325 (2023)

- 14k Accesses
- 3 Citations
- 103 Altmetric
- Metrics details

## Abstract

Rare CD4 T cells that contain HIV under antiretroviral therapy represent an important barrier to HIV cure[1,2,3], but the infeasibility of isolating and characterizing these cells in their natural state has led to uncertainty about whether they possess distinctive attributes that HIV cure-directed therapies might exploit. Here we address this challenge using a microfluidic technology that isolates the transcriptomes of HIV-infected cells based solely on the detection of HIV DNA. HIV-DNA$^+$ memory CD4 T cells in the blood from people receiving antiretroviral therapy showed inhibition of six transcriptomic pathways, including death receptor signalling, necroptosis signalling and antiproliferative Gα12/13 signalling. Moreover, two groups of genes identified by network co-expression analysis were significantly associated with HIV-DNA$^+$ cells. These genes ($n$ = 145) accounted for just 0.81% of the measured transcriptome and included negative regulators of HIV transcription that were higher in HIV-DNA$^+$ cells, positive regulators of HIV transcription that were lower in HIV-DNA$^+$ cells, and other genes involved in RNA processing, negative regulation of mRNA translation, and regulation of cell state and fate. These findings reveal that HIV-infected memory CD4 T cells under antiretroviral therapy are a distinctive population with host gene expression patterns that favour HIV silencing, cell survival and cell proliferation, with important implications for the development of HIV cure strategies.

## Main

Understanding how HIV persists during antiretroviral therapy (ART) can advance the search for a safe and scalable HIV cure. A central example of

this is the latent reservoir concept, in which some HIV proviruses are thought to persist by maintaining a quiescent state that spares their host cells from virus- or immune-mediated killing[2]. Evidence supporting this concept includes the presence of rare memory CD4 T cells in ex vivo samples that inducibly express HIV[1,3,4], as well as data from culture models demonstrating molecular blocks to HIV transcription, particularly in resting cells[5,6,7,8,9,10,11]. These and other findings have prompted the development of latency-reversing agents (LRAs) that can induce HIV transcription with the goal of exposing infected cells to elimination in vivo. However, the lack of a demonstrable reduction in reservoir size in clinical trials of LRAs[12,13,14,15,16] has emphasized how much remains unknown about the barriers to an HIV cure. Of particular importance is the long-standing uncertainty about the biology of HIV-infected CD4 T cell reservoirs. As cells containing quiescent viruses in the blood and tissues have not been identifiable without substantial manipulation, it has been impossible to establish whether these rare cells have special attributes that favour HIV latency or otherwise help to account for HIV persistence under ART. Studies attempting to circumvent this obstacle by detecting HIV enrichment in phenotypic, functional or anatomic CD4 T cell subsets[17,18,19,20,21,22,23,24,25,26,27]—in some cases using advanced single-cell analyses[28,29]—have found low levels of infected cells across subsets and emphasized the heterogeneity of the infected cell pool. Thus, the identification of distinctive biological signatures among HIV-infected CD4 T cells under ART has emerged as a central challenge in HIV cure research.

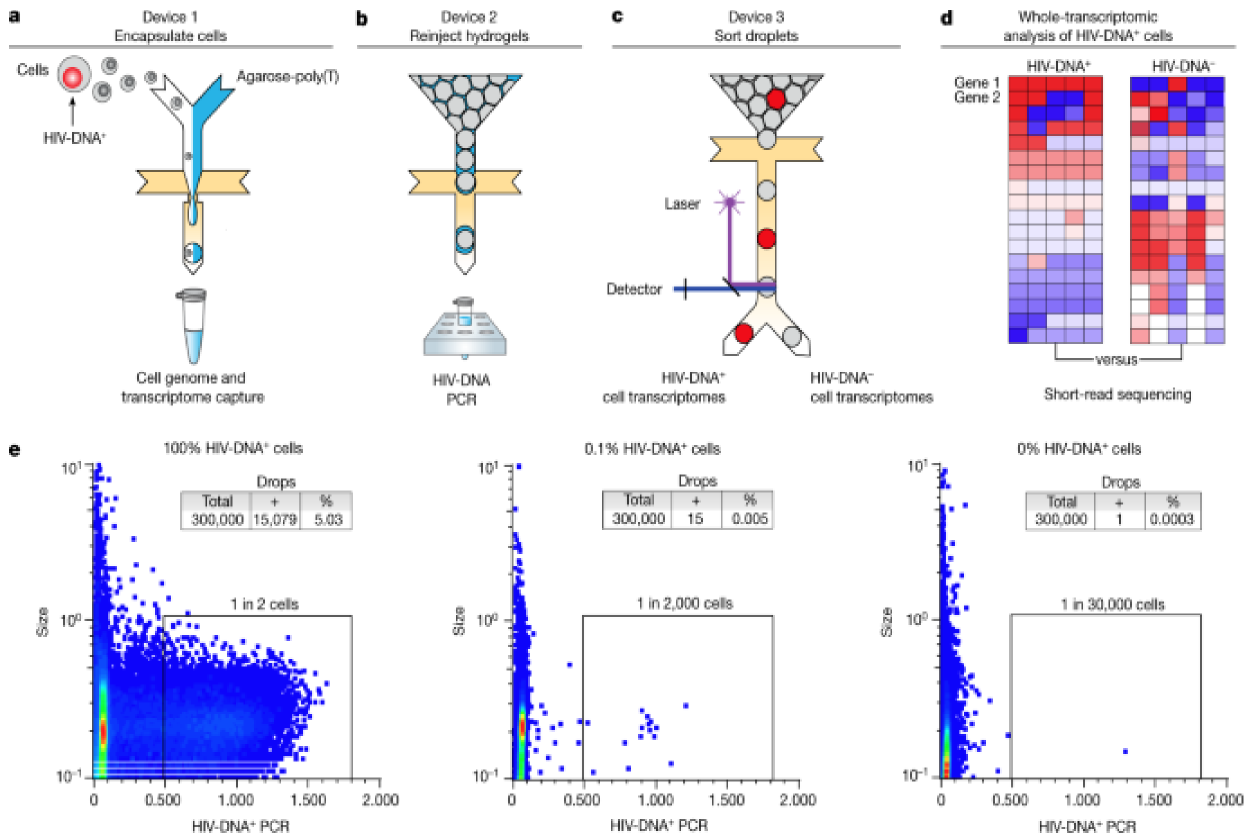
To help address this challenge, we developed a custom microfluidic technology that enables the unbiased detection and gene expression profiling of HIV-infected cells directly ex vivo. The technology, termed focused interrogation of cells by nucleic acid detection and sequencing (FIND-seq)[30], separates millions of single cells within water-in-oil droplets for immediate lysis, followed by polyadenylated RNA sequence recovery and then sorting according to HIV DNA detection. This approach isolates whole transcriptomes from cells containing quiescent viruses without the need for in vitro latency reversal, thereby capturing a transcriptome-wide profile of these cells in their natural state. Here we used FIND-seq in people with HIV receiving long-term ART to analyse host gene expression patterns of memory CD4 T cells containing HIV *gag* DNA—a marker of the HIV-

infected cell reservoir that encompasses both intact and defective virus sequences[31]. Our results reveal distinctive transcriptomic signatures that help to explain HIV-infected CD4 T cell persistence despite the suppression of virus replication, highlighting important opportunities for further progress towards an HIV cure.

# HIV-DNA$^+$ cell transcriptome sorting

FIND-seq uses three microfluidic devices to isolate polyadenylated RNA sequences from HIV-DNA$^+$ cells (Fig. 1a–c). The first device loads millions of single cells into water-in-oil droplets with a strongly denaturing lysis buffer and molten agarose covalently conjugated to oligo-dT (Fig. 1a). After encapsulation, the agarose in each single-cell droplet is cooled to form a hydrogel that retains high-molecular-mass DNA as well as polyadenylated RNA. This approach maintains compartmentalization among cells during oil removal, incubations, washes and reagent exchanges, therefore enabling optimized cell lysis, mRNA reverse-transcription and subsequent PCR while preventing interference between steps (Extended Data Fig. 1a–d). The second device reinjects washed hydrogels containing single-cell transcriptome cDNA and genomic DNA into a second emulsion for HIV *gag* DNA detection (Fig. 1b). The third device uses an accurate dielectrophoretic sorter[32] to separate droplets on the basis of their fluorescence (Fig. 1c) for subsequent whole-transcriptomic analysis (Fig. 1d and Extended Data Fig. 1e). Using dilutions of latently infected human J-Lat T cells in uninfected human Jurkat T cells, FIND-seq droplet cytometry detected HIV-DNA$^+$ cells with an estimated sensitivity of 50% and a per-droplet false-positive rate of 1 in 300,000 (Fig. 1e). Transcriptome sequencing in HIV-DNA$^+$ droplets sorted from a 1:1 mixture of J-Lat and mouse cells revealed >99% human sequences (Extended Data Fig. 1f,g). These findings demonstrate that FIND-seq accurately detects rare HIV-DNA$^+$ cells and isolates the transcriptomes from these cells.

**Fig. 1: Whole-transcriptomic analysis of HIV-DNA$^+$ cells using FIND-seq.**




**a**–**d**, Overview of the workflow, including three sequential microfluidic devices separated by handling steps. **a**, On the first device, single cells are encapsulated at a limiting dilution in a water-in-oil emulsion with lysis buffer and molten agarose-poly(T). The agarose is then cooled to form a hydrogel bead that retains genomic DNA and polyadenylated RNA. After oil removal, whole-transcriptome cDNA is covalently linked to the hydrogel by reverse transcription for subsequent whole-transcriptome amplification (WTA) using PCR (see Extended Data Fig. 1a–e). **b**,**c**, Hydrogel beads re-encapsulated on the second device are analysed using droplet PCR for HIV *gag* (**b**) and then sorted on the third device (**c**). **d**, The processing steps performed after droplet sorting include WTA, library preparation and sequencing, and bioinformatic comparison of HIV-DNA$^{+}$ cells and HIV-DNA$^{-}$ cells. **e**, Droplet cytometry plots demonstrating the analysis of pure HIV-DNA$^{+}$ J-Lat T cells (left), pure HIV-DNA$^{-}$ Jurkat T cells (right), and a mixture of 0.1% J-Lat and 99.9% Jurkat cells (middle). Cells were encapsulated at 1 cell per 10 droplets.

# Transcriptome sequencing after FIND-seq

We tested whether FIND-seq-sorted transcriptomes accurately represent the cells from which they are sorted by using mixtures of J-Lat T cells and Raji human B cells (Extended Data Fig. 2a). We cultured J-Lat and Raji cell lines separately and performed RNA sequencing (RNA-seq) analysis of each using standard protocols. At the same time, a 1:100 mixture of J-Lat and Raji cells was analysed using FIND-seq (Extended Data Fig. 2b). Gene expression differences between J-Lat and Raji cells after standard processing were highly correlated with differences between HIV-DNA$^{+}$ and HIV-DNA$^{-}$ cells after FIND-seq processing ($R = 0.47$, $P = 2.2 \times 10^{-16}$; Extended Data Fig. 2c). Furthermore, differential expression between J-Lat and Raji cells analysed using FIND-seq identified canonical T cell and B cell genes (Extended Data Fig. 2d) and agreed with published findings (Extended Data Fig. 2e). These results demonstrate that FIND-seq can be used to study the transcriptomic signatures of rare HIV-DNA$^{+}$ cells.

## FIND-seq of HIV-DNA$^{+}$ cells ex vivo

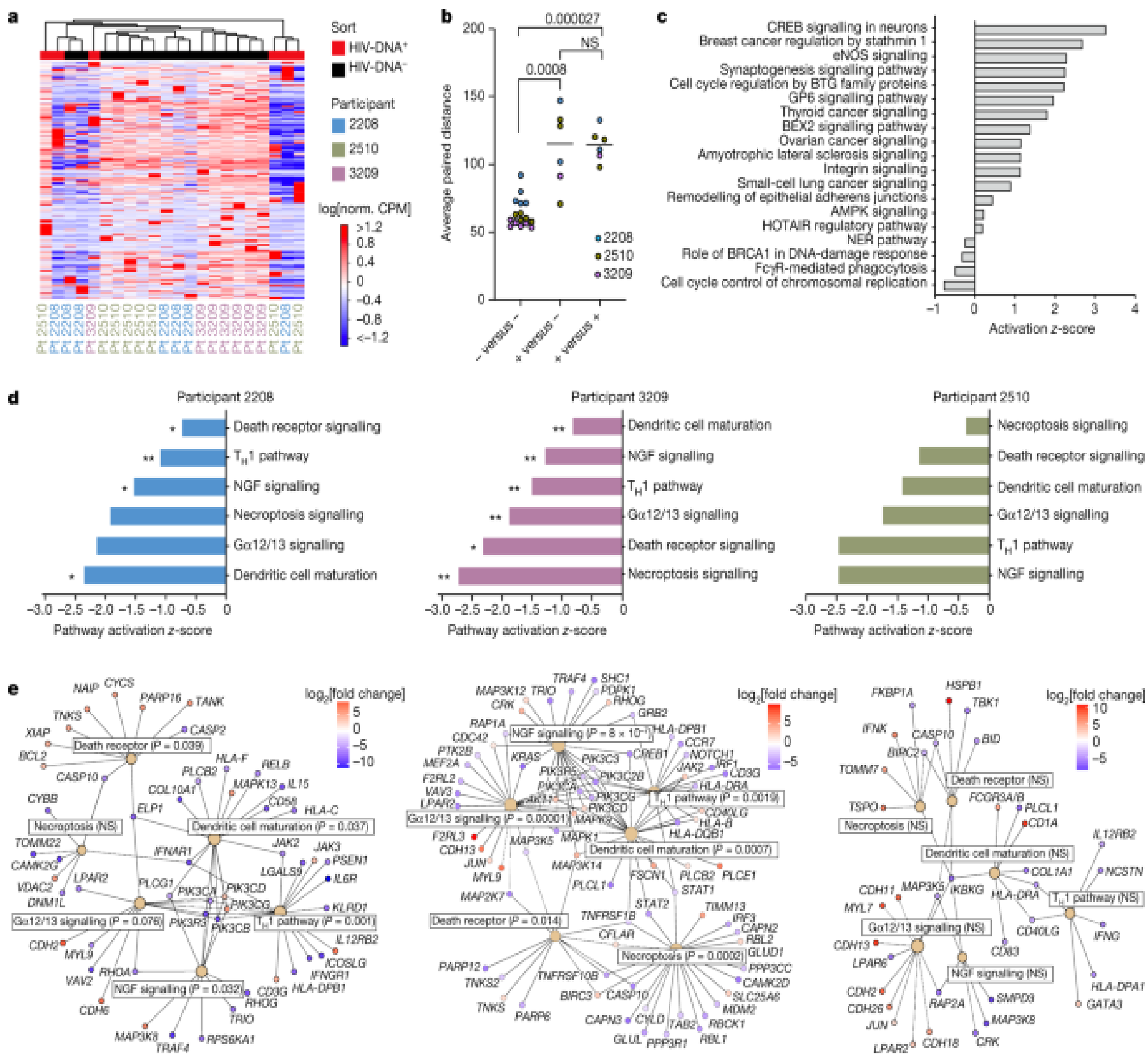
To define gene expression patterns of HIV-DNA$^{+}$ memory CD4 T cells under ART, we applied FIND-seq to magnetically purified memory CD4 T cell samples from five people with HIV receiving long-term ART that was initiated during chronic infection (Supplementary Table 1). Droplet cytometry data acquired during sorting demonstrated between 534 and 2,153 HIV-DNA$^{+}$ cells per million (Extended Data Fig. 3a), consistent with previous studies using quantitative PCR analysis of extracted DNA[19,20]. False-positive frequencies of HIV-DNA$^{+}$ memory CD4 T cells measured in three HIV-uninfected control participants ranged between 7 and 19 per million (Extended Data Fig. 3b). To maximize sorted transcriptome cDNA quantity and therefore reduce the need for extensive whole-transcriptome amplification (WTA) that could skew gene abundance in the sequencing libraries, we collected all droplets after HIV detection PCR in aliquots of 100 cell-equivalents. Sorting resulted in different numbers of aliquots collected across participants owing to the different frequencies of HIV-DNA$^{+}$ cells (Extended Data Fig. 3c). After WTA and sequencing, we used a prospective curation process to select only those samples with a high library quality for further analysis (Methods). This resulted in a set of 22 curated

samples from three people with HIV (Supplementary Table 2 and Extended Data Fig. 4).

## Host transcriptomes of HIV-DNA$^+$ cells

Using the curated dataset (Supplementary Table 3), we first compared host gene expression between HIV-DNA$^+$ and HIV-DNA$^-$ memory CD4 T cells at the global level. Unsupervised clustering revealed partial segregation between HIV-DNA$^+$ and HIV-DNA$^-$ cell transcriptomes (Fig. 2a), and the use of Euclidean distance as a summary measure of transcriptomic relatedness demonstrated that distances between HIV-DNA$^+$ and HIV-DNA$^-$ cell samples were significantly greater than distances among HIV-DNA$^-$ cell samples ($P = 8.0 \times 10^{-4}$; Fig. 2b). However, we also observed sample clustering by participant (Fig. 2a) as well as significantly greater Euclidean distances among HIV-DNA$^+$ cell samples than among HIV-DNA$^-$ cell samples ($P = 2.7 \times 10^{-5}$; Fig. 2b). We conclude that the whole-transcriptome clustering analysis suggested distinctive host gene expression by HIV-DNA$^+$ memory CD4 T cells, but also indicated that transcriptomic differences among populations of HIV-DNA$^+$ cells and across study participants are substantial sources of variation in the dataset.

**Fig. 2: Host transcriptomic pathways in HIV-DNA$^+$ memory CD4 T cells under ART.**



**a**, Unsupervised clustering analysis of HIV-DNA$^{+}$ (red) and HIV-DNA$^{-}$ (black) cell samples by expression of all protein-coding genes in the measured transcriptome. Norm., normalized; Pt, participant. **b**, The average Euclidean distances between sorted samples, defined by pairwise comparison of each HIV-DNA$^{-}$ sample to all other HIV-DNA$^{-}$ samples (negative versus negative); each HIV-DNA$^{+}$ sample to all HIV-DNA$^{-}$ samples (positive versus negative); and each HIV-DNA$^{+}$ sample to all other HIV-DNA$^{+}$ samples (positive versus positive). $n = 16$ biologically independent HIV-DNA$^{-}$ and 6 biologically independent HIV-DNA$^{+}$ samples sorted separately from three participants. Median values and $P$ values calculated using Mann–Whitney $U$-tests are shown. **c**, Biological pathways

enriched among DEGs (absolute fold change > 1.5 and FDR ≤ 0.05; Wald Test, Benjamini–Hochberg multiple-testing correction) between HIV-DNA$^{+}$ and HIV-DNA$^{−}$ cells in an analysis treating samples from distinct participants as biological replicates. *z*-scores for pathways with $P < 0.05$ (right-tailed Fisher's exact test) are shown. **d**, Ingenuity pathways with a concordant direction of difference between HIV-DNA$^{+}$ and HIV-DNA$^{−}$ cells in all three participants analysed separately. Statistical analysis was performed using right-tailed Fisher's exact tests; $*P < 0.05$, $**P < 0.001$. Numeric *P* values corresponding to the asterisks are shown in **e**. $T_H1$, T helper 1 cells. **e**, Network plots showing DEGs identified separately in each participant that were part of shared Ingenuity pathways that were found to be inhibited in HIV-DNA$^{+}$ cells across all three participants. Pathways are indicated by tan nodes labelled with the pathway name and *P* value; the node size is proportional to the number of DEGs identified within the pathway. Nodes indicating individual genes are coloured according to the relative expression between HIV-DNA$^{+}$ and HIV-DNA$^{−}$ cells (red, higher in HIV-DNA$^{+}$ cells; blue, lower in HIV-DNA$^{+}$ cells).

Source data

## Host gene differential expression

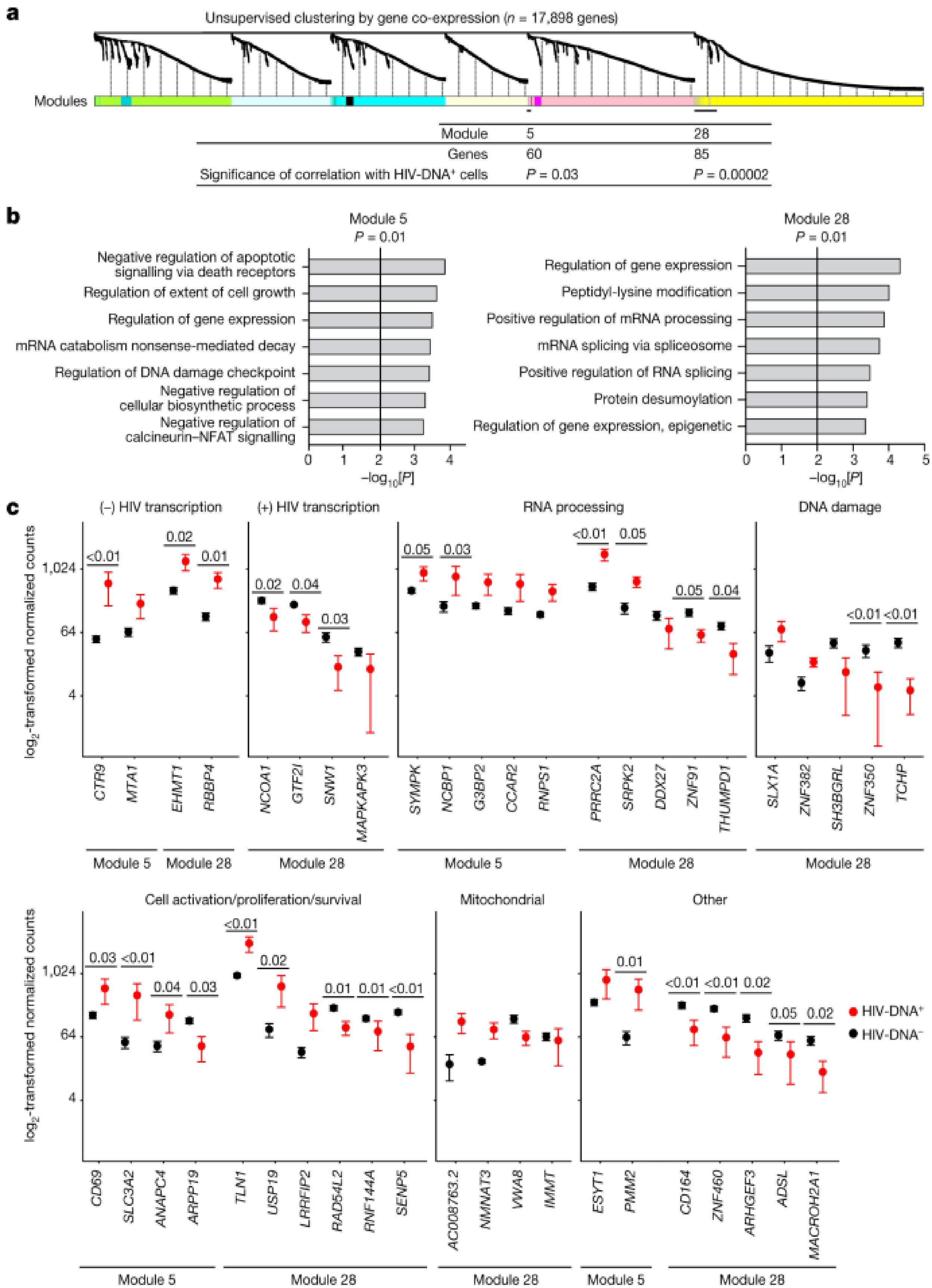
To identify individual genes and transcriptomic pathways that were characteristic of HIV-DNA$^{+}$ memory CD4 T cells, we performed differential gene expression (DGE) analysis using two distinct approaches (Supplementary Table 4). Using a combined approach that analysed participants as biological replicates, we identified 2,776 differentially expressed genes (DEGs; absolute fold change > 1.5, FDR ≤ 0.05) (Extended Data Fig. 5a). Pathway enrichment analysis on the basis of these DEGs yielded several cancer- and cell-cycle-related pathways (Fig. 2c), suggesting differences between HIV-DNA$^{+}$ and HIV-DNA$^{−}$ memory CD4 T cells related to cell proliferation and survival. Notably, a comparison of DEG lists defined for each of the participants separately revealed only 11 DEGs common to all three participants (Extended Data Fig. 5b–d). However, pathway enrichment analysis using participant-specific DEG lists (absolute fold change ≥ 2, $P \leq 0.01$) identified six pathways that shared concordant

direction across participants (Fig. 2d and Supplementary Table 5). All six concordant pathways showed *z*-activation scores of <0, indicating pathway inhibition in HIV-DNA$^+$ cells relative to HIV-DNA$^-$ cells. Notably, these inhibited pathways in HIV-DNA$^+$ cells included death receptor signalling, necroptosis signalling and the anti-proliferative Gα12/13 signalling pathway[33]. Inferences of pathway inhibition arose from both decreased expression of pathway activators and increased expression of pathway inhibitors in HIV-DNA$^+$ cells and depended on differential expression of distinct pathway genes in different participants (Fig. 2e). We conclude that although many individual DEGs distinguishing HIV-DNA$^+$ cells from HIV-DNA$^-$ cells differed between the participants, higher-order analysis revealed that inhibition of cell death and anti-proliferative signalling are shared attributes of HIV-DNA$^+$ memory CD4 T cells under ART.

# Analysis of co-expressed gene signatures

We anticipated that pooled sequencing from diverse HIV-DNA$^+$ memory CD4 T cells under ART could dilute signals from infected cell subpopulations, thereby limiting the detection of informative features of HIV-infected cells in conventional DGE analysis. To identify transcriptomic signatures of HIV-DNA$^+$ cells as groups of genes, we used weighted gene co-expression network analysis (WGCNA) to define gene modules on the basis of correlation patterns across samples (Supplementary Table 6). Within the curated set of 22 samples that together expressed 17,898 different genes, this process produced 28 distinct gene modules of varying sizes (Fig. 3a). Correlating module gene expression patterns with cell infection status (that is, HIV-DNA$^+$ versus HIV-DNA$^-$) identified significant correlations for module 5 (60 genes, $R = 0.46$, $P = 0.03$) and module 28 (85 genes, $R = 0.78$, $P = 2 \times 10^{-5}$) (Fig. 3a). Thus, unsupervised clustering using WGCNA revealed two groups of genes that account for only 0.81% of the measured transcriptome that distinguished HIV-DNA$^+$ from HIV-DNA$^-$ memory CD4 T cells in ART-treated people with HIV.

**Fig. 3: Co-expressed gene signatures in HIV-DNA$^+$ memory CD4 T cells under ART.**


a
Unsupervised clustering by gene co-expression (n = 17,898 genes)
Modules
Module 5 28
Genes 60 85
Significance of correlation with HIV-DNA⁺ cells P = 0.03 P = 0.00002
b
Module 5
P = 0.01
Negative regulation of apoptotic signalling via death receptors
Regulation of extent of cell growth
Regulation of gene expression
mRNA catabolism nonsense-mediated decay
Regulation of DNA damage checkpoint
Negative regulation of cellular biosynthetic process
Negative regulation of calcineurin–NFAT signalling
−log10[P]
Module 28
P = 0.01
Regulation of gene expression
Peptidyl-lysine modification
Positive regulation of mRNA processing
mRNA splicing via spliceosome
Positive regulation of RNA splicing
Protein desumoylation
Regulation of gene expression, epigenetic
−log10[P]
c
(−) HIV transcription
(+) HIV transcription
RNA processing
DNA damage
log2-transformed normalized counts
CTR9 MTA1 EHMT1 RBBP4
NCOA1 GTF2I SNW1 MAPKAPK3
SYMPK NCBP1 G3BP2 CCAR2 RNPS1 PRRC2A SRPK2 DDX27 ZNF91 THUMPD1
SLX1A ZNF382 SH3BGRL ZNF350 TCHP
Module 5 Module 28 Module 28 Module 5 Module 28 Module 28
Cell activation/proliferation/survival
Mitochondrial
Other
CD69 SLC3A2 ANAPC4 ARPP19 TLN1 USP19 LRRFIP2 RAD54L2 RNF144A SENP5
AC008763.2 NMNAT3 VWA8 IMMT
ESYT1 PMM2 CD164 ZNF460 ARHGEF3 ADSL MACROH2A1
Module 5 Module 28 Module 28 Module 5 Module 28
HIV-DNA⁺
HIV-DNA⁻

**a**, The 17,898 genes detected in ≥2 samples from the curated dataset were processed for WGCNA as described in the Methods. A total of 28 resulting modules of genes defined by distinct co-expression patterns across the samples are indicated as coloured segments, with the relatedness among genes indicated by the dendrogram. The two modules that were significantly correlated with the HIV DNA status of the samples are indicated at bottom (module 5, 60 genes, $R = 0.46$, $P = 0.03$; module 28, 85 genes, $R = 0.78$, $P = 2 \times 10^{-5}$; weighted Pearson correlation). **b**, Gene ontology (GO) analysis of module 5 and module 28 gene lists. All significant terms (adjusted $P \leq 0.05$, Fisher's exact test, Benjamini–Hochberg multiple-testing correction) are shown, except for redundant terms that are shown in Supplementary Table 6, but were omitted here for clarity. **c**, Genes from modules 5 and 28 with normalized expression levels that differed by an average of at least twofold between HIV-DNA$^+$ and HIV-DNA$^-$ cells and had a concordant direction of difference in all of the participants. Genes are grouped in individual plots according to putative biological function. *P* values calculated using Wald tests are shown for genes with $P < 0.05$ in the differential expression analysis between HIV-DNA$^+$ and HIV-DNA$^-$ cells. $n = 16$ biologically independent HIV-DNA$^-$ and 6 biologically independent HIV-DNA$^+$ samples sorted separately from 3 participants. Data are mean ± s.e.m.

To characterize the differences between HIV-DNA$^+$ and HIV-DNA$^-$ memory CD4 T cells reflected by these modules, we analysed the module gene lists using Gene Ontology (GO). In both modules, we found statistically significant enrichment (adjusted $P \leq 0.05$) for genes related to the regulation of gene expression at the transcriptional and post-transcriptional levels (Fig. 3b). Module 28 was enriched for GO terms related to mRNA splicing and processing. Module 5 was enriched for genes involved in mRNA degradation by nonsense-mediated decay, which has been linked to negative post-transcriptional regulation of HIV gene expression in vitro[34]. Moreover, module 5 was enriched for terms related to cell survival, activation and proliferation, including regulation of death receptor signalling, regulation of calcineurin–NFAT signalling and DNA-damage checkpoint regulation. We conclude that GO analysis of WGCNA module genes identified transcriptional and post-transcriptional gene regulation as well as several cell state regulatory processes as distinguishing attributes of HIV-DNA$^+$ memory CD4 T cells under ART.

Furthermore, we examined the transcriptomic differences between HIV-DNA$^{+}$ and HIV-DNA$^{-}$ memory CD4 T cells by inspecting a filtered list of the 44 genes in WGCNA modules 5 and 28 that showed at least twofold average difference between HIV-DNA$^{+}$ and HIV-DNA$^{-}$ cell populations and a concordant direction between populations across the participants (Fig. 3c, Extended Data Table 1 and Supplementary Table 6). We noted that 8 out of 44 genes were previously implicated in the regulation of HIV transcription. Four genes were linked to negative regulation of HIV transcription through histone modification (*EHMT1*[35], *RBBP4*[36] and *MTA1*[37]) or promoter-proximal pausing of RNA polymerase II (*CTR9*[38]), and were higher in HIV-DNA$^{+}$ cells. The remaining four genes were linked to positive regulation of HIV transcriptional initiation (*GTF2I*[39] and *MAPKAPK3*[40]) or elongation (*NCOA1*[41] and *SNW1*[42]), and were lower in HIV-DNA$^{+}$ cells. We conclude that host gene expression signatures of HIV-DNA$^{+}$ memory CD4 T cells under ART were relatively non-permissive for HIV transcription.

We next examined the remaining 36 genes from the filtered module 5 and 28 gene lists. Ten of these genes encoded RNA-processing factors. In module 5, these included higher levels in HIV-DNA$^{+}$ cells of antiviral defence factor *NCBP1*[43] and post-splicing complex component *RNPS1*[44], both of which have been linked to nonsense-mediated decay. Module 5 also included higher levels in HIV-DNA$^{+}$ cells of *G3BP2*, a stress granule factor in a gene family that has been implicated in cytoplasmic sequestration and translational inhibition of HIV mRNAs[45]. mRNA-processing factors in module 28 included higher levels in HIV-DNA$^{+}$ cells of *PRRC2A*—a reader of $N^6$-methyladenosine RNA modifications that can be induced by HIV infection in vitro[46]—and the splicing regulator SRPK. Among the additional 26 genes, we noted that module 28 included *USP19* and *LRRFIP2*, which can inhibit apoptosis[47] or pyroptosis[48] and were higher in HIV-DNA$^{+}$ cells, and *TLN1*[49], which is required for antigen-driven T cell proliferation mediated through immunological synapses[49] and was also higher in HIV-DNA$^{+}$ cells. Finally, we noted multiple module 28 genes involved in the DNA-damage response and mitochondrial function. We conclude that the transcriptomic signatures of HIV-DNA$^{+}$ memory CD4 T cells under ART suggest that these cells have the capacity for post-transcriptional HIV

silencing, and are also consistent with DGE-based indications of increased cell survival and proliferation.

## Enrichment of signatures in cell subsets

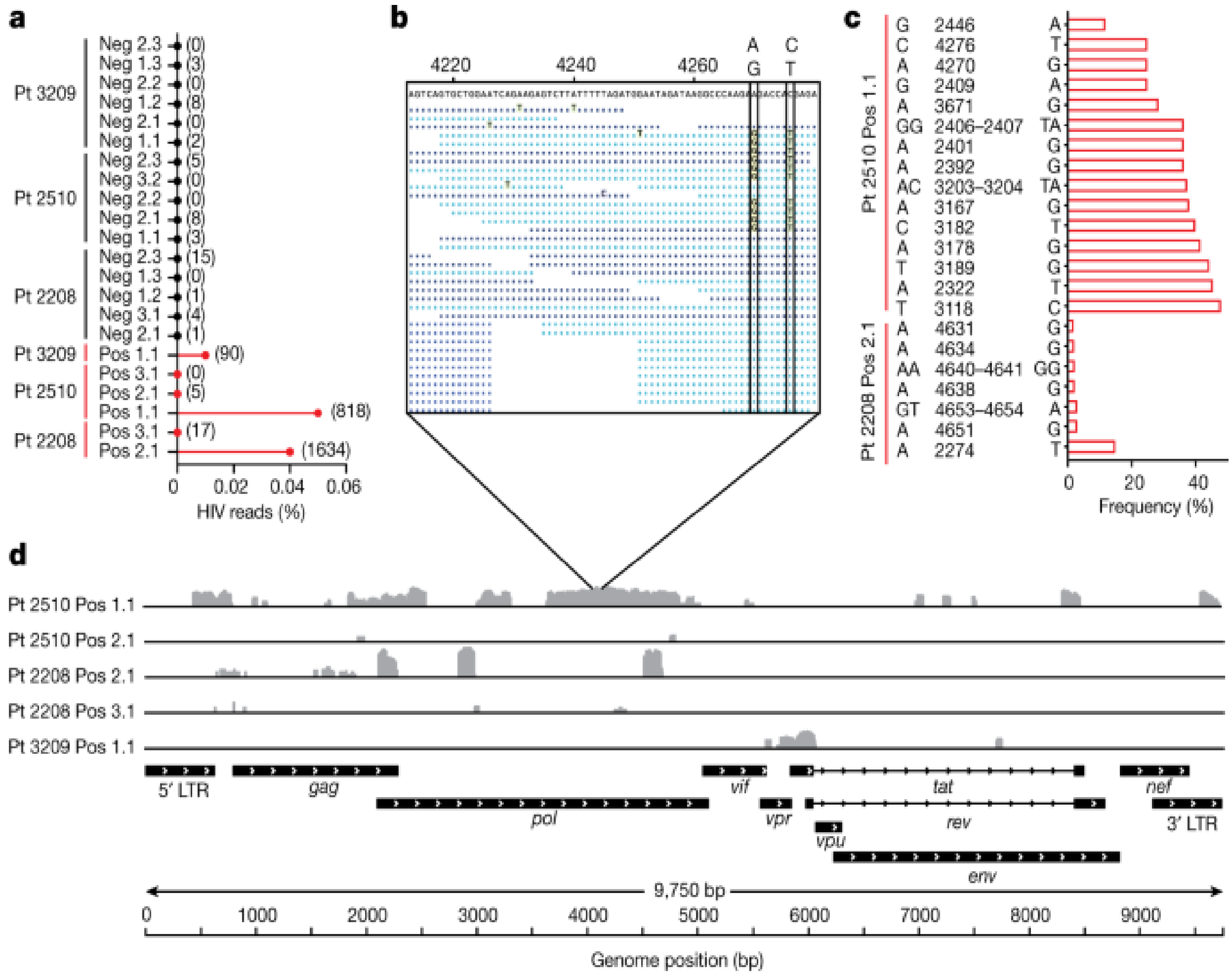
To investigate the origins of HIV-DNA$^+$ memory CD4 T cell transcriptomic signatures identified by co-expression network analysis, we compared these signatures with the transcriptomes of defined CD4 T cell subsets. We isolated circulating naive and memory CD4 T cell subsets from nine ART-treated people with HIV (Supplementary Table 1) using fluorescence-activated cell sorting (FACS) (Extended Data Fig. 6), defined subset gene expression using RNA-seq and finally used gene set enrichment analysis (GSEA) to compare gene expression signatures in the sorted memory subsets (defined by expression relative to the naive subset) against co-expression network analysis signatures of HIV-DNA$^+$ cells (Extended Data Table 2). This revealed significant enrichment of the module 5 signature in memory CD4 T cells of the CD27$^+$CCR7$^+$CD45RO$^+$CXCR5$^+$CCR6$^-$ peripheral T follicular helper ($T_{FH}$) phenotype[50]. No significant enrichment was observed for the module 5 signature in any other subset, or for the module 28 signature in any of the subsets. We conclude that, taken together, the transcriptomic signatures of HIV-DNA$^+$ memory CD4 T cells under ART did not map to defined CD4 T cell subsets, although the module 5 signature showed partial similarity to the signature of CCR6$^-$ peripheral $T_{FH}$ cells in ART-treated people with HIV.

## HIV RNA expression analysis

Finally, we used the curated set of 22 samples to analyse HIV transcriptional patterns in HIV-DNA$^+$ memory CD4 T cells under ART by aligning transcriptome sequence reads to a reference HIV genome (Fig. 4). We found that some HIV-DNA$^+$ cell samples showed hundreds of HIV reads (Fig. 4a), including one sample from participant 2510 with two distinct virus sequences (Fig. 4b,c) that suggested processive HIV transcripts from at least two cells in the sorted aliquot of 100 cells. Nevertheless, HIV read percentages for all HIV-DNA$^+$ cell samples were $<0.05\%$ (Fig. 4a), which is

100-fold lower than previously reported for HIV-expressing cells sequenced after in vitro stimulation[51]. These findings are consistent with latent infection and/or HIV sequence defects that limit virus transcription in HIV-DNA$^+$ cells. HIV genome coverage patterns of mapped reads were notable for isolated peaks interspersed with areas of no coverage (Fig. 4d), suggesting atypical transcription start sites[52], transcripts from proviruses with deletion mutations and/or chance sampling variations. Spliced transcripts were not detected even by manually inspecting and mapping individual mates of read pairs using BLAST. The use of assembly-based tools to produce contigs from reads that did not initially map to the human reference yielded no HIV contigs from 5/6 HIV-DNA$^+$ cell samples and did not substantially increase mapped HIV read counts in the remaining sample (not shown). We conclude that polyadenylated RNA-seq in HIV-DNA$^+$ memory CD4 T cells from ART-treated people with HIV did not reveal either full-length genomic HIV transcripts or spliced HIV messages encoding accessory proteins.

**Fig. 4: HIV RNA sequences in memory CD4 T cells under ART.**




**a**, The percentages of all exonic reads mapping to a clade B HIV reference genome for all samples. Absolute read counts are shown in parentheses. HIV-DNA$^{-}$ samples are shown in black, and HIV-DNA$^{+}$ samples are shown in red. **b**, Expanded view of coverage for sample 2510 Pos 1.1, with the vertical boxes indicating two linked variant positions within the given region. Reads shown in light blue and dark blue are those mapped in the forward and reverse orientations. Nucleotide bases that match the sample consensus at the top are shown as dots. **c**, Graphical representation of HIV reference genome base positions at which variation was detected among sequence reads, as described in the Methods. Samples with no detectable variation are not shown. **d**, The coverage of mapped reads across the HIV reference genome for HIV-DNA$^{+}$ cells. Individual samples are labelled with the participant ID number, followed by the HIV DNA status (HIV-DNA$^{+}$ (pos) and HIV-DNA$^{-}$ (neg)), and then an identifier denoting the replicate

number. Sample 2510 Pos 3.1 is omitted from this panel owing to a lack of HIV reads in that sample.

# Discussion

The absence of evidence for HIV reservoir size reduction in ‘shock and kill’ clinical trials has bred uncertainty about the role of therapeutic HIV latency reversal and the use of the latent reservoir concept. Meanwhile, attempts to understand the mechanisms of HIV persistence under ART by identifying distinctive attributes of HIV-infected CD4 T cells have faced major technical obstacles. Using microfluidic technology developed to study HIV-DNA$^{+}$ memory CD4 T cells under ART in their natural state, we identified host gene expression signatures in these rare cells that were intrinsically non-permissive for the transcription of the virus. This supports the concept that these cells are a latent reservoir and links HIV transcriptional quiescence in vivo to host gene expression patterns that are specific to infected cells. Furthermore, host transcriptomic signatures of HIV-DNA$^{+}$ memory CD4 T cells under ART indicated that the persistence of these cells may involve additional mechanisms beyond HIV transcriptional silencing, including post-transcriptional HIV silencing, resistance to cell death and resistance to anti-proliferative signalling. These findings are consistent with incomplete latency reversal by early LRAs[53,54,55,56,57,58] and the persistence of infected cells observed even after cell stimulation both in vitro[59] and in vivo[12,13,14,15,16]. Overall, our results in this study therefore reveal a host cell transcriptomic signature of which further elucidation may lead to the development of new HIV cure strategies.

The origins of the gene expression patterns that we identified in this study will require further investigation. In part, these patterns may arise progressively under ART through the selective elimination of cells that do not express them. Selection for an HIV-silencing signature may occur among cells that are competent to express toxic virus gene products in vivo, while selection for cell survival and proliferation could apply to the entire HIV-DNA$^{+}$ cell pool. Importantly, this selection model implies that there are pre-existing differences among CD4 T cells in the expression of HIV silencing, cell survival and cell proliferation signatures that did not trace in their entirety to a single memory CD4 T cell subset. These signatures may

therefore reflect mixed contributions from multiple subsets, each with modest enrichment for the virus, perhaps exemplified by our partial mapping of one co-expressed module signature to peripheral $T_{FH}$ cells. At the same time, it is also possible that some gene expression patterns of HIV-infected memory CD4 T cells are a consequence of HIV infection in these cells. Cellular transcriptomic reprogramming could represent a host response to HIV integration or other life cycle steps, as suggested by co-expressed module signature genes encoding virus-induced and DNA-damage response factors. Alternatively, although we detected little evidence of polyadenylated HIV RNA expression in HIV-DNA$^+$ cells, it remains possible that components of infecting HIV virions or HIV expression products of which transcripts went undetected in our sequencing—due to transient expression or method sensitivity—might actively reprogram host cell gene expression. Future studies elucidating such mechanisms may yield new targets for HIV cure strategies.

Our findings in this study have several limitations. First, owing to technical challenges, we sorted and sequenced pools of HIV-DNA$^+$ cell transcriptomes without distinguishing between intact and defective HIV genomes[31]. As a result, technical advances in FIND-seq and/or new technologies will be required to define how the transcriptomic signatures identified here are distributed among individual cells. Analysis of HIV-DNA$^+$ cells at the single-cell level will avoid dilution of signatures from reservoir subpopulations, thereby refining and extending the findings from this study. Single-cell transcriptomic analyses that distinguish between intact and defective HIV may also clarify whether HIV silencing signatures arise strictly by selection within translation-competent reservoirs, or whether these signatures can arise even when the infecting virus genome has acquired lethal mutations during reverse transcription. Second, although many of the transcriptomic signature genes identified here have well-defined roles in regulating HIV gene expression, cell survival or cell proliferation, the roles of other genes in HIV persistence will require further study. Those signature genes that have RNA-processing functions but have not previously been linked with HIV replication will be of particular interest, as some of these could contribute to post-transcriptional regulation of HIV gene expression while others might serve only as markers of infected cells. Third, our findings address neither the durability of transcriptomic signature

expression within each infected cell nor the distribution of cells expressing signature genes across diverse tissue compartments, raising important questions about reservoir cell dynamics that impact the development of HIV cure strategies. Fourth, as our study included a small number of participants, it is possible that larger FIND-seq studies performed in diverse participant populations and incorporating technical improvements to increase the recovery of high-quality data will reveal signatures that were not detected here. Finally, it is important to acknowledge that the barriers to HIV cure under ART may include virus reservoirs outside the memory CD4 T cell pool[60,61,62].

Notwithstanding these limitations, our findings highlight two parallel but complementary paths in translational and basic research towards an HIV cure. The first is an increased emphasis on in vivo studies targeting the full range of mechanisms that both maintain HIV quiescence and prevent the death of HIV-infected cells. The approaches taken may include synergistic combinations of LRAs targeting diverse HIV transcriptional and translational blocks, paired with therapies that potentiate physiological CD4 T cell death. However, as the complexity of therapeutic combinations increases, their potential for significant toxicity may become a growing concern. Thus, the second path forward is an ongoing effort to define gene expression patterns within HIV-infected cellular reservoirs and to understand their mechanistic basis. The intent is for these approaches to reveal how HIV silencing, cell survival and cell proliferation programs come to be expressed among the diverse memory CD4 T cells present in vivo, therefore generating additional insights that may be translated to effective and safe HIV-cure-directed therapies.

# Methods

## Study participants

Recruitment of study participants with HIV was performed in compliance with relevant ethical regulations under the IRB-approved SCOPE protocol (NCT00187512) at San Francisco General Hospital. Participants were enrolled from the SCOPE cohort on the basis of sample availability at the time of study, without use of sample size calculations, blinding or

randomization. Demographic and clinical laboratory data were collected at San Francisco General Hospital and are reported in Supplementary Table 1. All of the participants provided informed consent before study. Prescreening of participant samples to ensure adequate numbers of HIV-DNA$^+$ memory CD4 T cells for FIND-seq analysis was performed in parallel sample aliquots using fluorescence-assisted clonal amplification[63].

## Cell lines

Jurkat human T cells (TIB-152, ATCC), HIV-DNA$^+$ J-Lat full-length human T cells (clone 6.3, ARP-9846)[64] and Raji human B cells (CCL-86, ATCC) were cultured in Gibco RPMI Medium 1640 (Thermo Fisher Scientific, 11875093) with penicillin and streptomycin (Thermo Fisher Scientific, 15140122) and 10% fetal bovine serum (FBS). Mouse fibroblasts (NIH/3T3, CRL-1658, ATCC) were cultured in Dulbecco's modified Eagle's medium (DMEM) with penicillin and streptomycin (Thermo Fisher Scientific, 15140122) and 10% FBS. Before use, 3T3 cells were dissociated using 0.25% trypsin-EDTA (Thermo Fisher Scientific, 25200-072) and neutralized in DMEM with 10% FBS. Cell lines were used without authentication or mycoplasma contamination testing.

## Fabrication of microfluidic devices

Standard photolithography techniques were used to fabricate microfluidic devices at the Harvard Medical School Microfluidics Facility. Silicon wafers were spin-coated with SU-8 2025/2050 photoresist (Kayaku Advanced Materials) and ultraviolet-patterned using a mask aligner. After developing, the wafers were baked overnight and used as master moulds for soft-lithography. In brief, the PDMS prepolymer and curing agent were mixed by hand at a ratio of 10 to 1 (Momentive, RTV615), degassed for at least 1 h, poured onto the mould and degassed until no bubbles remained. PDMS was baked overnight at 65 °C before holes were punched using a 0.75 mm biopsy punch and bonded to a glass slide (75 × 50 × 1.0 mm, Thermo Fisher Scientific, 12–550C) with a plasma bonder (Technics Plasma Etcher 500-II). Bonded devices were made hydrophobic with Aquapel with a 30 s contact time, flushed with HFE-7500, purged with air and baked for at least 1 h before use.

## Cell line validation studies

Cells were washed twice with Hanks' balanced salt solution (HBSS, no calcium, no magnesium, Thermo Fisher Scientific, 14170112) and then counted, mixed (mouse:human 1:1; J-Lat:Raji 1:100), and resuspended in HBSS containing 18% OptiPrep Density Gradient Medium (Sigma-Aldrich) for FIND-seq. For standard RNA-seq studies performed in parallel, aliquots of $5 \times 10^4$ cells were lysed in RNAzol RT (Molecular Research Center) and stored at −80 °C until subsequent total RNA extraction according to the manufacturer's instructions. Whole-transcriptome cDNA was then generated from total RNA by reverse transcription using 6 mM $MgCl_2$, 1 M betaine, 7.5% PEG-8000, 1 mM dNTP, 2 U $\mu l^{-1}$ Maxima H-minus reverse transcriptase (Thermo Fisher Scientific, EP0753), 0.5 U $\mu l^{-1}$ RNase inhibitor (Lucigen, NxGen) and 2 µM SMART TSO (AAGCAGTGGTATCAACGCAGAGTGAATrGrGrG). This cDNA was purified using AMPure XP beads (Beckman Coulter), and was then processed for WTA by PCR, with library preparation as previously described[65]. FIND-seq sample processing and library preparation were performed as described below. The correlation between the DGE results from standard RNA-seq and FIND-seq was analysed using stat_cor (method = "pearson") in R (v.4.1.0). The results from the J-Lat:Raji mixing study were compared with published transcriptomic signatures of CD4 T cells and B cells[66] using GSEA.

## PBMC processing for FIND-seq

Approximately 20–30 million cryopreserved peripheral blood mononuclear cells (PBMCs) from each study participant were used for FIND-seq. Cryopreserved PBMC suspensions were thawed in a 37 °C water bath, washed in prewarmed RPMI with 10% FBS, and sedimented by centrifugation at 300 rpm (Sorvall Legend XT). Untouched memory CD4 T cells were then isolated by magnetic-column-based negative selection (Miltenyi, 130-091-893). Cells were counted manually with a haemocytometer using Trypan blue, and aliquots of $5 \times 10^4$ cells were lysed and stored in RNAzol RT.

## FIND-seq

FIND-seq was performed as described previously[30]. In brief, four syringes were prepared for microfluidic cell encapsulation: lysis buffer, agarose, cells and oil. The lysis buffer consisted of 20 mM Tris-HCl pH 7.5, 1,000 mM LiCl, 1% LiDS, 10 mM EDTA, 10 mM DTT and 0.4 µg $\mu l^{-1}$ proteinase K. Conjugated agarose-dT was heated to 95 °C for 1 h before use and was kept heated throughout the run using a custom syringe heater. A 10 ml syringe was loaded with oil (Bio-Rad, 186–3005) for droplet generation. All of the syringes were connected to the microfluidic device using PE/2 tubing (Scientific Commodities, BB31695-PE/2). To make droplets, pumps were run at 600 µl $h^{-1}$ (cell mixture), 1,200 µl $h^{-1}$ (agarose), 600 µl $h^{-1}$ (lysis buffer), and 5,000 µl $h^{-1}$ (oil) using a bubble-triggered drop generator[67]. Air was controlled to break the jet and generate 53–55 µm droplets. After lysis at 55 °C for 2 h, droplets were cooled at 4 °C overnight to allow agarose gelation. Solid agarose microspheres (beads) were removed from the oil using a drop-breaking procedure. All of the steps were performed at 4 °C to prevent dissociation of mRNA from the poly(T) oligonucleotides. The beads were removed from the oil and washed five times. For each wash, the beads were incubated in wash buffer for 5 min on ice, centrifuged at 4,700 rpm for 10 min and aspirated before the next wash. Beads were first washed in wash buffer 1 containing 20 mM Tris-HCl pH 7.5, 500 mM LiCl, 0.1% LiDS and 0.1 mM EDTA. Next, the beads were washed twice with wash buffer 2 containing 20 mM Tris-HCl pH 7.5 and 500 mM NaCl. Finally, the beads were washed twice in 5× reverse transcription buffer containing 250 mM Tris-HCl pH 8.3, 375 mM KCl, 15 mM $MgCl_2$ and 50 mM DTT and filtered with a 100 µm cell strainer. The beads were resuspended in reverse transcription master mix to a final concentration of 6 mM $MgCl_2$, 1 M betaine, 7.5% PEG-8000, 1 mM dNTP, 2 U $\mu l^{-1}$ Maxima H-minus reverse transcriptase (Thermo Fisher Scientific, EP0753), 0.5 U $\mu l^{-1}$ RNase inhibitor (Lucigen, NxGen) and 2 µM SMART TSO (AAGCAGTGGTATCAACGCAGAGTGAATrGrGrG). Reverse transcription was completed at 25 °C for 30 min, followed by 90 min at 42 °C. The tubes were mixed continuously with an inverter during all incubations. After reverse transcription, the beads were washed five times with 0.1% Pluronic in RNase/DNase-free water.

After reverse transcription, the cell occupancy of agarose beads was quantified by microscopy and successful reverse transcription was checked using WTA before continuing with bead reinjection and sorting. Agarose beads containing cellular genomes and transcriptomes were reinjected into droplets to perform single-cell HIV detection PCR. Beads were mixed with PCR reagents to achieve a final concentration of 1× TaqPath Mastermix (Thermo Fisher Scientific, A30866), PEG-6000 (0.5% (w/v)), Tween-20 (0.5% (w/v)), F-127 Pluronic (0.5% (w/v)), BSA (0.1 mg $ml^{-1}$), HIV *gag* forward primer (CACTGTGTTTAGCATGGTGTTT, 900 nM), HIV *gag* reverse primer (TCAGCCCAGAAGTAATACCCATGT, 900 nM) and HIV *gag* hydrolysis probe (CY5-ATTATCAGAAGGAGCCACCCCACAAGA-3′ Iowa Black RQ, 250 nM)[68]. To generate the final 1× reaction mixture concentration, beads were soaked in 2× PCR master mix on a shaker for 30 min in the dark. Next, the beads were centrifuged and loaded into a 3 ml syringe. The remaining 1× PCR master mix (supernatant) was loaded into a separate 3 ml syringe. Finally, the beads and 1× PCR master mix were reinjected in the microfluidic device to encapsulate the beads into 70 µm droplets[69]. Agarose beads were re-encapsulated in droplets with about 70% loading, which is not accounted for in the detection efficiency calculation. Droplets were collected in 40 µl aliquots in PCR strips and thermocycled as follows: 88 °C for 10 min; then 55 cycles of 88 °C for 30 s and 60 °C for 1 min. After thermocycling, droplets were transferred into a 3 ml syringe for microfluidic sorting.

HIV-$DNA^+$ and HIV-$DNA^-$ droplets were sorted on the basis of the HIV PCR signal using a concentric sorter as previously described[32]. For HIV-$DNA^-$-sorted samples, we sorted 100 cell equivalents based on the number of genomes per hydrogel bead determined previously, collecting a mixture of HIV-$DNA^-$ cell droplets and cell-free droplets. For HIV-$DNA^+$-sorted samples, we sorted aliquots of 100 droplets. The sorter was run with the following flow rates: 180 µl $h^{-1}$ cell droplets, 6,000 µl $h^{-1}$ bias oil (HFE-7500), 250 µl $h^{-1}$ spacer oil (HFE-7500) and 3,500 µl $h^{-1}$ extra spacer oil (HFE-7500). To sort, the 2 M NaCl on-chip electrode was polarized using a high-voltage amplifier at 1,200 V, 4,000 Hz for 15 cycles with 120 µs delay. We sorted into 1.5 ml Eppendorf tubes, removed all but 20 µl of the oil, added 50 µl of distilled nuclease-free water and centrifuged the sample at 20,000*g* for 5 min, and then stored the samples at −80 °C.

Before performing WTA on sorted HIV-DNA$^+$ droplets in each participant, we determined the WTA cycle number that was required to amplify transcriptome cDNA from 100 cells in that participant. Accordingly, we first performed WTA on HIV-DNA$^-$-sorted sample aliquots. Sorted HIV-DNA$^-$ sample aliquots (frozen at −80 °C) were heated to 60 °C on a heat block for 10 min, mixed carefully by pipet and centrifuged at 20,000*g* for 5 min. The aqueous layer was then transferred to PCR strips and a WTA PCR reaction was performed using the 1× KAPA HiFi Master mix (Roche, KK2601) and 0.4 µM Smart-seq2 primer (AAGCAGTGGTATCAACGCAGAGT). Sorted material was thermocycled as follows: 95 °C for 3 min; then 18–22 cycles of 98 °C for 15s, 67 °C for 20s and 68 °C for 4 min; then 72 °C for 5 min, with a 4 °C terminal hold. The WTA was performed at three different cycle numbers—18, 20, and 22 cycles. All reactions were subsequently purified using a 1.2:1 ratio of AMPure XP beads (Beckman Coulter), with the final elution performed in 20 µl of nuclease-free water. After WTA, the DNA yield was quantified using the Qubit 4 Fluorometer and DNA size distribution was assayed using a Bioanalyzer 2100 with High Sensitivity DNA chip. On the basis of these results, the HIV-DNA$^+$-sorted samples were processed as above using the minimal cycle number required to achieve a concentration of greater than 2 ng µl$^{-1}$ in 20 µl of elution volume.

## Sequencing and read preprocessing

Libraries were prepared from transcriptome material sorted by FIND-seq using the Nextera XT Library Preparation Kit with v2 indexes. Individual sample libraries were combined at equimolar amounts to produce a single library pool. The library was quantified using the KAPA SYBR FAST Universal qPCR Kit. The library concentration and fragment size distribution were confirmed using the Agilent Bioanalyzer 2100 with High Sensitivity DNA chip. The library was diluted and denatured in accordance with the Illumina MiSeq System Denature and Dilute Libraries Guide (document 15039740). Cell line libraries were sequenced on the Illumina MiSeq system in 2 × 75 bp runs, and the selected libraries were subsequently sequenced again on the Illumina HiSeq 4000 system in a 2 × 75 bp run, operated using the Illumina HiSeq Control Software (HCS) v.3.4.0. For samples from people with HIV, libraries were first pooled and run on the Illumina MiSeq system in a 2 × 75 bp run, then rebalanced and run on the

Illumina HiSeq 4000 system in a 2 × 75 bp run. Raw sequencing data were converted to fastq format using the bcl2fastq2 script (v.2.20) from Illumina and the reads were demultiplexed using sample-specific indexes. The resulting fastq files were trimmed for quality, ambiguity and presence of read-through adapters using the ‘Trim reads’ tool with the default settings in CLC Genomics Workbench (GWB) v.21.0.3. The quality of the raw and trimmed reads was assessed using QC tools in GWB.

## Participant sample data quality filtering

Owing to the abundance of HIV-DNA$^{-}$ cells in samples from ART-treated people with HIV, HIV-DNA$^{-}$ cells were sorted in multiple replicates. Sequencing data were generated from 53 HIV-DNA$^{+}$ and HIV-DNA$^{-}$ cell samples sorted by FIND-seq from 5 people with HIV. A prospective curation approach was used to exclude low-quality samples from downstream transcriptomic analysis. HIV-DNA$^{-}$ sample quality was assessed according to the following parameters: (1) the total number of reads sequenced; (2) the percentage of intergenic and intronic reads; (3) the proportion of ribosomal RNA (rRNA) reads; and (4) the exonic fragment count (Supplementary Table 2). Samples that had a paired-end read count of less than $10^6$ and had >35% mapped intergenic reads were excluded. Furthermore, within each participant, HIV-DNA$^{-}$ samples that differed qualitatively from other replicates by having lower exonic reads or higher rRNA content were removed. If all HIV-DNA$^{-}$ samples were removed for a participant, that participant was excluded from further analysis. After the removal of 31 FIND-seq-sorted samples in this curation process, 22 HIV-DNA$^{+}$ and HIV-DNA$^{-}$ samples belonging to participants 2208, 2510 and 3209 remained (Supplementary Table 2).

## Analysis pipeline testing

The transcriptomes of primary cell samples generated by FIND-seq showed high proportions of intronic and intergenic reads (Extended Data Fig. 4). We therefore performed a second, deeper sequencing of libraries from the J-Lat:Raji cell mixing study and tested whether bioinformatics pipelines that address coverage bias and/or genomic DNA contamination might mitigate

the effects of these patterns on the gene expression results. In total, we evaluated nine different pipelines using control data from the J-Lat:Raji cell line mixing study. The details of each pipeline are found below; the default options and parameters were used for all tools unless otherwise noted. Reads were mapped against the GRCh38 (ENSEMBL v.100) reference with coding gene annotations only for all pipelines tested.

### CLC Genomics Workbench

CLC Genomics Workbench (GWB) v.20 and v.21 (https://digitalinsights.qiagen.com/) were tested using the default settings for mapping and abundance estimation using the RNA-seq analysis tool. For DGE analysis in GWB v.21, the option to filter average expression before FDR correction was selected.

### 3′ tag counting

Raw reads were preprocessed and mapped using GWB v.21. As in a previous study[70], reads were mapped to the region within 1,500 bp from the 3′ end of the gene and expression values were calculated in GWB. Analysis of DGE was also performed in GWB.

### Salmon with positional bias correction

Salmon v.1.3.0 was implemented as it includes an algorithm for transcript expression quantification that incorporates bias modelling to account for position specific and other biases that are commonly seen in RNA-seq data[71]. Read mapping generated from GWB v.20 was used as the input. Post-quantification analysis of DGE was performed using EdgeR (v.3.32.1)[72] and DESeq2 (v.1.30.1)[73].

### SeqMonk DNA contamination correction

We considered that relatively high intergenic read proportions in sorted samples might be due to library incorporation of the genomic DNA retained with each cell during FIND-seq. We therefore used the SeqMonk expression

quantification (http://www.bioinformatics.babraham.ac.uk/projects/seqmonk/) pipeline v.1.47.2, which estimates and corrects count data for each transcript using the density of intergenic reads. Read mapping previously processed in GWB v.20 was used as the input. Analysis of DGE was performed in DESeq2. Expression qualification and DGE with or without DNA contamination correction (SeqMonk) was evaluated, and each was tested with or without automatic independent filtering (DESeq2).

## Selection of the analysis pipeline

For each pipeline, transcriptome accuracy was assessed by comparing J-Lat:Raji FIND-seq mixing study DGE results with the DGE detected between J-Lat cells and the unsorted J-Lat:Raji mixture in standard RNA-seq. DEGs were considered as those with an absolute fold change of ≥1.5 and FDR ≤ 0.05. DEGs identified in standard RNA-seq but not in FIND-seq were considered to be false negatives (FN); those identified only after FIND-seq as false positives (FP); and those identified in both FIND-seq and standard RNA-seq as true positives (TP). Based on this, the sensitivity (or recall) as TP/(TP + FN) and positive predictive value (PPV) as TP/(TP + FP) for each analysis process were calculated (Supplementary Table 7).

GWB v.20 and v.21 yielded the highest combination of sensitivity and PPV. Pipelines that corrected for coverage bias and DNA contamination did not increase the sensitivity, and in several cases showed lower PPV. Although GWB v.20 had a higher PPV than GWB v.21, there were developments in the GWB v.21 transcriptome analysis pipeline that were anticipated to reduce noise in primary cell samples. Thus, the pipeline in GWB v.21 was selected for the analysis of participant samples.

## DGE between HIV-DNA$^{+}$ and HIV-DNA$^{−}$ memory CD4 T cells

As described above, transcriptome data from FIND-seq-sorted material contained higher proportions of intronic and intergenic sequences than the standard RNA-seq data. These non-exonic sequences were also abundant in material that was subjected to only the hydrogel encapsulation and cDNA synthesis steps of FIND-seq, consistent with the requisite co-retention of cell

genomic DNA with transcriptome material and with efficient nuclear lysis and capture of immature transcripts in our hydrogel-based workflow. Accordingly, after curating the participant samples on the basis of quality, differential expression using only exonic reads was performed (Supplementary Table 3). Using GWB v.21, a combined analysis was performed using the Wald test with Benjamini–Hochberg multiple-testing correction by defining DEGs between HIV-DNA$^+$ and HIV-DNA$^-$ samples using data from the three participants as biological replicates, while controlling for any interparticipant differences in expression. Moreover, a participant-specific analysis was performed by determining DEGs within each participant separately (Supplementary Table 4). The default settings for all other parameters for the differential expression for RNA-seq tool were used except for Filter on average expression for FDR correction, which was enabled for all analyses. Unless otherwise noted, cut-offs for statistical significance of DEGs were absolute fold change of ≥1.5 and FDR ≤ 0.05.

## Euclidean distance calculation

Pairwise Euclidean distances between the curated samples were calculated using the dist function in R (v.4.1.0) using a matrix of counts per million mapped reads (CPM) gene expression values as input. For each sample of a given HIV DNA status group (that is, HIV-DNA$^+$ or HIV-DNA$^-$), average intragroup and intergroup distances to all other curated samples were calculated, with values plotted in GraphPad Prism (v.9.3.1). Statistical significance of distance differences between groups was calculated using Mann–Whitney *U*-tests.

## Transcriptomic pathway expression differences between HIV-DNA$^+$ and HIV-DNA$^-$ cells

Ingenuity Pathway Analysis (Qiagen, summer release 2021) was used to identify enriched biological pathways (Supplementary Table 5) on the basis of DEG lists. For the combined analysis considering samples from different participants as biological replicates, DEGs with an absolute fold change of ≥1.5 and FDR ≤ 0.05 were used. For the participant-specific analysis, DEGs with a fold change of ≥2 and raw $P \leq 0.01$ were used and pathways regulated in the same direction for all three participants were identified.

The directionality of enrichment of pathways for each analysis was determined from the *z*-score, which is calculated in Ingenuity Pathway Analysis to represent predicted relative pathway activity. The *z*-score for each pathway was calculated using the list of genes annotated to that pathway and meeting criteria for statistically significant differential expression between HIV-DNA$^+$ and HIV-DNA$^-$ cells. A simplified *z*-score was calculated as follows: $Z = (N^+ - N^-)/(\sqrt{N})$, where $N^+$ and $N^-$ are those genes of which the direction of regulation is concordant or discordant with predictions from the literature. A positive *z*-score implies activation of a pathway, whereas a negative *z*-score implies inhibition. Statistical significance of the enrichment of a pathway was determined using a right-tailed Fisher's exact test as described previously[74]. Networks of pathways identified as inhibited across participants and their corresponding genes were plotted using ClusterProfiler (v.4.1.1)[75].

## WGCNA

Weighted gene co-expression network analysis[76] was performed in R using the WGCNA package (v.1.70) with a gene expression matrix of CPM values. Genes detected in <2 samples were excluded from analysis. The one-step automatic method was used for network construction and module detection. A soft thresholding power ($\beta$) of 6 was selected based on approximate scale-free topology using the function pickSoftThreshold. The co-expression network was built with a minimum module size of 30, reassignThreshold of 0 and mergeCutHeight of 0.25. The default values were used for the other parameters. Co-expressed modules of genes that correlated with HIV-DNA$^+$ and HIV-DNA$^-$ status were identified. Modules that were correlated with the traits with $P \leq 0.05$ were considered to be significant. GO enrichment analysis for the genes belonging to the two WGCNA modules significantly correlated with cell HIV DNA status was performed using Enrichr (29 March 2021 release)[77,78]. Enrichment analysis was performed using a Fisher's exact test with Benjamini–Hochberg multiple-testing correction.

## Analysis of HIV reads

To identify sequence reads representing HIV RNA, we created a combined human (GRCh38, ENSEMBL v.100) and HIV (GenBank: KT284371)

reference. The HIV sequence for this reference was derived from the clade B representative in the 2016 LANL HIV sequence compendium, with deletions in the LTR regions replaced by the corresponding sequence and annotations from HXB2CG (GenBank: K03455 M38432), and with masking of the *gag* amplicon detected in FIND-seq. Reads were aligned to the combined reference using the Map reads to reference tool with the default settings in GWB (v.21). Counts were obtained for reads extracted from mapping to the combined reference. Mapped reads were visualized using GWB and Integrated Genome Viewer (v.2.11.9).

The frequencies of sequence variants in HIV reads compared to the reference sequence were examined to assess the presence of multiple virus sequences. To do this, a consensus of aligned sequences was generated and reads mapping to the HIV genome were extracted. These reads were then mapped against the consensus reference sequence. The resulting mapping was improved by local realignment in areas containing insertions and deletions (indels). Variants were then identified using the ‘low frequency’ variant caller in GWB v.21 with a minimum coverage of 2, minimum count of 1, inclusion of broken reads and without relative read direction filter applied. The default options for the other parameters were used. The list of variants obtained was manually inspected and filtered to remove (1) those with a frequency above 50% (thus representing the predominant sequence rather than a minor variant) and (2) those with read count = 1 or that represented presumptive technical insertions in homopolymeric regions.

Moreover, the Sequences from HIV Easily Reconstructed (SHIVER)[79] pipeline (v.1.5.8) was tested to create a hybrid reference from de novo assembled contigs of HIV reads for individual samples and closely matched reference sequences. In brief, reads were mapped to the GRCh38 (ENSEMBL v.100) reference using the Map reads to reference tool in GWB v.21 with stringent settings, with the length fraction and similarity fraction parameters set to 0.8. Unmapped reads were then collected and paired reads among them were processed using the de novo assembly tool in GWB (v.21) with the default settings. We also tested the iterative virus assembler (IVA; v.1.0.11) to perform de novo assembly from the unmapped reads using the default settings, but did not recover HIV contigs using this tool. Contig sequences obtained from GWB (v.21) were exported in fasta format and were processed using the SHIVER pipeline with the default settings. A clade

B HIV genome obtained from the 2016 LANL sequence compendium was used as a reference.

## Enrichment analysis of WGCNA modules in defined CD4 T cell subsets

Viably cryopreserved PBMCs from ART-treated people with HIV were thawed and stained for FACS with LIVE/DEAD Aqua stain (Molecular Probes) and the following antibodies (with the indicated dilutions): CXCR5-Alexa Fluor 488 (1:7; BD), CCR5-Cy7PE (1:10; BD), CD27-Cy5PE (1:10; Beckman Coulter), CD45RO-PE-Texas Red (1:12; Beckman Coulter), CD14-PE (1:80; BD), CD11c-PE (1:40; BD), CD3-H7APC (1:5; BD), CCR7-Alexa Fluor 700 (1:8; BD), CD20-APC (1:5; BD), CD56-APC (1:10; BD), T cell receptor gamma delta (TCR-γδ)-APC (1:5; BD), PD1-Brilliant Violet 711 (1:10; BioLegend), CD8-Qdot 655 (1:200; Invitrogen), CD4-Qdot 605 (1:200; Invitrogen), CD57-Qdot 585 (1:50; Invitrogen) and CCR6-Brilliant Violet 421 (1:10; BD). Stained samples were sorted into CD4 T cell subsets using the FACSAria (BD) system by first gating for single cells that were $CD3^{+}$, $Aqua^{low}$ and negative for CD11c, CD14, CD20, CD56 and TCR-γδ. The remaining events that were $CD4^{+}$ and $CD8^{-}$ were then collected as naive ($CD27^{+}CD45RO^{-}$) or memory CD4 T cell subsets (see memory subset definitions in Extended Data Table 2). Sorted cell subsets were processed for total RNA extraction and whole-transcriptome sequencing as described previously[63]. The resulting data were processed using the standard pipeline in GWB v.21 using the human reference (GRCh38, ENSEMBL v. 100) with only the coding gene annotations. The resulting CPM values were exported and provided as an input to GSEA (v.4.2.3)[80,81]. Enrichment of module 5 and 28 signatures (separated into genes upregulated and downregulated between $HIV\text{-}DNA^{+}$ and $HIV\text{-}DNA^{-}$ cells) was identified in transcriptome data from each memory CD4 T cell subset (with data from the naive CD4 T cell subset serving as a reference). GSEA was run using the default settings for all of the parameters.

## Reporting summary

Further information on research design is available in the Nature Portfolio Reporting Summary linked to this article.

## Data availability

Transcriptome sequencing data from human study participants were deposited with controlled access in the database of Genotypes and Phenotypes (dbGaP; phs003095.v1.p1). Transcriptome sequencing data from cell line experiments were deposited in the NCBI Sequencing Read Archive (SRA; accessions PRJNA819479 and PRJNA893817). Gene sets M3077 and M3076 analysed in Extended Data Fig. 2 are available online (https://www.gsea-msigdb.org/). Source data are provided with this paper.

## References


1. Finzi, D. et al. Identification of a reservoir for HIV-1 in patients on highly active antiretroviral therapy. *Science* **278**, 1295–1300 (1997).

2. Siliciano, J. D. & Siliciano, R. F. In vivo dynamics of the latent reservoir for HIV-1: new insights and implications for cure. *Annu. Rev. Pathol.* **17**, 271–294 (2022).

3. Wong, J. K. et al. Recovery of replication-competent HIV despite prolonged suppression of plasma viremia. *Science* **278**, 1291–1295 (1997).

4. Procopio, F. A. et al. A novel assay to measure the magnitude of the inducible viral reservoir in HIV-infected individuals. *EBioMedicine* **2**, 874–883 (2015).

5. Barboric, M. et al. Tat competes with HEXIM1 to increase the active pool of P-TEFb for HIV-1 transcription. *Nucleic Acids Res.* **35**, 2003–2012 (2007).

6. Bosque, A. & Planelles, V. Induction of HIV-1 latency and reactivation in primary memory $CD4^+$ T cells. *Blood* **113**, 58–65 (2009).

7. Ghose, R., Liou, L. Y., Herrmann, C. H. & Rice, A. P. Induction of TAK (cyclin T1/P-TEFb) in purified resting $CD4^+$ T lymphocytes by combination of cytokines. *J. Virol.* **75**, 11336–11343 (2001).

8. Kinoshita, S. et al. The T cell activation factor NF-ATc positively regulates HIV-1 replication and gene expression in T cells. *Immunity* **6**, 235–244 (1997).

9. Nabel, G. & Baltimore, D. An inducible transcription factor activates expression of human immunodeficiency virus in T cells. *Nature* **326**, 711–713 (1987).

10. Sedore, S. C. et al. Manipulation of P-TEFb control machinery by HIV: recruitment of P-TEFb from the large form by Tat and binding of HEXIM1 to TAR. *Nucleic Acids Res.* **35**, 4347–4358 (2007).

11. Van Lint, C., Emiliani, S., Ott, M. & Verdin, E. Transcriptional activation and chromatin remodeling of the HIV-1 promoter in response to histone acetylation. *EMBO J.* **15**, 1112–1120 (1996).

12. Archin, N. M. et al. Interval dosing with the HDAC inhibitor vorinostat effectively reverses HIV latency. *J. Clin. Invest.* **127**, 3126–3135 (2017).

13. Archin, N. M. et al. Administration of vorinostat disrupts HIV-1 latency in patients on antiretroviral therapy. *Nature* **487**, 482–485 (2012).

14. Elliott, J. H. et al. Short-term administration of disulfiram for reversal of latent HIV infection: a phase 2 dose-escalation study. *Lancet HIV* **2**, e520–e529 (2015).

15. Rasmussen, T. A. et al. Panobinostat, a histone deacetylase inhibitor, for latent-virus reactivation in HIV-infected patients on suppressive antiretroviral therapy: a phase 1/2, single group, clinical trial. *Lancet HIV* **1**, e13–e21 (2014).

16. Sogaard, O. S. et al. The depsipeptide romidepsin reverses HIV-1 latency in vivo. *PLoS Pathog.* **11**, e1005142 (2015).

17. Banga, R. et al. PD-1$^+$ and follicular helper T cells are responsible for persistent HIV-1 transcription in treated aviremic individuals. *Nat. Med.* **22**, 754–761 (2016).

18. Banga, R. et al. Blood CXCR3$^+$ CD4 T cells are enriched in inducible replication competent HIV in aviremic antiretroviral therapy-treated individuals. *Front. Immunol.* **9**, 144 (2018).

19. Brenchley, J. M. et al. T-cell subsets that harbor human immunodeficiency virus (HIV) in vivo: implications for HIV pathogenesis. *J. Virol.* **78**, 1160–1168 (2004).

20. Chomont, N. et al. HIV reservoir size and persistence are driven by T cell survival and homeostatic proliferation. *Nat. Med.* **15**, 893–900 (2009).

21. Douek, D. C. et al. HIV preferentially infects HIV-specific CD4$^+$ T cells. *Nature* **417**, 95–98 (2002).

22. Gosselin, A. et al. Peripheral blood CCR4$^+$CCR6$^+$ and CXCR3$^+$CCR6$^+$CD4$^+$ T cells are highly permissive to HIV-1 infection. *J. Immunol.* **184**, 1604–1616 (2010).

23. Hiener, B. et al. Identification of genetically intact HIV-1 proviruses in specific CD4$^+$ T cells from effectively treated participants. *Cell Rep.* **21**, 813–822 (2017).

24. Lee, G. Q. et al. Clonal expansion of genome-intact HIV-1 in functionally polarized Th1 CD4$^+$ T cells. *J. Clin. Invest.* **127**, 2689–2696 (2017).

25. Mendoza, P. et al. Antigen-responsive CD4$^+$ T cell clones contribute to the HIV-1 latent reservoir. *J. Exp. Med.* **217**, e20200051 (2020).

26. Simonetti, F. R. et al. Antigen-driven clonal selection shapes the persistence of HIV-1-infected CD4$^+$ T cells in vivo. *J. Clin. Invest.* **131**, e145254 (2021).

27. Yukl, S. A. et al. Differences in HIV burden and immune activation within the gut of HIV-positive patients receiving suppressive antiretroviral therapy. *J. Infect. Dis.* **202**, 1553–1561 (2010).

28. Collora, J. A. et al. Single-cell multiomics reveals persistence of HIV-1 in expanded cytotoxic T cell clones. *Immunity* **55**, 1013–1031 (2022).

29. Weymar, G. H. J. et al. Distinct gene expression by expanded clones of quiescent memory CD4$^+$ T cells harboring intact latent HIV-1 proviruses. *Cell Rep.* **40**, 111311 (2022).

30. Clark, I. C. et al. Identification of astrocyte regulators by nucleic acid cytometry. *Nature* https://doi.org/10.1038/s41586-022-05613-0 (2023).

31. Ho, Y. C. et al. Replication-competent noninduced proviruses in the latent reservoir increase barrier to HIV-1 cure. *Cell* **155**, 540–551 (2013).

32. Clark, I. C., Thakur, R. & Abate, A. R. Concentric electrodes improve microfluidic droplet sorting. *Lab Chip* **18**, 710–713 (2018).

33. Herroeder, S. et al. Guanine nucleotide-binding proteins of the G12 family shape immune functions by controlling CD4$^+$ T cell adhesiveness and motility. *Immunity* **30**, 708–720 (2009).

34. Rao, S. et al. Host mRNA decay proteins influence HIV-1 replication and viral gene expression in primary monocyte-derived macrophages. *Retrovirology* **16**, 3 (2019).

35. Ding, D. et al. Involvement of histone methyltransferase GLP in HIV-1 latency through catalysis of H3K9 dimethylation. *Virology* **440**, 182–189 (2013).

36. Wang, J. et al. Retinoblastoma binding protein 4 represses HIV-1 long terminal repeat-mediated transcription by recruiting NR2F1 and histone deacetylase. *Acta Biochim. Biophys. Sin.* **51**, 934–944 (2019).

37. Cismasiu, V. B. et al. BCL11B is a general transcriptional repressor of the HIV-1 long terminal repeat in T lymphocytes through recruitment of the NuRD complex. *Virology* **380**, 173–181 (2008).

38. Gao, R. et al. Competition between PAF1 and MLL1/COMPASS confers the opposing function of LEDGF/p75 in HIV latency and

proviral reactivation. *Sci. Adv.* **6**, eaaz8411 (2020).

39. Malcolm, T., Kam, J., Pour, P. S. & Sadowski, I. Specific interaction of TFII-I with an upstream element on the HIV-1 LTR regulates induction of latent provirus. *FEBS Lett.* **582**, 3903–3908 (2008).

40. Yang, X., Chen, Y. & Gabuzda, D. ERK MAP kinase links cytokine signals to activation of latent HIV-1 infection by stimulating a cooperative interaction of AP-1 and NF-κB. *J. Biol. Chem.* **274**, 27981–27988 (1999).

41. Kino, T., Slobodskaya, O., Pavlakis, G. N. & Chrousos, G. P. Nuclear receptor coactivator p160 proteins enhance the HIV-1 long terminal repeat promoter by bridging promoter-bound factors and the Tat-P-TEFb complex. *J. Biol. Chem.* **277**, 2396–2405 (2002).

42. Bres, V., Gomes, N., Pickle, L. & Jones, K. A. A human splicing factor, SKIP, associates with P-TEFb and enhances transcription elongation by HIV-1 Tat. *Genes Dev.* **19**, 1211–1226 (2005).

43. Gebhardt, A. et al. The alternative cap-binding complex is required for antiviral defense in vivo. *PLoS Pathog.* **15**, e1008155 (2019).

44. Lykke-Andersen, J., Shu, M. D. & Steitz, J. A. Communication of the position of exon-exon junctions to the mRNA surveillance machinery by the protein RNPS1. *Science* **293**, 1836–1839 (2001).

45. Cobos Jimenez, V. et al. G3BP1 restricts HIV-1 replication in macrophages and T-cells by sequestering viral RNA. *Virology* **486**, 94–104 (2015).

46. Csosz, E. et al. Analysis of networks of host proteins in the early time points following HIV transduction. *BMC Bioinform.* **20**, 398 (2019).

47. Mei, Y., Hahn, A. A., Hu, S. & Yang, X. The USP19 deubiquitinase regulates the stability of c-IAP1 and c-IAP2. *J. Biol. Chem.* **286**, 35380–35387 (2011).

48. Jin, J. et al. LRRFIP2 negatively regulates NLRP3 inflammasome activation in macrophages by promoting Flightless-I-mediated caspase-1 inhibition. *Nat. Commun.* **4**, 2075 (2013).

49. Wernimont, S. A. et al. Contact-dependent T cell activation and T cell stopping require talin1. *J. Immunol.* **187**, 6256–6267 (2011).

50. Pallikkuth, S. et al. Peripheral T follicular helper cells are the major HIV reservoir within central memory CD4 T cells in peripheral blood from chronically HIV-infected individuals on combination antiretroviral therapy. *J. Virol.* **90**, 2718–2728 (2015).

51. Cohn, L. B. et al. Clonal $CD4^+$ T cells in the HIV-1 latent reservoir display a distinct gene profile upon reactivation. *Nat. Med.* **24**, 604–609 (2018).

52. Kuniholm, J. et al. Intragenic proviral elements support transcription of defective HIV-1 proviruses. *PLoS Pathog.* **17**, e1009982 (2021).

53. Blazkova, J. et al. Effect of histone deacetylase inhibitors on HIV production in latently infected, resting $CD4^+$ T cells from infected individuals receiving effective antiretroviral therapy. *J Infect Dis* **206**, 765–769 (2012).

54. Falcinelli, S. D. et al. Combined noncanonical NF-kappaB agonism and targeted BET bromodomain inhibition reverse HIV latency ex vivo. *J. Clin. Invest.* **132**, e157281 (2022).

55. Grau-Exposito, J. et al. Latency reversal agents affect differently the latent reservoir present in distinct $CD4^+$ T subpopulations. *PLoS Pathog.* **15**, e1007991 (2019).

56. Sannier, G. et al. Combined single-cell transcriptional, translational, and genomic profiling reveals HIV-1 reservoir diversity. *Cell Rep.* **36**, 109643 (2021).

57. Yukl, S. A. et al. HIV latency in isolated patient $CD4^+$ T cells may be due to blocks in HIV transcriptional elongation, completion, and

splicing. *Sci. Transl. Med.* **10**, eaap9927 (2018).

58. Baxter, A. E. et al. Single-cell characterization of viral translation-competent reservoirs in HIV-infected individuals. *Cell Host Microbe* **20**, 368–380 (2016).

59. Ren, Y. et al. BCL-2 antagonism sensitizes cytotoxic T cell-resistant HIV reservoirs to elimination ex vivo. *J. Clin. Invest.* **130**, 2542–2559 (2020).

60. Cochrane, C. R. et al. Intact HIV proviruses persist in the brain despite viral suppression with ART. *Ann. Neurol.* **92**, 532–544 (2022).

61. Heesters, B. A. et al. Follicular dendritic cells retain infectious HIV in cycling endosomes. *PLoS Pathog.* **11**, e1005285 (2015).

62. Pinzone, M. R. et al. Naive infection predicts reservoir diversity and is a formidable hurdle to HIV eradication. *JCI Insight* **6**, e150794 (2021).

63. Boritz, E. A. et al. Multiple origins of virus persistence during natural control of HIV infection. *Cell* **166**, 1004–1015 (2016).

64. Jordan, A., Bisgrove, D. & Verdin, E. HIV reproducibly establishes a latent infection after acute infection of T cells in vitro. *EMBO J.* **22**, 1868–1877 (2003).

65. Picelli, S. et al. Smart-seq2 for sensitive full-length transcriptome profiling in single cells. *Nat. Methods* **10**, 1096–1098 (2013).

66. Hutcheson, J. et al. Combined deficiency of proapoptotic regulators Bim and Fas results in the early onset of systemic autoimmunity. *Immunity* **28**, 206–217 (2008).

67. Yan, Z. H., Clark, I. C. & Abate, A. R. Rapid encapsulation of cell and polymer solutions with bubble-triggered droplet generation. *Macromol. Chem. Phys.* 218, 1600297 (2017).

68. Pasternak, A. O. et al. Highly sensitive methods based on seminested real-time reverse transcription-PCR for quantitation of human

immunodeficiency virus type 1 unspliced and multiply spliced RNA and proviral DNA. *J. Clin. Microbiol.* **46**, 2206–2211 (2008).

69. Clark, I. C. & Abate, A. R. Microfluidic bead encapsulation above 20 kHz with triggered drop formation. *Lab Chip* **18**, 3598–3605 (2018).

70. Sigurgeirsson, B., Emanuelsson, O. & Lundeberg, J. Sequencing degraded RNA addressed by 3′ tag counting. *PLoS ONE* **9**, e91851 (2014).

71. Patro, R., Duggal, G., Love, M. I., Irizarry, R. A. & Kingsford, C. Salmon provides fast and bias-aware quantification of transcript expression. *Nat. Methods* **14**, 417–419 (2017).

72. Robinson, M. D., McCarthy, D. J. & Smyth, G. K. edgeR: a Bioconductor package for differential expression analysis of digital gene expression data. *Bioinformatics* **26**, 139–140 (2010).

73. Love, M. I., Huber, W. & Anders, S. Moderated estimation of fold change and dispersion for RNA-seq data with DESeq2. *Genome Biol.* **15**, 550 (2014).

74. Kramer, A., Green, J., Pollard, J. Jr & Tugendreich, S. Causal analysis approaches in Ingenuity Pathway Analysis. *Bioinformatics* **30**, 523–530 (2014).

75. Wu, T. et al. clusterProfiler 4.0: a universal enrichment tool for interpreting omics data. *Innovation* **2**, 100141 (2021).

76. Langfelder, P. & Horvath, S. WGCNA: an R package for weighted correlation network analysis. *BMC Bioinform.* **9**, 559 (2008).

77. Chen, E. Y. et al. Enrichr: interactive and collaborative HTML5 gene list enrichment analysis tool. *BMC Bioinform.* **14**, 128 (2013).

78. Kuleshov, M. V. et al. Enrichr: a comprehensive gene set enrichment analysis web server 2016 update. *Nucleic Acids Res.* **44**, W90–W97 (2016).

79. Wymant, C. et al. Easy and accurate reconstruction of whole HIV genomes from short-read sequence data with shiver. *Virus Evol.* **4**, vey007 (2018).

80. Mootha, V. K. et al. PGC-1α-responsive genes involved in oxidative phosphorylation are coordinately downregulated in human diabetes. *Nat. Genet.* **34**, 267–273 (2003).

81. Subramanian, A. et al. Gene set enrichment analysis: a knowledge-based approach for interpreting genome-wide expression profiles. *Proc. Natl Acad. Sci. USA* **102**, 15545–15550 (2005).

# Acknowledgements

We thank the participants in this study; and N. Morgan for discussions. J-Lat full-length cells, clone 6.3, contributed by E. Verdin, were obtained through the NIH HIV Reagent Program, Division of AIDS, NIAID. This work was supported by NIH U01 AI129206-01 (to E.A.B. and A.R.A.), the CZ Biohub (to A.R.A.), the American Foundation for AIDS Research investment grant 109537-61-RGRL (to E.A.B.), the Delaney AIDS Research Enterprise (DARE) to Find a Cure 1UM1AI126611-01 (to S.G.D.), the NIH Office of AIDS Research Strategic Fund (to E.A.B.), the Intramural AIDS Targeted Antiviral Program (IATAP; to D.C.D.), the NIH Intramural Research Program (to D.C.D. and E.A.B.) and by NIH R01AI149699 (to F.J.Q. and A.R.A.). I.C.C. is supported by a transition grant from the NIH (K22AI152644).

# Author information

Author notes

1. These authors contributed equally: Adam R. Abate, Eli A. Boritz

## Authors and Affiliations

1. Department of Bioengineering and Therapeutic Sciences, School of Pharmacy, University of California, San Francisco, San Francisco, CA,

USA

Iain C. Clark & Adam R. Abate

2. Ann Romney Center for Neurologic Diseases, Brigham and Women’s Hospital, Harvard Medical School, Boston, MA, USA

Iain C. Clark, Shravan Thaploo, Michael A. Wheeler & Francisco J. Quintana

3. Department of Bioengineering, California Institute for Quantitative Biosciences, QB3, University of California, Berkeley, Berkeley, CA, USA

Iain C. Clark & Sakshi Shah

4. Virus Persistence and Dynamics Section, Vaccine Research Center, National Institute of Allergy and Infectious Diseases, National Institutes of Health, Bethesda, MD, USA

Prakriti Mudvari, Samuel Smith, Mohammad Abu-Laban, Mehdi Hamouda, Marc Theberge, Sung Hee Ko, Liliana Pérez, Divya Kilam, Saami Zakaria, Sally Choi & Eli A. Boritz

5. Human Immunology Section, Vaccine Research Center, National Institute of Allergy and Infectious Diseases, National Institutes of Health, Bethesda, MD, USA

Daniel G. Bunis, James S. Lee, Samuel Darko, Amy R. Henry & Daniel C. Douek

6. Broad Institute of MIT and Harvard, Cambridge, MA, USA

Michael A. Wheeler & Francisco J. Quintana

7. Department of Medicine, University of California, San Francisco, San Francisco, CA, USA

Rebecca Hoh & Steven G. Deeks

8. Department of Chemical and Biomolecular Engineering, California Institute for Quantitative Biosciences, QB3, University of California, Berkeley, Berkeley, CA, USA

Salwan Butrus

### Contributions

Conceptualization: D.C.D., A.R.A. and E.A.B. Methodology: I.C.C., A.R.A. and E.A.B. FIND-seq analysis of HIV-DNA$^{+}$ cells: I.C.C., S.T., M.A.W. and S. Shah. Molecular optimization studies: I.C.C., S.T., S. Smith, M.H., S.H.K., D.G.B., J.S.L., D.K., S.Z., S.C. and S.D. Library preparation and sequencing: S. Smith and A.R.H. Flow cytometry analysis of CD4 T cell subsets: M.A.-L., M.T. and L.P. Bioinformatic analysis: P.M., I.C.C. and S.B. Resources: I.C.C., R.H., S.G.D., F.J.Q., D.C.D., A.R.A. and E.A.B. Manuscript preparation: I.C.C., P.M. and E.A.B. Supervision: F.J.Q., D.C.D., A.R.A. and E.A.B.

### Corresponding authors

Correspondence to Adam R. Abate or Eli A. Boritz.

## Ethics declarations

### Competing interests

I.C.C., A.R.A. and E.A.B. have prepared a provisional patent application for submission related to the technology used in this study.

## Peer review

### Peer review information

*Nature* thanks the anonymous reviewers for their contribution to the peer review of this work.

# Additional information

**Publisher's note** Springer Nature remains neutral with regard to jurisdictional claims in published maps and institutional affiliations.

# Extended data figures and tables

## Extended Data Fig. 1 FIND-seq workflow details and sorted transcriptome purity.

(**a**–**d**) Transcriptome recovery and HIV *gag* DNA detection steps in FIND-seq, including (**a**,**b**) capture of single-cell genomes and transcriptomes in agarose, (**c**) reverse-transcription of polyadenylated RNA in agarose following oil removal and washes, generating single-cell agarose hydrogel beads with retained genomic DNA and covalently linked whole transcriptome cDNA that incorporates a template-switch oligonucleotide (TSO) for subsequent WTA, and (**d**) HIV detection PCR using *gag* primers and hydrolysis probe after hydrogel re-encapsulation on Device 2 (Fig. 1). (**e**) Diagram of whole transcriptome amplification and library preparation from material sorted by FIND-seq, with representative microelectrophoresis traces. (**f**,**g**) Purity of transcriptome material sorted by FIND-seq. (**f**) HIV DNA$^{+}$ J-Lat human T cells and HIV DNA$^{-}$ 3T3 mouse fibroblasts were mixed and subjected to FIND-seq followed by whole transcriptome sequencing. (**g**) Percentages of transcriptome reads from pure input cell populations, the 1:1 mixture of 3T3 and J-Lat, and HIV DNA$^{+}$ cell transcriptomes sorted by FIND-seq that aligned unambiguously to human (red) or mouse (black) references. Results from a single experiment are shown.

## Extended Data Fig. 2 Validity of HIV DNA$^{\pm}$ cell transcriptome sequencing after FIND-seq.

(**a**) HIV DNA$^{+}$ J-Lat T cells and HIV DNA$^{-}$ Raji B cells were mixed at a 1:100 ratio and then subjected to FIND-seq and whole transcriptome sequencing. In parallel, extracted RNA samples from J-Lat cells and Raji

cells were subjected to standard RNA-seq processing for comparison. (**b**) Droplet cytometry plot representing sorting of HIV DNA$^{+}$ cells from the J-Lat:Raji mixture. (**c**) Correlation of gene expression differences between HIV DNA$^{+}$ cells and HIV DNA$^{-}$ cells (determined after FIND-seq) with gene expression differences between J-Lat cells and Raji cells (determined after standard RNA-seq). Points are coloured according to concordance of statistical significance in differential gene expression (DGE) results between FIND-seq and standard RNA-seq. Purple denotes genes significantly different ($p < 0.05$) in both FIND-seq and standard RNA-seq; grey denotes genes not significantly different in either FIND-seq or standard RNA-seq; blue denotes genes with discordant significance between standard and FIND-seq samples. Pearson's R and p values were calculated in R v4.1.0. (**d**) Volcano plot of genes that were differentially expressed between HIV DNA$^{+}$ and HIV DNA$^{-}$ cells after FIND-seq, coloured by expected direction of change. Blue: differentially expressed genes found in gene set GSE10325 (M3077: CD4 T cell vs B cell down), red: differentially expressed genes found in GSE10325 (M3076: CD4 T cell vs B cell up). (**e**) Gene set enrichment pre-ranked analysis (GSEA) comparing transcriptomic differences between HIV DNA$^{+}$ and HIV DNA$^{-}$ cell samples sequenced from the J-Lat:Raji mixture after FIND-seq to previously reported differences between CD4 T cells and B cells (CD4 TCELL VS BCELL UP, M3076; CD4 TCELL VS BCELL DN, M3077).

## Extended Data Fig. 3 FIND-seq droplet cytometry of HIV DNA$^{+}$ memory CD4 T cells *ex vivo*.

(**a**) Droplet cytometry plots from the sorting of HIV DNA$^{+}$ and HIV DNA$^{-}$ memory CD4 T cells from five ART-treated people with HIV (PWH). Two PWH where transcriptome data were excluded from later analyses based on data quality are indicated with * (see "Participant sample data quality filtering" in Methods). (**b**) Negative control droplet cytometry plots of memory CD4 T cells from three HIV-uninfected participants. (**c**) Numbers of HIV DNA$^{+}$ cells per million memory CD4 T cells, as measured by droplet cytometry during FIND-seq of samples from PWH and HIV-uninfected participants. *n* = 1 measurement for each of 5 PWH and each of 3 HIV-

uninfected participants. Bars indicate median values. Total numbers of HIV $DNA^+$ cells collected for each PWH are indicated in the table.

## Extended Data Fig. 4 Transcriptome sequence composition and yield after FIND-seq from PWH.

(**a**) Percentages of exonic, intergenic, and intronic reads, and total yields of sequencing reads, in curated samples. (**b**) Numbers of mapped exonic reads and genes detected in curated samples. (**c**) Rank abundance plots of genes in each sample, grouped by participant. Red bars and traces indicate HIV $DNA^+$ samples, and black traces indicate HIV $DNA^-$ samples.

## Extended Data Fig. 5 Host gene expression by HIV $DNA^+$ and HIV $DNA^-$ memory CD4 T cells under ART.

(**a**) Volcano plot of DGE between HIV $DNA^+$ and HIV $DNA^-$ cells from DGE analysis that considered samples from participants as biological replicates. Genes showing Fold Change >1.5 and FDR ≤0.05 between HIV $DNA^+$ and HIV $DNA^-$ cells are highlighted in red. (**b**) DGE between HIV $DNA^+$ and HIV $DNA^-$ cells, analysed separately in each participant. Genes with absolute fold change >1.5 and p ≤0.1 are highlighted in red. Labels indicate DEGs that were common to all three participants. (**c**) Overlap of DEGs (absolute fold change ≥1.5, p ≤0.1) between HIV $DNA^+$ and HIV $DNA^-$ after separate analysis of each participant. (**d**) RNA expression of DEGs that were common to all participants. Each plotted point indicates the expression level of the given gene in a single sorted sample ($n = 16$ biologically independent HIV $DNA^-$ and 6 biologically independent HIV $DNA^+$ samples). Box plots indicate the median with the lower and upper hinges corresponding to the 25th and 75th percentiles and whiskers corresponding to 1.5 x the interquartile range.

## Extended Data Fig. 6 Fluorescence-activated cell sorting of circulating CD4 T cell subsets in ART-treated PWH.

Leukocytes (**a**) not part of multi-cell conjugates (**b**) that were viable and stained with the T cell marker CD3 (**c**) but not lineage markers CD20, CD56, TCR-γδ, CD14, or CD11c (**d**) and were $CD4^{+}$ and $CD8^{-}$ (**e**) were identified by CD27 and CD45RO staining as phenotypically naïve (**f**, top-left gate, $CD27^{+}CD45RO^{-}$ population) or memory (**f**, top-right and bottom gates) CD4 T cells. $CD27^{+}$ memory CD4 T cells (**f**, top-right gate) were further separated into three populations by CXCR5 and CCR7 expression (**g**). Each of these three populations was then collected in two subsets defined by CCR6 expression (**h**–**j**). $CD27^{-}$ memory CD4 T cells (**f**, bottom gate) were collected in three subsets defined by CCR6 and CD57 expression (**k**). The sorting strategy yielded purified naïve and 9 subsets of memory CD4 T cells. The marker expression patterns of the sorted memory CD4 T cell subsets are shown in Extended Data Table 2. Percentages of all events on each plot falling within the indicated gates are indicated. Results are shown for participant ID 2013.

**Extended Data Table 1 Transcriptomic Signature Genes of HIV $DNA^{+}$ Memory CD4 T Cells under ART**

**Extended Data Table 2 Enrichment of Signature Genes within Sorted Memory CD4 T Cell Subsets from ART-Treated PWH**

# Supplementary information

## Reporting Summary

## Supplementary Table 1

Clinical characteristics of study participants with HIV. a, Participants studied by FIND-seq. b, Participants studied using FACS analysis.

## Supplementary Table 2

Sample curation. a, Sequencing characteristics of all of the samples, including the numbers of sequencing reads, percentages of reads mapped and genomic distributions of mapped reads. b, Sequencing characteristics of

FIND-seq-sorted samples that passed a prospective process of curation for library quality (described in the Methods).

## Supplementary Table 3

Whole-transcriptome gene expression for curated samples. Raw counts of all genes for all 22 curated samples are shown, determined using GWB v.21 as described in the Methods.

## Supplementary Table 4

DGE analysis between HIV-DNA$^{+}$ and HIV-DNA$^{-}$ memory CD4 T cells. The analysis was restricted to protein-coding genes. a, DEGs identified by analysing samples from all of the participants as biological replicates. b, DEGs from participant 2208. c, DEGs from participant 2510. d, DEGs from participant 3209. Statistical significance of differential expression was calculated using Wald Test in GWB v.21.0.3 with Benjamini–Hochberg multiple-testing correction.

## Supplementary Table 5

Pathway analysis of DEGs. a, Pathways derived from significant DEGs (defined by absolute fold change ≥ 2, $P \leq 0.01$) from each participant that were shared and had concordant direction among all three participants. a, Summary of pathway *z*-scores and predicted direction of regulation across participants. b–g, Pathway genes that were differentially expressed in each participant for Gα12/13 signalling (b), NGF signalling (c), Th1 pathway (d), necroptosis signalling (e), dendritic cell maturation (f) and death receptor signalling (g). Significance of differential expression for each gene was calculated using Wald Test in GWB v.21.0.3 with Benjamini–Hochberg multiple-testing correction. Right-tailed Fisher's exact test was used for statistical testing of pathway enrichment.

## Supplementary Table 6

Listing and GO analysis of HIV-DNA$^{+}$ memory CD4 T cell signature genes. Gene modules 5 and 28 were defined and correlated with cell HIV DNA

status using WGCNA as described in the Methods. a, Differential expression results of module 5 genes in each participant and for all participants combined. b, GO analysis of module 5 genes. c, Differential expression results of module 28 genes in each participant and for all of the participants combined. d, GO analysis of module 28 genes. Gene co-expression modules were identified using WGCNA v.1.7.0 with weighted Pearson correlation. GO enrichment analysis was performed in Enrichr using Fisher's exact test with Benjamini–Hochberg multiple-testing correction.

### Supplementary Table 7

Selection of analysis pipeline. The sensitivity and positive-predictive value of gene expression quantification and differential expression analysis performed using GWB v.20, GWB v.21 or other pipelines that address coverage bias and/or genomic DNA contamination were tested using J-Lat-Raji cell mixing study data as described in the Methods.

## Source data

### Source Data Fig. 2

## Rights and permissions

**Open Access** This article is licensed under a Creative Commons Attribution 4.0 International License, which permits use, sharing, adaptation, distribution and reproduction in any medium or format, as long as you give appropriate credit to the original author(s) and the source, provide a link to the Creative Commons licence, and indicate if changes were made. The images or other third party material in this article are included in the article's Creative Commons licence, unless indicated otherwise in a credit line to the material. If material is not included in the article's Creative Commons licence and your intended use is not permitted by statutory regulation or exceeds the permitted use, you will need to obtain permission directly from the copyright holder. To view a copy of this licence, visit http://creativecommons.org/licenses/by/4.0/.

Reprints and Permissions

# About this article

## Cite this article

Clark, I.C., Mudvari, P., Thaploo, S. *et al.* HIV silencing and cell survival signatures in infected T cell reservoirs. *Nature* **614**, 318–325 (2023). https://doi.org/10.1038/s41586-022-05556-6

- Received: 21 March 2022
- Accepted: 11 November 2022
- Published: 04 January 2023
- Issue Date: 09 February 2023
- DOI: https://doi.org/10.1038/s41586-022-05556-6

## Share this article

Anyone you share the following link with will be able to read this content:

Get shareable link

Sorry, a shareable link is not currently available for this article.

Copy to clipboard

Provided by the Springer Nature SharedIt content-sharing initiative

# This article is cited by

- **Silence, escape and survival drive the persistence of HIV**
  - Nicolas Chomont

*Nature* (2023)

- **[Identification of astrocyte regulators by nucleic acid cytometry]**
    - Iain C. Clark
    - Michael A. Wheeler
    - Adam R. Abate

  *Nature* (2023)

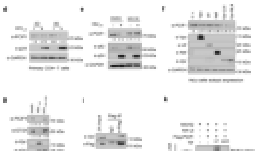
## Silence, escape and survival drive the persistence of HIV

- Nicolas Chomont

Nature News & Views 04 Jan 2023

---

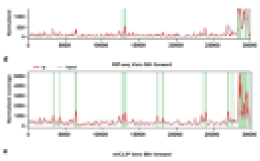
This article was downloaded by **calibre** from https://www.nature.com/articles/s41586-022-05556-6



## HIV reprograms host m6Am RNA methylome by viral Vpr protein-mediated degradation of PCIF1

20 September 2021

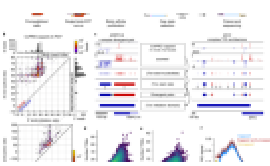
Qiong Zhang, Yuqi Kang, … Tariq M. Rana



## The m6A methylome of SARS-CoV-2 in host cells

28 January 2021

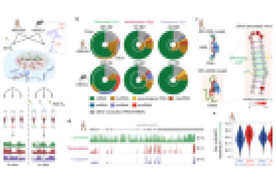
Jun’e Liu, Yan-Peng Xu, … Cheng-Feng Qin



## Single-molecule nascent RNA sequencing identifies regulatory domain architecture at promoters and enhancers

22 October 2018

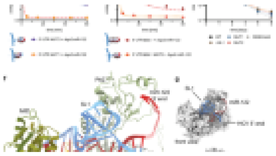
Jacob M. Tome, Nathaniel D. Tippens & John T. Lis



[RNA structure maps across mammalian cellular compartments](#)

18 March 2019

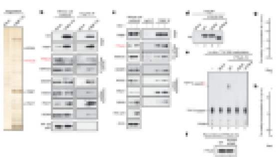
Lei Sun, Furqan M. Fazal, … Qiangfeng Cliff Zhang



[A structured RNA motif locks Argonaute2:miR-122 onto the 5’ end of the HCV genome](#)

25 November 2021

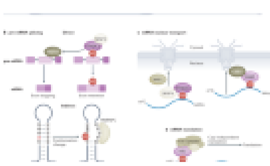
Luca F. R. Gebert, Mansun Law & Ian J. MacRae



[FTSJ3 is an RNA 2′-O-methyltransferase recruited by HIV to avoid innate immune sensing](#)

09 January 2019

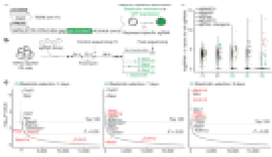
Mathieu Ringeard, Virginie Marchand, … Yamina Bennasser



[Biological roles of adenine methylation in RNA](#)

19 October 2022

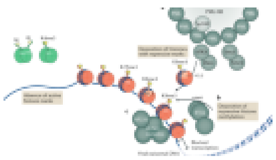
Konstantinos Boulias & Eric Lieberman Greer



[**m6A RNA methylation regulates the fate of endogenous retroviruses**]

13 January 2021

Tomasz Chelmicki, Emeline Roger, … Deborah Bourc’his



[**Epigenetic and epitranscriptomic regulation of viral replication**]

12 June 2020

Kevin Tsai & Bryan R. Cullen

- Article
- Published: 01 February 2023

# mRNA ageing shapes the Cap2 methylome in mammalian mRNA


- Vladimir Despic &
- Samie R. Jaffrey


*Nature* **volume 614**, pages 358–366 (2023)


- 15k Accesses

- 90 Altmetric

- Metrics details

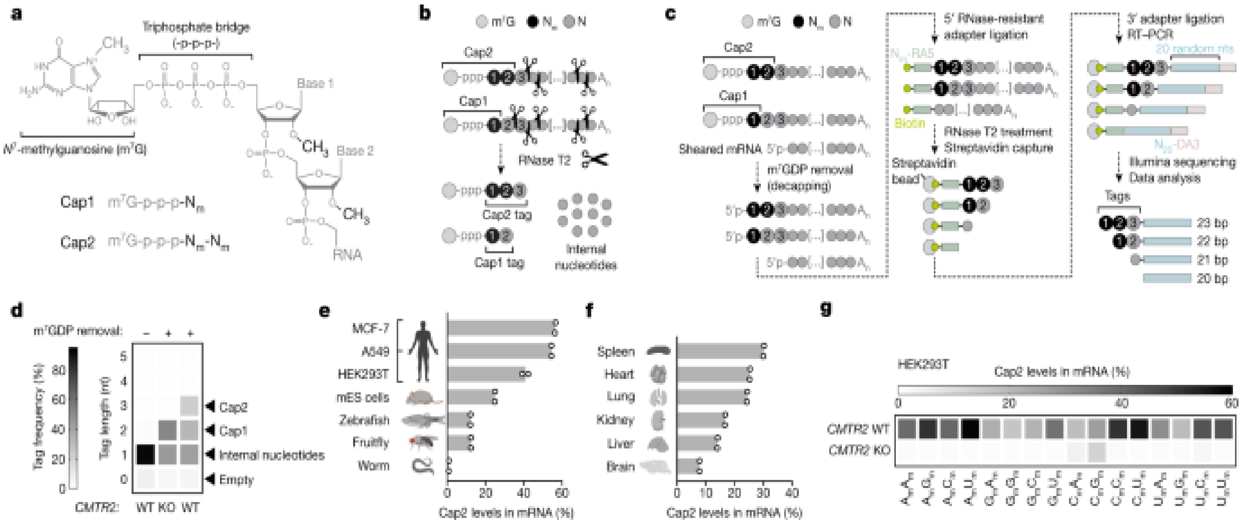
## Abstract

The mRNA cap structure is a major site of dynamic mRNA methylation. mRNA caps exist in either the Cap1 or Cap2 form, depending on the presence of 2′-*O*-methylation on the first transcribed nucleotide or both the first and second transcribed nucleotides, respectively[1,2]. However, the identity of Cap2-containing mRNAs and the function of Cap2 are unclear. Here we describe CLAM-Cap-seq, a method for transcriptome-wide mapping and quantification of Cap2. We find that unlike other epitranscriptomic modifications, Cap2 can occur on all mRNAs. Cap2 is formed through a slow continuous conversion of mRNAs from Cap1 to Cap2 as mRNAs age in the cytosol. As a result, Cap2 is enriched on long-lived mRNAs. Large increases in the abundance of Cap1 leads to activation of RIG-I, especially in conditions in which expression of RIG-I is increased. The methylation of Cap1 to Cap2 markedly reduces the ability of RNAs to bind to and activate RIG-I. The slow methylation rate of Cap2 allows Cap2 to accumulate on host mRNAs, yet ensures that low levels of Cap2 occur on newly expressed viral RNAs. Overall, these results reveal an immunostimulatory role for Cap1, and that Cap2 functions to reduce activation of the innate immune response.

## Main

The mRNA cap structure is a critical component of eukaryotic mRNAs but varies between transcripts based on its methylation state. Each cap structure comprises a $N^7$-methylguanosine ($m^7G$) cap at the 5′ end of mRNA, adjacent to the first transcribed nucleotide[3,4,5]. During mRNA biogenesis, the first nucleotide of all mRNAs becomes 2′-*O*-methylated ($N_m$) by cap methyltransferase 1 (CMTR1) to form a Cap1-modified mRNA terminus ($m^7G$-ppp-$N_m$)[6,7]. Upon mRNA export into the cytosol, a subset of Cap1 mRNAs is subjected to 2′-*O*-methylation of the ribose on the second nucleotide by cap methyltransferase 2 (CMTR2) to form Cap2-modified mRNA 5′ ends ($m^7G$-ppp-$N_m$-$N_m$)[7,8,9] (Fig. 1a). However, the basis for this selectivity in mRNA cap methylation and the function of Cap2 are unclear.

**Fig. 1: Cap2 is a variable mRNA modification found in diverse sequence contexts.**



**a**, Structure of Cap1-modified and Cap2-modified 5′ mRNA termini. **b**, RNase T2 (scissors) cleaves RNA only after non-2′-*O*-methylated nucleotides. RNase T2 selectively releases Cap1 and Cap2 from mRNA in the form of two-nucleotide-long and three-nucleotide-long cap tags. **c**, CapTag-seq. mRNAs are decapped and a biotinylated 5′ end adapter composed of 2′-*O*-methylated nucleotides ($N_m$-RA5) is ligated to the first mRNA nucleotide. The ligated mRNAs are digested with RNase T2, resulting in the formation of the 5′ adapter-linked cap tags. The released 5′ adapter-linked cap tags are captured on streptavidin beads and ligated to the 3′ end DNA adapter containing 20 randomized nucleotides ($N_{20}$-DA3). After RT–PCR and next-generation sequencing, read length identifies Cap1 (22 base pair (bp)) and Cap2 (23 bp) cDNA origins. Reads that are 21 bp long reflect 5′ adapter ligations to uncapped, sheared mRNA. Reads that are 20 bp long represent adapter dimers. **d**, CapTag-seq specifically detects Cap1 and Cap2 mRNA species in bulk mRNA. CapTag-seq was conducted on mRNA extracted from *CMTR2* WT and KO HEK293T cells with (+) or without (–) the $m^7$GDP removal step. A heatmap of the length-based tag frequency is shown for each sample. Average of $n = 2$ biological replicates. **e**, Cap2 levels in bulk mRNA from different organisms and mammalian cell types. Average of $n = 2$ biological replicates. **f**, Cap2 levels in bulk mRNA from different mouse tissues. Average of $n = 2$ biological replicates. **g**, A heatmap showing Cap2 levels on each of the 16 possible $m^7$G-proximal dinucleotides

in *CMTR2* WT and KO HEK293T cell transcriptomes. Average of $n = 2$ biological replicates.

Source data

Cap2 appears to have important regulatory roles in higher organisms, as deletion of the *Cmtr2* gene causes preweaning lethality in mice[10] and affects growth and proliferation of *KRAS*-driven lung cancer cells[11]. As Cap2 methylation is an abundant non-constitutive mRNA modification[2], these data suggest that Cap2 exerts important cellular functions via controlling a subset of mRNAs.

The identity of Cap2-modified mRNAs and the rules that govern the specificity of Cap2 methylation have remained unknown since the original discovery of Cap2 nearly 50 years ago. This is largely due to the lack of methods for transcriptome-wide mapping of Cap2 methylation.

Using a set of new methods to quantify and map Cap2, here we reveal unique features and function of this epitranscriptomic modification. Our quantitative transcriptome-wide map of Cap2 reveals an unexpected topology of the Cap2 methylome in mammalian transcriptomes, with essentially all mRNAs susceptible to Cap2 methylation. Cap2 methylation specificity is largely guided by mRNA age. We found that this age-directed mechanism for Cap2 methylation provides a novel strategy to distinguish viral RNA from self RNA and to control the activation of the innate immune response.

## Cap2 levels vary between cell types

As Cap2 is a non-constitutive mRNA modification[1,2], it has a potential for dynamic regulation in different cellular contexts and conditions. However, current methods for measuring Cap2 dynamics are cumbersome, as they rely on metabolic mRNA radiolabelling and chromatographic separation of Cap1 and Cap2 from the nuclease digests of mRNA[1]. These methods utilize RNase T2 to selectively release the cap structures from mRNA. RNase T2 liberates the cap structures from mRNA as it cleaves all phosphodiester bonds in RNA except those after $N_m$ (ref. [12]) (Fig. 1b). Thus, RNase T2

digestion of Cap1 mRNA releases $m^7G$-ppp-$N_m$-N, whereas the digestion of Cap2 mRNA releases $m^7G$-ppp-$N_m$-$N_m$-N (Fig. 1b). We refer to these $m^7G$-linked two-nucleotide-long or three-nucleotide-long fragments as ‘cap tags’, as they directly indicate the Cap1 or Cap2 status of an mRNA, respectively.

To quantify the levels and dynamics of Cap2 in any cellular sample, we developed CapTag-seq. In CapTag-seq, mRNAs are first subjected to enzymatic $m^7GDP$ removal (decapping), and the resulting 5′-monophosphorylated mRNA ends are ligated to a 5′ adapter composed of $N_m$, thus rendering it resistant to RNase T2 (Fig. 1c). The resulting 5′ adapter-linked mRNAs are fully digested with RNase T2, leaving the cap tags attached to the 5′ adapter. A conversion of the 5′ adapter-linked cap tags into cDNA libraries allows quantification of the cap tags by next-generation sequencing (Fig. 1c; see Methods). In addition, the identity of nucleotides in the cap tags can reveal sequence contexts associated with Cap2 methylation.

We first assessed whether CapTag-seq specifically detects Cap1 and Cap2 mRNAs. CapTag-seq libraries prepared from HEK293T cells comprised almost exclusively three-nucleotide-long, two-nucleotide-long and one-nucleotide-long cap tags (Fig. 1d). The lack of longer cap tags demonstrates the specificity and efficiency of the RNase T2 cleavage step. In control mRNA samples that were not decapped, only the one-nucleotide tags remained (Fig. 1d), indicating that these tags probably reflect contamination from sheared mRNA with uncapped 5′ ends that can be subjected to 5′ adaptor ligation. They are unlikely to derive from Cap0 mRNAs (that is, no 2′-*O*-methylation at the first and second nucleotides), as Cap0 mRNAs are not detected in orthogonal biochemical assays[1,2].

To further confirm that the three-nucleotide-long cap tags derive from Cap2 mRNAs, we performed CapTag-seq on *CMTR2* knockout (KO) HEK293T cells (Extended Data Fig. 1a). Here we found a near-complete loss of the three-nucleotide-long cap tags (Fig. 1d), thus confirming their Cap2 origin and simultaneously validating Cap2 depletion in *CMTR2* KO HEK293T cells. CapTag-seq was quantitative, as mixtures of mRNA from CMTR2-overexpressing wild-type and *CMTR2* KO HEK293T cells at predefined ratios produced the expected Cap2 stoichiometries (Extended Data Fig. 1b).

We found that relative Cap2 abundance varied considerably between mammalian cell lines, with as low as approximately 25% in mouse embryonic stem (mES) cells and 40% in HEK293T cells, and as high as 54% in A549 cells and 56% in MCF-7 cells (Fig. 1e and Extended Data Fig. 1c). Of note, Cap2 was nearly absent in the *Caenorhabditis elegans* transcriptome (0.9%) and present at low levels in fruitfly and zebrafish (approximately 12%) mRNA (Fig. 1e). Cap2 was also highly variable in mouse tissues, ranging from approximately 8% in the mouse brain to 30% in the mouse spleen (Fig. 1f and Extended Data Fig. 1d). These results show that Cap2 levels vary widely between organisms, tissues and cell types, suggesting regulation of Cap2 methylation in different cellular contexts.

# Cap2 resides within diverse sequences

We next used CapTag-seq to determine whether Cap2 is associated with specific $m^7$G-proximal nucleotides. To test whether certain sequences are selectively methylated by CMTR2, we examined Cap2 levels on all 16 possible $m^7$G-proximal dinucleotides. In all cell types, we found that all 16 dinucleotides can be subjected to Cap2 methylation (Fig. 1g and Extended Data Fig. 1e). However, the extent of Cap2 methylation differed between individual dinucleotides (Fig. 1g and Extended Data Fig. 1e). Unexpectedly, we found that the sequences with the highest Cap2 methylation differed slightly among mouse tissues (Extended Data Fig. 1f). This was surprising as the sequence preferences of CMTR2 would be expected to be identical regardless of the tissue. Overall, these data suggest that the pattern of Cap2 in the transcriptome may not be driven simply based on the sequence preferences of CMTR2, but, as will be shown below, is instead dictated in combination with other mechanisms.

Together, these data indicate that Cap2 is an abundant and promiscuous mRNA modification. The tissue-specific enrichment of Cap2 in different sequence contexts suggests that some mRNAs may have higher levels of Cap2 than other mRNAs, raising the possibility that Cap2 may have specific regulatory roles or functions.

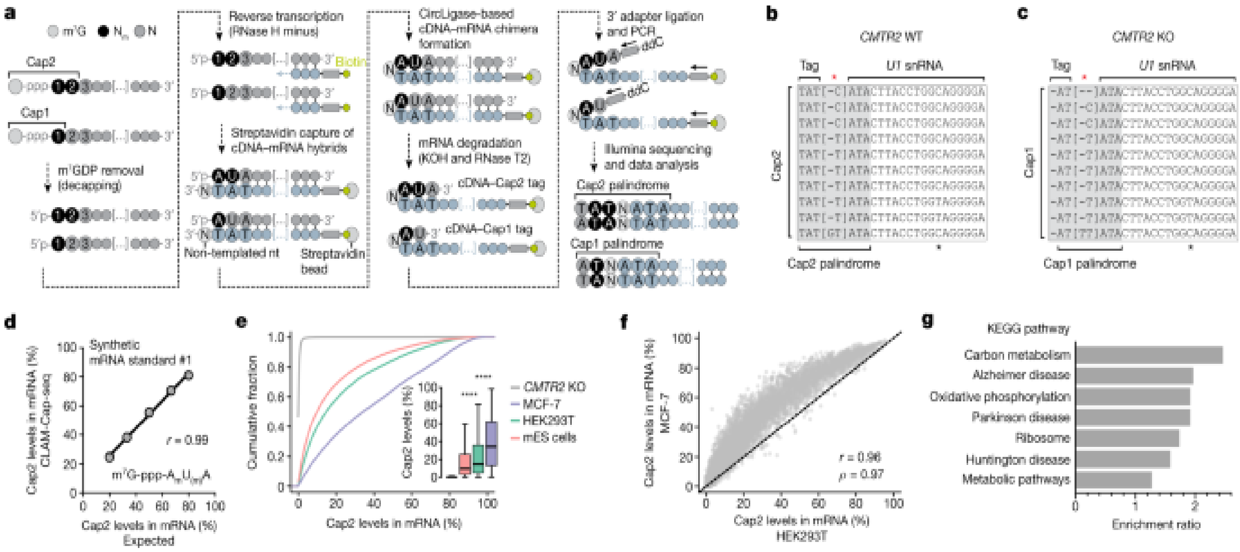
# CLAM-Cap-seq creates cDNA–mRNA chimeras

To understand pathways and processes that may be regulated by Cap2 methylation, we wanted to identify Cap2-modified mRNAs. $N_m$ has been mapped at internal sites within ribosomal RNA based on the ability of $N_m$ to stochastically stall certain reverse transcriptases and induce termination of cDNA synthesis[13]. However, $N_m$-induced terminations are often inconsistent and influenced by sequence contexts surrounding modified nucleotides[14]. We therefore sought to develop a novel method for detection and quantification of Cap2 in individual mRNAs.

Although RNase T2 selectively releases Cap1 and Cap2 cap tags from mRNA, it destroys the sequence information of the mRNA from which the cap tag originated (Fig. 1b). To overcome this, we developed CLAM-Cap-seq (CircLigase-assisted mapping of caps by sequencing), a method which entails generating cDNA that is physically attached to the cap tag of its template mRNA. By creating a chimera between the cDNA and the cap tag, each cDNA sequence contains a record of the cap status of the original mRNA.

In CLAM-Cap-seq, decapped mRNA is first reverse transcribed to generate a cDNA–mRNA hybrid. Next, the cDNA 3′ end is ligated to the first 5′ mRNA nucleotide to create a cDNA–mRNA chimera (Fig. 2a). Subsequently, RNase T2 removes the entire mRNA except the cap tag, which remains covalently attached to the cDNA. Finally, a DNA adapter is ligated to the cap tag to enable the conversion of cDNA–cap tags into a sequencing library (Fig. 2a; see Methods). The resulting sequencing reads begin with ‘palindromes’ that reflect the cap tag of the mRNA followed by the first cDNA nucleotides, which are the reverse complement of the cap tag (Fig. 2a). Overall, CLAM-Cap-seq physically couples a remnant of the mRNA in the form of the cap tag to the cDNA, thus revealing the Cap1 or Cap2 status for each mRNA in the transcriptome.

**Fig. 2: CLAM-Cap-seq identifies Cap2 methylation enrichment on specific mRNAs.**




**a**, In CLAM-Cap-seq, mRNAs are decapped and reverse transcribed using a 5′-biotinylated primer. Non-templated nucleotides added to the 3′ cDNA ends by reverse transcriptase are indicated. cDNA–mRNA hybrids are captured on streptavidin beads. mRNA and cDNA ends are ligated by CircLigase to form a cDNA–mRNA chimera. The mRNA is degraded by KOH and RNase T2, leaving two-nucleotide-long and three-nucleotide-long cap tags attached to the cDNA. A DNA adapter is ligated to the cap tags, enabling the conversion of the cDNA–cap tag chimera into sequencing libraries. Sequencing reads begin with a palindrome, comprising the reverse complement of the cap tag followed by the transcript sequence. **b**,**c**, *U1* snRNA CLAM-Cap-seq PCR sequences obtained from *CMTR2* WT (**b**) and KO (**c**) HEK293T cells. The red asterisk indicates non-templated nucleotides, and the black asterisk denotes a mutation in the *U1* snRNA. **d**, CLAM-Cap-seq-predicted Cap2 stoichiometry plotted against the expected Cap2 stoichiometry of a luciferase mRNA standard starting with $A_mU_{(m)}A$. Pearson's *r* is shown. *n* = 2 technical replicates. **e**, Cumulative distribution plot of Cap2 stoichiometry in TSN isoforms from mES cells (*n* = 12,773), *CMTR2* WT (*n* = 12,776) and KO (*n* = 16,102) HEK293T cells, and MCF-7 cells (*n* = 10,630). Each box shows the first quartile, median and third quartile, and whiskers represent 1.5× interquartile ranges. Two-sided Wilcoxon signed-rank test, ****$P < 0.00001$. **f**, Cap2 stoichiometry is correlated between human cell lines. Cap2 stoichiometry for a shared set of TSN isoforms in HEK293T and MCF-7 cells was plotted. Pearson's (*r*) and Spearman's ($\rho$) are shown. Average of *n* = 4 (HEK293T) and *n* = 2 (MCF-7) biological replicates. *n* = 7,187 TSN isoforms. **g**, Gene enrichment

analysis performed for highly Cap2-modified mRNAs from HEK293T cells. The bar graph shows the enrichment ratio of the KEGG pathways associated with highly Cap2-modified mRNAs relative to all mRNAs with measurable Cap2 stoichiometry. FDR < 5%.

Source data

Although the ligation of cDNA to mRNA has not been described, we considered the possibility that this could be achieved with CircLigase, which has previously been used to ligate annealed DNA strands[15]. We tested CircLigase-assisted formation of chimeric cDNA–cap tags on *U1* small nuclear RNA (snRNA), which is nearly 100% Cap2-modified in various cell types[16]. First, we confirmed successful generation of cDNA–cap tags by performing PCR across the cDNA–cap tag ligation junction (Extended Data Fig. 2a). Sequencing of individual PCR products revealed the expected Cap2 palindromes at the beginning of the reads derived from *U1* snRNA extracted from wild-type cells (Fig. 2b). By contrast, only Cap1 palindromes were observed in *CMTR2* KO cells, demonstrating the specificity of this method (Fig. 2c). Overall, these data show that CLAM-Cap-seq selectively generates cDNA–cap tag chimeras that report the RNA identity as well as its Cap1 or Cap2 status.

In the centre of the palindromes, we routinely observed 0, 1 or 2 nucleotides (Fig. 2b,c), probably added to the cDNA ends by the terminal nucleotidyl-transferase activity of the reverse transcriptase[17]. Despite the presence of non-templated nucleotides, the complementary sequences within the palindrome are easily identified and demarcate the exact cap tag region (Fig. 2b,c). Thus, the cap tag can be extracted from the palindrome to determine whether the original mRNA was Cap1 or Cap2.

We next tested the ability of CLAM-Cap-seq to accurately predict Cap2 stoichiometry in mRNA. To test this, we mixed Cap1-modified and Cap2-modified luciferase mRNAs in specific molar ratios and spiked them into cellular poly(A)$^{+}$ RNA. We found that CLAM-Cap-seq accurately predicted Cap2 stoichiometry present in the mixture of synthetic luciferase mRNA standards (Fig. 2d and Extended Data Fig. 2b). Collectively, these data demonstrate that CLAM-Cap-seq can accurately measure Cap2 stoichiometry in mRNA.

## CLAM-Cap-seq reveals the Cap2 methylome

We next identified Cap2-modified mRNAs in mES, HEK293T and MCF-7 cells. Gene transcription can initiate at different locations within a gene promoter, giving rise to transcript isoforms that differ in the start nucleotides (transcript-start nucleotide (TSN) isoforms)[18,19]. To identify Cap2 stoichiometry for each TSN isoform, rather than genes, we first identified TSN isoforms in the transcriptome by transcription start site-sequencing (TSS-seq)[20,21] (Extended Data Fig. 2c–e).

Next, we performed CLAM-Cap-seq on mRNA extracted from mES, HEK293T and MCF-7 cells and calculated Cap2 stoichiometry for each TSN isoform identified by TSS-seq. CLAM-Cap-seq produced sufficient read coverage for prediction of Cap2 stoichiometry in 10,630–12,776 TSN isoforms, spread across 3,745–4,267 genes in the examined cell lines. CLAM-Cap-seq datasets showed low variability of Cap2 measurements across replicates (Extended Data Fig. 2f,g).

The specificity of CLAM-Cap-seq is supported by the lack of Cap2 reads in CLAM-Cap-seq datasets from *CMTR2* KO HEK293T cells (Fig. 2e). Furthermore, the Cap2 stoichiometry was low (1–11%) in nuclear poly(A)$^+$ RNAs compared with cytosolic mRNAs (2–84%), consistent with the formation of Cap2 in the cytosol[8] (Extended Data Fig. 2h). The overall levels of Cap2 methylation and the Cap2 dinucleotide preferences identified by CLAM-Cap-seq were highly similar to those identified by CapTag-seq (Extended Data Fig. 2i,j).

To biochemically validate the levels of Cap2 measured using CLAM-Cap-seq, we developed an approach to measure Cap2 levels on specific cellular mRNAs. In this method, named CapOligo-PAGE, a self-splinting DNA oligo is selectively ligated to the radiolabelled 5′ end of an mRNA of interest. Following RNase T2-mediated removal of the mRNA, the self-splinting oligo remains attached to the radiolabelled cap tags. A subsequent PAGE electrophoresis resolves DNA oligo-attached cap tags to establish the Cap1 or Cap2 status of the mRNA of interest (Extended Data Fig. 3a–c; see Methods). Using CapOligo-PAGE, we confirmed that Cap2 was present in *OAT* and *RPS12* mRNAs, with markedly higher Cap2 stoichiometry in

*RPS12* mRNA (Extended Data Fig. 3d,e), as predicted by CLAM-Cap-seq (Extended Data Fig. 2h). Thus, the Cap2 stoichiometry measurements obtained with CLAM-Cap-seq are consistent with our orthogonal assay for determination of Cap1 and Cap2 status in individual mRNAs.

We next assessed the overall stoichiometry of Cap2 throughout transcriptomes. In all three cell lines, we detected transcripts with Cap2 stoichiometries that ranged from 0% to approximately 100% (Fig. 2e). Of note, the overall level of Cap2 varied substantially between cell types, with MCF-7 cell transcripts exhibiting threefold higher Cap2 methylation than mRNAs of the mES cell transcriptome (Fig. 2e). To understand the basis for the differences in Cap2 levels in different cell types, we compared Cap2 stoichiometry at the shared set of TSN isoforms between HEK293T and MCF-7 cells (Fig. 2f). We found that TSN isoforms with low Cap2 stoichiometry in HEK293T cells also exhibited low levels of Cap2 in MCF-7 cells. Similarly, high Cap2 stoichiometry TSN isoforms from HEK293T cells were also highly Cap2-modified in MCF-7 cells (Fig. 2f). The major difference was that the Cap2 stoichiometry of each TSN isoform was proportionally higher in MCF-7 cells (Fig. 2f). Thus, rather than distinct Cap2 epitranscriptomes in each cell type, we found that Cap2 levels at all TSN isoforms are largely correlated in these two human cell lines.

We next used gene enrichment analysis to determine whether Cap2-modified mRNAs are linked to specific cellular pathways. These analyses showed that transcripts with high Cap2 stoichiometry were significantly enriched in gene sets associated with general metabolic pathways and other housekeeping functions in all three cell lines (Fig. 2g and Extended Data Fig. 4). Thus, Cap2 enrichment on specific mRNA cohorts appears to be a conserved phenomenon in mammalian cells.

Overall, these data suggest that Cap2 could influence the function of specific groups of genes and thus regulate cell functions.

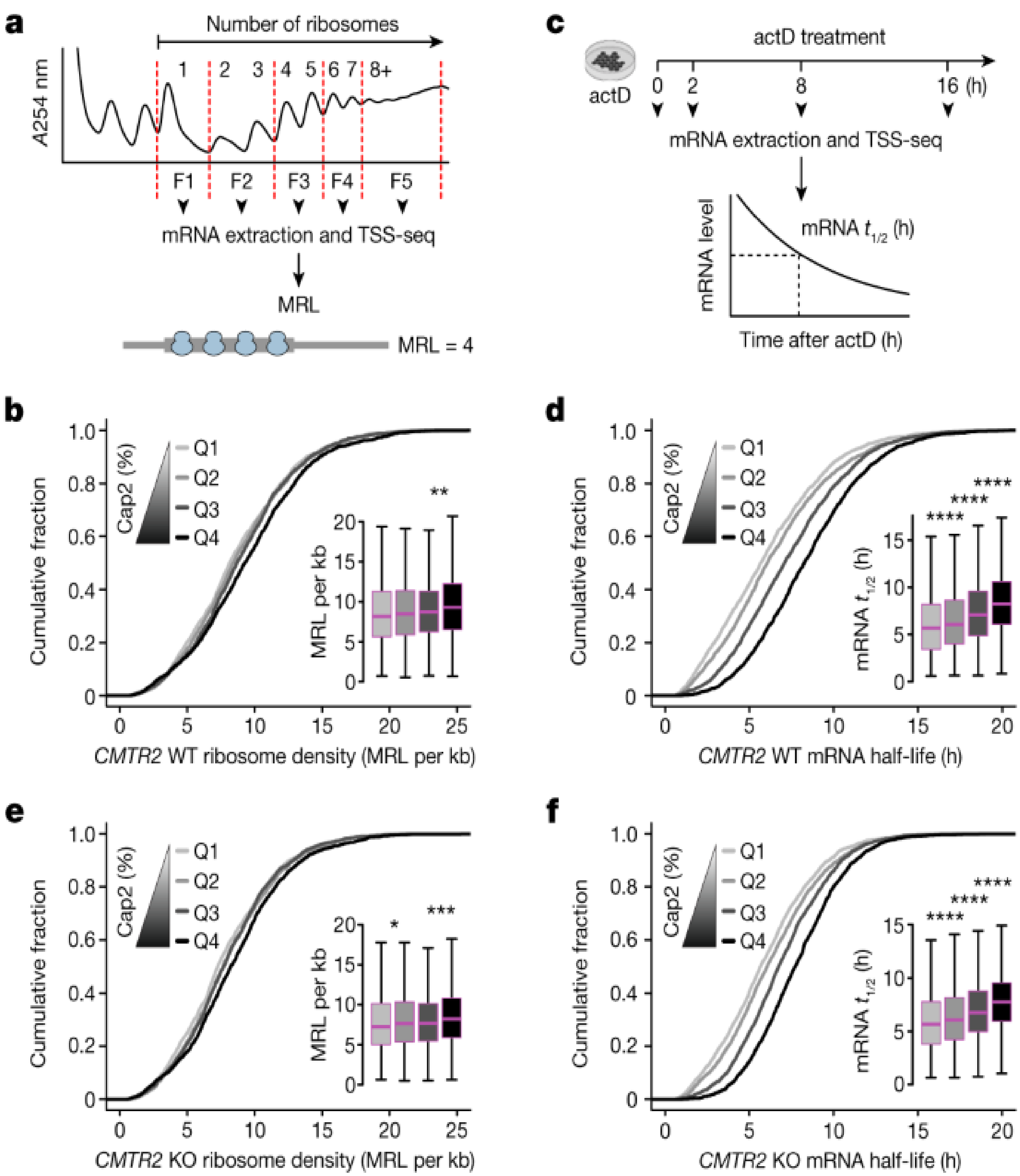
## Cap2 is enriched on long-lived mRNAs

As Cap2 is added in the cytosol, we asked whether Cap2 is associated with cytoplasmic mRNA processing events, such as translation or mRNA

stability. Current approaches for measuring mRNA translation and stability generate sequencing reads that cannot be linked to specific TSN isoforms. To measure translation and stability of every Cap2-modified TSN isoform, we first developed methods for TSN-specific translation and stability analyses.

To specifically assess translation of TSN isoforms, we combined polysome profiling with TSS-seq (polysome–TSS-seq). The abundance of each TSN isoform along the sucrose gradient can be used to calculate the average number of actively translating ribosomes bound to each TSN isoform (mean ribosome load (MRL))[22] (Fig. 3a).

**Fig. 3: Cap2 methylation is highly enriched on long-lived mRNAs.**




**a**, Polysome–TSS-seq. Translated mRNAs were isolated from different polysome fractions (F1–F5) and subjected to TSS-seq. The average number of ribosomes bound to each TSN isoform was calculated, termed mean ribosome load (MRL). **b**, Cumulative distribution plot of the ribosome density (MRL per kb) for TSN isoforms binned into equally sized quartiles

of increasing Cap2 stoichiometry (Q1–Q4) in *CMTR2* WT HEK293T cells. $Q_n = 1{,}782$. **c**, ActD-TSS-seq. mRNA was extracted from cells treated with actinomycin D (actD) for 0, 2, 8 and 16 h. Purified mRNA was subjected to TSS-seq for half-life measurements of each TSN isoform. **d**, Cumulative distribution plot of the half-lives for TSN isoforms binned into equally sized quartiles of increasing Cap2 stoichiometry in *CMTR2* WT HEK293T cells. $Q_n = 2{,}115$. **e**, Analysis of mRNA translation, as in **b**, using *CMTR2* KO HEK293T cells. $Q_n = 1{,}938$. **f**, Analysis of mRNA half-lives, as in **d**, using *CMTR2* KO HEK293T cells. $Q_n = 2{,}150$. In **b**,**d**–**f**, average of $n = 2$ biological replicates. Two-sided Wilcoxon signed-rank test, $^{*}P < 0.01$, $^{**}P < 0.001$, $^{***}P < 0.0001$ and $^{****}P < 0.00001$. Each box shows the first quartile, median and third quartile, and whiskers represent 1.5\(\times \) interquartile ranges.

Source data

We quantified TSN isoforms in five polysome fractions of HEK293T cells using TSS-seq. As a control, we showed that mRNAs known to be highly and lowly translated were found in the expected positions within the sucrose gradient (Extended Data Fig. 5a). Next, we calculated the MRL for each TSN isoform in two replicates (Extended Data Fig. 5b,c).

To determine whether Cap2 is associated with translation efficiency, we stratified all TSN isoforms into equally sized quartiles based on their Cap2 stoichiometry. When we examined the distribution of the ribosome density (MRL per kilobase of the open reading frame (MRL per kb)) for each Cap2 stoichiometry quartile, we observed slightly higher ribosome density in highly Cap2-modified transcripts relative to the mRNAs with the lowest levels of Cap2 (median Δ ribosome density ($Q_4 - Q_1$) = ~1 MRL per kb; Fig. 3b and Extended Data Fig. 5d–f). Overall, these data suggest that Cap2 shows a slight enrichment on mRNAs with increased translation efficiency.

We next asked whether Cap2 is associated with mRNA stability. To calculate the half-lives of each TSN isoform, we quantified TSN isoform abundance by TSS-seq at different time points after transcriptional shut off with actinomycin D (actD-TSS-seq) (Fig. 3c and Extended Data Fig. 5g). TSN

isoform half-lives were quantified in two replicates (Extended Data Fig. 5h,i).

When we compared the distribution of half-lives between mRNAs of different Cap2 stoichiometry, we observed a large difference in the half-lives and abundance of mRNAs with the highest and lowest Cap2 levels (median $\Delta\ t_{1/2}\ (Q_4 - Q_1) = 2.5$ h; Fig. 3d and Extended Data Fig. 5j–m).

A similarly strong positive relationship between Cap2 methylation and mRNA stability was also observed in mES and MCF-7 cells (Extended Data Fig. 5n–t), suggesting a conserved relationship between Cap2 and mRNA stability across different cell types and species.

Overall, these data show that Cap2 methylation is enriched on mRNAs with high translation and stability, with a much more prominent association between Cap2 methylation and mRNA stability.

## Cap2 does not confer high mRNA stability

We next wanted to determine whether Cap2 directly influences mRNA translation. We therefore measured mRNA translation in *CMTR2* KO HEK293T cells by polysome–TSS-seq (Extended Data Fig. 6a). We noticed that *CMTR2* KO HEK293T cells exhibited slower growth and overall reduced translation based on the puromycin incorporation and polysome profiling (Extended Data Fig. 6b–d). Despite the global reduction in translation, we asked whether CMTR2 depletion causes a selective decrease in the translation efficiency of mRNAs with the highest Cap2 stoichiometry. Consistent with the overall impairment of growth and translation (Extended Data Fig. 6b–d), all transcripts exhibited a reduction in translation after CMTR2 depletion independent of their Cap2 status (median Δ ribosome density = −0.8 MRL per kb; Extended Data Fig. 6e). However, the slight difference in translation efficiency between the high and low Cap2-modified mRNAs observed in *CMTR2* WT cells remained largely unchanged in the *CMTR2* KO cells (Fig. 3e). These data suggest that CMTR2 depletion does not regulate the translation capacities of transcripts based on their Cap2 stoichiometry.

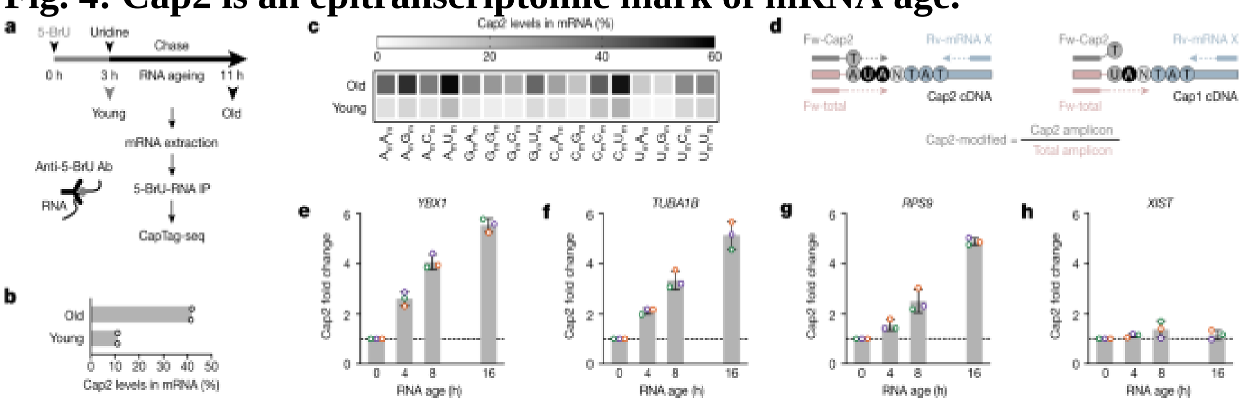
We then wanted to determine whether Cap2 confers long half-lives to mRNA. To test this, we measured changes in mRNA half-lives ($\Delta\ t_{1/2}$) in *CMTR2* KO HEK293T cells with actD-TSS-seq (Extended Data Fig. 6f,g). Here we observed that highly Cap2-modified transcripts exhibited a subtle decrease in half-lives in *CMTR2* KO cells (Extended Data Fig. 6h). However, the large difference in mRNA stability observed between the high and low Cap2-modified mRNAs in *CMTR2* WT cells remained in the *CMTR2* KO cells (Fig. 3f and Extended Data Fig. 6i). These data suggest that the mild stabilizing effect of Cap2 on mRNA does not explain the unusual longevity of Cap2-marked mRNAs.

# Cap2 levels increase with mRNA age

As Cap2 methylation does not confer long half-life to an mRNA, we considered the possibility that long half-life might cause high Cap2 methylation. Long-lived mRNAs persist longer in cells and therefore may have more time to acquire high Cap2 methylation during their cytoplasmic lifetime.

To test this, we used BruChase to capture mRNAs of increasing age[23]. In this approach, cells were pulsed with 5-bromouridine (5-BrU) for 3 h to label newly synthesized RNA. Then, the cells were chased in uridine-rich media to allow for ageing of BrU-labelled transcripts. BrU-containing RNA was immunopurified from mRNA with an anti-5-BrU antibody at 0 and 8 h (Fig. 4a).

**Fig. 4: Cap2 is an epitranscriptomic mark of mRNA age.**



**a**, Transcripts were metabolically labelled using a 3 h 5-BrU pulse and chased in uridine-containing media for 0 h and 8 h to allow isolation of young and old RNA, respectively. BrU-containing mRNAs of different age were immunopurified using an anti-5-BrU antibody (Ab) and Cap2 levels were measured using CapTag-seq. IP, immunoprecipitation. **b**, Cap2 levels in young and old mRNA. Average of $n = 2$ biological replicates. **c**, Cap2 levels on each of the 16 possible $m^7G$-proximal dinucleotides in young and old transcriptomes. Average of $n = 2$ biological replicates. **d**, CLAM-Cap–qPCR, a transcript-specific Cap2 methylation measurement method. Following generation of cDNA–cap tags attached to the 3′ end DNA adapter, Cap2 levels were measured by qPCR using a gene-specific reverse (Rv-mRNA X) and Cap2 tag-specific forward (Fw-Cap2) primer. Total (Cap1 and Cap2) cDNA–cap tags were amplified in parallel by qPCR with a primer pair comprising Rv-mRNA X and a primer that anneals to the DNA adapter (Fw-total). **e**–**h**, Fold change in Cap2 methylation as a function of mRNA age for *YBX1* (**e**), *TUBA1B* (**f**) and *RPS9* (**g**) mRNAs and for the nuclear non-coding RNA *XIST* (**h**). The level of Cap2 methylation at 0 h of the uridine chase was set to 1 ($t_0 = 1$, dashed line). $n = 3$ biological replicates. Data shown as mean ± s.d. Coloured data points denote measurements from the same experiment.

Source data

We next performed CapTag-seq on young (0 h) and old (8 h) mRNA. We found that young mRNA was 11% Cap2-modified, whereas old mRNA exhibited approximately 42% Cap2 methylation (Fig. 4b), suggesting that Cap2 methylation increases throughout the transcriptome as transcripts age in the cytosol. All 16 $m^7G$-proximal dinucleotides exhibited an increase in Cap2 methylation over time (Fig. 4c), indicating the generality of age-dependent increases in Cap2 levels across all mRNA sequence contexts.

To examine the levels of Cap2 on individual transcripts as they age, we developed CLAM-Cap–quantitative PCR (CLAM-Cap–qPCR), an amplification-based method for measurement of Cap2 levels on low-abundance mRNAs. CLAM-Cap–qPCR involves preparation of cDNA–cap tag chimeras with a DNA adapter ligated to the 3′ end of the cap tag according to the CLAM-Cap-seq protocol. Next, the levels of Cap2 are measured in an mRNA of interest by qPCR using a transcript-specific primer

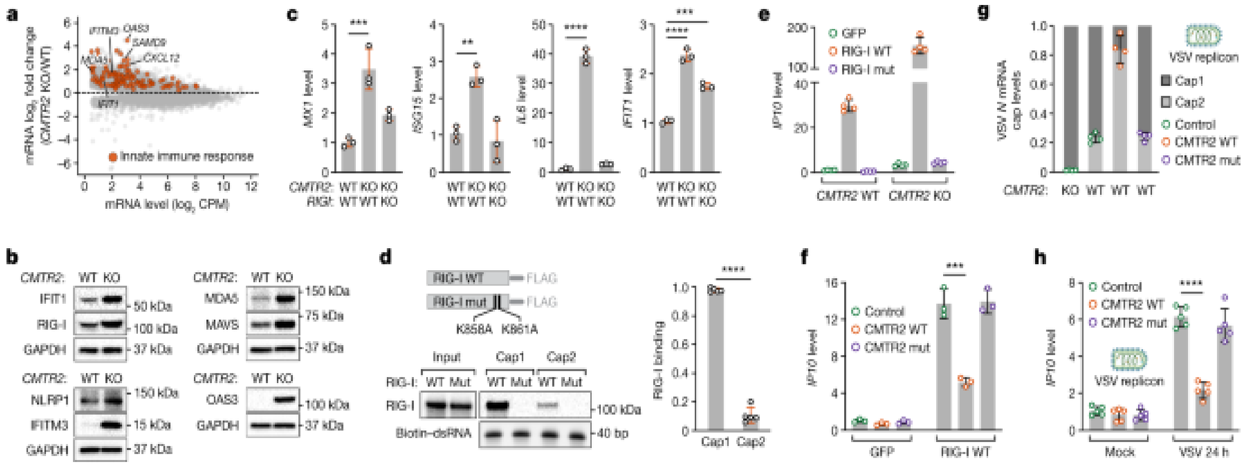
and a primer that hybridizes to the DNA adapter and the first nucleotide of the three-nucleotide-long cap tag that is unique to the Cap2 form of the mRNA (Fig. 4d). To determine the total abundance of the mRNA, a parallel qPCR is performed using a primer that hybridizes only to the 3′ adapter, but not to any portion of the cap tag (Fig. 4d). We confirmed the accuracy of this method using luciferase mRNA standards with known Cap2 stoichiometries (Extended Data Fig. 6j). Overall, this approach allowed us to calculate the Cap2 levels in an mRNA of interest.

We performed CLAM-Cap–qPCR on three long-lived mRNAs: *YBX1*, *TUBA1B* and *RPS9*. In each case, we observed that the Cap2 levels continuously increased as each mRNA aged (Fig. 4e–g). As a control, we examined the nuclear RNA *XIST*[24], which is not expected to encounter CMTR2. Indeed, we found largely unchanged Cap2 levels on *XIST* for the entire duration of the uridine chase (Fig. 4h). Overall, these data suggest that Cap2 methylation represents a dynamic mRNA modification that continuously increases throughout the mRNA lifetime.

# CMTR2 depletion induces antiviral genes

We next wanted to understand the functional implication of Cap2 methylation. To test this, we analysed gene expression changes in *CMTR2* KO HEK293T cells using RNA-seq. We found that downregulated genes were enriched in translation and RNA processing pathways, whereas markedly upregulated genes were related to the innate immune response and inflammatory pathways (Fig. 5a and Extended Data Fig. 7a). Among upregulated genes, we noticed numerous interferon-stimulated genes (ISGs), a gene group that is transcriptionally induced after cell infection with viruses, as well as other pathogens[25]. We confirmed the induction of ISGs at the protein and RNA level (Fig. 5b and Extended Data Fig. 7b–g). Similar effects were seen in *CMTR2* KO A549 cells (Fig. 5c and Extended Data Fig. 7h–j).

**Fig. 5: Cap2 methylation suppresses RIG-I activation and virus-induced innate immune response.**



**a**, RNA-seq-based measurements of gene expression changes upon CMTR2 depletion. $n = 4$ biological replicates. $n = 9{,}507$ genes. $P < 0.05$. CPM, counts per million. **b**, Expression of antiviral proteins in *CMTR2* WT and KO HEK293T cells. GAPDH was the loading control. **c**, Expression of innate immune response genes in *CMTR2* KO A549 cells requires RIG-I. Transcript levels were quantified by RT–qPCR. $n = 3$ biological replicates. **d**, HEK293T lysates expressing RIG-I or the RIG-I K858A/K861A cap-binding mutant were incubated with immobilized Cap1 and Cap2 double-stranded RNAs (dsRNAs). The pulled-down RIG-I protein was detected by western blot. The bars show quantification from $n = 5$ pulldowns. Two-tailed unpaired Student's *t*-test with Welch's correction, ****$P < 0.00001$. **e**, *CMTR2* WT and KO HEK293T cells were transfected with GFP, RIG-I WT or RIG-I mutant (mut) from **d**. *IP10* expression was measured 48 h post-transfection by RT–qPCR. $n = 4$ biological replicates. **f**, *CMTR2* WT HEK293T cells were transfected with control, CMTR2 (CMTR2 WT) and CMTR2 W85A (CMTR2 mut) constructs for 24 h. Each sample was further transfected with GFP or RIG-I WT. *IP10* expression was measured by RT–qPCR 48 h after the second transfection. $n = 3$ biological replicates. **g**, HEK293T *CMTR2* KO cells expressing control and *CMTR2* WT cells expressing control, CMTR2 WT or CMTR2 mut for 24 h were either mock-infected or VSV-infected. Cap2 methylation on viral *N* mRNA was assessed with CLAM-Cap–qPCR 24 h post-infection. The stacked bar plot shows the fraction of Cap1-modified and Cap2-modified VSV *N* mRNA. The Cap1 fraction was calculated as 1 − Cap2 fraction. $n = 4$ biological replicates. **h**, *CMTR2* WT HEK293T cells were treated as in **g**. *IP10* expression was assessed 24 h post-infection by RT–qPCR. $n = 5$ biological replicates. In **c**–**h**, data shown as mean ± s.d. In **c**,**f**,**h**, one-way ANOVA with Bonferroni

multiple comparison test was used; $^{**}P < 0.01$, $^{***}P < 0.001$ and $^{****}P < 0.0001$.

Source data

The magnitude of the ISG induction was comparable to that of the induction seen after wild-type HEK293T cells were treated with interferon (750 U $ml^{-1}$) for 6 h (Extended Data Fig. 7k). The induction of ISGs was sufficient to sensitize cells to diverse inflammatory signals (Extended Data Fig. 7l–p).

Overall, these data suggest that the lack of Cap2, and thus the increase in Cap1 mRNA levels, leads to the activation of pathways that are normally triggered in response to viral RNA. As *CMTR2* KO cells are not exposed to an exogenous virus, the induction of the innate immune response may be mediated by the change in cap methylation of endogenous RNAs.

# Cap2 suppresses RIG-I activation

The effects of Cap2 loss may be mediated by a specific RNA-binding protein whose RNA-binding activity is affected by Cap2 methylation. RIG-I is a well-established sensor of foreign RNA that becomes activated upon binding to the triphosphate bridge of $m^7G$-capped RNAs[26,27]. RIG-I is markedly activated by Cap0 RNA due to the low nanomolar affinity (2 nM) of RIG-I for Cap0 RNA[27,28].

Methyl modifications of RNA impair the binding of capped RNA to RIG-I. A 2′-*O*-methylation at the first nucleotide in Cap1 RNA leads to markedly reduced binding affinity (425 nM)[27]. 2′-*O*-methylation at the second nucleotide also reduces RIG-I activation[26]. In this study, the RNA only contained a single methyl modification at the second position, and not a dual methylation as seen in Cap2. Therefore, it remains unclear whether dual methylation in Cap2 would further reduce the binding affinity of Cap1 RNA to RIG-I. Overall, these studies raise the possibility that some of the cellular effects of CMTR2 depletion may be mediated by RIG-I.

To address this, we first asked whether RIG-I activity contributes to the induction of ISGs in *CMTR2* KO cells. We generated *CMTR2*, *RIG-I* double

KO A549 cells and monitored the expression of several ISGs by qPCR with reverse transcription (RT–qPCR) (Fig. 5c and Extended Data Fig. 7h,j). We found that RIG-I depletion markedly reduced the expression of ISGs in *CMTR2* KO cells, demonstrating RIG-I involvement in the induction of the innate immune response in these cells.

Next, we directly measured the effect of Cap2 on the RNA-binding capacity of RIG-I. We incubated equal amounts of streptavidin-immobilized Cap1 and Cap2 double-stranded RNAs with cell lysates expressing FLAG-tagged RIG-I. Consistent with previous studies[27], RIG-I readily bound to Cap0 RNA (Extended Data Fig. 8a). RIG-I also showed lower, but clear binding to Cap1 RNA. However, RIG-I exhibited markedly lower interaction with Cap2 RNA (Fig. 5d and Extended Data Fig. 8a,b). Neither Cap1 nor Cap2 RNA bound to RIG-I K858A/K861A, a RIG-I mutant that cannot interact with the triphosphate bridge of the cap structure[29] (Fig. 5d). These results confirm the cap-dependent nature of the observed interactions. Overall, these data demonstrate that the dual methylation in Cap2 RNAs further reduces the ability of Cap1 RNAs to bind RIG-I.

Although Cap1 is not thought to be an activating ligand for RIG-I, we wanted to know whether high levels of Cap1 could activate RIG-I in cells. To measure RIG-I activation, we overexpressed RIG-I in HEK293T cells, which led to the induction of *IP10* (Fig. 5e), a frequently used marker for RIG-I activation[28,30]. However, overexpression of RIG-I in *CMTR2* KO cells, whose transcriptome is solely composed of Cap1 RNA, resulted in markedly increased levels of *IP10* (Fig. 5e). These data suggest that Cap1 RNA can activate RIG-I if it is present at high levels.

Of note, the observed activation of RIG-I depends on the RNA cap structure as overexpression of RIG-I K858A/K861A failed to induce *IP10* (Fig. 5e). Expression of RIG-I constructs remained similar in all tested samples (Extended Data Fig. 9a).

To determine whether the low level of activation of RIG-I in wild-type HEK293T cells was due to Cap1 mRNAs (approximately 60% of mRNAs; see Fig. 1e), we overexpressed CMTR2 to convert Cap1 to Cap2 mRNAs before RIG-I overexpression. Here we found that RIG-I expression led to markedly reduced *IP10* levels relative to control RIG-I-expressing cells (Fig.

5f). Conversely, RIG-I activation was not reduced in cells expressing CMTR2 W85A, a mutant that cannot methylate the cap structure[7] (Fig. 5f). RIG-I expression remained similar across all tested samples (Extended Data Fig. 9b). Overall, these data suggest that the function of the dual methylation in Cap2 is to further reduce the binding of Cap1 to RIG-I, thus decreasing the immunostimulatory effects seen at high concentrations of Cap1.

We confirmed previous studies showing that transfected Cap1 RNA is unable to activate RIG-I probably due to the low level of transfected RNA and its weak binding affinity (Extended Data Fig. 9c). However, the transcriptome-wide increase in Cap1 levels due to CMTR2 depletion may be sufficient to achieve Cap1 concentrations needed to activate RIG-I.

## Cap2 in viral RNA impairs host response

Although our data demonstrate that Cap2 suppresses the ability of endogenous Cap1 RNA to induce the innate immune response, the purpose of a slow, time-dependent methylation of Cap1 to Cap2 is unclear. We considered the possibility that slow Cap2 methylation allows the host cell to detect and respond to rapidly replicating viral Cap1 RNAs before the viral RNA acquires high levels of Cap2 over time.

To test this model, we used vesicular stomatitis virus (VSV), an RNA virus that triggers the expression of antiviral genes, in part through RIG-I activation[31]. Although VSV RNA acquires Cap1 by virally encoded enzymes, it utilizes host CMTR2 to achieve low Cap2 levels[32]. Therefore, we used CMTR2 overexpression to enhance Cap2 methylation efficiency in VSV RNA. In this way, we could determine whether the normally low Cap2 methylation efficiency enables efficient induction of the innate immune response by VSV.

To test this, we first infected control HEK293T cells with propagation-incompetent VSV[33] (Extended Data Fig. 9d). Consistent with previous studies[34,35], VSV infection resulted in the rapid accumulation of viral RNA to an amount comparable to the entire mRNA transcriptome of mock-infected cells (Extended Data Fig. 9e,f). Viral transcripts were

predominantly Cap1-modified (Fig. 5g and Extended Data Fig. 9g,h). This increase in Cap1 levels was associated with the expected induction of *IP10* mRNA (Fig. 5h). Thus, the VSV-induced increase in Cap1 may contribute to the activation of the innate immune response.

We next attempted to increase Cap2 methylation efficiency of viral RNA by overexpressing CMTR2. Overexpression of CMTR2 markedly increased Cap2 stoichiometry on viral RNA, resulting in the concomitant reduction in Cap1 levels (Fig. 5g and Extended Data Fig. 9g,h). In CMTR2-overexpressing cells, VSV infection failed to induce *IP10* mRNA to the levels seen in control infected cells (Fig. 5h). This was due to cap-mediated methylation, as CMTR2 W85A failed to suppress *IP10* induction (Fig. 5g,h and Extended Data Fig. 9g,h). Overall, these data suggest that cells maintain low efficiency of Cap2 methylation to prevent viral RNA from acquiring Cap2 and evading host defence mechanisms.

As a control, we asked whether CMTR2 overexpression nonspecifically suppresses the innate immune response. To test this, we activated the innate immune response using noncapped RIG-I ligands, such as triphosphorylated double-stranded RNA and poly(I:C)[36]. Although HEK293T cells express RIG-I protein at low levels (Fig. 5b), they have previously been shown to respond to double-stranded RNA ligands in a RIG-I-dependent manner[37]. Consistent with this, we found that both stimuli readily induced *IP10* mRNA expression (Extended Data Fig. 9i). However, CMTR2 overexpression did not suppress their effects on *IP10* mRNA levels (Extended Data Fig. 9i). These data are consistent with a model in which increased expression of CMTR2 selectively suppresses antiviral responses induced by Cap1 RNAs.

# Discussion

Cap2 was discovered nearly 50 years ago as one of the five major methyl modifications that decorate mRNA along with $m^7G$, $N^6$,2′-*O*-dimethyladenosine ($m^6A_m$), Cap1 and $N^6$-methyladenosine ($m^6A$). Despite the high prevalence of Cap2 in the transcriptome, Cap2 is the last major unmapped nucleotide modification. Using CLAM-Cap-seq, we generated a transcriptome-wide map of Cap2, which revealed strong Cap2 enrichment on long-lived mRNAs, occurring as a result of mRNA age-guided Cap2

deposition in the transcriptome. Rather than controlling mRNA processing events such as translation or stability, a major function of Cap2 is to further suppress the ability of endogenous RNAs to activate the innate immune response. Mechanistically, the dual methylation in Cap2 acts to prevent Cap1 from binding to RIG-I, thus suppressing the autoimmune potential of endogenous Cap1 RNA. We also show that slow, time-dependent accumulation of Cap2 in mRNAs represents a cellular adaptation used to cloak host RNAs from activating RIG-I. Simultaneously, slow Cap2 methylation reduces the likelihood that rapidly replicating viral RNA acquires Cap2 and thus evades recognition by host cell defences.

The cell requires mechanisms to distinguish self from non-self RNA. Methylation of mRNA caps is one of the major mechanisms to mark self mRNAs. Cap0 RNAs that lack ribose methylation are high-affinity ligands and potent activators of RIG-I[27]. Small amounts of Cap0 can therefore activate the innate immune response. The presence of a single methyl group in Cap1 is sufficient to reduce the ability of RNA to activate RIG-I. Although the binding affinity of Cap0 to RIG-I is 2 nM, Cap1 still binds at an affinity of 425 nM (ref. [27]). We found that large amounts of Cap1 RNA, achieved by depletion of CMTR2 or by viral infection, can provide sufficient levels of Cap1 to activate RIG-I. Thus, even though Cap1 only activates RIG-I weakly, the large amount of Cap1 in the cell, coupled with the induction of RIG-I expression in response to viral infection, can make Cap1 RNA an important agonist of RIG-I signalling.

Previous studies have shown that methylation at either the first or second position of RNA is sufficient to reduce activation of RIG-I[26]. We showed that the dual methylation in Cap2 functions to reduce the ability of Cap1 RNA to bind to and activate RIG-I. Although our study identifies RIG-I as an ‘anti-reader’ of Cap2, *RIG-I* KO did not completely reduce the induction of the ISGs after CMTR2 depletion. Other proteins, such as IFITs[38,39] or other foreign RNA sensors such as MDA5 (ref. [40]), may also be sensitive to Cap2 methylation and therefore regulate aspects of mRNA biology.

Of note, some viruses have acquired CMTR2 homologues, such as Mimivirus and African swine fever virus[9]. The CMTR homologue in vaccinia virus has been proposed to methylate the first, second and possibly

other nucleotides[41]. Thus, viral CMTR homologues may have broader methylation functions than previously recognized, including Cap2 methylation, which may help to them to evade host responses.

The levels of Cap1 and Cap2 vary in different cells and tissues, which correlate in part with CMTR2 levels (Extended Data Fig. 1c,d). Although higher Cap1 levels may be deleterious for cells, we found that these cells typically exhibit lower RIG-I expression, which may reduce the autoinflammatory potential of high levels of Cap1 RNA (Extended Data Fig. 10a–c). Cells may adjust the levels of CMTR2 to influence their cellular responses to either host or viral RNAs, and aberrant levels of Cap1 may contribute to diseases that are linked to excessive activation of the innate immune response (Extended Data Fig. 10d).

In addition to suppressing the immunostimulatory effects of cellular RNAs, Cap2 may affect mRNAs in other ways. Our global analyses showed small but clear effects of Cap2 on mRNA translation or stability. Cap2 may thus shape gene expression, particularly for long-lived transcripts, to further enhance their stability in cells and to increase their protein expression. In addition, some RNAs may have a stronger dependence on Cap2 for preventing their interaction with RIG-I, and thus may have a more important role in suppressing the innate response when Cap2-modified. Other RNAs may contribute to the biology of Cap2, including snRNAs[16]. Finally, Cap2 has been linked to neuronal functions in *Drosophila*[41], suggesting different roles of Cap2 in lower organisms.

We developed a suite of tools to profile and measure Cap2 in transcriptomes and on specific mRNAs of interest. Measurements of Cap1 and Cap2 cap tags using CapTag-seq reveals the overall Cap2 prevalence in bulk mRNA, whereas CLAM-Cap-seq involves creating cDNA–cap tag chimeras that directly link the Cap2 status of an mRNA to the cDNA that is generated from it. Along with newly developed biochemical and PCR-based methods, the Cap1 or Cap2 state of any mRNA of interest can be readily measured.

Our data show that Cap2 is fundamentally different from other epitranscriptomic mRNA modifications. First, Cap2 methylation is a dynamic process, as it continuously accumulates throughout the lifetime of an mRNA in the cytoplasm. This contrasts other mRNA modifications such

as $m^6A$, which are largely ‘written’ in the nucleus and thus exhibit little or no potential for dynamics once the mRNA has left the nucleus. Although CMTR2 exhibits slight preferences for methylation of some $m^7G$-proximal sequences, it does not require strictly defined sequence motifs. Furthermore, the primary purpose of Cap2 is not to regulate mRNA fates, as is seen with $m^6A$[42], but is instead to lower the overall burden of Cap1 RNAs on the intracellular defence mechanisms designed to fight against invading pathogens.

# Methods

## Cell culture

HEK293T, A549 and MCF-7 cells were purchased from the American Type Culture Collection. mES cells were obtained as a kind gift from J. Hanna’s laboratory. HEK293T and MCF-7 cells were maintained in DMEM (11995065, Gibco) supplemented with 10% FBS and 100 U penicillin–streptomycin (15140148, Gibco). A549 cells were grown in Ham’s F-12K medium (21127022, Gibco) supplemented with 10% FBS and 100 U penicillin–streptomycin. mES cells were cultured in Knockout DMEM (10829018, Gibco) supplemented with 15% heat-inactivated FBS, 100 U penicillin–streptomycin, 1× GlutaMAX (35050061, Gibco), 55 µM β-mercaptoethanol, 1× MEM non-essential amino acid solution (11140076, Gibco), $10^3$ U $ml^{-1}$ LIF (ESG1107, ESGRO), 3 µM CHIR99021 (72052, STEMCELL Technologies) and 1 µM PD0325901 (72182, STEMCELL Technologies). All cell types were grown in sterile cell culture incubators at 37 °C and 5% $CO_2$. Cell lines were not authenticated. All cell types tested negative for mycoplasma contamination. Mycoplasma contamination was routinely tested with Hoechst staining.

## Generation of KO cell lines

To generate *CMTR2* KO HEK293T cells, $6 \times 10^5$ HEK293T cells were seeded in a single well of a six-well cell culture plate. The next day, cells were transfected with 1 µg FTSJD1 double nickase plasmid (SC-412604-NIC, Santa Cruz Biotechnology) using 2 µl LipoD239 transfection reagent

(SL100668, SignaGen Laboratories). After 36 h, GFP-positive cells were sorted by flow cytometry and seeded into a single well of a 12-well cell culture plate. After 24 h, GFP-positive cells were treated with 5 μg $ml^{-1}$ puromycin for 36 h. The remaining viable cells were washed twice with PBS and grown until 30–50% confluency was reached. Single-cell clones were isolated and screened for CMTR2 depletion using western blot. To generate *CMTR2* KO and *CMTR2 RIG-I* double KO A549 cells, $2.5 \times 10^5$ A549 cells were seeded in a single well of a six-well plate. The following day, cells were transfected with either 2.5 μg FTSJD1 double nickase plasmid or a mixture of 1.5 μg FTSJD1 and 1.5 μg RIG-I (SC-400812-NIC, Santa Cruz Biotechnology) double nickase plasmids using Lipofectamine 3000 transfection reagent (L3000001, Invitrogen) according to the manufacturer's instructions. The procedure for isolation of single-cell KO clones was performed as described for HEK293T cells.

## Animal maintenance and procedures

All animals used in this study were maintained in compliance with Weill Cornell Medicine Institutional Animal Care and Use Committee (IACUC) protocols. Eight-week-old CL57B/L wild-type female mice were purchased from Charles River Laboratory and housed in standard cages with unrestricted supplies of water and food with 14 h light–10 h dark cycle at 18–23 °C and 40–60% humidity. Sixteen-week-old female mice were dissected for isolation of the brain, liver, kidney, lung, heart and spleen. Upon isolation, organs were stored in TRIzol reagent at −80 °C until further use. The zebrafish wild-type AB line was used in this study. Embryos were maintained in E3 medium at 28 °C and staged as previously described[43]. Forty-eight-hour-old zebrafish embryos were collected in TRIzol reagent and stored at −80 °C until further use.

## Total RNA isolation

Total RNA was isolated from cells using TRIzol reagent according to the manufacturer's instructions unless otherwise stated. For isolation of total RNA from mouse tissues, TRIzol-submerged tissues were homogenized with high-impact zirconium 1.5-mm beads (D1032-15, Benchmark Scientific) twice at 50 Hz for 3 min using TissueLyser II (Qiagen). For

isolation of total RNA from zebrafish samples, embryos were dissolved in TRIzol reagent and passed three times through a 21-gauge needle.

## mRNA extraction

Total RNA (20 µg) was diluted in 75 µl nuclease-free water. Oligo$(dT)_{25}$ magnetic beads (50 µl; bed volume; S1419S, NEB) were resuspended in 75 µl 2× mRNA binding buffer (40 mM Tris-HCl pH 7.5, 1 M LiCl, 2 mM EDTA and 0.1% Triton X-100) and mixed with total RNA. Samples were heated at 65 °C for 5 min, placed on ice for 3 min and incubated at room temperature for 10 min with constant rotation. Beads were washed twice with 150 µl mRNA wash buffer (20 mM Tris-HCl pH 7.5, 150 mM LiCl, 1 mM EDTA and 0.01% Triton X-100) and resuspended in 75 µl mRNA elution buffer (10 mM Tris-HCl pH 7.5). Samples were heated at 75 °C for 2.5 min and placed on ice for 2 min. To ensure pure mRNA isolation, a second round of poly$(A)^+$ RNA purification was conducted. 75 µl 2× mRNA binding buffer was mixed with the beads from the previous step, followed by incubation for 10 min at room temperature with constant rotation. Beads were then washed once with 150 µl mRNA wash buffer and resuspended in 25 µl water. To allow for the final mRNA elution from the beads, samples were heated at 75 °C for 3 min and the supernatant was collected. The extracted mRNA was further purified using a Zymo Research Clean and Concentrator-5 (RCC-5) column (R1013, Zymo Research). In the experiments in which a higher or lower amount of total RNA was used, mRNA was isolated by upscaling or downscaling of the mRNA isolation reagents.

## CapTag-seq

mRNA (2 µg) was treated with 25 U Quick CIP (M0525L, NEB) in a 30-µl reaction for 30 min at 37 °C. The reaction was cleaned using a Zymo RCC-5 column and mRNA was eluted with 20 µl water. $m^7$GDP was removed from mRNA 5′ termini (decapping) using 5 U Cap-Clip acid pyrophosphatase (C-CC15011H, CELLSCRIPT) in a 20-µl reaction for 1 h at 37 °C. The mRNA decapping reaction was cleaned with Zymo RCC-5 column and mRNA was eluted in 11.5 µl water. A biotinylated 5′ adapter composed of 2′-*O*-methylated nucleotides (biotin-$N_m$-RA5) was ligated to the 5′-

monophosphorylated mRNA ends using 60 U T4 RNA ligase 1 (M0437M, NEB) in the following 30 µl reaction mixture: 3 µl 10× RNA ligase buffer, 10 µl decapped mRNA, 3 µl 10 mM ATP, 1 µl 30 µM biotin-$N_m$-RA5, 10.5 µl 50% PEG-8000, 0.5 µl 40 U $µl^{-1}$ RNaseOUT and 2 µl 30 U $µl^{-1}$ T4 RNA ligase 1 for 4 h at 25 °C. To successfully remove non-ligated biotin-$N_m$-RA5, the ligation reaction was cleaned three times with Zymo RCC-5 column following the manufacturer's protocol for isolation of RNA longer than 200 nucleotides. Ligated mRNA was eluted in the third cleanup step in 40 µl water. Next, ligated mRNA was digested to completion with 5 U RNase T2 (GE-NUC00400-02, MoBiTec) in 30 mM Na-acetate pH 4.5 overnight at 37 °C. The resulting adapter-linked cap tags were captured on M-280 streptavidin Dynabeads (20 µl bed volume, Invitrogen) in 300 µl binding buffer (10 mM Tris-HCl pH 7.5, 300 mM NaCl and 0.05% Triton X-100) for 30 min at room temperature. Beads were washed twice with 500 µl high-salt buffer (10 mM Tris-HCl pH 7.5, 2 M NaCl and 0.1% Triton X-100), twice with 500 µl binding buffer, and twice with 500 µl low-salt buffer (10 mM Tris-HCl pH 7.5, 50 mM NaCl and 0.025% Triton X-100). The removal of the 2′,3′-cyclic phosphate from the 3′ end of cap tags was conducted using 10 U T4 PNK (M0201L, NEB) in a 20 µl dephosphorylation buffer (100 mM Na-acetate pH 6.0, 10 mM $MgCl_2$ and 5 mM DTT) for 20 min at 23 °C. Beads were washed twice with 500 µl binding buffer, and twice with 500 µl low-salt buffer. Next, the preadenylated DNA adapter with a 20-nucleotide randomized region ($N_{20}$-DA3) was ligated to the dephosphorylated 3′ ends of cap tags with 200 U T4 RNA ligase 2, truncated KQ (M0373L, NEB) in a 20 µl ligation mix (2 µl 10× RNA ligase buffer, 1 µl 20 µM DA3, 7 µl water, 1 µl 200 U $µl^{-1}$ T4 RNA ligase 2, truncated KQ, 8.5 µl 50% PEG-8000 and 0.5 µl 40 U $µl^{-1}$ RNaseOUT) for 4 h at 27 °C. The non-ligated $N_{20}$-DA3 was removed with 25 U yeast 5′-deadenylase (M0331S, NEB) and 15 U RecJf (M0264S, NEB) for 45 min at 30 °C. Beads were washed twice with 500 µl high-salt buffer, twice with 500 µl binding buffer and twice with 500 µl low-salt buffer. For cDNA preparation, beads were first resuspended in 12 µl reverse transcription annealing mix (1 µl 10 µM reverse transcription primer (RTP), 4 µl 250 mM Tris-HCl pH 8.3, 5 µl 300 mM KCl and 2 µl water), heated at 90 °C for 2 min, and slowly cooled down to 25 °C with a rate of 0.1 °C $s^{-1}$. Following the RTP annealing, 7.25 µl RT mixture (4 µl water, 1 µl 0.1 M DTT, 1 µl 10 mM dNTPs (each), 1 µl 60 mM $MgCl_2$ and 0.25 µl 40 U

ul$^{-1}$ RNaseOUT) and 0.75 µl SuperScript III (18080051, Invitrogen) were added to the annealing mix. The reaction was incubated for 30 min at 55 °C, and heat inactivated for 10 min at 75 °C. PCR amplification of cDNA was performed with 2× Phusion High Fidelity PCR master mix with HF buffer (M0531L, NEB). The resulting PCR products were purified twice with 1.8× PCR volume AMPure XP beads (A63881, Beckman Coulter). Amplified cDNA libraries were sequenced on Illumina instruments in a single-end or paired-end modes.

## CapTag-seq data analysis

Low-quality sequencing reads were filtered out and the 3′ end adapter (DA3) was trimmed off using Flexbar v2.5 (ref. [44]). Duplicated reads were removed using the pyFastqDuplicateRemover.py script within the pyCRAC package[45]. Next, the 20-bp-long randomized region was removed from the 3′ end of sequencing reads using the UNIX cut command. The remaining portion of the reads represents RNase T2-released tags. Tag length distribution, quantification of the two-nucleotide and three-nucleotide-long cap tags from Cap1 and Cap2 mRNAs, respectively, and Cap1 and Cap2 $m^7$G-proximal sequences of cap tags were obtained using basic UNIX commands.

## TSS-seq

mRNA (200 ng) was treated with 25 U Quick CIP in a 30-µl reaction for 30 min at 37 °C. The reaction was cleaned using a Zymo RCC-5 column and mRNA was eluted in 17 µl water. $m^7$GDP was removed from the mRNA 5′-termini using 5 U Cap-Clip acid pyrophosphatase in a 20-µl reaction for 1 h at 37 °C. The decapped mRNA was isolated by mixing the decapping reaction with 44 µl RNAClean XP beads (A63987, Beckman Coulter). After 15 min of incubation at room temperature, the beads were washed twice with 80% ethanol and mRNA was eluted from the beads in 10 µl water for 5 min. Next, a biotinylated 5′ RNA adapter with the eight-nucleotide-long unique molecular identifiers (biotin-RA5-UMIs) was ligated to the 5′-monophosphorylated mRNA ends with 60 U RNA ligase 1 in the 30-µl reaction as described in CapTag-seq. Ligated mRNA was purified by mixing the ligation reaction with 44 µl 1.5 M NaCl and 31 µl RNAClean XP beads.

After 10 min of incubation at room temperature, beads were washed twice with 80% ethanol and RNA was eluted from the beads in 20 µl water for 5 min. Eluted RNA was further mixed with 28 µl RNAClean XP beads and incubated for 10 min at room temperature. Beads were washed twice with 80% ethanol and RNA was eluted as before in 20 µl water. Next, the ligated mRNA was subjected to a partial alkaline-based fragmentation by mixing 20 µl mRNA with 5 µl 240 mM $NaHCO_3$ and 5 µl 360 mM $Na_2CO_3$. The fragmentation mixture was incubated for 11 min at 60 °C and immediately placed on ice. Fragmented RNA was extracted using a Zymo RCC-5 column, eluted in 20 µl water and stored at −80 °C until further use. The following day, ligated mRNA 5′ ends were captured on M-280 streptavidin Dynabeads (20 µl bed volume) in 100 µl binding buffer for 30 min at room temperature. Next, the beads were washed twice with 500 µl high-salt buffer, twice with 500 µl binding buffer and twice with 500 µl low-salt buffer. Dephosphorylation of the 3′ ends of RNA fragments, ligation of the preadenylated DNA adapter (DA3) and reverse transcription steps were conducted as described in the CapTag-seq protocol. For the reverse transcription reaction, samples were incubated for 45 min at 55 °C, followed by heat inactivation for 10 min at 75 °C. cDNA was PCR amplified using 2× Phusion High Fidelity PCR master mix with HF buffer and the resulting PCR products were purified twice with 0.9× PCR volume AMPure XP beads. Amplified cDNA libraries were sequenced on the Illumina instrument in a paired-end mode.

## TSS-seq data analysis

Low-quality sequencing reads were filtered out and the 3′ end adapter (DA3) was trimmed off using Flexbar v2.5 (ref. [44]). Duplicated reads were removed using the pyFastqDuplicateRemover.py script within the pyCRAC package v1.3.2 (ref. [45]). Only the read R1 was considered for further analysis. Eight-nucleotide-long randomized region (UMIs) was removed from the 5′ end of sequencing reads using seqtk. UMI-free reads were then shortened from the 3′ end to the universal length of 25 bp using seqtk. The first nucleotide of the processed, 25-bp-long reads represents the TSN of an mRNA. The processed reads were first aligned to the *Drosophila melanogaster* genome (dm6) using Bowtie v1.2.3 (ref. [46]). The remaining, unmapped reads were then aligned to the human (h38) or mouse (mm10) genome using Bowtie v1.2.3. The 5′ end

read coverage (representing a TSN coverage) per each genomic position was obtained using BEDTools v2.28.0 (ref. [47]). The Ensembl gene annotation file was obtained from Ensembl[48] and annotated gene starts were extended by 250 bp. The aligned reads were annotated with BEDTools using the modified Ensembl gene annotation file. For each sample, 5′ end read coverage per each genomic position was normalized to the total number of mapped reads (mapped reads per million (RPM)). Genomic positions with the normalized 5′ end coverage < 2 RPM were discarded. A genomic position with the maximum coverage within an annotated gene was identified as the major TSN isoform of a gene. All other genomic positions within that gene with normalized 5′ end coverage more than 10% of the maximum (major) TSN were considered as alternative TSN isoforms for that gene.

## ActD-TSS-seq

*CMTR2* WT or *CMTR2* KO HEK293T cells ($1.8 \times 10^6$) were seeded in a 6-mm cell culture dish. The day after seeding, cells were treated with 5 µg $ml^{-1}$ actD to block synthesis of new transcripts. Total RNA was extracted from cells after 0, 2, 8 and 16 h of actD treatment. Total RNA of each sample was spiked-in with 40 ng *D. melanogaster* poly(A)$^+$ RNA (636222, Takara). Cellular poly(A)$^+$ RNA was extracted using oligo(dT)$_{25}$ magnetic beads. mRNA (200 ng) from each time point of actD treatment was subjected to the TSS-seq protocol as described above.

## ActD-TSS-seq data analysis

Sequencing reads were processed as described above with minor modifications.

The annotated TSN isoforms with expression more than 4 RPM at 0 h of actD treatment were considered for calculations of mRNA half-lives. The TSN isoform expression at each time point of actD treatment was first normalized to the total number of reads mapping to the *D. melanogaster* genome in each sample. The normalized TSN expression was then transformed with a sample-specific scale factor determined from the general mRNA decay rate in HEK293T cells (see Extended Data Figs. 5g and 6f). The scaling factors were as follows: for 0 h actD = 1, for 2 h actD = 0.77, for

8 h actD = 0.56 and for 16 h actD = 0.41. The fully normalized TSN isoform expression values at each time point after actD treatment were then used for the calculation of the mRNA decay rates with a one-phase decay model using the drm function in the drc R package[49]. TSN isoform half-lives were calculated as: $t_{1/2} = \ln 2/k$, where $k$ represents the TSN isoform-specific decay constant derived from the drm function.

## Polysome–TSS-seq

*CMTR2* WT or *CMTR2* KO HEK293T cells ($8 \times 10^6$) were seeded onto a 150-mm cell culture dish. The following day, cells were treated with 100 µg ml$^{-1}$ cycloheximide (CHX; C7698, Sigma) for 5 min at 37 °C. Cell dishes were placed in ice, washed once with 10 ml ice-cold PBS supplemented with 100 µg ml$^{-1}$ CHX (PBS + CHX), and scraped in 8 ml PBS + CHX. Cells were pelleted at 300*g* for 3 min at 4 °C, supernatant aspirated, and cell pellet was resuspended in 0.5 ml ice-cold polysome extraction buffer (20 mM Tris-HCl pH 7.5, 100 mM KCl, 1% Triton X-100, 5 mM $MgCl_2$, 2 mM DTT, 100 µg ml$^{-1}$ CHX and 1× Halt protease and phosphatase inhibitor cocktail (78440, Thermo Scientific)). Cells were left on ice for 5 min to lyse. The cell lysis process was facilitated by passing cells through a 21-gauge needle. Cell lysate was centrifuged for 5 min at 16,000*g* at 4 °C, the supernatant was transferred to a new 1.5-ml tube and snap frozen in liquid nitrogen. Frozen cell lysates were stored at −80 °C until further use. Frozen cell lysates were thawed on ice. Lysate (500 µl) was layered on top of the 10–50% linear sucrose gradient prepared with polysome extraction buffer. The gradient was centrifuged for 2 h at 36,000*g* in a SW-41 Ti swinging bucket rotor at 4 °C. Polysome fractionation was performed using an automated fraction collector (BioComp) with a continuous monitoring of the 254-nm absorbance. Fractions corresponding to a one, two–three, four–five, six–seven and more than eight ribosomes were collected manually. *Drosophila* poly(A)$^+$ RNA (3 µl of 2.5 ng µl$^{-1}$) was spiked-in to each fraction to account for differences in RNA extraction between fractions. Next, an equal volume of TRIzol LS was added to each isolated polysome fraction along with 15 mM EDTA (final concentration). Tubes were briefly vortexed and left at room temperature for 30 min. Total RNA was isolated as instructed by the TRIzol LS manufacturer’s protocol and precipitated using isopropanol. mRNA was

extracted from the total RNA of each polysome fraction with oligo(dT)$_{25}$ magnetic beads. Poly(A)$^+$ RNA (200 ng) from each fraction was subjected to the TSS-seq protocol as described above.

## Polysome–TSS-seq data analysis

Sequencing reads were processed as described in the actD-TSS-seq data analysis with minor modifications. The genomic positions with 5′ end read coverage of more than 1 RPM in each polysome fraction were considered. Genomic positions that passed this expression threshold were then annotated to the TSN isoforms identified in the input sample (0 h actD-TSS-seq libraries) using BEDTools. The expression (RPM) of the annotated TSN isoforms was further normalized to the total number of reads mapping to the *D. melanogaster* genome in each polysome fraction. Following the normalization, an average number of ribosomes bound to each TSN isoform was calculated as follows: total abundance of a TSN isoform ($N_{\mathrm{total}}$) was calculated as the sum of the TSN isoform expression levels ($N$) in each of the five isolated polysome fractions ($F_n$): $N_{\mathrm{total}} = N_{\mathrm{F1}} + N_{\mathrm{F2}} + N_{\mathrm{F3}} + N_{\mathrm{F4}} + N_{\mathrm{F5}}$, where $F$ denotes polysome fraction number. Total number of ribosomes ($R_{\mathrm{total}}$) associated with each TSN isoform was calculated as $R_{\mathrm{total}} = f_1 \times N_{\mathrm{F1}} + f_2 \times N_{\mathrm{F2}} + f_3 \times N_{\mathrm{F3}} + f_4 \times N_{\mathrm{F4}} + f_5 \times N_{\mathrm{F5}}$, where $f$ denotes the number of ribosomes present in each polysome fraction ($f_1 = 1$, $f_2 = 2.5$, $f_3 = 4.5$, $f_4 = 6.5$ and $f_5 = 12$). The average number of ribosomes bound to each TSN isoform (MRL) was then calculated as MRL = $R_{\mathrm{total}}/N_{\mathrm{total}}$. Translation efficiency of each TSN isoform was defined as the average ribosome density on each TSN isoform. Ribosome density (MRL per kb) was calculated as MRL per kilobase of the mRNA open reading frame.

## CLAM-Cap-seq

mRNA (1 µg) was partially fragmented in a 60-µl reaction containing 40 mM $NaHCO_3$ and 60 mM $Na_2CO_3$ for 8.5 min at 60 °C. Seven independent fragmentation reactions were combined (7 µg poly(A)$^+$ RNA in total) and collectively purified using a Zymo RCC-5 column. Fragmented mRNA was eluted from the column in 31 µl water. Next, the internal mRNA fragments

were 5′ end phosphorylated with 10 U T4 PNK in two separate 30-μl reactions (15 μl mRNA, each) for 30 min at 37 °C. Two phosphorylation reactions were combined and cleaned as described before. mRNA was eluted from the column in 21 μl water. Next, 5′-phosphorylated internal mRNA fragments were removed with 1 U Terminator 5′ phosphate-dependent exonuclease (TER51020, Lucigen) in two separate 15-μl reactions (10 μl mRNA, each) for 1 h at 30 °C. The remaining $m^7G$-protected 5′ mRNA fragments were purified by mixing two combined Terminator reactions (30 μl total) with 45 μl RNAClean XP beads. The mixtures were left at room temperature for 15 min, followed by two bead washes with 80% ethanol. RNA was eluted from the beads in 16 μl water for 5 min. Enriched 5′ mRNA fragments were subjected to $m^7GDP$ removal with 7.5 U Cap-Clip acid pyrophosphatase in a 20-μl reaction for 1 h at 37 °C. The decapping reaction was mixed with 36 μl RNAClean XP beads and 84 μl 100% ethanol, and left at room temperature for 15 min. The beads were washed twice with 80% ethanol, and decapped mRNA fragments were eluted from the beads in 11 μl water for 5 min. Next, the decapped mRNA fragments were incubated in the annealing mix (10 μl decapped mRNA fragments, 1 μl 10 μM biotin-$N_6$-DA3-RTP, 2 μl 500 mM Tris-HCl pH 8.3, and 2 μl 750 mM KCl) at 90 °C for 1.5 min and cooled down quickly to 4 °C. Following $N_6$-DA3-RTP annealing, 4.25 μl RT mix (2 μl 0.1 M DTT, 1 μl 10 mM dNTPs (each), 1 μl 60 mM $MgCl_2$ and 0.25 μl 40 U $μl^{-1}$ RNaseOUT) was added to the annealing mix along with 0.75 μl 200 U $μl^{-1}$ Maxima reverse transcriptase RNase H minus (EP0752, Thermo Scientific). The reverse transcription reaction was incubated at 25 °C for 7.5 min, followed by a 10-min incubation at 52 °C and a 30-min incubation at 57 °C. Reactions were cooled down to 4 °C, mixed with M-280 streptavidin Dynabeads (10-μl bed volume) in 100 μl binding buffer and incubated at room temperature for 30 min. The beads were washed twice with 500 μl binding buffer and twice with 500 μl low-salt buffer. Next, the beads were resuspended in 18.5 μl 1× CircLigase mix (2 μl 10× CircLigase buffer, 4 μl 5 M betaine, 1 μl 50 mM $MnCl_2$, 1 μl 1 mM ATP and 10.5 μl water), and 1 μl 100 U $μl^{-1}$ CircLigase II was added. The CircLigase reaction was incubated for 8 h at 60 °C with occasional pipetting of the beads. The reaction was then resuspended in 100 μl binding buffer containing fresh M-280 streptavidin Dynabeads (5-μl bed volume) and incubated for 30 min at room temperature. Beads were then

washed once with 500 µl high-salt buffer, twice with 500 µl binding buffer and once with 500 µl low-salt buffer. Next, the beads were resuspended in 50 µl 0.2 M KOH and incubated overnight at 37 °C. The following day, HCl was added to the solution to obtain the pH of 7.5, and new M-280 streptavidin Dynabeads (10-µl bed volume) were added. Sample was incubated for 30 min at room temperature, followed by bead washes with 500 µl high-salt buffer, twice with 500 µl binding buffer and once in 500 µl low-salt buffer. Beads were then incubated for 2.5 h at 37 °C in a 50-µl reaction containing 30 mM Na-acetate pH 4.5 and 5 U RNase T2. Beads were then washed once with 500 µl high-salt buffer, twice with 500 µl binding buffer and twice with 500 µl low-salt buffer. The removal of the 2′,3′-cyclic phosphate from the 3′ ends of cap tags and the ligation of the preadenylated DNA adapter with UMIs (DA5-UMIs) was performed as described in the CapTag-seq protocol. After ligation, the beads were washed twice with 500 µl high-salt buffer, twice with 500 µl binding buffer and twice with 500 µl low-salt buffer. Beads were then resuspended in 20 µl cDNA buffer (10 mM Tris-HCl pH 7.5) and used for subsequent PCR amplification of cDNA–cap tags with 2× Phusion High Fidelity PCR master mix with HF buffer. The resulting PCR products were purified twice with 0.9× PCR volume AMPure XP beads. Purified cDNA libraries were sequenced on Illumina instrument in a paired-end mode.

## CLAM-Cap-seq data analysis

Low-quality sequencing reads were filtered out and the 3′ end DNA adapter (DA3) was trimmed off using Flexbar v2.5 (ref. [44]). Duplicated reads were removed using the pyFastqDuplicateRemover.py script within the pyCRAC package v1.3.2 (ref. [45]). Following the removal of PCR duplicates, only the read R1 was considered for further analysis. The six-nucleotide-long UMI was first removed from the 5′ end of sequencing reads using seqtk. Next, we determined Cap1 and Cap2 origins of the sequencing reads. To achieve that, 5′ ends of processed reads were screened for the presence of Cap1 and Cap2 palindromes containing zero and one non-templated nucleotide using grep UNIX command. The palindrome search was focused on all 64 possible trinucleotide sequences that an mRNA may begin with (for example, AGA, CTT, and so on), except for the homopolymeric trinucleotide stretches (for example, AAA, GGG, CCC and UUU), as these can generate palindromes

with ambiguous Cap1 and Cap2 assignment. Of note, as U-starting mRNAs are very rare in mammalian transcriptomes (see Extended Data Fig. 2d), they were also excluded from the Cap1 and Cap2 palindrome search. Next, the sequencing reads containing Cap1 and Cap2 palindromes were separated, followed by the removal of cap tags and a non-templated nucleotide with seqtk to obtain mappable reads whose starts represent the first mRNA nucleotide. Cap tag-free Cap1-derived and Cap2-derived reads were then trimmed at their 3′ end to obtain the universal read length of 25 bp. After processing, Cap1 and Cap2 reads were separately mapped to the human (hg38) or mouse (mm10) genome using Bowtie v1.2.3. 5′ end read coverage per each genomic position was assessed using BEDTools. The aligned reads were then annotated to the TSN isoforms identified via TSS-seq using BEDTools. Cap2 stoichiometry for each TSN isoform was calculated as the Cap2 read fraction of the total (Cap1 + Cap2) reads. Only TSN isoforms whose total (Cap1 + Cap2) CLAM-Cap-seq read coverage was higher or equal to 30 were considered for Cap2 stoichiometry calculations. TSN isoforms showing low variability in Cap2 stoichiometry between replicates (standard deviation of less than 5%) were used for all downstream analysis.

## Gene enrichment analysis

For gene enrichment analysis (WebGestalt (http://www.webgestalt.org/)), Cap2 stoichiometry of a gene was calculated as a weighted Cap2 stoichiometry average of all TSN isoforms of that gene. In these calculations, the contribution of each TSN isoform to the average Cap2 stoichiometry for a gene was based on the relative expression level of each Cap2-modified TSN isoform. Genes with the highest and lowest Cap2 stoichiometry (top 20%) were identified. The overrepresentation analysis[50] for KEGG pathways was performed using all genes with measured Cap2 stoichiometry as a reference gene set. In the RNA-seq dataset, genes were ranked based on the level of the changes in their expression between *CMTR2* KO and *CMTR2* WT cells ($\log_2$ fold change) and subjected to the gene set enrichment analysis[50] for identification of gene sets enriched in specific Reactome pathways.

## CapOligo-PAGE

Small or poly(A)$^+$ RNA (3 µg) was subjected to m$^7$GDP removal with 5 U Cap-Clip acid pyrophosphatase in a 20-µl reaction for 1 h at 37 °C. The decapped RNA was purified using a Zymo RCC-5 column and eluted in 20 µl water. RNA 5′ ends were dephosphorylated using 25 U Quick CIP in a 30-µl reaction at 37 °C. RNA was purified as described above and eluted in 10 µl water. RNA (7 µl) from the previous step was radiolabelled in a 10-µl reaction using 10 U T4 PNK and 1 µl 10 mCi ml$^{-1}$ [$^{32}$P]-ATP for 30 min at 37 °C. The reaction was heat inactivated at 85 °C for 2 min. Next, 1 µl 10 µM 5′-biotinylated self-splinting DNA oligonucleotide was added to the reaction mix. The sample was heated at 85 °C for 4 min and left at room temperature for 20 min to allow DNA oligo annealing to the 5′ end of the target RNA. Ligation mix (3.7 µl; 0.56× PNK buffer, 0.15 mM ATP, 22.8% DMSO and 1.9 U µl$^{-1}$ T4 DNA ligase (EL0011, Thermo Scientific)) was added to the reaction, mixed and incubated for 4 h at 37 °C. M-280 streptavidin Dynabeads (7-µl bed volume) in 100 µl binding buffer were added to the ligation mix and incubated for 30 min at room temperature with constant shaking. Next, the beads were washed twice with 500 µl high-salt buffer, twice with 500 µl binding buffer and twice with 500 µl low-salt-buffer. After the last wash, beads were resuspended in 45 µl 30 mM Na-acetate pH 4.5, and 4 µg Monarch RNase A (T3018L, NEB) and 5 U RNase T2 were added. Samples were incubated overnight at 37 °C to completely degrade mRNA, leaving the cap tags attached to the self-splinting DNA oligonucleotide. The following day, the beads were washed twice with 500 µl binding buffer and twice with low-salt buffer. The beads were then resuspended in 50 µl 10 mM HCl and incubated for 30 min at 37 °C to open up the 2′,3′-cyclic phosphate at the 3′ end of RNase-derived cap tags. Binding buffer (150 µl) was added, and the pH of the reaction was adjusted with KOH to 7.5. M-280 streptavidin Dynabeads (5-µl bed volume) were added to the mixture and incubated for 30 min at room temperature. Next, the beads were washed once with 500 µl binding buffer and once with low-salt buffer. Beads were then resuspended in 10 µl 1.1× CutSmart buffer and digested with 20 U BamHI HF (3136L, NEB) for 1.25 h at 37 °C. Beads were gently washed once with 150 µl binding buffer and once with 150 µl low-salt buffer. Beads were then resuspended in 10 mM Tris-HCl pH 7.5, heated at 85 °C for 7 min and supernatants were quickly collected into a fresh tube. The eluted samples containing DNA oligo-linked cap tags were mixed with 2× Novex TBE-urea sample buffer (LC6876, Invitrogen) and

loaded onto a 20-cm-long 15% TBE-urea sequencing gel. Samples were run on the gel until the bromephenol blue dye reached the end of the gel. The resolved DNA oligo-linked cap tags were transferred onto a nylon membrane, UV crosslinked and exposed to the phosphor screen. Autoradiographs were developed using the FLA7000IP Typhoon Phosphorimager.

## BruChase

HEK293T cells ($5 \times 10^6$) were seeded in a 10-cm cell culture dish. The following day, cells were incubated in growing media containing 200 μg $ml^{-1}$ 5-BrU (850187, Sigma) for 3 h to allow for metabolic labelling of newly synthesized transcripts. Then, BrU-containing media were withdrawn, and cells were chased in growing media containing 2 mM uridine (U3750, Sigma) for 0, 4, 8 and 16 h. Total RNA was extracted from cells at each time point of the uridine chase using TRIzol reagent and isopropanol precipitation. Next, 100 μg total RNA for each time point was incubated with 10 μg anti-bromodeoxyuridine antibody (MI-11-3, MBL Life Science) in 500 μl IP buffer (5 mM Tris-HCl pH 7.5, 0.5× PBS, 0.05% Triton X-100, 1 mM EDTA and 40 U $ml^{-1}$ RNaseOUT) for 2 h at 4 °C with constant rotation. Pierce Protein A/G magnetic beads (30-μl bed volume; 88802, Thermo Scientific) in 100 μl IP buffer were added to the RNA–antibody mix and incubated for an additional 1 h at 4 °C with constant rotation. Beads were then washed four times with 700 μl IP buffer. The immunopurified RNA was eluted from the beads via proteinase K treatment. Beads were mixed in 300 μl proteinase K buffer (100 mM Tris-HCl pH 7.5, 50 mM NaCl, 0.5% SDS and 10 mM EDTA) and 10 μl 20 mg $ml^{-1}$ proteinase K solution (RNA grade; 25530049, Invitrogen), and incubated for 45 min at 50 °C. Next, the supernatant was collected and mixed with 300 μl phenol:chloroform:IAA, 25:24:1, pH 6.6 (AM9730, Invitrogen) in a Phase Lock Gel Heavy tube (2302830, QuantaBio). The mixture was incubated for 5 min at 30 °C and centrifuged at 13,000*g* for 5 min. Following centrifugation, the aqueous phase was collected, and BrU-containing RNA was precipitated with 0.3 M Na-acetate pH 5.5, 2.5× sample volume 100% ethanol and 2 μl 15 mg $ml^{-1}$ Glycoblue (AM9515, Invitrogen). Two independent immunopurifications were combined and subjected to the

CLAM-Cap-seq protocol. DNA adapter-linked cDNA–cap tags were resuspended in 40 µl water and subjected to the RT–qPCR analysis.

## BruChase-CapTag-seq

HEK293T cells ($9 \times 10^6$) were seeded in a 15-cm cell culture dish. The following day, cells were incubated in growing media containing 200 µg $ml^{-1}$ 5-BrU (850187, Sigma) for 3 h to allow for metabolic labelling of newly synthesized transcripts. Then, BrU-containing media were withdrawn, and cells were chased in growing media containing 2 mM uridine (U3750, Sigma) for 0 h and 8 h. Total RNA was extracted from cells at both time points of the uridine chase using TRIzol reagent and isopropanol precipitation. mRNA was extracted from total RNA using oligo(dT) capture as described above. Isolated mRNA from three 15-cm cell culture dishes constituted a single biological replicate. BrU-labelled mRNA was immunopurified as described above. BrU-labelled mRNA (200 ng) from each time point of the uridine chase was subjected to the CapTag-seq procedure.

## RNA-seq

Total RNA was extracted from $2 \times 10^6$ *CMTR2* WT or *CMTR2* KO HEK293T cells using TRIzol reagent. The RNA quality was assessed by Bioanalyzer analysis. Total RNA was spiked in with ERCC RNA spike-in mix 1 according to the manufacturer's instructions (4456740, Invitrogen). Total RNA (1 µg) was used for RNA-seq library preparation with the NEBNext Ultra II RNA Library Prep kit for Illumina (E7770S, NEB). Ribosomal RNA was removed using the NEBNext rRNA Depletion kit (E6310L, NEB). The libraries were sequenced on the Illumina instrument in a paired-end mode. Four independent biological replicates were sequenced for each condition.

## RNA-seq data analysis

Sequencing reads of low quality were discarded and reads shorter than 18 bp were removed. Ribosomal rRNA reads were removed using STAR aligner[51]. The remaining reads were then mapped to the human (hg38) protein-coding

transcriptome using STAR aligner. Trimmed mean of M values (TMM) normalization, empirical Bayes estimate of the negative binominal dispersion, and measurement of the changes in gene expression ($\log_2$ fold change) were performed for all samples and replicates at the same time using edgeR[52].

## Western blotting and antibodies

Cell pellets were collected by centrifugation at 300*g* for 5 min. After a single wash in ice-cold PBS, cell pellets were resuspended in cell lysis buffer (50 mM Tris-HCl pH 7.5, 150 mM NaCl, 1% NP-40, 0.1% SDS and 1× Halt protease and phosphatase inhibitor cocktail) and lysed on ice for 10 min. Cell lysis was facilitated by sonication with the following parameters: four times 5 s on, 10 s off at 10% amplitude (Branson). Cell lysates were cleared by a 5 min of centrifugation at 20,000*g* at 4 °C. Protein concentration in isolated cell lysates was determined using the Pierce BCA Protein Assay kit (23225, Thermo scientific). Protein (20–25 µg) was loaded per lane onto a NuPAGE 4–12% Bis-Tris gel (NP0322BOX, Invitrogen). Resolved proteins were transferred onto a PVDF membrane and probed with an antibody recognizing a protein of interest. The following antibodies were used in this study: rabbit anti-FTSJD1 polyclonal antibody (1:500 dilution; PA5-61696, Invitrogen), rabbit anti-RIG-I (D14G6) monoclonal antibody (1:1,000 dilution; 3743T, CST), rabbit RIG-I/DDX58 (EPR18629) monoclonal antibody (1:2,000 dilution; ab180675, Abcam), rabbit anti-MDA5 (D74E4) monoclonal antibody (1:1,000 dilution; 5321T, CST), rabbit anti-IFIT1 (D2X9Z) monoclonal antibody (1:1,000 dilution; 14769S, CST), rabbit anti-IFITM3 (D8E8G) XP monoclonal antibody (1:1,000 dilution; 59212T, CST), mouse anti-NLRP1 monoclonal antibody (1:1,000 dilution; 679802, BioLegend), rabbit anti-MAVS polyclonal antibody (1:1,000 dilution; 3993T, CST), rabbit anti-OAS3 polyclonal antibody (1:1,000 dilution; ab154270, Abcam), mouse anti-puromycin (12D10) monoclonal antibody (1:5,000 dilution; MABE343, Millipore Sigma), mouse anti-GAPDH monoclonal antibody (1:10,000; GT239, GeneTex), mouse anti-β-actin monoclonal antibody (1:4,000; AM4302, Thermo), horseradish peroxidase-conjugated donkey anti-rabbit IgG (1:5,000; NA934, Cytiva) and horseradish peroxidase-conjugated sheep anti-mouse IgG (1:5,000; NA931, Cytiva). For anti-RIG-I (D14G6), anti-NLRP1 and anti-MDA5 (D74E4)

antibodies, membranes were incubated with 3% BSA in TBS supplemented with 0.1% Tween-20 (TBST). All other antibodies were used with 3% milk in TSBT.

## RT–qPCR

To remove potential DNA contamination, total RNA was first treated with 1 U DNase I (EN0521, Thermo Scientific) for 20 min at 37 °C and purified using a Zymo RCC-5 column. Total RNA (1–3 μg) was reverse transcribed to cDNA with the SuperScript III First Strand synthesis system (18080051, Invitrogen) using either random hexamers (N8080127, Invitrogen) or oligo(dT)$_{20}$ (18418020, Invitrogen) as reverse transcription primers. The same amount of total RNA was used for directly compared conditions. qPCR was performed using the iQ SYBR Green Supermix (1708880, Bio-Rad) with 150 nM primers in a 10-μl reaction. The amplifications were conducted with the following protocol in all experiments: 95 °C for 10 min, 40 cycles of 95 °C for 15 s, 58 °C for 15 s and 68 °C for 20 s. The specificity of primer pairs was tested with melting curves at the end of the 40th amplification cycle. *GAPDH*-normalized gene expression was calculated and presented. Normalized gene expression values were set to 1 for control conditions with a propagation of variability across all samples and replicates.

## Puromycin incorporation assay

*CMTR2* WT or *CMTR2* KO HEK293T cells ($1.8 \times 10^6$) were seeded in a 6-mm cell culture dish. The following day, cells were incubated in growing media containing 0.8 μg ml$^{-1}$ puromycin for 0, 30, 60 and 90 min. Cells were washed twice with ice-cold PBS and collected by centrifugation at 300*g* for 5 min. Cell lysate preparation and western blotting were performed as described above. The PVDF membrane with transferred proteins was probed with anti-puromycin antibody for the detection of nascent proteins. Following anti-puromycin western blot, the membrane was washed and stained with Amido Black Staining solution (A8181, Sigma-Aldrich) to ensure equal protein loading in all lanes.

## MTT cell proliferation assay

Changes in cell growth upon CMTR2 depletion were tested using MTT (3-(4,5-dimethylthiazol-2-yl)−2,5-diphenyltetrazolium bromide) cell proliferation assay. *CMTR2* WT or *CMTR2* KO HEK293T cells ($2 \times 10^4$) were seeded in a single well of a 12-well plate. The MTT assay was performed on cells at 1, 2 and 3 days following the initial seeding. For each time point, cells were washed once with pre-warmed PBS, followed by incubation in the solution containing 1:1 mixture of phenol red-free DMEM and MTT reagent (5 mg $ml^{-1}$ MTT (ab 146345, Abcam) for 3 h at 37 °C. MTT solvent (1.5× volume) (4 mM HCl and 0.1% NP-40 in isopropanol) was added to the cells, and formazan crystals were dissolved by pipetting. Samples were incubated for 15 min at room temperature and 570-nm absorbance read to estimate the number of viable cells. A well without seeded cells was used for background subtraction.

## VSV infections

HEK293T cells ($3.5 \times 10^5$) were seeded in a poly-d-lysine (A3890401, Gibco) coated well of a six-well plate. The following day, cells were transfected with 800 ng pcDNA4.0/TO-NeonGreen, pcDNA4/TO-NeonGreen-CMTR2 or pcDNA4/TO-NeonGreen-CMTR2 W85A plasmids using 1.2 µl LipoD293T transfection reagent. Twenty-four hours after transfection, cells were infected with $1.25 \times 10^8$ propagation-incompetent VSV particles. After 24 h of the VSV infection, cells were washed once with PBS and collected in 1 ml TRIzol reagent for total RNA extraction. Isolated total RNA was treated with DNase I, purified and subjected to CLAM-Cap–qPCR and RT–qPCR analysis.

## Poly(I:C) and 3p-hpRNA cell treatments

HEK293T cells ($3.5 \times 10^5$) were seeded in a well of a six-well plate. The following day, cells were transfected with 800 ng pcDNA4.0/TO-NeonGreen, pcDNA4/TO-NeonGreen-CMTR2 or pcDNA4/TO-NeonGreen-CMTR2 W85A plasmids using 1.2 µl LipoD293T transfection reagent. Twenty-four hours after transfection, cells were transfected with either 500 ng LMW poly(I:C) (InvivoGen) or 750 ng 3p-hpRNA (InvivoGen) using LyoVec transfection reagent (InvivoGen) according to the manufacturer’s instructions. After 24 h (for poly(I:C) and 8 h (for 3p-hpRNA), cells were

collected in 1 ml TRIzol reagent for total RNA extraction. Isolated total RNA was treated with DNase I, purified and subjected to RT–qPCR analysis.

## Plasmids

The CMTR2 open reading frame was obtained by RT–PCR on mRNA extracted from HEK293T cells. The CMTR2 open reading frame was cloned into the pcDNA4/TO-NeonGreen plasmid between the KpnI and XbaI restriction sites to obtain the N-terminal NeonGreen-tagged CMTR2 expression construct. The pcDNA4/TO-NeonGreen-CMTR2 W85A mutant construct was generated by PCR-based site-directed mutagenesis of the pcDNA4/TO-NeonGreen-CMTR2 plasmid. The pcDNA3.1(+)-FLAG-RIG-I plasmid was purchased from OriGene (OHu25414). The pcDNA3.1(+)-FLAG-RIG-I K858A/K861A, H830A and C829A mutant constructs were generated by PCR-based site-directed mutagenesis of the original pcDNA3.1(+)-FLAG-RIG-I plasmid. All generated plasmids are available from the lead contact on request.

## Preparation of the biotinylated dsRNA oligos for RIG-I pulldown

Single-stranded Cap0-modified, Cap1-modified and Cap2-modified RNA oligonucleotides were provided by TriLink Biotechnologies. To remove any residual non-capped RNA, the oligos were treated with Terminator exonuclease for 1 h at 30 °C and purified using RNAClean XP beads. A complementary 5′-biotinylated RNA oligo was annealed to Cap0-modified, Cap1-modified and Cap2-modified RNA oligos in a 1.1:1 ratio in 50 µl annealing buffer (10 mM Tris-HCl pH 7.5, 100 mM NaCl and 1 mM EDTA). Biotinylated Cap0-terminated, Cap1-terminated or Cap2-terminated dsRNA (700 ng) was incubated with M-280 streptavidin Dynabeads (40 µl bed volume) in 300 µl binding buffer supplemented 1 U $\mu l^{-1}$ RNaseOUT at room temperature for 30 min with constant rotation. The RNA-bound beads were washed three times with 500 µl binding buffer, resuspended in 150 µl cell lysis buffer (20 mM Tris-HCl pH 7.5, 100 mM KCl, 5 mM $MgCl_2$, 0.5% NP-40, 40 U $ml^{-1}$ RNaseOUT and 1× Halt protease and phosphatase inhibitor cocktail), and kept on ice.

## RIG-I pulldown assay

HEK293T cells ($4.8 \times 10^6$) were seeded on a 10-cm Petri dish. The following day, cells were transfected with 4.8 µg pcDNA3.1(+)-FLAG-RIG-I, pcDNA3.1(+)-FLAG-RIG-I K858A/K858A, pcDNA3.1(+)-FLAG-RIG-I H830A or pcDNA3.1(+)-FLAG-RIG-I C829A plasmids using 10 µl LipoD293 transfection reagent. Forty-eight hours after transfection, cells were washed once with 5 ml ice-cold PBS and scraped in 8 ml ice-cold PBS. Cell pellets were collected by 5 min of centrifugation at 300*g* at 4 °C, supernatant was removed by aspiration and cells were resuspended in 500 µl cell lysis buffer (20 mM Tris-HCl pH 7.5, 100 mM KCl, 5 mM $MgCl_2$, 0.5% NP-40, 40 U $ml^{-1}$ RNaseOUT and 1× Halt protease and phosphatase inhibitor cocktail). Cells were left to lyse on ice for 10 min. To facilitate cell lysis, cells were passed three times through a 21-gauge needle and incubated on ice for an additional 10 min. The lysates were cleared by centrifugation at 16,000*g* for 10 min and the supernatants were saved. Protein concentration was measured by the Pierce BCA Protein Assay kit according to the manufacturer's instructions. Protein lysate (0.75 mg) at the concentration of 1 mg $ml^{-1}$ was incubated with streptavidin-immobilized Cap0, Cap1 and Cap2 dsRNA for 45 min at room temperature with agitation. Following the incubation, the beads were washed four times with 750 µl cell lysis buffer and separated in two equal parts. RNA-bound proteins were eluted in 25 µl 1.5× NuPAGE LDS sample buffer (NP0007, Invitrogen) from one bead fraction. The eluted proteins were loaded onto the NuPAGE 4–12% Bis-Tris gel and run at 180 V for 60 min. The resolved proteins were transferred onto the PVDF membrane and western blot was performed using anti-RIG-I antibody. To show equal amount of RNA bait across different samples, the remaining part of the beads was subjected to the proteinase K treatment for RNA isolation. Isolated RNA was loaded onto the 20% TBE non-denaturing PAGE and run at 150 V for 2.5 h. RNA was visualized after the gel was stained with 1× SYBR Gold nucleic acid gel stain (S11494, Invitrogen).

## CMTR2 and RIG-I co-overexpression in *CMTR2* WT HEK293T cells

HEK293T cells (3.5 × $10^5$) were seeded in a single poly-d-lysine (A3890401, Gibco) coated well of a six-well plate. The following day, cells were transfected with 800 ng pcDNA4.0/TO-NeonGreen, pcDNA4/TO-NeonGreen-CMTR2 or pcDNA4/TO-NeonGreen-CMTR2 W85A plasmids using 1.2 µl LipoD293T transfection reagent. After 24 h, cells were transfected with either 1 µg pcDNA3.1(+)-FLAG-GFP or pcDNA3.1(+)-FLAG-RIG-I. After 48 h, cells were washed once with PBS, scraped and collected by 5 min centrifugation at 300*g* at 4 °C. Cell pellets were divided into equal parts for protein and total RNA extraction.

## RIG-I overexpression in *CMTR2* WT and *CMTR2* KO HEK293T cells

*CMTR2* WT or *CMTR2* KO HEK293T cells (3.5 × $10^5$) were seeded in a single well of a six-well plate. The following day, cells were transfected with 1 µg pcDNA3.1(+)-FLAG-GFP, pcDNA3.1(+)-FLAG-RIG-I or pcDNA3.1(+)-FLAG-RIG-I K858A/K861A constructs. After 48 h, cells were washed once with PBS, scraped and collected by 5 min of centrifugation at 300*g* at 4 °C. Cell pellets were divided into equal parts for protein and total RNA extraction.

## Oligonucleotides

The sequences of the oligonucleotides used in this study are provided in Supplementary Table 3.

## Quantification and statistical analysis

Quantitative and statistical methods are described above and in the figure legends. R v4.0.1, GraphPad Prism v9.0.1 and ImageJ 1.53a were used for all statistical analysis and data visualization. Figures were prepared using Graphic v3.1 and Adobe Illustrator v27.0.1. All statistical tests and *P* values are provided in Supplementary Table 2. Experimental results shown as representative blots were successfully replicated two or more times to ensure the reproducibility of the reported findings.

### Reporting summary

Further information on research design is available in the Nature Portfolio Reporting Summary linked to this article.

## Data availability

Raw and processed sequencing data can be accessed from the NCBI Gene Expression Omnibus under the accession number GSE196043. In addition, TSS-seq, CLAM-Cap-seq, polysome–TSS-seq and actD-TSS-seq processed data are provided as Supplementary Table 1. The following public datasets were used in this study: GSE49831, GSE99978, GSE69352, GSE141507 and GSE52662. The detailed description of the data processing can be found in the Methods section and within GSE196043. Any additional information for the analyses of the data reported in this study is available from the corresponding author on request. Source data are provided with this paper.

## References


1. Adams, J. M. & Cory, S. Modified nucleosides and bizarre 5′-termini in mouse myeloma mRNA. *Nature* **255**, 28–33 (1975).

2. Furuichi, Y. et al. Methylated, blocked 5 termini in HeLa cell mRNA. *Proc. Natl Acad. Sci. USA* **72**, 1904–1908 (1975).

3. Cho, E. J., Takagi, T., Moore, C. R. & Buratowski, S. mRNA capping enzyme is recruited to the transcription complex by phosphorylation of the RNA polymerase II carboxy-terminal domain. *Genes Dev.* **11**, 3319–3326 (1997).

4. McCracken, S. et al. 5′-Capping enzymes are targeted to pre-mRNA by binding to the phosphorylated carboxy-terminal domain of RNA polymerase II. *Genes Dev.* **11**, 3306–3318 (1997).

5. Moteki, S. & Price, D. Functional coupling of capping and transcription of mRNA. *Mol. Cell* **10**, 599–609 (2002).

6. Belanger, F., Stepinski, J., Darzynkiewicz, E. & Pelletier, J. Characterization of hMTr1, a human Cap1 2′-*O*-ribose methyltransferase. *J. Biol. Chem.* **285**, 33037–33044 (2010).

7. Smietanski, M. et al. Structural analysis of human 2′-*O*-ribose methyltransferases involved in mRNA cap structure formation. *Nat. Commun.* **5**, 3004 (2014).

8. Langberg, S. R. & Moss, B. Post-transcriptional modifications of mRNA. Purification and characterization of cap I and cap II RNA (nucleoside-2′-)-methyltransferases from HeLa cells. *J. Biol. Chem.* **256**, 10054–10060 (1981).

9. Werner, M. et al. 2′-*O*-ribose methylation of cap2 in human: function and evolution in a horizontally mobile family. *Nucleic Acids Res.* **39**, 4756–4768 (2011).

10. Dickinson, M. E. et al. High-throughput discovery of novel developmental phenotypes. *Nature* **537**, 508–514 (2016).

11. Cai, H. et al. A functional taxonomy of tumor suppression in oncogenic KRAS-driven lung cancer. *Cancer Discov.* **11**, 1754–1773 (2021).

12. Motorin, Y. & Marchand, V. Detection and analysis of RNA ribose 2′-*O*-methylations: challenges and solutions. *Genes (Basel)* **9**, 642 (2018).

13. Maden, B. E., Corbett, M. E., Heeney, P. A., Pugh, K. & Ajuh, P. M. Classical and novel approaches to the detection and localization of the numerous modified nucleotides in eukaryotic ribosomal RNA. *Biochimie* **77**, 22–29 (1995).

14. Motorin, Y., Muller, S., Behm-Ansmant, I. & Branlant, C. Identification of modified residues in RNAs by reverse transcription-

based methods. *Methods Enzymol.* **425**, 21–53 (2007).

15. Dorsett, Y. et al. HCoDES reveals chromosomal DNA end structures with single-nucleotide resolution. *Mol. Cell* **56**, 808–818 (2014).

16. Krogh, N., Kongsbak-Wismann, M., Geisler, C. & Nielsen, H. Substoichiometric ribose methylations in spliceosomal snRNAs. *Org. Biomol. Chem.* **15**, 8872–8876 (2017).

17. Wulf, M. G. et al. Non-templated addition and template switching by Moloney murine leukemia virus (MMLV)-based reverse transcriptases co-occur and compete with each other. *J. Biol. Chem.* **294**, 18220–18231 (2019).

18. Consortium, F. et al. A promoter-level mammalian expression atlas. *Nature* **507**, 462–470 (2014).

19. Reyes, A. & Huber, W. Alternative start and termination sites of transcription drive most transcript isoform differences across human tissues. *Nucleic Acids Res.* **46**, 582–592 (2018).

20. Yamashita, R. et al. Genome-wide characterization of transcriptional start sites in humans by integrative transcriptome analysis. *Genome Res.* **21**, 775–789 (2011).

21. Tsuchihara, K. et al. Massive transcriptional start site analysis of human genes in hypoxia cells. *Nucleic Acids Res.* **37**, 2249–2263 (2009).

22. Sample, P. J. et al. Human 5′ UTR design and variant effect prediction from a massively parallel translation assay. *Nat. Biotechnol.* **37**, 803–809 (2019).

23. Paulsen, M. T. et al. Use of Bru-seq and BruChase-seq for genome-wide assessment of the synthesis and stability of RNA. *Methods* **67**, 45–54 (2014).

24. Brown, C. J. et al. The human XIST gene: analysis of a 17 kb inactive X-specific RNA that contains conserved repeats and is highly localized within the nucleus. *Cell* **71**, 527–542 (1992).

25. Schneider, W. M., Chevillotte, M. D. & Rice, C. M. Interferon-stimulated genes: a complex web of host defenses. *Annu. Rev. Immunol.* **32**, 513–545 (2014).

26. Wang, Y. et al. Structural and functional insights into 5′-ppp RNA pattern recognition by the innate immune receptor RIG-I. *Nat. Struct. Mol. Biol.* **17**, 781–787 (2010).

27. Devarkar, S. C. et al. Structural basis for m7G recognition and 2′-*O*-methyl discrimination in capped RNAs by the innate immune receptor RIG-I. *Proc. Natl Acad. Sci. USA* **113**, 596–601 (2016).

28. Schuberth-Wagner, C. et al. A conserved histidine in the RNA sensor RIG-I controls immune tolerance to N1-2’*O*-methylated self RNA. *Immunity* **43**, 41–51 (2015).

29. Takahasi, K. et al. Nonself RNA-sensing mechanism of RIG-I helicase and activation of antiviral immune responses. *Mol. Cell* **29**, 428–440 (2008).

30. Brownell, J. et al. Direct, interferon-independent activation of the CXCL10 promoter by NF-κB and interferon regulatory factor 3 during hepatitis C virus infection. *J. Virol.* **88**, 1582–1590 (2014).

31. Kato, H. et al. Cell type-specific involvement of RIG-I in antiviral response. *Immunity* **23**, 19–28 (2005).

32. Moyer, S. A. & Banerjee, A. K. In vivo methylation of vesicular stomatitis virus and its host-cell messenger RNA species. *Virology* **70**, 339–351 (1976).

33. Berger Rentsch, M. & Zimmer, G. A vesicular stomatitis virus replicon-based bioassay for the rapid and sensitive determination of multi-species type I interferon. *PLoS ONE* **6**, e25858 (2011).

34. Lodish, H. F. & Porter, M. Translational control of protein synthesis after infection by vesicular stomatitis virus. *J. Virol.* **36**, 719–733 (1980).

35. Neidermyer, W. J. Jr & Whelan, S. P. J. Global analysis of polysome-associated mRNA in vesicular stomatitis virus infected cells. *PLoS Pathog.* **15**, e1007875 (2019).

36. Kato, H. et al. Length-dependent recognition of double-stranded ribonucleic acids by retinoic acid-inducible gene-I and melanoma differentiation-associated gene 5. *J. Exp. Med.* **205**, 1601–1610 (2008).

37. Wienert, B., Shin, J., Zelin, E., Pestal, K. & Corn, J. E. In vitro-transcribed guide RNAs trigger an innate immune response via the RIG-I pathway. *PLoS Biol.* **16**, e2005840 (2018).

38. Kumar, P. et al. Inhibition of translation by IFIT family members is determined by their ability to interact selectively with the 5′-terminal regions of cap0-, cap1- and 5’ppp- mRNAs. *Nucleic Acids Res.* **42**, 3228–3245 (2014).

39. Abbas, Y. M. et al. Structure of human IFIT1 with capped RNA reveals adaptable mRNA binding and mechanisms for sensing N1 and N2 ribose 2′-*O* methylations. *Proc. Natl Acad. Sci. USA* **114**, E2106–E2115 (2017).

40. Zust, R. et al. Ribose 2′-*O*-methylation provides a molecular signature for the distinction of self and non-self mRNA dependent on the RNA sensor Mda5. *Nat. Immunol.* **12**, 137–143 (2011).

41. Haussmann, I. U. et al. CMTr cap-adjacent 2′-*O*-ribose mRNA methyltransferases are required for reward learning and mRNA localization to synapses. *Nat. Commun.* **13**, 1209 (2022).

42. Zaccara, S., Ries, R. J. & Jaffrey, S. R. Reading, writing and erasing mRNA methylation. *Nat. Rev. Mol. Cell Biol.* **20**, 608–624 (2019).

43. Kimmel, C. B., Ballard, W. W., Kimmel, S. R., Ullmann, B. & Schilling, T. F. Stages of embryonic development of the zebrafish. *Dev. Dyn.* **203**, 253–310 (1995).

44. Dodt, M., Roehr, J. T., Ahmed, R. & Dieterich, C. FLEXBAR-Flexible barcode and adapter processing for next-generation sequencing platforms. *Biology (Basel)* **1**, 895–905 (2012).

45. Webb, S., Hector, R. D., Kudla, G. & Granneman, S. PAR-CLIP data indicate that Nrd1-Nab3-dependent transcription termination regulates expression of hundreds of protein coding genes in yeast. *Genome Biol.* **15**, R8 (2014).

46. Langmead, B., Trapnell, C., Pop, M. & Salzberg, S. L. Ultrafast and memory-efficient alignment of short DNA sequences to the human genome. *Genome Biol.* **10**, R25 (2009).

47. Quinlan, A. R. & Hall, I. M. BEDTools: a flexible suite of utilities for comparing genomic features. *Bioinformatics* **26**, 841–842 (2010).

48. Yates, A. D. et al. Ensembl 2020. *Nucleic Acids Res.* **48**, D682–D688 (2020).

49. Ritz, C., Baty, F., Streibig, J. C. & Gerhard, D. Dose–response analysis using R. *PLoS ONE* **10**, e0146021 (2015).

50. Wang, J., Vasaikar, S., Shi, Z., Greer, M. & Zhang, B. WebGestalt 2017: a more comprehensive, powerful, flexible and interactive gene set enrichment analysis toolkit. *Nucleic Acids Res.* **45**, W130–W137 (2017).

51. Dobin, A. et al. STAR: ultrafast universal RNA-seq aligner. *Bioinformatics* **29**, 15–21 (2013).

52. Robinson, M. D., McCarthy, D. J. & Smyth, G. K. edgeR: a Bioconductor package for differential expression analysis of digital gene expression data. *Bioinformatics* **26**, 139–140 (2010).

53. Lizio, M. et al. Gateways to the FANTOM5 promoter level mammalian expression atlas. *Genome Biol.* **16**, 22 (2015).

54. Schueler, M. et al. Differential protein occupancy profiling of the mRNA transcriptome. *Genome Biol.* **15**, R15 (2014).

55. Batista, P. J. et al. $m^6A$ RNA modification controls cell fate transition in mammalian embryonic stem cells. *Cell Stem Cell* **15**, 707–719 (2014).

56. Weber, R. A. et al. Maintaining iron homeostasis is the key role of lysosomal acidity for cell proliferation. *Mol. Cell* **77**, 645–655.e7 (2020).

57. Floor, S. N. & Doudna, J. A. Tunable protein synthesis by transcript isoforms in human cells. *eLife* **5**, e10921 (2016).

58. Herzog, V. A. et al. Thiol-linked alkylation of RNA to assess expression dynamics. *Nat. Methods* **14**, 1198–1204 (2017).

59. Wei, J. et al. Genome-wide CRISPR screens reveal host factors critical for SARS-CoV-2 infection. *Cell* **184**, 76–91.e13 (2021).

# Acknowledgements

We thank A. Mirza for helpful suggestions on the development of the CapOligo-PAGE; members of the Jaffrey laboratory for comments and suggestions throughout the duration of this project; J. Dittman and J. Cao laboratories for providing us with worm and zebrafish samples, respectively; the R. Schwartz laboratory for propagation-incompetent VSV; members of the Genomics Core Facility at Weill Cornell Medicine; and A. McCaffrey and his colleagues at TriLink Biotechnologies for providing us with chemically synthesized Cap1 and Cap2 luciferase mRNAs, as well as short Cap1 and Cap2 RNA oligonucleotides. This work is supported by US National Institutes of Health grants S10OD030335, R35NS111631, RM1HG011563 and MH121072 (to S.R.J).

# Author information

## Authors and Affiliations

1. Department of Pharmacology, Weill Cornell Medicine, Cornell University, New York, NY, USA

   Vladimir Despic & Samie R. Jaffrey

## Contributions

V.D. and S.R.J. designed the study. V.D. performed the experiments, analysed the data and prepared the figures. V.D. and S.R.J. wrote the manuscript.

## Corresponding author

Correspondence to Samie R. Jaffrey.

# Ethics declarations

## Competing interests

S.R.J. is an advisor to and owns equity in 858 Therapeutics. V.D. declares no competing interests.

# Peer review

## Peer review information

*Nature* thanks the anonymous reviewers for their contribution to the peer review of this work.

# Additional information

**Publisher's note** Springer Nature remains neutral with regard to jurisdictional claims in published maps and institutional affiliations.

# Extended data figures and tables

## Extended Data Fig. 1 Cap2 methylation resides in diverse sequence contexts.

**a**, Representative western blot showing CMTR2 expression in the parental (P) and three *CMTR2* KO HEK293T cell clones (#14, #19, #21). GAPDH, loading control. *CMTR2* KO clone #21 was used for all experiments throughout the manuscript, unless otherwise indicated. sgRNA, single-guide RNA. **b**, CapTag-seq accurately measures Cap2 levels in bulk mRNA. CapTag-seq-determined Cap2 stoichiometry was plotted against the expected Cap2 stoichiometry of a predefined mixture of mRNAs from *CMTR2* KO and CMTR2-overexpressing cells in specific molar ratios. Pearson's (*r*), n = 1 experiment. **c**, CMTR2 levels vary between human cell lines. Representative western blot showing CMTR2 expression in three human cell lines; HEK293T, A549 and MCF-7 cells. ACTB, loading control. **d**, CMTR2 is highly expressed in mouse spleen. Representative western blot showing CMTR2 expression in mouse organs. A549 cell lysate was used to identify mouse CMTR2 protein on the blot. ACTB, loading control. **e**-**f**, Heatmaps showing Cap2 levels across all 16 $m^7G$-proximal dinucleotides in transcriptomes of different organisms, mammalian cell lines (**e**) and mouse tissues (**f**). Average of n = 2 biological replicates.

Source data

## Extended Data Fig. 2 CLAM-Cap-seq quantitatively measures Cap2 stoichiometry in individual mRNAs transcriptome-wide.

**a**, CircLigase-assisted formation of cDNA-mRNA chimera requires $m^7GDP$ removal from the mRNA 5′-terminus. Fully Cap2- and Cap1-modified *U1* snRNAs from *CMTR2* WT and *CMTR2* KO HEK293T cells, respectively, were subjected to the CLAM-Cap-seq protocol. cDNA-cap tags were PCR-amplified with primers that surround cDNA-cap tag ligation junction (red

arrow). PCR product representing cDNA-cap tag was detected only upon the enzymatic $m^7$GDP removal from the *U1* snRNA 5′-end. The total amount of synthesized cDNA in all samples was determined by a parallel PCR using a primer pair that hybridizes to the internal portion of the U1 cDNA. Representative nondenaturing, 6% TBE gel pieces with the respective PCR products are shown. **b**, CLAM-Cap-seq accurately predicts Cap2 stoichiometry in mRNA. The CLAM-Cap-seq-determined Cap2 stoichiometry plotted against the expected Cap2 stoichiometry of a synthetic luciferase mRNA standard with $m^7$G-proximal $A_m$-$G_m$-G sequence. The expected Cap2 stoichiometry refers to a predefined mixture of Cap1- and Cap2-terminated luciferase mRNAs in specific molar ratios. Pearson's (*r*), n = 2 technical replicates. **c**, TSS-seq, an approach for identification of the TSN (transcript-start nucleotide) mRNA isoforms. Poly(A)+ RNA is subjected to the enzymatic $m^7$GDP removal (decapping). Following mRNA decapping, a biotinylated 5′ RNA adapter with unique molecular identifiers (RA5-UMIs) is ligated to the first mRNA nucleotide. After a partial alkaline-based mRNA fragmentation, ligated mRNA 5′-ends are captured on streptavidin beads to perform a 3′-end DNA adapter ligation (DA3). Following reverse transcription, cDNA libraries are PCR amplified, sequenced, and sequencing data analyzed. After UMI removal from the 5′-end of sequencing reads, the first nucleotide of the UMI-free sequencing reads defines a TSN (a circle denoted with 1) of each mRNA in the transcriptome. A single nucleotide position in an annotated gene exhibiting the highest 5′-end read coverage is marked as the major, maximum TSN isoform. All other positions within an annotated gene with 5′-end read coverage higher than 10% of the maximum TSN are considered as TSN isoforms produced from a gene. **d**, TSS-seq-identified TSN isoforms are consistent with previous TSN mapping methods. Stacked bar plots show the observed frequency of different TSNs in the indicated transcriptomes (A>G>C>>U). Pie charts below show the percent of TSNs from TSS-Seq found within and outside the established CAGE (cap analysis of gene expression) peaks[53]. **e**, TSS-seq accurately measures mRNA expression. Correlation plots between TSS-seq-derived and RNA-seq-based calculations of mRNA expression in different cell llines[54,55,56]. Pearson's (*r*) and Spearman's (*ρ*). (**d-e**) Average of n = 2 for HEK293T and n = 1 for mES and MCF-7 cells. **f**, Cumulative distribution plot of the Cap2

stoichiometry variation between replicates (Cap2 standard deviation, StDev, %) for TSN mRNA isoforms binned based on the total number of CLAM-Cap-seq (Cap1 and Cap2) reads. n = 4 biological replicates. Each box shows the first quartile, median, and third quartile, whiskers represent 1.5× interquartile ranges. **g**, Reproducibility of the CLAM-Cap-seq. Pearson's correlation coefficient (*r*) of the CLAM-Cap-seq-predicated Cap2 stoichiometry across biological replicates was calculated and plotted for different cell lines. **h**, Cap2 stoichiometry for a selected set of cytoplasmic and nuclear poly(A)+ RNAs in *CMTR2* WT and *CMTR2* KO HEK293T cells was plotted. Cap2 stoichiometry of the major TSN isoform was considered. Blue data points indicate mRNAs whose Cap2 stoichiometry was biochemically validated (see Extended Data Fig. 3d,e). Average of n = 4 and n = 2 biological replicates for *CMTR2* WT and *CMTR2* KO HEK293T cells, respectively. **i**, Bar plot showing global Cap2 levels in cells based on CapTag-seq and CLAM-Cap-seq measurements. Average of n = 2 and n = 4 biological replicates. **j**, Correlation between CapTag-seq- and CLAM-Cap-seq-derived Cap2 measurements for $m^7$G-proximal dinucleotides in three different mammalian cell lines. Pearson's (*r*), F test, grey area denotes 95% confidence interval for predictions from a linear model. Average of n = 2 and n = 4 biological replicates.

Source data

## Extended Data Fig. 3 A biochemical assessment of Cap2 stoichiometry in individual mRNAs with CapOligo-PAGE.

**a**, CapOligo-PAGE, a biochemical assay for Cap2 measurements in individual transcripts. A mixture of Cap1- and Cap2-terminated mRNAs is subjected to enzymatic $m^7$GDP removal, followed by T4 PNK 5′-end radiolabeling with [$^{32}$P]-ATP (green P with an asterisk). Next, a 5′-biotinylated self-splinting DNA oligonucleotide (blue) containing BamHI restriction site (pink) is ligated to the first radiolabeled mRNA nucleotide of a target transcript. Following splint ligation of the DNA oligonucleotide, an mRNA of interest is captured on streptavidin beads. A subsequent RNaseA- and RNase T2-mediated mRNA removal creates self-splinting DNA-cap tag chimeras. BamHI cleaves the self-splinting DNA oligo, thus liberating radiolabeled Cap1 and Cap2 cap tags in a form of short oligonucleotides

that differ by a single nucleotide in length. The released cap tag-containing DNA oligos are separated on the 15% sequencing TBE-Urea PAGE, transferred onto the nylon membrane, and visualized by autoradiography. **b**, CapOligo-PAGE specifically detects Cap2 and Cap1 in individual transcripts. Fully Cap2- and Cap1-modified *U1* snRNAs from *CMTR2* WT and *CMTR2* KO cells, respectively, were subjected to the CapOligo-PAGE protocol. Representative autoradiograph with resolved oligonucleotides containing radiolabeled cap tags is shown. Asterisk indicates a background band detected in all samples, including the sample in which the decapping step was omitted. **c**, CapOligo-PAGE accurately measures Cap2 stoichiometry in individual transcripts. Small RNA from *CMTR2* WT and *CMTR2* KO cells were mixed in predefined molar ratios and subjected to CapOligo-PAGE. Representative autoradiograph is shown. A plot shows linear regression of the expected and CapOligo-PAGE-derived Cap2 stoichiometries. Pearson's (*r*), n = 1 experiment. **d-e**, CapOligo-PAGE reveals Cap2 levels on cellular mRNAs. Representative autoradiographs showing Cap1 and Cap2 status of the (**d**) *OAT* and (**e**) *RPS12* mRNAs in *CMTR2* WT and *CMTR2* KO HEK293T cells. Asterisk, background band.

Source data

## Extended Data Fig. 4 Cap2 is enriched on a conserved set of specific mRNAs in mammalian cell lines.

**a**, Gene enrichment analysis for lowly Cap2-modified mRNAs in HEK293T cells. **b-c**, Gene enrichment analysis for lowly and highly Cap2-modified mRNAs in (**b**) mES and (**b**) MCF-7 cells. Bar graphs show the enrichment ratio of the KEGG pathways associated with highly (dark grey) or lowly (light grey) Cap2-modified mRNAs relative to all mRNAs with measurable Cap2 stoichiometry. The enrichment analyses were performed using the overrepresentation analysis (ORA) method with a false discovery rate (FDR) threshold of 5%.

Source data

## Extended Data Fig. 5 Cap2 methylation is highly enriched on long-lived mRNAs.

**a**, Bar graph showing the percent of *ACTB* and *ATF4* mRNAs found in each polysome fraction (F1-5) of the linear sucrose density gradient. Average of n = 2 biological experiments. **b**, Reproducibility of the translation measurements in *CMTR2* WT cells. The mean ribosome load (MRL) measurements of TSN isoforms from two independent polysome-TSS-seq experiments plotted against each other. Pearson's ($r$) and Spearman's ($\rho$). **c**, Polysome-TSS-seq-derived MRL measurements are consistent with the previously published mRNA translation dataset. An average MRL of all TSN isoforms for a gene plotted against gene-level MRL calculated from previously published polysome-RNA-seq HEK293T data[57]. Spearman's ($\rho$). **d**, Cap2 methylation is poorly correlated with translation. Scatter plot showing correlation between Cap2 stoichiometry and ribosome density (MRL/kb) for each TSN isoform in HEK293T cells. Pearson's ($r$) and Spearman's ($\rho$). F test, light blue area denotes 95% confidence interval for predictions from a linear model. **e**, Cap2 methylation is enriched on highly translated mRNAs. Cumulative distribution plot of the ribosome densities (MRL/kb) for HEK293T-expressed mRNAs[57] binned into equally sized quartiles (Q) of increasing Cap2 stoichiometry. **f**, Highly translated mRNAs exhibit subtle Cap2-enrichment. Cumulative distribution plot of the Cap2 stoichiometry for the TSN isoforms binned into equally sized quartiles (Q) of increasing ribosome density (MRL/kb). Only the first and fourth quartiles were plotted. Average of n = 2 biological replicates. **g**, Global mRNA decay rate in *CMTR2* WT cells. The remaining amount of poly(A)+ RNA isolated from 20 µg total RNA at different time points following transcription block by actinomycin D, actD, was plotted. n = 2 biological replicates. **h**, Reproducibility of the mRNA half-life measurements in *CMTR2* WT cells. TSN isoform half-lives derived from two independent actD-TSS-seq experiments plotted against each other. Pearson's ($r$) and Spearman's ($\rho$). **i**, ActD-TSS-seq-derived mRNA half-lives are consistent with previous mRNA half-life measurements. An average half-live of all TSN isoforms for a gene plotted against previously reported gene-level half-lives in HEK293 cells[54]. Spearman's ($\rho$). **j**, Cap2 methylation is well-correlated with mRNA half-lives. Scatter plot showing the correlation between Cap2 stoichiometry and half-lives for each TSN isoform in HEK293T cells. Pearson's ($r$) and Spearman's ($\rho$). F test, light blue area denotes 95% confidence interval for predictions from a linear model. **k**, Cap2 methylation is enriched on long-lived mRNAs. Cumulative

distribution plot of the half-lives for HEK293-expressed mRNAs[54] binned into equally sized quartiles (Q) of increasing Cap2 stoichiometry. **l**, Cap2 methylation is enriched on highly abundant mRNAs in HEK293T cells. Cumulative distribution plot of the expression levels (RPM; reads per million, $\log_2$) for TSN isoforms in HEK293T cells binned into equally sized quartiles (Q) of increasing Cap2 stoichiometry. Average of n = 2 biological replicates. **m**, Long-lived mRNAs exhibit strong Cap2-enrichment in HEK293T cells. Cumulative distribution plot of the Cap2 stoichiometry for the TSN isoforms binned into equally sized quartiles (Q) of increasing half-lives. Only the first and fourth quartiles were plotted. Average of n = 2 biological replicates. **n**, Highly Cap2-modified mRNAs exhibit long half-lives in mESCs. Cumulative distribution plot of the half-lives for mESC-expressed mRNAs[58] binned into equally sized quartiles (Q) of increasing Cap2 stoichiometry. **o**. Long-lived mRNAs exhibit high Cap2 stoichiometry in mESCs. Cumulative distribution plot of the Cap2 stoichiometry for mESC-expressed mRNAs[58] binned into equally sized quartiles (Q) of increasing half-lives. Only the first and fourth quartiles were plotted. **p**, Cap2 methylation is enriched on highly abundant mRNAs in mESCs. Cumulative distribution plot of the expression levels (RPM; reads per million, $\log_2$) for TSN isoforms in mESCs binned into equally sized quartiles (Q) of increasing Cap2 stoichiometry. n = 1 experiment. **r**, Highly Cap2-modified mRNAs exhibit long half-lives in MCF-7 cells. Cumulative distribution plot of the half-lives for MCF-7-expressed mRNAs[54] binned into equally sized quartiles (Q) of increasing Cap2 stoichiometry. **s**, Long-lived mRNAs exhibit high Cap2 stoichiometry in MCF-7 cells. Cumulative distribution plot of the Cap2 stoichiometry for MCF-7-expressed mRNAs[54] binned into equally sized quartiles (Q) of increasing half-lives. Only the first and fourth quartiles were plotted. **t**, Cap2 methylation is enriched on highly abundant mRNAs in MCF-7 cells. Cumulative distribution plot of the expression levels (RPM; reads per million, $\log_2$) for TSN isoforms in MCF-7 cells binned into equally sized quartiles (Q) of increasing Cap2 stoichiometry. n = 1 experiment. (**e-f, k-t**) Each box shows the first quartile, median, and third quartile, whiskers represent 1.5\(\times \) interquartile ranges. Two-sided Wilcoxon signed-rank test; * $p < 0.01$, ** $p < 0.001$, *** $p < 0.0001$, **** $p < 0.00001$.

Source data

## Extended Data Fig. 6 Cap2 methylation does not confer high translation and stability to mRNA.

**a**, Reproducibility of the MRL measurements in *CMTR2* KO HEK293T cells. TSN isoform MRLs derived from two independent polysome-TSS-seq experiments plotted against each other. Pearson's ($r$) and Spearman's ($\rho$). **b**, A loss of Cap2 causes global reduction in translation in HEK293T cells. Polysome profiles of *CMTR2* WT and *CMTR2* KO HEK293T cells. The percent of the RNA signal (A254 nm, absorbance at 254 nm) observed at different positions across the linear (10-50%) sucrose gradient was plotted. n = 1 experiment. **c**, A loss of Cap2 results in the reduced synthesis rate of nascent proteins in HEK293T cells. *CMTR2* WT and *CMTR2* KO HEK293T cells were incubated in the growing media containing low levels of puromycin (0.8 μg $ml^{-1}$) for the indicated time periods to label nascent proteins. The left panel represents the western blot showing levels of puromycin-labeled proteins synthesized in the respective cell lines. The right panel shows the amido black-stained membrane from the left panel to indicate equal protein loading in all lanes. **d**, *CMTR2* KO cells exhibit slower growth rate. A plot showing *CMTR2* WT and *CMTR2* KO cell growth rate over time. The y-axis indicates the absorbance signal at 570 nm that is directly proportional to the number of viable, growing cells. n = 3 biological replicates. **e**, Cap2 loss does not lead to selective change in the translation of highly Cap2-modifed transcripts. Cumulative distribution plot of changes in the ribosome density (MRL/kb) between *CMTR2* KO and *CMTR2* WT HEK293T cells for TSN isoforms binned into equally sized quartiles (Q) of increasing Cap2 stoichiometry. Average of n = 2 biological replicates. **f**, Global mRNA decay rate in *CMTR2* KO cells. The remaining amounts of poly(A)+ RNA isolated from 20 μg total RNA at different time points following transcriptional block by actD were plotted. n = 2 biological replicates. **g**, Reproducibility of the mRNA half-life measurements in *CMTR2* KO HEK293T cells. TSN isoform half-lives derived from two independent actD-TSS-seq experiments plotted against each other. Pearson's ($r$) and Spearman's ($\rho$). **h**, Cap2 loss leads to mild, but selective change in the half-lives of highly Cap2-modifed transcripts. Cumulative distribution plot of changes in the half-lives between *CMTR2* KO and

*CMTR2* WT HEK293T cells for TSN isoforms binned into equally sized quartiles (Q) of increasing Cap2 stoichiometry. Average of n = 2 biological replicates. **i**, Cap2 loss does not lead to selective change in the expression of highly Cap2-modifed transcripts. Cumulative distribution plot of the RNA-seq-determined fold changes in gene expression between *CMTR2* KO and *CMTR2* WT HEK293T cells for genes binned into equally sized quartiles (Q) of increasing Cap2 stoichiometry. n = 4 biological replicates. **j**, CLAM-Cap-qPCR accurately detects differences in Cap2 levels in mRNA. CLAM-Cap-qPCR-determined Cap2 levels were plotted against the expected Cap2 stoichiometry of a synthetic luciferase mRNA standard. The expected Cap2 stoichiometry refers to Cap1- and Cap2-terminated luciferase mRNAs mixed in specific molar ratios. A linear regression line with the Pearson's ($r$). n = 2 technical replicates. (**e, h, i**) Each box shows the first quartile, median, and third quartile, whiskers represent 1.5× interquartile ranges. Two-sided Wilcoxon signed-rank test; * $p < 0.01$, ** $p < 0.001$, *** $p < 0.0001$, **** $p < 0.00001$.

Source data

## Extended Data Fig. 7 Loss of Cap2 causes activation of the innate immune response.

**a**, Cap2 loss causes the upregulation of genes related to the innate immune response and inflammatory pathways. Bar graph shows the normalized enrichment score (NES) of the Reactome pathways for differentially regulated genes in *CMTR2* KO HEK293T cells. Dark grey, upregulated genes. Light grey, downregulated genes. The analysis was conducted using the gene set enrichment analysis (GSEA) method with a false discovery rate (FDR) threshold of 5%. **b-f**, Cap2 depletion causes the upregulation of the interferon-stimulated genes (ISGs). *GAPDH*-normalized expression level for the selected set of ISGs measured in *CMTR2* WT and *CMTR2* KO HEK293T cells by RT-qPCR. n = 3 and n = 5 biological replicates, mean ± s.d. **g**, Prevention of Cap2 formation induces the upregulation of antiviral proteins. Western blots showing the expression levels of the selected antiviral proteins in *CMTR2* WT and *CMTR2* KO HEK293T cells. GAPDH, loading control. **h**, Generation of the *CMTR2* KO and *CMTR2, RIG-I* double KO A549 cell lines. Representative western blot showing

CMTR2 and RIG-I expression in WT, *CMTR2* KO and *CMTR2, RIG-I* double KO A549 cells. GAPDH, loading control. **i**, A loss of Cap2 has no effect on the synthesis rate of nascent proteins in A549 cells. *CMTR2* WT and *CMTR2* KO A549 cells were incubated in the growing media containing low levels of puromycin (1 μg $ml^{-1}$) for 90 min to label nascent proteins. The left panel represents a western blot showing levels of puromycin-labeled proteins synthesized in the respective cell lines. The right panel shows the amido black-stained membrane from the left panel to indicate equal protein loading in all lanes. **j**, CMTR2 loss causes the induction of the innate immune response in A549 cells across different cell clones in a RIG-I-dependent manner. Western blots showing CMTR2 and RIG-I expression levels in multiple knockout cell clones. GAPDH, loading control. Bar plots below show *GAPDH*-normalized expression of *MX1*, *ISG15* and *IFIT1* mRNAs determined using RT-qPCR. RNA samples were extracted from the respective clones at the time of the western blot screens in search for knockout cell clones. n = 1 experiment. *CMTR2* KO clone #1, *CMTR2, RIG-I* double KO clone #3 were selected for all downstream experiments. Note that the magnitude of the ISG induction decreases in the selected clones over several cell passages (Fig. 5c and Extended Data Fig. 7h), indicating A549 cell adaptation to chronic inflammation caused by permanent CMTR2 depletion. **k**, Antiviral protein induction caused by CMTR2 depletion is comparable to interferon (IFN) treatment in HEK293T cells. Representative western blot shows RIG-I and IFITM3 expression in *CMTR2* WT and *CMTR2* KO cells treated with PBS or IFN for 6 h at 750 U $ml^{-1}$. GAPDH, loading control. **l**, Poly(I:C) treatment of *CMTR2* KO cells induces RNase L activation. Representative Bioanalyzer trace of total RNA extracted from *CMTR2* WT and *CMTR2* KO HEK293T cells pretreated with RNase L inhibitor (valoneic acid dilactone, VAL) followed by mock (Lipo) or poly(I:C) transfection for 6 h. rRNA cleavage products appeared only in *CMTR2* KO cells transfected with poly(I:C). rRNA cleavage products disappeared when cells were pretreated with RNase L inhibitor. **m**, *CMTR2* KO HEK293T cells are sensitive to treatment with triphosphorylated hairpin RNA (3p-hpRNA). *GAPDH*-normalized *IP10* transcript levels in *CMTR2* WT and *CMTR2* KO HEK293T cells transfected with 3p-hpRNA for 8 h. n = 4 biological replicates, mean ± s.d. **n**, *CMTR2* KO HEK293T cells are sensitive to viral infection. *GAPDH*-normalized *IP10* transcript levels in *CMTR2* WT and *CMTR2* KO

HEK293T cells 24 h after the infection with the propagation-incompetent VSV replicon. n = 4 biological replicates, mean ± s.d. **o**, *CMTR2* KO A549 cells are sensitive to viral infection. *GAPDH*-normalized *RSAD2* transcript levels in *CMTR2* WT and *CMTR2* KO A549 cells 24 h after the infection with the propagation-incompetent VSV replicon. n = 3 biological replicates, mean ± s.d. **p**, CMTR2 depletion sensitizes cells to SARS-CoV-2 infection. Plots showing the gene rank with respect to the effect of gene knockout (CRISPR z-score) on cell growth upon SARS-CoV-2 infection[59]. Negative CRISPR z-score indicates negative effect of SARS-CoV-2 infection on cell growth, whereas positive score denotes positive effect of SARS-CoV-2 infection on cell growth upon the knockout of each gene.

Source data

## Extended Data Fig. 8 Cap2 methylation inhibits RIG-I binding to capped RNA.

**a**, Equal amounts of biotinylated Cap0, Cap1, and Cap2 double-stranded, dsRNAs were immobilized on streptavidin beads and incubated with HEK293T cell lysates expressing FLAG-tagged RIG-I wild-type (RIG-I WT), RIG-I H830A and RIG-I C829A mutant proteins. Representative western blots show the amount of the respective RIG-I proteins recovered by each capped RNA bait. **b**, Western blot showing RIG-I levels from three independent pulldowns with biotinylated Cap1 and Cap2 dsRNAs. A SYBR Gold-stained nondenaturing 20% TBE gel below shows equal amounts of streptavidin-immobilized dsRNA baits used in each pulldown experiment.

## Extended Data Fig. 9 Cap2 methylation suppresses RIG-I activation and VSV-induced innate immune response.

**a**, Representative western blot showing RIG-I levels in *CMTR2* WT and *CMTR2* KO HEK293T cells transfected with constructs encoding FLAG-tagged GFP (Control - gfp), RIG-I wild-type (RIG-I WT) and RIG-I K858A/K861A mutant (RIG-I mut) proteins. GAPDH, loading control. **b**, Representative western blots showing CMTR2 and RIG-I levels in cells transfected with constructs encoding either FLAG-tagged GFP or RIG-I wild-type proteins, and plasmids expressing NeonGreen (Control - ng),

NeonGreen-tagged CMTR2 wild-type (CMTR2 WT) or CMTR2 W85A (CMTR2 mut) proteins. GAPDH, loading control. **c**, Cap0 RNA transfection results in the induction of the innate immune response. *GAPDH*-normalized *RSAD2* mRNA levels in wild-type A549 cells transfected with transfection reagent only (LyoVec), and equal amounts (1.5 micrograms) of Cap0, Cap1, and Cap2 dsRNA were plotted. Average of n = 2 biological replicates. **d**, VSV RNA efficiently replicates in HEK293T cells. Line plot showing RT-qPCR-measured VSV RNA levels 0, 6 and 24 h of VSV infection at the indicated multiplicity of infection (MOI). *GAPDH*-normalized VSV *N* mRNA levels were plotted. n = 1 experiment. **e**, Correlation plot of the predefined number of the firefly luciferase (FLuc) transcripts and RT-qPCR-derived Ct values. To obtain FLuc mRNA standard curve, a 10× serial dilutions of FLuc mRNA standard were added to the fixed amount of total RNA extracted from HEK293T cells and quantified by RT-qPCR. Pearson's (*r*). n = 2 technical replicates. **f**, Viral RNA accumulates at high levels in VSV-infected cells. Bar plot showing the absolute number of *N*, *P*, and *M* VSV mRNAs per ng total RNA. Absolute number of viral transcripts was determined using the FLuc mRNA standard curve from Extended Data Fig. 9e. The number of endogenous mRNAs in mock-infected cells was determined based on the three independent measurements of oligo(dT)-isolated mRNA from fixed amount of total RNA. The calculations of the absolute mRNA numbers were based on the average size of mRNA in human cells of 2.5 kb. n = 3 biological replicates, mean ± s.d. **g**, A schematic of the Cap2 methylation measurement in VSV mRNAs by CLAM-Cap-qPCR. VSV mRNAs start with $A_mA_{(m)}C$ $m^7G$-proximal sequence. Thus, after the creation of the DNA adapter-ligated cDNA-cap tags, VSV mRNAs Cap2 levels were measured by qPCR using a *N*, *P*, or *M* mRNA-specific reverse primer (Rv-mRNA X, blue arrow) and a forward primer that hybridizes to the DNA adapter and the first C nucleotide of the CAA three-nucleotide cap tag of the Cap2 form of VSV mRNAs (Fw-Cap2, grey arrow). Total abundance of (Cap1 and Cap2) cDNA-cap tags was determined via parallel qPCR using a primer pair comprising a VSV mRNA-specific reverse primer and a primer that only anneals to the DNA adapter and not to any portion of the VSV mRNA cap tags (Fw-total, pink arrow). **h**, CMTR2 overexpression leads to increased Cap2 levels in viral *P* and *M* mRNAs. *CMTR2* KO HEK293T cells expressing Control, and *CMTR2* WT HEK293T cells expressing

Control, CMTR2 WT or CMTR2 mut were infected with propagation-incompetent VSV replicon. Twenty-four h post-infection, RNA was collected, and CLAM-Cap-qPCR was conducted on viral *P* and *M* mRNAs. Stacked bar plot shows the fraction of Cap1- and Cap2-modified VSV *P* and *M* mRNAs. Cap1-modified fraction was inferred from Cap2 measurements as 1-Cap2 fraction. Average of n = 2 biological replicates. **i**, CMTR2 overexpression does not suppress the innate immune response triggered by non-capped RNA ligands. Bar plot showing *IP10* mRNA levels in poly(I:C)- and 3p-hpRNA-stimulated HEK293T cells expressing Control, CMTR2 WT or CMTR2 mut proteins. *GAPDH*-normalized *IP10* mRNA expression levels. Average of n = 2 biological replicates for Control and 3p-hpRNA treatments. n = 4 biological replicates for poly(I:C) treatment, mean ± s.d.

Source data

## Extended Data Fig. 10 Cap1 RNA levels anticorrelate with RIG-I expression.

**a**, RIG-I levels vary between human cell lines. Representative western blot showing RIG-I expression in three human cell lines; HEK293T, A549 and MCF-7 cells. ACTB, loading control. **b**, RIG-I levels vary between mouse organs. Representative western blot showing RIG-I expression in mouse organs. ACTB, loading control. **c**, *Ddx58* mRNA expression anticorrelates with Cap1 levels in mouse organs. Scatter plot showing strong negative correlation between Cap1 levels and *Ddx58* mRNA expression level determined via CapTag-seq and RT-qPCR, respectively. *Ddx58* mRNA expression was normalized to the expression of *Eef2* housekeeping mRNA. n = 2 biological replicates. *Ddx58* mRNA encodes for RIG-I protein. **d**, Schematic of how RIG-I and cap methylation regulate the activation of the innate immune response. In this model, cellular homeostasis is achieved by balancing Cap1 and RIG-I levels. Regulation of Cap2 methylation via CMTR2 expression and mRNA ageing contributes to the establishment of this balance, allowing cell homeostasis. Low levels of Cap1 can induce RIG-I activation only if RIG-I levels are high. However, when Cap1 levels are elevated, even small amounts of RIG-I are sufficient to mediate Cap1 effects and lead to inflammation. Notably, Cap1 levels can increase with

CMTR2 depletion or when large amounts of new viral RNA are synthesized, leading to activation of RIG-I. Additionally, situations associated with increased RIG-I expression, such as viral infection and autoimmune diseases, may further sensitize cells to Cap1 RNAs of the viral or host origins.

Source data

## Supplementary information

### Supplementary Figure 1

Uncropped images

### Reporting Summary

### Supplementary Table 1

Processed sequencing data

### Supplementary Table 2

Statistical tests and p-values

### Supplementary Table 3

List of oligonucleotides

## Source data

### Source Data Fig. 1

### Source Data Fig. 2

### Source Data Fig. 3

**Source Data Fig. 4**

**Source Data Fig. 5**

**Source Data Extended Data Fig. 1**

**Source Data Extended Data Fig. 2**

**Source Data Extended Data Fig. 3**

**Source Data Extended Data Fig. 4**

**Source Data Extended Data Fig. 5**

**Source Data Extended Data Fig. 6**

**Source Data Extended Data Fig. 7**

**Source Data Extended Data Fig. 9**

**Source Data Extended Data Fig. 10**

## Rights and permissions

Springer Nature or its licensor (e.g. a society or other partner) holds exclusive rights to this article under a publishing agreement with the author(s) or other rightsholder(s); author self-archiving of the accepted manuscript version of this article is solely governed by the terms of such publishing agreement and applicable law.

Reprints and Permissions

## About this article

## Cite this article

Despic, V., Jaffrey, S.R. mRNA ageing shapes the Cap2 methylome in mammalian mRNA. *Nature* **614**, 358–366 (2023). https://doi.org/10.1038/s41586-022-05668-z

- Received: 10 February 2022
- Accepted: 16 December 2022
- Published: 01 February 2023
- Issue Date: 09 February 2023
- DOI: https://doi.org/10.1038/s41586-022-05668-z

## Share this article

Anyone you share the following link with will be able to read this content:

Get shareable link

Sorry, a shareable link is not currently available for this article.

Copy to clipboard

Provided by the Springer Nature SharedIt content-sharing initiative

---

This article was downloaded by **calibre** from https://www.nature.com/articles/s41586-022-05668-z

# Amendments & Corrections

- **Author Correction: Heterochromatin silencing of p53 target genes by a small viral protein** [24 Jan 2023]
  -
- **Author Correction: Layered subsurface in Utopia Basin of Mars revealed by Zhurong rover radar** [24 Jan 2023]
  -

- Author Correction
- Published: 24 January 2023

# Author Correction: Heterochromatin silencing of p53 target genes by a small viral protein

- Conrado Soria,
- Fanny E. Estermann,
- Kristen C. Espantman &
- …
- Clodagh C. O’Shea

Show authors

*Nature* **volume 614**, page E29 (2023)

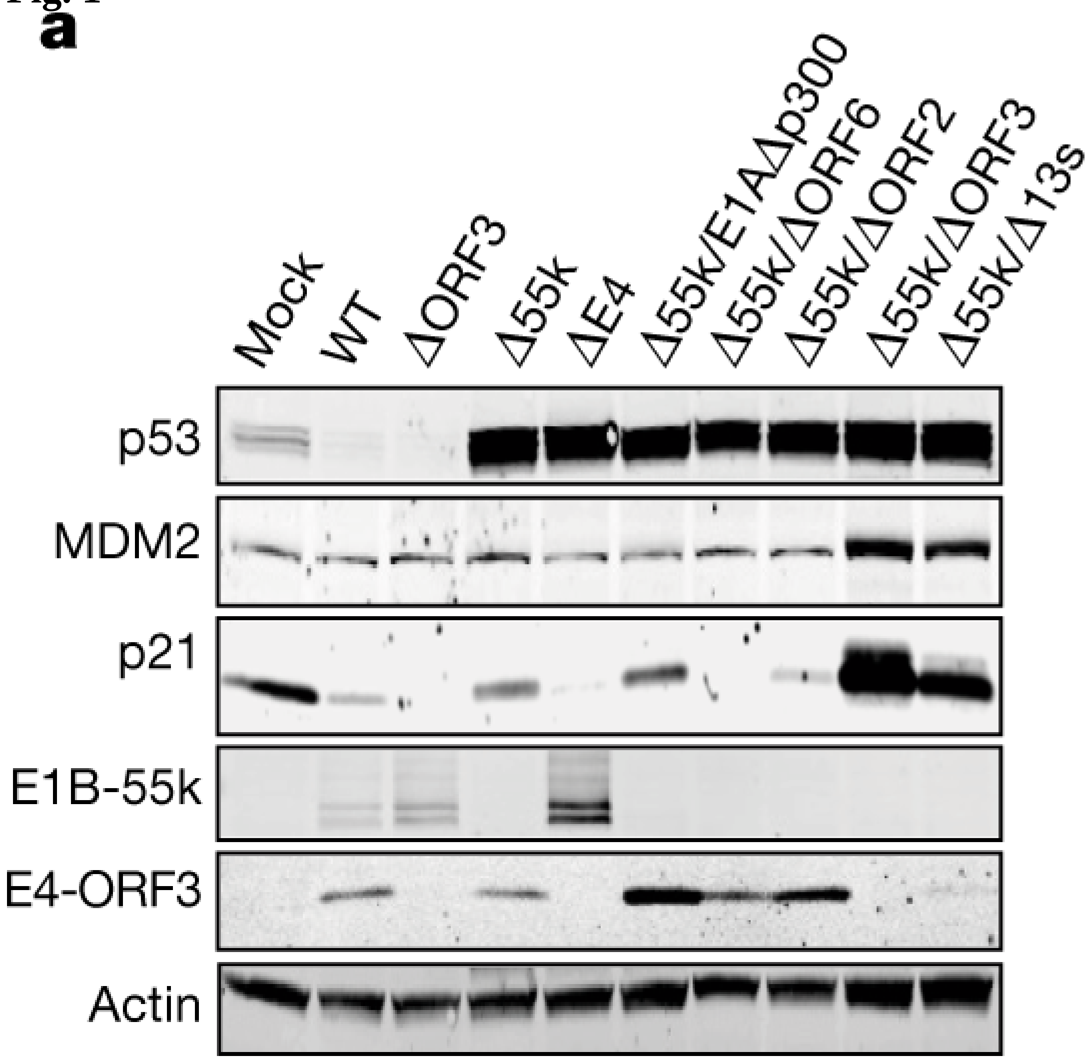
- 858 Accesses
- 10 Altmetric
- Metrics details

The Original Article was published on 26 August 2010

Correction to: *Nature* https://doi.org/10.1038/nature09307 Published online 26 August 2010

In the version of this article initially published, due to a cropping error that occurred upon rescanning and replacing the actin blot in Fig. 2a in response to a reviewer’s request, the actin lane for an additional lysate that had been run at the end of the gel, but that was not part of the figure, was inadvertently included. This was an editing error and does not affect any results or conclusions in the article. The actin panel in Fig. 2a has now been cropped to remove the additional lane and is shown as Fig. 1, below. The original article has not been corrected online

**Fig. 1**




Corrected Fig. 2a.

# Author information

Author notes

1. These authors contributed equally: Conrado Soria, Fanny E. Estermann

## Authors and Affiliations

1. Molecular and Cell Biology Laboratory, Salk Institute for Biological Studies, 10010 N. Torrey Pines Road, La Jolla, California, USA

   Conrado Soria, Fanny E. Estermann, Kristen C. Espantman & Clodagh C. O'Shea

## Corresponding author

Correspondence to Clodagh C. O'Shea.

# Rights and permissions

Reprints and Permissions

# About this article

## Cite this article

Soria, C., Estermann, F.E., Espantman, K.C. *et al.* Author Correction: Heterochromatin silencing of p53 target genes by a small viral protein. *Nature* **614**, E29 (2023). https://doi.org/10.1038/s41586-022-05494-3

- Published: 24 January 2023
- Issue Date: 09 February 2023
- DOI: https://doi.org/10.1038/s41586-022-05494-3

## Share this article

Anyone you share the following link with will be able to read this content:

Get shareable link

Sorry, a shareable link is not currently available for this article.

Copy to clipboard

Provided by the Springer Nature SharedIt content-sharing initiative

---

This article was downloaded by **calibre** from https://www.nature.com/articles/s41586-022-05494-3

- Author Correction
- Open Access
- Published: 24 January 2023

# Author Correction: Layered subsurface in Utopia Basin of Mars revealed by Zhurong rover radar


- Chao Li,
- Yikang Zheng,
- Xin Wang,
- Jinhai Zhang,
- Yibo Wang,
- Ling Chen ,
- Lei Zhang,
- Pan Zhao,
- Yike Liu,
- Wenmin Lv,
- Yang Liu,
- Xu Zhao,
- Jinlai Hao,
- Weijia Sun,
- Xiaofeng Liu,
- Bojun Jia,
- Juan Li,
- Haiqiang Lan,
- Wenzhe Fa,
- Yongxin Pan &
- …
- Fuyuan Wu


Show authors

*Nature* **volume 614**, page E30 (2023)

- 358 Accesses
- 1 Altmetric
- Metrics details

The Original Article was published on 26 September 2022

Correction to: *Nature* https://doi.org/10.1038/s41586-022-05147-5
Published online 26 September 2022

In the version of this article initially published, in Fig. 1a, the longitude of the Viking-2 landing site was wrongly shown at 225.7E, and has now been corrected to appear at 225.7W in the HTML and PDF versions of the article.

# Author information

Author notes

1. These authors contributed equally: Chao Li, Yikang Zheng, Xin Wang, Jinhai Zhang

## Authors and Affiliations

1. Key Laboratory of Earth and Planetary Physics, Institute of Geology and Geophysics, Chinese Academy of Sciences, Beijing, China

   Chao Li, Xin Wang, Jinhai Zhang, Lei Zhang, Wenmin Lv, Xu Zhao, Jinlai Hao, Weijia Sun, Juan Li & Yongxin Pan

2. Key Laboratory of Petroleum Resource Research, Institute of Geology and Geophysics, Chinese Academy of Sciences, Beijing, China

Yikang Zheng, Yibo Wang & Yike Liu

3. College of Earth and Planetary Sciences, University of Chinese Academy of Sciences, Beijing, China

   Yibo Wang, Ling Chen, Juan Li, Yongxin Pan & Fuyuan Wu

4. State Key Laboratory of Lithospheric Evolution, Institute of Geology and Geophysics, Chinese Academy of Sciences, Beijing, China

   Ling Chen, Pan Zhao, Haiqiang Lan & Fuyuan Wu

5. State Key Laboratory of Space Weather, National Space Science Center, Chinese Academy of Sciences, Beijing, China

   Yang Liu

6. Center for Excellence in Comparative Planetology, Chinese Academy of Sciences, Hefei, China

   Yang Liu

7. Institute of Remote Sensing and Geographical Information System, School of Earth and Space Sciences, Peking University, Beijing, China

   Xiaofeng Liu, Bojun Jia & Wenzhe Fa

### Corresponding author

Correspondence to Ling Chen.

## Rights and permissions

**Open Access** This article is licensed under a Creative Commons Attribution 4.0 International License, which permits use, sharing, adaptation, distribution and reproduction in any medium or format, as long as you give appropriate credit to the original author(s) and the source, provide a link to the Creative Commons license, and indicate if changes

were made. The images or other third party material in this article are included in the article's Creative Commons license, unless indicated otherwise in a credit line to the material. If material is not included in the article's Creative Commons license and your intended use is not permitted by statutory regulation or exceeds the permitted use, you will need to obtain permission directly from the copyright holder. To view a copy of this license, visit http://creativecommons.org/licenses/by/4.0/.

Reprints and Permissions

# About this article

## Cite this article

Li, C., Zheng, Y., Wang, X. *et al.* Author Correction: Layered subsurface in Utopia Basin of Mars revealed by Zhurong rover radar. *Nature* **614**, E30 (2023). https://doi.org/10.1038/s41586-023-05734-0

- Published: 24 January 2023
- Issue Date: 09 February 2023
- DOI: https://doi.org/10.1038/s41586-023-05734-0

## Share this article

Anyone you share the following link with will be able to read this content:

Get shareable link

Sorry, a shareable link is not currently available for this article.

Copy to clipboard

Provided by the Springer Nature SharedIt content-sharing initiative

This article was downloaded by **calibre** from https://www.nature.com/articles/s41586-023-05734-0